Optical Remote Sensing

Science and Technology

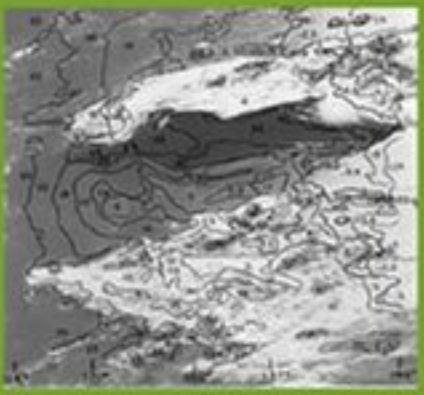

Walter G. Egan

Optical Remote Sensing

Science and Technology

Walter G. Egan
York College
City University of New York
Queens, New York, U.S.A.

MARCEL DEKKER, INC. NEW YORK • BASEL

Library of Congress Cataloging-in-Publication Data
A catalog record for this book is available from the Library of Congress.

ISBN: 0-8247-4131-5

This book is printed on acid-free paper.

Headquarters
Marcel Dekker, Inc., 270 Madison Avenue, New York, NY 10016, U.S.A.
tel: 212-696-9000; fax: 212-685-4540

Distribution and Customer Service
Marcel Dekker, Inc., Cimarron Road, Monticello, New York 12701, U.S.A.
tel: 800-228-1160; fax: 845-796-1772

Eastern Hemisphere Distribution
Marcel Dekker AG, Hutgasse 4, Postfach 812, CH-4001 Basel, Switzerland
tel: 41-61-260-6300; fax: 41-61-260-6333

World Wide Web
http://www.dekker.com

The publisher offers discounts on this book when ordered in bulk quantities. For more information, write to Special Sales/Professional Marketing at the headquarters address above.

Current printing (last digit):

10 9 8 7 6 5 4 3 2 1

PRINTED IN THE UNITED STATES OF AMERICA

OPTICAL ENGINEERING

Founding Editor

Brian J. Thompson

University of Rochester
Rochester, New York

1. Electron and Ion Microscopy and Microanalysis: Principles and Applications, *Lawrence E. Murr*
2. Acousto-Optic Signal Processing: Theory and Implementation, *edited by Norman J. Berg and John N. Lee*
3. Electro-Optic and Acousto-Optic Scanning and Deflection, *Milton Gottlieb, Clive L. M. Ireland, and John Martin Ley*
4. Single-Mode Fiber Optics: Principles and Applications, *Luc B. Jeunhomme*
5. Pulse Code Formats for Fiber Optical Data Communication: Basic Principles and Applications, *David J. Morris*
6. Optical Materials: An Introduction to Selection and Application, *Solomon Musikant*
7. Infrared Methods for Gaseous Measurements: Theory and Practice, *edited by Joda Wormhoudt*
8. Laser Beam Scanning: Opto-Mechanical Devices, Systems, and Data Storage Optics, *edited by Gerald F. Marshall*
9. Opto-Mechanical Systems Design, *Paul R. Yoder, Jr.*
10. Optical Fiber Splices and Connectors: Theory and Methods, *Calvin M. Miller with Stephen C. Mettler and Ian A. White*
11. Laser Spectroscopy and Its Applications, *edited by Leon J. Radziemski, Richard W. Solarz, and Jeffrey A. Paisner*
12. Infrared Optoelectronics: Devices and Applications, *William Nunley and J. Scott Bechtel*
13. Integrated Optical Circuits and Components: Design and Applications, *edited by Lynn D. Hutcheson*
14. Handbook of Molecular Lasers, *edited by Peter K. Cheo*
15. Handbook of Optical Fibers and Cables, *Hiroshi Murata*
16. Acousto-Optics, *Adrian Korpel*
17. Procedures in Applied Optics, *John Strong*
18. Handbook of Solid-State Lasers, *edited by Peter K. Cheo*
19. Optical Computing: Digital and Symbolic, *edited by Raymond Arrathoon*
20. Laser Applications in Physical Chemistry, *edited by D. K. Evans*
21. Laser-Induced Plasmas and Applications, *edited by Leon J. Radziemski and David A. Cremers*

22. Infrared Technology Fundamentals, *Irving J. Spiro and Monroe Schlessinger*
23. Single-Mode Fiber Optics: Principles and Applications, Second Edition, Revised and Expanded, *Luc B. Jeunhomme*
24. Image Analysis Applications, *edited by Rangachar Kasturi and Mohan M. Trivedi*
25. Photoconductivity: Art, Science, and Technology, *N. V. Joshi*
26. Principles of Optical Circuit Engineering, *Mark A. Mentzer*
27. Lens Design, *Milton Laikin*
28. Optical Components, Systems, and Measurement Techniques, *Rajpal S. Sirohi and M. P. Kothiyal*
29. Electron and Ion Microscopy and Microanalysis: Principles and Applications, Second Edition, Revised and Expanded, *Lawrence E. Murr*
30. Handbook of Infrared Optical Materials, *edited by Paul Klocek*
31. Optical Scanning, *edited by Gerald F. Marshall*
32. Polymers for Lightwave and Integrated Optics: Technology and Applications, *edited by Lawrence A. Hornak*
33. Electro-Optical Displays, *edited by Mohammad A. Karim*
34. Mathematical Morphology in Image Processing, *edited by Edward R. Dougherty*
35. Opto-Mechanical Systems Design: Second Edition, Revised and Expanded, *Paul R. Yoder, Jr.*
36. Polarized Light: Fundamentals and Applications, *Edward Collett*
37. Rare Earth Doped Fiber Lasers and Amplifiers, *edited by Michel J. F. Digonnet*
38. Speckle Metrology, *edited by Rajpal S. Sirohi*
39. Organic Photoreceptors for Imaging Systems, *Paul M. Borsenberger and David S. Weiss*
40. Photonic Switching and Interconnects, *edited by Abdellatif Marrakchi*
41. Design and Fabrication of Acousto-Optic Devices, *edited by Akis P. Goutzoulis and Dennis R. Pape*
42. Digital Image Processing Methods, *edited by Edward R. Dougherty*
43. Visual Science and Engineering: Models and Applications, *edited by D. H. Kelly*
44. Handbook of Lens Design, *Daniel Malacara and Zacarias Malacara*
45. Photonic Devices and Systems, *edited by Robert G. Hunsperger*
46. Infrared Technology Fundamentals: Second Edition, Revised and Expanded, *edited by Monroe Schlessinger*
47. Spatial Light Modulator Technology: Materials, Devices, and Applications, *edited by Uzi Efron*
48. Lens Design: Second Edition, Revised and Expanded, *Milton Laikin*
49. Thin Films for Optical Systems, *edited by François R. Flory*
50. Tunable Laser Applications, *edited by F. J. Duarte*
51. Acousto-Optic Signal Processing: Theory and Implementation, Second Edition, *edited by Norman J. Berg and John M. Pellegrino*
52. Handbook of Nonlinear Optics, *Richard L. Sutherland*
53. Handbook of Optical Fibers and Cables: Second Edition, *Hiroshi Murata*

54. Optical Storage and Retrieval: Memory, Neural Networks, and Fractals, *edited by Francis T. S. Yu and Suganda Jutamulia*
55. Devices for Optoelectronics, *Wallace B. Leigh*
56. Practical Design and Production of Optical Thin Films, *Ronald R. Willey*
57. Acousto-Optics: Second Edition, *Adrian Korpel*
58. Diffraction Gratings and Applications, *Erwin G. Loewen and Evgeny Popov*
59. Organic Photoreceptors for Xerography, *Paul M. Borsenberger and David S. Weiss*
60. Characterization Techniques and Tabulations for Organic Nonlinear Optical Materials, *edited by Mark Kuzyk and Carl Dirk*
61. Interferogram Analysis for Optical Testing, *Daniel Malacara, Manuel Servín, and Zacarias Malacara*
62. Computational Modeling of Vision: The Role of Combination, *William R. Uttal, Ramakrishna Kakarala, Sriram Dayanand, Thomas Shepherd, Jagadeesh Kalki, Charles F. Lunskis, Jr., and Ning Liu*
63. Microoptics Technology: Fabrication and Applications of Lens Arrays and Devices, *Nicholas F. Borrelli*
64. Visual Information Representation, Communication, and Image Processing, *Chang Wen Chen and Ya-Qin Zhang*
65. Optical Methods of Measurement: Wholefield Techniques, *Rajpal S. Sirohi and Fook Siong Chau*
66. Integrated Optical Circuits and Components: Design and Applications, *edited by Edmond J. Murphy*
67. Adaptive Optics Engineering Handbook, *edited by Robert K. Tyson*
68. Entropy and Information Optics, *Francis T. S. Yu*
69. Computational Methods for Electromagnetic and Optical Systems, *John M. Jarem and Partha P. Banerjee*
70. Laser Beam Shaping: Theory and Techniques, *edited by Fred M. Dickey and Scott C. Holswade*
71. Rare-Earth-Doped Fiber Lasers and Amplifiers: Second Edition, Revised and Expanded, *edited by Michel J. F. Digonnet*
72. Lens Design: Third Edition, Revised and Expanded, *Milton Laikin*
73. Handbook of Optical Engineering, *edited by Daniel Malacara and Brian J. Thompson*
74. Handbook of Imaging Materials, *edited by Arthur S. Diamond and David S. Weiss*
75. Handbook of Image Quality: Characterization and Prediction, *Brian W. Keelan*
76. Fiber Optic Sensors, *edited by Francis T. S. Yu and Shizhuo Yin*
77. Optical Switching/Networking and Computing for Multimedia Systems, *edited by Mohsen Guizani and Abdella Battou*
78. Image Recognition and Classification: Algorithms, Systems, and Applications, *edited by Bahram Javidi*
79. Practical Design and Production of Optical Thin Films: Second Edition, Revised and Expanded, *Ronald R. Willey*

80. Ultrafast Lasers: Technology and Applications, *edited by Martin E. Fermann, Almantas Galvanauskas, and Gregg Sucha*
81. Light Propagation in Periodic Media: Differential Theory and Design, *Michel Nevière and Evgeny Popov*
82. Handbook of Nonlinear Optics: Second Edition, Revised and Expanded, *Richard L. Sutherland*
83. Polarized Light: Second Edition, Revised and Expanded, *Dennis Goldstein*
84. Optical Remote Sensing: Science and Technology, *Walter G. Egan*

Additional Volumes in Preparation

Nonlinear Optics: Theory, Numerical Modeling, and Applications, *Partha P. Banerjee*

Preface

In recent years, much has transpired in the field of remote sensing and, in particular, polarization. Polarization is an outgrowth of multiple, highly accurate photometric measurements. Plane polarization is the difference between precision photometric measurements in two mutually perpendicular directions. Circular polarization is used as a refinement in the complete description of the optical properties of surfaces and of the atmosphere in terms of Stokes parameters.

This book explores advanced concepts in the mathematical representation of polarization, descriptors, and various optical elements used in the analysis of polarization in multiple applications—highlighting tried and proven techniques to enhance aircraft and satellite technology and determine the photometric and polarimetric properties of atmosphere, ground surfaces, and inner and outer space. Experiments such as the NASA Lear Airborne Observatory and the Mariner explorers are presented as a basis for many of the recent advances in remote sensing and polarization.

Designed for use in remote sensing courses and as a reference text, the level of treatment is appropriate for undergraduates, but advanced high school students may investigate the material with great advantage. The book also serves as a reference for graduate-level college students and researchers.

The book will be useful to students and workers in aircraft and satellite remote sensing in geology and atmospheric sciences, the military, natural resources, agriculture, forestry, ranching, urban resources, hydrology, pollution (marine and atmospheric), the environment, limnology, seismology, and oceanography.

I am especially grateful to the following scientists and engineers who helped with the programs described in the book: Alexandre Salman, Michael Duggin, Theodore Hilgeman, Miriam Sidran, Jerry Krassner, Charles Harvey, Victor Whitehead, Steve Israel, Robert Erath, Kenneth Keen, Arthur Speidel (deceased), Herbert Hallock, Joe Grusaskas, Elizabeth Larson, Edward Hindman, and Austin Hogan. I would like to thank the helicopter and aircraft pilots, ship captain George Tweedy, shop technicians Chris Clamser and John Augustine, and all the research laboratory technicians. I am especially grateful to Shaneeza Kahn for her invaluable proofreading and Joan Egan, my wife, for her continual support. I would also like to thank the staff at Marcel Dekker, Inc., for their editorial and production assistance.

Walter G. Egan

Contents

12. Planetary Remote Sensing Atmospheres

13. Effect of Aerosols on Optical Remotely Sensed Data

14. Comparison Between Infrared Martian Disk Spectra and Optical Properties of Terrestrial Analogs

15. The Interstellar Medium: Ultraviolet Complex Index of Refraction of Several Candidate Materials

16. Anomalous Refractive Index of Submicrometer-Sized Particulates

17. Ultraviolet Spectra of Organic Molecules and the Interstellar Medium

18. Complex Index of Refraction of Bulk Solid Carbon Dioxide

19. Star Environments

20. Optical Properties of Continental Haze and Cumulus and Orographic Clouds Based on Space Shuttle Polarimetric Observations

21. Volumetric Scattering and Absorption by Aerosols: Parametric Sensitivity in Mie Modeling and Comparisons to Observations

22. Radiative Transfer Properties of the Sahara Region

23. Meteorological Analysis of Chemical Exchange Events in the Arctic Basin

24. Optical Enhancement of Aircraft Detection Using Polarization

25. Detection of Vehicles and Personnel Using Polarization

26. Optical Remote Sensing of the Sea: A Caribbean Example

1

Polarization and Remote Sensing

I. INTRODUCTION

Photometry has been used as a technique for optical sensing ever since humans first looked at the horizon. Interpretation of photometric data is of value in obtaining geological or geophysical information from aircraft, earth meteorological or planetary satellites, or planetary landing craft. However, extensive spectral reflectance measurements are necessary to reduce ambiguity in data interpretation. Vast amounts of photometric data are readily obtained from observations of planetary surfaces. Such measurements were made by Krinov [1] on various soils, rocks, and sands and some vegetation. Additional measurements were made by Bauer and Dutton [2] on farmlands and wooded hills of Wisconsin and by Romanova [3] where sand deposits. The data may ultimately be presented graphically or as a picture.

However, reflected light in itself is a function of the angle of incidence i of radiation upon the surface being investigated as well as the viewing angle ε (see Fig. 1). Also, the reflected light may be depicted in terms of a phase angle α and measured in the "plane of vision" containing the lines of incidence and emergence (e.g., the source, planetary surface, and sensor; see Fig. 1). The effect of incident angle has been shown by Kondratiev and Manolova [4], and the effect of viewing angle by Ashburn and Weldon [5] and Coulson [6]. In lunar surface simulation, Orlova [7], Hapke and Van Horn [8], and Halajian and Spagnolo [9] sought to depict the directional reflectance of the lunar surface.

The data are frequently ambiguous, but the ambiguity may be reduced or the data rendered unique by the use of polarimetry. Polarization informa-

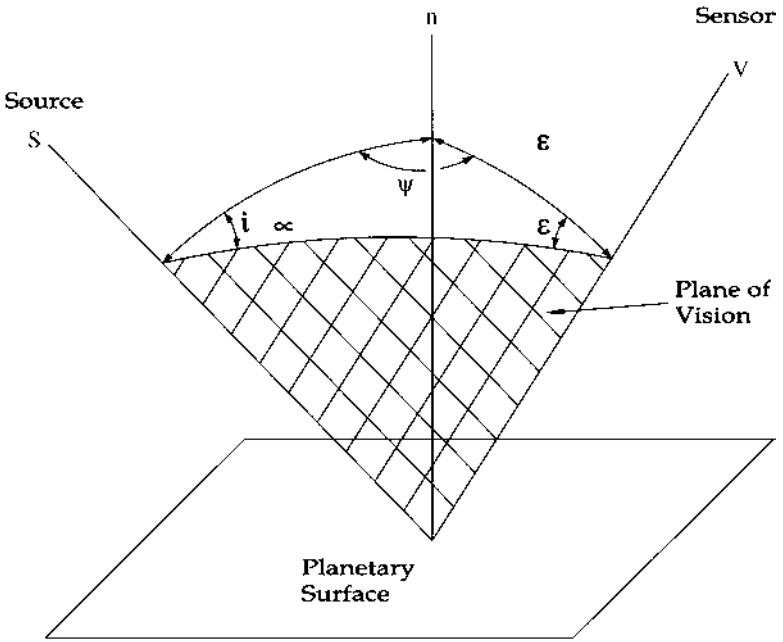

FIGURE 1 Geometrical definitions.

tion already exists in the sensor's photometric data and can usually be obtained by a simple modification of the sensor's optical path for polarimetry during data acquisition.

Polarimetry too is not a newcomer, having been used by Lyot [10], Dollfus [11,12], Gehrels et al. [13], and Coffeen [14] for lunar analysis and simulation. Coulson [6] and Ashburn and Weldon [5] studied the polarimetric properties of a desert surface. Further work was done on sands, loam, and grass by Coulson et al. [15] and Coulson [16]. Also, Egan and Hallock [17] investigated the polarimetric properties of various minerals and some vegetation, and Egan [18] investigated simulated lunar and planetary surface materials.

The effect of the atmosphere through which the polarimetric and photometric observations are made must not be neglected. This effect can be photometric (affecting the intensity or spectral distribution of the illuminating light) or polarimetric. The intensity effect was considered by Gordon and Church [19] and Coulson and coworkers, [15,16], and the specular effect by Henderson and Hodgkiss [20]. Atmospheric polarization was also considered by Coulson and coworkers [15,16], Lyot [10], Dollfus [11,12], and Egan and Foreman [21].

Because of all the factors involved, the interpretation of high spectral resolution photometry or polarimetry from surfaces beneath an atmosphere is complicated, but it is not beyond the realm of analysis. In other words, spectral photometry and polarimetry are a function of the surface, the angles of illumination and viewing, and the effect of the atmosphere. The factors involved may be readily separated by sequential optical measurements, as from a satellite, and by subsequent analysis in terms of "ground truth" data obtained by previous observations and measurements. For unknown planetary surfaces, the interpretation is dependent upon terrestrial simulation until the first in situ verifying measurements are made.

II. MISSION PLANNING CONSTRAINTS

On earth or in aircraft, scientific instruments such as a polarimeter or photometer are required to perform under rather limited ranges of maneuver loads or extreme environments and with the active participation of people. In unmanned satellites and planetary flybys or landers, the scientific equipment is exposed to a more severe environment. The facts that a high vacuum generally exists and that somewhat greater accelerations accompany launching can complicate the design of rotating components and electronics. For planetary landers, instrumentation is further subjected to the high heating rates of atmospheric entry as well as landing shock loads.

The following typical factors and their combinations can make otherwise conventional earth-based laboratory measurement techniques functionally unsuitable for planetary exploration from unmanned spacecraft:

- Thermal sterilization processes to minimize planetary biological contamination in the case of capture or landing
- Extended soaking in the interplanetary space environment (radiation and hypervelocity particle hazard, outgassing, etc.)
- Limited payload capability (e.g., requirement for very compact, lightweight, low-power-consumption equipment)
- Exposure to a low-density ionosphere or atmosphere (e.g., possibility of electrical breakdown and chemically reactive gas combinations)
- Instrument alignment requirements and tracking accuracy relative to position in space and planetary surface features
- Hypersonic flight environment (e.g., high thermal load, plasma, large Doppler shifts, flight attitude variations caused by deceleration through the planetary atmosphere)
- The passive role of humans in the system

The unique situation presented by a mission profile and the appreciation of the tremendous financial investment, not only in the exploratory program

as a whole but in each launching, signals the need to exploit our most advanced technology for exploration of the planets. There is an underlying urgency to create a highly integrated payload–vehicle system, uncompromising in performance and reliability and sympathetic, but objectively unyielding, to the provincial viewpoint of any one single discipline.

A typical avenue of scientific instrumentation payload optimization, within the mission constraints of an exploratory spacecraft, is that of shared components or modules. This is especially attractive when equipment is passive during interplanetary travel but must be functional in the proximity of the planet (e.g., a photometric-polarimetric analyzer). Some of the most likely areas of potential benefit from this principle are the power supply and power conditioning, telemetry, and physical support. However, measures for equipment sharing and vehicle compatibility must preclude such mutual interference as electric or magnetic fields, physical actuators, and chemical contamination.

Form factors are especially important for instruments included on landers. To fit within the launch vehicle's physical envelope and power capability, the entire spacecraft dimensions and weight must meet one group of restrictions. For successful atmospheric entry, a lander mass and physical dimensions must meet still another restrictive condition. Within these boundaries, the scientific payload must share space with vital engineering equipment to ensure the proper carrying out of the lander's mission objectives. The shape of each experimental apparatus must make optimum use of the final available space, must not impose excessive internal heat load on itself or adjacent components, must be accessible for preflight check-out and servicing, and must not compromise the reliability of the power supply or data processing and transmitting equipment, in either normal or unusual operating conditions.

Against this formidable background of unmanned spacecraft design specifications, a scientific measurement technique must remain attractive. The prospects for photometry-polarimetry, in particular, under such constraints are very favorable because of the relative simplicity of the system and the ready availability of space-qualified building blocks for its necessary components. The sun is the usual source of illumination of the planetary surface, although artificial illumination is possible, for example, with a laser. The planetary surface or the planet's atmosphere provides the reflecting medium that alters the intensity as a function of phase and viewing angles of the incident light. Phase and viewing angle referencing is given primarily by the spacecraft trajectory and attitude, although some variability, such as retractable and rotating booms, can be provided in the spacecraft.

A vital instrumental element is the polarizer that enables reflected light to be measured by photoelectric detectors along two mutually perpendicular

planes. A color filter element can also be used in conjunction with the polarizer to obtain spectral discrimination.

Perhaps the most vulnerable component of this relatively simple system is the photoelectric detector. However, sufficient development has been conducted, in conjunction with space programs like the Orbiting Astronomical Observatory (OAO), to ensure the availability of specialized detectors that are reliable, predictable, and even capable of being remotely checked for calibration before and after an active measurement period.

Having considered some of the design constraints and requirements for the equipment readiness of a photometer-polarimeter for planetary surface exploration, it is proper to examine the various factors that could influence interpretation of photometric-polarimetric measurements.

III. INTERPRETATION FACTORS

A. Minerals

The effect of surface minerals and associated structure on the polarimetric and photometric curves may be seen by comparing Figs. 2–7 (from Egan and Hallock [17]). Ilmenite (curves of Figs. 2 and 3) is a blue-gray-black opaque, hexagonally crystalline mineral [22]. The sample consisted of 1–10 cm chunks

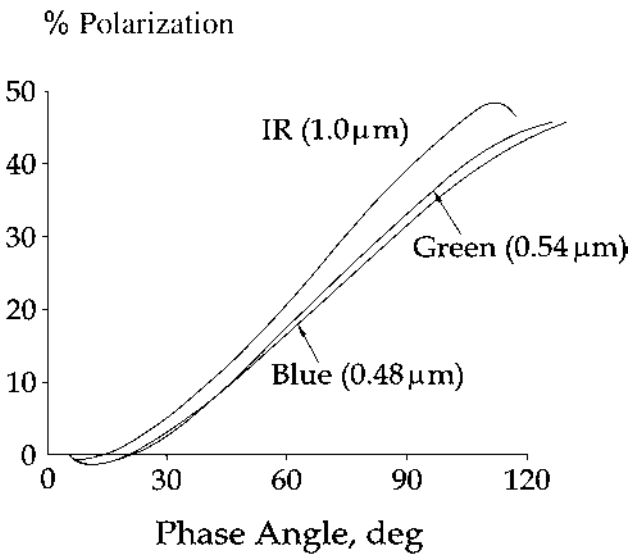

FIGURE 2 Polarization curves of ilmenite ($FeTiO_3$) from New York State. $\varepsilon = 60°$. (From Ref. 17.)

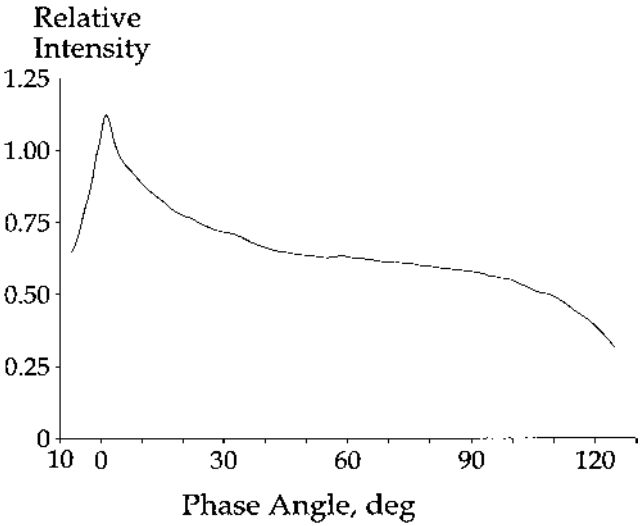

FIGURE 3 Photometric curve of ilmenite. $\varepsilon = 60^\circ$ at 0.54 μm. (From Ref. 17.)

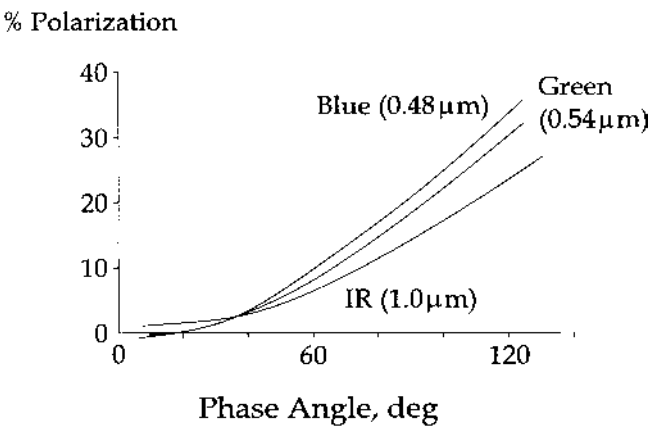

FIGURE 4 Polarization curves of niccolite (NiAs) from Cobalt, Ontario, Canada. $\varepsilon = 60^\circ$. (From Ref. 17.)

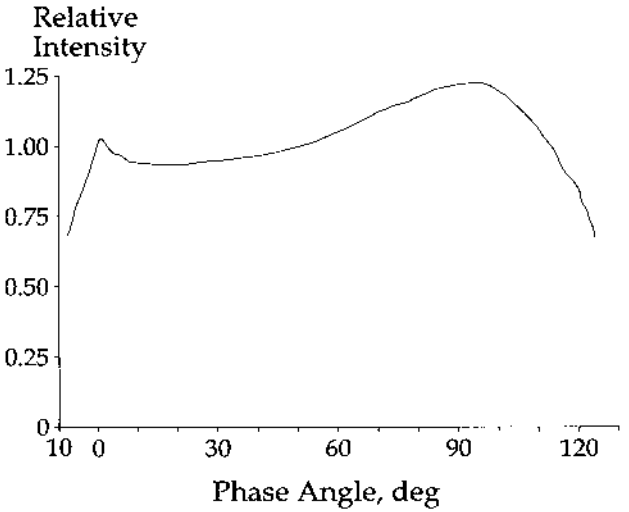

FIGURE 5 Photometric curve of niccolite. $\varepsilon = 60^\circ$ at 0.54 μm. (From Ref. 17.)

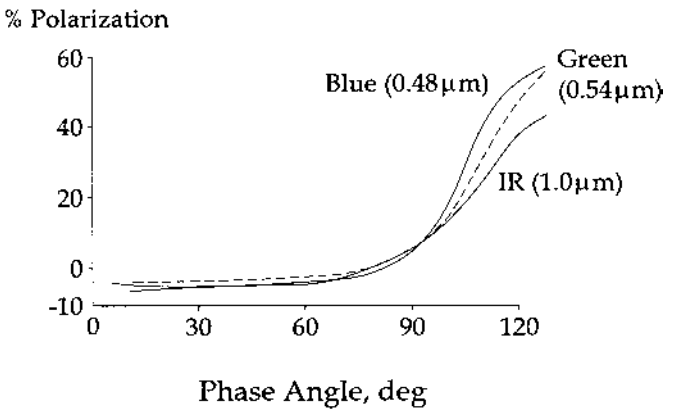

FIGURE 6 Polarization curves of rose quartz (SiO_2) from Maine. $\varepsilon = 60^\circ$. (From Ref. 17.)

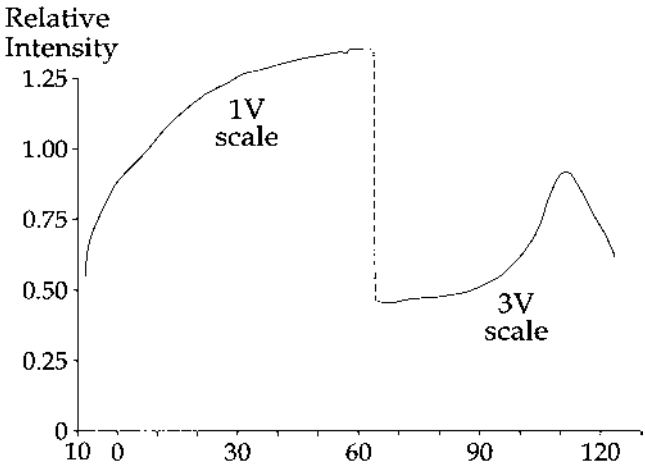

FIGURE 7 Photometric curves of rose quartz. $\varepsilon = 60°$ at 0.54 μm. (From Ref. 17.)

of ore (from New York State) unmixed with foreign matter. The infrared polarization is highest (Fig. 2) and the blue the lowest for phase angles greater than 60°. The photometry (Fig. 3) indicates a fairly diffusing surface for the ore because of the lack of a specular photometric peak at a phase angle equal to twice the viewing angle. A niccolite sample (from Cobalt, Ontario, Canada), consisting of chunks 1–5 cm in average diameter, is largely composed of niccolite (NiAs) with traces of cobaltite (CoAsS) and calcite ($CaCO_3$). Niccolite is pale copper red and has a hexagonal crystal lattice [22]. The polarimetric curves (Fig. 4) do not reach a peak and have an inverted color order, with the highest polarization in the blue and the lowest in the infrared. Photometrically, however, the sample produces a peak at about 100° (Fig. 5) and less backscatter at 0° than the ilmenite.

A sample 10 cm block of rose quartz (low quartz) with a hexagonal crystal lattice, being translucent and birefringent, produced polarization curves that remained slightly negative up to about a 70° phase angle, where they rose steeply (Fig. 6). The polarization in blue light was higher than that in infrared at a phase angle of about 110°. Photometrically (Fig. 7), the quartz produced a specular photometric peak near 120° phase angle and negligible backscatter at 0°. A small amount of titanium, as an impurity, appears to cause the rose color.

Surface structure has been found to affect polarimetric curves (see the following), and the curves representing effects of mineral composition could be expected to be affected somewhat by surface structure. Also, contaminants, such as those in the niccolite sample, can affect the polarimetry.

The photometry has been presented only in green light, because it is largely unaffected by the observational light wavelength [9].

B. Particle Sizes and Combinations

Although implicit in the investigations of Dollfus and others, the explicit effect of particle size on the polarimetric curves was shown by Egan [18] for a sample of Haleakala (Hawaii) volcanic ash. Representative curves are shown in Figs. 8 and 9 for a particle size ranging from 6.35 mm to below 1 μm. The investigation was directed toward lunar surface simulation, and hence comparison curves for a mare (Crisium) and a highland (Clavius) are shown, derived from data of Gehrels et al. [13]. The greatest effect on polarization is

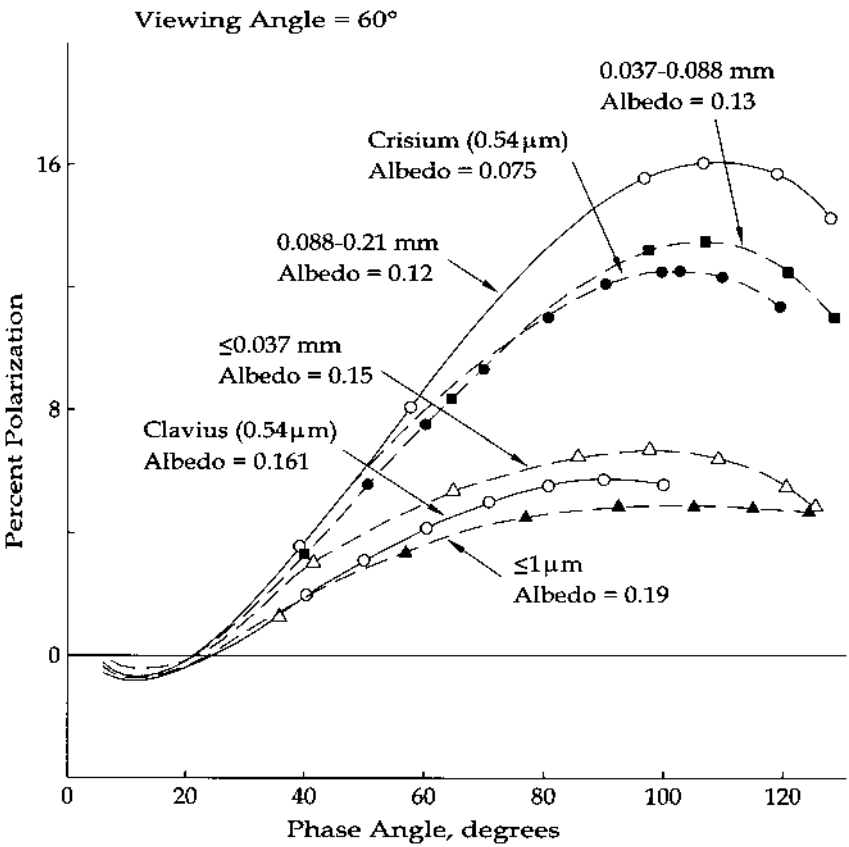

FIGURE 8 Haleakala volcanic ash. Percent polarization as a function of smaller particle size; integrated visible light (λ_{eff} = 0.55 μm); 5° albedo. (From Ref. 39.)

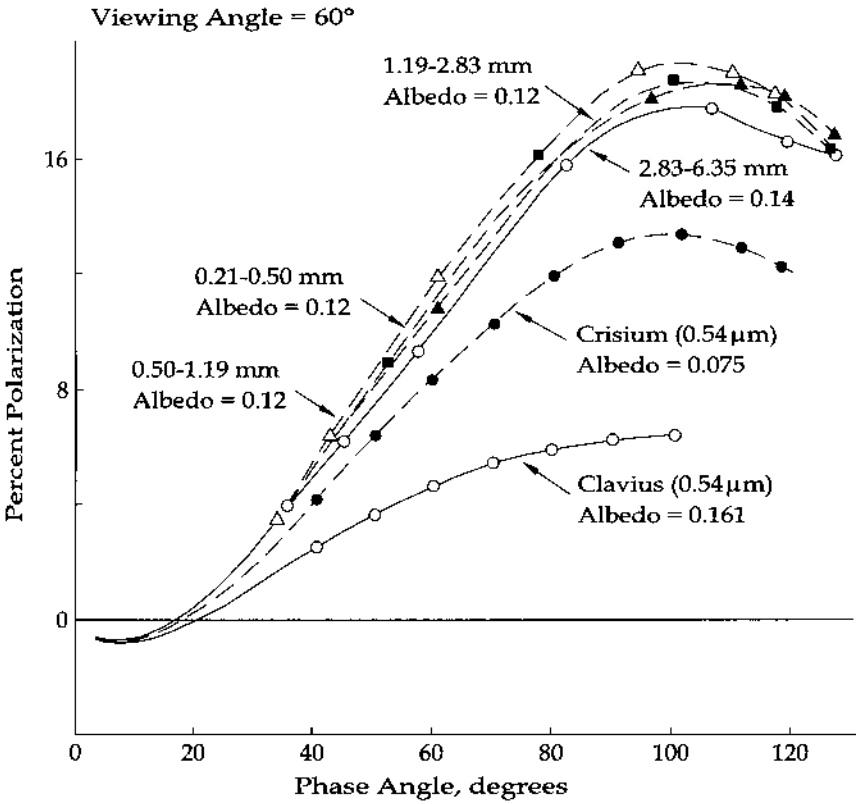

FIGURE 9 Haleakala volcanic ash. Percent polarization as a function of larger particle size; integrated visible light (λ_{eff} = 0.55 μm); 5° albedo. (From Ref. 39.)

for the smaller particle sizes (Fig. 8), where it is seen that the smaller, brighter (higher albedo) particles produce the lowest polarization. There is a smaller effect on polarization for the larger particles (Fig. 9). These results would be expected to vary somewhat depending upon how the crystalline structure of a material affects its fracture into smaller particles. This could be influenced by the technique of pulverization.

The photometric curves also depend upon particle size [23], differing most at the highest phase angles, where the smaller particles have the higher photometric curves.

An effect of combinations of polarimetric and photometric models can be seen in Fig. 10. Here, a coarse Haleakala volcanic ash was lightly coated with a powder of itself of particles smaller than 1 μm. The effect is to reduce the maximum polarization (here intended to achieve a better match to Mare

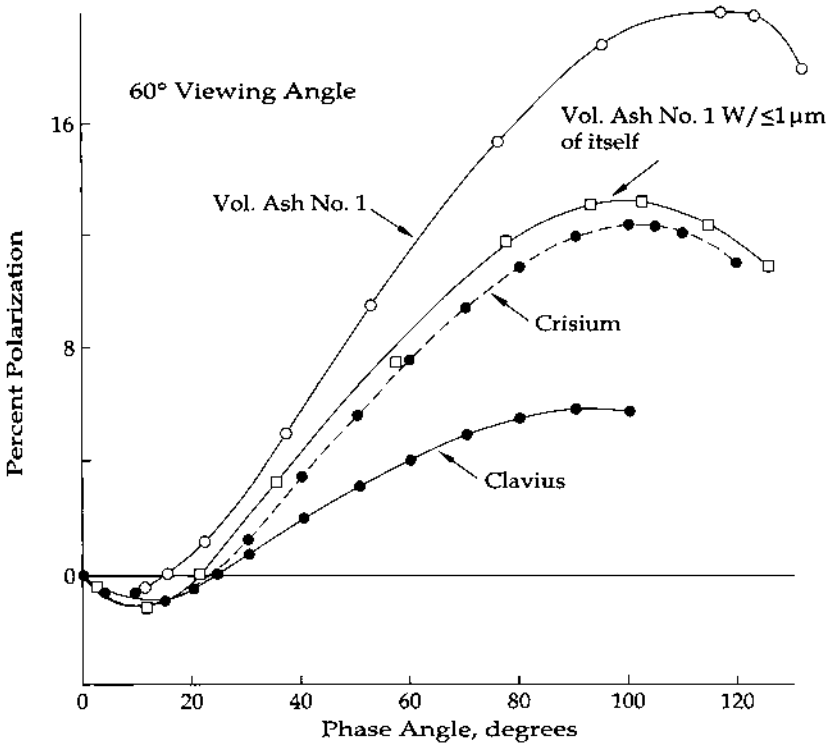

FIGURE 10 Effect of combination of models. A Haleakala volcanic ash is compared to itself coated with a light powder. (From Ref. 39.)

Crisium) and have relatively no effect on the photometry. The composite photometric curve is shown in Fig. 11. The photometry is basically produced by the shadowing by the larger sample scale and is relatively unaffected by the powder (see Ref. 9, for instance). The polarization, on the other hand, is primarily the result of the particulate surface scattering.

C. Porosity

The term porosity may be used to express the looseness or denseness of a granular material such as soil. Its numerical value is given by the ratio of the void volume to the total volume of the soil mass. Because many soil properties (strength, permeability, etc.) depend to some degree upon porosity, it would be useful to establish a porosity–photometry or porosity–polarization relationship. The use of surface porosity in lieu of bulk porosity is necessary for this type of relationship because the polarization

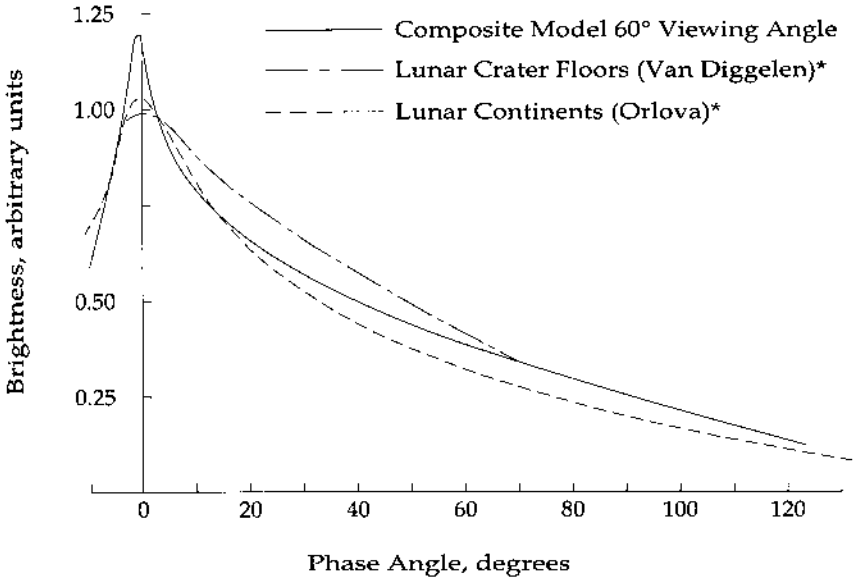

FIGURE 11 Photometry of composite model of a Haleakala volcanic ash topped with particles of itself $\leq$ 1 μm (integrated visible light, λ_{eff} = 0.54 μm). *See, for instance, Ref. 18.

characteristics of a powder are basically a function of surface or near-surface effects in the visible and near-infrared spectral regions. (The surface porosity of a material may be defined as the ratio of the apparent surface voids to the total projected surface area.)

Egan and Nowatzki [24] showed that a surface porosity–polarization relation does exist for basalt powder consisting of particles of less than 38 μm when it constitutes a surface having *z*-axis symmetry. Three samples were investigated, all having the same particle size but each having a different surface porosity. The surface roughness of each sample was defined in terms of the distribution of slope lengths and was determined semiphotographically by a technique described elsewhere [25]. It was shown that the less porous a surface, the greater was its total length of near-horizontal slopes. The curves in Fig. 12 clearly show the trend of increasing polarization for decreasing porosity in the infrared (1.0 μm) region at a 60° viewing angle. This effect may be the result of the greater length of near-horizontal slopes producing a specular reflection and a greater positive polarization maximum at high phase angles. The results of photometric measurements on the same samples are shown in Fig. 13; these indicate that the surface with the lowest porosity has

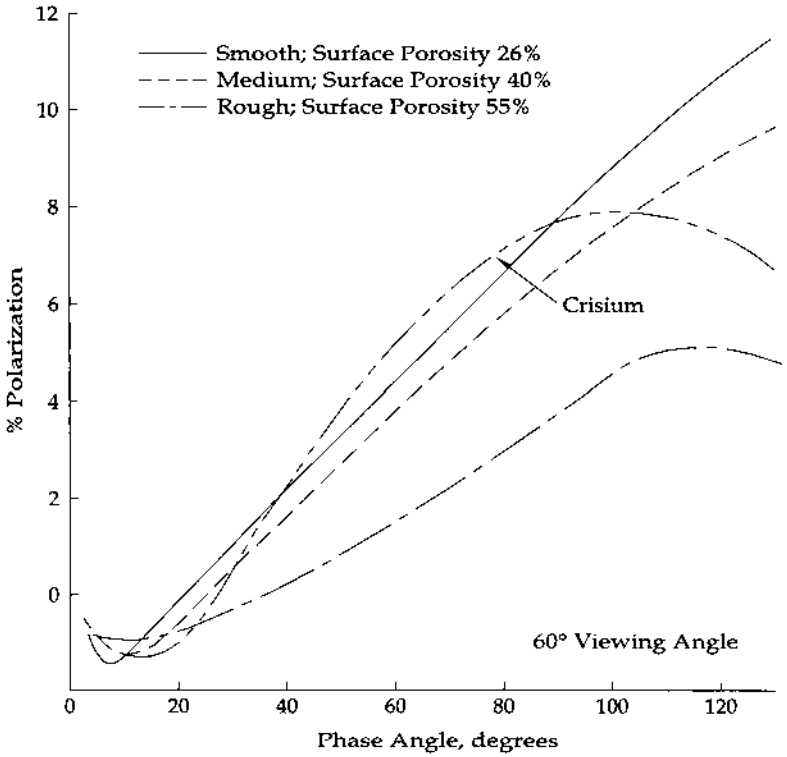

FIGURE 12 Effect of surface porosity on polarization curves of basalt powder < 38 μm in particle size.

the highest specular peak and greatest backscatter. The albedo tends to decrease with increasing porosity.

Before a universally applicable authoritative relationship between porosity and polarization or photometry can be established, it will be necessary to obtain much more experimental evidence. Analytically, the subject is very difficult, and at this time it lends itself best to an empirical approach.

D. Orientation

Following the results of the investigation into the porosity–polarization relationship of a powdered material, the question arose as to whether the same concepts applied to an intact vesicular material. Prompted by the anomalous polarimetric results at low phase angles obtained by Egan and Hallock [17] from experiments on rhyolytic pumice, a study was initiated

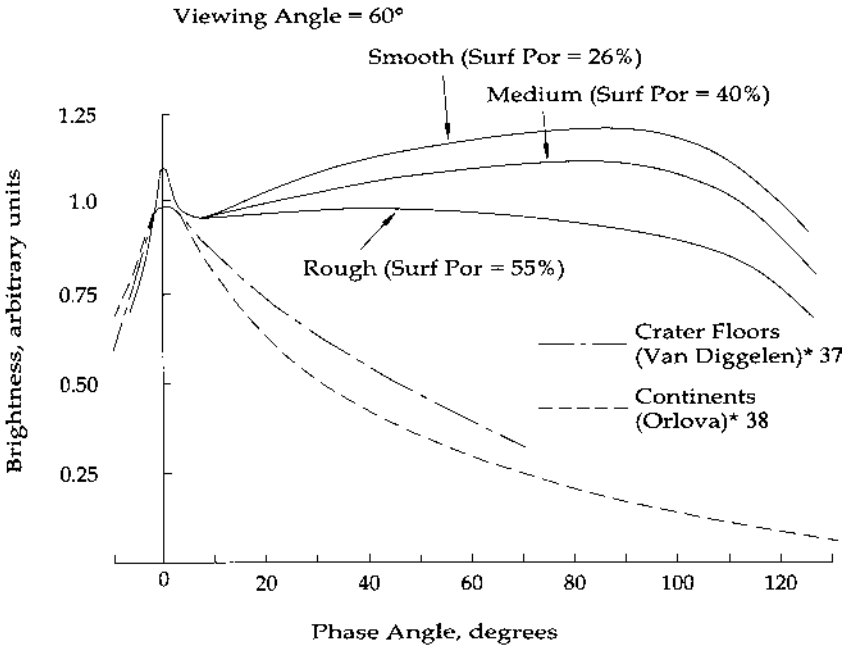

FIGURE 13 Effect of surface porosity on photometric curves of basalt powder < 38 μm in particle size (integrated visible light). *See, for instance, Ref. 18.

to investigate both the porosity question and the possibility of an orientation effect for this type of material. As could be deduced from the fact that a given pumice specimen has the same surface porosity regardless of the viewing direction, a porosity–polarization relationship could not be established. However, it was observed that the polarimetric characteristics of a given pumice specimen were very much dependent upon the plane of vision.

Figure 14 shows the results of measurements made on a typical pumice specimen. When the axes of the elongated pores on the surface of the specimen are oriented parallel to the plane of vision, the maximum value of the percent polarization is greater and the minimum value less than when the pores lineation of the same specimen are oriented perpendicular to the plane of vision. An inversion occurs in the parallel orientation that does not occur in the perpendicular orientation. From this, it was inferred that the orientation of the surface pores lineation appears to control the inversion angle and the minimum value of the percent polarization at low phase

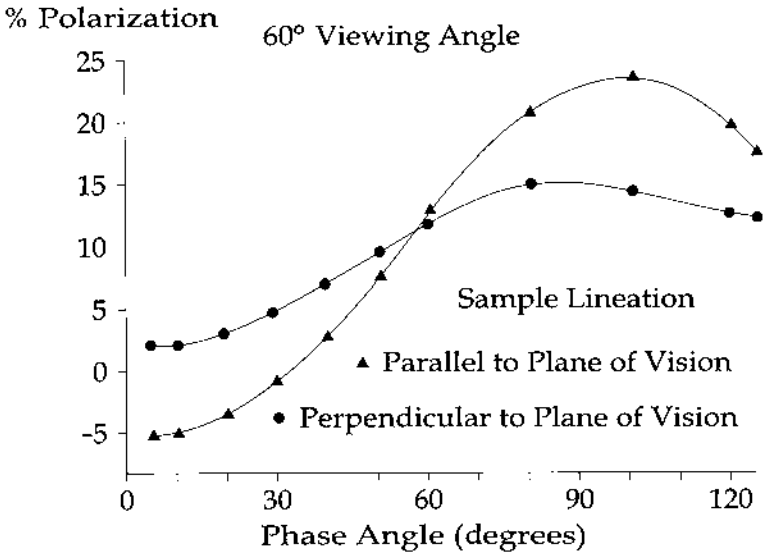

FIGURE 14 Effect of suface orientation on polarization curves of rhyolytic pumice (Mono Crater, California, region).

angles. The effect of surface structure, defined in terms of a distribution of slope lengths, was also investigated.

Figure 15 shows that a greater total length of near-horizontal surface slopes occurs when the pore lineation of the sample is oriented parallel to the plane of vision. The fact that the greater maximum polarization occurs in this orientation seems to confirm the results of the porosity–polarization study performed on powders, namely, that the greater length of near-horizontal slopes produces a greater positive polarization maximum.

Work is currently in progress to determine a parameter that could be used as an orientation index. Preliminary results suggest that the difference in residual polarization between two orientations should be used. The residual polarization is defined as the percent polarization (positive or negative) when the curve is extrapolated to zero phase angle.

The research reported here is admittedly preliminary, and it would be naive to say that the effect of a specific parameter has been isolated. For instance, neither the powder study nor the pumice study specified the effects of diffraction, microstructure, or multiple scattering. However, contrived laboratory models have been used in which the effect of some of these other influences are minimized; the general effects of porosity and orientation on the polarization have been verified.

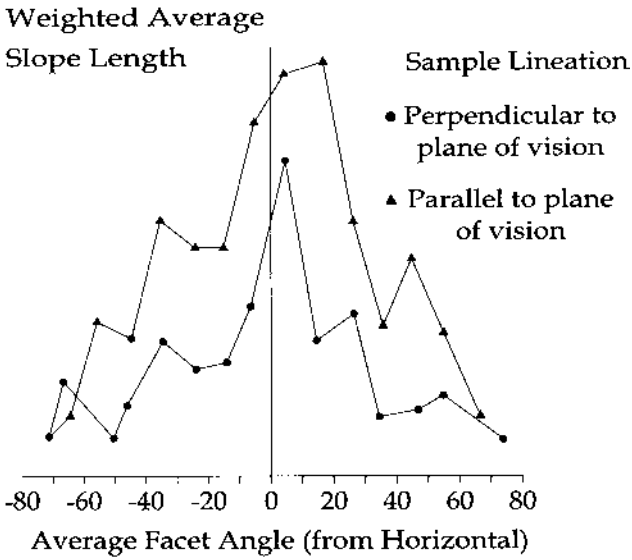

FIGURE 15 Effect of surface orientation on surface slope distribution at 90° phase angle (rhyolytic pumice).

E. Chemistry

Attempts have been made to explain the seasonal color changes in certain regions of Mars by chemical reactions [26]. Investigations [27] have shown that iron-rich brucite of the New Idria serpentinite formation of California, when exposed to various controlled environments of oxygen, carbon dioxide, and water, reacts chemically with these agents and may form products interesting from the viewpoint of color transformation. Table 1 shows the color change results of laboratory experiments starting with bluish-gray reactant minerals.

An experiment was conducted at Grumman on a serpentine–brucite slurry in $CO_2 + O_2$ atmosphere at reduced pressure to see if any of the reactions reported in Ref. 27 could be duplicated. Although the anticipated color change was achieved, the reverse reaction could not be effected. The photometric and polarimetric characteristics of the material were obtained before and after the chemical reaction. The results show that although neither matches the observed Martian surface characteristics, there is a distinct difference between the two. A chemical change occurred between the initial and final states of this material. This chemical change affected the albedo and probably the physical structure. Thus, chemistry is not a readily

TABLE 1 Laboratory Reactions of Iron-Rich Brucite from New Idria Serpentinite

Experiment	Starting material	Sample preparation	Gas environment	Time period	Products[d]	Color
I	Serpentine + brucite[a]	Dry mount[b]	Lab. atmosphere	6 mo	Serpentine + s. coalingite + s. brucite	Tan
II	Serpentine + brucite	Slurry	$O_2 + CO_2$[c]	1 h	Serpentine (+ hydromagnesite precipitate from solution)[e]	Brown
III	Serpentine + brucite	Dry mount	$O_2 + CO_2 + H_2O$	5 d	Serpentine + s. coalingite	Brown
				16 d	Serpentine + nesquehonite	Brown
IV	Reagent grade brucite	Dry mount	$O_2 + CO_2 + H_2O$	3 d	Nesquehonite	Gray
V	Serpentine + brucite	Slurry	O_2	50 d	Serpentine + tr. coalingite	Tan
VI	Serpentine + brucite	Dry mount	$O_2 + H_2O$	50 d	Serpentine + tr. coalingite	Tan
VII	Serpentine + brucite	Slurry	CO_2	1 h	Serpentine	Olive-green
VIII	Coalingite concentrate	Slurry	CO_2	18 h	Amorphous (+ hydromagnesite precipitate from solution)[e]	Red-brown

[a] Sample 487-52-7, about 25% brucite, powdered, magnetite removed.
[b] Packed into an X-ray holder.
[c] Gases bubbled through a water trap and then onto the dry sample or into the water slurry.
[d] Identified by X-ray diffraction technique: s = some; tr. = trace.
[e] The clear filtrates were heated for about 1 h; a white fluffy precipitate of hydromagnesite then formed.

isolated variable but produces a complex change involving other variables that affect polarimetry.

The chemistry of a mineral such as limonite, which has been hypothesized as forming the major constituent of the visible Martian desert surface [11], could fundamentally affect its polarization and photometry. Limonite is largely $FeO(OH) \cdot nH_2O$ with some $Fe_2O_3 \cdot nH_2O$ and often contains small amounts of hematite, clay minerals, and manganese oxides, with widely varying water content [22]. Individual samples of limonite therefore vary. Some of the discrepancies in the observed polarimetry [21] of limonite may arise because of the chemistry of the specific type of limonite used.

F. Foliage

The polarimetry of lichens was investigated by Dollfus [11], a grass turf was observed by Coulson [16], and by Egan and Hallock [17] measured the polarimetric properties of *Rhododendron maximum* (rosebay) leaves. The curves of polarimetry and photometry are shown in Figs. 16 and 17, as a case in point and not as representative of all foliage. The polarization curves are widely divergent between the green and infrared, and a peak occurs at about 120° in infrared light whereas the maximum is approached only in

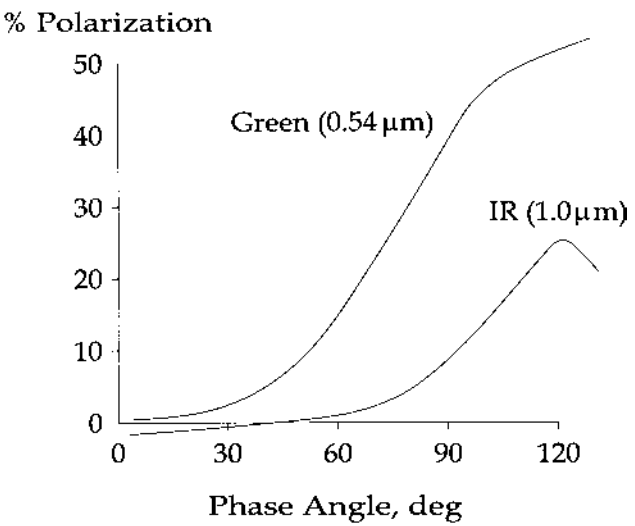

FIGURE 16 Polarization curves of *Rhododendron maximus* (rosebay) leaves. $\varepsilon = 60°$ at 0.54 μm. (From Ref. 17.)

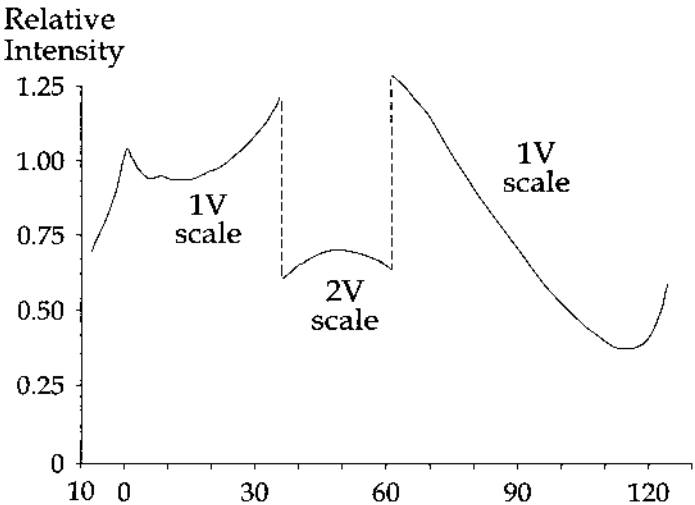

FIGURE 17 Photometric curves of *Rhododendron maximus* (rosebay) leaves. $\varepsilon = 60°$ at 0.54 μm. (From Ref. 17.)

green light. The leaves were placed in the beam of the large-scale photometer on a platen; they would not normally be arranged in such a manner on a bush. It is expected that a polarimetric orientation effect would exist for leaves occurring in nature.

The photometric curves are presented in Fig. 17; it can be seen that there is a peak at about 45°. This could be the result of the physical placement of the leaves. Also, another photometric effect was observed by Chia [28] whereby the albedo of Barbados sugar cane increases as crop height increases until the leaves achieve complete cover. The albedo of the vegetation, but not the bare soil, depended upon the zenith angle of the sun.

G. Atmosphere and Aerosols

The effect on polarimetry of an atmosphere above a surface was noted by Lyot [10], Dollfus [11], Coulson [16], Egan and Foreman [21], and Rea and O'Leary [29]. Essentially, the effect depends upon the optical thickness and scattering properties of the atmosphere. The contributions of the molecules of the air are analyzed in terms of Rayleigh scattering, but aerosol polarimetric effects must be deduced in terms of the Mie theory.

A typical set of theoretical curves depicting the comparative effects of a molecular atmosphere hypothesized for Mars, containing aerosols, is shown in Fig. 18. Curve *a* depicts Rayleigh scattering for a pure molecular

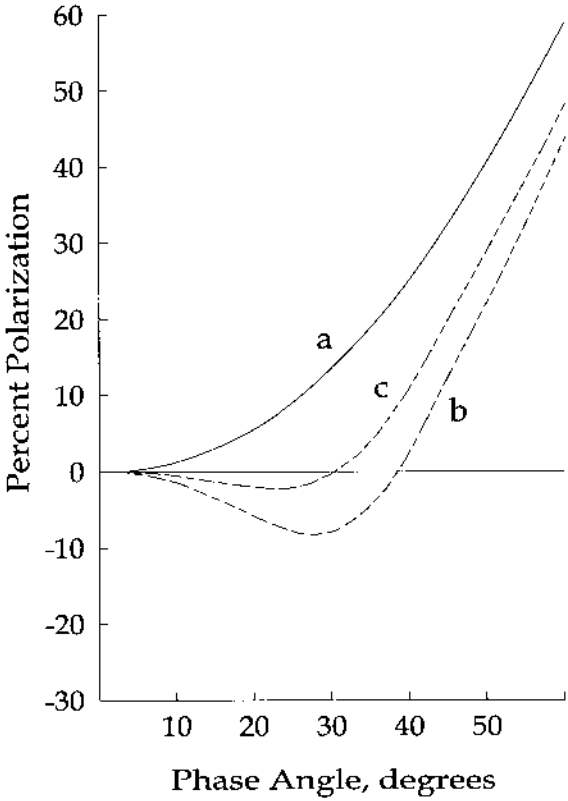

FIGURE 18 Polarimetric effect of atmospheric aerosols (calculated). (From Ref. 29.)

mixture, and curve *b* depicts Mie scattering for aerosols of 0.58 μm diameter at $\lambda = 6100$ Å; a mixture of the molecules *a* and aerosols *b* in a relative brightness ratio of 25:65 at zero phase angle is shown by curve *c*. These curves are illustrative and serve to exemplify the effect of aerosols on the polarization curves at small phase angles. Experimental laboratory investigations of the effect of aerosols and ice crystals in polarization photometry were initiated by Lyot [10], Dollfus [11], Zander [30], and Egan [21]. Problems exist in the control of aerosol particle sizes and containment for polarimetric observations.

The significance of the photometric effects of aerosols has been indicated by most of the polarimetric investigators cited above. It appears that the separation of the various parameters relating to the atmosphere (with and without aerosols) can be accomplished by narrow spectral band polarimetric

and photometric observations over a wide spectral range for many different phase and viewing angles.

It should be mentioned in connection with the atmosphere that Rayleigh polarization of the incoming sunlight occurs strongly at sunrise and sunset. At noon, and for 3 or 4 h on each side of noon, the sunlight polarization is small and has been observed [31] to be under 1% in the Long Island (NY) area on a cold winter day. Toward sunset, the polarization of the sunlight increased to about 5% on the same day. This polarization of the illuminating light, as well as sky light polarization, must be taken into account when using the observed or inferred depolarization characteristics of the surfaces observed polarimetrically.

IV. APPLICATIONS

In considering the use of multispectral photometry and polarimetry in the determination of planetary surface characteristics, a distinction must be made between large-scale surface features such as topography and small-scale properties such as porosity.

Contingent on the development of a photometric-polarimetric satellite system suitable for both earth and planetary orbital missions, a large-scale observation phase may include the mapping of topographic features of a planet such as Mercury, for which no visual observations of topography exist, or Mars, about which there is currently much controversy regarding as basic a topographic identification as highlands and lowlands. The atmospheric structure may also be investigated. Of course, before extraterrestrial measurements are attempted, a basis for comparison must be established. Consequently, observations from earth orbiters must be made and correlated to ground truth. Atmospheric and surface-covering effects (foliage, aerosols, etc.) must be taken into account. It has been shown that the orientation of relatively large-scale surface features affects the polarization characteristics of natural materials [25]. By analogy, each of the topographic features shown in Fig. 19 may be expected to exhibit polarimetric results characteristic of its orientation relative to a viewing satellite. Serial scanning of such topographic features from an orbiter would allow for systematic variation of sensor parameters such as color and phase angle. Observational series of this type would be necessary for reliable identification of the features being observed. By adjusting the resolution of the instruments it may be possible to observe a range of features extending from boulders to mountain ranges.

It may also be possible to use photometric and polarimetric observations from orbiting satellites in the mapping and possible identification of the general soil types of a planetary surface. Figure 20 shows the distribution of the great soil groups on earth emphasizing the desert regions which are shown

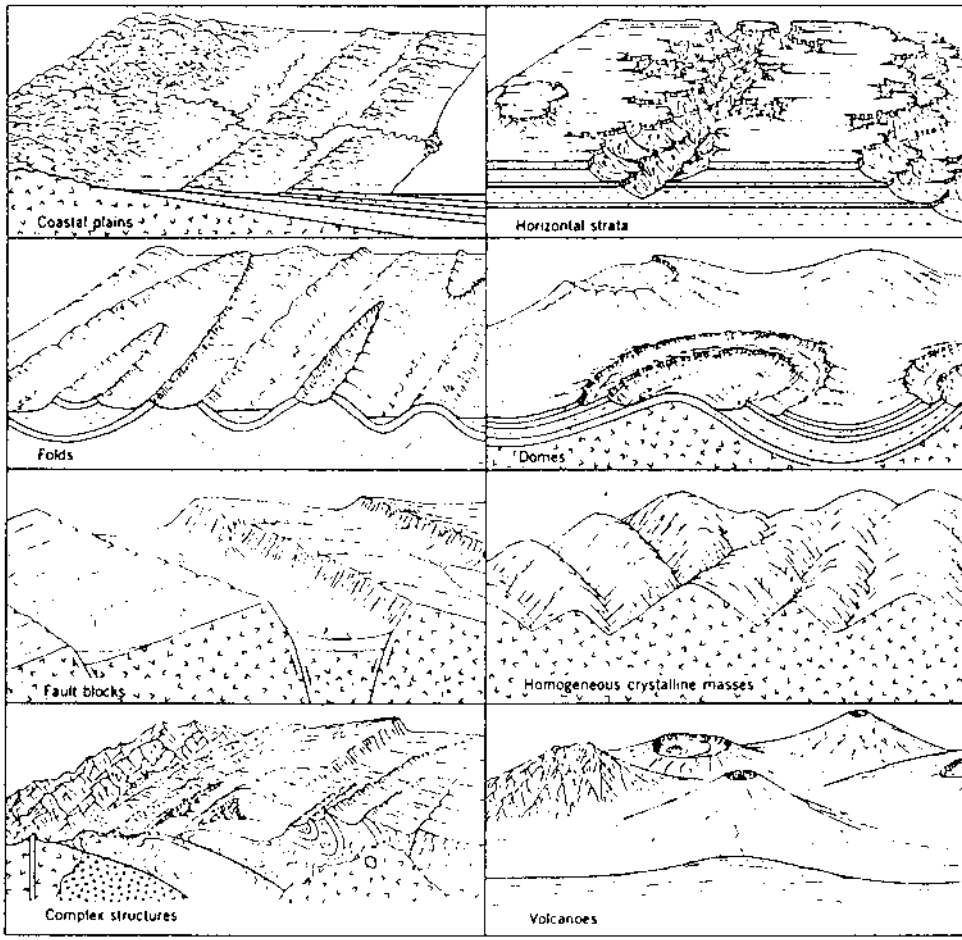

FIGURE 19 Effect of geologic structure and lithology on the morphology of landscapes. (From Ref. 32.)

shaded [33]. Before attempting to obtain a similar map for another planet it would be necessary to establish a correlation between terrestrial ground truth and the results of earth orbiters. Obviously, it would be desirable to have already obtained, by prior surveillance, an accurate map of large-scale topographic features, so that the soil type identification would not conflict physically with the topography associated with the area under consideration.

Because the physical properties and chemical composition of each of the great soil groups are closely related to climatic conditions, we may possibly

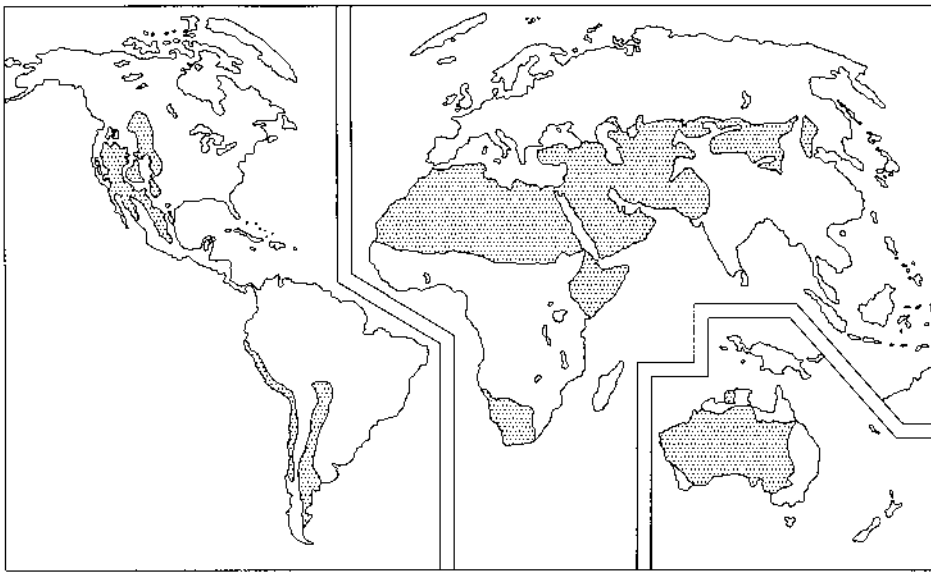

FIGURE 20 World distribution of great soil groups. (From Ref. 33.)

learn something of the climatic history of an earth-like planet, once having identified some of its soil types. Figure 21 illustrates a classification of soils in relation to climatic conditions [34]. The regional relationship between the climatic information in Fig. 21 and the desert areas in Fig. 20 is obvious. Some evidence of the usefulness of such an approach is found in the widely held opinion that iron oxides constitute a polarimetrically significant portion of the Martian surface [10,35,36]. If, as some of these investigators maintain, a hydrated form of iron oxide (limonite) exists on the martian surface then the atmosphere and general surface conditions must be amenable to the existence of water at some time since the genesis of the planet. A climatic condition is thereby imposed.

It has already been noted that photometry and polarimetry can be affected by chemical reactions. The ambient conditions under which chemical reactions occur in nature are influenced by regional climate. For example, the chemical weathering of minerals is much stronger in the humid tropics than in the tundra regions. Consequently, each climatic region has its characteristic soil types. The identification of a regional soil type may be an indirect means of determining the climatic history of a region on an earth-like planet.

Aside from ground truth correlations, other uses of photometric and polarimetric observations of the earth from a satellite seem to be directed

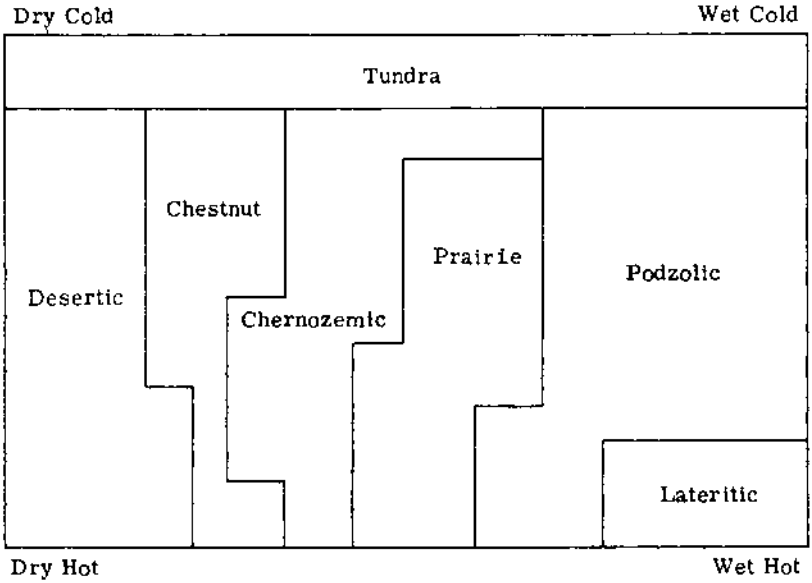

FIGURE 21 Classification of soils in relation to climatic conditions. (Adapted from Ref. 34.)

toward earth resources studies. It is believed, however, that earth resources investigations represent a necessary refinement of large-scale topographic and soil group mapping that must be conducted first to establish a correlation with terrestrial ground truth prior to any ventures for planetary exploration.

The usefulness of multispectral photometry and polarimetry is not limited to astronautical applications. It may be possible to ascertain terrestrial soil properties for engineering projects by remote sensing from an airplane. It has been shown [24] that a porosity–polarization relationship exists for a granular material constituting a surface with z-axis symmetry. It may be possible to use this small-scale effect for the density control so important in the construction of an earth-fill dam. In compacting natural soils, the density obtained is a function of the moisture content of the soil and the applied compactive effort. The construction of an earth-fill dam may be considered to proceed in a series of layers or lifts. The height of each lift is usually specified on the basis of the particle sizes of the materials being used in the fill. If the compaction specifications (moisture content, lift height, number of roller passes, etc.) are followed, then the surface density should be fairly representative of the density of the entire lift. At present, the density or compaction control for an earth-fill dam is generally accomplished by manually perform-

ing a series of tedious and time-consuming field tests on each lift. However, because density is related to porosity for a given fill material, the density of any lift may be inferred from the polarimetric characteristics of the in-place fill as obtained from an airplane flying over the construction site. As a control, one manually performed test would have to be conducted on each lift and correlated polarimetrically with the aircraft observation. The spectral range could be adjusted to suit the size and material of the fill being used for a particular phase of the construction project.

Research in the field of laser depolarization has been conducted at Grumman. Results of preliminary experiments indicate that the amount of laser depolarization is a function of the moisture content of the target material [31]. The fact that, for soils, moisture content and density are related implies that laser depolarization offers another approach to the rapid determination of densities in earth-fill dam construction.

V. CONCLUSION

Polarimetry and photometry are valuable techniques in the estimation of ground truth not readily available by any other direct means. Airborne and spacecraft systems are possible within the engineering performance and reliability constraints imposed. Many factors are involved in the proper interpretation of polarimetric and photometric data; however, they are amenable to analysis. The applications of multispectral photometry and polarimetry discussed above are a mere sampling of those possible once a more complete understanding of the fundamentals behind these phenomena has been obtained. Unfortunately, theory is lagging experiments at this time, so all of the relationships discussed must be expressed in an empirical manner. Despite this limitation, multispectral photometry and polarimetry represent a promising new approach to the investigation of both large-scale and small-scale surface features.

REFERENCES

1. Krinov, E.L. Spectral Reflectance Properties of Natural Surfaces, Tech. Transl. TT-439, 1947. Ottawa: Natl. Research Council of Canada, 1953.
2. Bauer, K.G.; Dutton, J.A. Albedo variations measured from an airplane over several types of surfaces. J. Geophys. Res. 1962, 67, 2367–2376.
3. Romanova, M.A. Air Survey of Sand Deposits by Spectral Luminance. Laboratory of Aeromethods of the Academy of Sciences of the USSR; State Scientific Technical Press for Literature on Petroleum and Solid Fuels, 1962. Translation by Consultants Bureau, New York, 1964.
4. Kondratiev, K.I.; Manolova, M.P. The problem of incoming diffuse and to-

tal radiation on the surface of a slope. Meteorol. Gidrol (Leningrad) 1955, 6, 31–34.
5. Ashburn, E.V.; Weldon, R.G. Spectral diffuse reflectance of desert surfaces. J. Opt. Soc. Am. 1956, 46, 583–586.
6. Coulson, K.L. Characteristics of solar radiation reflected from desert soil. Sci. Rep. No. 2, Contract AF19(604)-1303, Univ. California, Los Angeles, 1966.
7. Orlova, N.S. Radial diagrams of scattering for several materials. Tr. Astron. Obs. (Leningrad State Univ.) 1952, 16, 166–193.
8. Hapke, B.; Van Horn, H. Photometric studies of complex surfaces. J. Geophys. Res. 1963, 68, 4545–4570.
9. Halajian, J.D.; Spagnolo, F.A. Photometric measurements of simulated lunar surfaces. Final Report on NASA Contract No. NAS 9-3182. Grumman Res. Dept. Rep. RE-245, April 1966.
10. Lyot, B. Recherches sur la polarisation de la lumiere des planets et de quelques substances terrestres. Ann. Obs. Paris, Sect. de Meudon 8, 1929.
11. Dollfus, A. Etude des planets par la polarization de leur lumiere. Ann. Astrophys. Suppl. No. 4, 1957.
12. Dollfus, A. Polarization studies of the planets. In: Kuiper, G.P.; Middlehurst, B.M., Eds. Planets and Satellites. Chicago, IL: Univ. Chicago Press, 1961, Chap. 9.
13. Gehrels, T.; Coffeen, T.; Owings, D. Wavelength dependence of polarization. III. The lunar surface. Astron. J. 1964, 69(December), 826–852.
14. Coffeen, D.L. Wavelength dependence of polarization. IV. Volcanic cinders and particles. Astron. J. 1965, 70(August), 403–413.
15. Coulson, K.L.; Gray, E.L.; Bouricius, G.M. Effect of surface reflection on planetary albedo. Icarus 1966, 5(March), 139–148.
16. Coulson, K.L. Effects of reflection properties of natural surfaces in aerial reconnaissance. Appl. Opt. 1966, 5(6), 905–917.
17. Egan, W.G.; Hallock, H.B. Polarimetry signature of terrestrial and planetary materials. Proc Fourth Symp Remote Sensing of Environment, Ann Arbor: Univ. Michigan, April 1966.
18. Egan, W.G. Polarimetric measurements of simulated lunar surface materials. J. Geophys. Res. 1967, (June), 3233–3245.
19. Gordon, J.I.; Church, P.V. Overcast sky luminances and directional luminous reflectances of objects and backgrounds under overcast skies. Appl. Opt. 1966, 5, 919–923.
20. Henderson, S.T.; Hodgkiss, D. The spectral energy distribution of daylight. Br. J. Appl. Phys. 1964, 15, 947–952.
21. Egan, W.G.; Foreman, K.M. A new perspective on Martian polarimetric measurements. Am. Astronaut. Soc., Nat. Symp., Huntsville, AL, June 1967.
22. Hurlbut, C.S. Jr. Mineralogy. 17th Ed. New York: Wiley, 1966.
23. Halajian, J.D. Photometric measurements of simulated lunar surfaces. Interim Report on NASA Contract No. NAS 9-3182, Grumman Res. Dept. Rep. RE-219, July 1965.
24. Egan W.G.; Nowatzki, E.A. A porosity-polarization relationship applicable to

the lunar surface. Paper presented to the 123rd Meeting of the American Astronomical Society, Univ. California, Los Angeles, CA, Dec. 27, 1966.
25. Egan W.G.; Nowatzki, E.A. An investigation of the relationship between polarization and surface structure of rhyolytic pumice. Paper presented at 48th Annual Meeting of the American Geophysical Union, Sheraton Park Hotel, Washington, DC, April 18, 1967.
26. Cohen, A.J. Seasonal color changes on Mars. Astron. J. 1966, 71(9), 849–850. (abstr)
27. Mumford, F.A.; Thompson, C.S. The stability of brucite in the weathering zone of the New Idria serpentinite. Clays and Clay Minerals, Proc. 14th Natl. Conf. Oxford, UK: Pergamon Press, 1966, 490.
28. Chia, L. Albedos of natural surfaces in Barbados. Quart. J. Roy. Meteorol. Soc. 1967, 93(395), 116–120.
29. Rea D.G.; O'Leary, B.T. Visible polarization data of Mars. Nature 1965, 206(4889), 1138–1140.
30. Zander, R. Spectral scattering properties of ice clouds and hoarfrost. J. Geophys. Res. 1966, 71(2), 375–378.
31. Egan, W.G. Unpublished observations.
32. Thornbury, W.D. Principles of Geomorphology, New York: Wiley, 1954.
33. Winters, E.; Simonson, R.W. The subsoil. Adv. Agron. 1951, 3, 1–92.
34. Millar C.E.; Turk, F.M. Fundamentals of Soil Science. New York: Wiley, 1943.
35. Binder, A.B.; Cruikshank, D.P. Comparison of the infrared spectrum of Mars with spectra of selected terrestrial rocks and minerals. Commun. Lunar Planetary Lab., Univ. Arizona 1964, 2, 193.
36. Pollack, J.B.; Sagan, C. Interpretation of surface features. Presented at Symposium on the Surface of Mars, Goddard Institute for Space Studies, Feb. 3 and 4, 1967. Unpublished.
37. Van Diggelen, L. Photometric properties of lunar cater floors. Recherche Astronomique de l'Observatoire d'Utrecht, 1959.
38. Orlova, N.S. Selected articles on light scattering and photometric relief of the lunar surface. Astron. Zh. 33(1), NASA TTF-75, 1962.
39. Egan, W.G. Photometry and Polarization in Remote Sensing. New York: Elsevier Science, 1985.

2

Photometry

I. INTRODUCTION

Radiative energy is carried through space (including earth's atmosphere) by invisible electromagnetic waves. Evidence of the presence of these waves is given when they interact with a sensor. In the optical region, the sensor may be the eye, a phototube, a solid-state photosensor, or some combination of one or more of these devices in a system. The system may be a telescope, a scanner, or a mosaic system.

Electromagnetic radiation travels through free space at the velocity of light (3×10^{10} cm/s). Because electromagnetic radiation has a wave property, it has a wavelength and therefore a frequency. The relationship between the wavelength and frequency is given by the relationship

$$\lambda = c/v \tag{1}$$

where c is the velocity of light (radiation) in a vacuum (3×10^{10} cm/s), λ is the wavelength (in centimeters), and v is the frequency, in hertz (sinusoidal cycles per second).

When electromagnetic radiation passes through a nonabsorbing atmosphere or any lossless dielectric, it is slowed down by a factor equal to the refractive portion of the index of refraction of the medium. This slowing down can cause a bending or refraction of the wave. The frequency v remains the same in the dielectric, but the wavelength decreases in accordance with the expression given above for the wavelength. The electromagnetic wave consists of two field components, an electric field **E** and a magnetic field **H**; these components are mutually perpendicular and follow the same amplitude

variations. In the simplest form, the amplitudes are represented as sine waves of one frequency (Fig. 1).

This sine wave disturbance ξ can be expressed mathematically as

$$\xi = \mathbf{A} \sin(\omega t - 2\pi z/\lambda) \tag{2}$$

where the quantities are defined as follows: $\mathbf{A}$ is the vector amplitude of the wave (half the peak-to-peak deviation), ω is the angular frequency, and z is the distance along the direction of propagation. An alternative representation in complex notation is

$$\xi = \mathbf{A} e^{i(\omega t - 2\pi z/\lambda)} \tag{3}$$

or, alternatively,

$$\xi = \mathbf{A} e^{i\phi} \tag{4}$$

where ϕ is termed the *phase angle* (not to be confused with the phase angle in astronomy, mentioned later in this chapter); here

$$\phi = \omega t - \frac{2\pi z}{\lambda} \tag{5}$$

$\mathbf{A}$ is a vector quantity (i.e., it has a direction and an amplitude $|\mathbf{A}|$) and may represent the $\mathbf{E}$ or $\mathbf{H}$ field. When $\mathbf{A}$ is directed along the x axis (the real axis), a

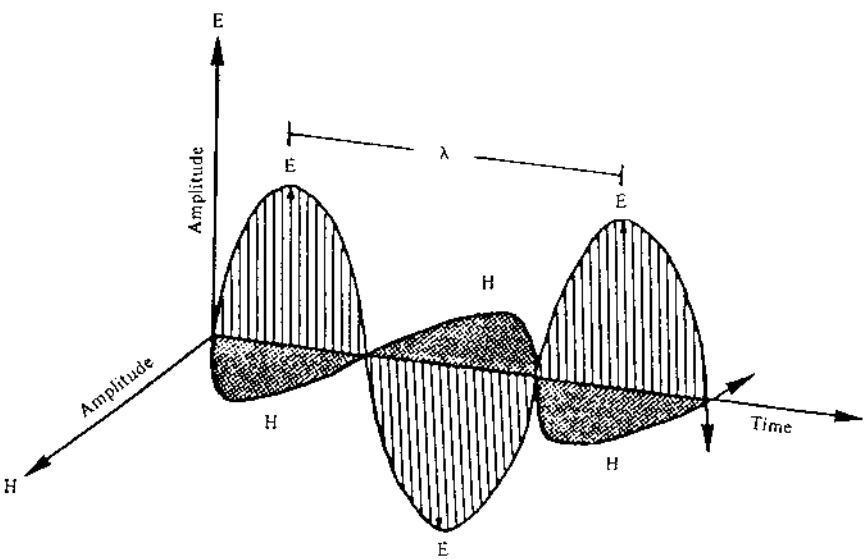

FIGURE 1 Electric (E) and magnetic (H) vectors of a plane electromagnetic wave.

unit vector **i** lying on the x axis and directed in the positive sense is used as a prefix as in i|**A**|; if the unit vector prefix **j** is used (i.e., **j**|**A**|), the direction of the absolute magnitude is along the positive y-axis direction. Similarly, the unit vector **k** is directed along the positive z axis.

The intensity (the physically measurable quantity) is the amplitude squared (i.e., $|\mathbf{A}|^2$). The plot of Fig. 1 is versus time (or position). The wavelength is shown, and the direction of the **E** field is taken conventionally as the plane of polarization (historically, though, the **H** field was once taken as the polarization direction). Figure 1 represents a plane-polarized wave, and the polarization direction may assume any direction in a plane perpendicular to the direction of propagation. Unpolarized radiation would be represented by an infinite number of plane-polarized waves of equal infinitesimal amplitude A oriented in all directions perpendicular to the direction of propagation. Another representation would be two mutually orthogonal plane-polarized waves not having phase coherence.

The techniques for producing and analyzing polarized radiation are described in Chapter 3. The mathematical representation of the phenomena is outlined in Chapter 4.

II. QUANTITATIVE DESCRIPTORS

The radiant energy Q (in ergs or joules; see Table 1) is transported by electromagnetic waves; the energy is proportional to the product of the amplitudes of **E** and **H**. The magnitudes of **E** and **H** are related by a constant of proportionality, the intrinsic impedance η of the medium:

$$E = \eta H \tag{6}$$

When radiation enters a medium other than a vacuum, it is slowed down. The index of refraction m is the ratio of the velocity c of energy flow in free space (a vacuum) to v, its velocity in the medium:

$$m = \frac{c}{v} \tag{7}$$

The rate of flow of this energy (in ergs per second, joules per second, or watts) is termed the radiant flux Φ (Table 1), and this flux striking a surface is the irradiance E_c (watts per square meter, or Btu per square foot) (Table 1). A flux being emitted from a surface is described by the radiant emittance M_c. The radiation occupies a volume, with a radiant density w_e.

The ideal of all radiation moving in parallel rays is not met in practice. Both radiation sources and sensors are at finite distances, and as a result the radiation diverges radially from sources and converges radially on sensors. This concept must be brought into the mathematical representation by way of

TABLE 1 Radiometric and Analogous Photometric Units

Quantity	Symbol	Description	Defining equation	Representative units
		Radiometric units		
Radiant energy[a,b]	Q_e		$Q_e = \int_0^\tau \Phi_e dt$	joules (1 J = 10^6 erg $= \frac{1}{4.186}$ cal)
Radiant density[a,b]	w_e	Radiant energy per unit volume	$w_e = \frac{\partial Q_e}{\partial V}$	joules per cubic meter
Radiant flux[a]	Φ_c	Radiant energy per unit time	$\Phi_e = \frac{\partial Q_e}{\partial t}$	watts (1 W = I J/s)
Radiant intensity[a]	I	Radiant power per unit solid angle	$I = \frac{\partial \Phi_e}{\partial \omega}$	watts per steradian
Radiant emittance[a]	M_e	Radiant power emitted per unit area of source	$M_e = \frac{\partial \Phi_e}{\partial A}$	watts per square meter
Irradiance[a]	E_e	Radiant power impacting per unit area of receiver	$E_e = \frac{\partial \Phi_e}{\partial A}$	watts per square meter
Differential irradiance (directional radiance)	dE_e	Elemental contribution of flux at a point from a single direction (θ, ϕ)	$dE_e = L_e \cos\theta \, d\omega$	watts per square meter
Radiance	L_c	Radiant power per unit solid angle per unit projected area of source	$L_e = \frac{\partial^2 \Phi_e}{\partial \omega \, (\cos\theta \, \partial \, A)}$	watts per steradian per square meter

Photometric units

Luminous energy[a,b]	Q_v	Portion of radiant energy in visible region	$Q_v = \int_0^\tau \Phi_v dt$	lumen second, talbot
Luminous density[a,b]	w_v	Luminous energy per unit volume	$w_v = \frac{\partial Q_v}{\partial V}$	lumen seconds per cubic meter
Luminous flux[a,b]	Φ_v	Luminous energy per unit time	$\Phi_v = \frac{\partial Q_v}{\partial t}$	lumens
Luminous intensity[a]	I_v	Luminous power per unit solid angle; candlepower	$I_v = \frac{\partial \Phi_v}{\partial \omega}$	lumens per steradian; candela
Luminous exitance[a]	M_v	Luminous power emitted per unit area of source	$M_v = \frac{\partial \Phi_v}{\partial A}$	lumens per square meter
Illumination[a] (illuminance)	E_v	Luminous power impacting per unit area of receiver	$E_v = \frac{\partial \Phi_v}{\partial A}$	lumens per square meter
Differential illuminance (directional illuminance)	dE_v	Elemental contribution of flux at a point from a single direction (θ, ϕ)	$dE_v = L_v \cos\theta \, d\omega$	lumens per square meter
Luminance	L_v	Luminous power per unit solid angle per unit projected area from a source; brightness	$L_v = \frac{\partial^2 \Phi_v}{\partial \omega (\cos\theta \, \partial A)}$	lumens per steradian per square meter

[a] Radiometric and photometric quantities may be limited to a narrow-wavelength band by adding the word *spectral* and indicating the wavelength; the corresponding symbols may be modified by adding the subscript λ.

[b] Radiant and luminous energy and flux can be expressed as areal densities at a surface (quantity per unit area at a given point on a surface, e.g., $\partial Q/\partial A$) or as intensity (quantity per unit solid angle in a given direction, e.g., $\partial Q/\partial\omega$), or as specific intensity (quantity per unit solid angle in a given direction per unit projected area at a given point, e.g., $\partial\omega(\cos\theta \, \partial \, A)$. The spectral quantities can be described in a similar manner.

solid angles. A sphere encloses a solid angle ω of 4π steradians in space; the solid angle ω enclosed by *part* of a sphere is the sphere's surface area divided by the sphere's radius squared (Fig. 2) or, mathematically,

$$\omega = 4\pi \sin^2(\theta/4) \tag{8}$$

where θ is the vertex angle.

A point source of radiant flux will radiate into a solid angle of 4π steradians (a sphere) and produce a radiant intensity I of $\Phi/4\pi$ (Table 1) in units of watts per steradian. But since the actual radiant surfaces have a finite area, as do the sensors, the radiant intensity I per unit source surface area (the radiance L in Fig. 3a; see also Table 1) is the quantity to be reckoned in source–sensor calculations. For a diffusely radiating source of area A_1 and radiance L_1, the radiation intercepted by a sensor of area A_2 located at an angle θ_1 relative to the surface normal of A_1 (having the surface normal at angle θ_2 relative to A_1) at a distance r is

$$P_2 = L_{e1} A_1 \cos\theta_1 \frac{A_2 \cos\theta_2}{r^2} \tag{9}$$

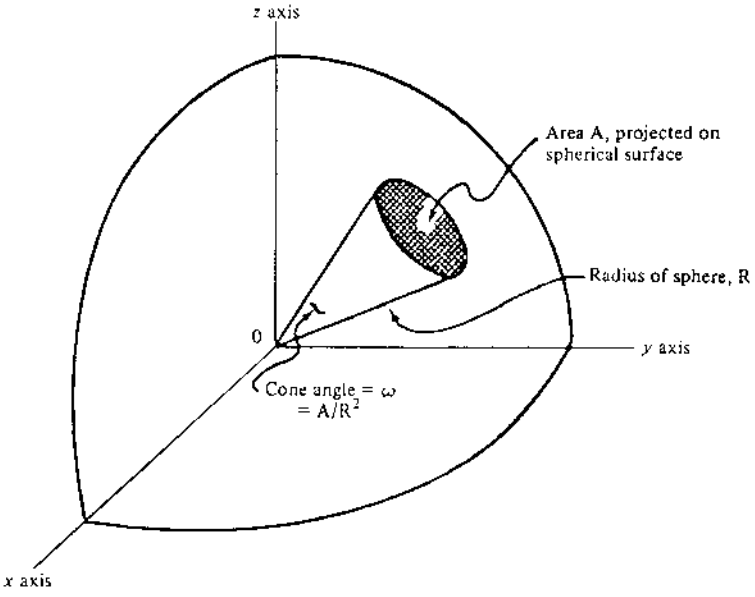

FIGURE 2 The concept of the solid angle in angular measure. (Copyright 1975 by the American Society of Photogrammetry. Reproduced with permission.) (From Ref. 1.)

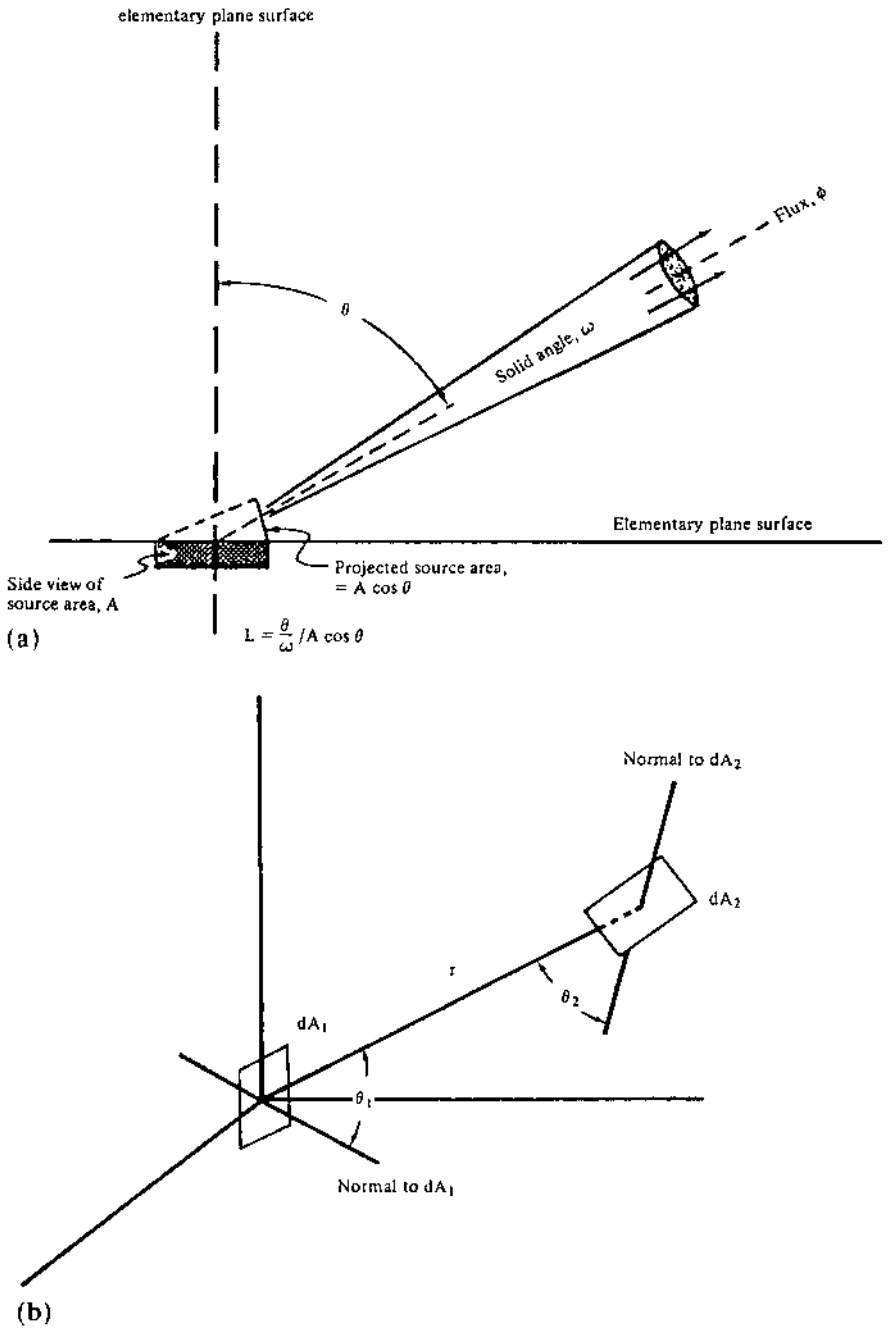

FIGURE 3 (a) The concept of radiance. (Adapted from Ref. 1.) (b) Geometrical relationships.

(See Fig. 3b.) The differential irradiance at the sensor of area A_2 will be

$$dE_2 = L_{e1}\cos\theta_1 \frac{dA_2}{r^2} \tag{10}$$

In terms of photometry (Table 1), the analogous symbolism applies, with the exception that the luminous flux Φ_v is limited to that in the spectral region to which the eye is sensitive. However, in the more general sense (as used in this text), the term photometry characterizes radiation in the spectral range from the ultraviolet to the infrared.

In remote sensing photometry, the brightness of surfaces is the basic parameter of interest. The brightness of a surface is the product of the bidirectional reflectance and the irradiance. Bidirectional reflectance of a surface is the ratio of radiant flux reflected or scattered in a particular direction (measured relative to the surface normal, θ') to that incident at an angle θ (also measured relative to the surface normal) (Fig. 4). Both θ and θ' may assume any value from $0°$ to $\pm 90°$; further, the reflected or scattered ray may be in a direction other than in the projection of the incident direction on the surface. It may thus take any value between $0°$ and $360°$, the azimuthal variation ϕ, measured counterclockwise from above. Another angle of interest is the phase angle α, measured in a plane including the incident and reflected or scattered rays. The bidirectional reflectance yields the specular reflectance when $\theta = \theta'$ and $\phi = 180°$; the sum (integral) of the bidirectionally

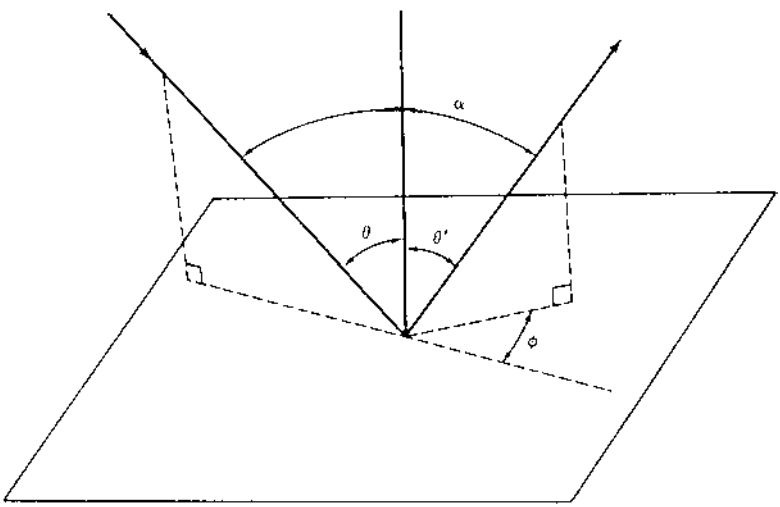

FIGURE 4 Geometrical relationships.

reflected and scattered flux over a hemisphere enclosing the surface yields the total diffuse reflectance. Specular reflectance is important in the remote sensing of water surfaces or smooth man-made surfaces. Diffuse reflectance is of no interest because remote sensors do not measure it.

III. ABSOLUTE PHOTOMETRIC MEASUREMENTS

The irradiance of a surface is usually composed of two components: (1) a directional incident (collimated) flux and (2) a diffuse incident flux. For instance, the incident solar radiation is directionally incident (or at least spatially collimated to 0.5°, this being the angular diameter of the sun as seen from earth), and the incident flux from the sky (and clouds, when present) is diffuse. Accurate measurement of these specular and diffuse components may be accomplished by various types of photometers. Several kinds are manufactured by The Eppley Laboratory, Inc. Newport, Rhode Island. Figure 5 shows a normal incidence pyrheliometer (with a solar tracker), which is used for measurement of direct solar irradiance (in watts per square meter). The instrument is mounted on a solar tracker to permit aiming the sensor directly at the sun throughout the day without manual attention. Filters may be mounted on the optical system when a particular spectral range is to be measured. The acceptance angle of the sensor system is 5°43′30″, which is about 10 times the sun is angular diameter. Thus, the system also will sense the "halo" around the sun caused by scattering of the particulate aerosols in the earth's atmosphere [2]. The irradiance on a horizontal surface will be the projection, i.e., the irradiance multiplied by the cosine of the angle that the sun's radiation makes with the perpendicular to the surface (i.e., the solar zenith angle, which is the complement of the solar elevation angle).

For the measurement of total incident radiation (direct plus diffuse), a pyranometer, such as shown in Fig. 6a,b may be used. The diffuse radiation is the difference between the radiation on the pyranometer and that on the normal incidence pyrheliometer. An improved version is shown in Fig. 6b with up to ±0.5% over the temperature range.

For both the normal incidence pyrheliometer and the pyranometer, as well as other related instruments, a certification of the calibration is furnished (Fig. 7). Traceability to primary standards is noted, as well as the calibration factors.

The diffuse radiation alone may be measured if a paddle (a circular disk) is held at an appropriate distance in front of the pyranometer so as to form a shadow of the sun on the pyranometer; the object is to have this disk block the direct solar rays from striking the pyranometer. In addition, a pyranometer must be located free of nearby walls, buildings, or obstacles in order to

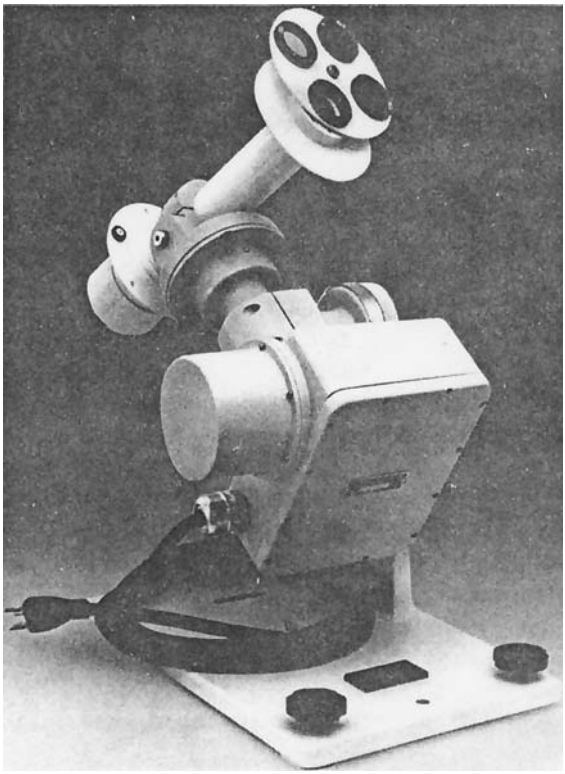

FIGURE 5 Eppley normal incidence photometer.

prevent radiation scattered off these objects from causing erroneous contributions to the sensed irradiance.

The spectral variation of the incident solar radiation may be measured by using narrowband filters of the thin-film interference type. The filters transmit a narrow wavelength band nominally given at 566 nm as shown in Fig. 8. The peak transmission of the filter is 44.0% at a wavelength of 569 nm; the bandwidth (FWHM; full width at half-maximum) of 19 nm is shown.

The irradiance transmitted by this filter is the wavelength-by-wavelength product of the incident radiance and the filter transmission (solid line). Equivalently, when the incident radiance does not vary significantly over the filter passband, a 100% (or 50%) transmitting bandwidth hypothetical filter may be chosen. This hypothetical filter will have the same transmission–wavelength product as the actual filter. The determination is made using a

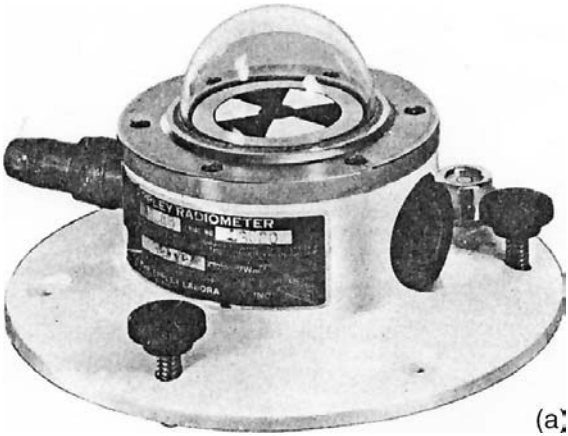

(a)

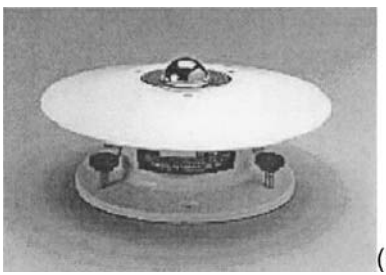

(b)

FIGURE 6 (a) Eppley black and white pyranometer. (b) Newest version.

planimeter or other area-measuring device on the actual transmission curve shown, and the result is the dashed line shown in Fig. 8. If the incident radiance varies significantly over the transmission band of the filter, the "equivalent filter" is then broken up into as many ranges as required to adequately represent the overall irradiance.

A variant of the pyranometer and pyrheliometer, with all spectral filters included in one instrument, is the Volz photometer. This versatile device has been and still is used as a tertiary standard for sun and sky measurements with purported ± 1–2% accuracy. The device is portable, self-contained, and intended for handheld measurements of direct and scattered solar radiation for determination of atmospheric aerosol extinction and precipitable water. Four interference filters are normally used (0.865, 0.500, 0.380 μm as recommended by the World Meteorology Organization and EPA/NOAA, and a supplementary one at 0.945 μm for water vapor). Additional bands are

EPLAB

THE EPPLEY LABORATORY, INC.
SCIENTIFIC INSTRUMENTS
NEWPORT, R.I. 02840 U.S.A.

STANDARDIZATION
OF
EPPLEY BLACK AND WHITE PYRANOMETER

(horizontal surface receiver - 180°)

Model 8-48 Serial Number 16209 Resistance 345 ohm at 26°C

Temperature Compensation

Range -20 to + 40 °C

This radiometer has been compared with the Eppley group of reference standards, under radiation intensities of about 700 watts meter^{-2} (roughly one-half a solar constant), the adopted calibration temperature is 25 °C.

As a result of a series of comparisons, it has been found to develop an emf of:

11.91 x10^{-6} volts/watt meter^{-2}

8.30 millivolts/cal cm^{-2} min^{-1}

The calculation of this constant is based on the fact that the relationship between radiation intensity and emf is rectilinear to intensities of 1400 watts meter^{-2}. This pyranometer is linear to within ± 1.0 percent up to this intensity.

The calibration of this instrument is traceable to standard self-calibrating cavity pyrheliometers in terms of the Systems Internationale des Unites (SI units), which participated in the Fourth International Pyrheliometric Comparisons (IPCIV) at Davos, Switzerland in October 1975.*

Useful conversion facts: 1 cal-cm^{-2} min^{-1} = 697.3 watts/meter^2

1 BTU/ft^2-hr^{-1} = 3.153 watts/meter^2

Date of Test: August 19, 1977 IN CHARGE OF TEST

Richard H. Hatch

The Eppley Laboratory, Inc.

By: W. J. Schulze S. O. 35206

Newport, R. I. Date August 26, 1977

FIGURE 7 Typical photometer certification.

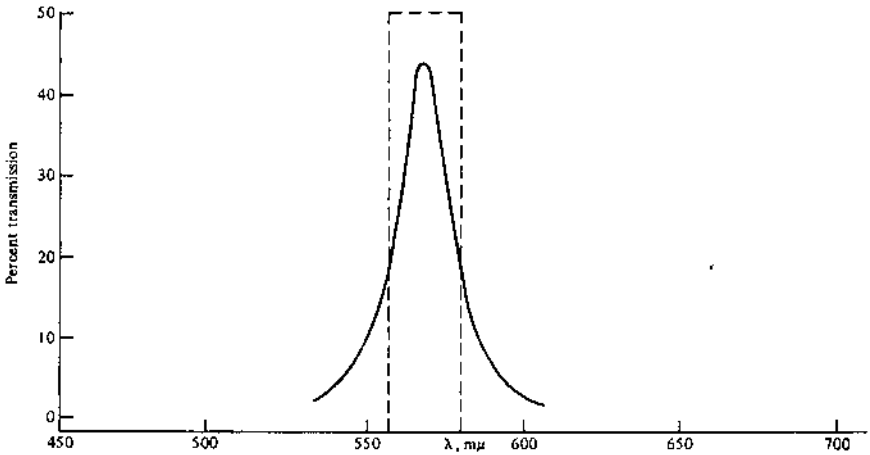

FIGURE 8 Typical interference filter transmission curve and equivalent (shown as dashed line).

furnished, on special request, at 0.342 and 1.67 μm. The field of view is less than 2°, and an air mass diopter is furnished to correct for solar elevations other than directly at the zenith.

By using calibration factors (furnished with each instrument), the effect of ozone and Raleigh absorption is theoretically eliminated. The aerosol extinction may then be calculated for 1 air mass (i.e., sun at the zenith) at the wavelengths sensed. At 0.945 μm, both aerosol and water vapor extinction are sensed; by rationing the extinction at 0.945 μm to that at 0.865 μm, the precipitable water vapor may be deduced. By shifting the viewing area off the incident solar direction and maintaining the same elevation angle, the brightness of the solar aureole can be determined. This measurement is actually along the solar almucantar, and the sky (aerosol) brightness as a function of displacement angle is a function of aerosol size. This sky brightening near the sun is caused by the diffraction of solar radiation by aerosol particles. To a first approximation, it is similar to Fraunhofer diffraction by a disk of radius r. The diffracted radiation is mainly within a scattering angle θ_0, where

$$\theta_0 = \sin^{-1}(0.6\lambda/r) \tag{11}$$

For instance, for radiation of wavelength 0.5 μm ($= \lambda$) and particles of 10 μm radius, the brightening region (solar aureole) has a radius of 2°, whereas for 1 μm radius particles, the aureole radius is 20°.

TABLE 2 Solar Spectral Distribution

λ (μm)	B_λ (10^{10} erg sr^{-1} cm^{-2} μm^{-1} sec^{-1})	B'_λ	$I_\lambda(0)$	$I'_\lambda(0)$	f_λ (erg cm^{-2} Å^{-1} sec^{-1})	$\frac{I_{\lambda(0)}}{I'_\lambda}$	$\frac{B'_\lambda}{I'_\lambda(0)}$	$\frac{B_\lambda}{I'_\lambda(0)}$
0.20	0.018	0.04	0.03	0.06	1.2	0.5	0.60	0.30
0.22	0.066	0.13	0.10	0.21	4.5	0.5	0.62	0.31
0.24	0.094	0.19	0.14	0.29	6.4	0.5	0.63	0.32
0.26	0.19	0.39	0.30	0.60	13	0.5	0.64	0.32
0.28	0.37	0.85	0.66	1.30	25	0.51	0.66	0.29
0.30	0.87	1.65	1.30	2.45	59	0.53	0.67	0.36
0.32	1.25	2.24	1.88	3.25	85	0.58	0.687	0.39
0.34	1.68	2.68	2.37	3.77	114	0.63	0.710	0.44
0.36	1.69	3.03	2.56	4.13	115	0.62	0.730	0.42
0.37	1.87	3.15	2.45	4.23[a]	127	0.58	0.737	0.43
0.38	1.78	3.35	2.59	4.63	121	0.56	0.710	0.39
0.39	1.69	3.54	2.62	4.95	115	0.53	0.711	0.34
0.40	2.35	3.71	3.24	5.15	160	0.63	0.720	0.46
0.41	2.75	3.82	3.68	5.26	187	0.70	0.728	0.52
0.42	2.78	3.90	3.85	5.28	189	0.73	0.736	0.53
0.43	2.69	3.91	3.73	5.24	183	0.71	0.743	0.51
0.44	2.95	3.90	4.14	5.19	201	0.80	0.750	0.57
0.45	3.13	3.87	4.38	5.10	213	0.86	0.757	0.61
0.46	3.16	3.82	4.35	5.00	215	0.87	0.763	0.63
0.48	3.13	3.71	4.16	4.79	213	0.87	0.774	0.65
0.50	3.00	3.57	3.96	4.55	204	0.87	0.783	0.66
0.55	2.90	3.25	3.72	4.02	198	0.92	0.803	0.72
0.60	2.75	2.86	3.42	3.52	187	0.97	0.817	0.78
0.65	2.46	2.54	3.00	3.06	167	0.98	0.832	0.80
0.70	2.19	2.25	2.65	2.69	149	0.985	0.843	0.82
0.75	1.90	1.93	2.25	2.28	129	0.986	0.853	0.83
0.8	1.68	1.73	2.01	2.03	114	0.987	0.863	0.83
0.9	1.32	1.35	1.54	1.57	90	0.98	0.878	0.85
1.0	1.08	1.11	1.25	1.26	74	0.99	0.887	0.87
1.1	0.90	0.91	1.00	1.01	61	0.99	0.895	0.89
1.2	0.73	0.74	0.80	0.81	50	0.99	0.900	0.90
1.4	0.48	0.48	0.52	0.53	33	0.99	0.910	0.91
1.6	0.328	0.33	0.36	0.36	22.3	0.993	0.918	0.92
1.8	0.218	0.220	0.235	0.238	14.8	0.994	0.925	0.92
2.0	0.150	0.151	0.159	0.160	10.2	0.996	0.930	0.93
2.5	0.073	0.073	0.78	0.078	4.97	0.998	0.940	0.94
3.0	0.039		0.041		2.63	1.0	0.947	0.95
4	0.013 7		0.014 2		0.93	1.0	0.957	0.96
5	0.006 0		0.006 2		0.41	1.0	0.963	0.96

TABLE 2 (continued)

λ (μm)	B_λ (10^{10} erg sr^{-1} cm^{-2} μm^{-1} sec^{-1})	B'_λ	$I_\lambda(0)$	$I'_\lambda(0)$	f_λ (erg cm^{-2} Å^{-1} sec^{-1})	$\frac{I_{\lambda(0)}}{I'_\lambda}$	$\frac{B'_\lambda}{I'_\lambda(0)}$	$\frac{B_\lambda}{I'_\lambda(0)}$
6	0.003 1		0.003 2		0.21	1.0	0.968	0.97
8	0.000 93		0.000 95		0.063	1.0	0.976	0.98
10	0.000 34		0.000 35		0.023	1.0	0.983	0.98
12	0.000 18		0.000 18		0.012	1.0	0.985	0.98

[a] Hypothetical continuum between Balmer lines: 5.6.
Source: Adapted from Ref. 3.

Photometric calculations with polarized radiation sometimes can cause difficulties. For instance, when 100% plane-polarized radiation is incident on a perfectly diffusing surface, the scattered radiation will be completely depolarized and the geometrical factor that describes the spatial distribution of radiation ($1/\pi$) is identical to that for unpolarized incident radiation, providing a non–polarization-sensitive radiation detector is used. If the detector is polarization-sensitive (i.e., has a polaroid in front of it to detect plane-polarized radiation), the corresponding factor is $1/2\pi$. Because most surfaces are imperfect diffusers, the dominant plane-polarized scattered (reflected) radiation will lie in the same plane of polarization as the incident radiation. In this case, a calculation of the scattered radiation must take into account the phase function of the surface (Chap. 3).

The sun itself is not exactly a blackbody radiator. The internal nuclear furnace, which supplies the solar energy by transforming hydrogen into helium, is enclosed by a shell of hot gases. These gases have absorption and produce the Fraunhofer absorption spectrum. The solar output as a function of wavelength between 0.2 and 12 μm (above the earth's atmosphere) is shown in Table 2. This table is from an astronomy text, and the radiance per unit wavelength (i.e., μm^{-1}) is termed *intensity*. Also, 10^{10} erg sr^{-1} cm^{-2} μm$^{-1} \cdot$ s^{-1} = 10^7 W m^{-2} sr μm. The quantity B_λ is the average solar intensity in the presence of the Fraunhofer absorption lines, and B'_λ is that observed between the Fraunhofer lines. Because the solar intensity decreases toward the outer rim of the sun's disk (limb darkening), the center of the sun is brighter, and the quantities $I_\lambda(0)$ and $I'_\lambda(0)$ are those representing B_λ and B'_λ at the center of the solar disk.

The appropriate absolute reference values depend on the sensor system. If the sensor measures the average output of the entire sun or the

reflected and scattered energy produced therefrom, then B_λ is correct. If a very high resolution spectrometer is used to look at the entire sun or, similarly, the specularly reflected or scattered energy, then B'_λ is appropriate. For atmospheric observations whereby the center of the sun is viewed (within the 0.5° sun diameter), then $I_\lambda(0)$ or $I'_\lambda(0)$ is appropriate, depending upon whether the sensor is broadband or very high resolution, respectively.

IV. SURFACE REFLECTANCE

The bidirectional reflectance of a surface is the result of the interaction of radiant flux with the surface. The radiant flux, for instance, may consist of direct sunlight plus diffuse sky light. (We are considering wavelengths shorter than about 3 μm, where surface emission is negligible.) The interaction of the incident radiant flux with the surface is through scattering and absorption of the radiation, which occurs by virtue of the microstructure of the surface and the optical complex index of refraction. Various successful surface models relate the optical complex index of refraction and the surface geometry with the reflectance. These are generally based on radiative transfer analyses such as the Kubelka–Munk or modified Kubelka–Munk. However, the fundamental property is the optical complex index of refraction of the surface material.

An example of a typical material is silica sand from Cape Hatteras, (see Table 3) where n is the refractive index and nk is the absorption index (both are dimensionless) and t is the diffuse transmission of the sample used in the Modified-Kubelka-Munk (M-K-M) Model [3]. The graph shows plot of n and the log base 10 of nk, the absorption index. A model is needed to relate these basic optical properties to observed optical phenomena; the model ties the refractive and absorptive indices to the observations in the most general case. The structural properties of a surface affect the relative effect of the refractive portion on scattering and that of the absorptive portion on absorption. Because of the almost infinite range of measurable combinations, a surface model is appropriate to represent the phenomena most generally. Other complex indices of refraction are available [2,4]. (See Fig. 9.)

Surfaces as they occur in nature are almost never ideal, whether diffuse or specular; the surfaces generally exhibit some combination of specularity, diffuseness, shadowing, and retroreflection. The properties of specularity and diffuseness have already been alluded to; interparticulate shadowing occurs even from surfaces that have a detailed small-scale microstructure. Shadowing causes a diminished surface reflectance as the incident radiation angle increases; also, as the viewing angle increases, the surface reflectance

TABLE 3 Optical Constants for Sand, Cape Hatteras, North Carolina[a]

λ	T	r(μm)	nk	n
0.185	0.495E-03	0.190	0.192E-03	1.449
0.190	0.112E-02	0.193	0.174E-03	1.451
0.200	0.832E-03	0.200	0.183E-03	1.454
0.210	0.807E-03	0.204	0.189E-03	1.457
0.215	0.806E-03	0.214	0.183E-03	1.459
0.220	0.861E-03	0.210	0.189E-03	1.462
0.225	0.108E-02	0.218	0.180E-03	1.464
0.233	0.122E-02	0.220	0.181E-03	1.467
0.240	0.126E-02	0.221	0.184E-03	1.470
0.260	0.197E-02	0.237	0.173E-03	1.472
0.280	0.248E-02	0.247	0.171E-03	1.475
0.300	0.422E-02	0.236	0.176E-03	1.478
0.325	0.488E-02	0.265	0.162E-03	1.480
0.360	0.826E-02	0.298	0.141E-03	1.483
0.370	0.110E-01	0.317	0.126E-03	1.486
0.400	0.135E-01	0.348	0.115E-03	1.488
0.433	0.232E-01	0.330	0.116E-03	1.491
0.466	0.299E-01	0.436	0.769E-04	1.493
0.500	0.399E-01	0.470	0.658E-04	1.496
0.533	0.484E-01	0.490	0.604E-04	1.499
0.566	0.552E-01	0.601	0.381E-04	1.501
0.600	0.597E-01	0.558	0.471E-04	1.504
0.633	0.614E-01	0.554	0.497E-04	1.507
0.666	0.821E-01	0.578	0.409E-04	1.509
0.700	0.800E-01	0.578	0.434E-04	1.512
0.817	0.798E-01	0.529	0.627E-04	1.515
0.907	0.858E-01	0.571	0.557-04	1.517
1.000	0.906E-01	0.563	0.616E-04	1.520
1.105	0.870E-01	0.587	0.622E-04	1.522

[a] *nk* determined from MKM theory. Effective sample thickness = 0.0144 cm.

decreases nonlinearly (see Fig. 8 and Fig. 9 in chapter 1). Furthermore, as the incident radiation and sensor come into alignment (phase angle of 0°), there is a strong increase in reflected (scattered) radiation; this effect is termed retroreflectance see ref. 2 pp 25 and ref. 4 pp 139–152 (or in astronomy, the opposition effect).

The atmosphere can significantly affect the remotely sensed photometry of surfaces, sometimes by an order of magnitude, particularly visibility. The almost infinite variety of possible atmospheric effects again

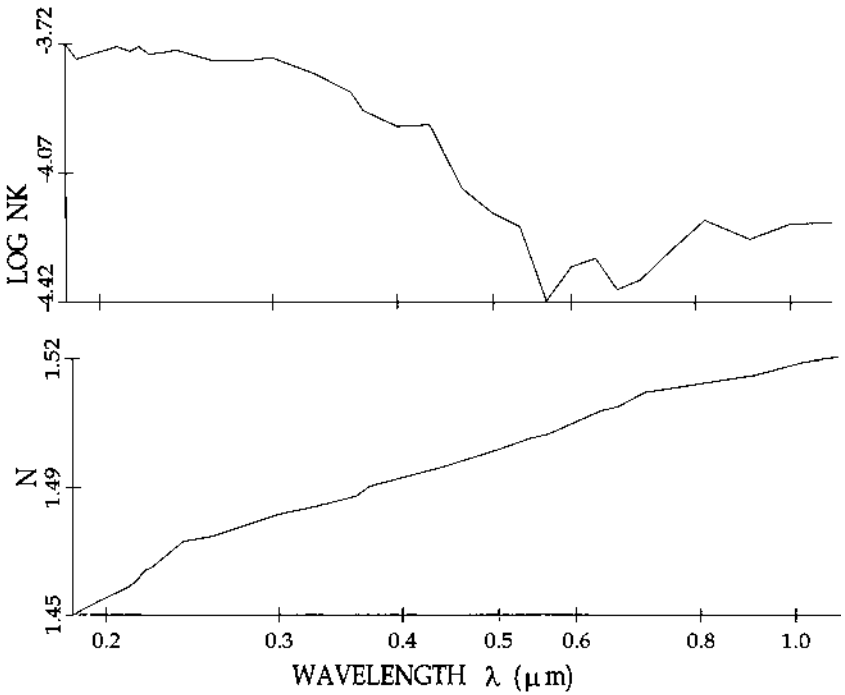

FIGURE 9 Complex index of refraction of Haleakala volcanic ash: nk, absorption index and n, refractive index.

requires the use of modeling to represent them. Basically, atmospheric effects broadly include scattering and absorption: Rayleigh scattering, molecular absorption, aerosol scattering, and aerosol absorption. The aerosol scattering and absorption again require a knowledge of their optical complex index of refraction for modeling. The Rayleigh scattering may be readily represented theoretically, but molecular absorption is particularly tricky, because it depends on the molecular line shapes; these in turn depend on the pressure and temperatures near the molecules. The latter vary throughout the earth's atmosphere, particularly vertically but also to some extent horizontally. The modeling of molecular absorption bands (which are the sums of the effects of many lines) is dependent on the line parameters and the combination techniques, and these techniques are still being developed and evaluated. More specifically, water vapor, carbon dioxide, ozone, nitrogen oxides, methane, carbon monoxide, nitrogen, and oxygen are the strong molecular absorbers of interest. A thorough

discussion of the present state of knowledge is embodied in a section on atmospheric effects, see chapter 21.

REFERENCES

1. Reeves, R.G. Manual of remote sensing Falls Church: American Society of Photogrammetry, 1975.
2. Egan, W.G.; Shaw, G.E. Effect of Aerosols on Optical Remotely Sensed Data, Proc Fifteenth Int Symp Remote Sensing. ERIM, 1981; 476–503.
3. Allen, C.W. Astrophysical Quantities. 2nd Ed.; Athlone Press: London, 1963.
4. Egan, W.G.; Hilgeman, T.W. Optical Properties of Inhomogeneous Materials, Academic Press Inc.: New York, 1979; 81–125.

3

Polarization

I. INTRODUCTION

Polarization was initially introduced and characterized in Chapter 2 (see Fig. 1 of Chap. 2). Polarization is quite common in nature. However, its use in remote sensing has been limited to astronomy, where every bit of information available in the optical spectral region must be used in analyses because most astronomical objects will not be reached for in situ measurements within our lifetime.

Terrestrial polarization occurs in the reflection and scattering of light from water and land surfaces, roads and highways, windows, and vehicle bodies, to name a few. Contrast enhancement of clouds may be achieved by using a polaroid filter on a camera (with color film). Glare from polarized reflection from water surfaces can be minimized by using polarizing eyeglasses. The radiation scattered from the moon's surface is partially polarized, and this property was used to advantage to model it prior to the lunar landing; the object was to determine the surface bearing strength in order to design the lunar lander (the LM; lunar module) appropriately. All gas lasers with Brewster angle mirrors produce 100% polarized radiation. In fact, every surface produces some polarization of the scattered radiation, even if only very slight.

This chapter continues with the description of polarization, its production, and its detection by virtue of the interaction of radiation with matter. The emphasis is on the spectral region between 0.185 and 3.0 μm, where reflected and scattered radiation dominate; polarization of emitted radiation is mentioned briefly. The present status of surface and atmospheric modeling is described.

II. RADIATION SOURCES

A single atom emitting a photon of radiation would be expected to produce plane-polarized waves, though of random orientation. Many atoms of different elements clustered together, with pressure-broadened spectral lines—as in the sun or stars—would produce blackbody radiation (Fig. 1). The radiation behaves in accordance with the Planck function, with the radiation intensity plotted as a function of wavelength. The radiation from the sun would be expected to be unpolarized; however, the existence of magnetic fields causes preferential orientation of atoms located therein (Zeeman effect), and plane-polarized or circularly polarized radiation occurs depending upon the field direction.

Terrestrially, blackbody radiation sources are incandescent or heated solids. In solids, the atoms are linked to each other by lattice forces, and the resulting effect is the smearing out of the sharp spectral lines that would normally be emitted by the individual atoms. The result is a continuous radiation emission, although not usually quite equal to that of a blackbody. In this case, the radiation is less, and the emission is termed graybody (i.e., the emissivity of the surface is less than 1). For solids (and liquids), where a well-defined surface exists, a directional radiation property exists whereby polarized radiation is emitted. The polarization is described by Fresnel's equations. These expressions arise from the application of Maxwell's equations to surfaces, with the appropriate boundary conditions; the fundamental optical properties of the surfaces (i.e., the complex index of refraction) determine the fields that exist within and outside the surface. In reality, surfaces are not perfectly smooth, and modifications to Fresnel's equations are necessary to account for the surface roughness.

However, for a smooth surface, the emissivity ε is made up of two components relative to the plane of emission, one parallel ($\|$) and one perpendicular ($\perp$):

$$\varepsilon = \frac{1}{2}(\epsilon_{\|} + \epsilon_{\perp}) \tag{1}$$

$$\varepsilon_{\|} = \left[\frac{2\sin\theta\cos\phi}{\sin(\theta+\phi)\cos\phi-\theta)}\right]^2 \tag{2}$$

$$\varepsilon_{\perp} = \left[\frac{2\sin\theta\cos\phi}{\sin(\theta+\phi)}\right]^2 \tag{3}$$

where θ is the angle of emission measured from the normal to the surface and ϕ is the angle of incidence for internally generated blackbody radiation. Snell's law is obeyed:

$$\sin\theta = m\sin\phi \tag{4}$$

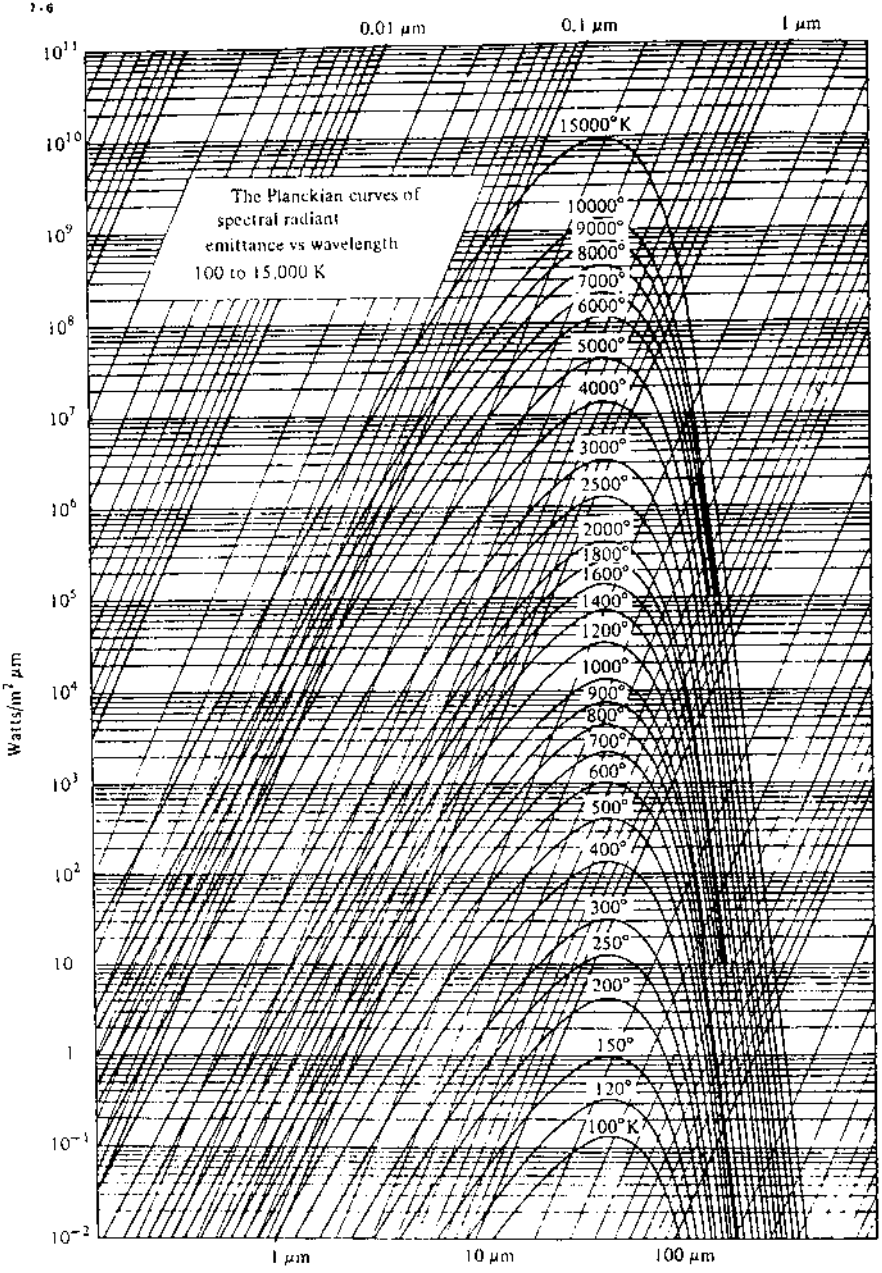

FIGURE 1 An interesting and very useful diagram of Planckian curves is obtained by inclining the vertical lines of the log-log representation so that the peaks of the maximum spectral emittance are aligned vertically. The entire range of temperatures from 100 to 15,000 K can thus be shown most conveniently with good separation between the curves, including the long-wavelength area of the spectral band.

where m is the optical complex index of refraction:

$$m = n - ik_0 \tag{5}$$

Equations (1)–(4) can, in principle, be combined to give the total emissivity ε as a function of the angle of emission from the surface normal (θ) and the optical complex index of refraction n:

$$\varepsilon = \varepsilon(\theta, n, k_0) \tag{6}$$

Typically, the total normalized emissivity and the parallel and perpendicular components are shown versus emission angle as in Fig. 2. It can be seen that the parallel component is stronger than the perpendicular component. The emission is Lambertian (cosine function) near normal

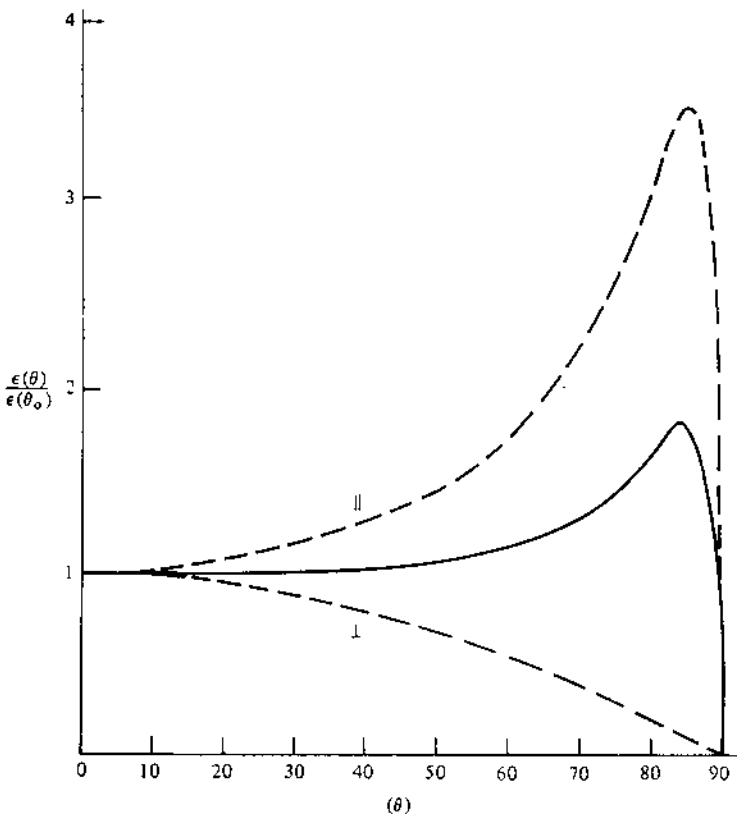

FIGURE 2 Normalized emissivity vs. emission angle.

up to about $\theta = 55°$, for instance, for a glass radiator having a refractive index of 1.5 (Fig. 3). For larger angles of emission θ, the directional spectral emissivity decreases; the ∞ curve is for a thick plate of glass, and the other curves are for thinner plates having the dimensionless product of thickness and spectral absorption coefficient equal to 2, 1, 0.3, and 0.1. The reason for the decrease in emissivity with increased angle of emission is that the directional transmittance of the glass/air surface decreases at the larger angles.

Thus, tungsten incandescent filaments can be expected to produce some polarized radiation at all wavelengths depending on their physical structure. A convenient optical structure that serves to remedy this situation is the Lyot depolarizer. It is placed in the optical path between the tungsten lamp source and the object to be illuminated. The depolarizer [2] is made of two quartz or gypsum plates cut parallel to their optic axes. Their thicknesses are in the ratio of 2:1, and they are glued together with Canada balsam so that their optic axes make an angle of 45°. Because noncoherent radiation of varying wavelength undergoes varying retardation passing through the assembly, any broadband polarization in the incident radiation will be eliminated. It should be noted that the Lyot depolarizer will not be effective for monochromatic, coherent radiation.

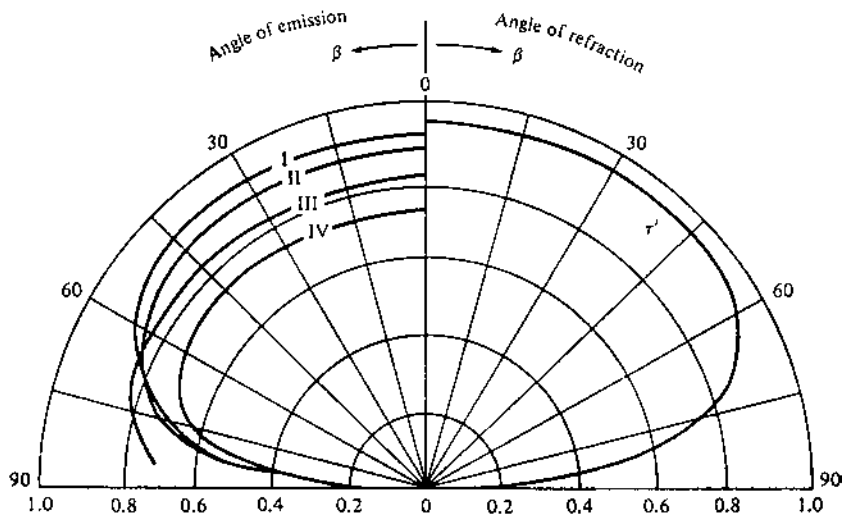

FIGURE 3 Angular variation of the transmissivity τ' of glass/air surface calculated for $n_{glass} = 1.5$ (right-hand side), and the emissivities of various metals (left). I, glass; II, clay; III, alumina (coarse); IV, copper oxide. (After Ref. 1.)

III. MATHEMATICAL REPRESENTATION

Plane-polarized radiation was depicted in Fig. 1 of Chapter 2 and represented as Eq. (2), (3), or (4) of that chapter. The plane of polarization of this wave could also rotate continuously in the same plane, resulting in a circularly polarized wave. It could rotate clockwise (viewed end on from the left), producing right circularly polarized radiation, or counterclockwise, producing left circularly polarized radiation. It is to be noted that the **E** and **H** fields do not necessarily occur concurrently in phase (maximum **E** with maximum **H**) in free space. In some crystals and at metal surfaces, the **E** and **H** amplitudes can be out of phase. In another variant, the **E** vector could simultaneously rotate and periodically change in amplitude, resulting in elliptically polarized radiation.

The preceding characteristics can be expressed mathematically. A circularly polarized wave ξ can be represented as the sum of two equal-amplitude sine waves in mutually perpendicular directions, with the second one phase-displaced by 90° ($\pi/2$):

$$\xi = \mathbf{i}|\mathbf{A}|e^{i\phi} + \mathbf{j}|\mathrm{A}|e^{i(\phi \pm \pi/2)} \tag{7}$$

where the + and – signs refer to positive and negative circular polarization, respectively.

Elliptically polarized radiation is represented by a wave consisting of nonequal mutually perpendicular components A_1 and A_2:

$$\xi = \mathbf{i}A_1 e^{\mathrm{i}\phi} + \mathbf{j}A_2 e^{\mathrm{i}(\phi \pm \pi/2)} = \mathbf{E}_1 + \mathbf{E}_2 \tag{8}$$

If the A_1 and A_2 plane-polarized waves are out of phase by some angle ϕ_2, then the representation is

$$\mathbf{E}_1 = \mathbf{i}A_1 e^{i\phi}, \qquad \mathbf{E}_2 = \mathbf{j}A_2 e^{i(\phi+\phi_2)} \tag{9}$$

The phase angle ϕ_2 can be the result of scattering (or reflection) of the second plane wave off a material having a significant absorption (see, for instance, Ref. [3], Eq. I-19).

When temporally incoherent radiation is partially plane-polarized and the intensities (absolute amplitudes squared) measured in mutually perpendicular directions are I_x and I_y, a convenient representation of plane polarization is percent plane polarization:

$$\%\ \text{polarization} = \frac{I_x - I_y}{I_x + I_y} \times 100 \tag{10}$$

The plane of polarization θ_0 is given by

$$\theta_0 = \tan^{-1}(I_x/I_y) \tag{11}$$

If circular polarization exists, these expressions represent only the values resulting from plane polarization. It is thus seen [Eq. (10)] that polarization is generally highly accurate photometry, because it may be the small difference between two terms $|I_x|$ and $|I_y|$, which in themselves may each be large.

Polarization is produced by Fresnel reflections of radiation at a surface. The vector expressions for the parallel and perpendicular reflected components are

$$\hat{R}_{\|} = \left\{ \frac{(\hat{m}_{i'}/\hat{m}_i)^2 \cos\hat{\theta}_i - [(\hat{m}_{i'}/\hat{m}_i)^2 - \sin^2\,\hat{\theta}_i]^{1/2}}{(\hat{m}_{i'}/\hat{m}_i)\cos\hat{\theta}_i + [(\hat{m}_{i'}/\hat{m}_i)^2 - \sin^2\,\hat{\theta}_i]^{1/2}} \right\}^2 \tag{12a}$$

and

$$\hat{R}_{\perp} = \left\{ \frac{\cos\hat{\theta}_i - [(\hat{m}_{i'}/\hat{m}_i)^2 - \sin^2\,\hat{\theta}_i]^{1/2}}{\cos\hat{\theta}_i + [(\hat{m}_{i'}/\hat{m}_i)^2 - \sin^2\,\hat{\theta}_i]^{1/2}} \right\} \tag{12b}$$

where $\hat{\theta}_i$ is the angle of incidence of the wave to the surface normal, $\hat{m}_i$ is the complex index of refraction of the incident medium, and $\hat{m}_{i'}$ is the complex index of refraction of the second refractive medium.

Figure 4 shows typical properties of the reflected intensities as a function of incident angle for dielectric reflection, where both $\hat{m}_i$ and $\hat{m}_{i'}$ are real. The Brewster angle occurs at ϕ, where the smaller parallel component goes to zero and there is 100% polarization with the perpendicular component. The tangent of ϕ yields the index of refraction of the dielectric.

For metallic reflection, where $\hat{m}_{i'}$ is complex, a typical set of reflectance curves is shown in Fig. 5; here it can be seen that the trends in the reflecting power are analogous to those of the dielectric case. However, the perpendicular component does not go to zero but achieves a minimum at ϕ, termed in this instance the *principal angle of incidence*.

From the application of Fresnel's equations to dielectric and metallic reflection it is found that a phase change occurs for the electric vector. This is shown in Fig. 6 for the typical dielectric case and in Fig. 7 for metallic reflection. For pure dielectric reflection (Fig. 6), a phase change (δ_s) of 180° (π) occurs for the perpendicular component, but the parallel component has no phase change (δ_p) up to the Brewster angle (ϕ), when a phase change of π occurs with increased angle of incidence. A phase change of π merely means a polarity reversal of the wave. However, for metallic reflection (Fig. 7), the phase change is more involved; of particular interest is the difference δ between δ_p and δ_s. This difference is always 90° at the principal angle of incidence ϕ. The principal azimuth ψ is given by

$$\tan\psi = R_{\|}/R_{\perp} \tag{13}$$

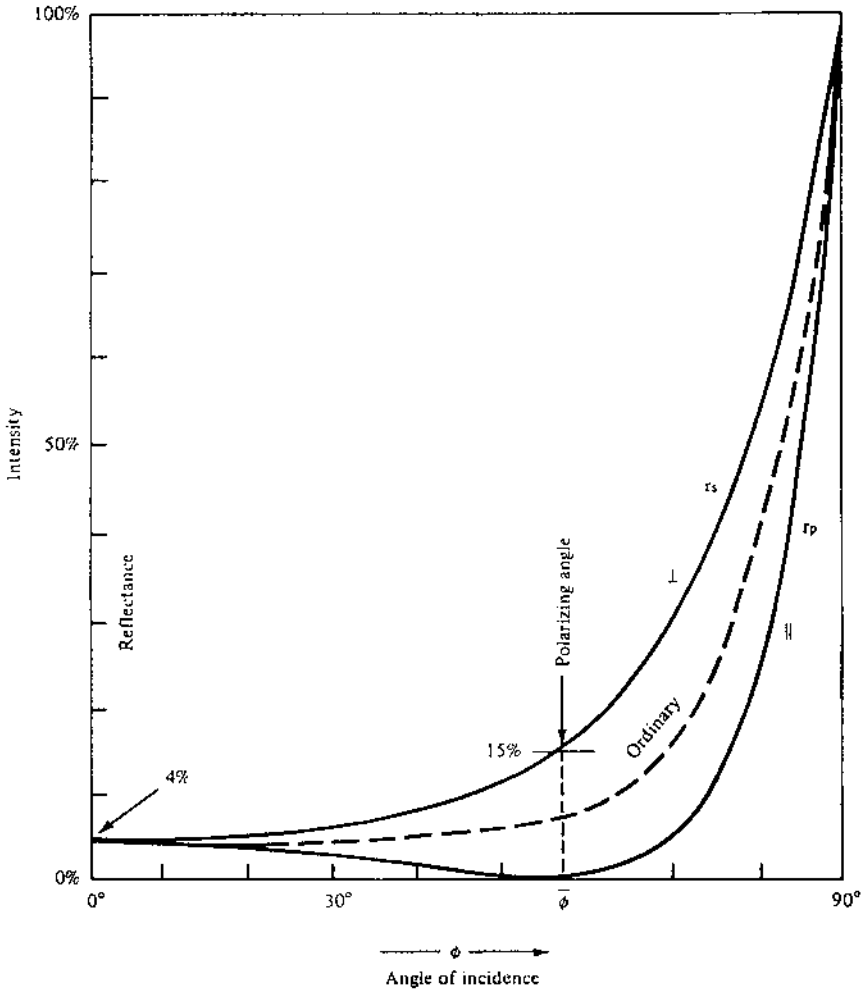

FIGURE 4 Reflectances for a dielectric having $n = 1.50$. (From Ref. 4.)

For metallic reflection at angles other than ϕ, the phase change δ will be some other value. This will result in $\delta = \phi_2$ in Eq. (9), and the amplitudes A_1 and A_2 will be given by the Fresnel reflectivity.

For rough surfaces, an approach frequently used is to assume that an assemblage of facets can be employed to represent the irregularities. Then the Fresnel laws of reflectance can be applied statistically to characterize the reflectance (and scattering). However, in these models, as carefully as they

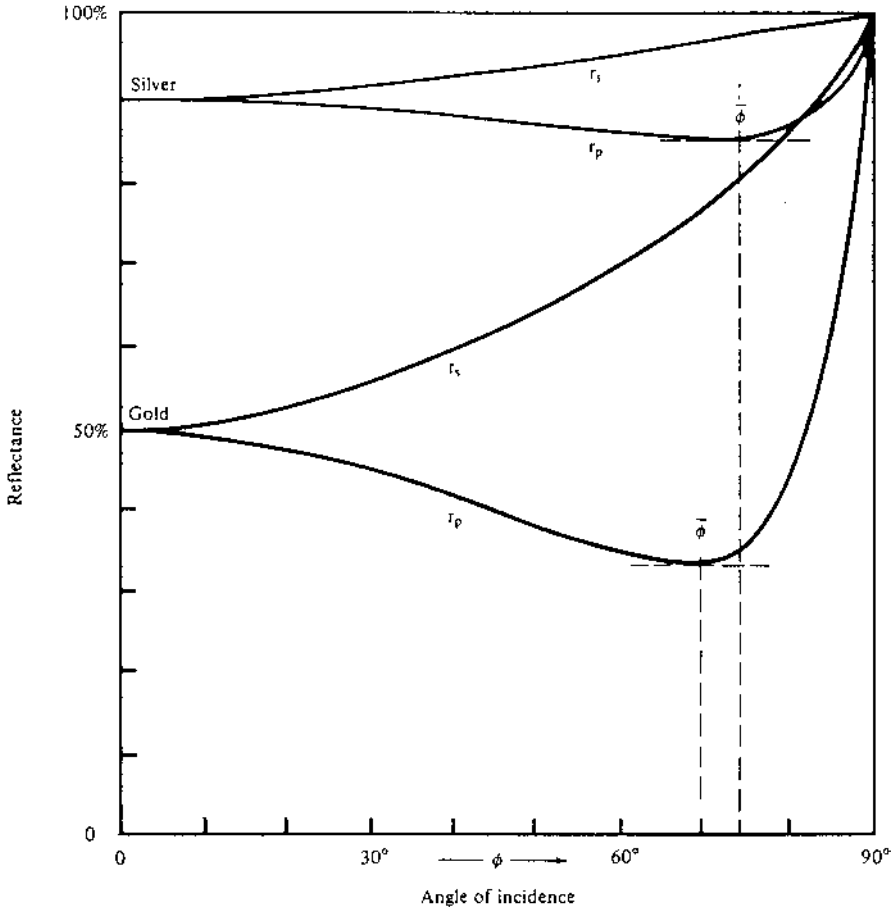

FIGURE 5 Reflectances for plane-polarized white light off gold and silver mirrors. (From Ref. 4.)

may be constructed, an empirical factor is always needed somewhere to represent certain uncalculable effects.

IV. DETECTION AND MEASUREMENT OF POLARIZED RADIATION

To sense polarization in an electromagnetic wave, an optical element is necessary that responds nonuniformly to the vector directional property of

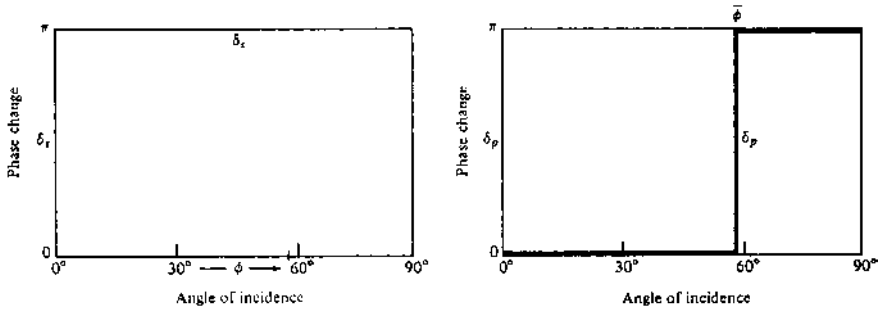

FIGURE 6 Phase change of the electric vector of plane-polarized light externally reflected from a dielectric. (From Ref. 4.)

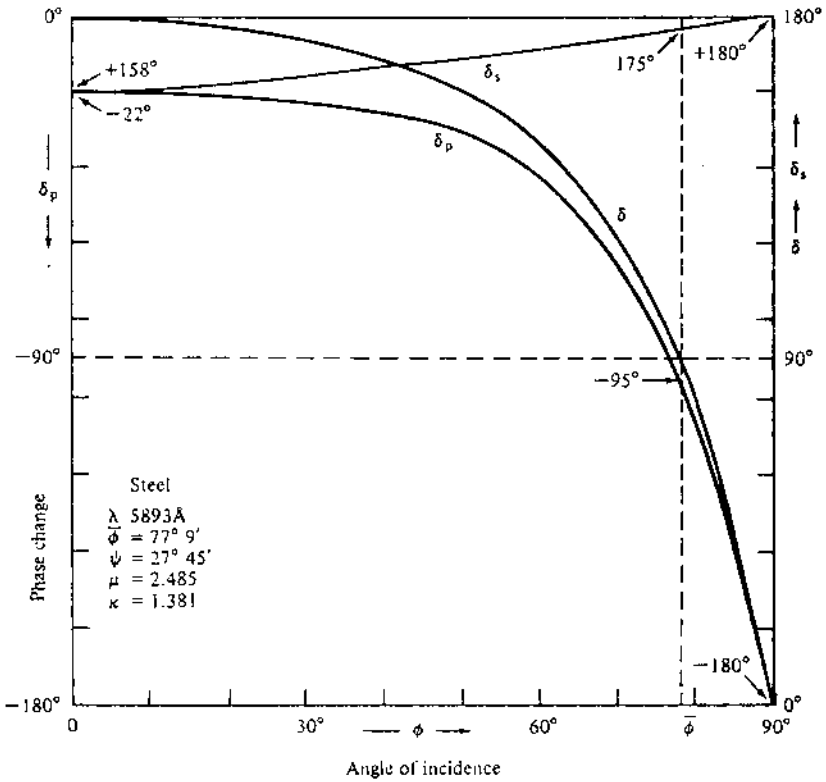

FIGURE 7 Phase changes of the electric vector for reflection from a metallic steel mirror. (From Ref. 5.)

the incident radiation. Such devices are polaroids, wire grid polarizers, dichroic polarizers, piles of plates, double refraction prisms (Glan-Foucault, Nicol, Wollaston, or Rochon, for instance), or asymmetrical scatterers. Various degrees of mechanization and computational facilities have been described in the extensive literature on polarization analysis. This section describes some of the convenient polarization analyzers, the basic reasoning for the analysis of polarized radiation, and a few mechanized versions.

The most antique instrument for analyzing polarization is the wire grid; Heinrich Hertz was the first to use the wire grid as a polarizer in 1888 to evaluate the properties of the then recently discovered radio waves. The grid, consisting of 1 mm copper wires spaced 3 cm apart, was used to check the properties of 66 cm radio waves. By orienting the grid parallel and perpendicular to the electric vector of the radiation, the electric field was either "short-circuited" or permitted to pass through respectively. This property of asymmetrical absorption is termed dichroism [6].

This same principle was extended into the infrared by duBois and Rubens in 1911 with 25 μm diameter noble metal wires for polarization analyses of radiation from 24 to 314 μm. The most recent application was by Bird and Parrish in 1960 [7]; wire grids were made by evaporating gold onto a plastic replica of a diffraction grating (Fig. 8). Such grids are available commercially from Perkin-Elmer with transmission in the wavelength range from 2.5 μm to well beyond 333 μm. The wavelength range from 2.5 to 35 μm uses a silver bromide substrate, and the region between 20 and 333 μm employs a polyethylene substrate. The polarization properties of these wire grid polarizers are shown in Fig. 9; the plot is the ratio of the parallel component of intensity to the perpendicular versus wavelength. The larger the ratio, the

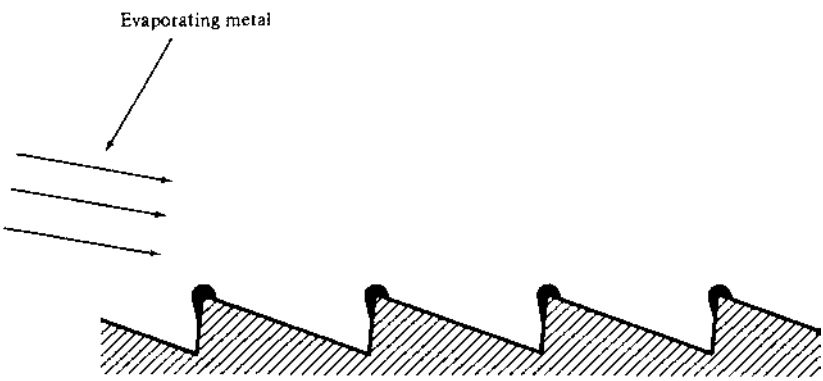

FIGURE 8 Evaporation of metal on a plastic grating replica.

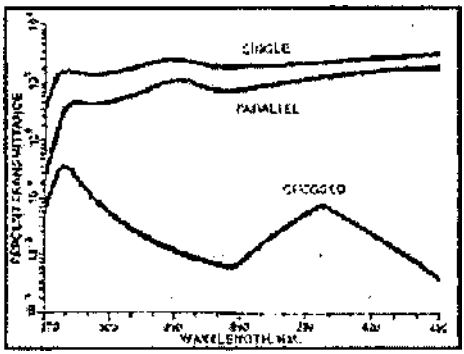

FIGURE 9 HNP'B-Linear polarizer for near-ultraviolet. Features: Broad-bandpolarizer (275–750 mm) for the near-ultraviolet as well as the visible region. Product Application: Photometric instruments, photography, microscopy, fluorescence.

better the performance of the wire grid as an analyzer. There is some inherent attenuation of the wire grid analyzer (64% at 2.6 μm) because of the obscuration of the optical path through it by the wires.

As a result of research by E. H. Land, in 1938 the chemical analog of the wire grid was invented. Long, thin polymer molecules aligned nearly parallel to each other, with high conductivity produced by free electrons associated with the iodine atoms in the molecules, served to absorb the electric field parallel to the molecules: the perpendicular component then passed through with little absorption.

The transmittance, T, of a single-sheet polarizer in a beam of linearly polarized incident light is given by

$$T = k_1 \cos^2 \theta + k_2 \sin^2 \theta$$

where θ is the angle between the plane of polarization of the incident beam (more accurately, the plane of the electric field vector of the incident beam) and the plane of preferred transmission of the polarizer. k_1 and k_2 are the principal transmittances of the polarizer, and both are functions of wavelength. Ideally, $k_1 = 1$ and $k_2 = 0$. In reality, k_1 is always somewhat less than unity, and k_2 always has some small but nonzero value.

If the incident beam is unpolarized and the angle θ is redefined to be the angle between the planes of preferred transmission (planes of polarization) of two sheet polarizers in near contact, it can easily be shown that the transmittance of the pair is given by

$$T_{pair} = k_1 k_2 \sin^2 \theta + 1/2(k_1^2 + k_2^2) \cos^2 \theta \tag{14}$$

If we define

$$H_{90} = T_{\text{pair}}(90°) = k_1 k_2 \tag{15}$$

$$H_0 = T_{\text{pair}}(0°) = 1/2(k_1^2 + k_2^2) \tag{16}$$

Equation (16) can be simplified to

$$\begin{aligned} T_{\text{pair}} &= H_{90}\sin^2\theta + H_0\cos^2\theta \\ &= H_{90} + (H_0 - H_{90})\cos^2\theta. \end{aligned}$$

The quantity H_{90} is called the closed transmittance or extinction ratio, and the quantity H_0 is called the open transmittance. Both quantities are wavelength-dependent, as is shown in Fig. 10. Because of the large ranges of open and closed transmission, it is convenient to graph the optical densities corresponding to these transmissions rather than the transmissions themselves. The open and closed optical densities are defined as follows:

$$\Delta_0 = \log\left(\frac{1}{H_0}\right) \qquad \text{and} \qquad \Delta_{90} = \log\left(\frac{1}{H_{90}}\right)$$

Various polarizers are available from Melles-Griot (www.mellesgriot.com) and the 3M Corporation. The usable wavelengths cover the region from 0.275 to 2.0 μm. Table 1 lists some significant linear polarizers, their region of operation, and the reference curves for their performance. The list is not all-inclusive but represents practical, inexpensive polarization analyzers that are available in 2 in. (51 mm) diameter, some mounted in holders appropriate for use in laboratory and field measurements.

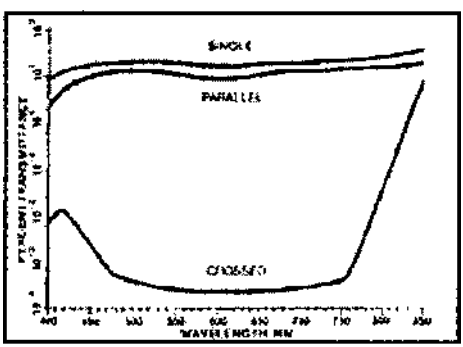

FIGURE 10 HN32 - Neutral linear polarizer. Features: Represents the best balance between transmission and extinction for general use. Extinction transmission is about 0.005%. Product Application: Variable-density filter systems, photoelastic stress analysis, and other applications where light modulation is necessary.

TABLE 1 Linear Fixed Wavelengths, Polarizers—Operating Ranges and Reference Curves

Polarization analyzer	Wavelength region μm (cm^{-1})	Reference curve
L1271025 KRS-5 (Perkin-Elmer, wire grid)	2–22 (450–5000)	Mid-IR
L1271026 Polyethylene (Perkin-Elmer, wire grid)	22–1000 (10–450)	Far-IR
L1271027 CaFl (Perkin-Elmer, wire grid)	1–4 (2500–10,000)	Near-IR
HNP′B (3M)	0.275–0.750	Fig. 9
HN32 (3M)	0.450–0.750	Fig. 10
HN38 (3M)	0.470–0.700	Fig. 11
HN42 (3M)	0.400–0.700	Fig. 12
HN42HE (3M)	0.400–0.700	Fig. 13
HR (3M)	0.8–2.0	Fig. 14
O3FPGXXX (Melles Griot)	0.350–0.50	Fig. 15
O5FPI00X (Melles Griot)	0.8–1.2	Fig. 16
O3FPI01X (Melles Griot)	1.2–1.6	Fig. 17

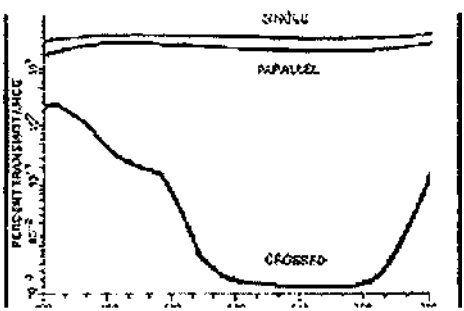

FIGURE 11 HN38 - Neutral linear polarizer. Features: Exceptionally free from color distortion. Product Application: Camera filters, studio light filters, variable color filter systems, other applications where high transmission is required along with a medium extinction density.

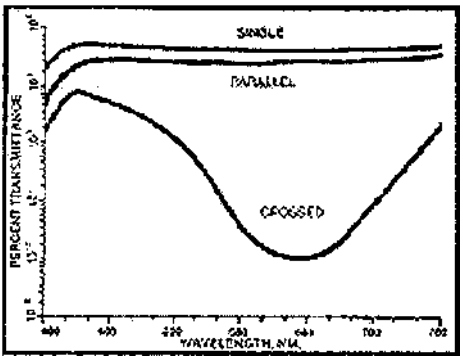

FIGURE 12 HN42 - Neutral linear polarizer. Features: High transmission. Product Application: Photographic, spectrographic, and other applications where insertion losses must be kept to a minimum.

More exotic laboratory-type polarization analyzers are piles of plates, double refraction prisms, and asymmetrical scatterers. These devices are described in the vast literature on polarization and generally cause mounting and alignment problems, particularly when the analyzer is to be rapidly rotated as in a system with a wide optical acceptance angle. The additional requirement is that the operation be automated and computerized with a minimum accuracy of $\pm 0.1\%$ polarization.

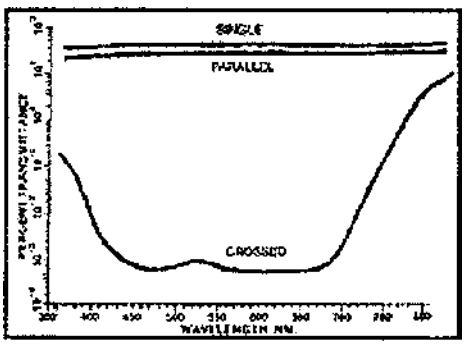

FIGURE 13 HN42HE - Neutral linear polarizer. Features: Very high efficiency linear polarizer. Both maximum and minimum transmittance show low color saturation. Product Application: Recommended for applications requiring high transmission and high dynamic range.

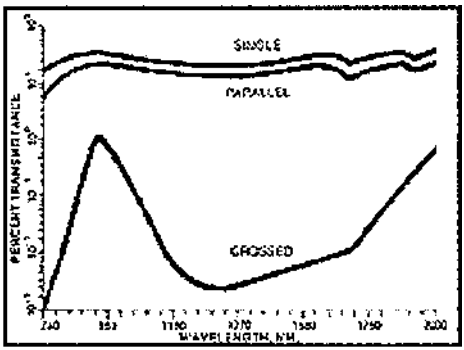

FIGURE 14 HR - Linear polarizer for near-infrared. Features: Broadband polarizer for the region 800–2000 mm. Product Application: Shutter and light control devices for IR lasers, LED and other infrared sources, photodetectors in non-visible security systems, infrared photography, crystallographic studies.

In polarization observations, measurements are required as a function of wavelength. In the original astronomical observations, the ultraviolet, blue, and visible (UBV) regions were sensed using Schott-Jena glass filters; this was before the advent of precision interference filters. However, interference filters are now available that span the range from the ultraviolet to the infrared. Also, some are available in a liquid crystal filter tunable and narrow band that is applicable to polarization measurements.

Two liquid crystal tunable filters are available from Cambridge Research and Instrumentation, Inc., the sole commercial supplier of these

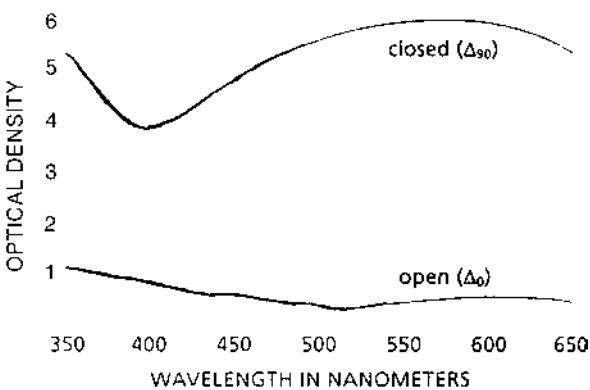

FIGURE 15 Optical density for pair of 03 FPG dichroic sheet polarizers.

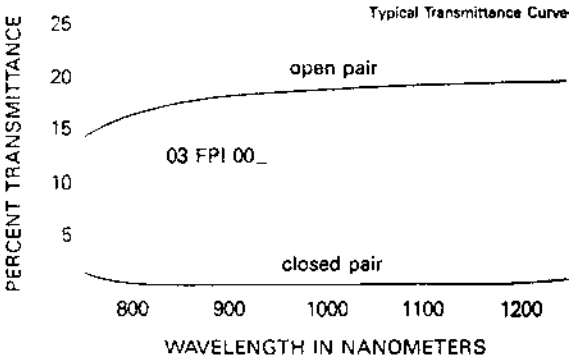

FIGURE 16 Typical polaroid transmittance curve for wavelength 800 to 1200 nm.

devices. The near-infrared unit covers the spectral region from 650 to 1050 nm. A second visible range liquid crystal tunable filter covers the spectral region from 400 to 720 nm, see Table 2. These devices use a unique Lyot [2] birefringent filter–based design. A Lyot filter is composed of two or more modules, each of which consists of an entrance polarizer, a birefringent crystal, and an exit polarizer. This design provides a unique capability to produce a device that provides for a rapidly tunable narrowband pass filter that can cover a broad spectral range. However, this design introduces significant polarization artifacts that must be calibrated if this device is to be exploited for hyperspectral polarization imaging experiments.

Liquid crystal tunable filters provide a selectable 10 nm wide spectral bandwidth. Random access time to a selected wavelength is 50 ms. The

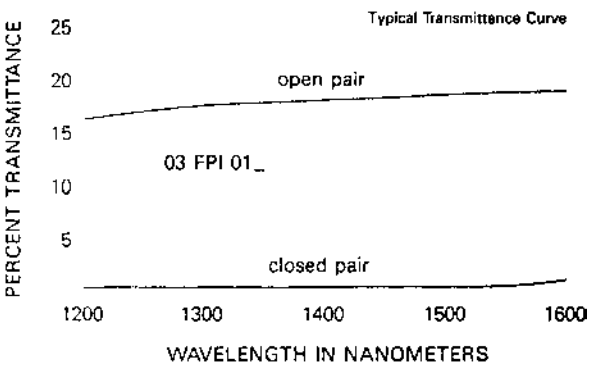

FIGURE 17 Typical polaroid transmittance curve for wavelength 1200 to 1600 nm.

TABLE 2 Equivalent Optical Wavelengths

μm (wavelength)	cm^{-1} (wavenumber)	Å (Angstroms)	mμ(nm) (wavelength)	mm (wavelength)
0.4	25,000	4000	400	0.004
1.0	10,000	10,000	1000	0.01
10.0	1000	100,000	10,000	0.1

The wavenumber (cm^{-1}) is used instead of wavelength to obviate the necessity of a large number of zeros to designate the wavelength.

clear aperture is 20 nm. The field of view is ($\pm 7°$). The transmission curves for the visible band and near-infrared liquid crystal tunable filters are shown in Fig. 18.

In order to sense polarized radiation, much less radiation itself, an appropriate detector is necessary. The human eye is one of the oldest polarization sensors but is rather inadequate for quantitative work. The eye has been used quite extensively in photometry to judge matching brightness, but

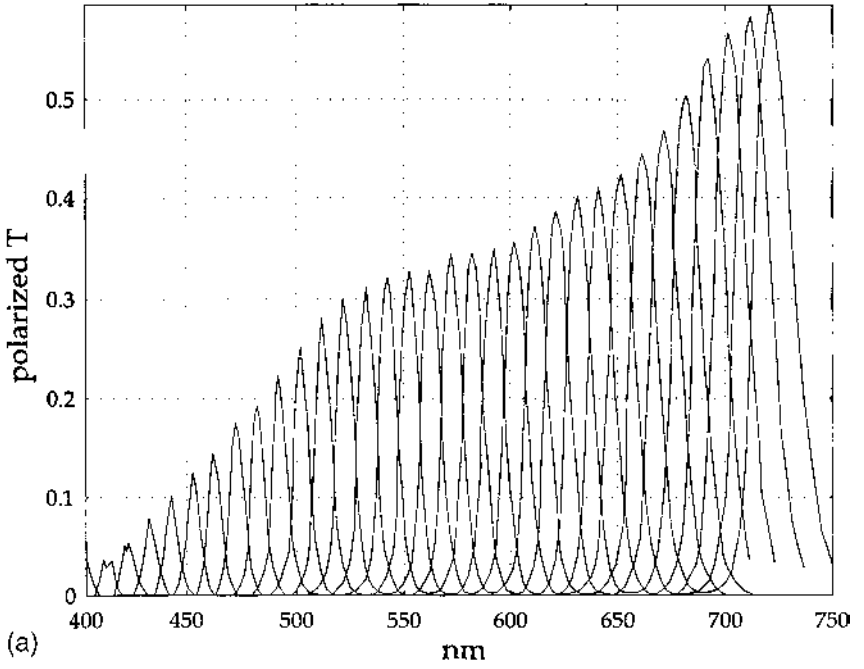

FIGURE 18 Transmission curves for (a) visible and (b) near-infrared liquid crystal tunable filter units.

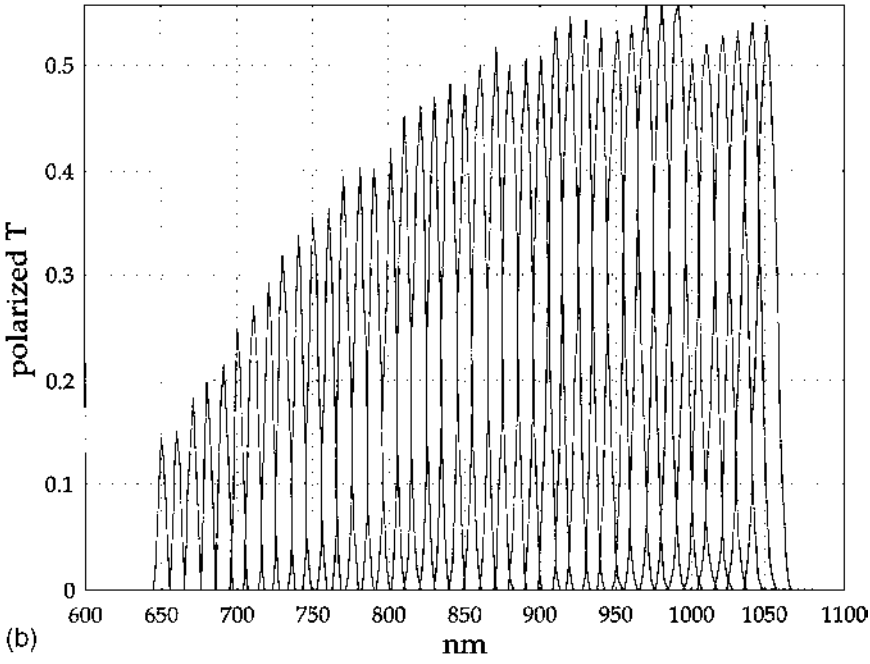

FIGURE 18 Continued.

the range of brightnesses occurring in polarimetry and the need for quantification require some form of accurate photometric detector. Types of detectors include phototubes, photomultipliers, photodiodes, thermocouples, thermopiles, pneumatic bolometers, and photoconductive or photovoltaic semiconductors. The chapter on sensor systems (Chapter 6) discusses detectors in detail, because the choice of appropriate detector is tied into system considerations such as wavelength sensitivity of the detector, the frequency response, and the sensor area.

To characterize polarization, a series of logical steps are necessary: these steps are presented in Fig. 19. The steps require a polarization analyzer and a device that serves to retard one radiation component relative to the component perpendicular to it; this device is termed a retardation plate or wave plate. The retardation plate, when appropriately chosen, can efficiently convert any form of polarization into any other form. More specifically, a primary function of retarders is to produce and analyze unusual circular and elliptical polarization.

Physically, a retarder is a thin crystalline plate, such as calcite, with its optic axis parallel to the plane of the plate. The index of refraction that it sees depends upon whether the incident ray from the left is polarized parallel to the

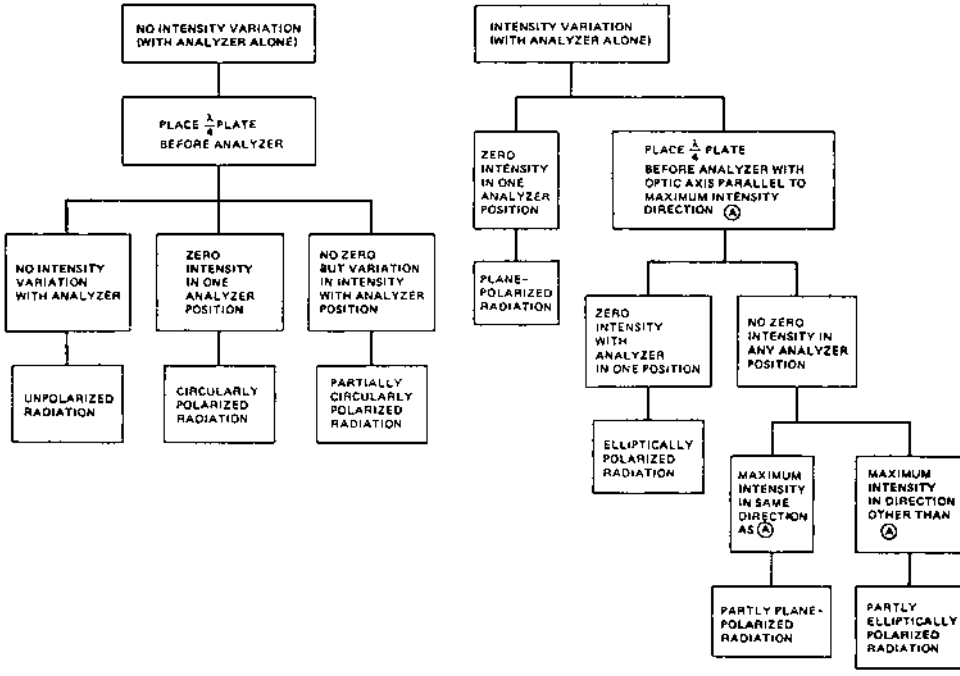

FIGURE 19 Characterization of polarization.

x axis or the y axis. The index of refraction along the y axis (o ray) is larger than that along the x axis (e ray), resulting in a wave that travels faster when polarized along the x axis. Thus, when a wave is plane-polarized at an angle of 45° (halfway between the x and y axes), it is split into two components along the respective axes. If the relative delay of the fast and slow waves is an integral multiple of a wavelength, there is no effect on the ray emerging from the retarder except for some slight loss due to external reflection from the left side of the plate, internal reflection on the right side of the plate, and absorption within the plate (and possibly scattering from molecules within the plate). However, if the delay is some fraction of a wavelength, various things may happen. Thus, if the delay is 90° (i.e., $\pi/2$ or $\lambda/4$), it may be seen [Eq. (7)] that circularly polarized radiation is produced. Conversely, circular polarization can be converted to linear polarization by using a $\lambda/4$ (quarter-wave) plate. If the incident plane-polarized radiation were at an angle other than 45°, then elliptical polarization would be produced, the ellipticity depending upon the angle.

Most quarter-wave plates have chromatism; that is, the phase shift depends on the wavelength of the radiation. A quarter-wave plate cut for one

wavelength would produce a different phase shift at another wavelength. Because of the need for a fixed phase shift ($\lambda/4$, for instance) to analyze polarized radiation, adjustable phase shifters are available (made by Continental Optics, Hauppauge, NY), transmitting the range from the ultraviolet to the long-wavelength infrared. However, the Polaroid Corporation makes a variety of circular polarizers, restricted to producing a quarter-wave phase shift at one wavelength.

Returning to Fig. 19 and using the quarter-wave plate, we can characterize the polarization of an incident beam of radiation. The quantitative specification depends upon a mathematical description, a convenient one being Stokes parameters, the subject of Chapter 4.

REFERENCES

1. Schmidt, E.; Eckert, E. Über die Richtungsverteilung der wärmestrahlung von oberflächen (Angular distribution of thermal radiation from surfaces). Forsch, Gebiete Ingenieuw 1935, 6, 175–183.
2. Lyot, B. Recherches sur la polarisation de la lumiere des plantes et de quelques substances terrestres. Ann. De l'obs. de Paris, Sect. de Meudon 8, 1929.
3. Egan, W.G.; Hilgeman, T.W. Optical Properties of Inhomogeneous Materials. Academic Press Inc.: New York, 1979; 81–125.
4. Jenkins, F.A.; White, H.E. Principles of Optics. Mc.Graw-Hill: New York, 1957.
5. Birge, R.T. The Velocity of Light. Nature 1934, 134, 771–772.
6. Egan, W.G. Photometry and Polarization in Remote Sensing. Elsevier Science Publishing Co., Inc.: New York, 1985.
7. Shurcliff, W.A.; Ballard, S.S. Polarized Light. Van Nostrand: New York, 1964.

4

Stokes Parameters

I. INTRODUCTION

The general representation of radiation—unpolarized, partially polarized, completely polarized, circularly or elliptically polarized—is achieved through the use of the Stokes vector [1]. The Stokes vector consists of a set of four numbers arranged in matrix form defining a particular form of radiation:

$$\begin{bmatrix} 1 \\ 0 \\ 0 \\ 0 \end{bmatrix} \quad \text{unpolarized radiation of unit intensity} \tag{1}$$

$$\begin{bmatrix} 1 \\ \pm 1 \\ 0 \\ 0 \end{bmatrix} \quad \text{horizontally } (+) \text{ or vertically } (-) \text{ polarized radiation of unit intensity} \tag{2}$$

$$\begin{bmatrix} 1 \\ 0 \\ \pm 1 \\ 0 \end{bmatrix} \quad \text{radiation of unit intensity polarized linearly at } \pm 45^\circ \text{ to the reference axes} \tag{3}$$

$$\begin{bmatrix} 1 \\ 0 \\ 0 \\ \pm 1 \end{bmatrix} \quad \text{right } (+) \text{ or left } (-) \text{ circularly polarized radiation of unit intensity} \tag{4}$$

$$\begin{bmatrix} I \\ Q \\ U \\ V \end{bmatrix}$$ general form of the Stokes vector, where I, Q, U, and V are the Stokes parameters (5)

NOTE: The quantities S_1, S_2, S_3 have been used in the literature and are here defined for the sake of completeness.

The four Stokes parameters are defined by

$$\begin{aligned} I &= \langle A_x^2 + A_y^2 \rangle = A^2 = S_0 \\ Q &= \langle A_x^2 - A_y^2 \rangle = S_1 \\ U &= \langle 2A_xA_y \cos\gamma \rangle = S_2 \\ V &= \langle 2A_xA_y \sin\gamma \rangle = S_3 \end{aligned} \tag{6}$$

where A_x, A_y are the amplitudes of the electromagnetic waves in mutually perpendicular directions, A^2 is the intensity, γ is the phase angle between A_x and A_y, $\langle\ \rangle$ indicates time averaging, and $I^2 = Q^2 + U^2 + V^2$.

Briefly, the quantity I, the intensity of radiation, is the result of photometric measurement. The quantity Q is the difference between the intensities of radiation in the mutually perpendicular directions used to specify A_x and A_y. If the mutually perpendicular directions used in the remote sensing program are those perpendicular and parallel to the plane of vision (i.e., the plane defined by the sun, the viewed point on the remotely sensed surface, and the sensor), then it has been found that, because of symmetry, $U = 0$. The quantity U indicates the excess of radiation in the $+45°$ direction over that in the $-45°$ direction relative to the plane of vision; V is a quantity that indicates the amount of circularly polarized radiation. The quantity Q is also measured by a plane polarization sensor; Q/I is then proportional to the percent polarization [Eq. (10)]:

$$\%\ \text{polarization} = 100\frac{\langle A_x^2 - A_y^2 \rangle}{\langle A_x^2 + A_y^2 \rangle} = 100\frac{Q}{I} \tag{7}$$

A number of apparatuses have been described that perform automated analyses of polarized radiation, some generating values for the Stokes parameters. Plane-polarized radiation is the most commonly occurring form of radiation in remote sensing of natural objects. Strong circular or elliptical polarization occurs with metallic reflection but may occur to a slight degree in atmospheric scattering by particulate aerosols, especially if they are anisotropic.

A spectropolarimeter-photometer that I have used for laboratory and aircraft measurements is described in Chapter 14. The system uses quartz optics, and observations may be made in the spectral range from 0.185 to

2.7 μm. In operation, the spectral region is chosen by the appropriate filter–sensor–polarization analyzer combination. The polarization analyzer is rotated by an electric motor at 6.5 Hz that produces a fluctuating voltage, for polarized incoming radiation, of 13 Hz. Simultaneously, a sine/cosine resolver electrically indicates the angular position of the polaroid on an oscilloscope. The voltage from the output anode of the photomultiplier may be simultaneously fed to both ac and dc recorders. Provision must be made for elimination of dark current from the photomultiplier or PbS system sensor. The dc and ac outputs are proportional to the Stokes parameters I and Q (S_0 and S_1). The plane of polarization is read from the oscilloscope from a Lissajous figure. The analysis of circularly polarized radiation of a particular wavelength requires the use of a quarter-wave plate before the analyzer in accordance with the procedures outlined in Fig. 20 of Chapter 3.

Conventional ellipsometers, on the other hand, are designed to determine the polarization of radiation reflected from thin films or metallic surfaces, where elliptically polarized radiation is normally produced. Plane polarization and photometry are generally available within the system but are of little interest. However, astronomers are interested in both photometry and polarization, and their polarimeters are designed to function in the manner of the spectropolarimeter-photometer just described, to produce Stokes parameters. There are also polarimeters, based on Fresnel's equations, that yield only polarization, the photometry being submerged into a calibration procedure.

A short description of these three representative types of polarimeters follows.

II. ELLIPSOMETER

The conventional Gaertner ellipsometer (1968) consists of a light source, a polarizer, a compensator or a quarter-wave plate, an experimental surface, an analyzer, and a detector in Fig. 20 of Chapter 3. The ellipsometer is intended to measure the polarizing properties of surfaces (i.e., ultimately the Stokes parameters of the surface); the polarimetric properties of remotely scattered or reflected radiation are not determined with this type of instrument. There is a need to characterize surfaces in the laboratory in terms of Stokes parameters for subsequent use in mathematical models. For measurement with the Gaertner ellipsometer, the polarizer and analyzer positions must first be manually adjusted (or the compensator could be adjusted) to provide a null position. The azimuthal positions of the polarizer and analyzer yield the phase retardation Δ and amplitude attenuation ψ that represent the phase relationship change of the $\parallel$ and $\perp$ components upon reflection from the experimental

surface (i.e., elliptical polarization). The plane-polarized components are obtained for the polarizer and analyzer both oriented $\parallel$ or $\perp$ (with no compensator), and the cross-polarized components for the polarizer $\parallel$, analyzer $\perp$, and polarizer $\perp$, analyzer $\parallel$. These plane polarization measurements imply a reference plane, usually taken as the plane of vision, as indicated previously. The ellipsometric procedure requires a double balancing, which is time-consuming.

At this point, it is appropriate to digress again and bring in the matrix representation of the Stokes parameters for a general surface that has both Fresnel reflectivity and scattering. In essence, the surface causes a transformation of the properties of the radiation incident upon it, just as a polarizer, analyzer, or quarter-wave plate does. For instance, a linear polarizer with the transmission axis horizontal ($\theta = 0°$) would be represented in either of two ways—by the Mueller matrix,

$$\frac{1}{2}\begin{bmatrix} 1 & 1 & 0 & 0 \\ 1 & 1 & 0 & 0 \\ 0 & 0 & 0 & 0 \\ 0 & 0 & 0 & 0 \end{bmatrix} \tag{8a}$$

or by the Jones matrix,

$$\begin{bmatrix} 1 & 0 \\ 0 & 0 \end{bmatrix} \tag{8b}$$

To discuss these matrices in general, we use the representations

$$\begin{bmatrix} A_{11} & A_{12} & A_{13} & A_{14} \\ A_{21} & A_{22} & A_{23} & A_{24} \\ A_{31} & A_{32} & A_{33} & A_{34} \\ A_{41} & A_{42} & A_{43} & A_{44} \end{bmatrix} \quad \text{and} \quad \begin{bmatrix} A_{11} & A_{12} \\ A_{21} & A_{22} \end{bmatrix} \tag{9}$$

The various properties of surface reflection and scattering are then given in terms of the matrix coefficients. Thus A_{11} represents $\parallel$ polarizer, $\parallel$ analyzer conditions; A_{22}, $\perp$ polarizer, $\perp$ analyzer; and A_{12} and A_{21} are the cross-polarization components. The coefficients in the other positions in the Mueller matrix, as well as admitting the possibility of the elements in the Jones matrix assuming values of $A_{12} = A_{21} = \pm i$ and $A_{12} = -i$, $A_{21} = i$, permit the assumption of a reference plane that is not the plane of vision (i.e., at $\pm 45°$) and right circular polarization. This brief exposure will serve to introduce the concept of matrix representation that will be developed more fully in later chapters.

We now return the discussion to the ellipsometer. Ord constructed a null-balancing ellipsometer with the polarizer and analyzer positions controlled by a computer. However, the system requires a high signal-to-noise ratio, which can be achieved only with a laser. The first rotating polarizer unit

was suggested by Kent and Lawson and elaborated upon by Van der Meulen and Hien. The Van der Meulen and Hien device samples the light passing through a rotating analyzer at 512 equally spaced intervals and subjects the data to Fourier analysis to obtain the ellipse parameters. A more recent embodiment employs a double-modulation configuration of Stobie, Rao, and Dignam; double modulation is achieved by the use of a polarizer and analyzer at fixed azimuths and a rotating polarizer either before or after the reflecting surface. The system has the advantage that it is not a null system in the conventional sense and does not involve signal amplitude measurements. However, to obtain the Stokes parameters for a surface, the plane-polarized components must be determined.

III. ASTRONOMICAL POLARIMETER-PHOTOMETER

A typical astronomical polarimeter-photometer was used by Gehrels [2] at the University of Arizona for measurements of planetary photometry and polarization. It consists of a cryostat (icebox) containing photomultiplier sensors preceded by a Wollaston prism polarization analyzer. Dual photomultipliers are used with integrators, one set with an S-1 response (RCA-7102) and one set with an S-20 response (RCA-7265)—see Chapter 6 for description of response curves. Dry ice is used to cool the photomultipliers, although liquid nitrogen could also be used. Precautions must be taken to ensure that no moisture accumulates on the photomultiplier tube terminals. The purpose of the dual photomultipliers is to ensure measurement reliability because the sensitivity of end window photomultipliers can vary greatly over the sensitive area. The cryostat is positioned at the telescope's focal plane and can be rotated to determine the polarization properties of the incoming radiation. A telescope-guiding eyepiece is included; the photometer system contains a Lyot depolarizer (see Chap. 3), a field-viewing eyepiece, a focal plane diaphragm slide, a centering eyepiece, and a filter holder. Although originally set up as a UBV photometer (see Chap. 3) narrowband interference filters may also be used.

During operation, the integration times were usually between 10 and 40 s, although photon counting could be used for weak sources. The Wollaston prism gave full transmission down to a wavelength of 0.290 μm and up to the infrared at 1.0 μm. Frequent calibration ensured the accuracy and precision of the measurements. The removable depolarizer allows determination of the first Stokes parameter with the same apparatus.

IV. LYOT POLARIMETER

The *Lyot* polarimeter is a visual device that measures only polarization; the photometry is canceled out by the calibration technique inherent in its

operation. The polarimeter has the advantage that no electronic instrumentation is necessary for its operation, but the considerable disadvantages are that it is limited to the visual range, is nonrecording, and does not supply photometry. The device directly measures the percent polarization and is an outgrowth of the Savart polariscope. The amazing sensitivity of the unit is that a polarization of 0.001 can be measured. It has been used to measure planetary and terrestrial polarization.

The principle of operation consists of slightly polarizing the light rays that enter the polariscope alternately parallel and perpendicular to the principal axis of the analyzer. With this technique interference fringes become quite visible. By rotating the polarimeter around its axis to assume orthogonal positions, the equality of the fringe intensity is achieved through adjustment of a compensating plate. The percent polarization is then read directly from a calibrated sector.

A few words are now in order about the Stokes vector as a tool for interpreting the photometric and polarimetric properties of surfaces.

Assume that the exact nature of the surface scatterer is known. Then the scattered field could, in principle, be determined from the incident field:

$$\begin{bmatrix} E_{\perp} \\ E_{\parallel} \end{bmatrix} = \begin{bmatrix} A_2 & A_3 \\ A_4 & A_1 \end{bmatrix} \begin{bmatrix} E_{0\perp} \\ E_{0\parallel} \end{bmatrix}$$

where $E_{\perp}$ and $E_{\parallel}$ are the components of the scattered fields perpendicular and parallel, respectively, to the plane of vision, and $E_{0\perp}$ and $E_{0\parallel}$ represent the same quantities for the incident field. The elements of matrix A depend on the detailed nature of the scatterer as well as on the propagation vectors of both the incident and scattered fields. The analysis of a scattering problem consists essentially of determining the matrix $[A]$. In the optical region, the features of the incident and scattered beams that are usually observed are the energy intensities in various polarization modes. The most complete description of such a beam is given by the four-element Stokes vector, which can be determined by experiment.

The Stokes vectors of the incident and scattered beams are also related by a matrix transformation

$$\begin{bmatrix} I \\ Q \\ U \\ V \end{bmatrix} = \begin{bmatrix} F_{11} & F_{12} & F_{13} & F_{14} \\ F_{21} & F_{22} & F_{23} & F_{24} \\ F_{31} & F_{32} & F_{33} & F_{34} \\ F_{41} & F_{42} & F_{43} & F_{44} \end{bmatrix} \begin{bmatrix} I_0 \\ Q_0 \\ U_0 \\ V_0 \end{bmatrix}$$

where I, Q, U, and V provide information about the intensity of the light, the intensity of polarized light, the position of the plane of polarization, and the extent of the circular polarization present. The elements of matrix $[F]$ can be expressed in terms of the elements of matrix $[A]$. Thus, given a knowledge of

the scatterer, one can, in principle, determine the properties of the scattered beam, i.e., the Stokes vector.

However, in the problem of interpreting a remotely sensed signature, we are given the Stokes vector and seek to determine the properties of the scatterer. This requires (1) determining the elements of matrix $[F]$ from the observational data [3], (2) inverting the relationship between $[A]$ and $[F]$ so that the elements of $[A]$ can be determined from the elements of $[F]$ [4], and (3) determining the properties of the scatterer from a knowledge of matrix $[A]$. The last of these is the mathematically difficult inverse scattering problem. A determination of matrix $[A]$ provides more insight than is available from the Stokes vector alone. Before this can be done, the first of the requirements above must be completed, namely, the determination of matrix $[F]$.

The elements of $[F]$ are functions of wavelength and the propagation vectors of the incident and scattered fields. It is clear that to determine $[F]$ for one wavelength and at each phase angle, one must perform four experiments, each of which measures the Stokes vector of the scattered beam. The incident beam for the four experiments must be, respectively, (1) linearly polarized parallel to the plane of vision, (2) linearly polarized perpendicular to the plane of vision, (3) linearly polarized at some angle to the plane of vision other than 90° or 0°, and (4) circularly polarized.

When an atmosphere intervenes that is itself a scatterer and absorber, a second scattering matrix operates on both the source components and the surface scattered components. The ensuing requirement for the determination of the Stokes parameters of the intervening atmosphere as well as the underlying scattering surface is even more difficult mathematically.

A procedure for determining certain optical properties of the atmosphere (such as the aerosol particle size distribution) is constrained linear inversion [4]. In essence, the atmospheric absorption and scattering problem is set up in terms of certain significant variables that are permitted to vary within specified bands so that singularities will not occur in the possible solutions.

REFERENCES

1. Egan, W.G. Photometry and Polarization in Remote Sensing. Elsevier Science Publishing Co., Inc.: New York, 1985.
2. Gehrels, T. Planets, Stars, and Nebulas Studied with Photopolarimetry. University of Arizona Press: Tucson, Az, 1974.
3. Shurcliff, W.A.; Ballard, S.S. Polarized Light. Van Nostrand: New York, 1964.
4. Egan, W.G.; Shaw, G.E. Effect of Aerosols on Optical Remotely Sensed Data. Proc. 15th Int Symp Remote Sensing. ERIM 1981, 959–973.

5

Instrumentation

I. INTRODUCTION

The object of instrumentation is to gather polarimetric and photometric data that are to be interpreted to yield information applicable to a specific program. The polarization and photometry are expressed as Stokes parameters (Chap. 4) [1], which are defined spectrally, spatially, and temporally. This is a big order and produces data in the range of terabytes and much greater. It is no trick to assemble tremendous amounts of optical data, but the storage and interpretation can be a horrendous problem. In this chapter the emphasis is on optical data, but ancillary data, which we call "ground truth," [4] must be acquired. The ground truth and atmospheric properties are available from various sources [1].

Many systems can be used to collect polarization and photometric data simultaneously; some are imaging and some are nonimaging (or field-averaging). One important consideration in any system is the calibration that is necessary for any quantitative work. Another consideration is how the assembled data can be fitted to an appropriate mathematical model.

The simplest focal plane collection system for the first Stokes parameter (S_0) is a camera. The first Stokes parameter (intensity) is easily collected as imagery without a polarization analyzer in front of the camera lens. The second Stokes parameter (S_1) is acquired as imagery with a linear polarizer in front of the lens but with the polarizer axis (for simplicity of the subsequent analysis) oriented either parallel or perpendicular to the principal plane (Chap. 2), with both orientations used in sequence. Two images are necessary; these are acquired either with one camera

sequentially or with two cameras, the latter collated later using control points in the scene.

The third Stokes parameter (S_2) can be acquired with two more observations (polarization) with the polarization analyzer oriented at 45° to the perpendicular and parallel planes used to determine the second Stokes parameter. The fourth Stokes parameter (S_3) is circular polarization (which is usually small except for birefringent scattering surfaces such as plants); detection requires a quarter-wave retardation plate, appropriately oriented with respect to the plane polarizer (see Chap. 3).

The simplest camera to use is a Hasselblad 2 1/4 in. format calibrated using the imagery subsequent to film development. This has been used successfully from the Space Shuttle for farm crop identification and cloud and atmospheric polarization measurements (see Chap. 11).

A program using the WILD 9 in. format camera was used to image wetlands in Maryland. Precision calibration employed step wedges with image densitometry in red, green, and blue and near-infrared imagery, along with calibrated ground panels in the field of view.

Beyond simple photographic data acquisition is the digital camera approach. It uses the Bayer pattern to separate red (R), green (G), and blue (B) and a filter to eliminate the near-infrared (NIR) response of the sensor. A proprietary algorithm separates out the NIR response to yield RGB data (see Chap. 24).

Duggin used a special Kodak Color Infrared (CIR) camera with the blue eliminated and the NIR retained along with the red and green to acquire remote sensing imagery. The focal plane array has a density of 2048 × 3072 pixels approximately 1 mil (12 μm) in size. Data from this camera are presented in Chapter 24. The polarimetric accuracy is about 0.2%, and the photometric accuracy is about 2% with careful calibration.

Subsequently Kodak developed a 6 megapixel CCD camera with a focal plane array of 2008 × 3040 pixels and a 12 bit depth (36 colors). This is the Kodak 660 digital camera, ISO range 80–200. Another digital camera, the Kodak 330, has a 1504 × 2008 (3 M pixel) focal plane indium-tin oxide CCD array, 10 bit depth per pixel (30 colors), and an ICO range of 125–400. The Kodak 330 is heavier in weight (3.49 lb; 1.58 kg), than the Kodak 660 (2.8 lb; 1.08 kg). The smaller size makes it more suitable for use in remotely piloted vehicles (RPVs). Battery requirements are similar.

Space Shuttle images were acquired with dual Hasselblad cameras (single-lens reflex) looking through the Space Shuttle window (Chap. 11). The film used in the cameras was Ektachrome 5036. The film images were digitized by NASA's Video Digital Analyzer (VDAS) Laboratory in Texas and spatially registered in a procedure described in detail in Chapter 11. These three-color photographs were given a preliminary characterization

on a 512 × 512 pixel system to the 8 bit (0–255) level. The digitization system has the capability of producing 2048 pixels horizontally and 6000 vertically. Registration of the pixels was to 0.01 with Laboratory of Image Processing Systems (LIMS). Polarimetric accuracy was 0.5%, and photometric accuracy was of the order of 5%.

Another version of a focal plane array is described in patents registered by Egan in 1991. It is appropriate for polarization measurements at long infrared wavelengths. Long-wavelength semiconductor detectors require cooling to liquid nitrogen or liquid helium temperatures (at higher temperatures, operation is possible only with diminished sensitivity). Multiple detectors and wavelength-scanned photometric measurements are currently produced, but they do not do polarization in this implementation (see Table 1, for instance).

Illustrations from the Egan patent are shown in Figs. 1–3. Figure 1 shows the implementation of the system for multiple-wavelength polarimetric sensing. Polarization filters *12* are oriented with axes perpendicular and parallel to the principal plane and are deposited by thin-film evaporation in this layer over a substrate with appropriate bandpass filters *14*, also thin evaporated films. The filters extend the width of the focal plane.

The detectors are evaporated or chemically deposited on the substrate. Figure 2 shows the cooled substrate *42* assembly with additional layered

TABLE 1 Performance Specifications for the Northrop-Grumman Advanced Remote Sensing Unit

Performance/Specifications	Multispectral	Hyperspectral
Bands	5	200
	Pan 0.675 μm	0.4–2.0 μm
	1 0.485 μm	
	2 0.565 μm	
	3 0.660 μm	
	4 0.830 μm	
Resolution	P:1 m MS: 1–4 m	<10 m
Swath	8 km	3 km
Altitude	550 km	550 km
Aperture	0.55 m	0.55 m
Design life	5 yr	5 yr
Weight	55 kg	70 kg
Power	55 W	75 W
Volume	0.33 m^3	0.4 m^3

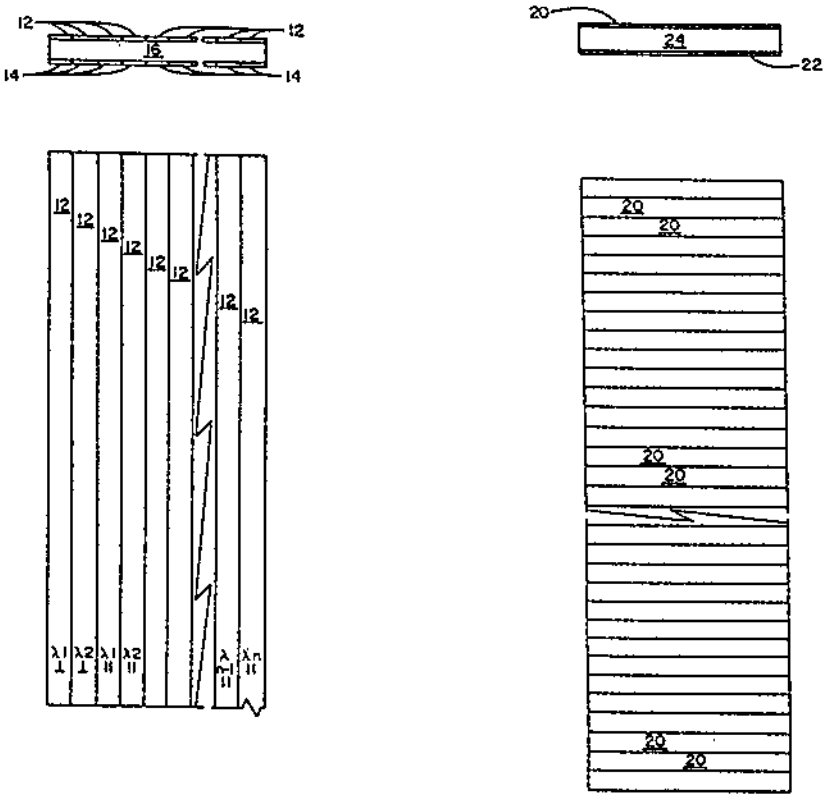

FIGURE 1 Focal plane filter structure for polarimetric remote sensing. (From Ref. 2.)

thin-film filters to characterize the sensor acceptance bandpass. Quarter-wave plate filters may be added to sense circular polarization. Because the third Stokes parameter is to be sensed, this requires a 45° orientation of the sensors as shown in Fig. 3.

Another implementation, shown in Fig. 4, uses fiber optics, with resolution determined by the sizes of the sensor fibers. Scanning is required by a scanning mirror (colloquially called a "pushbroom" technique). The mirror implementation with two perpendicular mirrors is shown in Fig. 5. The two perpendicular mirrors cancel the polarization from the front surface reflection of each mirror. The technique was originally used in the large-scale polarimeter described by Egan for lunar surface simulation [1].

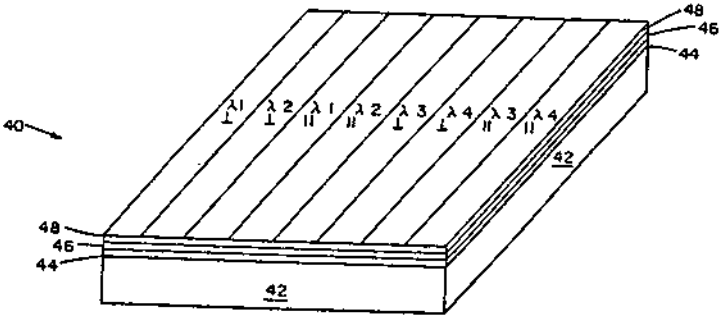

FIGURE 2 Cooled substrate focal plane. (From Ref. 2.)

The same technique was used in the design of the Earth Orbiting Scanning Polarimeter (EOSP) shown in cutaway view in Fig. 6. The ultimate implementation of the EOSP is the Research Scanning Polarimeter (RSP) shown in Fig. 7, developed by L. Travis of the NASA Goddard Institute for Space Studies of Columbia University, New York City.

II. INSTRUMENT DESCRIPTION

The Research Scanning Polarimeter (RSP) was developed by SpecTIR Corporation in association with the Goddard Institute for Space Studies of

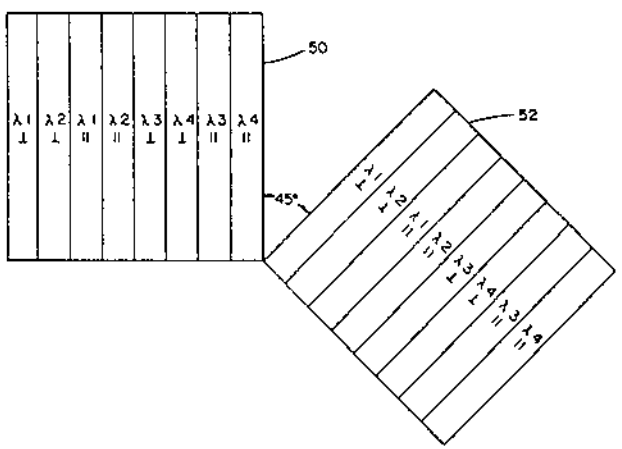

FIGURE 3 Skewed focal plane array for third Stokes parameter. (From Ref. 3.)

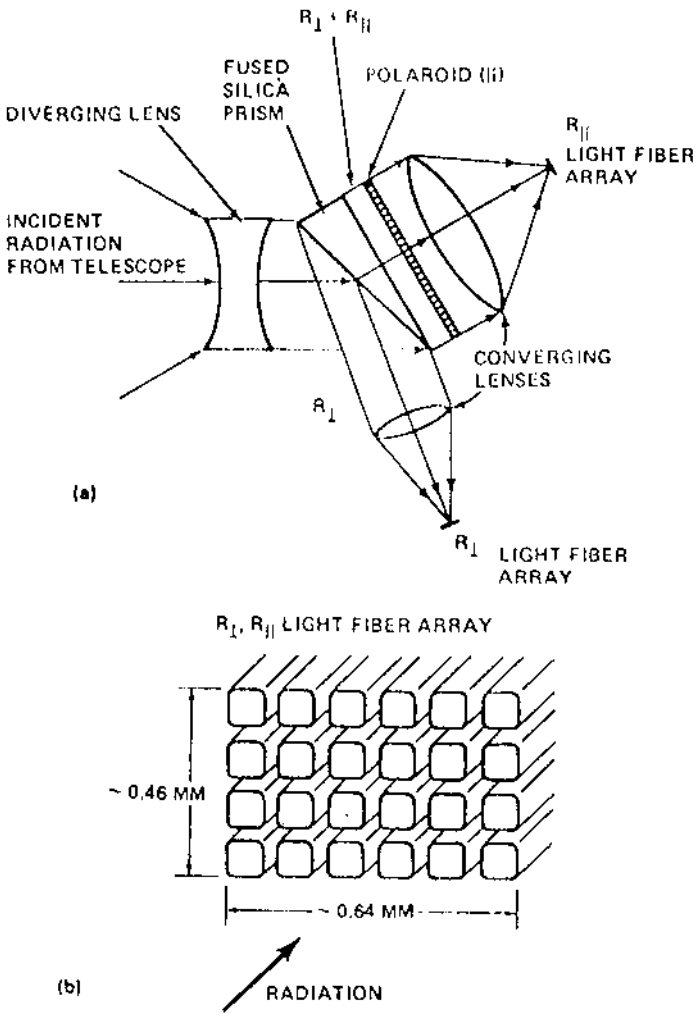

FIGURE 4 Beam-splitter arrangement. (a) Fused silica prism as a polarizing beam splitter. (b) Associated optics and light fiber array to the detectors. (From Ref. 5.)

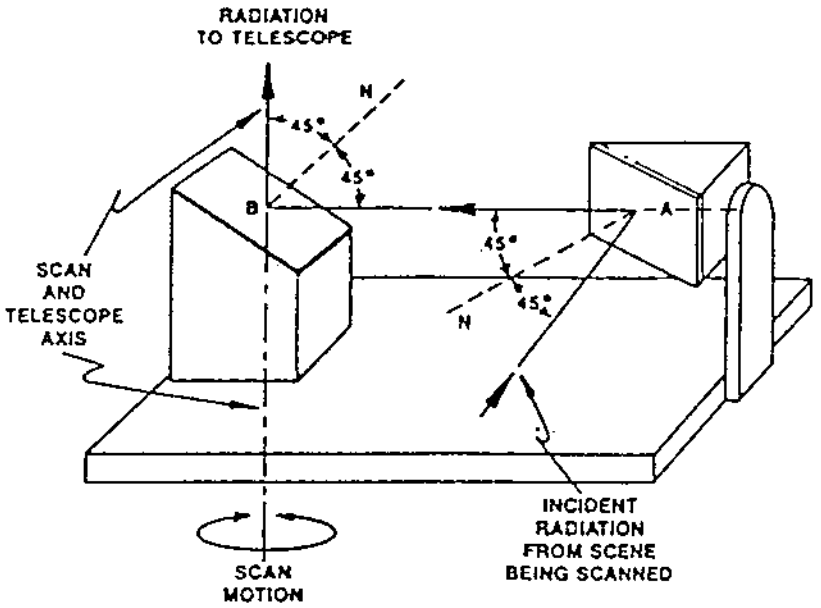

FIGURE 5 Scanning mirrors. If the mirrors are arranged so that the planes of incident and reflected radiation are interchanged in reflections from mirrors A and B, the overall polarization is canceled.

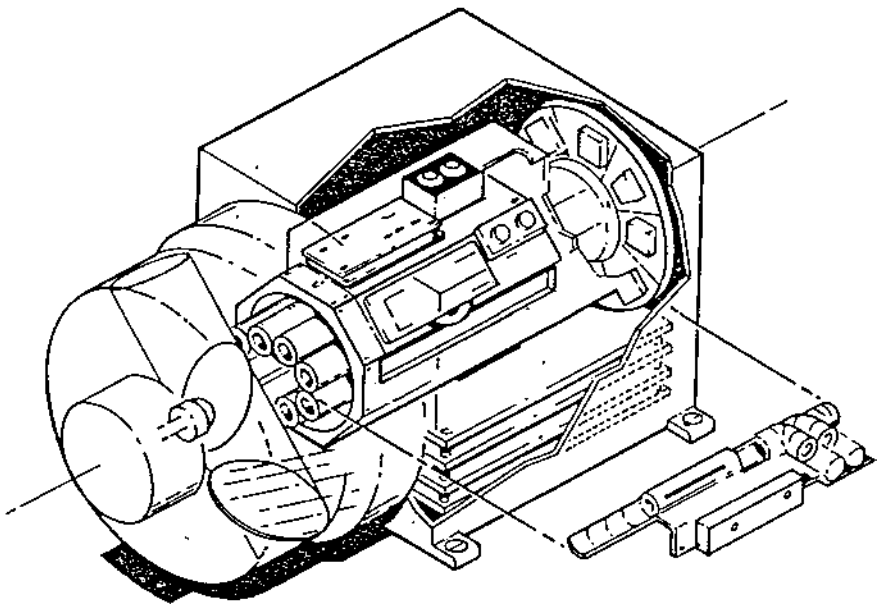

FIGURE 6 Cutaway view of the Earth Orbiting Scanning Polarimeter (EDSP). L. Travis (Private Communication).

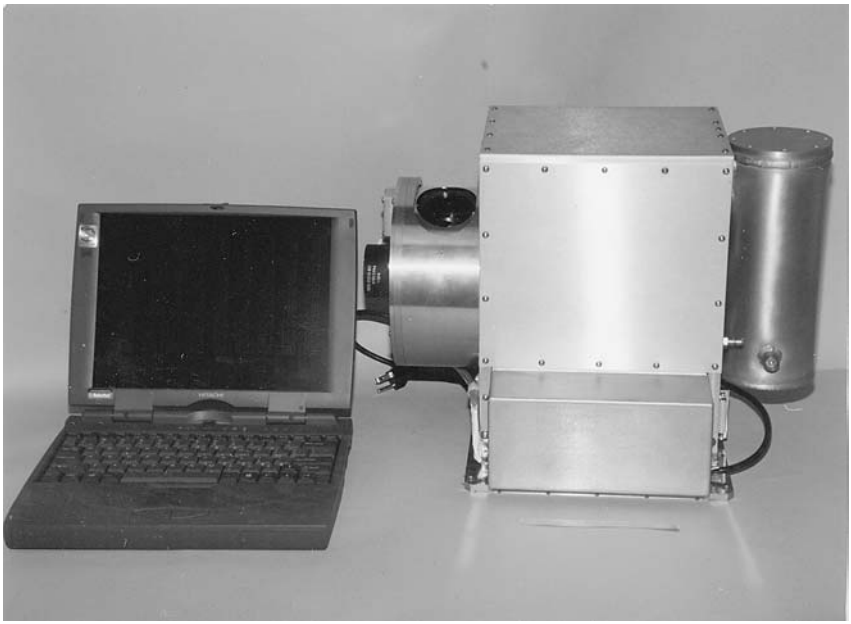

FIGURE 7 Research Scanning Polarimeter (RSP), (Photo courtesy of L. Travis).

Columbia University. Figure 7 shows the assembled RSP instrument with its liquid nitrogen Dewar on the left side and scanner assembly on the right. Data acquisition is performed on a laptop computer, which is shown here and gives an indication of the size of the instrument. The scientific requirements for the polarimetric measurements are satisfied by the RSP through its high measurement accuracy, the wide range of viewing angles measured, and its ability to sample the spectrum of reflected solar radiation over most of the radiatively significant range. The RSP instrument uses a polarization-compensated scanning mirror assembly to scan the fields of view of six boresighted refractive telescopes through $\pm 60^\circ$ from the normal with respect to the instrument baseplate. The refractive telescopes are paired, with each pair making measurements in three spectral bands. One telescope in each pair makes simultaneous measurements of the linear polarization components of the intensity in orthogonal planes at 0° and 90° to the meridional plane of the instrument, while the other telescope simultaneously measures equivalent intensities in orthogonal planes at 45° and 135°. This approach ensures that the polarization signal is not contami-

nated by uncorrelated spatial or temporal scene intensity variations during the course of the polarization measurements, which could create false polarization. These measurements in each instantaneous field of view in a scan provide the simultaneous determination of the intensity and the degree and azimuth of linear polarization in all nine spectral bands.

III. SPECIFICATIONS

Spectral bands. The instrument has four telescopes with nine spectral channels that are divided into two groups based on the type of detector used: visible/near-infrared (VNIR) bands at 410 (30), 470 (20), 550 (20), 670 (20), 865 (20), and 960 (20) nm and shortwave infrared (SWIR) bands at 1590 (60), 1880 (90), and 2250 (120) nm. [The parenthetic figures are the full width at half-maximum (FWHM) bandwidths of the spectral bands.]

Scanner. The desired polarization-insensitive scanning function of the RSP is achieved by the use of a two-mirror system with the mirrors oriented such that any polarization introduced at the first reflection is compensated for by the second reflection.

Optics. The optics are simple refractive telescopes that define the 14 mrad field of view. Dichroic beam splitters are used for spectral selection, interference filters define the spectral bandpass, and Wollaston prisms are used to spatially separate the orthogonal polarizations onto the pairs of detectors.

Detectors. The detectors for the VNIR wavelengths are pairs of UV-enhanced silicon photodiodes. The detectors for the SWIR wavelengths are pairs of HgCdTe photodiodes with a 2.5 μm cutoff cooled to 163 K (−110°C).

Electronics. With the exception of the dual preamplifiers located near each detector pair, the RSP electronics are contained within three stacked, interconnected modules. The electronics provide the amplification of the signals detected by the 36 detector channels, sampling and 14 bit analog-to-digital conversion of the resultant signals, the servo control of the scanner rotation and the temperature of the SWIR detectors, and the control logic that formats the instrument signal and housekeeping data and supports transmission of the digital data to a personal computer for storage.

Cooler. A liquid nitrogen Dewar is used to cool the SWIR detectors during both ground and airborne operation. To optimize the performance of the SWIR channels, the temperature of the detectors is servo controlled at 163 K during operation.

Data Handling. Digital data from 152 scene sectors (IFOVs) over 121° of scan, dark samples from 10 sectors, and instrument status data are formatted by the RSP electronics and transmitted for each scan to a personal computer for storage (Fig. 7). The average data rate of 110 kilobytes per second (kbps) provides readout of the 36 signal channels together with instrument status data at a scan rate of 71.3 rpm. This scan rate results in an IFOV dwell time of 1.875 ms and yields contiguous (scan line-to-line) coverage at nadir when the aircraft is traveling at a Velocity/Height (V/H) ratio of 0.017 s^{-1}, e.g., 100 knots at an altitude of 3048 m (10,000 ft.).

Mass. 24 kg [including Liquid Nitrogen (LN2)].
Size. 48 × 28 × 34 cm (length × width × height) including Dewar.
Power. 18 W (27 W peak).

In any telescope system, there is inherent reflective (and/or refractive) optical polarization. This is shown for a typical Cassegrainian reflecting telescope in Fig. 8. If only the center of the field of view is used, there is negligible plane polarization. However, this is highly restrictive and must be corrected optically or in the data reduction process.

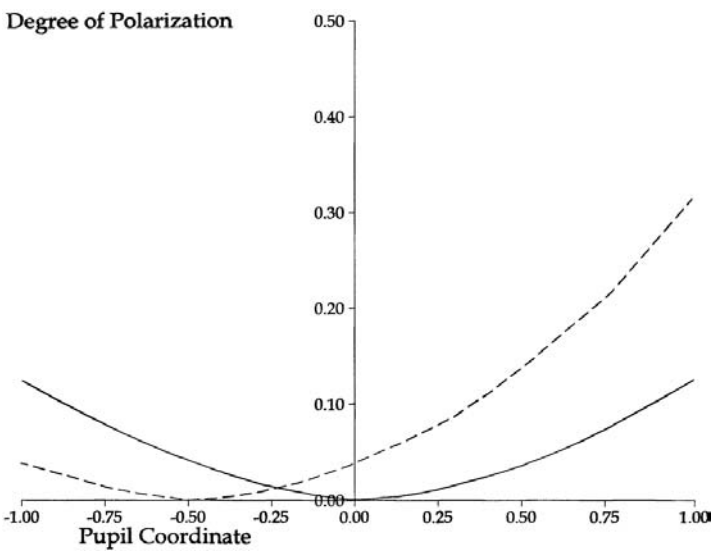

FIGURE 8 The degree of polarization of unpolarized incident light after transmission through the Cassegrain telescope for field angles of 0° and 3° for a *y*-fan of meridional rays. (From Ref. 6.)

REFERENCES

1. Egan, W.G. Photometry and Polarization in Remote Sensing. Elsevier Science Publishing Co., Inc.: New York, 1985.
2. Egan, W.G. US Patent 5,038,041 (assigned to Grumman Aerospace Corp.), August 6, 1991.
3. Egan, W.G. US Patent 5,029,990 (assigned to Grumman Aerospace Corp.), July 9, 1991.
4. Egan, W.G.; Hilgeman, T.W. Optical Properties of Inhomogeneous Materials: Academic Press Inc.: New York, 1979; 81–125.
5. Duggin, M.G.; Egan, W.G. Optical Enhancement of Aircraft Detector Using Polarization. 44th Annual Meeting of SPIE, July 30–August 4 2000, Session AM108.
6. Shurcliff, W.A.; Ballard, S.S. Polarized light. Van Nostrand: New York, 1964.

6

Data Acquisition and Storage

I. INTRODUCTION

There are many sources of remote sensing data. The primary sources are ground-based, aircraft, or satellite optical scanners. The data may be acquired digitally as with a multispectral scanner (MSS) or a coastal zone scanner (CZS), for example, or from digitized photographic imagery as taken with Hasselblad cameras from the Space Shuttle. A technique that is currently being applied is optical remote sensing with three- or four-color digital cameras with focal plane arrays. The pixel range of quantification is generally 16 bits but may be less.

One camera, the cooled KODAK CCD Model A7p, has been used to image military aircraft onto a 512 × 512 focal plane array, for example. The camera is cooled to 50–55° below ambient. The SIT S1A502AB back-illuminated CCD chip provides greater than 300,000 electron well depth with a typical noise figure of 7–11. The spectral response of the camera in the visible is between 375 and 900 nm with a quantum efficiency of better than 50%. The camera is computer-controlled with the aid of an astronomical software package. The interface uses eight parallel ports, which limits the image download speed.

It should be noted in passing that in remote sensing a significant time is generally needed to acquire the extensive amount of optical data required for analysis. For military applications, the time must be kept to a minimum, ideally zero, which is not possible. For instance, in battlefield conditions, loss in time can cause the loss of a conflict. In research, sometimes it can take

days, weeks, or months (even years) to acquire data, and the analysis of the data can take even longer.

An evolving source of data is spectral optical polarimetry. There are many systems in development in addition to those in current use. One such is the NASA GISS and Columbia University Research Scanning Polarimeter (RSP), described in Chapter 5. The optical Stokes parameter (S_0, S_1, S_2) are measured in nine spectral bands between 410 and 2250 nm, see Chapter 4. One run of data collection is on a 650 megabyte (MB) CD when used with a PC, but in a main frame data would be of the order of quadrabytes.

One image scan of 80° both along and across track (using a Cessna 210 aircraft) fills a 650 MB disc on a PC. On the order of 100 discs have been acquired with data running in the terabytes.

The data include a sample piece of C code for dumping a binary file on the CD for those who wish to use other (C or Fortran) codes for analysis. If one uses his own code, the correct relative gains, C12, K-band, K2, and radiometric calibration must be included, as described in an SPIE99 publication [1].

One need not go to the professional CCDs; there is much that can be accomplished with a 35mm frame. A 6 MB CCD can capture roughly the same amount of image data. For example, the Canon 3.3 MB PowerShot S20.

Almost all available digital cameras can accept digital data in at least 24-bit color, which is compatible with 16.7 million colors. Some can provide images in 30-, 36-, and 48-bit color. Many cameras have zoom capability, either optical or digital or both, a factor of 5 being usual.

CompactFlash cards will store up to 320 Mbytes of image data, or in between 512 Mbytes or a gigabyte (1GB) are available. Digital cameras that support Type II C CompactFlash cards can also take the higher capacity Microdrives, which were developed by IBM and hold up to 1 GB. CompactFlash cards are versatile and can be used in a wide variety of electronic devices for the transfer of images. Transferring images from SmartMedia and CompactFlash cards has become easier using USB plug-and-play card readers and floppy disc FlashPath adapters. Another form of removable media is Sony's Memory Sticks. The company's DSC-D770 Cyber-shot camera can use CompactFlash and Memory Sticks Sony has a line of digital movie cameras that use floppy discs for image storage. This is convenient because the image are saved in a standard JPEG format and can be read in a personal computer with a floppy drive.

The preceding discussion is imagery, but a considerable amount of data is acquired regarding the climate and weather and atmospheric properties. These data can be related to optical measurements of the transmission of light in the atmosphere, solar radiation, and absorption of atmospheric gases. For instance, atmospheric water vapor is indicated by absorption in the optical

wavelength region. This vapor is a significant greenhouse gas absorber even stronger than all the rest put together; its importance has not been realized even though it is alluded to in climate predictions. Carbon dioxide, which is presently assumed to be the most important greenhouse gas, forms part of the resulting sensed data bands. In light of the Kyoto Accord and the present position of the United States, the uncertainties in climate prediction are being emphasized, and remote sensing on a global basis not only by means of satellite, but also ground-based observations and interpretations as discussed in the following chapter, can lessen these uncertainties. The timeliness of remote sensing observations is important for many applications, for weather prediction and characterization as well as for military purposes. To benefit from having access to data on a timely basis, computing capability is important. Recent articles have indicated that the Europeans have better computing capability than the United States, but this could change in light of the need for better climate research.

There is an adage in the computer industry that processing power will double every 18 months, the speed will concurrently increase, the size will decrease, and the price will be cut in half. The original IBM PC had a processing speed of 4.77 megabytes per second when produced in 1981, but there are now available desktop systems that run at 1400 MB/s, and the end is not in sight. Currently the top-of-the-line G4 Power Mac system runs at 733 MHz, and there are computers containing Pentium processors running at 1500 MHz.

Another technique for data storage is to use a removable hard drive. It is not as compact as a floppy, but the Maxell can hold up to 80 GB, with 10 ms access time. Also, Digital video discs (DVDs) can accept up to 40 GB.

In this discussion, it has been assumed that the remote sensing of data is "locally" accessible and does not require transmission over phone lines (copper or fiber optics) (fiber optics are usable only with distances less than 1 km from the central office, without additional amplification). But frequently, and in the future, this will not be the case. We will use microwave or satellite. The top transfer rate of copper wires is 56 kHz and with coaxial cables up to as high as 5 MHz to a home or university PC. Higher data rates are necessary to accommodate remote sensing data and imagery. Wavelength division multiplexing (WDM) appears to be the best way to increase the capacity of fiber-optic lines. Present technology permits up to 60 channels; this means that 60 fiber-optic lines are replaced by one multiplexed fiber. Other competing systems that have been considered are the Synchronous Optical Networking (SONET) and Global Ethernet; SONET requires more fibers than WDM.

WDM has not been perfected; there are problems with noisy "old fiber" lines made before 1960. Newer fibers are controlled better in manufacturing to be more uniform and better transmitters of optical pulses and can transmit

at 40 GB/s. A cable to transmit 300 modes needs amplifiers to compensate for attenuation; polarimetric and refractive effects in the cable cause problems in transmission, amplification, and associated equipment. These problems are currently being attacked and appear amenable to solution.

Applications can be conceived that require a vast amount of data memory such as perimeter monitoring around airports where terrorist actions can occur. For example, inserting a foreign object such as a rock into the compressor section of a jet aircraft engine intake will damage the blades and destroy the engine. Foreign objects could easily be thrown or injected into the aircraft engines. Birds do not pose a problem. Dead chickens have been thrown into jet engines with no effect. However, a .45 caliber bullet could cause sufficient damage causing the engine to self-destruct. A pipe launcher could be used to inject foreign objects. To countermand these actions a Research Scanning Polarimeter (RSP) could be used in perimeter observations to project an image to the web and terrorist activity would be monitored by changes in that imagery. The technique for resolving the changes in imagery would be that used by Tombaugh (1) for the detection of the planet Pluto in the star field. A star field contains millions of stars (points of light) and Tombaugh looked for changes in the light, one of which represented the planet Pluto. He used a low-technology technique for recognition and subsequent super positions to detect changes. The same technique could be used to monitor unfriendly satellites.

Terrorist attacks on luxury cruises could be monitored using RSP and any unidentified craft approaching the cruise ship would be indicated through the use of remote sensing. Border crossings could be monitored using this technique with computer analysis alerts for border penetration and identifying terrorists. Army troop movement could also be identified using this technique.

Optical resolutions are such that a pencil lying on an airstrip seen from an altitude of 3000m could be imaged using polarization and the angular position of the pencil determined. Another possible application is monitoring the production of weapons of mass destruction and launching sites by rogue nations as was done with Cuba during the missile crisis. Ship movements and locations can be monitored around the world using remote sensing.

REFERENCES

1. Tombaugh, C.W. The trans-Neptunian planet search. In Planets and Satellites; Kuiper, G.P., Middlehurst, B.M., Eds.; Univ. Chicago Press: Chicago, 1961.

7

Data Analysis

I. INTRODUCTION

In Chapter 6, we discussed data acquisition and storage. In remote sensing the data assemblage can be astronomical by large. It is not difficult to acquire volumes of data without an understanding of their significance. How do we glean significance from a vast volume of data? What are the significant variables? How great are the notable effects? Do we need more data, and if so, of what sort? How good are the present data? How do we present them? These are a few of the questions to be asked.

Also, how long will it take to get the analysis and, perhaps a related question, how much will it cost? Do we have the resources (talent plus computer) to do the job? A big order, and in this chapter an attempt is made to provide a few answers.

To set the stage, the objectives have been set out, but not a suitable path. The approach to the task in this chapter is visual, with graphics making use of imagery (color hard copy ultimately) to present data and help pick out anomalies and significant features of interest.

Appropriate software is required to produce images from the databank and point up correlations. There are two broad categories of computer-based graphics programs: (1) point and draw programs and (2) paint programs (that use a raster basis) that work point by point (pixel by pixel). One subset of the paint programs is Adobe Photoshop.

Illustration programs such as CorelDRAW and Adobe Illustrator are vector programs, representing lines, shapes, and color fills in a composition

mathematically. Because the elements are represented mathematically rather than pixel by pixel, vector files are much smaller than raster files.

Still, although the file types are different, raster files from the newer paint and imaging programs can incorporate vector design elements and the draw programs support and incorporate raster designs into their compositions. Some programs work with both raster and vector files. Ron Scott's QFX has a high-end imaging application that effectively integrates vector and raster tools into one functional package.

A newer category of imaging programs referred to as projects-oriented programs work with images, graphic elements, and text. Such programs are Adobe PhotoDeluxe and Microsoft Picture. They include many of the tools required for graphic design; these programs do many of the things that Ron Scott did but are easier to work with.

Although their emphasis on presenting imagery is of interest, they do not analyze the data but merely present it in graphic form. This may be adequate for target recognition, for instance in the identification of military aircraft. In general, this is not the case, because many data, although they are in graphical form, do not lend themselves to graphics. Digital data that are a function of two variables yield readily to an x–y plot; for three variables, an x–y–z plot is appropriate. Multivariate functions must be segmented into two or three variable functions for plotting. Correlation programs that yield statistics such as averages, standard deviations, and bounds can aid in determining correlation; but the bottom line is generally that human judgment is needed.

So far in this chapter, the PC has been considered a self-contained unit that works with data and has access to Web sites for data acquisition. As such, a question voiced by David Gelernter of Microsoft is appropriate: "Using your computer as a mere channel to reach Web sites, reaching to and beyond it instead of using it, is like renting a Hyundai and keeping your Porsche in the garage."

Bill Gates gave a presentation on Microsoft.NET in a symposium (March 8, 2001, in New York at the Waldorf Astoria) on a revolutionary new platform built on open Internet protocols and standards with tools and services that meld computing and communication in new ways.

Figure 1 shows the overall concept using XML protocols as the final step from the PC through a graphic user interface (GUI) and the Internet. Microsoft.NET is based on a common language specification (Fig. 2), meaning that any language can be used to enter and work in the system without prior conversion. The .NET framework (Fig. 3) uses active server pagers (ASPs) and is segregated and easily extended. As noted above, the system uses active servers to support the PC and allows the use and analyses of data beyond the local PC.

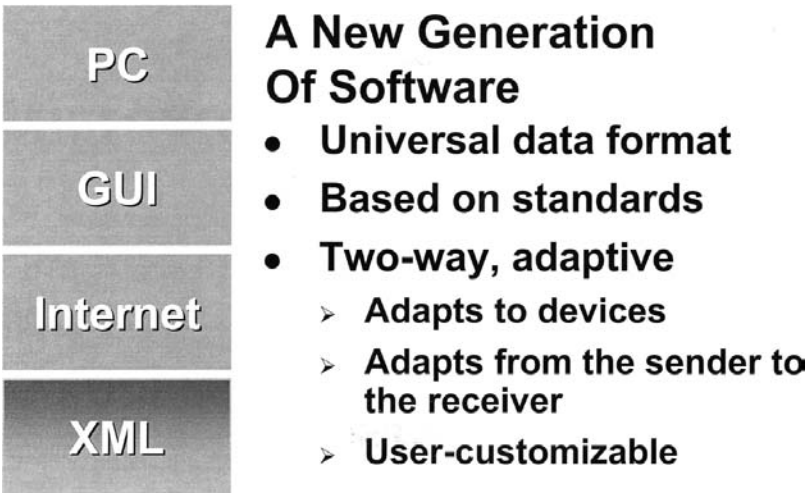

FIGURE 1 Overall concept XML protocol.

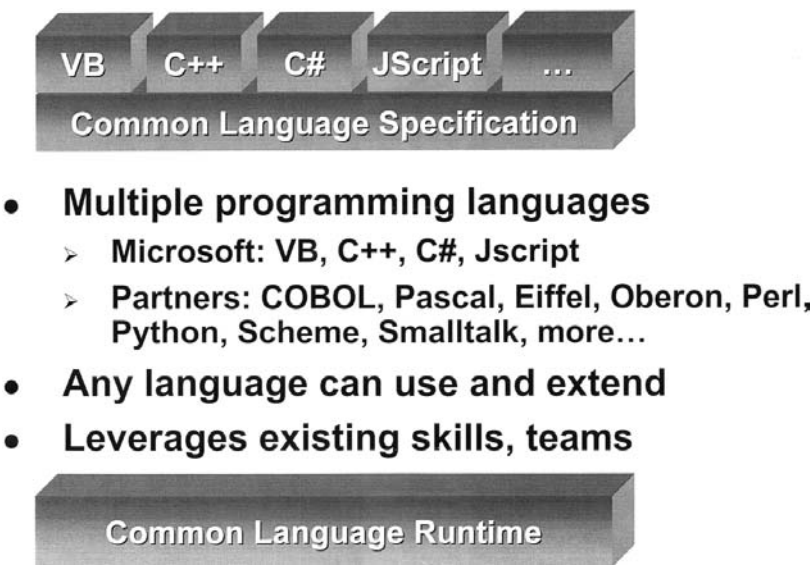

FIGURE 2 Microsoft.NET common language specification.

FIGURE 3 Microsoft.NET framework using active server pagers (ASPs).

II. DATA PRINTERS

Once the data are analyzed, and sometimes with the aid of hard copy, interpretation is enhanced by visual perception. Two types of digital printers are available: dye sublimation and inkjet. Even though dye sublimation is a digital process, it produces a continuous-tone print when the color or shades of gray fuse into each other, similar to photographic prints. Inkjet printer images are made up of individual dots that tend to separate under magnification. The images that dye sublimation printers produce is of higher quality than those produced by present inkjets.

Dye sublimation printers have heat-activated color ribbons that lay down the primary printing colors: cyan, magenta, and yellow (CYM, or CYMK when black is added). The colors are placed in multiple passes of the printing mechanism. Some printers add a clear ultraviolet-protective layer to increase the image durability of the print. Olympia has a newly developed sublimation printer, the Sony P-400, that produces full-page sublimation prints.

There are a number of sublimation printers available. Sony's FVP-1 produces photographic print–sized images; others, such as the Sony P-400, print full-sized pages. Most dye sublimation prints output at 300 dots per inch (dpi).

Inkjet printers have tiny inkjet nozzles in the printheads. The printer mode determines the number of colors that are printed. Newer designs have the nozzles built into the cartridge, making replacement simple. The cheaper models use the three primary colors (CYM) and print black by overlapping them. Newer models produce CYMK. Newer inkjets have two sets of primary colors, the primary colors and a second set of light-shaded primaries. The second set is useful if the imagery contains skin tones or requires smoother gradients.

Reasonable quality imagery is obtained at 720 dpi. Some models print at 1200 or 1400 dpi or even higher. The Lexmark Z42 generates output at 2400 $\times$ 1200 dpi.

With inkjet printers, the imagery is very sensitive to light and moisture. Daylight exposure of the imagery can cause fading in a few weeks, and moisture can destroy the imagery.

Epson has changed this with the Stylus Photo 2000P, which is capable of producing archival quality images. It uses proprietary inks and papers that are light- and moisture-resistant. Life expectancy is 200 years for the images. The durability of the imagery is important in field applications as well as for the military.

The ability to produce imagery on both sides of the papers as well as on sheets of various sizes is provided in the Hewlett Packard 1218. Epson has an option for roll printing on some inkjets. Some inkjets take 11 $\times$ 17 paper or even larger. Anywhere from 100 to 4000 images can be stored on a CD. Electronic images can be sent as e-mail or stored on one of the growing number of Internet sites that provide image storage space, usually at no cost.

Revolutionary systems will be updated as they evolve. The Microsoft.NET program description involves hundreds of pages and the material in this chapter briefly highlights the potential of the system. The program is described in part, on four 650MB disks which we have installed on computers at York College with help from the Microsoft staff who kindly supplied us with test programs to evaluate the system. We envisioned the system being used with Research Scanning Polarimeter (RSP) and disseminating the data over the web as tiff images. As computer memory increases, data collection can be more concentrated for the RSP. The projected goal of the Microsoft program will allow different government agencies, all with different systems, to communicate and exchange information with each other which is not possible at the present time.

8

Polarization and Surface Roughness

I. INTRODUCTION

Polarization is indicative of small-scale surface roughness, and photometry indicates large-scale surface roughness [1]. These phenomena are evident from measurements on natural and contrived surfaces. The original surface-scattering research was based on laboratory simulation of the lunar surface from astronomical observations prior to the lunar landing. It was found that large-scale irregularities on a surface cause shadowing to exert a major influence on the surface photometric scattering as well as on polarization. A dust coating on a coarse surface modifies both the photometric and polarimetric scattering functions. The dust coating causes depolarization and generally increases surface brightness. Percent polarization is found to be inversely proportional to surface optical albedo. In remote sensing, the fine structure of targets is related to percent polarization. Polarized retroreflectance is related to both coarse and fine structure of surfaces and is a valuable key to assessing contributing factors. Also, polarization can be used to advantage in military applications to distinguish targets from backgrounds.

Optical polarization has been used in astronomy for nearly 100 years [1] with applications familiar to everyone—sunglasses and stereovision. Other applications have been slow to arrive. A significant use of polarization has been to identify the clouds of Venus [2] and to characterize the lunar surface [1] and the surface composition of Mars [1]. In the past, spectrophotometry attracted the greatest amount of interest for surface characterization. However, both photometry and polarization are significantly paired in surface scattering.

The fundamental fact is that surface roughness drastically reduces the plane polarization of polarized incident radiation scattered by the surface [1]. Polarization is most conveniently represented by the dimensionless quantity percent polarization, the percent ratio of the magnitudes of the difference in the intensities of the polarized scattered radiation in mutually perpendicular planes to the total radiation [See Chap. 3, Eq. (10).]

Scattered radiation from an ideal rough surface obeys a cosine distribution function as the viewing angle is varied (diffusely scattered radiation). Very few surfaces are perfect diffusers, but all surfaces exhibit retroreflection, i.e., a strong backscatter at 0° incident, 0° scatter. The backscatter peak is usually twice the diffuse scatter but in some cases may be up to an order of magnitude higher [1]. Retroreflectance is independent of the tilt of the surface. Cross-polarization does not generally show any retroreflectance peak [3].

Three theories of the causes of retroreflectance are discussed in this chapter. The correlation of micro surface roughness with percent polarization and the modification of the photometric scattering function with macro surface roughness are also presented. Photometric and polarimetric measurements taken with a large-scale spectrophotopolarimeter are also presented.

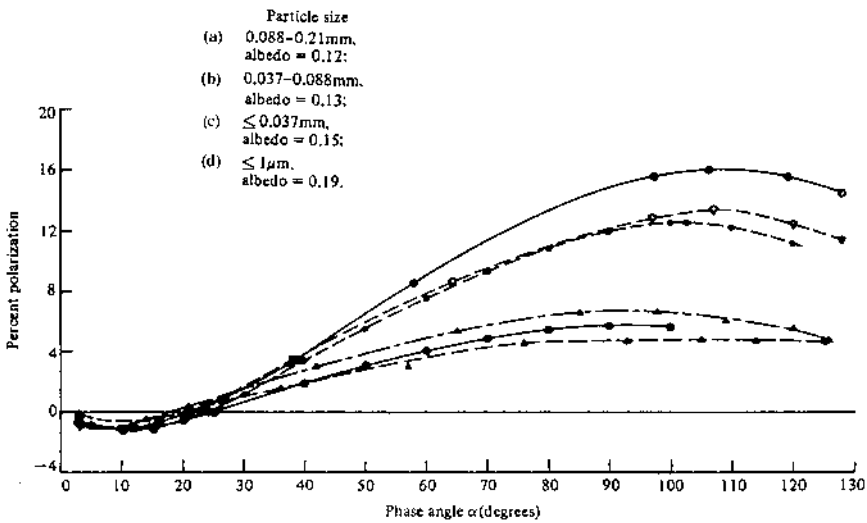

FIGURE 1 Haleakala volcanic ash. Percent polarization as a function of particle size for smallest particles, as determined with a 60° polarimeter. —○—○—, —○--○—, —▲—▲—, —▲--▲—, —●—●— Clavius albedo = 0.268, Lunar curves; —●--●— Crisium albedo = 0.137, Lunar curves. (Ref. 1.)

Other topics presented here include high angular resolution measurements made with laser illumination and with low temporal coherence illumination and the depolarization of surfaces as a significant factor in surface roughness characterization. An application of polarization to detect cross-polarized scattered radiation of an aircraft fuselage against the polarized sky will be presented in Chapter 24.

II. SCATTERING AND ABSORPTION

A. Polarization

Scattering by rough surfaces is basically governed by Fresnel's equations for coarse structures, with a subsidiary contribution caused by diffraction effects of the edges and asperities on the surface. In Fresnel's equations the optical index of refraction is an essential variable and is usually complex, i.e., includes an absorption factor as well as a refractive component.

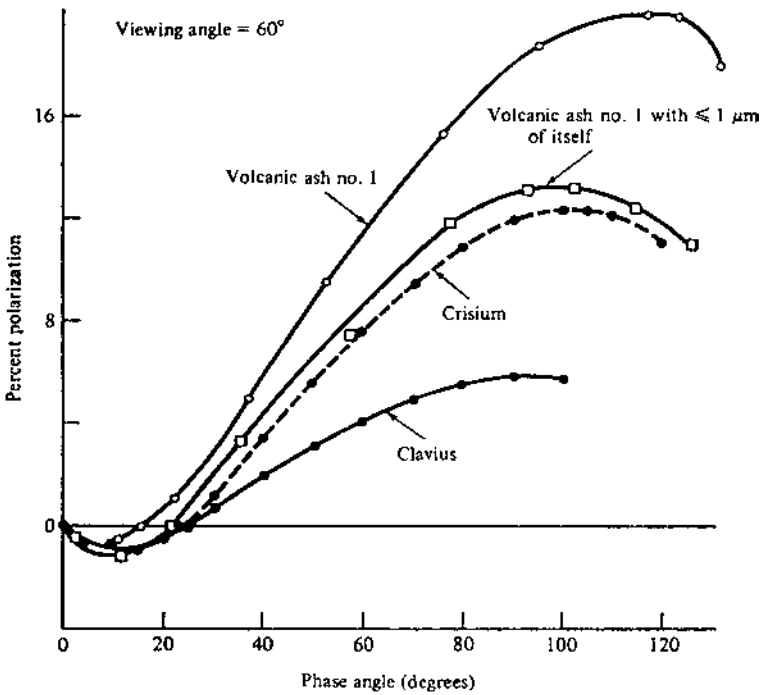

FIGURE 2 Effect of combination of models. A Haleakala volcanic ash is compared to particles of the same ash coated with a light powder. (Ref. 1.)

Polarization (or depolarization) of radiation incident upon a surface generally results from a single external scattering, and multiple scattering generally destroys polarization. Thus a surface with a large-scale structure (Fig. 1) composed of 0.088–0.21 mm particles has a higher maximum percent polarization (~16%) than one with ≤ 1 μm sizes (~4%) [4]. Powders have enhanced multiple scattering compared with geometrically rough surfaces. It is interesting to note that percent polarization is inversely related to surface optical albedo (the surface reflectance). Thus enhanced surface scattering makes the surface brighter and reduces the percent polarization. It is also evident that when a rough surface is coated with a powder, the percent polarization is reduced (Fig. 2). Hence percent polarization again is seen to be inversely proportional to the surface reflectance caused by the particulate microstructure.

However, things are not this simple (Fig. 3). For a given index of refraction, increased absorption causes decreased surface reflection, which then

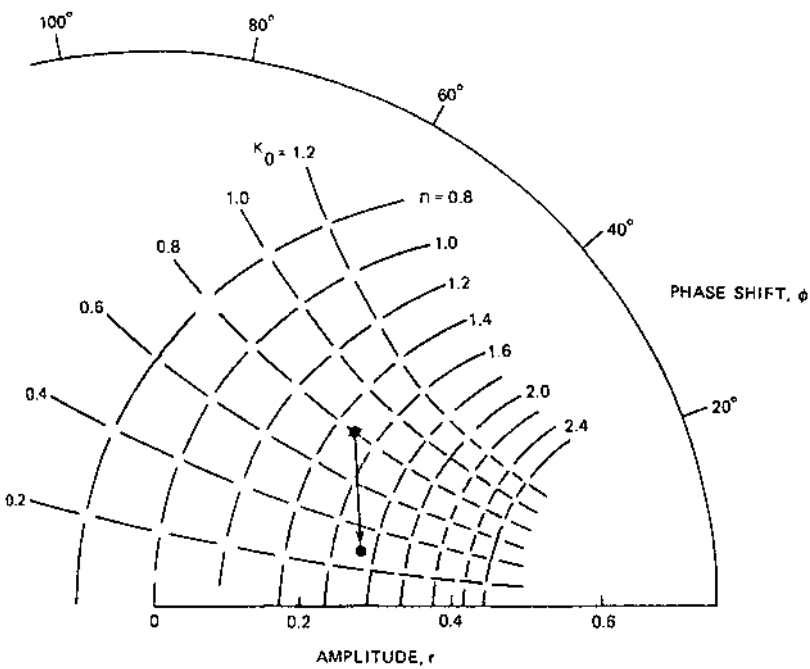

FIGURE 3 Smith diagram showing amplitude and phase of complex reflection coefficient and the effect of scattering for normal incidence.

augments the effect of particulate surface scattering. (Note that Fig. 3 is for normal incidence, and the effect of scattering is shown to be an increase in surface reflectance.)

B. Photometric Effects

In remote sensing of surfaces, where the source of illumination is at an angle (the phase angle) to the sensor (Fig. 4), the apparent reflectance of the surface is generally dependent on the phase angle. Thus in laboratory measurements to simulate the photometry of the lunar surface with a Hawaiian volcanic cinder (Fig. 5), it is seen that the brightness varies as a function of the phase angle (also the angle of incidence). Here the surface brightness can be shown to be a function of the surface microstucture. Halajian and Spagnolo [5] proposed various geometrical models that yield the required photometric function for the lunar surface (Fig. 6). The coarse structure is caused by the coarse porous structure of the lunar surface superimposed on the powder structure.

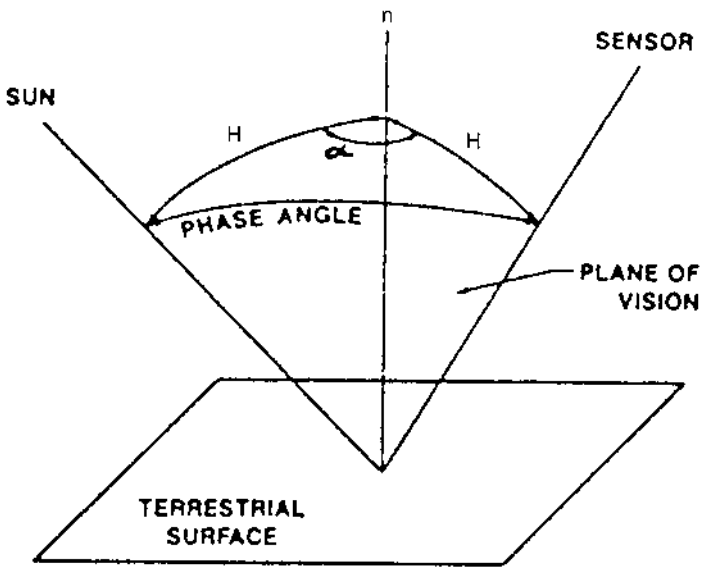

FIGURE 4 Geometrical relationships. Incident radiation from the sun (or sky) strikes the terrestrial surface and is scattered to the sensor system. The angle between the sun and sensor, in the plane (of vision) defined by the incident and scattered directions, is termed the phase angle.

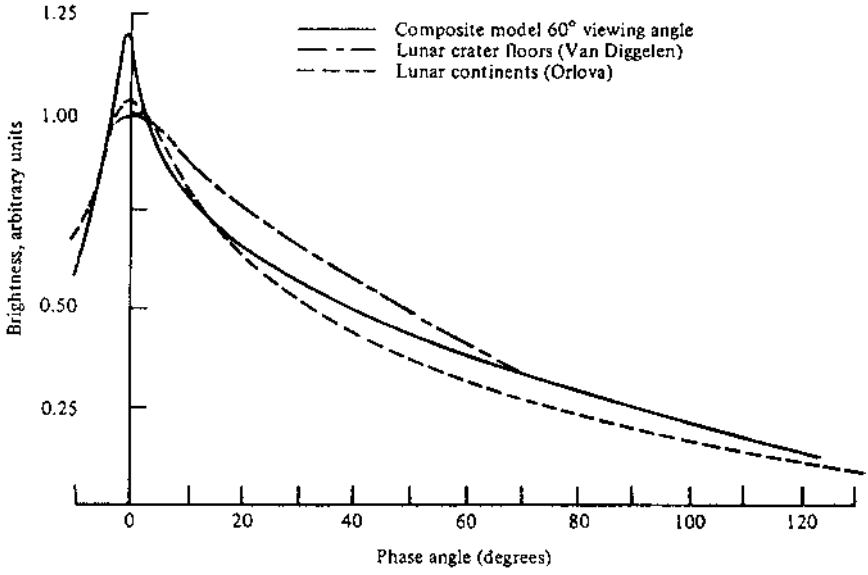

FIGURE 5 Photometry of a composite model of a Haleakala volcanic ash topped with particles of itself ≤ 1 μm in diameter (integrated visual light, $\lambda_{eff} = 0.54$ μm), for lunar crater floors and continents. (From Ref. 2.)

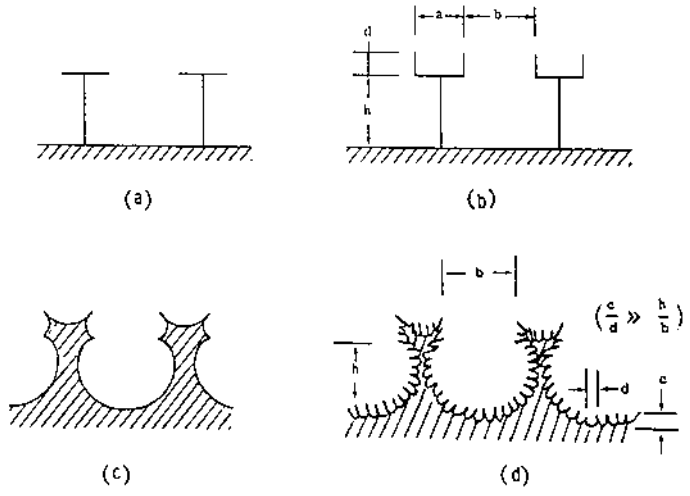

FIGURE 6 Evolution of building block for a lunar photometric model. (a) Basic T model; (b) modified T model (to improve backscatter); (c) cellular model (evolved from modified T model); and (d) modified cellular model (to account for opposition effect). (From Ref. 5.)

III. RETROREFLECTANCE

Another phenomenon that involves scattering is retroreflectance. This is a nonlinear increase in the brightness of a surface as the source and sensor are brought into alignment (so-called zero-zero). This nonlinear increase in brightness is shown in Fig. 7 for various lunar locations and compared to a Lambertian surface. The Halajian–Spagnolo model [5] accounts for this brightness increase. A model proposed by Hapke [6] that embodies particulate shadowing is also applicable, as is a model proposed by Trowbridge [7,8].

However, retroreflectance occurs for relatively smooth surfaces (such as smooth magnesium carbonate or paints) and is independent of surface tilt

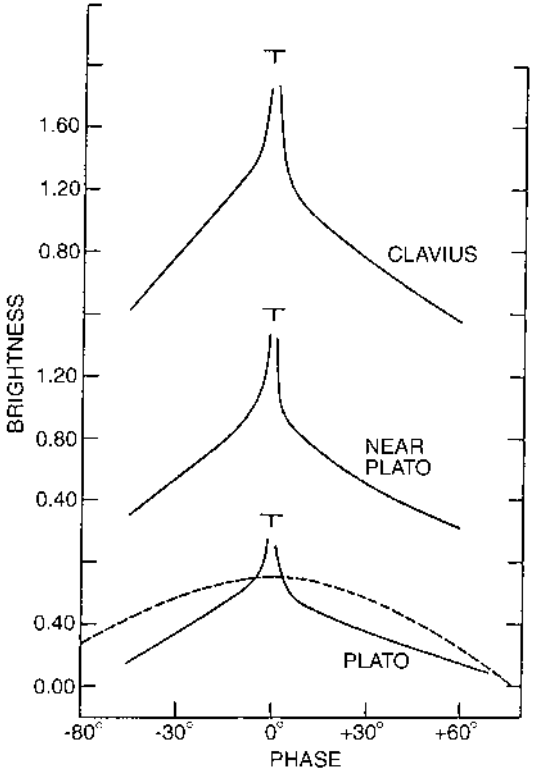

FIGURE 7 Lunar surface brightness observed in 1958–1959 as a function of phase. The ordinate represents the brightness in the V spectral region (effective wavelength 0.54 μm); the T symbols represent the extrapolated brightness at zero phase angle. The dashed curve represents a Lambertian surface. (From Ref. 4.)

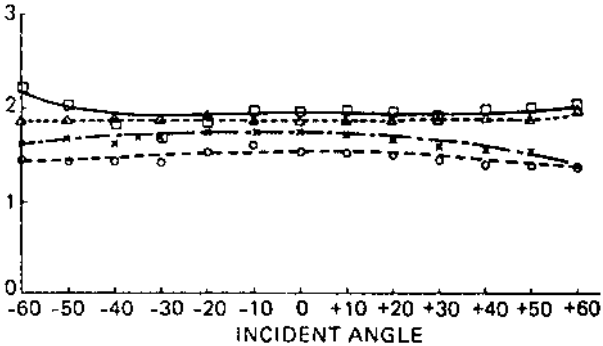

FIGURE 8 Retroreflectance effect at varying incident angles for $BaSO_4$ (×), $MgCO_3$ (○), white Nextel paint (△), and colloidal sulfur (□) for $\lambda = 0.6328$ μm He-Ne laser illumination with 1° source collimation and sensor acceptance angles. (From Ref. 1.)

(Fig. 8). It varies with the type of surface (Fig. 9) and can be up to a factor of 10× diffuse, Table 1, Reference 1, pp 139.

The explanation of a factor of 2× diffuse scatter is based on the theory of weak localization [9,10]. Electron localization and photon localization in a disordered material are governed by coherent backscattering caused by constructive interference of two wave traveling in opposite directions. The

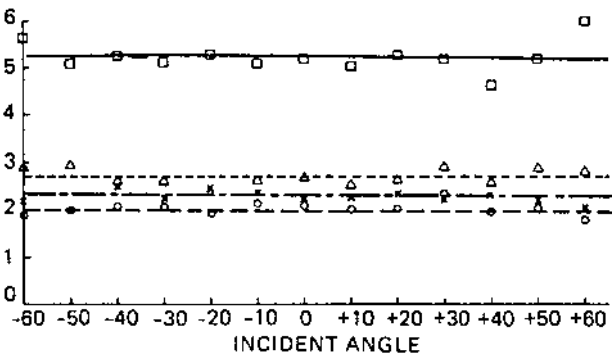

FIGURE 9 Retroreflectance effect at varying incident angles for $BaSO_4$ (×), $MgCO_3$ (○), white Nextel paint (△), and colloidal sulfur (□) for $\lambda = 0.6328$ μm He-Ne laser illumination with better than 1° source collimation and sensor acceptance angles. (From Ref. 1.)

TABLE 1 Laser (0.6328 μm) Opposition Effect[a] Referenced to 30° for Photometric Samples[b]

Sample	Opposition effect	Sample	Opposition effect
$MgCO_3$	1.35	Nextel blue	8
$BaSO_4$	1.49	Nextel red	1.40
Sulfur	1.76	Nextel black	11
Nextel white	1.31		

[a] From Ref. 1, pp 139.
[b] From Ref. 1, pp 142.

enhancement factor of 2 has an angular width governed by the diffusion length in the medium. However, the theory does not account for factors greater than 2 that have been observed (Table 1). The enhancement appears to be related to surface structure orientation that causes a coherent specular (physical optical) reflection that adds to the peaked retroreflectance.

IV. DEPOLARIZATION

A set of laser retroreflectance depolarization measurements at 0.6328 and 1.159 μm were made on white and red Nextel paints, magnesium carbonate, and Halon particulates for phase angles from 12.1° to 0° [3]. Depolarization is indicative of the amount of multiple scattering, because multiple scattering generally reduces polarization.

For instance, in Fig. 4 of Chapter 9 the 1.159 μm laser source is positioned so that its plane of polarization is either parallel or perpendicular to the plane of vision, and the sensor polarization is similarly positioned both for same-plane polarization and cross-polarization. The retroreflectance peak occurs only when the source and sensor polarizations are similarly aligned. The continuum at phase angles greater than about 4° is caused by multiple scattering, and the peak near 0° is the result of a single scattering. Note that exactly 0° is precluded by the lack of a beam splitter. There is no cross-polarization, indicating that the peak is caused by a single scattering. For a higher angular resolution with a beam splitter to permit measurements to exactly 0° (0.057° angular resolution at 0.6328 μm), more peaks are observed (Fig. 8 in Chapter 9). The double peaks near 0° are reproducible and indicative of weak field localization interference; shadowing cannot produce such a fine structure. Note that there is no retroreflectance in the cross-polarization traces.

V. REMOTE SENSING

The optical appearance of remotely sensed surfaces is affected by both coarse and fine-scale structure of the surfaces as previously noted. Large-scale surface variations cause a variable shadowing as a function of the phase angle and generally a minor variation in polarization. If the surface (which may be farm crops or forestry) has a small-scale structure (e.g., leaf structure or dust), the polarization is significantly affected. Thus far remote sensing has concentrated on wavelength-dependent photometry and has neglected polarization. It appears that, in the first place, the causes of polarization are not well enough understood, and second, the complication of polarization measurements doubles (if not quadruples) the amount of data obtained that have to be correlated with ground truth. The additional data are represented by the Stokes vector to include the plane of polarization and the amount of circular (or elliptical) polarization. However, the question arises as to whether the additional measurements are cost effective compared to single photometric observations. This determination is yet to be made except for specific applications (the clouds of Venus and the lunar surface).

VI. CONCLUSIONS

Polarization is significantly affected by fine-scale surface structure, which depolarizes incident polarized radiation by multiple scattering. When a single scatter exists as in polarized retroreflectance, the incident polarization is preserved. For specific structures, a fine-scale polarized retroreflectance structure exists.

On the macro scale, surface roughness produced by an oriented surface structure can cause high polarization in either of the two planes.

One military application of polarization is to characterize targets against backgrounds. This is possible with both ground-based and airborne targets. The additional data obtainable with polarization requires not only more elaborate sensing instrumentation (such as focal plane arrays) but also advanced analytical computing.

REFERENCES

1. Egan, W.G.; Hilgeman, T.W. In Optical Properties of Inhomogeneous Materials; Academic Press: New York, 1979.
2. Hansen, J.E.; Travis, L.D. Light scattering in planetary atmospheres. Space Sci. Rev. 1974, 16, 527–610.
3. Egan, W.G. Laser retroreflectance consistent with a polarized single-scatter weak electromagnetic field localization-interference phenomenon. Appl. Opt. 1994, 33, 535–543.

4. Egan, W.G. In Photometry and Polarization in Remote Sensing; Elsevier: New York, 1985.
5. Halajian, J.D.; Spagnolo, F.A. In Photometric Measurements of Simulated Lunar Surfaces; Grumman Res. Dept. Rep. RE-245, Grumman Corp.: Bethpage, NY, 1966.
6. Hapke, B.W. A theoretical photometric function for the lunar surface. J. Geophys. Res. 1963, 68, 4571–4586.
7. Trowbridge, T.S. Retroreflection from rough surfaces. J. Opt. Soc. Am. 1978, 68, 1225–1242.
8. Trowbridge, T.S. Rough surface retroreflection by focussing and shadowing below a randomly undulating surface. J. Opt. Soc. Am. 1984, A1, 1019–1027.
9. Ishimaru, A.; Tsang, L. Backscattering enhancment of random discrete scatterers of random size. J. Opt. Soc. Am. 1988, 5, 228–236.
10. Ishimaru, A. Experimental and theoretical studies on enhanced backscattering from scatters and rough surfaces. In Scattering in Volumes and Rough Surfaces; Nieto-Vesperinas, J., Dainty, J.C., Eds.; North-Holland: Amsterdam, 1990; 324 pp.

9

Polarized Laser Retroreflectance

I. INTRODUCTION

Retroreflectance by a rough surface is the brightness increase of a surface as the source–surface–observer angle (also termed the phase angle in astronomy) is decreased. Peaking is independent of the orientation of the surface relative to the source or observer. Retroreflectance (the opposition effect) was first discovered by Barabashev [1], who observed a sharp rise in the reflective intensity of lunar maria when the moon is full. This was further confirmed by Markov [2], van Diggelen [3], and Gehrels et al. [4].

A number of mechanisms have been proposed to explain theoretically the ubiquitous retroreflectance effect occurring not only with natural surfaces [5,6] but also with photometric standards and coatings. Trowbridge [7,8] proposed various geometrical optical (ray-tracing) mechanisms, such as lens retroreflectance and below-surface-shadowing retroreflectance. Hapke [9–11] and Hapke and Van Horn [12] proposed a theoretical lunar photometric function based on interparticulate shadowing.

For electromagnetic waves interacting with a dense medium, the energy scattered back in the retroreflection direction is significantly greater on average than in other directions [13]. This enhanced backscattering of light propagating in a dense medium has been reported for a dense random distribution of latex microspheres [14]. A sharp peak appears when the volume density is above 1%. The peak cannot be explained by Mie theory, double-passage effects, or radiative transfer theory. The peak has an angular width of between a few tenths of a degree and $\sim 2^\circ$. A second-order multiple scattering theory is used to calculate the scattered field, and Feynman diagrams

are used to represent the physical processes. The theory yields an angular width of the peak on the order of the attenuation rate divided by the wave number [15].

Further, in solid-state physics, electronic conduction in a disordered material is affected by coherent effects in its wave function, which is related to wave propagation. The probability that an electron will return to its starting point is not predicted in models based on the Boltzmann transport equation when the mean free path between consecutive collisions approaches their wavelength [13]. There is an enhanced probability that an electron will return to its starting point (enhanced backscattering), which reduces the electrical conductivity (weak electromagnetic field localization) [16]. This weak localization of photons with enhanced backscattering of light has only recently been recognized and promises to yield insight into the laser retroreflectance phenomena.

Oetking [17] was the first to demonstrate the opposition effect peaking in laboratory measurements. His system allowed observations to be made to within 1° of the incident direction. All of the materials measured showed the opposition effect. It was pointed out that the opposition effect could not be specular reflectance because it existed even when the surface was tilted at angles of up to 50° from the incident direction.

Subsequently Egan and Hilgeman [19–22] used various techniques including a cubic beam-splitting device to make retroreflectance measurements at exactly 0° incidence and viewing angles. Surfaces measured were photometric standards and coatings such as $MgCO_3$, $BaSO_4$ paint, sulfur, and Nextel white, red, blue, and black paints. The observations of Oetking were corroborated by the retroreflectance observations of Egan and Hilgemans [19] which included the use of lasers. The source collimation in their initial work was 1°.

The retroreflectance of the photometric samples in 0.6328 μm laser illumination varied somewhat from that in 0.600 μm incandescent illumination, with black Nextel paint having a retroreflection ratio (i.e., the ratio of retroreflection amplitude to reflected amplitude at the 30° phase angle) of 11 in laser radiation.

In a later set of experiments, Montgomery and Koh [23] made opposition effect measurements with a plane-polarized 0.6328 μm laser on $BaSO_4$ paint, leaves, grass, red clay, sand, and various other substances. Their measurements were of simple polarized and perpendicularly depolarized scattering not related to the plane of incidence. They showed that the scattered polarized retroreflectance peak occurred only when the analyzer was parallel to the polarization of the laser. They mentioned that the retroreflectance peak in the shadowing mechanism could result from single-scattering contributions, which should exhibit less depolarization than the multiply diffusely

scattered radiation. Equipment limitations yielded a lower limit of 10% of the incident radiation that could be established on the existence of perpendicularly (i.e., cross-polarized) diffuse backscatter at a phase angle of 0°.

The present research was similarly directed toward the measurement of the polarimetric properties of retroreflectance with 100% plane-polarized laser radiation at 0.6328 and 1.159 μm wavelengths down to 0° phase angles. The polarized and depolarized radiation scattered from various surfaces (e.g., white and red Nextel paint and $MgCO_3$) was sensed. A total of 39 surfaces were sensed, but only the results from the aforementioned surfaces are presented herein as representative. Various powder surfaces were also measured, but only Halon (powdered polystyrene) is discussed in this chapter.

II. EXPERIMENT

The measurement of retroreflectance requires positioning of the source and sensor so as to allow varying the phase angle from approximately 10° to exactly 0°. This positioning required two laser ranges: one (I) for angles from 0.26° to 12.1° (Fig. 1), and another (II) for phase angles from +1.2° to −0.1° (Fig. 2). The first system (Fig. 1) allowed the photomultiplier (RCA Type 6199 for 0.6328 μm and Type 7102 for 1.159 μm wavelengths) to be moved laterally in the horizontal plane [the plane of vision (POV)] in the x direction to achieve a range of phase angles. The laser used was usually the Keuffel & Esser alignment laser (now Cubic Precision Model 71–2610) having a 1.27 cm diameter beam, with improved collimation (to <0.5 mrad).

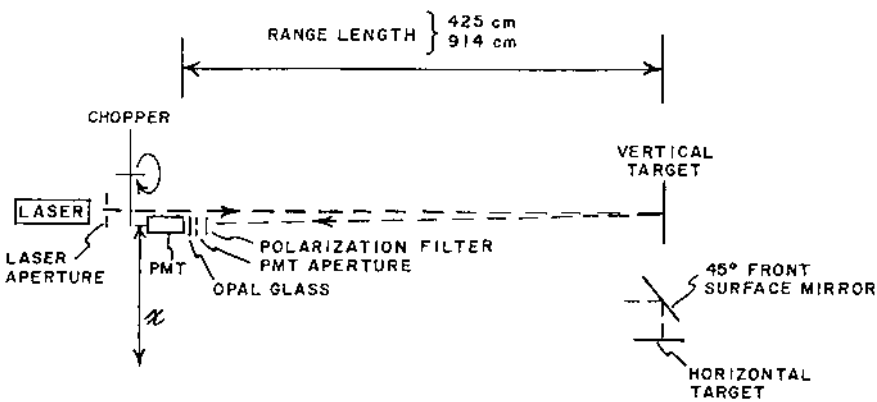

FIGURE 1 Laser range I. Layout showing laser and adjacent photomultiplier, chopper, baffles, and polarization filter. Targets may be placed vertically or, for powders, horizontally with the use of the 45° mirror.

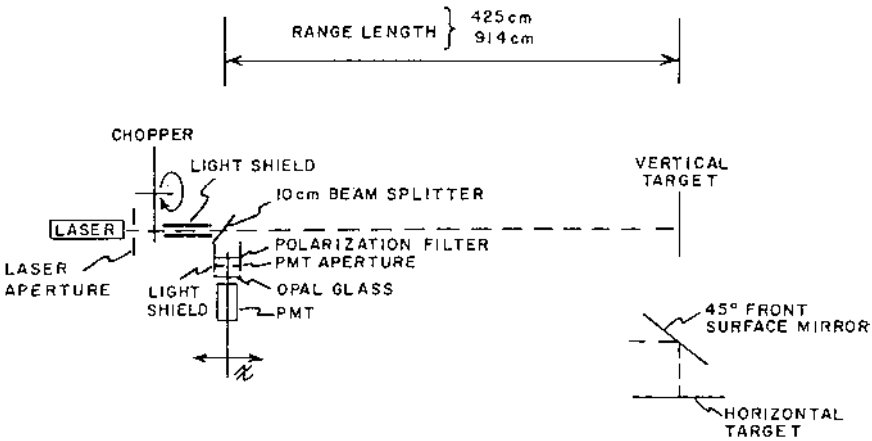

FIGURE 2 Laser range II. Layout showing laser and perpendicular photomultiplier viewing the 10 cm diameter beam splitter. Appropriate baffles are provided. Targets may be placed vertically or, for powders, horizontally with the use of the 45° mirror.

However, a Spectra-Physics Model 120 laser was used for 1.159 μm measurements (0.72 mm beam diameter, 2.1 mrad beam divergence). Some measurements were made with the Spectra-Physics Model 120 laser at 0.6328 μm (beam diameter 0.79 mm, beam divergence 1.0 mrad). Two sizes of apertures were used in front of the photomultiplier (PMT in the figure) and also in front of the Keuffel and Esser laser to improve the angular resolution of the measurements [24,25]. The photomultiplier aperture was 1.27 cm for measurements shown in Figures 3–7 and 9) and 0.424 cm for measurements shown in Figs. 8 and 10–12.

The angular resolution of the system was determined experimentally with a precision front-surface mirror located at the vertical (or horizontal) target. The photomultiplier was traversed across the reflected laser beam to measure the beam width at full width at half-maximum (FWHM). The position of the photomultiplier in the x direction was sensed by a potentiometer attached to the photomultiplier. The potentiometer was turned by a rack-and-pinion gear system affixed in the x direction. The potentiometer output was fed to the x position of a Houston Instruments X-Y recorder, and the photomultiplier output to the y position from a Princeton Applied Research phase-sensitive amplifier. The time for a single scan averaged 10 min, and this permitted improved speckle averaging. Powder samples were accommodated through the use of a 45° front-surface mirror located at the position of the vertical target.

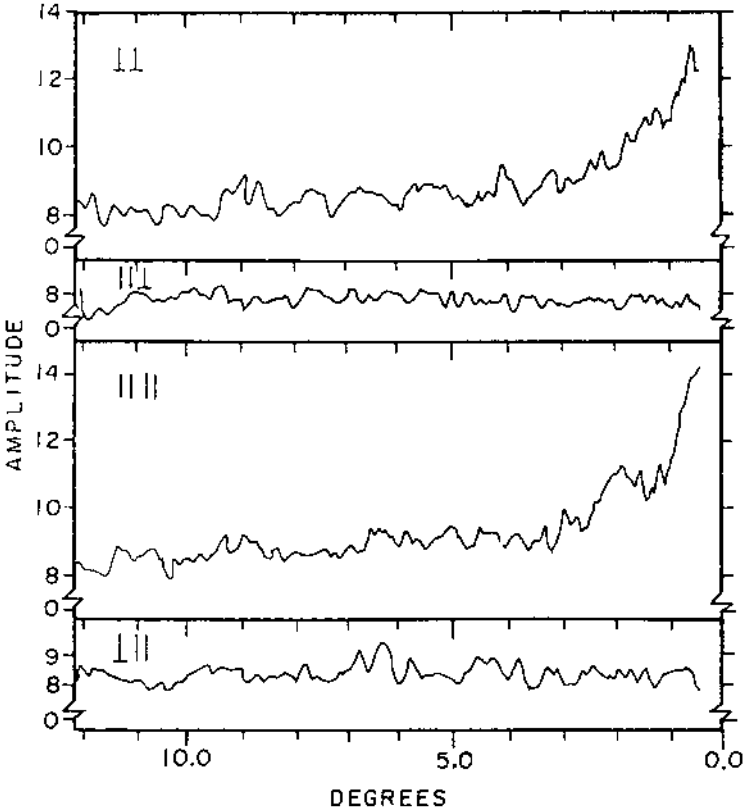

FIGURE 3 Retroreflectance amplitudes as a function of the included angle of white Nextel paint at 0.6328 μm laser wavelength for four laser–analyzer orientations on 425 cm range I. Optical angular resolution = 0.14°.

Range length was usually 425 cm, although the range could be increased to 914 cm to increase the angular resolution of the system. The polarization filter was located in front of the photomultiplier aperture, with an opal glass diffuser at the photomultiplier face.

Four polarization configurations were measured, which are identified first by the plane of polarization of the laser, then by the plane of polarization of the sensor relative to the plane defined by the laser, the sample, and the sensor (the POV). For example, $\perp \parallel$ means a configuration in which the plane of polarization of the laser was perpendicular to the POV and the sensed polarization was parallel to the POV.

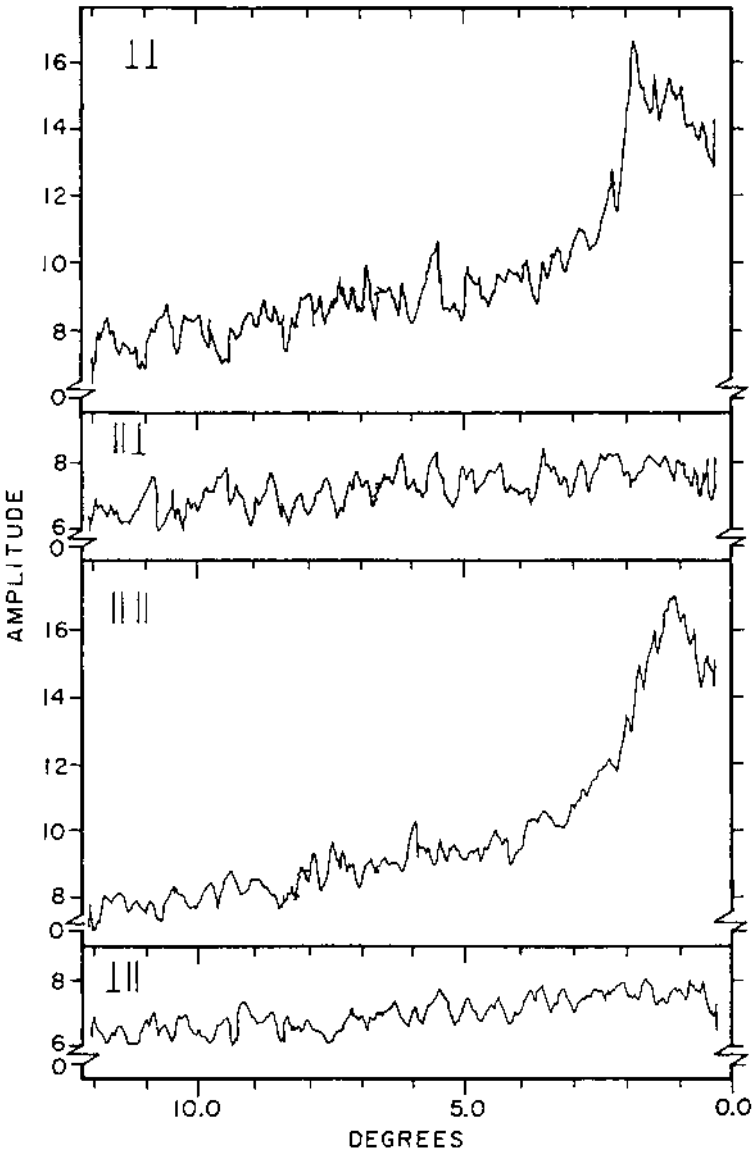

FIGURE 4 Retroreflectance amplitudes as a function of the included angle on a magnesium carbonate block at 1.159 μm laser wavelength for four laser–analyzer orientations on the 425 cm range I. The surface is tilted at 1° to the incoming laser radiation. Optical angular resolution = 0.18°.

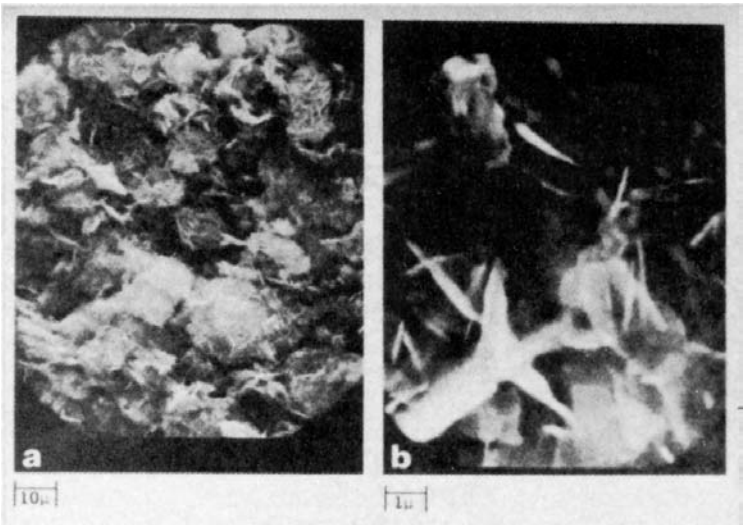

FIGURE 5 Scanning electron microscopic (SEM) images of the sample with a pressed $MgCO_3$ surface. (a) Magnification 1000×; (b) magnification 10,000×.

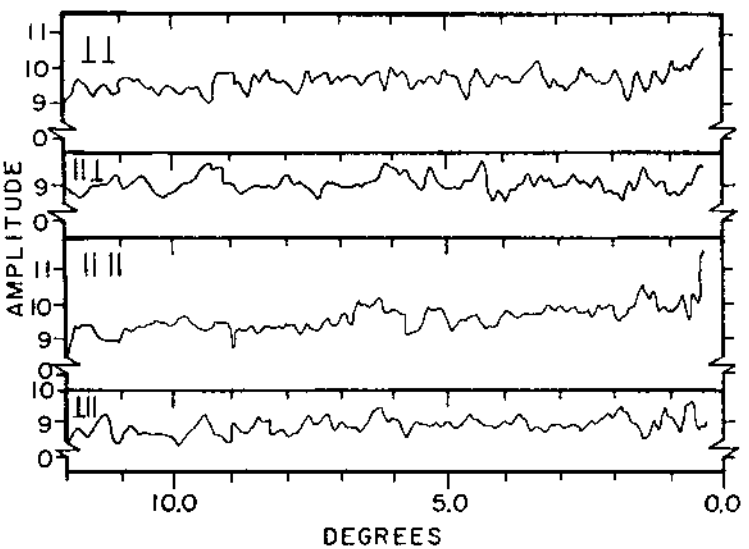

FIGURE 6 Retroreflectance amplitudes as a function of the included angle for Halon at 0.6328 μm laser wavelength for four laser–analyzer orientations on the 425 cm range I. Optical angular resolution = 0.14°.

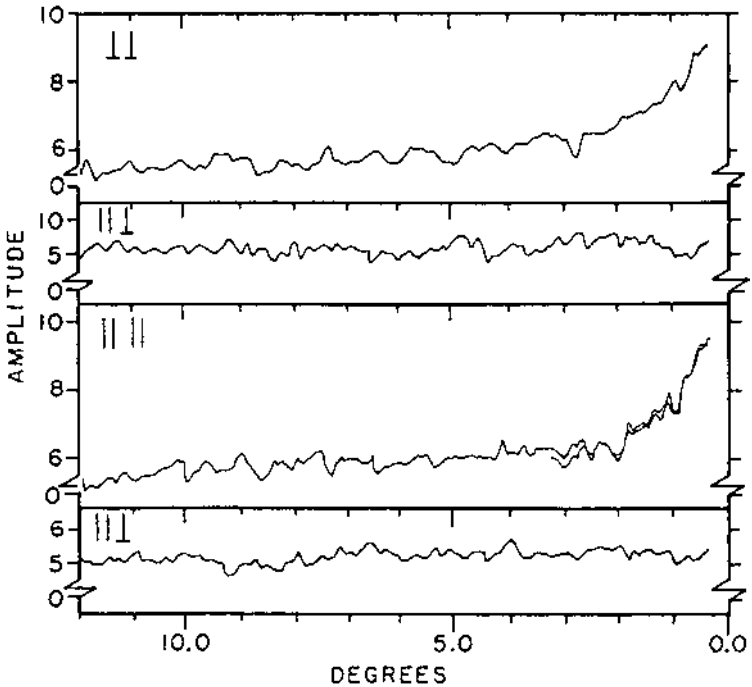

FIGURE 7 Retroreflectance amplitudes as a function of the included angle for red Nextel paint at 0.6328 μm laser wavelength for four laser–analyzer orientations on the 425 cm range I. Optical angular resolution = 0.14°.

The second laser range (II), shown in Fig. 2, allows measurements at exactly the 0° phase angle. Here the photomultiplier (and the rack-and-pinion potentiometer assembly) are located to permit transverse movement of the photomultiplier. The essential difference is a 10 cm diameter beam splitter; it is an Oriel general-purpose flat-glass component, flat to 1 wavelength over the 2.54 cm diameter and parallel to 30 seconds of arc or better. The surface is a standard optical polish with an Inconel front surface to provide increased reflection; the rear surface is coated with magnesium fluoride to reduce reflection to 1–2% between 400 and 700 nm. The transmitted wave-front distortion is less than 0.1 wave /2.54 cm. The position of 0° was set by autocollimation of the laser beam onto itself to the beam splitter.

Appropriate baffles are included, as are provisions for observing powder samples. The absolute amplitude accuracy of the polarization measurements is ±1% for measurements shown in Figs. 3, 4 and 6 and ±10% for measurements shown in Figs. 8–11.

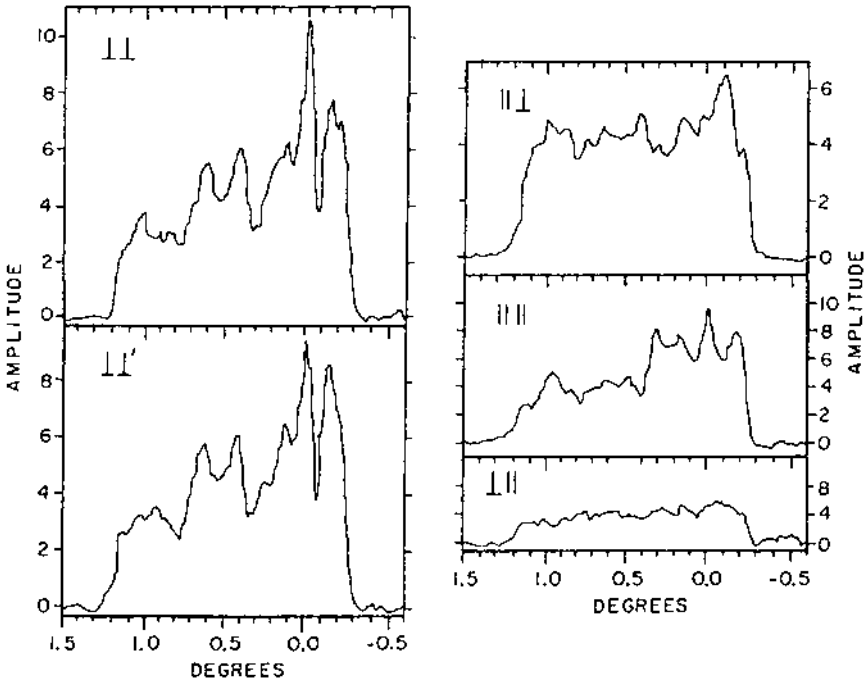

FIGURE 8 Retroreflectance amplitudes as a function of the included angle for a $MgCO_3$ block at 0.6328 μm laser wavelength for four laser–analyzer orientations on 425 cm range II. Optical angular resolution = 0.057°.

III. RESULTS

Experimental results for the four amplitudes of the polarized intensities are shown in Figs. 3, 4, and 6–12. Figures 3, 4, 6, and 7 show measurements at angles in the POV between 0.26° and 12.1° on white Nextel paint, $MgCO_3$, Halon, and red Nextel paint, respectively. Figure 5 shows a scanning electron microscopic (SEM) image of $MgCO_3$ used in the investigation. Figures 8–11 are measurements through the 0° phase angle from +1.2° to −0.1° for $MgCO_3$, white Nextel paint, and Halon. Figure 12 is a set of measurements at high resolution (0.076°) for white Nextel paint with the 914 cm range of laser II. The results are now analyzed in detail.

White Nextel paint is a standard diffuse photometric coating, but it has significant retroreflectance, as pointed out by Egan and Hilgeman [20], who also did scanning electron microscopic (SEM) imagery of the surface [20]. The present polarimetric determinations (Fig. 3) show significant retroreflectance for configurations ⊥ ⊥ and || || but no retroreflectance for || ⊥ or ⊥ ||.

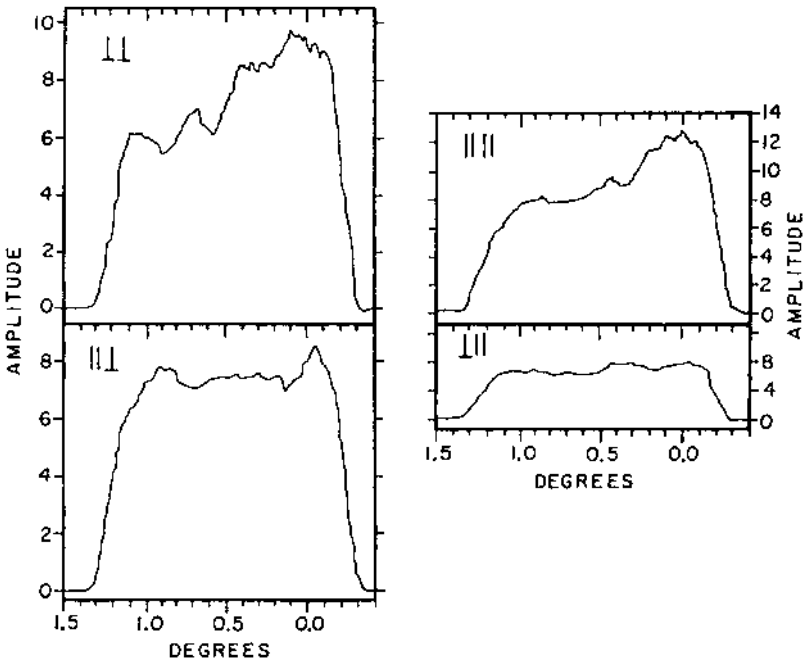

FIGURE 9 Retroreflectance amplitudes as a function of the included angle for $MgCO_3$ at 0.6328 μm laser wavelength for four laser-analyzer orientations on the 425 cm range II. Optical angular resolution = 0.17°.

The significance is that retroreflectance is produced only by a dominant single, polarized, in-plane scattering from the surface of the white Nextel paint, because only in that way will the perpendicular or parallel laser polarization be preserved. At larger phase angles, multiple scattering depolarizes the laser radiation scattered at the surface. As indicated in Fig. 3, the optical angular resolution of the system was 0.14°. Cross-polarized components resulting from geometrical multiple scattering with facets of the surface by the retroreflectance peak are down by several orders of magnitude and are not evident. The single scatter can then be geometrically shadowed by adjacent surface irregularities.

Going to Fig. 4 for the $MgCO_3$ block, which is tilted at an angle of ~1° to the incident radiation we see that the dominant retroreflectance peak does not occur at exactly 0° but is shifted by ~2°, revealing a sensitivity of retroreflectance to tilting of the sample surface, resulting from shadowing [7,8] in complex surfaces (Fig. 5). Again retroreflectance occurs only for the ⊥⊥ and || || orientations, not for the || ⊥ or ⊥ || orientations.

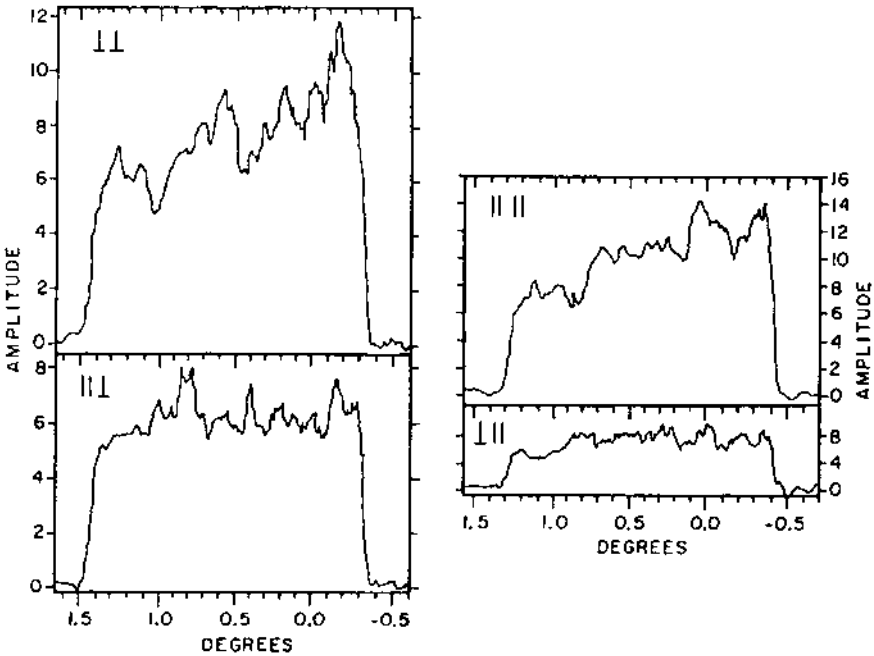

FIGURE 10 Retroreflectance amplitudes as a function of the included angle for white Nextel paint at 0.6328 μm laser wavelength for four laser–analyzer orientations on the 425 cm range II. Optical angular resolution = 0.057°.

The $MgCO_3$ surface (Fig. 5) is a random, apparently on-end, platelet structure as shown by the SEM imagery [26,27] (sometimes termed fairy castle); it is not amenable to systematic structure characterizations. It is difficult to conceive of the geometrical optical lens mechanism of Trowbridge [7] as an explanation of the observed retroreflectances. The present measurements (Fig. 4) were made at 1.159 μm wavelength with an optical angular resolution of 0.18°.

Figure 6 shows only a slight retroreflectance by Halon for the ⊥⊥ and || || configurations and the usual lack of retroreflectance for the || ⊥ and ⊥ || configurations. The Halon powder was measured on the horizontal surface, which had been previously checked with $MgCO_3$ and white Nextel paint for consistency with measurements of these samples when placed in the vertical position. Halon powder is not completely transparent, and it has a value nk 0.11×10^{-3} at a wavelength of 0.633 μm, where n is the refractive portion of the index of refraction and k is the absorption portion [27].

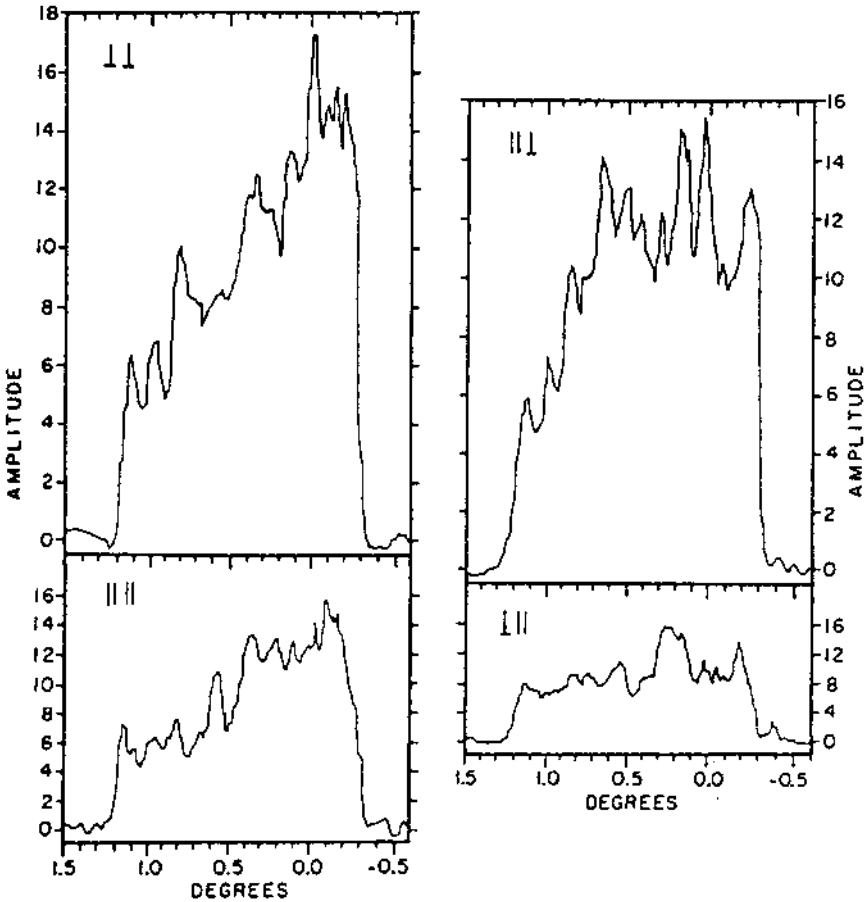

FIGURE 11 Retroreflectance amplitudes as a function of the included angle for Halon at 0.6328 μm laser wavelength for four laser–analyzer orientations on the 425 cm range II. Optical angular resolution = 0.057°.

It appears that the first surface-polarized scatter is probably masked by multiple internal depolarizing scattering, and the polarized retroreflectance peak cannot be seen. The optical angular resolution is 0.14°.

The retroreflectance observations for red Nextel paint at a wavelength of 0.6328 μm are presented in Fig. 7. Again we see strong retroreflectance in configurations ⊥⊥ and || || and none in || ⊥ or ⊥ ||. However, in || ||, a second run was made, overlapping the first. It can be seen that the resulting curves

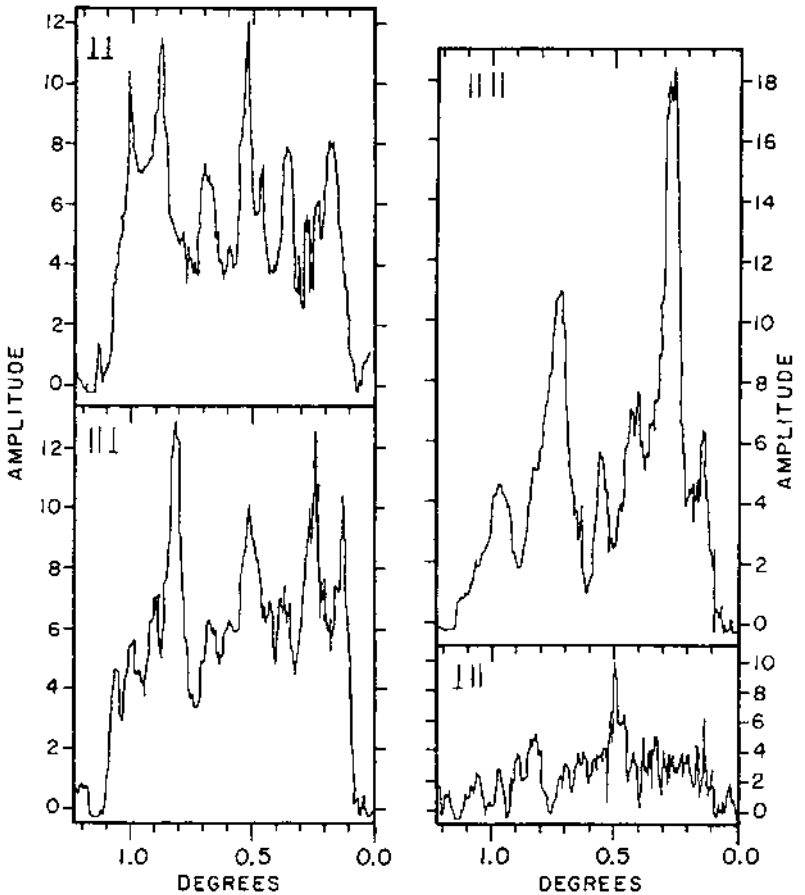

FIGURE 12 Retroreflectance amplitudes as a function of the included angle for white Nextel paint at 0.6328 μm laser wavelength for four laser–analyzer orientations on 914 cm range II. Optical angular resolution = 0.076°.

consistently have the same shape, with slight variations being caused by speckle noise. Optical angular resolution is 0.14°. The speckle noise is of the order of λ/a, where λ is the laser wavelength (0.6328 μm) and a is the sample dimension (~ 1 cm). These speckle fluctuations cause the deviations (the zero axis on the curves is suppressed as shown). A SEM image of red Nextel paint is in Ref. [18].

The question naturally arises as to whether geometrical optical surface shadowing [7,8] is causing the observed retroreflectance variations. Shad-

owing cannot occur for structures herein described that have dimensions on the order of, or shorter than, the wavelength of the illuminating radiation (i.e., because strong diffraction occurs). Or is an optical interference phenomenon arising from weak localization causing the polarized fine structure observed in the retroreflectance? Basically, the question is whether geometrical optics or physical optics or both apply to retroreflectance.

To test the concept of weak localization causing a constructive interference to produce a coherent wave front, a set of high resolution curves for $MgCO_3$ with $\perp\perp$ and $\perp\perp'$ was run sequentially; here the prime denotes a second curve with the same $\perp\perp$ geometry. As shown in Fig. 8, there are close similarities in the resulting curves. For interference to occur, as in a diffraction grating, the spacing of the lines would have to be on the order of 50 μm. Clearly (referring to Fig. 5), $MgCO_3$ does not resemble a diffraction grating, but coherent constructive interference can occur from waves diffracted under the effects of weak localization by the $MgCO_3$ platelets. For geometrical shadowing to occur, the $MgCO_3$ surface platelets must have an angle relative to the surface on the order of 1°, and they must be of large dimensions compared with the illuminating wavelength. Considering the $MgCO_3$ surface structure as shown by the SEM imagery (Fig. 5), the surface does have the structure required for shadowing, but the platelet dimensions are comparable to the laser wavelength. The surface also has a structure that could cause coherent interference in single scattering that would be affected by weak localization, which produces a coherent wave front. Again speckle noise is evident and causes small disagreements between the $\perp\perp$ and $\perp\perp'$ curves.

Another point to be made is that the optical angular resolution is 0.057° for these curves, which is enough to resolve microshadowing caused by crevices in the surface. Sharp peaks on the surface do not give microshadowing. The system resolution is apparently high enough that if the sensed area is changed, the retroreflectance pattern is changed, so the high resolution retroreflectance peaking cannot be used as a general surface characterization. The configurations $\perp\perp$, $\perp\perp'$, and $||\ ||$ do show significant peaks at $\sim -0.2°$; These peaks are probably a result of the alignment tolerance of the surface to $\sim \pm 0.1°$.

For configurations $||\ ||$ and $||\ \perp$, fine structures can be seen (Fig. 8). The $||\ ||$ constructive interference pattern arising from weak localization (with retroreflectance apparent) is understandable as single scattering, but the curve for $||\ \perp$ shows a small fine structure at small angles of incidence.

Figure 9 is a set of traces for the $MgCO_3$ surface, except that a lower resolution (0.17°) is used. Retroreflectance (with the constructive interference effects from weak electromagnetic field localization smoothed out) is apparent for configurations $\perp\perp$ and $||\ ||$ but not for $||\ \perp$ or $\perp\ ||$.

Figure 10 is a similar set of curves for white Nextel paint at 0.6328 μm wavelength, with an angular resolution of 0.057°. Again clear evidence of retroreflectance is shown for ⊥⊥ and || || but not for || ⊥ or ⊥ ||.

Halon (Fig. 11) shows clear evidence of retroreflectance plus constructive optical interference from weak electromagnetic field localization for the ⊥⊥ and || || configurations. The fine structure for || ⊥ appears to be the result of transparency of the Halon and internal scattering.

The last set of curves (Fig. 12) is for white Nextel paint on laser range II at an optical resolution of 0.076°. The 1° angular scale range has a fine structure that would not be revealed by shadowing; hence it must be an optical interference effect from the weak electromagnetic field localization coherent wave front. The peaks shown for configuration ⊥⊥ mask retroreflectance, although configuration || || shows some optical interference effect.

IV. DISCUSSION

This experimental investigation shows that configurations ⊥⊥ and || || exhibit sharp retroreflectance peaks, which are not exhibited when configurations ⊥ || and || ⊥ are measured. This occurs for all sample surfaces.

We find that the speckle noise is small, as a result of effects of the sample size, wavelength, sampling aperture, and long scan times for the conditions shown in Figs. 3–7 and 9. For the conditions shown in Figs. 8 and 10–12, there is somewhat more speckle noise, but it is not so excessive as to mask the retroreflectance signal.

The structures of the retroreflectance curves shown in Figs. 8 and 10–12 must be the result of a specific optical phenomenon because they are reproducible [see Fig. 7 (⊥⊥) and Fig. 8 (⊥⊥ and ⊥⊥′)]. What could cause such structure? The following factors are considered: noise, shadowing, simple interference, multiple scattering, and interference by weak electromagnetic field localization.

Noise. There is some speckle noise ($\lambda/a \cong 0.006$ average width), but it is small in the present experiment.

Shadowing. For shadowing to occur, there must be very sharp contours. It could occur, as with the platelets of MgCO3 that are perpendicular to the surface. Shadowing requires a surface structure that is large compared to the illuminating wavelength.

Simple interference. This could exist by virtue of the coherent laser radiation sources, but for simple interference to occur alone, some spatial (periodic) restrictions on the surface structure would be required.

Multiple scattering. A trough caused by suitably oriented platelets or facets in the sample surface could result in multiple scattering on the order of 2, which could cause a retroreflectance peak. Similarly, such a surface-scattering ensemble would also contain arbitrarily oriented facets that could cause a corresponding depolarization retroreflectance peak; however, such a peak is not observed.

Weak electromagnetic field localization. In the paper by Neito-Vesperinas [13], wave propagation in a random medium is characterized by the progress of the wave function in a multiple-scattering loop with a complex amplitude A_f. Each loop has its reverse (with complex amplitude A_b), and the outgoing waves from the two loops have the same complex amplitude $A = A_f = A_b$ and can interfere constructively so that the total intensity I is given by

$$I = |A_f|^2 + |A_b|^2 + 2\,\mathrm{Re}[A_f A_b] = 4|A|^2$$

whereas if the cross term were neglected the result would be $I = 2|A|^2$. Thus the constructive (retroreflectance) peak is twice the diffuse background, as seen (approximately) in the conditions shown in Figs. 3, 4, and 7 but not in the conditions for Halon, as shown in Fig. 6. Thus there appears to be considerable justification for the theory that weak electromagnetic field localization causes the retroreflectance peak obtained with certain samples. It is noted that the present one-dimensionality of the theory precludes the study of depolarization effects, here shown experimentally to be negligible. The weak electromagnetic field localization effect occurs in association with interference to augment the retroreflectance peak and produce a coherent and scattered wave front. The factor of 2 enhancement above the nonenhanced scattered light has also been predicted for discrete random media [14,28,29].

The curves for configuration || || (Fig. 7) were shown primarily to illustrate their reproducibility (including speckle noise). They are not a random fluke but are reproducible on any retroreflectance curve, allowing for the effect of speckle noise.

What can we conclude?

1. Multiple scatter (except under specific conditions, such as when caused by a trough with its long dimension oriented perpendicular or parallel to the plane of incidence), both internal and external, depolarizes radiation such as that caused by scatter from the $MgCO_3$ surface (Fig. 5). Therefore the retroreflectance peak could be the result of a single scattering by edges and asperities of the $MgCO_3$ surface. This is also inferred for the Nextel paints and Halon.

2. The signal-to-noise ratio is ~100:1 for laser range I and ~10:1 for laser range II.
3. Shadowing (microshadowing for narrow crevices) is physically realizable for a platelet structure ($MgCO_3$) and is inferred to exist similarly for the Nextel paints and Halon.
4. Interference (not in the diffraction grating sense, but in the sense of interference of a coherent scattered wave front) can exist and is caused by weak electromagnetic field localization. This appears to verify the physical theory that weak electromagnetic field localization causes the fine structure observed in the retroreflectance, modified as appropriate by geometrical shadowing.

Although the investigations were performed with lasers, the retroreflectance effect has been shown to be present for low coherence illumination as well [20]. We can infer that one explanation of the basic retroreflection phenomenon is that it could be the result of the polarized single scattering with incoherent illumination, as with laser radiation.

Thus geometrical theories based on simple surface shadowing do not explain the physical optical effects of the dominant polarized scatter of the incident radiation, and those theories need to be revised. An appropriate polarized scattering theory is not easily conceived because the surfaces observed for the aforementioned results have an ensemble of random edges and asperities and thus are transitional between geometrical optics and physical optics. A suitable model must await an appropriate mathematical treatment to include both polarization and depolarization.

Black Nextel paint, which had a demonstrated [21] retroreflectance ratio of 11, was observed to have a constructive interference fringe in the present experiments at 0° that produced this level of retroreflectance. I am aware of laser retroreflections from overhead wires that were 50 times that expected from their cross section; this again appears to be the effect of a coherent interference phenomenon for polarized radiation.

V. CONCLUSIONS

From the data presented in this chapter, it is evident that laser retroreflectance could be the result of a dominant single polarized backscattering with subsequent adjacent-particle shadowing, by asperities in the surfaces considered in this study. Also, selected multiple scattering (or weak electromagnetic field localization) could cause a similar effect, with constructive interference along the wave front. Where the surface is transparent, laser retroreflectance is small, apparently from much internal scattering, which reduces both the polarizing effect of the first surface-polarized single scattering and shadowing by adjacent surface particles. For incidence angles near normal and at higher

angular resolutions, polarized interference fringes appear that presumably would be masked in low coherence illumination.

From the evidence presented for retroreflectance it appears that surface models must be reformulated and based on a dominant, polarized single scattering by surface edges and asperities. Both the physical and geometrical optical properties of the scattering must be considered.

REFERENCES

1. Barabashev, N.P. Bestimmung der Erdalbedo und des Reflectiongesetzes fur die Oberflache der Mondmeere Theorie der Rillen. Astron. Nachr. 1922, 217, 445–452.
2. Markov, A.V. Les particularites dans la reflexion de la lumière par la surface de la lune. Astron. Nachr. 1924, 221, 65–78.
3. van Diggelen, J. The radiance of lunar objects near opposition. Planet. Space Sci. 1965, 13, 271–279.
4. Gehrels, T.; Coffeen, T.; Owings, D. Wavelength dependence of polarization. III. The lunar surface. Astron. J. 1964, 69, 826–852.
5. Halajian, J.D.; Spagnolo, F.A. Photometric measurements of simulated lunar surfaces. Grumman Res. Dept. Rep. RE-245, Bethpage, NY: Grumman Corp., 1966.
6. Halajian, J.D.; Spagnolo, F.A. Photometric measurements of simulated lunar surfaces. Grumman Res. Dept. Memo. RM-308, Bethpage, NY: Grumman Corp., 1966.
7. Trowbridge, T.S. Retroreflection from rough surfaces. J. Opt. Soc. Am. 1978, 68, 1225–1242.
8. Trowbridge, T.S. Rough-surface retroreflection by focusing and shadowing below a randomly undulating surface. J. Opt. Soc. Am. A 1984, 1, 1019–1027.
9. Hapke, B.W. A theoretical photometric function for the lunar surface. J. Geophys. Res. 1963, 68, 4571–4586.
10. Hapke, B.W. An improved theoretical lunar photometric function. Astron. J. 1966, *73*, 333–339.
11. Hapke, B.W. An improved lunar photometric function. Astron. J. 1966, 71, 386A.
12. Hapke, B.; Van Horn, H. Photometric studies of complex surfaces, with applications to the moon. J. Geophys. Res. 1963, 68, 4545–4570.
13. Neito-Vesperinas, M. Enhanced backscatter. Opt. Photon. News 1990, 1 (12), 50–52.
14. Tsang, L.; Ishimaru, A. Backscattering enhancement of random discrete scatterers. J. Opt. Soc. Am. A 1984, 1, 836–839.
15. Kuga, Y.; Ishimaru, A. Retroreflectance from a dense distribution of spherical particles. J. Opt. Soc. Am. A 1984, 1, 831–835.
16. Abrahams, E.; Anderson, P.W.; Licciardello, D.C.; Ramakrishnan, T.V. Scaling theory of localization: absence of quantum diffusion in two dimensions. Phys. Rev. Lett. 1979, 42, 673–676.

17. Oetking, P. Photometric studies of diffusely reflecting surfaces with applications to the brightness of the moon. J. Geophys. Res. 1966, 71, 2505–2513.
18. Hapke, B. Comments on paper by Philip Oetking. Photometric studies of diffusely reflecting surfaces with applications to the brightness of the moon. J. Geophys. Res. 1966, 71, 2515.
19. Egan, W.G.; Hilgeman, T. Retroreflection measurements of photometric standards and coatings, II. J. Opt. Soc. Am. 1976, 67, 252.
20. Egan, W.G.; Hilgeman, T. Retroreflectance measurements of photometric standards and coatings. Appl. Opt. 1976, 15, 1845–1849.
21. Egan, W.G.; Hilgeman, T. Retroreflection measurements of photometric standards and coatings, Part 2. Appl. Opt. 1977, 16, 2861–2864.
22. Egan, W.G.; Hilgeman, T.W. Optical Properties of Inhomogeneous Materials; Academic Press: New York, 1979.
23. Montgomery, W.W.; Kohl, R.H. Opposition-effect experimentation. Opt. Lett. 1981, 5, 546–548.
24. Johnson, N.L.; Stephensen, H.F. Influence of aperture size and photometry of retroreflectors. Appl. Opt. 1980, 19, 1247–1252.
25. Rennilson, J.J. Retroreflection measurements: a review. Appl. Opt. 1980, 19, 1234–1235.
26. Egan, W.G.; Hallock, H.B. Coherence-polarization phenomena in remote sensing. Proc. Inst. Elect. Eng. 1969, 57, 621–628.
27. Egan, W.G. Photometry and Polarization in Remote Sensing; Elsevier: New York, 1985.
28. Ishimaru, A.; Tsang, L. Backscattering enhancement of random discrete scatters of moderate size. J. Opt. Soc. Am. 1988, 5, 228–236.
29. Mishchenko, M.I. Enhanced backscattering of polarized light from discrete random media: calculations in exactly the backscattering direction. J. Opt. Soc. Am. 1992, 9, 978–980.

10

Remote Sensing of Seismic Disturbances*

I. INTRODUCTION

Space methods are widely used for investigations of seismically active regions. This approach is based mainly on the use of space images of the earth's surface in the visible and near-infrared spectral range (0.5–1.7 μm) with high spatial resolution. These images capture the spectral response of the earth's surface and its relief. Therefore, they are useful for the study of lineament morphological structures and neotectonic movements in seismically active regions [1]. On the other hand, space images in the far-infrared range (8–14 μm) detect the temperature of the earth's surface and are amenable to polarimetric measurements.

It has been reported that preseismic activity alters the characteristics of soils, including their moisture [2], gas content, and composition [3,4]. Polarization in the visible range is very sensitive to soil moisture content, with higher polarization occurring with increased moisture [5]. In the visible range, polarization is highly sensitive to surface structure and thus permits identifying all ground features with much more facility than photometry [6]. In the 8–12 μm infrared, the polarization of emitted radiation is also a function of surface structure and appears to be another aspect applicable to earthquake

*Adapted from a presentation by Aleksandr Salman, Walter G. Egan, and Andrew Tronin at the Society of Photo-Optical Instrumentation Engineers in San Diego, CA, 22–23 July 1992 at the conference "Polarization and Remote Sensing."

remote sensing [7]. There are also numerous observations of surface and near-surface temperature changes prior to core earthquakes. For example, soil temperature anomalies of 2.5 K were measured in the zone of preparation of the Tangshan earthquake (China, 1976; magnitude > 7.0) [8]. Thermal changes due to changing stress fields, as well as other naturally occurring phenomena have also been determined in laboratory studies of materials [9,10]. For example, infrared remote sensing was successfully used to determine the increase in surface temperature before the eruption of volcanoes [11]. Advanced spaceborne equipment for remote sensing in the IR spectrum (e.g., HCMM radiometer, AVHRR-2) makes it possible to monitor a thermal field with a spatial resolution of about 1 km and with a temperature resolution of 0.5 K. Surveys are repeated every 12 h for NOAA series satellites. Therefore, variations in outgoing IR radiation during the period of preparation of earthquakes can be closely monitored.

II. INFRARED IMAGERY OF SEISMICALLY ACTIVE REGIONS (SOVIET CENTRAL ASIA)

The facts described in Section I stimulated the analysis of long-term series of IR images in relation to seismic activity. The area of study was the seismically active region of Central Asia—Tien-Shan, Kizilkums, and Kazakhstan. A great number of cloudless days per year in this region and its flat relief form favorable conditions for infrared surveys; i.e., the corrupting contribution of these factors to the outgoing infrared flux tends to be minimum. A night period of infrared monitoring (an hour before dawn) avoids the effects of nonuniform solar heating over the region. As the very first step of the study, an attempt was made to determine the general features of infrared radiation in that area of Central Asia. The analysis of a series of night-time IR images (from NOAA satellites) showed the presence of positive spatial anomalies of infrared outgoing flux. The temperature range of these anomalies reaches approximately 3–5 K. These anomalies are associated with the largest linear structures and fault zones of the regions considered [12]. The study of a continuous series (100–250 days per year) of the night-time infrared images taken over the Central Asian regions for a period of six years allowed the identification of a set of infrared anomalies with their geological locations (Fig. 1). Positive infrared anomalies of an intensity of several degrees at the foot of Kopetdag area had a linear shape 25–30 km in width and about 500 km in length. This anomaly is spatially related to the Predkopetdag fault (Fig. 1, line I–I), a boundary structure of the first order separating alpine Kopetdag area formations from the Turan plate [13]. Besides that, the anomaly coincides with the "thermal line" of Kopetdag's waters, the discharge zone of groundwater.

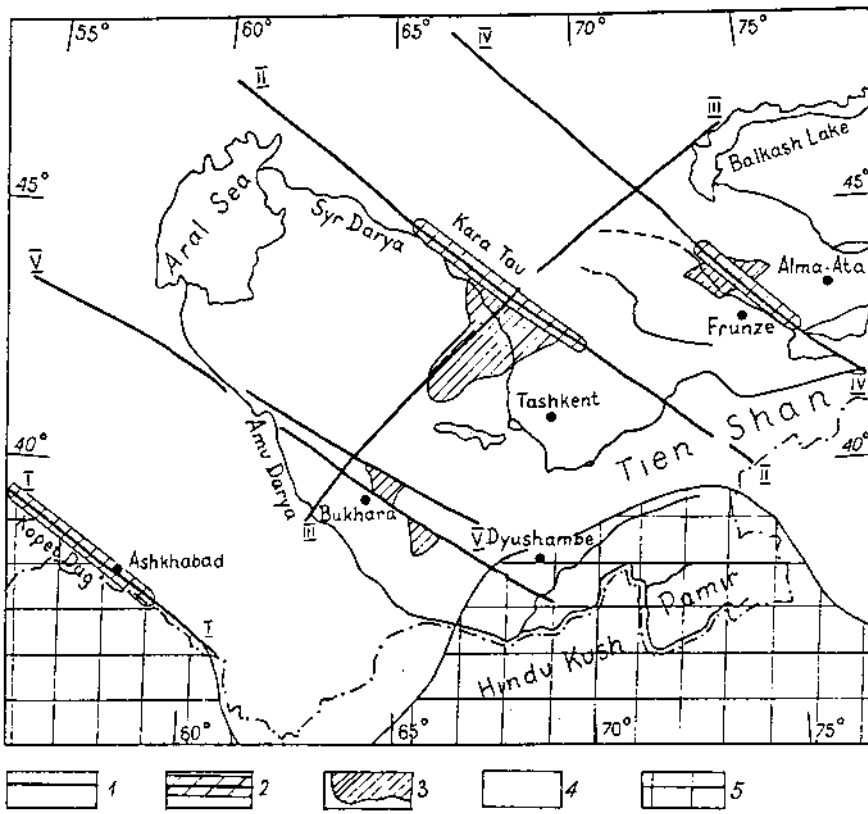

FIGURE 1 Tectonic sketch of the area of study in Central Asia. 1, faults; 2, stationary IR anomalies; 3, nonstationary IR anomalies; 4, Tien-Shan and Turan plates (Paleozoic); 5, Pamir and Hindu Kush (Meso-Cenozoic). faults: I–I, Predkopetdag; II–II, Karatau; III–III, Tamdi–Tokraus; IV–IV, Jalair-Naiman; V–V, Bukhara system.

Another significant anomaly about 50 km in width and 300 km in length was observed at the foot of the Karatau Range. Spatially this anomaly coincides with the Karatau fault (Fig. 1, line II–II), a structure of the first order separating the Turan plate from the Central Asian folded zone. The Karatau fault is the extension of the deep Talass-Fergana fault, which basically controls the geodynamics of the Central Asian region.

The permanent anomalies described above, however, contain variable components of intensity and dimensions. The anomaly at the foot of Karatau Ridge has the most significant variations in both of these components. Nonstationary properties of Karatau's anomaly occur occasionally at the

same position at the point of intersection of the Karatau and Tamdi-Tokraus faults (Fig. 1, line III–III). Similar properties of an infrared radiation field were observed over the Jalair-Naiman and Bukhara faults. The duration of these anomalies (several days) and their permanent spatial positions make it possible to reliably select them from among the temporary anomalies produced by meteorological factors.

III. NONSTATIONARY IR ANOMALIES AND CENTRAL ASIAN SEISMICITY

An earlier study [14] showed that there is a possible correlation between the nonstationary IR anomaly at the point of intersection of the Tamdi-Tokraus and Karatau faults and the seismic activity in the region of Gazli known because of Gazli earthquakes of 1976 and 1984, which had magnitudes exceeding 7.0 according to the Richter scale. The epicenters of these strong earthquakes were apparently located along the Tamdi-Tokraus fault zone. The examination of satellite night thermal images taken over this region several days before the events revealed the appearance of the IR anomaly mentioned above. The area of anomalies in both cases exceeds 100,000 km^2. This coincidence gave us the impetus to study a long series of thermal satellite images along with the seismicity of the Central Asian region. The results of this study are discussed next.

The indicator of seismic activity was calculated by using a conventional technique, i.e., by calculating the number of K_0 energy class (where K is the energy class and the energy class relates to earthquake magnitude) seismic events taking place in the region during the current period of time. The number of earthquakes different from the K_0 energy class was reevaluated in reference to the number of K_0 class events according to the equation

$$N_{K_0} = \sum\nolimits_K [\log\ N_K + \gamma(K - K_0)] \tag{1}$$

where K_0 is the number of K energy class earthquakes, $K_0 = 13$; and γ is the recurrent factor, which equals 0.49 for the Central Asian seismically active region.

The seismicity of the entire Central Asian region as well as the seismicity of its tectonically different provinces have been considered (Fig. 1). The first region the Paleozoic geosyncline, consists of the Turan plate and the Central Asian folded zone (Tien-Shan). Most earthquakes here have crustal origin with epicenters in Tien-Shan, Kizilkums, and southern Kazakhstan. The second region is related to the Mediterranean–Asian folded belt of the Meso-

Cenozoic Age and is characterized by Pamir-Hindukush earthquakes, which are intermediate and deep focused in origin.

The maximum of the annual activity of the IR anomaly at the point of intersection of the Tamdi-Tokraus and Karatau faults coincides with the peak of the annual seismic activity for the first region (Fig. 2). The correlation factor of these parameters is 0.86. This is statistically significant at the 0.95 confidence level. The seismic activity of the Pamir-Hindukush region does not correlate with time variations of the annual activity of the IR anomaly. The relation between seismic and infrared activity has been studied in more detail over time series with a monthly window of determination of seismic and infrared characteristics. The correlation factor between seismicity (earthquakes with $K > 12$ have been compared) and the IR anomaly activity is equal to 0.67 for the region of the Turan plate and Tien-Shan. The correlation coefficient is statistically significant with a confidence level of 0.99. Thus, there is statistical correlation between seismic activity and activity of infrared flux at the point of the intersection of two deep faults controlling the tectonics and seismicity of the Turan plate and Tien-Shan. Considering the infrared anomaly in terms of area $S(t) = \int s(\tau)d\tau$ S(t) is the summation of the smaller areas s(τ) we

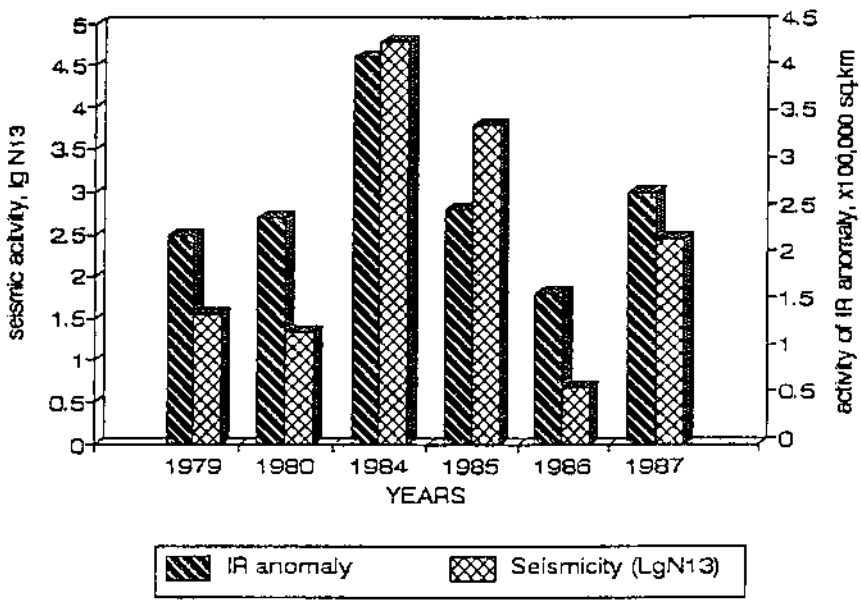

FIGURE 2 Correlation between active area of IR anomaly and seismicity of Turan plate and Tien-Shan (annual window of averaging).

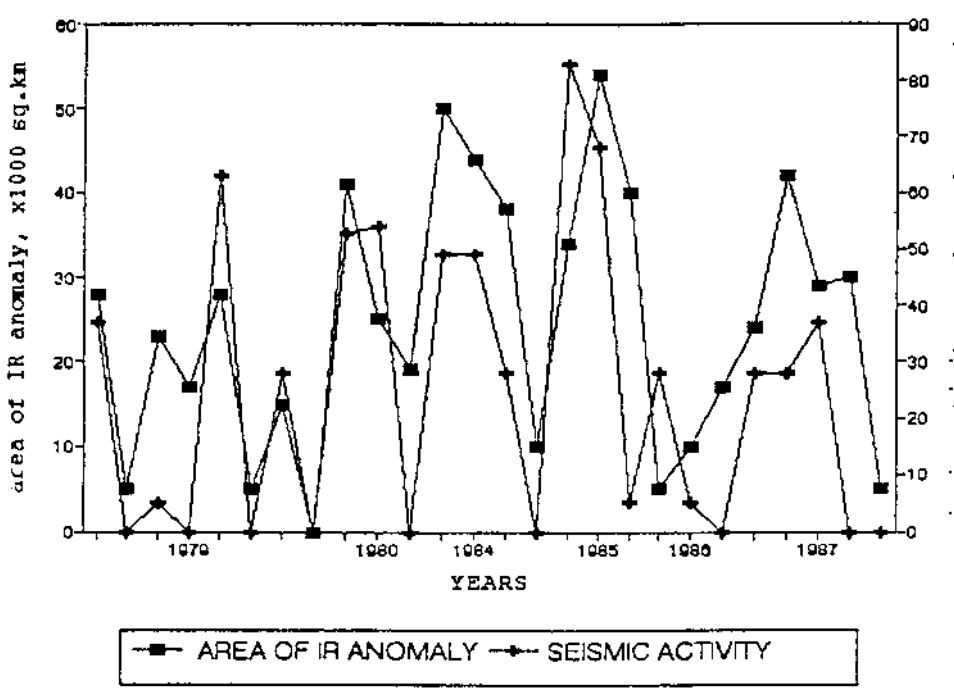

FIGURE 3 Correlation between active area of IR anomaly and seismicity of Turan plate and Tien-Shan (monthly window of averaging).

analyzed an area of IR anomaly $S(t)$, for a current area $s(\tau)$ of the anomaly per day, and seismic events being registered during this period of time on the Turan plate and in Tien-Shan, which showed that the most recent events were associated with periods of increasing accumulated energy of the infrared anomaly (Fig. 3). Practically all earthquakes with $K > 12$ registered in this region occurred during the growth periods of the anomalous area. It is a curious fact that the curve of the activity of the infrared field at the point of intersection of the Tamdi-Tokraus and Karatau faults and associated seismicity show a resemblance to the discontinuous deformation curve known for solids.

IV. MODELS OF THE ORIGIN OF INFRARED ANOMALIES ASSOCIATED WITH SEISMIC ACTIVITY

General consideration of the earth's outgoing infrared flux is based on the classical law of radiation of a heated body. According to the Stephan–

Boltzmann law, the integral radiation flux of a graybody (the earth's surface is usually considered as a graybody) is given as

$$R = \sigma \varepsilon T^4 \tag{2}$$

where σ is the Stephan–Boltzmann constant, ε is the emissivity of the surface, and T is temperature, in kelvins.

Wein's shift law,

$$\lambda_{\max} = 2897.8/T \tag{3}$$

allows the determination of the wavelength $\lambda_{\max}$ that corresponds to the maximum radiation density at any surface at temperature T. For example, in the case of an actual surface temperature range of 0–100°C, the radiation peak falls in the 7.75–10.50 μm wavelength range. Obviously, infrared radiation measured by a detector installed, for instance, onboard a satellite, is attenuated but negligibly polarized by the atmosphere. The minimal absorption of IR radiation by the atmosphere is observed over the ranges of 3–5 μm and 8–13 μm except at the water or carbon dioxide bands. Consequently, the spectral peak of the earth's radiation falls in one of the atmospheric passbands of 8–13 μm, which is called the second transparency window. The wavelength range contributes to the success of infrared monitoring in the range of 8–13 μm in surface temperature studies. The surface IR field is generated due to its temperature, which in turn is due to the absorbed solar energy and to a lesser extent the geothermal flux. The main parameters that define the conditions of IR signal generation are ε_s, the emissivity of the surface; A, the albedo (reflecting ability), or 1 - A, the absorbing ability of rocks over the wavelength range of the incident light flux; and thermophysical properties of rocks such as λ, thermal conductivity; C, heat capacity; and ρ, density. The equations of thermoconductivity,

$$c\rho \frac{\partial T(z,\tau)}{\partial \tau} = \lambda \frac{\partial^2 T(z,\tau)}{\partial z^2} \tag{4}$$

and heat balance,

$$\left.\frac{\partial T}{\partial z}\right|_{z=0} = q_r + q_t + q_{\text{ev}} + q_g \tag{5}$$

under the boundary conditions

$$T_{z\to\infty} = \text{const}; \qquad \left.\frac{\partial T}{\partial z}\right|_{z\to\infty} = \text{const} \tag{6}$$

describe the temperature regime at the surface ($z = 0$).

In Eq. (5), q_r is the radiation balance, q_t is the heat loss due to turbulent exchange between the atmosphere and the ground surface, q_{ev} is the heat loss

of evaporation, and q_g is geothermal flux. The radiation balance $q_r = q_L - q_s$ is defined by the short-wave component q_s associated with solar radiation Q as $q_s = (1-A)Q$ and long-wave component q_L related to the thermal radiation by the Stephan–Boltzmann law as

$$q_L = \varepsilon_s \sigma T^4 - b\varepsilon_s \varepsilon_a T^4 \tag{7}$$

Subscripts s and a refer to surface and air, respectively; b is the meteorological factor. Heat loss due to turbulent exchange q_t may be presented in general form as

$$q_t = f[u, (T_s - T_a)]$$

where u is the parameter of wind influence. Evaporation losses can be given as

$$q_{\text{ev}} = f(W_s - W_h)$$

where W_s and W_h are the moisture content of the air at the earth's surface and at some altitude h, respectively.

Thus, the daily range of the surface temperature depends on a number of factors: meteorological (wind speed, moisture content, air temperature, cloudiness, etc.) as well as on thermophysical parameters of the soil such as emissivity ε, albedo A, thermoconductivity λ, thermocapacity C, and density ρ. No data have been obtained on radiation coefficient variations. Therefore, the anomaly cannot be explained by these factors. The effect of the turbulent heat exchange q_t on the surface temperature may be significant. However, meteorological data related to periods of anomalous activity of IR radiation reveal insignificant values of wind speed. The latter defines convective heat exchange in near-surface layers of the atmosphere. According to data provided by meteorological stations located in the vicinity of the appearance of an IR anomaly (at the junction of the Tamdi-Tokraus and Karatau faults), minimal values of wind speed were observed during the night and did not exceed 2–3 m/s. In this case the effect of turbulent exchange does not exceed 0.1° regardless to surface temperature [15]. Geothermal flux q_g has a value smaller than other terms in Eq. (5) by several orders of magnitude. Therefore it is not necessary to consider variation of this parameter as the origin of surface temperature anomalies. In our particular case, the value of geothermal flux in the Central Asian region does not exceed 100–200 mW/m^2. In specific cases of rift origin, structures are characterized by abnormally high values of heat flow, which may exceed 10 W/m^2. Thus the geothermal flux may affect surface temperature as well as other meteorological parameters. Moisture content in the soil and humidity in the air remain important factors controlling surface temperature. These parameters affect the role of such processes as evaporation and condensation of moisture q_{ev}. The evaporation process is the most intense in daytime when solar heating takes place, and it leads to a decrease in surface temperature. Moisture content of the soil, in

addition to effects discussed above, alters the soil's thermophysical properties and affects the process of dew formation, which is known to be associated with the release of heat.

A brief consideration of factors affecting surface temperature [Eq. (5)] shows that their contributions strongly depend on time. Thus, to minimize the effect of solar heating, in terms of short-wave radiation q_s, turbulent heat exchange q_t, and evaporation q_{ev}, measurements of surface temperature have to be done during the night, preferably just before dawn. Therefore nighttime infrared imagery has been used to monitor surface temperature in seismically active regions.

The first step in considering the nature of the permanent anomaly of outgoing infrared flux as well as its temporary component in seismically active regions of Central Asia is to estimate the potential energy of these fluxes. Such a comparison gives the same order of magnitude of seismic energy and energy required to raise the temperature of an anomalous area of 10,000 km^2 by 1–2°. It is hard to assume that the observed increase in surface temperature is a result of direct conversion of mechanical energy into heat.

The fast rate of growth of the anomalous area over time which is on the order of magnitude of several days, does not allow consideration of thermoconductivity or convective transfer as possible mechanisms of surface temperature alteration prior to an earthquake. First of all, surface temperature alteration cannot be explained by direct thermoconductivity because of the very large time of thermal propagation from the seismic source to the surface, which is several orders of magnitude more than the characteristic periodicity of seismic events of K 13–14 energy class in the Central Asian seismically active region. The characteristic propagation time of a thermal impulse from a depth of about 10 km may be estimated as on the order of magnitude of 10^7–10^8 years. Also, there is no evidence of direct heat transport by different carriers. Therefore, the most probable source of sufficient energy for surface temperature alteration is solar heating reradiated nonuniformly over the surface. Reasons for nonuniform reradiation may be different, and it may have its origin at the surface. The question is whether or not these surface causes are connected to deep processes. Some of the possible variants are discussed below. It follows from the analysis of system (4)–(6) that thermophysical parameters ρ, λ, C (which is usually presented as thermal inertia $P = \sqrt{\rho\lambda C}$) determine the surface temperature pattern. As a first approach, the day-to-night temperature contrast is given by [16]

$$\Delta T = K\frac{1 - A}{P} \tag{8}$$

where K is an empirically obtained constant that depends on given conditions. It has been shown [17] that thermal inertia P is a direct function of soil moisture in the range of variation for the latter of 10–50% and a very

sensitive polarization parameter. The moisture change within this range leads to a change of several degrees in day-to-night temperature contrast. A moisture increase of 10–20% increases the thermal inertia coefficient P by 10–25%. At 50°, which is the usual day-to-night temperature variation for summer in the Central Asian regions, such a variation in the thermal inertia coefficient P leads to a decrease in day-to-night temperature contrast ΔT of 5–10°. This means that the increment of soil temperature during a night comes to about 2–5°. Such a temperature increment is sufficient to cause the infrared anomaly to be of the order of magnitude to fit the temperature range of the observed anomalies in the Central Asian region.

One of the possible mechanisms leading to the moisture variation is an alteration of the groundwater table. This effect does not contradict the existing hydrogeological conditions along the foot of the Kopetdag mountain system (permanent IR anomaly), where intensive discharge of groundwater is observed. A field study of this region was conducted, and its results, independent of the description above, follows.

The surface temperature regime can be affected by factors other than the variable thermophysical properties of rocks. We suppose that the near-surface atmosphere also contributes substantially to the outgoing infrared flux. The confirmation of this comes from meteorological observations of the area where there is the appearance of an infrared anomaly at the point of junction of the Tamdi-Tokraus and Karatau faults. Air temperature 2 m above the surface and the ground temperature were used. Data were collected six times a day for 2 weeks from meteorological stations located inside the area of the anomalous infrared radiation as well as outside this region. Current average temperatures (air and soil) T_a and T_b for active and background areas, respectively, were calculated. Temperature contrast at 6 a.m. for both air and ground temperatures is similar to the variation in the infrared activity presented in terms of the area of an anomaly. No correlation between daytime temperature contrast and infrared activity taken over nighttime periods is observed.

The field experiment showed an increase in the concentration of optically active CO_2 in the near-surface atmosphere across the active (in terms of seismicity) Kopetdag fault zone. A permanent anomaly of outgoing infrared radiation followed this structure. All these do not argue against the local greenhouse effect being considered as a possible mechanism of formation of an anomaly of outgoing infrared radiation. In addition to this, a possible connection between enriched gas content (CO, CO_2, CO_4, etc.) and crustal deformation processes along fault zones has been shown [4,18–21].

Field measurements of the concentration of CO_2 in the near-surface atmosphere and soil across the Kopetdag fault zone are shown in Fig. 4. The

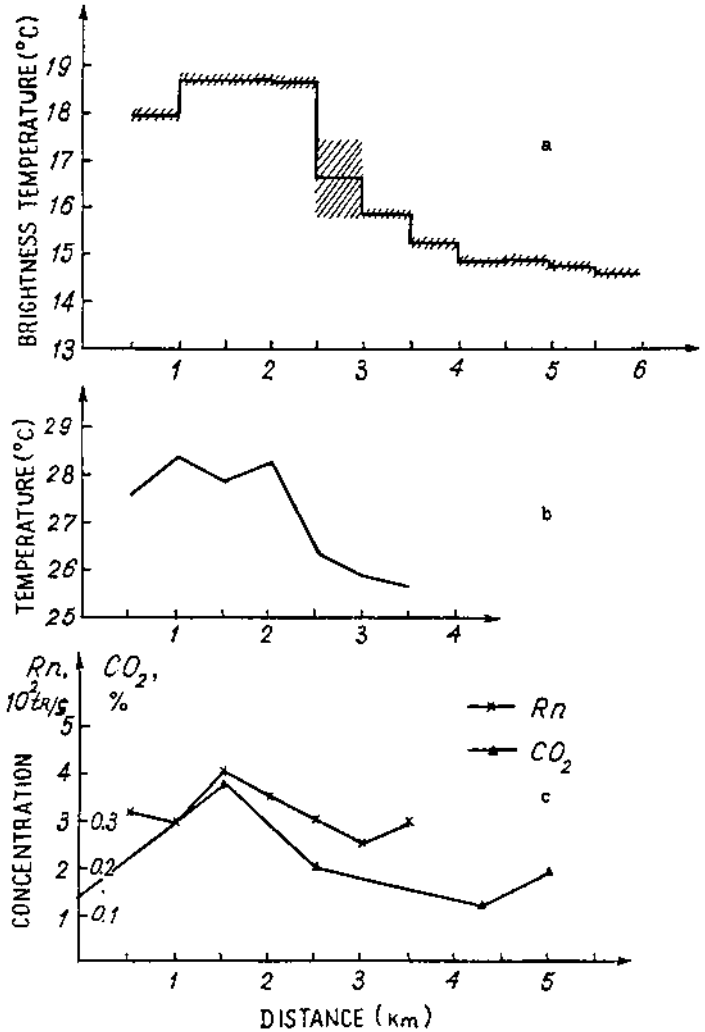

FIGURE 4 In situ measurements in the Predkopetdag fault zone (September 1987). (a) Infrared temperature of the surface; (b) temperature at a depth of 1.5 m; (c) concentrations of Rn and CO_2 in the soil.

increase in the CO_2 concentration was up to 0.3% in soil and up to 0.1% in the near-surface atmosphere, although the background value of the latter was about 0.03%. There is a correspondence between the zone of high CO_2 concentration and the increase in radon emanations as well as the increase in subsurface temperature at a depth of 1.5 m. The region of high infrared surface temperature taken at 6 o'clock in the morning follows the zone of high subsurface temperature and gas concentration.

Based on the foregoing, the effect of high concentrations of optically absorbing gaseous CO_2 on the accumulation of heat near the surface may be estimated. Optically absorbing gases such as CO_2, CH_4, and water vapor absorb a part of earth's infrared radiation. The value of absorbed infrared radiation may be estimated by using an empirical expression of Howard, Birch, and Williams:

$$\Delta E = \int_{\lambda_1}^{\lambda_2} E(\lambda, T) A(\lambda, T)\ d\lambda \tag{9}$$

where $E(\lambda,T)$ is the spectral density of IR flux, $A(\lambda,T)$ is the spectral absorption coefficient, and $(\lambda_2-\lambda_1)$ is an absorbance linewidth. The value of the spectral density $E(\lambda,T)$ is defined by Planck's law:

$$E(\lambda, T) = \frac{8\pi hc}{5}\left(\frac{1}{\exp(hc/\lambda KT)^{-1}}\right) \tag{10}$$

Spectral absorption factors $A(\lambda,T)$ in Eq. (9) can be defined experimentally and then tabulated. Equations (9) and (10) and tabulated values of the absorption coefficient allow estimation of the amount of absorbed infrared energy E for different temperatures and gas concentrations. Thus, the energy absorbed by a layer of pure CO_2 of thickness varying from 1 to 10 cm lies in the range of 10–60 W/m^2 (absorption lines of 4.29 and 14.8 μm were used for this calculation). A layer of CO_2 of such thickness corresponds to a 1 m layer of atmosphere with CO_2 bulk concentrations of 1–10%.

The energy absorbed by optically absorbing gases can be considered in addition to the term on the right-hand side of the balance equation Eq. (5). Numerical solution of the system of equations (4)–(6) showed that the daily temperature curve could shift by 1–5° when the right-hand side of the balance equation increased from 10 to 100 W/m^2. Therefore, anomalous concentrations of optically absorbing gases such as CO_2, CH_4, and water vapor in near-surface layers of atmosphere could generate additional heat along anomaly zones and as a result could be considered possible sources of anomalous outgoing infrared radiation. Observed values of the temperature increment do not contradict the values of temperature variations calculated according

to the increase in gas concentration in the near-surface atmosphere. Observed values of the concentration of CO_2 in the zone of anomaly infrared flux (the zone of the Kopertdag fault) are close by an order of magnitude to the values used for calculations.

The hypotheses discussed above do not disagree with each other. It appears that mechanisms that lead to increases in soil moisture and gas concentration are very similar. Groundwater motion may be the reason for both effects.

V. CONCLUSION

The problem of remote sensing of earthquakes is amenable to remote sensing analyses. The basic approach relies on the fact that the soil moisture is sensitively seemed by polarization and that groundwater motion will appear as a variation in surface moisture that causes the polarization of the surface in both the visible and infrared ranges.

The analyses presented are preliminary and are suggested as supplementary to already existing earthquake prediction methods.

REFERENCES

1. Veber, K. Remote sensing methods and catastrophes: the role of space image for prediction and reduction of losses due to geological catastrophes. 27th International Geological Congress, Moscow, 1984, Dokl., Sec. C Remote Sensing, 1984; Vol. 18, 681–687.
2. Roelffs E.A. Hydrogeological precursors for earthquakes: a review. PAGEOPH 1988, 126 (2–4), 177–210.
3. Sugisaki, R.; Anno, H.; Ui, H. Geochemical features of gases and rocks along active faults. Geochem. J. 1980, 14 (3), 101–112.
4. Rikitake, T. Earthquake prediction. Dev. Solid Earth Geophys; Elsevier: Amsterdam, 1976; Vol. 9.
5. Egan, W.G. Photometry and Polarization in Remote Sensing; Elsevier: New York, 1985.
6. Egan,W.G. High-resolution space-shuttle polarimetry for farm crop classification. Appl. Opt. 1982, 31, 1542–1548.
7. Sidran, M.; Egan, W.L. Analysis of sea surface polarization imagery of Hawaii environs by the space shuttle. Conference on Polarization and Remote Sensing, SPIE, San Diego, 1992.
8. Yongen, C.; Youquan, Y.; Ren, W. Acta Scissuol. Sin. 1987, *9*, (2), 167–175. in Chinese with English abstract.
9. Motovilov, E.A. Estimation of the stressed state of soils from measurement of infrared radiation flux trans (Transl.). Osnovania, Fundam. Mekh. Gruntov ed. 1989, 1, 24–26.

10. Gufeld, I.L.; Salman, A.G.; Stakhovsky, I.R. Thermal effects during the destruction of rocks. Gerland Beitr. Geophysik, Leipzig 1988, 97 (1), 35–39.
11. Cassinis, R.T.; Lechi, G.M. The use of infrared radiometry in geothermal areas. Phys. Volcan. Dev. Solid Earth Geophys. 1974, 6, 117–131.
12. Salman, A.; Tronin, A. Variations in the flux of the earth's infrared emission in seismically active regions of Central Asia. Izv. Acad. Sci. USSR, Phys. Solid Earth 1990, 26 (7), 586–588.
13. Bush, V.A. Transcontinental lineament systems of Eurasia. Geotectonika 1983 3, 15–31. in Russian.
14. Gorny, V.I.; Salman, A.G.; Tronin, A.A.; Shilin, B.V. The earth outgoing IR radiation as an indicator of seismic activity. Dokl. Akad. Nauk SSSR 1988, 301, (1), 67–69. in Russian.
15. Watson, K. Periodic heating of a layer over a semi-infinite solid. J. Geophys. Res. 1973, 78, 5904–5910.
16. Watson, K. Regional thermal inertia mapping from an experimental satellite. Geophysics 1982, 47, (12), 1681–1687.
17. Van de Griend, A.A.; Camillo, P.T. Estimation of soil moisture from diurnal surface temperature observation. Proc. IGARSS'86 Symp. Zurich, Sept, 8–11 1986, pp. 1227–1230.
18. Ammosov, S.M.; Voytoy, G.I.; Korobeinik, G.S. On the response of soil gas component on the signal of energy. Dokl. Akad. Nauk SSSR 1986, 290 (5), 1172–1175. in Russian.
19. King, C.-Y. Gas geochemistry applied to earthquake prediction: an overview. J. Geophys. Res. 1986, B91 (12), 12269–12281.
20. Sugisaki, R.; Anno, H.; Ui, H. Geochemical features of gases and rocks along active faults. Geochem. J. 1980, 14 (3), 101–112.
21. Sugisaki R. Deep seated gas emission induced by earth tide: basic observation for geochemical earthquake prediction. Science 1981, 212 (4500), 1264–1266.

11

High-Resolution Space Shuttle Polarimetry for Farm Crop Classification

I. INTRODUCTION

The monitoring of crop production on a global basis has been a major basic research program funded by NASA. The object is to investigate and improve the modeling of plant canopies and so acquire the potential information in remote sensing that is based on the fundamental physical properties in the input data. Vanderbilt et al. [1] used polarization measurements of two wheat canopies to measure a reflectance factor that is composed of two components of reflected light, specular and diffuse. They identify two key angles: (1) the angle of the polarizer for minimum flux and (2) the angle of incidence of sunlight specularly reflected by a leaf to a sensor. The data were acquired with an Exotech Model 20C spectroradiometer located 6 m above the soil. A rotatable piece of L-sheet was attached to the entrance port. Vanderbilt et al. [1] obtained quantities of maximum reflectance and minimum reflectance (which are related to the position of the polarizer) as well as quantities related to the first and second Stokes parameters and the degree of linear polarization. Their extensive series of measurements were possible only in a laboratory setup.

In a further step, including laboratory and aircraft measurements, Egan and coworkers [2–4] found that the linear polarization of light in a ground scene obtained by an airborne sensor provides additional discriminatory remote sensing scene classifications. The potentially important conclusion reached by Egan [2] was that the drying of leaves generally increases their ability to depolarize [1].

In a further investigation of the polarization of light that is scattered by vegetation and soils, Woessner and Hapke [5] studied the polarization of light scattered by clover. Their study was related to the seminal work of Lyot [6] and Dollfus [7], who attempted to use polarization to characterize possible vegetation on Mars. Lyot found that the polarization of light scattered by surfaces depends on the angle between the incident and scattered rays, which is also known as the phase angle, and is weakly dependent on the incident radiation zenith angle and the zenith angle of the scattered ray for a constant phase angle. The electric vector direction was found to lie either parallel or perpendicular to the scattering plane defined by the incident and scattered rays.

The object of the Woessner and Hapke [5] work was to determine whether the polarization of light by vegetative surfaces can be understood in terms of models of astrophysical data on soils or planetary regoliths. Measurements of a variety of soils were made by Coulson [8] and Egan and Hallock [3] Curran [9] also did an aerial reconnaissance study of the polarization of various types of crops and found that the polarization could be used to discriminate between rough and smooth vegetation canopies. Curran also used polarized photography to indicate soil moisture [10,11]. Other studies involving polarization, such as those of Vanderbilt et al. [1,12–14], Walraven [15], and Solomon [16], concluded that polarization contains surface information not identified by intensity alone.

More recently, in a space shuttle polarization experiment that used Hasselblad imagery of the Hawaiian Islands coming up on the Island of Hawaii from the southwest, it was shown that percent polarization indicates [17, 18] (1) soil texture, (2) atmospheric aerosols and haze, (3) sea state in a cloud-free area, (4) cloud particle size distribution, and (5) cloud optical depth. The data analysis was based on equipolarimetric contours on the imagery in three colors—red, green, and blue—that were defined by interference filters [18].

As an extension of this original work, imagery was acquired of a developed and documented farm area near New Madrid, Missouri [19,20]. The New Madrid area is known for having experienced a major earthquake in 1811, at which time the region fell approximately 15 m, rendering the area a swamp due to the influx of water from the adjacent Mississippi River. The area became fertile from the accumulation of organic material but still had the problem of excess surface water. Subsequently the U.S. Army Corps of Engineers instituted a sophisticated drainage system to drain the basin. Thus the New Madrid area is now highly irrigated and crisscrossed by a multitude of canals, one of which (No. 1 in Fig. 1) is 100 miles (161 km) long extending to the south.

As a result of this fertility and irrigation the area has been highly developed for farming. As shown in Fig. 1, the farm areas are laid out as a

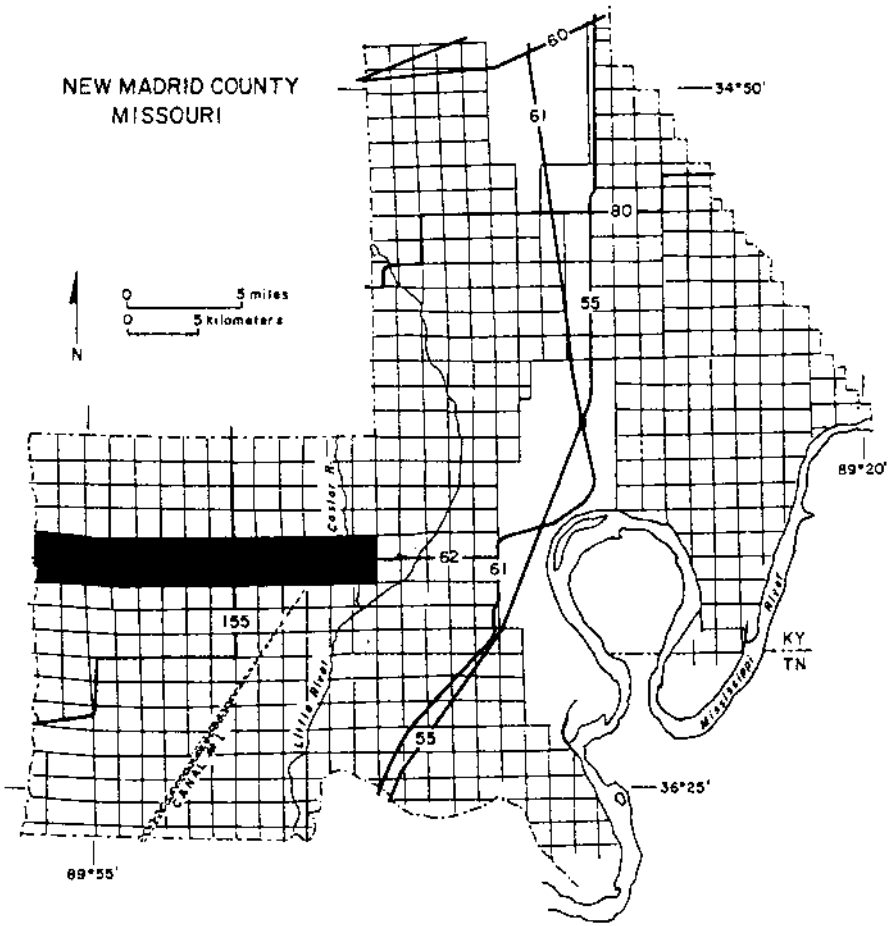

FIGURE 1 Map of New Madrid, Missouri, area showing the area polarimetrically imaged by the space shuttle cameras. The 2 mile × 14 mile (3.22 km by 22.52 km) ground-truthed area is shaded.

series of 1 mile-square quadrangles (2.59 km^2). These quadrangles are irregularly subdivided into farms. The annual documentation of the planted crops is maintained by the U.S. Department of Agriculture Soil and Conservation Service Unit at New Madrid. At the time of the shuttle overflight (August 1989) the detailed plantings were available for the entire county of New Madrid. In Fig. 1 the 2 mile × 14 mile (3.22 km × 22.5 km) ground-truthed area is shown by the shaded area. Details of a typical 1 mi × 2 mi

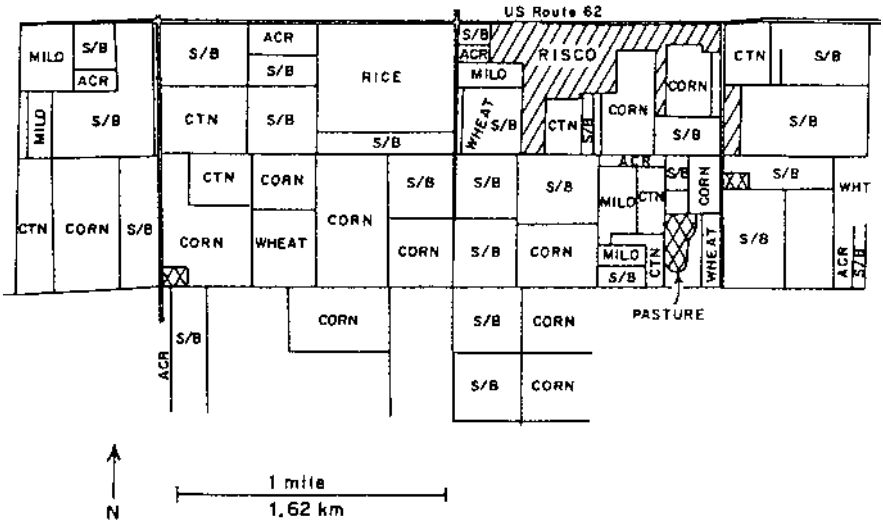

FIGURE 2 Detail of typical 1 mile × 2 mile (1.61 km × 3.22 km) ground-truthed area showing major crop plantings such as rice, cotton (CTN), soybeans (S/B), corn, milo (grain sorghum), and wheat (WHT) (to soybeans). Some areas are left fallow (ACR). The diagonally hatched area is the town of Risco.

(1.61 km × 3.22 km) area (shaded area in Fig. 1) is shown in Fig. 2. The major crops planted are rice, cotton, soybeans, corn, milo (grain sorghum), and wheat. Some areas are left fallow, and some pasture-land exists. The diagonally hatched area of Fig. 2 designates the developed town area of Risco. There is also a pasture area, which is shown cross-hatched.

II. OBSERVATION PROGRAM

The polarimetric imagery of the New Madrid area was obtained by dual Hasselblad cameras with a polarization filter on each camera, with the axes of the polarization filters being mutually perpendicular to each other. The detailed viewing geometry of the images is shown in Fig. 3. The space shuttle is at an altitude of 161 nm (298 km), and the central ray of viewing is located just west of New Madrid (36.6°N, 89.6°W). The average phase angle between the incident and viewing directions is 65.5°. Because the acceptance angle of the 100 mm lenses on the Hasselblad cameras is 32°, the zenith angle viewing directions are 19.5 ± 16°. Hence the phase angle range is between 49.5° and 81.5°. The sun lies low in the sky (early morning) at an elevation angle of 23.4° and an azimuth angle of 2.4° (south of east).

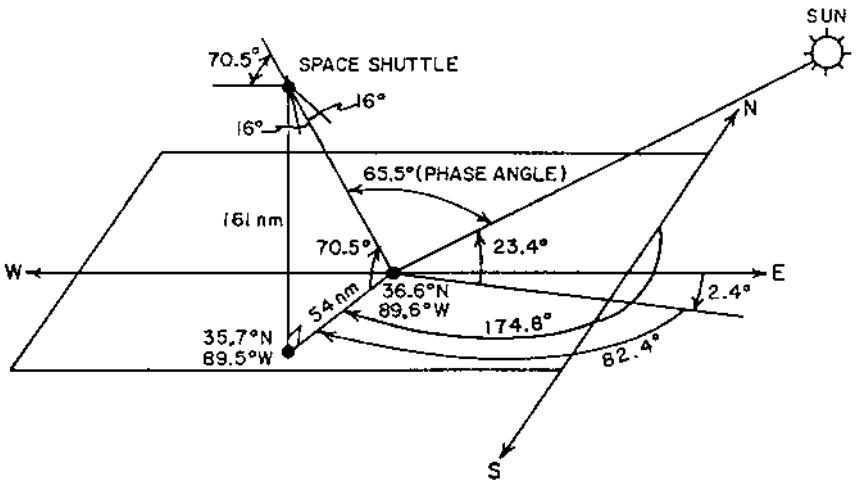

FIGURE 3 Viewing geometry shows the cameras on the space shuttle with a 32° acceptance angle. The phase angles between the incident solar direction and the camera acceptance angles lie between 49.5° and 81.5°; the principal plane is nearly coincident with the direction of polarization of the vertically oriented polarization analyzer on one of the cameras.

The Hasselblad cameras used for the imagery are single-lens reflex cameras, and for the observations the mission specialist was instructed to orient them to maximize or minimize the scene brightness by using a single viewfinder. In this way the polarization imagery was obtained with the planes of the polarization analyzers on the cameras close to parallel and perpendicular to the principal plane. For the New Madrid imagery the orientation of the polarization analyzers was within $\pm 5°$ of the principal plane (based on the minimum scene brightness seen in the camera viewfinder by the astronaut), and the analyzers themselves were mutually perpendicular to better than 1°. Thus by using two cameras the Stokes parameters I and Q were obtained. The quantity V/I (circular polarization) is likely to be quite small for natural surface features and is therefore not a significant factor [18].

The photographic images were taken through the overhead window of the space shuttle. The overhead window was a three-layer laminate with the following layers [21]: (1) outer thermal window of 7940 fused silicate; (2) middle window of 1723 $A1SiO_3$ for absorbing ultraviolet and with an antireflection material, and (3) 1723 $AlSiO_3$ coated with an antireflection coating, with an infrared reflector on either side. Because of the structure a small amount of polarization and distortion are introduced. The window polarization introduced is $\approx -1\%$ for oblique viewing, and the distortion

makes the use of focusing telescopes, such as the 5 in. Celestron or the 8 in. Meade, difficult; visual resolutions of 62–78 line pairs/mm and photographic resolutions of 20–44 line pairs/mm were observed, which depended sensitively on the window area. Ideally, for Hasselblad cameras with 100 mm lenses and image motion compensation, ground resolutions of 40 m should be possible, neglecting the blur when image motion compensation is not used.

The film used in the cameras was 5036 Ektachrome. The images were digitized at the VDAS (Video Digital Analysis Systems) Laboratory, NASA, Houston, Texas, and registered in a procedure that is described in detail below.

The two three-color photographs (STS-28-85-033, maximum polarization, and STS-28-86-033, minimum polarization) that are analyzed are given a preliminary digitization on a 512 × 512 pixel system to determine the maximum and minimum brightness (transparency) levels. These values are applied to each frame on the six images in the final 8 bit (0–255) digitization. This allows optimization and matching of the range of digital values. (A small section of the bottom of the image gives the date/time/roll/frame.) There is an approximately 55 mm^2 image space on the 70 mm^2 frame. The digitization system has the capability of 2048 pixels horizontally and 6000 vertically.

Color separation is achieved through the use of dichroic interference filters. The red filter has 50% transmission at 585 nm with 80% transmission at longer wavelengths and 1% or less transmission at wavelengths of 380–550 nm. The green filter has 50% transmission at 505 and 575 nm with 1% or less tranmission at 380–460 nm and 600–730 nm. Peak transmission at 540 nm is 70%. The blue filter has 50% transmission at 505 nm, 75% transmission at 390–480 nm, and less than 1% transmission at 540–750 nm.

To compare percent polarization, precise registration of the perpendicular and parallel images to 0.01 pixel is necessary. This is achieved through the use of a LIMS (Library of Image Processing Software) computer program. A selection is made of 12–15 corresponding points in the two images. The nearest-neighbor algorithm is used in the present procedure.

Following the registration, percent polarization was computed. The New Madrid imagery was cloud-free, although aerosol and Rayleigh scattering existed. The images were analyzed statistically both polarimetrically and photometrically to determine the frequency of occurrence of polarimetric and photometric values in the red, green, and blue images.

Digitization was accomplished with ground resolutions of 80–90 m.

III. CALIBRATION

In any remote sensing program, calibration is essential. For percent polarization, absolute photometric calibration of each image is unnecessary, be-

cause in percent polarization, which is the ratio of two intensities measured through similar optical systems, mutual photometric effects cancel (such as the infrared reflectance of the inner overhead shuttle window).

For the New Madrid program, optical ground truth was used for calibration. (The same technique was used for photometric calibration of the LANDSAT-1 photometers in a seawater quality remote sensing program in the Virgin Islands [22–24].) Thus in the Mississippi River off New Madrid there was a (dirty) silica sand island on the New Madrid Bend, from Mile 880 to Mile 885. The optical properties, both on the ground and as seen by the space shuttle, are listed in Table 1. The sand was readily distinguishable in the images.

The ground observation albedo values were obtained with a portable photometer, in comparison with a white Nextel painted panel and the percent polarization that are used in laboratory measurements. The red, green, and blue filters were interference types that peaked at 630, 535, and 440 nm with FWHM values of 16, 36, and 16 nm, respectively.

The sand albedo observed by the space shuttle is given as a value that is based on the brightest area in the scene.

Thus the atmospheric contribution is the difference between the ground observations and the space shuttle measurement, as shown in Table 2. At first sight Table 2 is puzzling because the blue polarization introduced by the atmosphere is less than that introduced in the red; Rayleigh scattering would dictate opposite trends. What is actually happening is that (due to multiple scattering of radiation by atmospheric haze) the atmosphere is depolarizing the polarized radiation scattered by the farm crops on the terrestrial surface. Thus the polarization has a dominant effect of depolarization from multiple scattering, which increases with decreasing wavelength; thus in Table 2 the polarization introduced by the atmosphere decreases with decreasing wavelength.

The atmospheric contribution is the sum of the effects of Mie and Rayleigh scattering. Hence in analyzing polarimetric and photometric data

TABLE 1 New Madrid Sand Optical Properties

	Ground observations		Space shuttle observations	
Spectral region	Albedo	Polarization (%)	Albedo	Polarization (%)
Red	0.354	6.9	0.410	32
Green	0.354	5.2	0.520	24
Blue	0.354	8.7	0.625	18

TABLE 2 Atmospheric Contributions

Spectral region	Photometry	Polarization (%)
Red	0.056	25.1
Green	0.166	18.8
Blue	0.271	9.3

the contributions of the atmosphere must be factored out. Here, as a first approximation, the contributions were assumed to be linear [25] and the imagery was corrected for atmospheric effects.

IV. EXPERIMENTAL RESULTS

Experimental results are presented in Figs. 4–9. Figures 4 and 5 are composite red, green, and blue photometry and polarization, respectively; Figs. 6 and 7 are breakouts of Fig. 5 that show detailed crop identification; and Figs. 8–10 are computer output renderings of a 122.6 acre (0.506 km^2) rice field in percent polarization.

The data in Figs. 4–7 are characterized in terms of the frequency of occurrence of a specific photometric or polarimetric pixel.

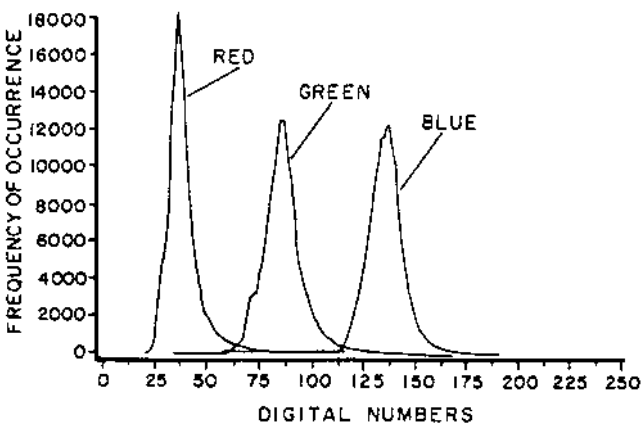

FIGURE 4 Photometry of the New Madrid area showing the frequency of occurrence of photometric pixels of intensities given in terms of digital numbers relative to the brightest pixel in each of the three spectral regions.

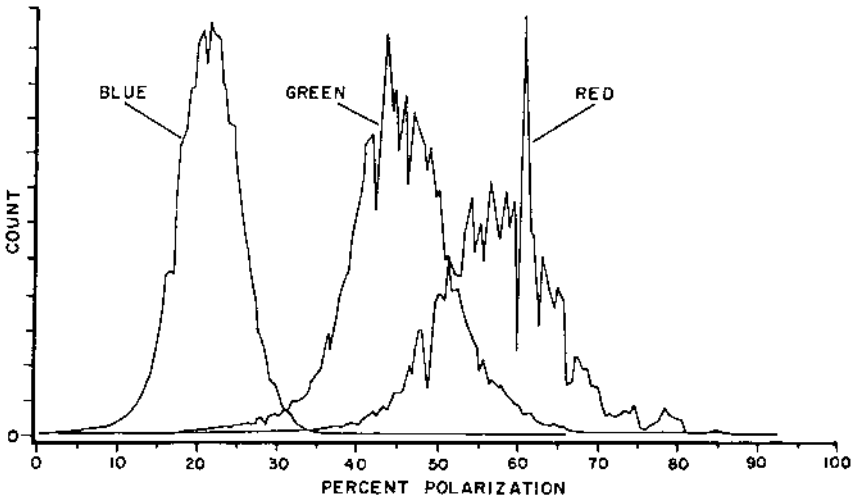

FIGURE 5 Percent polarization of the New Madrid area showing the relative frequency of occurrence of polarimetric pixels in each of the three spectral regions.

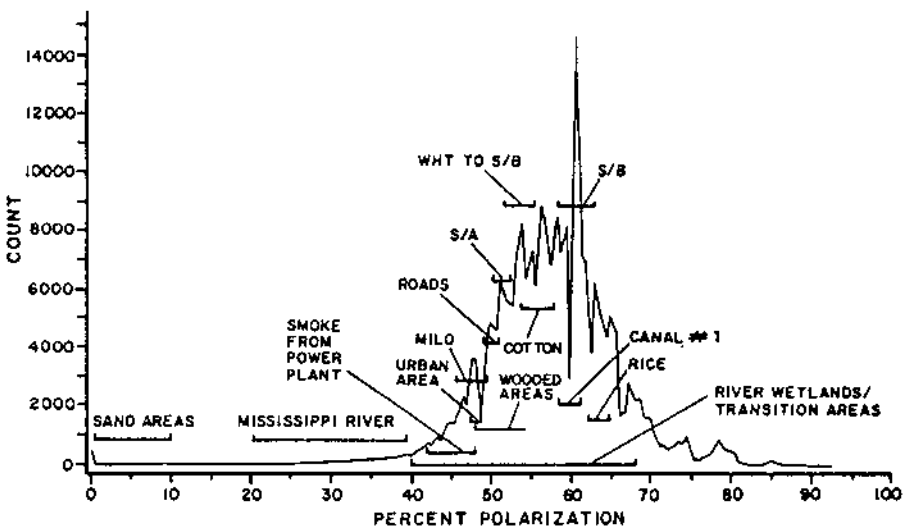

FIGURE 6 Breakout of the red percent polarization band of Fig. 5 identifying the peaks with corresponding ground features.

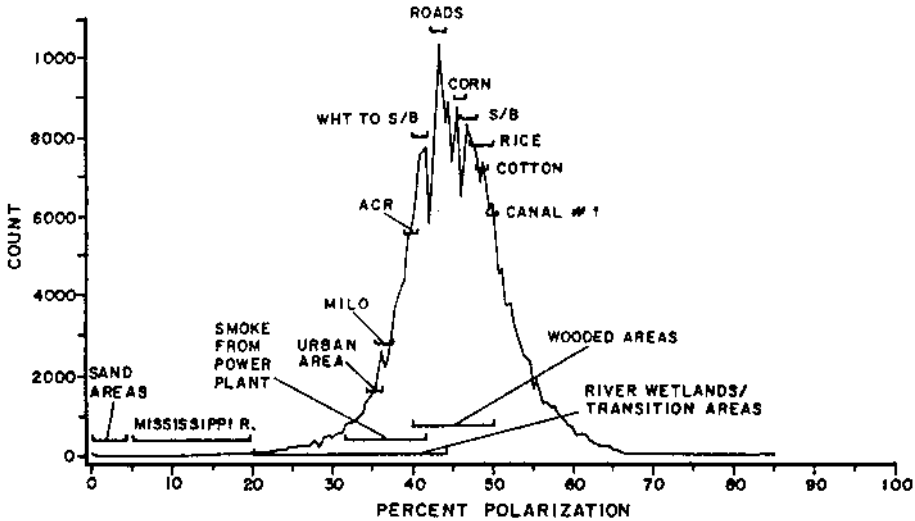

FIGURE 7 Breakout of the green percent polarization band of Fig. 5 identifying the peaks with corresponding ground features.

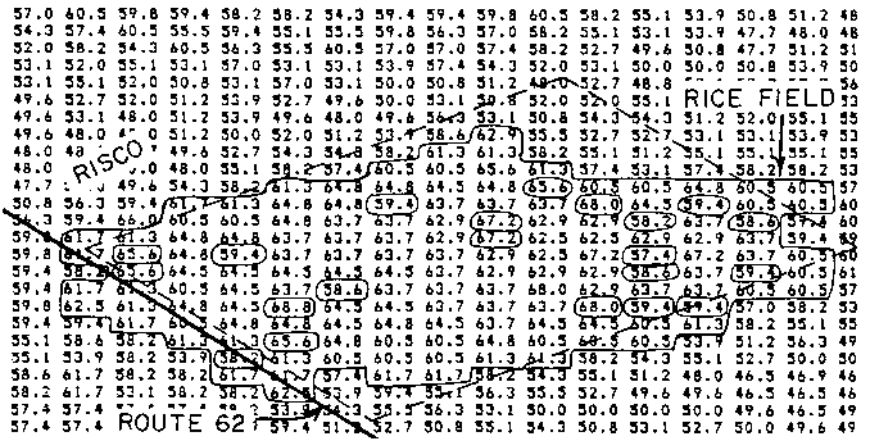

FIGURE 8 Digital output of the red band percent polarization showing a 122.6 acre (0.506 km^2) rice field. Encircled values within the field lie outside the recognition range of 60.5–64.8% polarization.

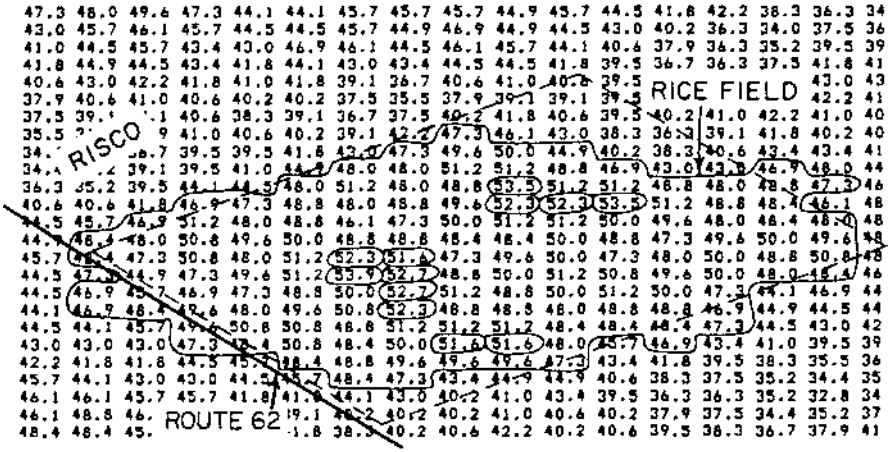

FIGURE 9 Digital output of the green band percent polarization showing a 122.6 acre (0.506 km^2) rice field. Encircled values within the field lie outside the recognition range of 46.9–51.2% polarization.

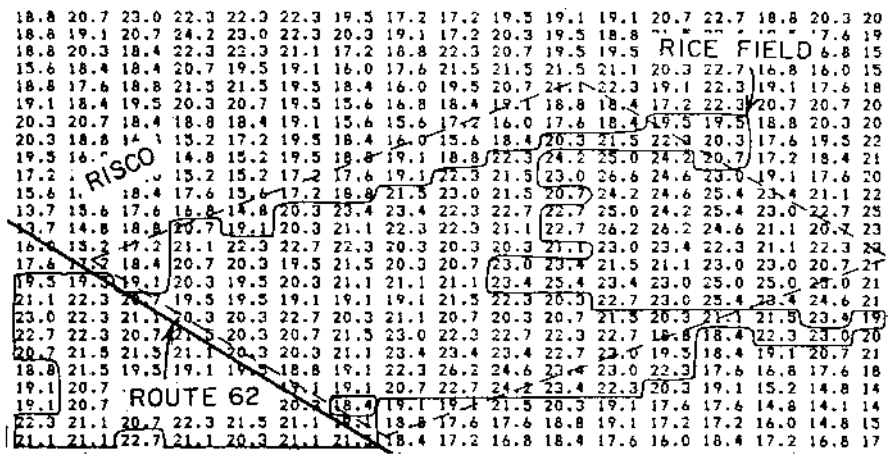

FIGURE 10 Digital output of blue band percent polarization showing a 122.6 acre (0.506 km^2) rice field. Encircled values within the field lie outside the recognition range of 19.5–22.3% polarization.

The most striking feature in a comparison of Fig. 4 (photometry) with Fig. 5 (percent polarization) is the jagged (reproducible) peaks in the polarimetric imagery. These peaks can be identified with specific crops by comparing the digital output with the corresponding ground truth of Fig. 1. The photometric frequencies are almost featureless except for small areas in which differentiation can be seen.

The overall red polarization discrimination is greatest (Figs. 5 and 6), and the blue polarization is the least (Fig. 5). This is to be expected on the basis of photometric considerations (Fig. 4) in which the blue photometry is highest (largest atmospheric multiple scattering and therefore depolarization) and red is the least (lowest atmospheric multiple scattering and therefore depolarization).

For the red percent polarization imagery (which is shown separately as Fig. 6), the percent polarization for various crops (milo, cotton, soybeans, and rice) is shown; the range of percent polarization is listed for each in Table 3. Also shown in Fig. 6 are the percent polarizations for the Mississippi River, sandbars, an urban area (the town of Risco), wooded areas, smoke from a power plant, and the range of transition pixels through the Mississippi River wetlands. Percent polarization is an extremely sensitive indicator of boundary areas, whether it be the Mississippi River or roads. At a higher

TABLE 3 Observed Percent Polarization of Various New Madrid Ground Features from the Space Shuttle

Feature	Red	Green	Blue
Canal #1	58–62	49–51	16–18
Roads	50–52	43–45	17–18
Soybeans	58–62	46–50	18–23
Corn	52–55	44–48	17–20
Milo	45–49	35–37	18–20
Acreage	48–52	38–40	17–19
Rice	61–65	47–51	19–22
Cotton	54–58	47–49	20–23
Risco	45–49	34–38	13–17
Sandbars	0–10	0–5	0–4
Smoke plume	42–48	30–42	10–20
Wooded areas	48–53	40–50	20–25
Mississippi River	20–40	7–20	4–19
Transition areas	40–68	20–45	19–24
Wheat to soybeans	50–55	38–42	—

resolution it could serve as a sensitive indicator of objects, vehicles, or personnel.

Another interesting feature is the separation of soybeans from areas that are first planted with wheat and, after harvest, are replanted with soybeans. This is clearly shown in Fig. 6.

By moving to the green percent polarization (Fig. 7), the distinctions of Fig. 6 can be seen again but on a more compressed scale. Here a significant feature is the characterization of roads as a strong peak. Where overlaps exist (i.e., cotton and rice in Fig. 7) the use of the red band (Fig. 6) can segregate the two crops, similar to urban and wooded areas.

The areas left fallow (set-aside areas) generally depend on what is being done with the land; perhaps grass, weeds, clover, or nothing may exist.

The range of percent polarization in the green band is shown in Table 3. Blue is also shown, but the distinction between crops is much less.

As a specific example of the use of polarization to characterize a crop, a 122.6 acre (0.506 km^2) rice field along Route 62 (in the central part of Fig. 2) is easily seen in the polarimetric image. The renditions are shown in Figs. 8–10.

In Fig. 8 (red percent polarization) the actual rice field is shown in the square broken-line outline, and the computer pixel range from 60.5% to 64.8% polarization is shown as the solid outline. Encircled pixels lie outside the range but could indicate variations in crop cover or quality.

A similar green percent polarization is shown in Fig. 9. There are relatively fewer pixels outside the green range from 46.9% to 51.2% than outside the red range, which makes the green band the better of the two bands for rice recognition.

The rice farm in the blue percent polarization is shown in Fig. 10; the acceptance polarization range is 19.5–22.3% polarization. The narrow range can be compared with the pixels that are exterior to the rice field. It can be seen that a significant number of pixels lie in the acceptance range, rendering identification of the rice field difficult.

V. DISCUSSION

In the space shuttle Hasselblad camera polarization and photometric program, it is evident that both atmospheric and terrestrial features may be uniquely characterized by using polarization, with secondary photometric information being obtained also. The combination of photometry with polarization is of particular value in the deduction of the effects of earth's atmosphere [25]. In regard to the polarization of terrestrial features, the connection of laboratory measurements of individual leaves to the area observations from space is tenuous; an attempt at this association is developed in the following paragraphs.

Of the various crops in the New Madrid area, the polarimetric and photometric properties of corn leaves have been measured in the laboratory [2]. The measurements of fresh corn leaves and tassels were determined for the long axes of the leaves perpendicular to and parallel to the plane of vision. Table 14.1 of Ref. 24 lists the polarimetric properties at an illumination angle of 30° to the horizontal (23.4° for the New Madrid imagery). Because the major contribution is corn leaf reflection and polarization and a linear relation up to 96° for the polarimetric phase curve is assumed, we obtain the empirical relationships.

$$\text{Red \% polarization} = 0.51 \times \text{phase angle} \qquad (0.633\ \mu\text{m})$$

$$\text{Green \% polarization} = 0.37 \times \text{phase angle} \qquad (0.533\ \mu\text{m})$$

This gives a polarization of 58% in red and 43% in green, compared with the observed values (Table 3) of 52–55% and 45–47%, respectively. Precise agreement with the laboratory measurements is not obtained because of the varying surface structures of the corn fields, ground cover, shadowing, and wavelength differences; however, the trend is evident.

It is highly desirable to use multiple wavelengths for polarimetric crop measurements, particularly for the assessment of crop quality. The crop ground cover is indicative of the growth stage, and this is evident in the effect of the polarization of the ground under the crops relative to the crop coverage. For instance, in Fig. 6 there is a distinct difference between the soybean plantings and the later wheat-to-soybean plantings.

Crop quality would be better indicated in near-infrared imagery, because reflectance in this spectral region strongly depends on leaf reflection and scattering [24]. Also, the moisture content of leaves in the red spectral area strongly affects their ability to depolarize [1].

Another point to be mentioned is the phase angle effect. In the current images only a portion of the entire available image was used, in which the central phase angle ranged from 59.7° to 67.7°. The phase angle variation across the images caused the polarimetric measurements near the Mississippi River at the upper portion of the image to differ sensitively from those at the lower portion of the image. Thus for the series of analyses in this chapter, in which only the centralmost region of the image was used, there was a small range of phase angles in the central region ($\sim 0.2°$) of the image, and the effect on the polarimetry was small. However, for analyses of the entire image or significant portions thereof, the phase angle effect must be considered in a modeling program.

Modeling of the polarimetric properties of complex surfaces is in progress with the Maxwell—Environmental Research Institute of Michigan polarimetric model [26]. The construction of such a model involves correlat-

ing surface polarimetric features with relatable model parameters to include phase angle effects.

VI. CONCLUSION

From the data presented, it is evident that polarization is an emerging new field for terrestrial and atmospheric remote sensing from space. Ground resolutions of 80–90 m are attainable by using Hasselblad cameras within the space shuttle cockpit; resolutions up to 40 m are possible with an optical quality space shuttle window and image motion compensation. Whereas sensed wavelengths were in the red, green, and blue spectral regions, longer and shorter wavelengths may be sensed with appropriate window optics and camera film.

It is evident that polarization is superior to photometry for farm crop classification, with a distinct peak characterizing each crop or surface feature. The sophistication of a second camera plus image registration software are added requirements.

The atmospheric properties above the New Madrid area have been defined to permit atmospheric modeling. It also appears that the observed crop properties may be tied to laboratory measurements.

ACKNOWLEDGMENTS

We thank L. Blunt, D. Kennedy, and the staff of the U.S. Department of Agriculture Soil Conservation Service in New Madrid, Missouri, for their cooperation in furnishing data on crop plantings at the time of the space shuttle overflight; we also thank T. Clark for river transportation to acquire sand samples. We thank D. Jones, L. Dowdy, and J. Pendergrass of the Hydraulics and Hydrology Branch, U.S. Army Corps of Engineers for Mississippi River data, and J. Keithley of the Soils Laboratory for soils data. Thanks to E. Anderson of the Charleston, Missouri, "Enterprise-Courier" newspaper for the 1811 earthquake data.

We thank the reviewer for his constructive comments.

This work was performed under NASA Contract No. NAS 9-17900, Lockheed Engineering and Sciences Company, Houston, TX.

REFERENCES

1. Vanderbilt, V.C.; Grant, L.; Biehl, L.L.; Robinson, B.F. Specular, diffuse and polarized light scattered by two wheat canopies. Appl. Opt. 1985, *24*, 2408–2418.

2. Egan, W.G. Optical Stokes parameters for farm crop identification. Remote Sensing Environ. 1970, *1*, 165–180.
3. Egan, W.G.; Hallock, H.B. Coherence polarization phenomena in remote sensing. Proc. IEEE 1969, *57*, 621–628.
4. Egan, W.G.; Grusauskas, J.; Hallock, H.B. Optical depolarization properties of surfaces illuminated by coherent light. Appl. Opt. 1968, *7*, 1529–1534.
5. Woessner, P.; Hapke, B. Polarization of light scattered by clover. Remote Sensing Environ. 1987, *21*, 243–261.
6. Lyot, B. Research on the Polarization of Light from Planets and Some Substances; Ann. Observatoire Paris Sect. Meudon VIII(1), 1929; NASA Tech. Transl. TTF-187; US Govt. Printing Office: Washington, DC, 1964.
7. Dollfus, A. Polarization de la lumiere renvoyée par les corps solides et les nuages naturels. Ann. Astrophys. 1956, *19*, 83–113.
8. Coulson, K. Effects of reflection properties of natural surfaces in aerial reconnaissance. Appl. Opt. 1966, *5*, 905–917.
9. Curran, P.J. Polarized visible light as an aid to vegetation classification. Remote Sensing Environ. 1982, *12*, 491–499.
10. Curran, P.J. A photographic method for recording of polarized visible light for soil moisture indications. Remote Sensing Environ. 1978, *7*, 305–322.
11. Curran, P.J. The use of polarized panchromatic and false color infrared film in the monitoring of soil surface moisture. Remote Sensing Environ. 1979, *8*, 246–266.
12. Vanderbilt, V.C.; Grant, L. Plant canopy specular reflectance model. IEEE Trans. Geosci. Remote Sensing 1985, *GE-23*, 722–730.
13. Vanderbilt, V.C.; Grant, L.; Daughtry, C.S.T. Polarization of light scattered by vegetation. Proc. IEEE 1985, *73*, 1012–1024.
14. Vanderbilt, V.C.; Biehl, L.L.; Robinson, B.F.; Bauer, M.E.; Vanderbilt, A.S. Linear polarization of light by two wheat canopies at many view angles. In Proceedings of the International Colloquium on Spectral Signatures of Objects in Remote Sensing; Guyot, G., Verbrugghe, M., Eds.; INRA Station de Bioclimatologie: Avignon, France, 1981; 217–224.
15. Walraven, R. Polarization imagery. Opt. Eng. 1981, *20*, 14–18.
16. Solomon, J.E. Polarization imaging. Appl. Opt. 1981, *20*, 1537–1544.
17. Whitehead, V.S.; Egan, W.G. Analysis of terrestrial polarization imagery obtained from the space shuttle. Trans. Am. Geophys. Union 1989, *70*, 301.
18. Egan, W.G.; Johnson, W.R.; Whitehead, V.S. Terrestrial polarization imagery obtained from the space shuttle: characterization and interpretation. Appl. Opt. 1991, *30*, 435–442.
19. Egan, W.G.; Israel, S.; Johnson, R.W.; Whitehead, V.S. High resolution space shuttle polarimetry for farm crop identification. In Annual Meeting 1990; OSA 1990 Tech. Dig. Ser.; Opt. Soc. Amer.: Washington, DC, 1990; Vol. 15, 52 p.
20. Egan, W.G.; Israel, S.; Johnson, W.R.; Whitehead, V.S. Enhanced hydrologic remote sensing using polarization. Trans. Am. Geophys. Union 1990, *71*, 499.
21. Scott, K. Draft of the final report on the shuttle window. Aerospace Corp: El Segundo, CA, 1989.

22. Egan, W.G. Water quality determinations in the Virgin Islands from ERTS-A data. In Proceedings of the Eighth International Symposium on Remote Sensing; Environ. Res. Inst. Mich.: Ann Arbor, MI, 1972; 658-708.
23. Egan, W.G. Boundaries of ERTS and aircraft data within which useful water quality information can be obtained. In Proceedings of the Ninth International Symposium on Remote Sensing; Environ. Res. Inst. Mich.: Ann Arbor, MI, 1973; 1319-1343.
24. Egan, W.G. Photometry and Polarization in Remote Sensing. Elsevier: New York, 1985; 211–231.
25. Egan, W.G.; Sidran, M. Modeling of atmospheric and cloud polarization using space shuttle imagery. In Annual Meeting 1990; OSA 1990 Tech. Dig. Ser.; Opt. Soc. Am.: Washington, DC, 1990; Vol. 15, 52 p.
26. Egan, W.G.; Maciulaitis, A. Modeling the Stokes parameter of surfaces. In Annual Meeting 1990; OSA 1990 Tech. Dig. Ser.; Opt. Soc. Am.: Washington, DC, 1990; Vol. 15, 260 p.

12

Planetary Remote Sensing Atmospheres

This chapter discusses planetary remote sensing. The emphasis will be on the terrestrial planet Mars. The information to be presented is admittedly dated, but the principles of analysis are fundamental and applicable to other planetary surfaces yet to be analyzed that have no vegetation. The Martian landers carried several experiments for determining the chemical composition of the Martian surface but not its mineralogical composition; this remains to be done with a sample return. The fine debris that was found at both landing sites had nearly the same chemical composition as a result of global dust storms that carried loose surface particles to all parts of the planet. The soil is rich in silicon and iron. It appears that highly oxidized iron compounds are responsible for the reddish color. Trenches 15 cm deep were dug by a scoop on a lander and it appears that bonding of the surface particles occurred. On the lunar surface, vacuum bonding is the result of van der Waals forces between the molecules. On the Martian surface, there is about 10 mbar surface pressure, and the bonding could be due to frost, shown to exist in the atmosphere. The evidence is inferred from the requirement of increasing the Martian air mass to 3.8, to satisfy the atmospheric modeling requirement. The additional carbon dioxide in the atmosphere could exist as frost or in association with the dust particles. On the earth trenches could not be dug easily in the dry soil as in wet beach sand. Because carbon dioxide exists as ice on the planet Mars and possibly on other planetary, asteroidal, and cosmic bodies it is appropriate to indicate a technique and the results of such a measurement. This is described following Egan and Spagnolo [1].

I. INTRODUCTION

Because of their color and origin, yellow Martian clouds are presumed to be very fine particles of material from the bright areas carried aloft by the wind. Identification of the dust particles provides valuable clues to the nature of the Martian surface material. Dollfus [2] concluded that finely pulverized limonite reproduced closely the polarization curve of the Martian bright areas as a function of phase angle. Adams and McCord [3] found that the reflectance spectrum of an oxidized basalt matched the spectral geometric albedo curve for Mars quite well. However, the match is not unique. Plummer and Carson [4] found that the reflection spectrum of Mars can also be well matched by that of polymers of carbon suboxide. Hanel et al. [5] observed the 1971 great yellow dust storm with the Mariner 9 infrared interferometer spectrometer (IRIS). Their analysis of spectral features due to the atmospheric dust indicates an SiO_2 content of $60 \pm 10\%$. Lowman [6] suggested that andesite, an intermediate igneous rock, would be a good candidate for Martian material. Hunt et al. [7] compared Mariner 9 IRIS radiance data with laboratory transmission spectra and suggested that the clay mineral montmorillonite could be the major component of the Martian dust cloud. It is beyond the scope of this chapter to discuss the pros and cons for each of these suggestions, nor have we exhausted the list of possibilities, but it seems fair to say that the question of what the Mars surface material is made of is far from settled at this time.

The Mariner 9 ultraviolet spectrometer (UVS) observed the 1971 dust storm at resolutions and phase angles not possible from the earth. The suspension of optically thick dust in the Mars molecular atmosphere gives a light intensity variation with phase angle and wavelength that can be compared with theoretical Mie scattering calculations. Measurements of the Mars surface reflectance, where the particles are in close contact, cannot easily be compared with theoretical calculations.

Previous studies of Martian aerosols using Mariner 9 ultraviolet data were published by Hord et al. [8], Pang and Hord [9], Ajello et al. [10], and Ajello and Hord [11]. This chapter reports on a study of the phase function and single-particle scattering albedo of the dust grains to determine their complex refractive index.

II. OBSERVATIONS

On November 17, 1971, the Mariner 9 spacecraft scan platform performed two pointing maneuvers designed specifically to study the phase function of the dust clouds obscuring the surface of Mars. During the sixth revolution a midlatitude target was observed from many different angles as the

spacecraft flew over. This maneuver was repeated for a target in the south polar region that was separated from the solid ice cap. The viewing geometry was graphically depicted by Koskela et al. [12]. Because the dust cloud was latitudinally inhomogeneous [13], data taken while the spectrometer field-of-view footprint was drifting off target were not used in this analysis. Sixty-nine spectra from Rev. 6 and 36 from Rev. 7 were selected for detailed analysis. The observations lasted 10 min 56 s on Rev. 6 and 7 min 20 s on Rev. 7. The midlatitude target was centered at 50.8°S and 124.5°W, and the polar target at 79.5°S and 18.3°W. The pointing errors were approximately 117 km in the east–west direction and 108 km in the north–south direction for the midlatitude target and 27 km E–W and 77 km N–S for the polar target. The solar zenith angle ($\cos^{-1}\mu_0$) ranged from 59.9° to 67.7° in Rev. 6 and from 53.4° to 58.8° in Rev. 7, while the observational zenith angle ($\cos^{-1}\mu$) varied from 8.8° to 35.2° and from 32.8° to 39.3°, respectively. The phase angle changed from 39.6° to 81.1° in the first observation and from 24.7° to 40.5° in the second. Phase angles outside the 15–84° range were unattainable owing to spacecraft constraints.

III. PHASE FUNCTION

The intensity observed by the spectrometer at a wavelength λ depends on the cosines of the incidence and emission angles μ_0 and μ and either the scattering angle α or the azimuth. We use α in this study. Hord et al. [8] found that dust storm measurements may be described by the equation

$$R = \frac{P(\alpha)\tilde{\omega}_0}{4}\left(\frac{\mu_0}{\mu + \mu_0}\right) \tag{1}$$

where R, the reflectance, is π times the observed intensity divided by the solar flux at Mars, $P(\alpha)$ is the phase function normalized to have a unit value when averaged over all angles, and $\tilde{\omega}_0$ is the single-scattering albedo or probability of reemission for an absorbed photon.

During the Mariner 9 dust storm observations, reflectance measurements made at a given phase angle were found to have a correlation coefficient within a few percent of unity with the quantity $\mu_0/(\mu + \mu_0)$. This high degree of correlation indicates that single scattering predominates over multiple scattering. Although the dust cloud was optically thick, the high absorptance of the particles, which follows from the extremely low observed albedo (~1%), suppressed higher order scattering except very near the forward direction, which is not applicable in our case.

If the dependence of R on μ and μ_0 can be represented so well by a formula that neglects multiple scattering, there is no reason why the R

dependence on the third angle, α, cannot be approximated by a single-scattering phase function for large α. Therefore, if the observed reflectance is divided by $(1/4)\ \mu_0/(\mu + \mu_0)$, one can obtain $P(\alpha)\tilde{\omega}_0$, the phase function times single-scattering albedo [cf. Eq. (1)]. $P(\alpha)\tilde{\omega}_0$, henceforth called the phase function, is the probability per unit solid angle that an incident photon is scattered in the direction α. The phase function observations on Revs. 6 and 7 are plotted as dots in Figs. 1 and 2. The 10 nm band centers are at 268 and 305 nm for Figs. 1 and 2, respectively. The Rev. 7 data are normalized to Rev. 6 data at phase angles common to both orbits, approximately 40°. A slight but significant latitudinal dependence was corrected for by

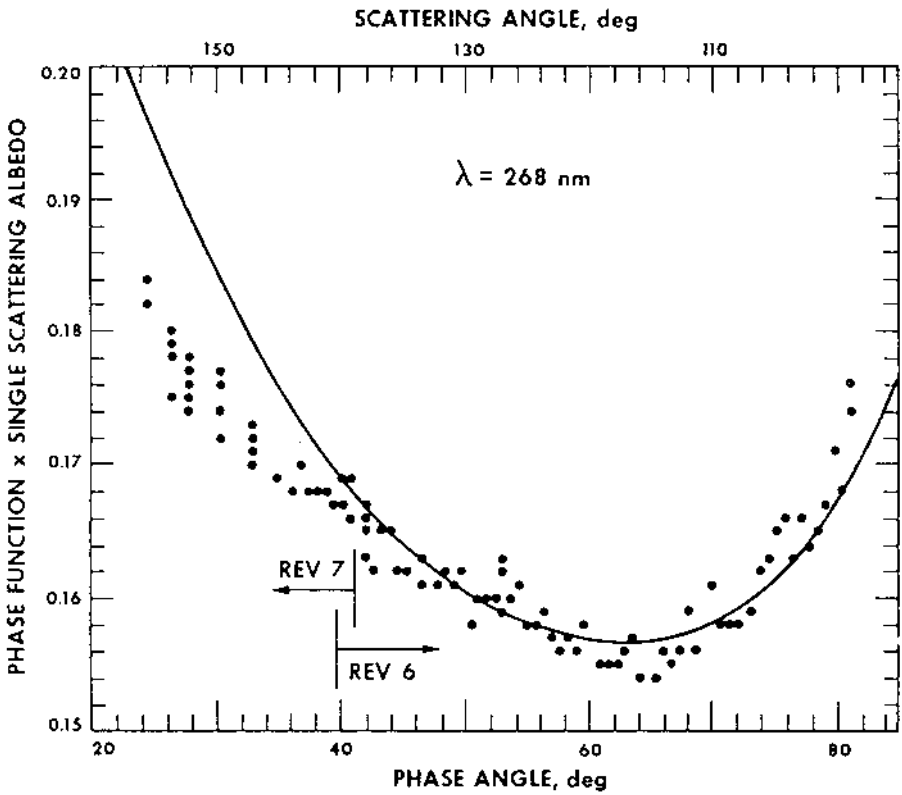

FIGURE 1 The phase function observed in a 10 nm band centered at $\lambda = 268$ nm during Revs. 6 and 7 is plotted as dots against the phase angle. The matching theoretical curve was calculated with a size distribution of spheres of effective radius $a = 1\ \mu$m, effective variance $b = 0.4$, complex refractive index $m = 2.0 - 0.02i$, and $f = 0.08$.

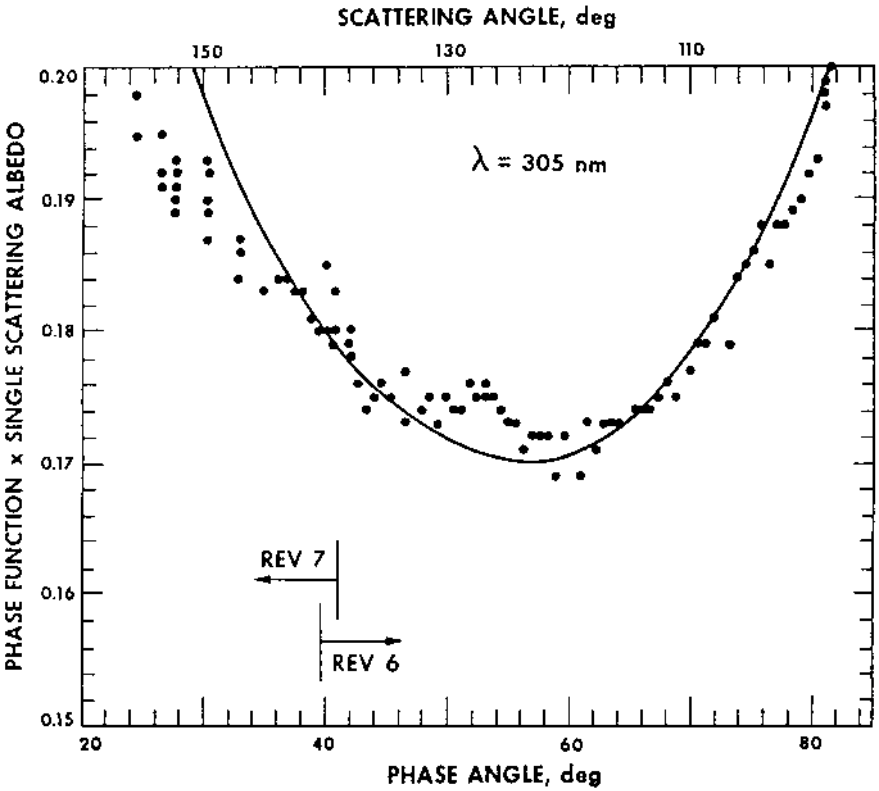

FIGURE 2 Same as Fig. 1, except for $\lambda = 305$ μm, $a = 1$ μm, $b = 0.4$, $m = 1.9-0.01i$, and $f = 0.075$.

using an equation derived from linear regressions between the phase function and latitude observed at a number of constant phase angles.

Figures 1 and 2 show that the long-wavelength phase function has higher values at all angles and is more symmetrical than the short-wavelength phase function. The phase functions exhibit a minimum at both wavelengths. The short-wavelength minimum is shifted to a larger phase angle (65°) than the long-wavelength minimum (60°).

IV. MIE SCATTERING CALCULATIONS

During dust storms, surface material is brought high into the atmosphere, where it is easily observed. Although modeling light scattered by rough

surfaces or particles in contact with one another is difficult, radiative transfer and scattering theory can be used to probe the optical properties of a cloud consisting of widely separated scattering centers.

For this study we assume that the dust particles can be approximated by a size distribution of spheres. Zerull and Giese [14] discussed the applicability of spherical particle Mie calculations to the case of randomly oriented, nonspherical particles. Our strategy is to find a theoretical fit to the observed phase functions.

Defining the size distribution with a minimum number of parameters facilitates inversion of the phase function measurements. The treatment used here follows Hansen and Travis [15]. The effective particle radius is chosen to be the particle radius r weighted by the particle cross-sectional area πr^2 and averaged over the distribution of particle sizes, giving

$$r_{\text{eff}} = \int_{r_1}^{r_2} r\pi r^2 n(r)\, dr \Big/ \int_{r_1}^{r_2} \pi r^2 n(r)\, dr = \frac{1}{G} \int_{r_1}^{r_2} r\pi r^2 n(r)\, dr \tag{2}$$

where $n(r)\, dr$ is the number of particles per unit volume with radius between r and $r + dr$, r_1 and r_2 are the smallest and largest particles in the distribution, and G is the geometrical cross-sectional area of particles per unit volume. Similarly, as a measure of the width of the size distribution, the effective variance is defined as

$$v_{\text{eff}} = \frac{1}{G r_{\text{eff}}^2} \int_{r_1}^{r_2} (r - r_{\text{eff}})^2\ \pi r^2 n(r)\, dr \tag{3}$$

where r_{eff}^2 in the denominator makes v_{eff} dimensionless.

The standard distribution as defined and graphically illustrated by Hansen and Travis [15] is

$$n(r) = \text{const}\ r^{(1-3b)/b}\ e^{-r/ab} \tag{4}$$

which has the properties

$$a = r_{\text{eff}}, \qquad b = v_{\text{eff}} \tag{5}$$

for the size distribution, Eq (4).

The standard distribution Eq. (4), is a variation of the gamma distribution. Calculations were also done using exponential and log-normal size distributions. As long as the effective radius and variance of the size distribution are the same as those of the standard size distribution, the results are unchanged.

The particles are assumed to be of homogeneous and isotropic material with the complex refractive index, m, measured with respect to free space. The real and imaginary parts of m are defined by the formula

$$m = n_r - in_i \tag{6}$$

where n_r alone is sometimes called the refractive index and $4\pi n_i/\lambda$ is the absorption coefficient.

The shift of the $P(\alpha)\tilde{\omega}_0$ minimum toward a 90° phase angle with decreasing λ [cf. Figs. 1 and 2, and Eqs. (8) and (9)] and with atmospheric clearing [16] indicates scattering by molecules in addition to dust. Ground-based polarimetric measurements of Mars made on the same day as the Mariner 9 ultraviolet observations show a polarization of ~1% with a definite inverse wavelength dependence, which is also indicative of some Rayleigh scattering [17]. Assuming a homogeneous mixture of gas and dust, the phase function for a unit volume of the atmosphere depends on the ratio of the Rayleigh scattering coefficient (per unit length) to the dust scattering coefficient,

$$f = k_{\text{sca,R}}/k_{\text{sca},d} \tag{7}$$

and the complete phase function is

$$P\tilde{\omega}_0 = \frac{\tilde{\omega}_d}{1+f}P_d + \frac{f}{1+f}P_{\text{R}} \tag{8}$$

where P_d and P_{R} are phase functions for dust particles and for Rayleigh scattering, respectively, and $\tilde{\omega}_d$ is single-scattering albedo for dust particles. The phase function for Rayleigh scattering is given by

$$P_{\text{R}} = (3/4)(1 + \cos^2\alpha) \tag{9}$$

The ratio f is of the order of the Rayleigh scattering optical thickness of the gaseous carbon dioxide atmosphere. As the proportion of dust decreases in the upper atmosphere, f increases. If the optical thickness of dust is larger than unity, f will be decreased.

The Mie phase function is dependent on four parameters; a, b, n_r, and n_i. The effective radius of the dust particles is known to within a factor of 2 from previous studies. Using the wavelength and time dependence of the ultraviolet extinction optical thickness of the dust clouds, Pang and Hord [9] estimated a mean radius of about 2 μm for the dust cloud particles. Moroz and Ksanfomaliti [18] estimated the particle radius to be 0.5–1 μm, based on the wavelength dependence of the contrast and dust sedimentation time observed by near-IR photometers on the Soviet spacecraft Mars-3. Using ground-based polarimetric measurements extending from ultraviolet to infrared

wavelengths, Veverka et al. [17] deduced the rate of clearing of the Martian atmosphere and concluded that the original dust cloud contained significant amounts of micro-sized particles ($a \simeq 0.5$ μm). Pollack et al. [19] compared the infrared brightness temperature spectra of hypothetical clouds of spherical dust particles with Mariner 9 IRIS spectra of the great Martian dust storm and found that particle size distributions with a mode radius of 2 μm fit the observations best. Conrath [20] examined the secular variation of the thermal structure of the Martian atmosphere during the dissipation phase of the 1971 dust storm, using temperatures obtained by the infrared spectrometer investigation on Mariner 9, and inferred a mean dust particle diameter of ~ 2 μm ($a \simeq 1$ μm). Hartmann and Price [21] analyzed trends in surface contrast in nearly 1000 Mariner 9 photographs and found that the particles were $\lesssim 5$ μm in diameter ($a \lesssim 2.5$ μm) high in the atmosphere, with a concentration of larger particles ($\lesssim 10$ μm) ($a \lesssim 5$ μm) near the ground in the lowest parts of Mars.

In contrast to the effective radius, the width of the dust particle size distribution is not known. However, effective variance values for the size distribution can be chosen to eliminate unreasonble possibilities and for computational efficiency. Theoretical studies by Sagan and Pollack [22] showed that a wide size range of particles (up to several hundred micrometers) can be moved by Martian winds and become airbone. However, large particles do not remain suspended long; theoretical calculations by Anderson [23] showed that particles larger than 25 μm have lifetimes in the Martian atmosphere of a few hours, and particles larger than 5 μm, only a few days. Ground-based observations by Capen and Martin [24], Veverka et al. [17], and Abramenko and Prokofieva [25] as well as Mariner 9 observations by Pang and Hord [9] and Hartmann and Price [21] have shown that the active dust-lifting phase of the storm persisted until mid-December. Resurgences and false clearings were observed as late as mid-December 1971. Because particles of all sizes were injected into the atmosphere for about 3 months and larger particles (> 5 μm) settled on a time scale much shorter than the life of the active storm, the conclusion is that the remaining dust became enriched with slowly settling small particles. Thus, the effective radius reported for the dust grains is small, in spite of lower threshold wind velocities required to set large particles into motion [22]. This small particle selection process will cause the particle size distribution of the mature and decaying dust cloud to skew strongly in the direction of decreasing size. Computations by Hansen and Travis [15] show that size distributions with $b > 0.1$ exhibit this behavior. Distributions with $b < 0.1$ are characteristic of condensation products that are not candidates for Martian yellow clouds. Size distributions skewed in the direction of increasing size, e.g., cloud-type distribution C.3 of Deirmendjian [26], are not considered in this study.

In choosing the complex refractive index, laboratory measurements of n_r and n_i for terrestrial analogs of Martian material were used [27]. No measurements were made for polymers of carbon suboxide.

Phase functions were computed for over 1000 combinations of the parameters a, b, n_r, n_i, and f using Eqs. (8) and (9) and a Mie Fortran code provided to us by J. E. Hansen. The ranges of values for the parameters, delimited as discussed above and then somewhat widened to estimate errors, are as follows: $0.45 \lesssim a \lesssim 3.32$, $0.05 \lesssim b < 0.5$, $1.555 \lesssim n_r \lesssim 2.33$, $0 \lesssim n_i \lesssim 0.1$, and $0 \lesssim f \lesssim 0.181$.

The limits of integration over particle size are as follows: $r_1 = 0$ and $r_2 =$ a radius sufficiently large that the phase function would not change significantly even if r_2 were increased. The interval between r_1 and r_2 was divided into 12 or 24 equal subintervals. Within each subinterval 96-point Gaussian quadratures were used. Decreasing the integration step size below the value used (~ 0.0025 μm) did not significantly change the phase function. The following procedure was used.

1. The five-dimensional space previously delimited was explored at coarse resolution to locate the regions where a solution was most likely to be found.
2. The effect of each parameter on the function was determined by changing the parameters one at a time, and a qualitative physical explanation was obtained using ray tracing methods [28].
3. The best solution was found by thoroughly searching the regions identified in step 1, taking into consideration the information gained in step 2.
4. One parameter at a time was varied. The fit was restored by changing one or more of the other parameters. The rms error of the fit was computed each time.

The last two steps enable one to establish confidence intervals for the parameters.

V. RESULTS

From over 1000 theoretical phase functions, the two shown in Figs. 1 and 2 (solid lines) are among those matching the observations. The effective radius ($a = 1.0$ μm) and effective variance ($b = 0.4$) of the size distribution are identical for both wavelength intervals. The value of f required (0.08 at 268 nm and 0.075 at 305 nm) is of the same order of magnitude as the optical thickness of molecular Rayleigh scattering from a carbon dioxide atmosphere. The values found for the complex refractive index are $m = 2.0 - 0.02i$ at 268 nm and $m = 1.9 - 0.01i$ at 305 nm.

The theoretical matching curves shown in Figs. 1 and 2 are not unique. A range of effective radii (0.8 μm $\lesssim a \lesssim$ 1.8 μm), effective variance ($b \gtrsim 0.2$), real indices ($n_r \gtrsim 1.8$), imaginary indices ($0.012 \lesssim n_i \lesssim 0.03$ at 268 nm and $0.007 \lesssim n_i \lesssim 0.023$ at 305 nm), and f ($0.06 \lesssim f \lesssim 0.09$ at 268 nm and $0.04 \lesssim f \lesssim 0.075$ at 305 nm) in the proper combinations can fit the data as well as the cases shown in Figs. 1 and 2. Figures 3 and 4 are examples using extreme values in the allowed range of parameters. The phase function in Fig. 3 was generated with nearly the smallest values of a (0.9 μm) and n_r (1.85) possible for 268 nm observations. Figure 4 uses nearly the largest effective radius ($a =$ 1.5 μm) and smallest effective variance ($b = 0.2$) possible.

The only large differences are found in the orbital Rev. 7 portion of the diagrams. These discrepancies may have arisen from the attempt to fit

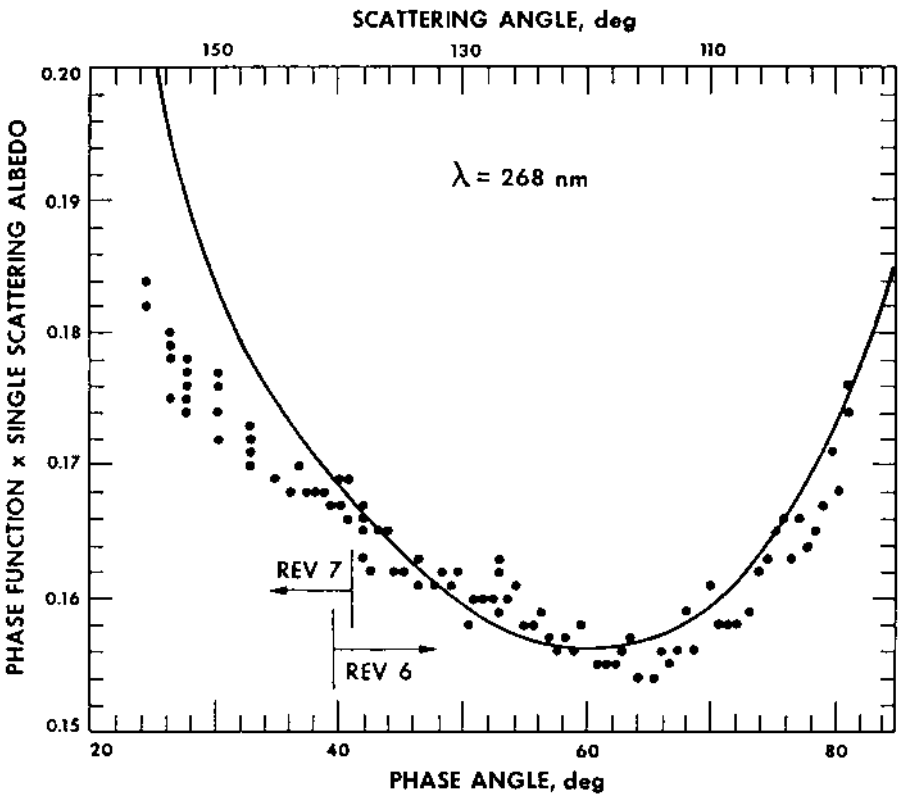

FIGURE 3 Same as Fig. 1, except for $\lambda = 268$ μm, $a = 0.9$ μm, $b = 0.4$, $m = 1.85 - 0.015i$, and $f = 0.085$.

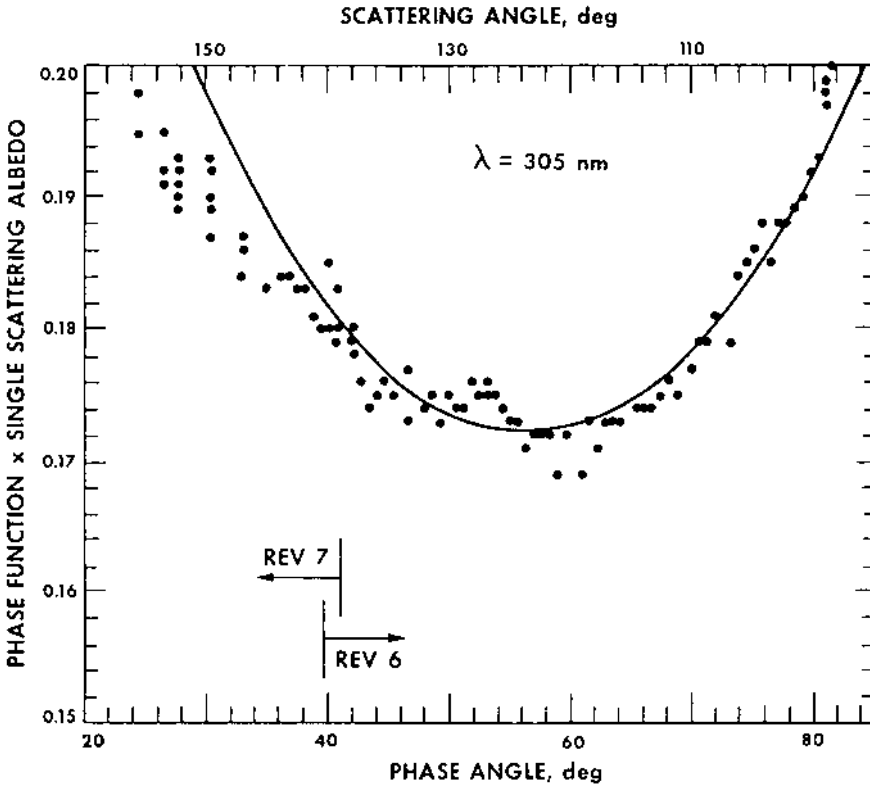

FIGURE 4 Same as Fig. 1, except for $\lambda = 305$ nm, $a = 1.5$ μm, $b = 0.2$, $m = 2.2-0.01i$, $f = 0.75$.

a single theoretical phase function to two sets of observations taken where the dust had different characteristics. If this is so, Rev. 7 data should not be normalized to Rev. 6 data. A horizontally inhomogeneous model could probably improve the fit, but we do not wish, at this time, to introduce additional complexity into the model. In this study, primary weight was assigned to the Rev. 6 data, and this portion of the data was matched by the theory. Only secondary consideration was given to the Rev. 7 data. The rms errors in fits to Rev. 6 data shown in Figs. 1–4 are about 1% of the mean value of the observed phase function. The rms errors are about four times as large if the Rev. 7 data are included.

Lower limits are given as estimates for the real component of the refractive index, n_r, and the effective variance of the size distribution, b,

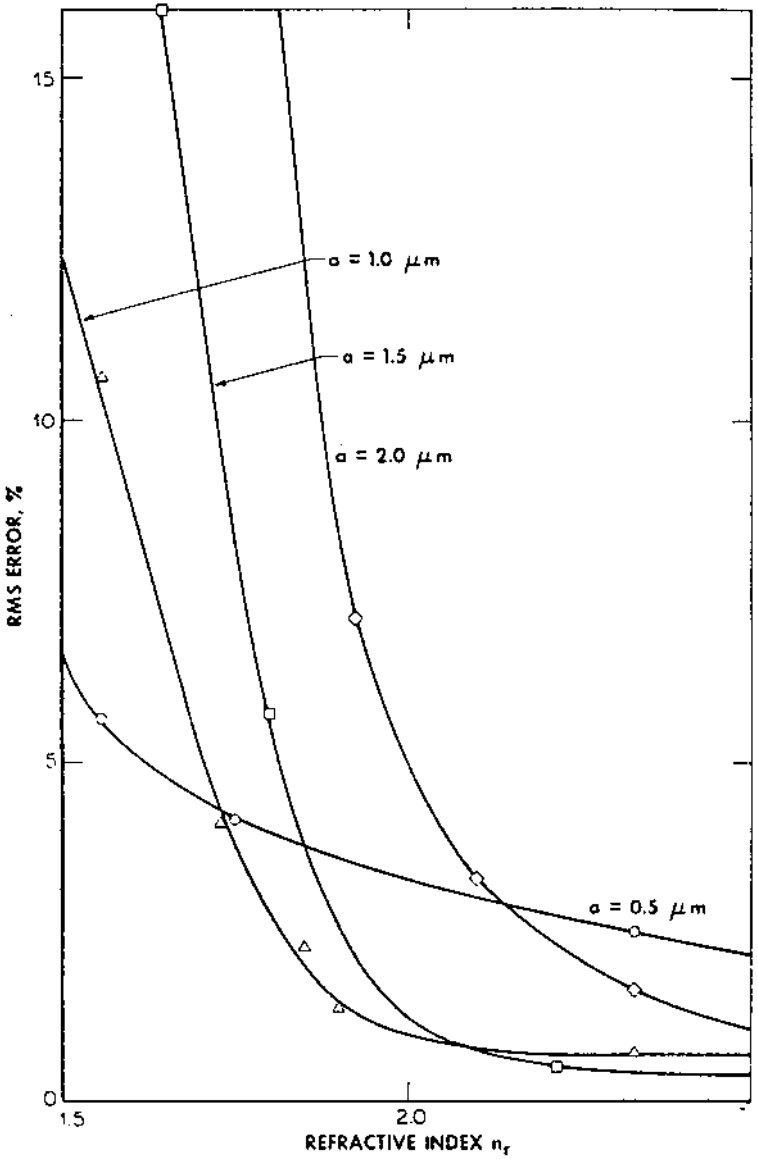

FIGURE 5 The approximate least rms error in fitting Rev. 6 data at a wavelength of 305 nm vs. the real component of the refractive index n_r at four effective radii: a = (○) 0.5 μm, (△) 1.0 μm, (□) 1.5 μm, and (◇) 2.0 μm.

because the rms error as a function of n_r or b does not show a distinct minimum. Figure 5 shows the approximate least rms errors as a function of the real component of the refractive index at four equally spaced values of the effective radius within the range established by previous independent studies: $a = 0.5$, 1.0, 1.5, and 2.0 μm. The parameters a and n_r were kept constant while b, n_i, and f were varied to obtain the best possible fit at each value of n_r. The approximate lower bounds to the rms errors (for Rev. 6 data, normalized to the mean value of the phase function observed at 305 nm) are drawn through the various symbols.

Figure 5 shows that certain effective radii ($a = 1.0$ and 1.5 μm) agree better than others ($a = 0.5$ and 2.0 μm). If a is assumed to be about 2 μm or larger, very large values of f or n_r are required to bring agreement with the measurements. If f and n_r are restricted to reasonable values, the $a = 2.0$ μm curve in Fig. 5 represents the best fit to the data. Values of $a \lesssim 0.7$ μm give phase function curves that have too much curvature about the minima.

The range of size estimates can be narrowed down. Figure 6 shows the approximate least rms errors for 268 and 305 nm data as a funtion of a. The

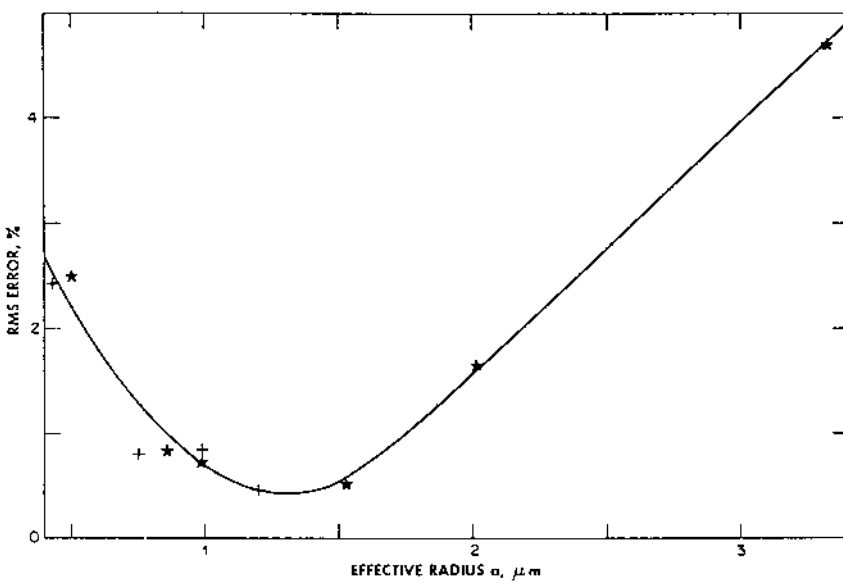

FIGURE 6 The approximate least-rms error in fitting Rev. 6 data vs the effective radius a for wavelengths of (+) 268 and (★) 305 nm.

effective radius, a, was held constant at various values along the abscissa while b, n_r, n_i, and f were adjusted to achieve the best agreement. Size estimates are independent of wavelength, because the rms errors for the two wavelength intervals are nearly identical. The effective radius is between 0.8 and 1.8 μm, or 1.3 ± 0.5 μm. Of all the parameters, the particle radius is the best determined, because it depends on the width of the observed phase function curve. This size estimate may be representative of dust grains in the upper dust layers rather than the entire atmosphere, because the ultraviolet spectrometer measured the dust cloud for optical depth 1.

The value of the effective variance, b, is the least known of the parameters. Increasing or decreasing b only moves the phase function up or down without changing its shape if b is greater than 0.2. Any error in the absolute calibration causes an error in b. On the other hand, an uncertainty in absolute calibration is absorbed as uncertainty in b without affecting the determination of other parameters. The effective variance, b, is estimated to be $\gtrsim 0.2$. This lower limit is typical of size distributions for terrestrial tropospheric aerosols and greater than, those for stratospheric condensates [15].

The same least-squares error analysis is used to determine the imaginary index, n_i. Figure 7 shows the least rms errors for the 268 and 305 nm

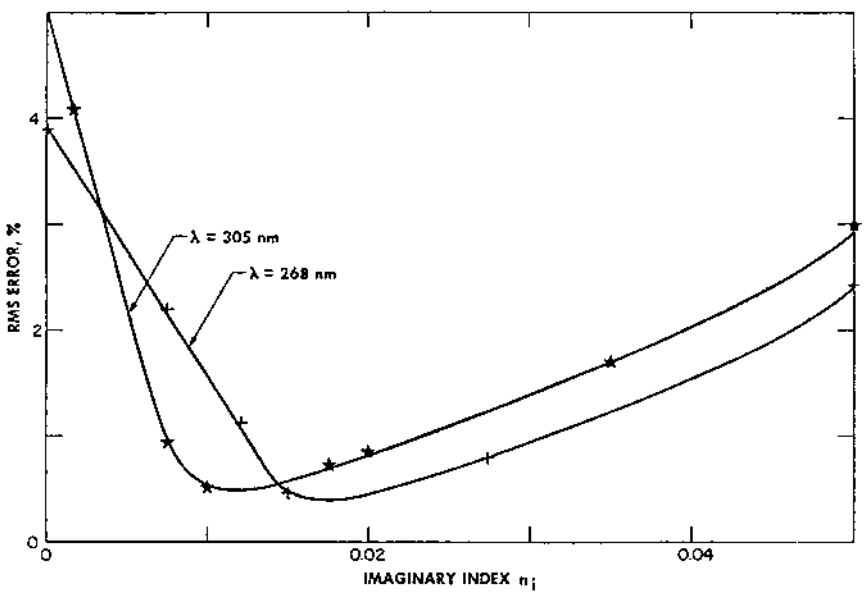

FIGURE 7 The approximate least-rms error in fitting Rev. 6 data vs. the imaginary index n_I at wavelengths of (+) 268 and (★) 305 nm.

TABLE 1 Properties of Martian Dust Particles

	Present work (active 1971 storm conditions)				
		Probable values			
Parameter	Acceptable range	Set A	Set B	Previous works	Remarks/references
Effective radius of size distribution, a	0.8–1.8 μm	1 μm	1.5 μm	0.5–2.0 μm	1971 storm, references listed in Section IV
Effective variance of size distribution, b	$\gtrsim$0.2	—	—	Unknown	
Rcal component of refractive index, n_r	$\gtrsim$1.8	2.0 at 268 nm; 1.9 at 305 nm	2.1 at 268 nm; 205 at 305 nm	1.55–1.75 at 360–1040 nm; 1.75 preferred	29
Imaginary component of refractive index, n_I	0.012–0.03 at 268 nm; 0.007–0.023 at 305 nm	0.02 at 268 nm; 0.01 at 305 nm	0.015 at 268 nm; 0.01 at 305 nm	Negligible from 360 to 1040 nm	29
Ratio of Rayleigh to dust scattering coefficients, f	0.06–0.09 at 268 nm; 0.04–0.075 at 305 nm	—	—	Unknown	

data of Rev. 6 as a function of n_i. The imaginary component of the refractive index, n_i, was fixed at different values along the abscissa while a, b, n_r, and f were changed to obtain the best agreement. Unlike the situation for the radius, the least rms errors are different for the two wavelength intervals in Fig. 7. Consequently, two different ranges of imaginary indices, 0.012–0.03–268 nm and 0.07–0.023 for 305 nm, are needed to fit the data at the respective wavelengths. Imaginary indices greater than $n_i \gtrsim 0.04$ give phase functions that cannot be adjusted to agree with the data by varying the other parameters. Nonabsorbing or weakly absorbing particles give too strong a backscatter peak to fit the data properly. A well-defined minimum in each lower-bound curve of the rms error gives values for the imaginary index of 0.015–0.02 at 268 nm and 0.01 at 305 nm.

The range of f values consistent with the data has been listed. These values of f are of the order of the molecular Rayleigh scattering optical thickness.

The results of this work are summarized in Table 1. Results of previous studies on Martian dust particles are included in the same table for comparison. We caution against overinterpretation of any similarity or difference found between these sets of results, because the 1971 dust storm, though most favorable for observing Martian dust, was not typical of Mars conditions. Also, these results may be representative of dust grains in the upper dust layers and not of the entire atmosphere.

VI. DISCUSSION

Mariner 9 ultraviolet spectrometer observations of the 1971 dust clouds have been analyzed by matching the observed dust phase function with Mie scattering calculations for size distributions of spheres of homogeneous and isotropic material. This method is successful in determining a value for the effective radius of the dust particles but gives only a lower limit for the effective variance. Similarly, one finds a value for the imaginary index but only a lower limit for the real refractive index. The phase curve–fitting technique was previously demonstrated to be capable of determining a range of values for the real index [29,30]. Polar nephelometer measurements of the phase functions of airborne soil particles give $0 \lesssim n_i \lesssim 0.005$ for the terrestrial dust in green light. In this case, the estimate of n_i was found to be insensitive to the assumed value of n_r used in computing the Mie functions [31]. This result is consistent with our study. Polarization measured simultaneously with intensity can add to the value of the observations [32].

Values of the real index found in this study are compatible with those found by Mead [30] for the visible and near-visible wavelengths, 1.55–1.75, with 1.75 preferred. The refractive index increases with decreasing wave-

length in going from the visible to the ultraviolet. Martian dust seems to have a normal dispersion in the wavelength range of near-ultraviolet and visible to near-infrared. This behavior in n_r, together with the rapid rise in the imaginary index from a negligible value in the visible and adjacent wavelengths to ~ 0.01 at 305 nm and ~ 0.02 at 268 nm, indicates that Mars material has an absorption band in the ultraviolet (e.g., Ref. 33). The same modeling technique used here is being extended to analyze data at other wavelengths between 195 and 350 nm. With the Mariner 9 ultraviolet data, the shape of this absorption band can be mapped out.

The presence of an ultraviolet absorption band is not only diagnostic of the composition of the Mars surface material but may also have implications for the development and evolution of life on Mars. Sagan and Pollack [34] pointed out that organisms can exist at about 1 cm subsurface in the Martian epilith, where they are protected from germicidal ultraviolet irradiation but can still use visible light for photosynthesis. If the Mars surface material absorbs ultraviolet light strongly as shown by this study but transmits visible light as shown by Mead [30], the conditions suggested by Sagan and Pollack will be easier to accomplish. If a millionfold attenuation of the solar ultraviolet flux is needed so that the organisms can repair and reproduce themselves at time scales shorter than the time to accumulate a lethal dose of irradiation, an approximately 30 μm layer of material with the optical properties listed in Table 1 can provide this protection. A hundredfold reduction in the depth of the euphotic zone means that about 1000 times as much visible light would be available for photosynthesis.

None of the rocks or minerals postulated or their combinations has the ultraviolet properties found in this study. Andesite, basalt, and montmorillonite have refractive indices that are too small. In addition, they do not absorb strongly in the ultraviolet. Limonite has acceptable properties at 305 nm, but the run with wavelength appears incorrect. Using values for limonite given by Egan et al. [27], we were unable to find a particle size distribution that fits the observed phase function properly for both wavelength intervals. The results of this study require candidate Mars materials to be strongly absorbing in the ultraviolet. This was also a criterion by previous Mariner 6 and 7 and OAO observations of Mars, which showed that the Mars surface albedo is low in the ultraviolet and decreases with decreasing wavelength [35,36]. Polymers of carbon suboxide have an upturn in their reflectance curves in the ultraviolet, a spectral feature inconsistent with the requirement just stated [4]. Laboratory measurements indicate that limonite, basalt, and montmorillonite have essentially flat reflectances between 200 and 400 nm, a behavior incompatible with the Mars surface spectral albedo.

ACKNOWLEDGMENT

We thank Charles A. Barth and members of the Mariner 9 ultraviolet spectrometer team for their support. We are grateful to James E. Hansen for providing us with a Mie scattering Fortran code.

REFERENCES

1. Egan, W.G.; Spagnolo, F.A. Complex index of refraction of bulk solid carbon dioxide. Appl. Opt. 1969, *8*, 2359–2360.
2. Dollfus, A. Polarization studies of planets. In Planets and Satellites; Kuiper, G.P., Middleburst, B.M., Eds.; Univ. Chicago Press: Chicago, 1961.
3. Adams, J.B.; McCord, T.B. Mars: interpretation of spectral reflectivity of light and dark regions. J. Geophys. Res. 1969, *74*, 4851–4856.
4. Plummer, W.T.; Carson, R.K. Mars: is the surface colored by carbon suboxide? Science 1969, *166*, 1141–1142.
5. Hanel, R.; Conrath, B.; Hovis, W.; Kunde, V.; Lowman, P.; Maguire, W.; Pearl, J.; Pirraglia, J.; Prabhakara, C.; Schlachman, B.; Levin, G.; Straat, P.; Burke, T. Investigation of the Martian environment by infrared spectroscopy on Mariner 9. Icarus 1972, *17*, 423–442.
6. Lowman, P. Personal communication, 1975.
7. Hunt, G.R.; Logan, L.M.; Salisbury, J.W. Mars: components of infrared spectra and the composition of the dust cloud. Icarus 1973, *18*, 459–469.
8. Hord, C.W.; Barth, C.A.; Stewart, A.I.; Lane, A.L. Mariner 9 ultraviolet spectrometer experiment: photometry and topography of Mars. Icarus 1972, *17*, 443–456.
9. Pang, K.; Hord, C.W. Mariner 9 ultraviolet spectrometer experiment: 1971 Mars' dust storm. Icarus 1973, *18*, 481–488.
10. Ajello, J.M.; Hord, C.W.; Barth, C.A.; Stewart, A.I.; Lane, A.L. Mariner 9 ultraviolet spetrometer experiment: afternoon terminator observations of Mars. J. Geophys. Res. 1973, *78*, 4279–4290.
11. Ajello, J.M.; Hord, C.W. Mariner 9 ultraviolet spectrometer experiment: morning terminator observations of Mars. J. Atmos. Sci. 1973, *30*, 1495–1501.
12. Koskela, P.E.; Helton, M.R.; Seeley, L.N.; Zawacki, S.J. Mariner Mars 1971 television picture catalog—sequence design and picture coverage. Jet Propulsion Lab. Tech. Memo. Pasadena, CA, 1972; Vol. 2, 33-585.
13. Barth, C.A.; Hord, C.W.; Stewart, A.I.; Lane, A.L. Mariner 9 ultraviolet spectrometer experiment: initial results. Science 1972, *175*, 309–312.
14. Zerull, R.; Giese, R.H. Microwave analog studies. In Planets, Stars and Nebulae Studied with Photopolarimetry; Gehrels, T., Ed.; Univ. Arizona Press: Tucson, AZ, 1974, 309–312.
15. Hansen, J.E.; Travis, L.D. Light scattering in planetary atmospheres. Space Sci. Rev. 1974, *16*, 527–610.
16. Ajello, J.M.; Pang, K.D. Mariner 9 ultraviolet spectrometer experiment: scattering properties of Hellas. Icarus 1975, *26*, 332–340.

17. Veverka, J.; Goguen, J.; Liller, W. Multicolor polarimetric observations of the great 1971 Martian duststorm. CRSR 550. Laboratory for Planetary Studies, Cornell Univ.: Ithaca, NY, 1973.
18. Moroz, V.I.; Ksanfomaliti, L.V. Preliminary results of astrophysical observations of Mars from Mars-3. Icarus 1972, *17*, 408–422.
19. Pollack, J.B.; Toon, O.B.; Sagan, C. Physical properties of the particles composing the great Martian dust storm of 1971. Bull. Am. Astron. Soc. 1974, *6*, 370.
20. Conrath, B.J. Thermal structure of the Martian atmosphere during the dissipation of the dust storm of 1971. Icarus 1975, *24*, 36–46.
21. Hartmann, W.K.; Price, M.J. Mars: clearing of the 1971 dust storm. Icarus 1974, *21*, 28–34.
22. Sagan, C.; Pollack, J.B. Windblown dust on Mars. Nature 1969, *223*, 791–794.
23. Anderson, A.D. Spherical particle terminal velocities in the Martian daytime atmosphere from 0 to 50 kilometers. J. Geophys. Res. 1967, *72*, 1951–1958.
24. Capen, C.F.; Martin, L.J. Mars' great storm of 1971. Sky Tel. 1972, *43*, 276–279.
25. Abramenko, A.N.; Prokofieva, V.V. Ground-based television patrol of Martian cloud formations in 1969 and 1971–1972. Icarus 1974, *21*, 191–195.
26. Deibmendjian, D. Electromagnetic Scattering on Spherical Polydispersions; American Elsevier: New York, 1969.
27. Egan, W.G.; Hilgeman, T.; Pang, K.D. Ultraviolet complex refractive index of Martian dust: laboratory measurements of terrestrial analogs. Icarus 1975, *25*, 344–355.
28. Liou, K.N.; Hansen, J.E. Intensity and polarization for single scattering by polydisperse spheres: a comparison of ray optics and Mie theory. J. Atmos. Sci. 1971, *28*, 995–1004.
29. Arking, A.; Porter, J. The phase curve of Venus and the nature of its clouds. J. Atmos. Sci. 1968, *25*, 617–628.
30. Mead, J.M. The contribution of atmospheric aerosols to the Martian opposition effect. Icarus 1970, *13*, 82–95.
31. Grams, G.W.; Blifford, I.H., Jr.; Gillette, D.A.; Russell, P.B. Complex index of refraction of airborne soil particles. J. Appl. Meteorol. 1974, *13*, 459–471.
32. Hansen, J.E.; Hovenier, J.W. Interpretation of the polarization of Venus. J. Atmos. Sci. 1974, *31*, 1137–1160.
33. Jenkins, F.A.; White, H.E. Fundamentals of Optics; McGraw-Hill: New York, 1957.
34. Sagan, C.; Pollack, J.B. Differential transmission of sunlight on Mars: biological implications. Icarus 1974, *21*, 490–495.
35. Hord, C.W. Mariner 6 and 7 ultraviolet spectrometer experiment: photometry and topography of Mars. Icarus 1972, *16*, 253–280.
36. Caldwell, J. Ultraviolet observations of Mars made by the Orbiting Astronomical Observatory. Icarus 1973, *18*, 489–496.

13

Effect of Aerosols on Optical Remotely Sensed Data

I. INTRODUCTION

The atmosphere is composed of nitrogen and oxygen molecules, trace gas constituents, and approximately micrometer-sized aerosol particles. The gaseous molecules produce broadband Rayleigh scattering and absorption of solar radiation in specific narrow spectral regions. The aerosols' primary effect is to scatter solar radiation, but they may absorb slightly over broad wavelength regions depending upon their composition and size. Water vapor, ozone, oxygen, and nitrogen dioxide also have weak absorption features in the visible spectrum and strong absorption features in the ultraviolet and near-infrared.

In aircraft or satellite data analysis these atmospheric absorption and scattering effects are often ignored. One technique frequently used to correct for atmospheric effects is to take ratios of ground target radiances (as sensed from a satellite or aircraft) from adjacent areas; the atmospheric contribution supposedly cancels out. This would be true, however, only if the atmospheric effects entered as simple multiplicative factors; actually the factors are additive or in combination with multiplicative, so the ratio technique is only approximate. Another disadvantage of the simple ratio technique is that it does not allow the establishment of absolute radiance levels of ground targets and thus does not permit a library of radiance values to be established for these ground targets for universal application in remote sensing. A database of radiances is essential when ground truth or "training areas" are not available,

whether because of inaccessibility of areas or lack of ground truthing teams for detailed and timely surveys.

One could ask, "Why worry about absolute calibration when useful information can be obtained from an uncalibrated black box?" The need is evident when we concern ourselves with the next generation of higher photometric and spatial resolution sensors. The LANDSAT D Thematic Mapper (TM) has 256 photometric quantification levels (which can be data processed to an effective 512 levels) compared with 64 for the MSS on LANDSATS I, II, and III. Also the instantaneous field of view (IFOV) of the TM is 30 m compared with 79 m for the Multispectral Scanner (MSS) on LANDSATS I, II, and III. The precision in radiation level measurement will be useless, because the approximations involved are already starting to present a difficulty at present photometric accuracy [1]; at the higher photometric accuracy, the value of the data will be vitiated. Further, at the projected higher angular resolution, scattering through small angles will have a greater effect on contrast, and it will vary from day to day as well.

The atmospheric degradations, which may be quite large, are logically expressed in terms of optical depths where an optical depth of unity produces an attenuation of 63%. Aerosol optical depths, unfortunately for modeling, undergo considerable spatial and temporal fluctuations. A paper by Rahn [2] for example, indicated that the vertical optical depth of midlatitude aerosols undergoes a factor of 2 seasonal variation (summer to winter) and that the urban-rural optical depth variation is greater than a factor of 10 (with a maximum urban optical depth of ~ 0.5 ($\lambda = 0.500$ μm) (Chicago, Baltimore, New York).

Optical effects from atmospheric aerosols, for all the remote sensing problems they cause, do have a beneficial side, because of the very fact that the atmospheric aerosols reduce incident earth surface radiation and affect sky intensity. Because there is a wavelength and angular dependence of this surface radiation and sky intensity, we can, in principle, infer from it the aerosol size spectrum, number density, complex index of refraction, and ultimately the composition. This, of course, has far-reaching implications for studies of weather, visibility, cloud formation, and the earth's heat balance. Considerable efforts have been made to assess quantitatively the optical effect of aerosols for application to LANDSAT date (see Refs. 3–5). However, the analysis of optical effects produced by aerosols can make use of their shapes and their complex index of refraction, including quantum size effects (see Ref. 6) for submicrometer-sized particles. Mie theory, an exact approach based on Maxwell's equations, represents scattering and absorption by spherical particles and is widely used in atmospheric radiative transfer models. More recently, modifications have been developed for ellipsoidal or platelet particles.

With the appropriate complex indices of refraction (see e.g., Ref. 7) and possible quantum size effects on aerosols [6], an appropriate radiative transfer model may be applied to correct aircraft and satellite data. This may require an assumption of an aerosol size distribution and number density with altitude. To infer the atmospheric aerosol size distribution and, in principle, the variation with altitude, as well as the optical constants, one must go in the reverse order, using optical field observations of sky intensity as a function of solar zenith angles and observer viewing angles. This inversion problem does not lend itself to an easy solution, nor is there necessarily a unique solution generated. Because the linear equations relating optical variables and the particle variables tend to be poorly conditioned, even tiny errors in the measured optical parameters can introduce severe instabilities in the solution [8–10]. Fortunately, many solution vectors that contain high frequency components cannot correspond to real particle distributions in the natural environment, because the larger and smaller peaks in the aerosol size distribution function would be smeared out rapidly. Aerosol particles normally range in size from $\sim 10^{-2}$ to ~ 10 μm in diameter; the smaller ones coagulate, and the larger ones fall out quickly.

The inversion procedure is most effectively applied in situations with azimuthal symmetry of atmospheric parameters, in contrast to conditions where perhaps a cold front may exist to cause decreased visibility and increased scattering from the location of the clouds. For these nonsymmetrical conditions, one could assume symmetry and a representative aerosol size and number density distribution and compare the results of a radiative transfer calculation with the observations, allowing for the nonrepresentative conditions in a particular direction. We prefer to have azimuthal symmetry, but it did not exist in either the Virgin Islands or Ft. Collins, Colorado, where our studies were carried out.

In any case, the optical measurements (usually radiance, but also flux) were made; this required exceptionally accurate ground photometry with carefully calibrated photometers. These determinations are referenced to the known solar radiance or flux at the top of the atmosphere [11] to characterize atmospheric absorption and scattering.

In this chapter we report on the results of major experimental tests of two complementary approaches to aerosol modeling. One approach, the Dave radiative transfer model, uses Mie theory, the optical properties of the aerosol, and size distribution to determine the optical effects on sky radiance, solar flux, and optical depths at various levels in the atmosphere, as well as downwelling solar direct and diffuse flux. The second approach, constrained linear inversion, uses optically observed effects such as the optical depth and variations of sky radiance on the solar almucantar to obtain the path-averaged optical depth of aerosols and the size distribution. The total down-

welling diffuse radiation may then be calculated and compared to measurement. Test areas for this comparison are ones that have a significant aerosol atmospheric loading, so that the effect of aerosols on optical remotely sensed data can be easily recognized. The ground and laboratory measurements that are made to furnish input to the models are described. The results of the modeling are quantitatively compared to experimental measurements. These comparisons include sky radiance, solar flux (at ground level), and angular width of the solar aureole. This comparison permits the validity of each of the models and also the reasonableness of inputs to be checked. The accuracy limitations of each of the models are indicated as well as the aerosol characteristics that affect the photometry.

II. STUDY AREAS

Two study areas were involved for this paper: (1) St. Thomas, U.S. Virgin Islands, and (2) Fort Collins, Colorado. The first area was the site of NASA Experiment No. 589 in 1972 [12,13], and the second area was the site of the First International Workshop on Light Absorption by Aerosols in 1980.

At St. Thomas, U.S.V.I., a mountain (altitude 458 m) located in the center of the island (Signal Mountain) was the site of the multidirectional solar flux and sky radiance measurements. Additionally, the sum of solar and sky flux were determined on a ground target using a calibrated photometric diffuse white plate at Signal Mountain, at Brewers Bay Beach, and at an offshore location in St. Thomas Harbor. The weather conditions were clear and sunny, temperature about 35°C, but the horizontal visibility decreased from the usual 60 miles (96.6 km) to 8 miles (12.9 km) during the measurements. The San Juan weather bureau indicated that the reduced visibility was the result of dust from storms over the Sahara desert being carried west by the easterly trade winds. Thus, at the time of the measurements, a below normal visibility existed, and by chance a tropical disturbance was building up east of Florida along with a cold front proceeding south over Florida. This resulted in a nonazimuthally symmetrical photometric condition.

The Fort Collins area is arid and has detectable pollution that changes throughout the day. The city is at an altitude of 519 m, thus being above a portion (16%) of the atmospheric air mass. Horizontal visibility was about 10–20 miles (16.1–32.2 km), and the sunsets were reddish. There was no rain preceding the observations.

III. EXPERIMENTAL APPROACH

The experimental field measurement approaches were dictated by the input needs of the aerosol modeling programs. Checking the Dave program

predictions required a number of angularly dependent photometric observations such as sky radiance solar flux at ground level and the radiance of a diffuse white panel at ground level. The constrained linear inversion, in contrast, required input data of path-average optical depths as a function of wavelength as well as sky intensity on the solar almucantar as a function of wavelength and scattering angle in order to determine the particle size distribution.

Sky radiance and solar flux data were gathered for the Dave model on Signal Mountain at St. Thomas. This provides a set of data that is compared to a radiative transfer model constructed by using the optical complex index of a sand representative of the Sahara and a representative aerosol size range and vertical distribution. Concurrent measurements of the sum of sky and solar flux on a ground target were made at Signal Mountain, Brewers Bay Beach, and offshore in St. Thomas Harbor between 0920 and 1448 local time. The radiance and flux measurements were made with a portable battery-operated Minneapolis-Honeywell photometer (with interchangeable narrowband interference filters). The field of view was 3°. The optical filters used in the measurements were peaked at 0.433, 0.533, and 0.633 μm; they were made by Optics Technology and had a bandpass of 0.02 μm. The photometer was calibrated with the filters in the laboratory with an Eppley thermopile. The diffuse panel used for the flux measurements was coated with white Nextel paint, having a reflectance of 70% at the wavelengths considered [12].

The Fort Collins measurements provided the total optical depths as a function of wavelength [$\tau(\lambda)$], and the sky intensity [$I_{sky}(\theta_0,\lambda)$] on the solar almucantar as a function of wavelength and scattering angle θ_0. These determinations were necessary in order to make an estimate of the aerosol particle size spectrum using constrained linear inversion.

For the constrained linear inversion program, the path-average optical depth or optical extinction was determined (at Fort Collins) by looking at the sun with a stable narrowband multiwavelength, parameter, calibrated [9] at Mauna Loa Observatory before and after the Fort Collins observations. One filter in the sun photometer was located at $\lambda = 0.945$ μm, a wavelength in the $\rho\sigma\tau$ complex of water vapor bands; this permitted a curve of growth to be determined relating water vapor amount (g/cm^2) along the solar ray path to the optical extinction. The water vapor information is obtained as a "fringe benefit" and is not use in the modeling. The sky intensity $I_o(\lambda)$ and its angular gradient within a few degrees of the sun were measured with the photoelectric coronameter [14]. These observations near the sun permit the aerosol particle size distribution to be determined; sky brightening near the sun arises from diffraction of sunlight by aerosol particles, similar to Fraunhofer diffraction. For light at 0.5 μm wavelength, the brightening (aureole) around the sun extends out 2° for 10 μm particles and out 20° for 1 μm particles.

In addition, the diffuse downwelling spectral flux from the sun was measured with a hemispherical flux detector. This served as a corroboration of the secant dependence of the optical thickness measurement made with the sun photometer.

IV. COMPUTATIONAL APPROACH

Two computational approaches were used for aerosol modeling: (1) The St. Thomas observations are compared to the Dave [15] radiative transfer model output, and (2) the Fort Collins data are used as input to a constrained linear inversion program to estimate the particle size distribution. Both approaches would benefit from detailed air truth. However, in lieu of detailed air truth, some assumptions are necessary. For the Dave program the complex index of refraction ($N + iK_o$) used for the aerosols was that determined for Sinai desert sand using the techniques of Egan and Hilgeman [7] and presented in Table 1. The Sinai desert sand is assumed to be representative of desert sand from the region of the Middle East. It is a lightly weathered silicate, with no organic inclusions.

Following a series of trial-and-error computer models in lieu of an inversion technique, a number of parameters were chosen for the Dave program. The vertical number density was that of Dave and Braslau multiplied by 10 (see Ref. 7). The particle size distribution used was a modified power law [16]: constant from radius 0.254 μm to 0.1 μm and decreasing as r^{-4} to 2 μm in radius. The Air Force Geophysical Laboratories [17] tropical temperature and pressure variation with altitude was used. Rayleigh scattering is included in the model as well as absorption by ozone. The solar zenith angle and the average ground albedo are also input parameter. The output of the model consists of sky radiance (and ground radiance) at selectable altitudes as a function of viewing zenith angles (in 2° increments) at selectable azimuth angles relative to the sun. The optical depth is output as a function of altitude as well as solar flux and ground target intensity. There were 40 plane parallel layers in the model extending upward to 44.75 km, and the total number of aerosol particles in a centimeter square column was

TABLE 1 Optical Constants for Sinai Desert Sano

λ (μm)	N	K_0
0.433	1.287	0.000138
0.533	1.287	0.000105
0.533	1.324	0.0000912

5.45×10^7. A ground albedo of 30% was assumed representative of the foliage-covered ground. This model was found empirically to represent the observed St. Thomas data where no weather fronts occur, as described subsequently in Section V.

The constrained linear inversion approach assumes that (1) the aerosol particles are heterodisperse and spherical; (2) the path-average optical depth as a function of radiation wavelength is a function of the aerosol number density and particle radius, and (3) the solar aureole brightening is a function of two Mie scattering matrix terms (M_1 and M_2), the radiation wavelength, and particle radius. An index of refraction of 1.50 was assumed, with no absorption. The kernels of these two functional relationships (integral equations) may be used to recover the overall particle size spectrum in the approximate particle size range $0.05\ \mu m < r < 10\ \mu m$. The integral equations are solved by breaking them up into quadratures to form a set of linear equations relating spectral extinctions, τ, aureole sky brightness, and particle size characteristics at angular position ϕ along the almucantar; a smoothing must be used to reduce the effect of experimental measurement error. The experimental inputs were the wavelength dependences of the path-average atmospheric optical thicknesses and the angular dependence of diffracted light within the angular scattering range of 1–28° from the sun; eight wavelengths between 0.400 and 0.850 μm were used. A particle size range of 0.05–10 μm was assumed, as well as the number density decreasing as r^{-4}. A correction was applied to account for Rayleigh scattering. The vertical number density profile does not enter into the calculations.

To a first approximation, the sky intensity in the solar almucantar, at wavelengths where the path-average optical depth is less than 1 and where no gaseous absorption occurs, is expressible as

$$I(\phi) = \frac{F_0}{\cos\theta_0}\left(\tau_a \frac{\rho_a}{4\pi} + \tau_R \frac{\rho_R}{4\pi}\right)\exp[(\tau_a + \tau_R)/\cos\theta_0]$$

where the subscripts a and R refer to aerosol and Rayleigh components, and P is the scattering phase function normalized so that the integral over 4π steradians equals 4π. ϕ is the scattering angle along the almucantar, θ_0 is the solar zenith angle, and F_0 is the solar irradiance at the top of the atmosphere.

The constrained linear inversion theory is applied to the solar aureole and optical extinction data to obtain the overall aerosol size distribution. The aerosol absorption can then be estimated by comparing the calculated downwelling monochromatic diffuse radiation for the inferred aerosol size distribution with actual measured values.

The amount of water vapor was inferred from a curve of growth (at $\lambda = 0.945\ \mu m$) relating water vapor amount along the solar ray path to the

optical thickness previously measured [9]. The water vapor absorption becomes significant if photometric observations are made in the water absorption band (i.e., sky radiance, solar flux, optical depth).

V. RESULTS

A. St. Thomas

The results of the photometric observations and modeling for St. Thomas are presented in Tables 2–6.

Table 2 lists the solar fluxes at Signal Mountain (altitude 458 m), both those observed and those calculated from the Dave model. Also shown for comparison is the solar flux at the top of the atmosphere [11]. The observations were made in early morning (before cloud formation), thus achieving long transmission paths through the lower aerosol layers where the major portion of Sahara dust existed. It is seen that the calculated values in the blue ($\lambda = 0.433$ μm) are systematically much higher than those observed (1.3–3.6 ×), whereas the green ($\lambda = 0.533$ μm) and red ($\lambda = 0.633$ μm) are distributed around 0.61–1.5 × and 0.44–1.6 ×, respectively, those observed. The experimental error of measurement was estimated to be ±10%, which

TABLE 2 Sun Observations at Signal Mountain, U.S.V.I., September 6, 1972[a]

	Local time									
	0725		0820		0850		0920		0930	
	Obs.	Calc.	Obs.	Calc.	Obs.	Calc.	Obs.	Calc.	Obs.	Calc.
Wavelength										
$\lambda = 0.433$ μm	0.26	0.35	0.32	0.47	0.37	0.81	0.32	1.15	0.34	0.93
Solar (top of atmos.) = 3.65										
$\lambda = 0.533$ μm	0.52	0.33	0.56	0.34	0.69	0.70	0.74	1.07	0.64	0.70
Solar (top of atmos.) = 3.94										
$\lambda = 0.633$ μm	0.59	0.27	0.59	0.26	0.42	0.49	0.79	0.71	0.73	0.60
Solar (top of atmos.) = 3.35										
Solar zenith angle (deg.)	69		56		51		43		35	
Solar azimuth angle (deg.)	80		90		100		105		115	

[a] Fluxes given in milliwatts per square centimeter.

TABLE 3 Diffuse White Panel Observations, U.S.V.I., September 6, 1972[a]

	Signal Mountain (Alt, = 458 m)						Brewers Bay Beach		Offshore Station	
	0920		0950		1030		1100		1448	
	Obs.	Calc.	Obs.	Calc.	Obs.	Calc.	Obs.	Calc.	Obs.	Calc.
λ = 0.433 μm	0.35	0.48	0.35	0.54	0.37	0.61	0.46	0.63	0.46	0.67
Panel (top of atmos.)		0.54		0.60		0.65		0.66		0.72
λ = 0.533 μm	0.49	0.53	0.43	0.60	0.61	0.65	0.46	0.67	0.49	0.73
Panel (top of atmos.)		0.57		0.64		0.69		0.70		0.77
λ = 0.633 μm	0.56	0.49	0.56	0.56	0.74	0.60	0.56	0.62	0.56	0.68
Panel (top of atmos.)		0.52		0.59		0.63		0.64		0.70
Solar zenith angle (deg.)	43		35		28		26		11	
Solar azimuth angle (deg.)	105		115		120		125		210	

[a] Intensity in milliwatts per square centimeter per steradian.

TABLE 4 Sky Radiance Measurements at a Signal Mountain, U.S.V.I., September 6, 1972[a]

Sensor viewing angle (deg.)		λ = 0.433 μm		λ = 0.533 μm		λ = 0.633 μm	
Zenith	Azimuth	Obs.	Calc.	Obs.	Calc.	Obs.	Calc.
45	270	0.13	0.11	0.041	0.061	0.037	0.032
74	180	0.18	0.21	0.066	0.13	0.061	0.071
80	0	0.25	0.25	0.17	0.18	0.36	0.11
81	270	0.40	0.25	0.066	0.18	0.099	0.096
0	90	0.11	0.12	0.038	0.078	0.037	0.051
33	90	0.40	0.12[b]	0.40	0.072[b]	0.40	0.042[b]
45	90	0.35	0.13[b]	0.30	0.074[b]	0.42	0.042[b]
56	90	0.43	0.15[b]	0.65	0.084[b]	0.84	0.047[b]
82	90	0.86	0.26[b]	1.21	0.19[b]	1.58	0.10[b]
88	90	0.80	0.25[b]	0.70	0.23[b]	0.91	0.18[b]

[a] Altitude = 458 m; 0745. local time; solar zenith angle = 82°; solar azimuth angle = 90°. Intensities in milliwatts per square centimeter per steradian.
[b] Low accuracy of model in vicinity of solar aureole.

TABLE 5 Sky Radiance Measurements at Signal Mountain, U.S.V.I., September 6, 1972[a]

Sensor viewing angle (deg.)		$\lambda = 0.433\ \mu m$		$\lambda = 0.533\ \mu m$		$\lambda = 0.633\ \mu m$	
Zenith	Azimuth	Obs.	Calc.	Obs.	Calc.	Obs.	Calc.
0	105	0.22	0.15	0.058	0.087	0.065	0.057
67	285	0.25	0.20	0.081	0.11	0.057	0.062
70	180	0.19	0.24	0.058	0.13	0.053	0.068
74	285	0.35	0.27	0.15	0.15	0.11	0.092
83	0	0.26	0.52[b]	0.19	0.45[b]	0.21	0.32[b]
89	0	0.15	0.53[b]	0.14	0.54[b]	0.14	0.48[b]
34	105	0.53	0.14[c]	0.46	0.076[c]	0.74	0.42[c]
63	105	0.57	0.19[c]	0.65	0.10[c]	0.97	0.53[c]
79	105	0.35	0.29[c]	0.43	0.19[c]	0.56	1.06[c]

[a] Altitude = 458 m; 0900 local time; solar zenith angle = 43°; solar azimuth angle = 105°. Intensities in milliwatts per square centimeter per steradian.
[b] Note: Model not representative of cold front approaching from the north (clouds).
[c] Low accuracy of model in vicinity of solar aureole.

TABLE 6 Sky Radiance Measurements at Signal Mountain, U.S.V.I., September 6, 1972[a]

Sensor viewing angle (deg.)		$\lambda = 0.433\ \mu m$		$\lambda = 0.533\ \mu m$		$\lambda = 0.633\ \mu m$	
Zenith	Azimuth	Obs.	Calc.	Obs.	Calc.	Obs.	Calc.
74	180	0.13	0.26	0.062	0.17	0.070	0.085
81	0	0.17	0.51[b]	0.11	0.41[b]	0.11	0.31[b]
89	0	0.17	0.54[b]	0.087	0.50[b]	0.11	0.49[b]
0	110	0.25	0.15[c]	0.066	0.093[c]	0.080	0.058[c]
57	110	0.49	0.17[c]	0.46	0.088[c]	0.64	0.048[c]
77	110	0.43	0.28[c]	0.21	0.18[c]	0.24	0.11[c]

[a] Altitude = 458 m; 0930 local time; solar zenith angle = 35°; solar azimuth angle = 110°. Intensities in milliwatts per square centimeter per steradian.
[b] Note: Model not representative of cold front approaching from the north (clouds).
[c] Low accuracy of model in vicinity of solar aureole.

would account in part for the random distribution in the comparison. However, the existence of low-level morning haze over the sea would be expected to produce a greater attenuation than the model predicted, particularly in the blue, and this may have caused the effect in Table 2.

Table 3 presents the intensities reflected from the diffuse white Nextel panel, both at Signal Mountain and at two sea-level locations, Brewers Bay Beach and the offshore station [12]. Also listed for comparison is the expected intensity of the white plate if it were to be placed at the top of the atmosphere.

There is fairly good agreement between the observed and calculated values of diffuse white panel intensities (Dave model) for all wavelengths. The calculated values are generally higher than the observed, for the same reasons as those indicated for Table 2.

Tables 4–6 list the observed and modeled sky radiances for the three observing wavelengths at various observing zenith and azimuth angles for three solar zenith angles (and corresponding azimuth angles). Agreement between the model and observations is good in the zenith direction and in azimuth directions away from the sun. Because of the large solar aureole (extending out to about 30° from the sun direction), the 90° azimuth values are high, particularly in the red (Table 4), which indicates many small particles (~ 1 μm) in the aerosol composition. This observation justifies the use of the complex indices of refraction measured on micrometer-sized particles presented above (in contrast to the values published by Patterson et al. [18]), for the Mie scattering calculations.

Tables 5 and 6 show similar results, although the effect of the solar aureole decreases. The reason for the inaccurate modeling of the solar aureole appears to be that the Dave model is a two-dimensional model, whereas the representation of the solar aureole is truly a three-dimensional scattering phenomenon, and the appropriate three-dimensional radiation transfer problem has not been solved yet.

B. Fort Collins

The results of the inversion of the atmospheric observations for Fort Collins are presented in Figs. 1–3. Although many detailed observations are necessary to produce each result [9], space limitations permit the presentation of only a sampling of some of significance.

The observed time variations in spectral radiation data produced the aerosol path-average optical depth data shown in Fig. 1 for four wavelengths. The day temperature reached about 40°C, and the sky appeared clear, but a distinct aureole appeared around the sun, about 15–20° in diameter. Also, the total aerosol load underwent a factor of 2 change during

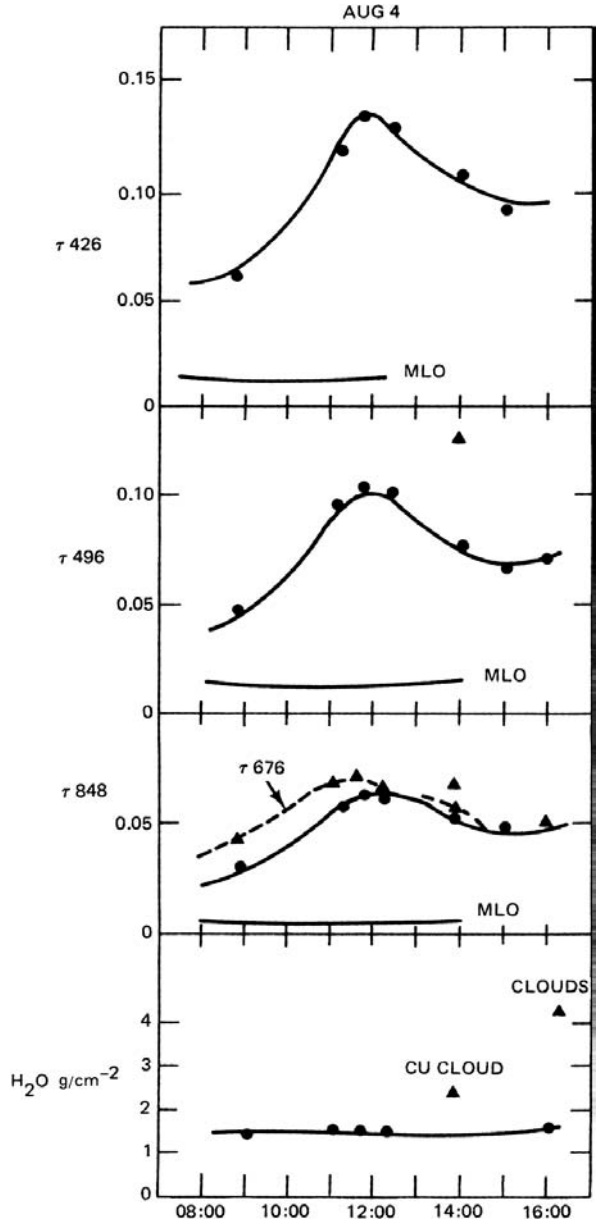

FIGURE 1 Temporal variation of Fort Collins aerosol optical thickness at four wavelengths and column water amounts. Only the O_3 absorption is taken out. The molecular continuum is uncertain; its effect is estimated to be of the order of 0.01 optical depth. MLO = Mauna Loa Observatory.

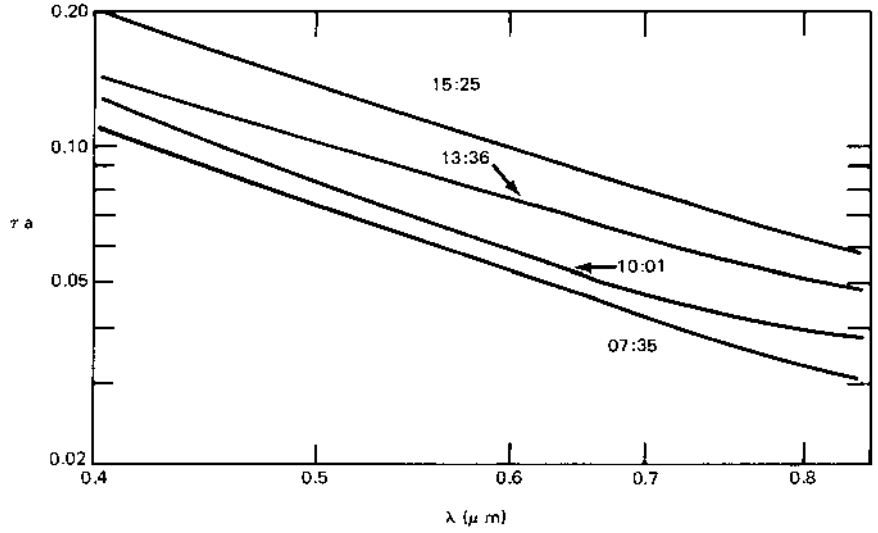

FIGURE 2 The spectral extinction spectrum for aerosols at Fort Collins at various times on August 6, 1980.

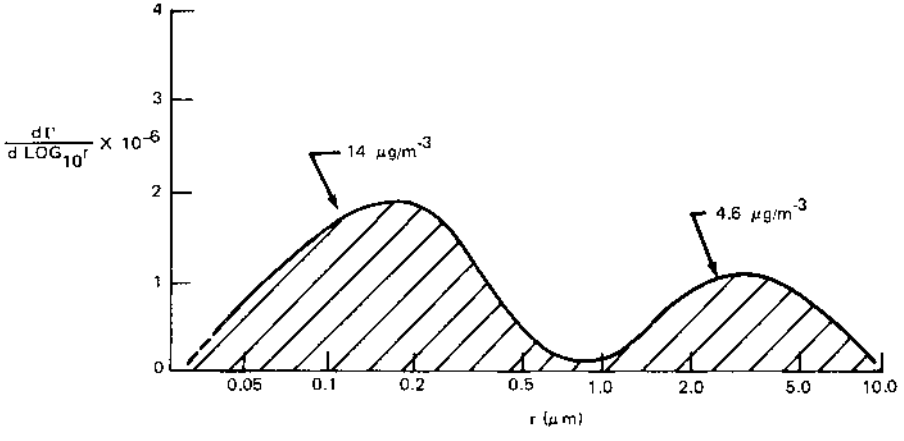

FIGURE 3 Aerosol column mass distribution function (g/cm^2) $d\Gamma/d \log r$ obtained by inverting sky intensity and spectral optical extinction measurements at 10:00 MDT, August 6, 1980, at Fort Collins. Cumulative mass in each mode, assuming a 1 km layer thickness, is 14 $\mu g/m^3$ in lower mode and 4.6 $\mu g/m^3$ in upper mode.

the day, with dominant increases in the morning and also about an hour before the onset of advection cloudiness in the afternoon. These optical depth variations appear to be caused by pollution advection from the south and east (Denver and Boulder) and by the growth of hygroscopic particles in the high humidities preceding cloud formation. The water vapor loading (Fig. 1) was estimated by the curve-of-growth method [9].

The spectral variations in aerosol path-average optical depth are shown in Fig. 2. The effect of O_3 has been taken out, but interband H_2O vapor and the molecular absorption continuum (estimated to be 0.01 optical depth) were not. Small variations in the wavelength dependence of optical depth indicate that the mean aerosol size varied slightly throughout the day (and also from day to day, it was found). Thus, the aerosol is not homogeneous but changes in concentration and, to a lesser extent, in size.

As one example, the aerosol column mass distribution derived from the inversion technique is shown in Fig. 3. It can be seen that there are two particle size modes, one at ~ 3 μm and one at ~ 0.2 μm. The particles are assumed to lie in a 1 km layer above the ground. The cause of the two particle modes appears to be that there are two different sources for each of the two sizes. An X-ray analysis of individual particles that had been collected onto Nuclepore filters showed that the large particles were rich in Al, Mg, and Si with significant Na, K, and Ca. These are evidently crustal derived material injected into the lower troposphere unstable air mass, i.e., blowing dust from the adjacent arid region. The small particles showed a significant amount of sulfur, but also some silicon, suggesting that the smaller particles are mixtures of sulfate and crustal silicates. The small silicate particles may act as condensation nuclei for industrially emitted sulfates from Fort Collins and adjacent industrial areas.

The accuracy of the inversion calculations in representing the experimental observations such as downwelling flux depends upon the observational accuracy. The precision photometric measurements of solar intensity at ground level are accurate to $\pm 0.1\%$ in the optical depth determination. However, in fitting the data to the model, a lesser accuracy of $\pm 3\%$ was achieved. A further limitation of $+1\%$ occurs in the photometric measurement of the solar aureole sky intensity as well as the total downwelling flux.

The results of the inversion calculations may be used in an atmospheric model. In such a model aerosol absorption can be estimated by comparing the calculated downwelling diffuse radiation for the aerosol size distribution shown in Fig. 3 to the actual values measure with the hemispherical flux detector [19,21]. A Schuster–Swarzschild two-stream approximation is used to represent the radiative transfer in the atmosphere. Intercomparisons of this two-stream calculation to the equation of radiative transfer carried out with the discrete ordinate method [20] indicated that the two-stream method

is accurate to about 2% for $\tau < 0.1$. In the red spectral region, the two-stream approximation is valid because τ is less than 0.1 (Fig. 1). For the aerosol size distribution shown in Fig. 3, at a wavelength of 0.710 μm and a ground surface albedo of 0.3 (estimated by viewing the terrain with a photometer), the calculated downwelling flux (ratioed to the solar irradiance at the top of the atmosphere) was 0.069; the measured value was 0.0695. This close agreement indicate that the model is good at this wavelength, and the albedo of single scattering is found to be close to unity. At shorter wavelengths the model will be poorer, because the optical depths are greater, and the approximation will be invalid.

VI. CONCLUSIONS

The results of two complementary approaches to the modeling of atmospheric aerosols in order to infer their effect on optical remotely sensed atmospheric and ground target data have been presented. There is now a realization [22] that aerosols may significantly affect radiation transfer in the near-ultraviolet, visible, and near-infrared regions and that as a result satellite and aircraft downward viewing data need to be corrected for atmospheric effects in order that a universal databank for ground targets can be established for remote sensing with no or poor ground truth. The atmospheric corrections, in themselves, furnish information that characterizes the effects of aerosols, although it does not give detailed description in terms of size, vertical distribution, and their optical complex indices of refraction.

The Dave two-dimensional radiative transfer program was used to model radiance and flux data acquired in St. Thomas, U.S. Virgin Islands, in angular detail (viewing, azimuthal, and solar elevation angles) in support of the NASA ERTS-1 satellite experiment. The model is quite good for detailed angular sky radiance calculations for regions far from the solar aureole but less accurate near the solar incident direction. This limitation may result in a calculated sky radiance a factor of 2 or 3 below the observed value and is attributed to the fact that the Dave model [15] does not include the earth's curvature and the measurements were made at sunrise; the appropriate three-dimensional radiative transfer problem has not yet been solved. The Dave program requires a number of input parameters that would arise from detailed air truth. These data would be furnished by radio sonds, LIDAR observations, low and high altitude aircraft flights as well as ground aerosol collection (and complex index of refraction determinations on the aerosols), and stratospheric balloon measurements and aerosol collections.

In lieu of detailed air truth, ground observations of incident diffuse and solar direct radiation at ground level may be sensed as a function of wavelength. Then, using reasonable assumed values of the optical complex index of

refraction, a particle size distribution, and vertical number density profile in the Dave radiative transfer model, a trial model can be constructed. Depending upon the match between the observed and calculated sky radiances and solar fluxes, the validity of the model is then determined. If large discrepancies occur, then the experience of the modeler is called upon to modify the assumptions to achieve a better fit.

From the application of the Dave program, it was concluded that dust from the Sinai desert could satisfy the requirements to produce the observed values of sky radiance and solar fluxes within $\pm 20\%$ in most cases.

In the second approach, the path-average aerosol optical extinction wavelength dependence and the angular distribution of sky radiance on the solar almucantar provided enough information to formally invert the Mie equations to derive the aerosol size distribution function and permit a calculation of integrated downwelling diffuse radiation. This approach was applied in Fort Collins on August 4, 6, and 7 in 1980 and involved passive optical ground measurements. The aerosol behavior in terms of particle size and in terms of transport, buildup, and decay can be determined as a function of time over given geographic regions. This technique has the advantage that the path-average aerosol parameters are sampled from the ground in-situ, but variations with altitude are not determined.

The particle size spectrum over Ft. Collins was deduced from the calculations to be bimodal, with the small mode (~ 0.2 μm radius) consisting of sulfate aerosol and the large mode (~ 3 μm radius) resulting from crustal material assumed to be dust from the surrounding arid region. This result was determined in the laboratory by an X-ray analysis of the composition of the aerosols. In this example, the surface aerosol was representative of the column aerosol, because the convective currents were strong. The match to the observations required for inversion resulted in an uncertainty of $\pm 3\%$ in the path-average optical depths. A comparison of observed and calculated downwelling diffuse radiation showed that values agreed to within 0.7%. The vertical number density profile is not obtained from the inversion, and the column mass loading is obtained by assuming that the aerosols lie in a 1 km layer above the ground. This would be expected to cause inaccuracies in sky radiance calculations at high elevation angles.

From the Dave model, it is of interest to note that the atmosphere primarily scatters radiation (see Table 7), with the specular solar radiation being transformed into diffuse radiation with very little absorption. This is in agreement with the results found for the Ft. Collins observations, where the aerosols were found to be lightly absorbing and highly scattering with a single scattering albedo (at $\lambda = 0.700$ μm) of close to unity. Even though the observations were not under the same conditions, similar trends are shown.

From the atmospheric modeling approaches presented, it is not evident whether the differences between the models and ground truth observations are

TABLE 7 Optical Depths

	Scattering			
Wavelength (μm)	Mie	Rayleigh	Absorption	Total
0.433	0.150	0.257	0.0006	0.406
0.533	0.122	0.110	0.017	0.232
0.633	0.115	0.0547	0.021	0.170

the result of inadequate input data or the model. The Dave model could well benefit from better input data, whereas the inversion technique does not yield a vertical number density profile. Both models show considerable aerosol effect: vertical optical depths of ~ 0.07 over Ft. Collins and ~ 0.12 over St. Thomas. Where there is urban pollution or dust, the optical depths may be considerably higher. The visibility (ground level or at higher altitudes) is inversely proportional to the optical depth at the altitude considered and is thus related to the determinations presented in this chapter.

It is concluded that by using ground-based observations, the Dave model provides detailed angular variation of sky radiance and solar flux to $\pm 20\%$ away from the solar aureole. The constrained linear inversion model furnishes the path-average optical depth to $\pm 3\%$, the total downwelling diffuse radiation to $\pm 1\%$ and the aerosol size distribution.

REFERENCES

1. Egan, W.G. Optical remote sensing of the sea—A Caribbean example. Proc. 14th Int. Symp. Remote Sensing Environ., 23–30 April 1980, pp. 563–586.
2. Rahn, K.A. On the causes, characteristics and potential environmental effects of aerosols in the arctic atmosphere. Presented at the Conference on the Arctic Ocean, London, 11–12 March 1980, sponsored by Arctic Committee of Monaco and Royal Geographical Society, 1980.
3. Dana, R.W. Solar and atmospheric effects on satellite imagery derived from aircraft reflectance measurements. Proc. 10th Int. Symp. Remote Sensing Environ., 6–10 Oct. 1975, 68–69.
4. Potter, J.F.; Mendlowitz, D. On the determination of haze levels from landsat data. Proc. 10th Int. Symp. Remote Sensing Environ., 6–10 Oct. 1975, 695–703.
5. Egan, W.G.; Fischbein, W.L. Optical atmospheric scattering and absorption limitations on offset pointing from earth observatory satellite (EOS) sensors. Proc. 10th Int. Symp. Remote Sensing Environ., 6–10 Oct. 1975, 783–792.
6. Egan, W.G.; Hilgeman, T. Anomalous refractive index of submicron-sized particulates. Appl. Opt. 1980, *19*, 3724–3727.
7. Egan, W.G.; Hilgeman, T. Optical Properties of Inhomogeneous Materials; Academic Press: New York, 1979.

8. Shaw, G.E. Inversion of optical scattering and spectral extinction measurements to recover aerosol size spectra. Appl. Opt. 1979, *18*, 988–993.
9. Shaw, G.E. Remote sensing of aerosol in free atmosphere by passive optical techniques. Report on the First Int. Workshop on Light Absorption by Aerosol Particles, July 28–Aug. 8, 1980, Colorado State Univ.: Boulder.
10. Twomey, S. Introduction to the Mathematics of Inversion in Remote Sensing and Indirect Measurements; Elsevier: New York, 1977.
11. Allen, C.W. Astrophysical Quantities; Athlone Press: London, 1963.
12. Egan, W.G. Water quality determinations in the Virgin Islands from ERTS-A data. Proc. 8th Int. Symp. Remote Sensing Environ., 2–6 Oct. 1972; ERIM: Ann Arbor, ME, 1972; 685–708.
13. Egan, W.G. Boundaries of ERTS and aircraft data within which useful water quality information can be obtained. Proc. 9th Int. Symp. Remote Sensing Environ., 15–19 April 1974; ERIM: Ann Arbor, 1974;1319–1343.
14. Shaw, G.E.; Deehr, C.S. A photoelectric coronameter for atmospheric turbidity studies. J. Appl. Meteor. 1975, *14*, 1203–1205.
15. Dave, J.V. Development of Programs for Computing Characteristics of Ultraviolet Radiation. NASA Rep. No. S80-RADTMO, Goddard Space Flight Center: Greenbelt, MD, 1972.
16. Deirmendjian, D. Electromagnetic Scattering on Spherical Polydispersions; American Elsevier: New York, 1969.
17. McClatchey, R.A.; Fenn, R.W.; Selby, J.E.A.; Volz, F.E.; Garing, J.S. Optical Properties of the Atmosphere; 3rd ed; Rep. AFCRL-72-0497, 24 Aug. 1972, Bedford, MA: Air Force Geophysical Lab., 1972, p. 3.
18. Patterson, E.M.; Gillette, D.A.; Stockton, B.H. Complex index of refraction between 300 and 700 nm for Saharan aerosols. J.G.R. 1977, 3153–3160.
19. Herman, B.; Browning, R.S.; DeLusi, J. Determination of the effective imaginary term of the complex index of atmospheric dust by remote sensing: the diffuse-direct method. J. Atmos. Sci. 1975, *32* (5);918–925.
20. Shaw, C.; Stamnes, K. Arctic haze: perturbation of the polar radiation budget. Aerosols: anthropogenic and natural sources and sinks. Ann. N.Y. Acad. Sci. 1980, *338*, 533–539.
21. Deirmendjian, D.; Clasen, R.; Vieze, W. Mie scattering with complex index of refraction. J. Opt. Soc. Am. 1961, *51*, 620–633.
22. Turner, R.E. Signature variations due to atmospheric effects. Proc. 10th Int. Symp. Remote sensing Environ., 6–10 Oct. 1975, pp. 671–682.

14

Comparison Between Infrared Martian Disk Spectra and Optical Properties of Terrestrial Analogs

I. INTRODUCTION

Comparisons between the Martian disk spectra and the optical properties of terrestrial analogs have been useful in characterizing the properties of the Martian soil [1–5]. However, these have not yet been accomplished with medium resolution (20 cm^{-1}) infrared Martian disk spectra between 2900 and 5600 cm^{-1}. We approached this problem by obtaining medium resolution (20 cm^{-1}) disk infrared spectra of Mars using the NASA Lear Airborne Observatory, with line modeling to deduce (and eliminate) the contribution to the observed spectrum by Martian and telluric CO_2. We then determined the optical complex index of refraction of terrestrial analogs of appropriate acceptable minerals and used the results in a surface scattering theory to represent the average Martian soil. From this model a characteristic particle size was obtained. The reflectivities of samples prepared with particles in this size range were then used to match the observed surface reflectivity.

The X-Ray Fluorescence Experiment of Vikings I and II revealed that the soil contains the elements (and oxides) listed in Table 1 in the abundances indicated (with 1σ the most probable range) [1,6,7].

Appropriate candidate rocks and minerals such as limonite, montmorillonite, andesite, and basalt contain varying proportions of these elements (except S and Cl) along with smaller portions of other elements (Ca, P, and Mn) [8]. The quantity of water chemically bound in the Martian soil sample

TABLE 1 Elements in Martian Soil

Element	Most probable abundance (%)	Oxide	Hypothesized oxide abundance (%)
Mg	2–8	MgO	3–10
Al	2–4	Al_2O_3	3–10
Si	18–24	SiO_2	39–52
S	2–4	SO_3	4–13
Cl	0.4–1	—	—
K	<0.25	K_2O	0–1
Ca	3–5	CaO	4–7
Ti	0.3–0.7	TiO_2	0.4–0.8
Fe	10–15	Fe_2O_3	17–22
O	45–55	—	—

at the Viking I landing area (Chryse Planitia) was from a few tenths of a percent to 1% [9] according to data from the Gas Chromatograph Mass Spectrometer Experiment. The delineation of the concentration of chemically bound water with depth in the soil is not indicated by any of the Viking experiments. The existence of bound water in the soil has been shown to be correlated with the water absorption band at 3570 cm^{-1} (2.8 μm) in candidate materials [10]. The delineation of this band on Mars is dependent upon the spectral resolution of the sensor system and the accuracy of the subtraction of the effect of the Martian atmosphere (and telluric atmosphere for ground-based observations). Critical to the determination is the depth of the absorption feature. The Houck et al. [10] estimation of the water content of the Martian soil (1% by weight) depended upon a determination of the molar abundance of water from a generalized single-scattering albedo formula of Sagan and Pollack [11]. An average particle size of 100 μm was assumed for the Martian soil; the Viking I results do not directly indicate the actual average surface particle size at Chryse Planitia. However, using a nominal engineering soil model based on the lunar soil, the particle sizes of surface and near-surface fines of sandy flats were estimated as being dominantly in the range of 10–100 μm [12]. The water in the Martian surface material appears to be chemically bound; the soil itself is quite dry [9]. The bound water has significance for the mineralogy of the planet, the environmental conditions during earlier epochs, and the possibility of life on the planet [13–15]. Initial ground-based infrared observations of Mars by Sinton [16] indicated the possibility of bound water, but the broad absorption band observed at 3300 cm^{-1} (3.0 μm) was actually from deuterated telluric water [17]. Stratoscope observations [18] provided a suggestion of Martian atmo-

spheric precipitable water based on the 3300–5880 cm^{-1} (1.7–3.0 μm) spectrum. Significantly higher resolution ground-based spectra of Mars in the 2500–3300 cm^{-1} (3–4 μm) region were provided by Beer et al. [19], found an albedo drop toward longer wavelengths attributed to surface water of hydration. They used a Connes-type Fourier spectrometer at the coude focus of the McDonald Observatory 2.7 m telescope. Subsequently, Houck et al. [20] made observations with an Ebert–Fastie 1/4 m spectrometer aboard the NASA Convair 990; the 2500–5000 cm^{-1} (2–4 μm) spectrum (72–265 cm^{-1} resolution) was obtained in 0.112 μm steps using a movable 19-slot Hadamard mask. They deduced that the wavelength minimum at 3510 cm^{-1} (2.85 μm) was the result of the O–H stretching vibrational frequency; they also eliminated nitrates from consideration because of the lack of a 2860 cm^{-1} (3.5 μm) absorption feature and the required narrownes of the 3510 cm^{-1} (2.85 μm) absorption feature. Strecker et al. [20] confirmed the corresponding water of hydration feature on observations of Mars on 22 and 23 December 1975 and 5 January 1976 from the NASA C-141 KAO 91 cm telescope; they used a circular variable filter wheel to obtain medium resolution spectra ($R \sim 2\%$) of Mars in the spectral region between 2380 and 8330 cm^{-1} (1.2 and 4.2 μm).

Other evidence of hydrated minerals and solid water was furnished by the Mariner Mars 6 and 7 infrared spectrometer data (IRS) [21]. The IRS scanned the 694–5260 cm^{-1} (1.9–14.4 μm) range with wavelength resolution better than 1% (7–53 cm^{-1}) [22]. The interpretation of the IRS data was based on the infrared laboratory spectra of a range of terrestrial mineral samples [23]; from the laboratory samples with 40–160 μm particle size, red oxidized tholeiitic basalt seemed to match the Martian reflection spectrum best, but not exactly [21]; the reflection spectra, which were measured using a nonstandard circular illumination geometry, were strongly influenced by the particle size of the sample. Also, a critical part of the matching depended upon the presence of a hypothesized solid CO_2 and H_2O ice layer on the red basalt. Further, the location of the CO_2 absorption edge between 3700 and 3850 cm^{-1} (2.6 and 2.7 μm) has been shown to depend upon the textural scale (particle size) of the CO_2 frost [24]. Thus, a fit could be made using another hydrated substrate mineral and the appropriate textural scale CO_2 frost. The use of laboratory reflectance spectra in matching planetary reflectance spectra can be misleading; as pointed out by Pimentel et al. [21], Egan et al. [8], and Egan and Hilgeman [25], particle size and shape as well as dust coating can produce significant changes in the laboratory (as well as planetary) reflectance spectra.

A desirable approach to modeling the Mars surface would be to use the optical complex indices of appropriate materials in the most probable amounts and vary the particle sizes and shapes in an appropriate surface

model including scattering and absorption by asperities. Also, the effect of the Martian (and telluric) atmospheres should be eliminated by using a high resolution spectrum of Mars with line modeling of the gaseous CO_2 and H_2O vapor. The actual shape and depth of the 3510 cm^{-1} (2.85 μm) water of hydration band of the Martian soil must be determined accurately. However, the state of the art is not yet this advanced [26]. In the following pages laboratory reflectance spectra are used to match the medium resolution Martian spectrum with theoretical surface modeling, providing justification through a parametric study of the effects of particle size.

II. MARTIAN SPECTRUM

Observations of the Martian disk between 2900 and 5600 cm^{-1} were made on 11 February 1976 from the NASA Lear Airborne Observatory. The aircraft altitude was 13.7 km during the observations. The precipitable water in the viewing direction external to the aircraft was less than 10 μm. The elevation angle of Mars was $20 \pm 1°$ during the observation.

The radiation from Mars entered the aircraft through a 2.54 cm thick Corning GE-105 water-free glass window. The radiation was then directed into a 30.5 cm f/23 folded Dall–Kirkham telescope by a gyroscopically stabilized heliostat. The Grumman-designed optical arrangement is shown schematically in Fig. 1. The spectrum is sensed by an Idealab Model IF-3 interferometer-spectrometer hard-mounted to the telescope. The fore-optics are of a symmetrical dual-beam type using the sky as a reference; only one side of the light path is shown traced to the detector. The field of observation is 6.3 arcmin. The double-beam, double-detector configuration gives automatic cancellation of the emitted light from the sky, telescope, and interferometer. The detectors are liquid nitrogen–cooled 1/2 mm InSb cells with a cold filter to cut off the long-wavelength response below 2800 cm^{-1} (above 3.5 μm), where the GE 105 window effectively stops transmitting. The telescope–interferometer system floats on a foam padding that rests on a plate bolted to the baggage compartment floor. The mechanical and electrical interference from the aircraft are below the electronic noise level. An entire spectrum is obtained in a 2 s scan, and the signal-to-noise ratio is improved by summing up hundreds of scans.

The data from the interferometer were recorded on a Lockheed Electronics Model STORE 4 analog tape recorder. Digitizing and summing up were performed on the ground after every flight using a Hewlett-Packard Model 21MX minicomputer. A phone link to a Hewlett-Packard Model 2000 computer at Bethpage, Long Island, was then employed. The single-sided interferograms are first-phase corrected using the technique of Forman et al. [27], cosine transformed, and apodized using a Hamming function [28]. The

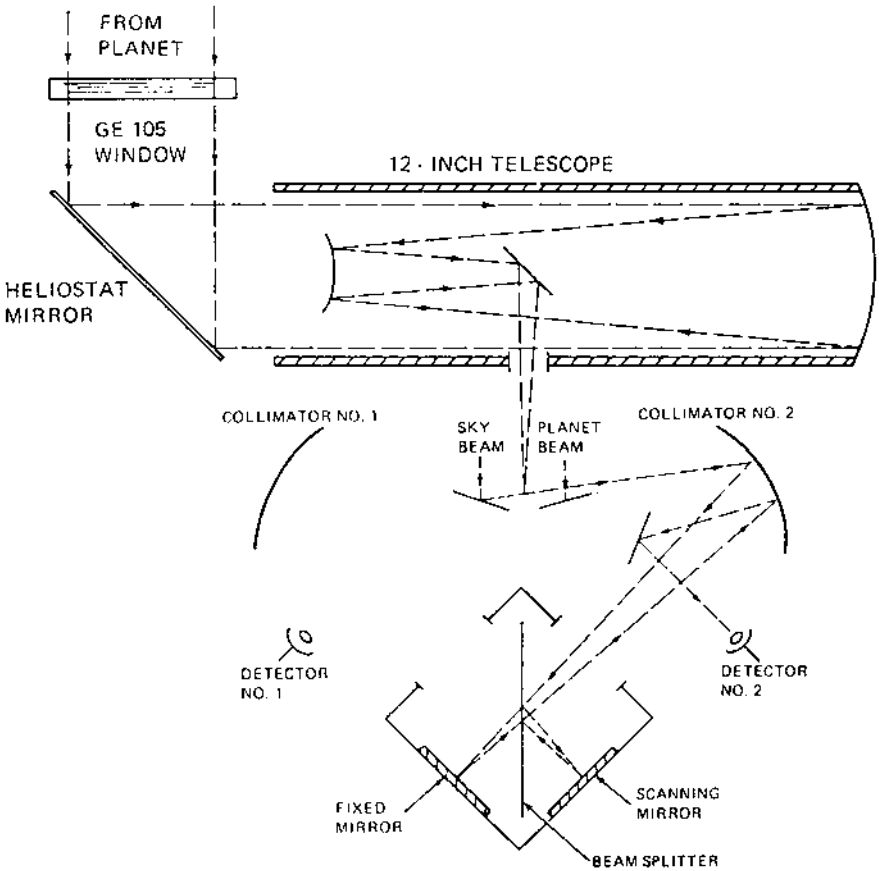

FIGURE 1 Schematic of optical system of telescope and interferometer as installed in NASA Lear Airborne Observatory, February 1976 (not to scale).

spectrum obtained (between 2900 and 5600 cm^{-1}) contained absorption effects from residual telluric H_2O and CO_2 as well as the CO_2 and H_2O of the Martian atmosphere.

In order to compare the Mars spectrum with those from terrestrial rock and mineral analogs, the telluric and Martian atmospheric effects must be subtracted from the raw data. First an approximate telluric absorption correction was applied by taking the ratio of the observed Martian spectrum to a lunar spectrum between 2900 and 5600 cm^{-1} taken during the February 1976 flights. The lunar curve was smooth except for the CO_2 band and a small amount of telluric H_2O. The ratio technique fails to correct exactly for

absorption where similar molecular constituents exist in the telluric and Martian atmospheres, but this is accounted for in the following through line-by-line modeling. The ratio spectrum was then multiplied by the calculated lunar flux of Russell et al. [29], assuming a 350 K blackbody and an albedo of 8%. This was scaled to the 6.3 arcmin aperture to get the relative Martian flux.

The absolute Martian flux in Janskys (1 Jy $= 10^{-26}$ W m^{-2} Hz^{-1}) was obtained from the visual (V) magnitude of Mars of $+0.1$ on 11 February 1976 [30] and the V–K color difference of $+2.11$ given by Mitchell [31]. Thus the K magnitude of Mars was -2. From this result, the ratio spectrum obtained as noted above can be scaled at K (4545 cm^{-1}) to yield the absolute Martian flux as seen by the Lear Jet telescope (Fig. 2). The spectral resolution

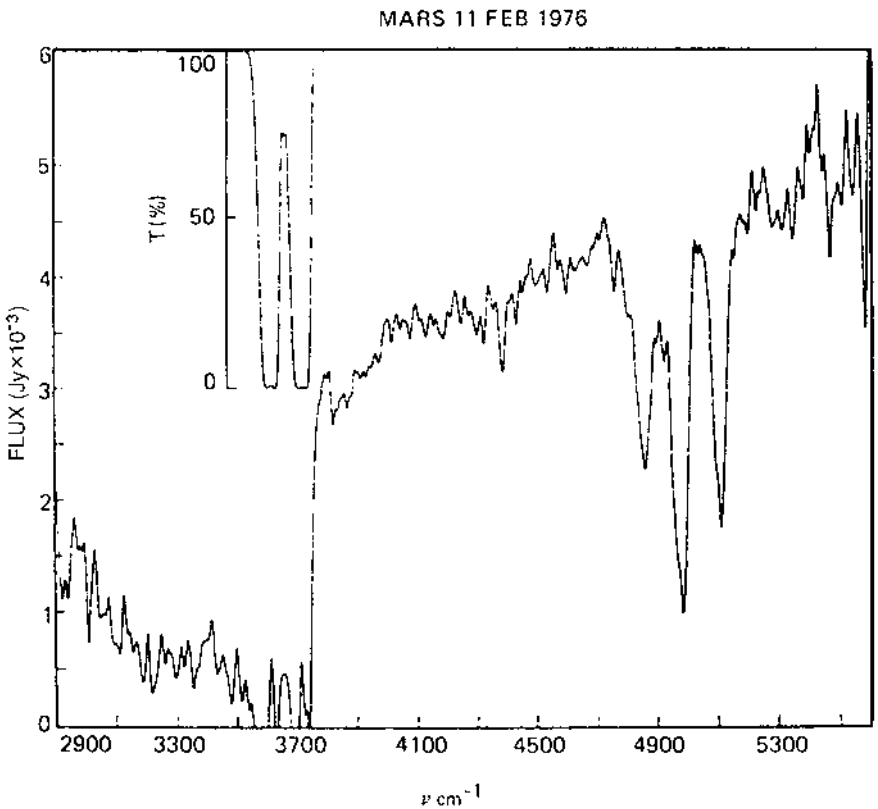

FIGURE 2 Absolute infrared spectrum of disk of Mars, 11 February 1976. Inset: Transmission of Martian CO_2 band at 3657 cm^{-1}, referred to abscissa scale.

of this spectrum was about 20 cm^{-1} at the strong (4900 cm^{-1}) CO_2 bands but varied from $\times 20$ cm^{-1} at 5000 cm^{-1} to $\times 17$ cm^{-1} at 3700 cm^{-1}. The resolution degradation from the theoretical maximum of 13 cm^{-1} for this observation can be attributed to image motion during the time of observation. In Fig. 2 the Martian soil-bound H_2O plus atmospheric CO_2 band at 3700 cm^{-1} can be seen.

The remaining effect of the Martian atmospheric CO_2 must be deduced before we can infer the average disk soil reflectance. This required line-by-line modeling of the Martian and telluric atmospheres and then smoothing to the spectral resolution of the Lear Jet interferometer system.

The CO_2 line parameters from McClatchy et al. [32] were used for the modeling. This listing gives the line strength S and Lorentz half-width α at STP for each line. These S and α values were scaled to the Martian average T and P, and the Lorentz line profiles were computed and Doppler-shifted

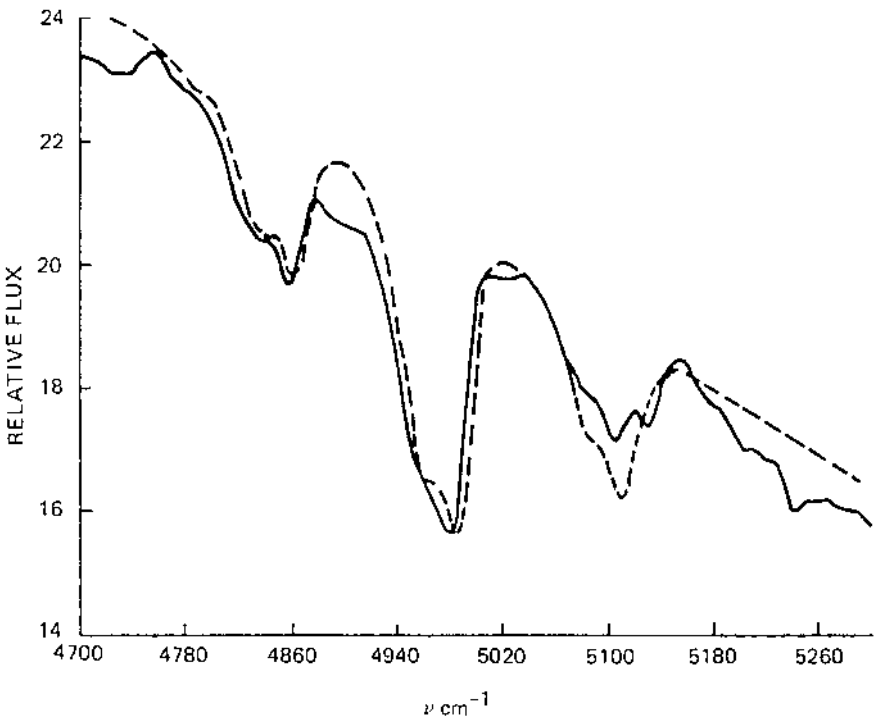

FIGURE 3 Relative observed lunar flux spectrum at ~17 cm^{-1} resolution (solid curve) with theoretical matching ashed curve using the telluric CO_2 triplet (CO_2 column density = 3.5×10^{21} molecules/cm^2; T = 217 K; P = 70.8 mbar).

to correspond to the experimental conditions. Then for an assumed column density of CO_2, in molecules/cm^2, the transmission was computed. The values assumed for the column density are determined by the fit to the three experimentally observed CO_2 bands at 4860, 4990, and 5100 cm^{-1} with the line profiles degraded from the convolution of the true spectrum with the Lear Jet interferometer resolution profile. In order to determine the residual telluric contribution, a telluric stratospheric model was used to fit the experimental lunar spectrum (Fig. 3) with an effective temperature of 217 K, an effective pressure of 70.8 mbar, and a column density of 3.5×10^{21} molecules/cm^2, corresponding to 2.9 air masses (20° elevation at time of observation). For Mars, a good fit was obtained with a 17 cm^{-1} resolution by adding to the telluric contribution a CO_2 column density of 8.9×10^{23} molecules/cm^2 (corresponding to 3.8 air masses) at Martian T and P (see Fig. 4). An average Martian temperature of 203 K and pressure of 7 mbar (close to that indicated by Gray-Young [33]) was used in the calculations for Mars.

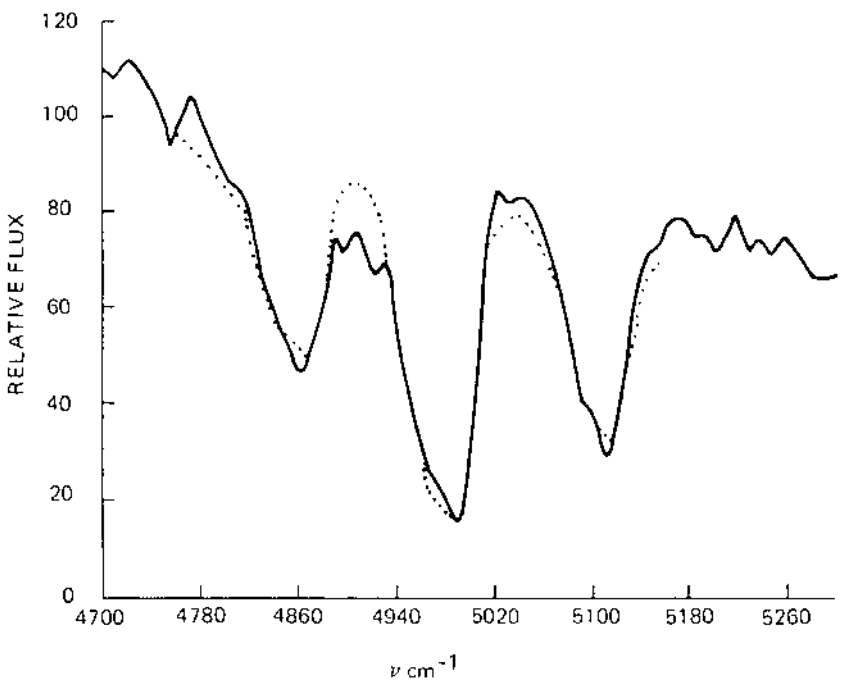

FIGURE 4 Relative observed Martian flux spectrum at ~17 cm^{-1} resolution (solid curve) with theoretical matching of CO_2 triplet (dotted curve) with a Martian atmosphere (CO_2 column density = 8.9×10^{23} molecules/cm^2; T = 203 K; P = 7 mbar).

Using the calculated CO_2 column density, the transmission of the Martian atmosphere in the region of the soil-bound H_2O ($v < 3700$ cm^{-1}) was computed to deduce the flux reflected from the Martian soil. At a wavelength of 3657 cm^{-1}, the calculated corresponding transmission of the Martian atmosphere (see inset of Fig. 2) was found to be 81%. This allows us to evaluate the reflectance of suitable candidate soils by interposing the requirement of a sharp dip at 3657 cm^{-1} (2.73 μm). The Martian water absorption band from $\times$3750 to 4200 cm^{-1} (Fig. 2) is weak, and no correction has been applied. The calculated transmission value of 81% could have a systematic error of $\pm$10% because of the use of the Lorentz profile instead of the more exact Voigt profile.

III. LABORATORY MEASUREMENTS

The laboratory measurements of terrestrial analogs were based on samples used for the interpretation of the Martian dust storm observed by Mariner 9 in 1971 [8]. The samples were andesite, basalt, limonite, and montmorillonite (Amory, MS); their chemical analyses were listed [8]; the bound water contents were 0.26, 1.41, 12.49, and 12.99%, respectively.

There was a question as to whether all four samples had a sufficiently deep (H_2O) absorption band at 3700 cm^{-1} to permit a reasonable fit to the observed Martian disk data. To check this, specular transmission measurement were made (perpendicular incidence and scattering) on layered KBr pellets containing $\sim$1 μm sample particles. The samples were prepared as described in Egan et al. [8]. The measurements were made between 5025 and 2427 cm^{-1}; the wavelength resolution, using a circular variable filter, was 33 between 4000 and 5025 cm^{-1}, 260 between 3584 and 4000 cm^{-1}, and 50 from 2427 to 3584 cm^{-1} (across the H_2O band and the 3657 cm^{-1} CO_2 transmission peak).

The results of these measurements of transmission (Figs. 5a, 5b) revealed the deepest relative 3600 cm^{-1} (2.77 μm) dip for (Amory, MS) montmorillonite and lesser relative dips for basalt, limonite, and andesite in that order. As a comparison, comparable measurements were made on thin sections of anorthosite and mica, which were suggested as Martian surface constituents [34] based on long-wavelength infrared spectra (between 200 and 1600 cm^{-1}). Also included is a montmorillonite sample from Clay Spur, Wyoming. The results (Figs. 5b) show that the anorthosite curve is similar to the basalt curve, and results derived for the basalt would be analogous to those that would be expected for anorthosite. The same would apply to the montmorillonite of Clay Spur, Wyoming, as compared to that of Amory, Mississippi, except that the Clay Spur sample has a deeper relative dip at the water band. The mica has a number of absorption bands (not

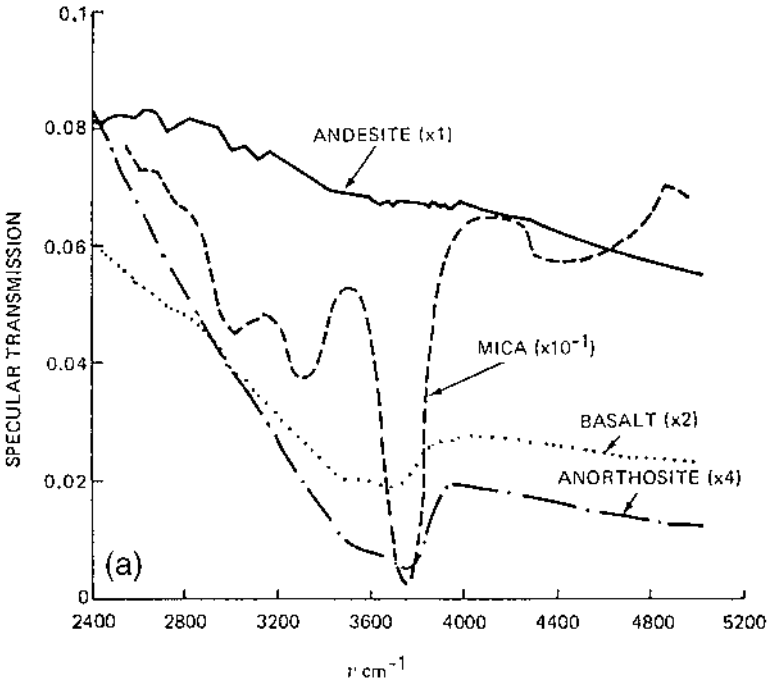

FIGURE 5 (a) Relative specular transmission of layered KBr pellets of andesite and basalt and thin sections of mica and anorthosite (effective thicknesses of 0.0025, 0.0028, 0.0297, and 0.0737 cm). (b) Relative specular transmission of layered KBr pellets of Amory, Mississippi, and Clay Spur, Wyoming, montmorillonites and one limonite sample (effective thicknesses of 0.0024, 0.00352, and 0.00029 cm).

the result of interference) that would produce a detailed spectral variation, with the sharp minimum apparently displaced to the short-wavelength side of the 3657 cm^{-1} transmission maximum in the Martian atmosphere.

Montmorillonite (Amory, MS), basalt, and limonite were selected as acceptable candidates (although not all-inclusive) for further optical measurements to determine the optical complex index of refraction because of their range of significant bound water content. Subsequently, the Viking I X-ray Fluorescence Experiment results indicated these to be good choices because of the large iron content (12.5–15%) [1,6] as well as the possibility of bound water. The object of further optical characterization was the determination of the optical complex index of refraction to permit optical mathematical modeling of suitable Martian soil candidates through a range of

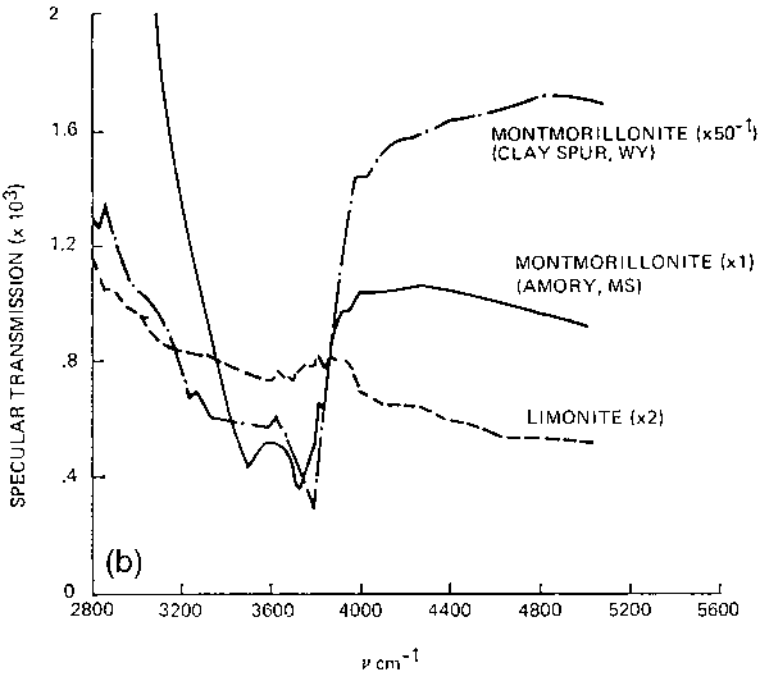

FIGURE 5 Continued.

particle sizes and combinations. The determination of the optical complex index of refraction requires total diffuse transmission and reflection measurements on the samples and a measurement of the real (refractive) portion by a Brewster angle technique. The total diffuse transmission and reflection measurements are then used in a Kubelka–Munk scattering model to determine the true absorption of the samples, free from the effect of scattering. The true optical complex of refraction thus obtained can be used in a scattering model of the Martian soil.

The detailed modeling procedure is described in the Appendix. It was found that the closest match to the Martian bound water feature was obtained with characteristic grain sizes in the range of 1–3 μm. Because this is close to the ~1 μm size of the laboratory samples, it was decided to use the laboratory sample reflectances to model the Martian surface (Fig. 2). Using this reflectance spectrum and the appropriate full disk geometry and atmospheric transmission, the emergent flux can be calculated from incident solar radiation for comparison to Fig. 2.

The absolute flux results for limonite, montmorillonite, and basalt are presented in Fig. 6 for an effective Martian CO_2 column density of 8.9×10^{23} molecules/cm^2, an average temperature of 203 K, and a surface pressure of 7 mbar. Also in Fig. 6 is superimposed the observed Martian flux curve of Fig. 2 The center of the CO_2 absorption band at 3657 cm^{-1} and the absorption edge at ~3750 cm^{-1} can be compared; the montmorillonite fits best at the center of the CO_2 band, but the limonite fits the absorption edge better. Note the agreement in reflection rise for $\nu < 3200$ cm^{-1} with that observed. The basalt gives too low a reflectivity for $\nu > 3700$ cm^{-1}.

From the comparisons here and in the Appendix, it appears that a mixture of small grains like montmorillonite or limonite with a negligibly absorbing interstitial material (KBr in the laboratory measurements) produces a good match to the observed flux spectrum. An alternative low-absorbing interstitial or underlying material different from the KBr could

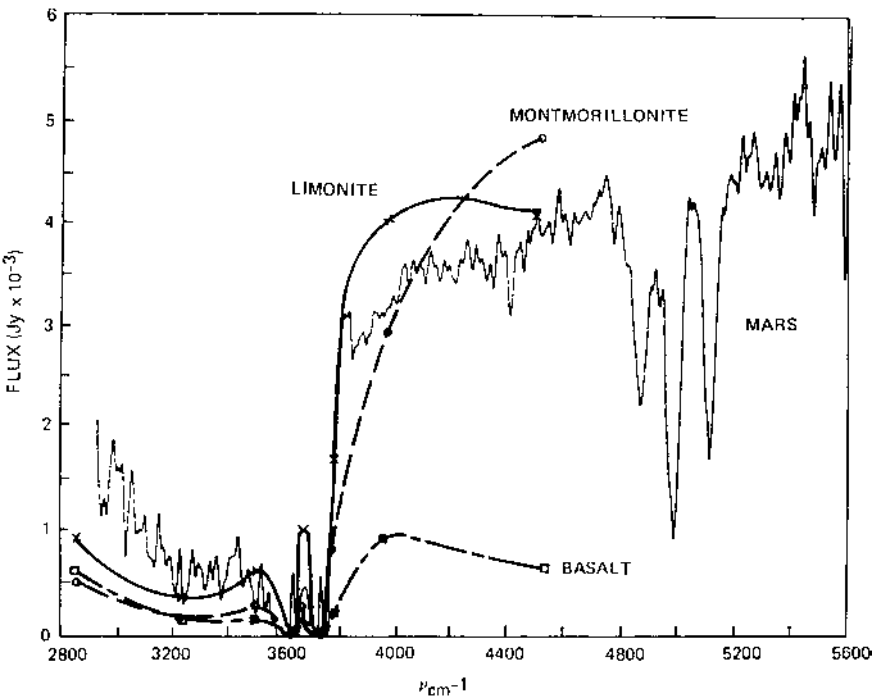

FIGURE 6 Absolute flux from an analog Martian soil layer composed of ~1 μm diameter loosely packed particles (corrected for Martian atmospheric CO_2 absorption). Comparison to Mars data of Fig. 2.

be basalt or voids. Basalt has a small wavelength dependence of absorption (see Appendix) and a higher absorption than KBr, but in a porous surface layer it could approximate the KBr pellet geometry.

IV. DISCUSSION

There appears to be no question that water of hydration is chemically bound into the surface soil of Mars. In particular, the Martian soils are "weathered." Let us consider the bound water aspect first, in the context of the present data. Houck et al. [10] estimated the bound water of the surface soil to be about 1% by weight; this value is based on a theoretical analysis using a water absorption coefficient for Lake County obsidian, an apparently inappropriate Martian soil material. Houck et al. [10] conjectured that the strength of the water band is more or less independent of the substrate and depends only on the amount of water present. However, our results (Fig. 5b) for the equal H_2O content montmorillonite and limonite show this to be false.

The minimum at 3700 cm^{-1} (2.7 μm) could also be caused by SiO_2 bands in combination, although that would also cause it to be quite broad. The geology and mineralogy of the Martian surface define what possible combinations of H_2O and SiO_2 are appropriate in terrestrial analogs. The measurements of the optical complex indices of refraction are thus the result of contributions of both SiO_2 and H_2O.

It is interesting to note that Huguenin [35] suggests that chemical weathering could remove H_2O from the atmosphere by hydration of Fe_2O_3 and clay minerals. The delineation of this water of hydration feature in the vicinity of 3700 cm^{-1} (2.7 μm) requires medium spectral resolution infrared spectroscopy as presented here, and the use of the 3657 cm^{-1} Martian atmospheric CO_2, 81% transmission peak, with mathematical modeling.

Pimentel et al. [21] in comparing the infrared laboratory spectra of a variety of igneous rocks, minerals, and basalts with the Martian spectrum, found that the best match was obtained with an oxidized red tholeiitic basalt. Because of the requirement of a solid CO_2 frost, the matching was unrealistic. Solid CO_2 should exist only at the poles.

The effect on soil matching of the use of medium spectral resolution Martian disk spectra presented here, rather than the high spatial resolution as used on Mariners 6, 7, and 9, is that an error could be produced by a fine CO_2 frost, such as could exist on the polar caps. This would be highly absorbing at 3657 cm^{-1} [24]. Thus, the CO_2 frost could make the apparent soil absorption appear greater than it really is. The CO_2 polar frost could contribute to sharpening the absorption edge at 3700 cm^{-1};

however, the visible portion of the polar cap contributing to our spectrum was quite small.

The Viking landers have consistently observed large optical depths of atmospheric aerosols, and, depending upon the particle sizes of the aerosol, the absorption bands may be stronger or weaker than those in the soil. The analysis of the atmospheric particulate scattering together with the molecular absorption in a multi-layered model would be desirable to resolve the interaction of radiation scattered by the soil and that by the atmosphere containing aerosols. This is an important phenomenon, but it represents too extensive an investigation to be treated here. Also, there did not appear to be any yellow haze enveloping Mars at the time of observation [36].

The Viking X-Ray Fluorescence Experiment report [6] was consistent with a montmorillonite as a dominant Martian soil in that there was 18–24% silicon in the soil. However, the average water of hydration is less than 1%, so the only way to reconcile this finding with the appearance of the strong water of hydration band at 3570 cm^{-1} (2.8 μm) is to hypothesize that there is a surface coating on the Martian soil of montmorillonite [or other material having a strong water of hydration band at 3570 cm^{-1} (2.8 μm)]. This configuration has been inferred from our optical modeling.

From Fig. 6 it appears that although the montmorillonite is more appropriate at 3657 cm^{-1}, the highly absorbing limonite fits the absorption edge at 3700 cm^{-1}. There is thus a possibility of both being found coating the Martian surface soil. Limonite may be a lesser constituent, because earth analog of limited chemical weathering of basaltic lava and volcanic ash occurred on Mars, the results in order of progression would be montmorillonite clays, kaolinite, hydrated free iron oxide (limonite), and heavy minerals. This progression is expected in arid terrestrial environments somewhat analogous to Martian conditions and would result in an increasing percentage of clay in the soil and a release of titanium from the parent material.

Thus one could expect to find montmorillonite in particulate form as the dominant clay from early chemical weathering with free oxides (limonite) and a small subsidiary contribution from basalt. This clay mineral would be light and would be transported readily as dust in the atmosphere but could form a coating on larger basalt particles. It is of interest to note that there is conflict of this model with that deduced for the atmospheric dust by Toon et al. [37] and provides an explanation for the difference between the suggested basaltic Martian crust composition and a possible basalt–montmorillonite composition for the atmospheric dust.

The nearest proposed model to match this physical situation is "desert varnish" [38]. Desert varnish is a weathered coating occurring on rocks under arid conditions; the coating would be a hydrated iron oxide such as

would be in limonite or montmorillonite. The polarimetric matching of desert varnish to the disk spectra is not too good, but because of the desert varnish variability, depending upon type, a match might be possible [39].

The thickness of an absorbing layer of limonite or montmorillonite would have to be at least skin depth for the absorption band to be fully developed. This thickness would be about 2 μm at 3600 cm^{-1} for montmorillonite and about 0.7 μm for limonite, implying no compositional differentiation within a single surface particle.

It might be desirable to make 2500–5000 cm^{-1} infrared airborne observations of a Martian dust storm to determine whether the dust itself has an ice or 3700 cm^{-1} (2.7 μm) water of hydration feature. These observations from an aircraft could be chosen to coincide with a Martian dust storm (after it occurs) and not require a continuously monitoring orbital space probe.

Huguenin [40] suggested that the 1973 dust cloud material was apparently more hydrated than the soils on the surface, thus lending credence to the model we propose.

V. SUMMARY

The bound water signature in the terrestrial analogs of the Martian surface, montmorillonite and limonite, has been shown to be consistent with the near-infrared spectrum of Mars. The medium resolution (20 cm^{-1}) Lear Jet Airborne Observatory data presented here, together with the results of modeling of the CO_2 bands in the Martian atmosphere, permit a characterization of the Martian soil that is better than previous ones. One important soil characterization is based on the low soil reflectivity within a CO_2 atmospheric absorption band at 3657 cm^{-1}. This low soil reflectance is caused by the water of hydration absorption feature also appearing in our terrestrial analogs. Our analysis indicates a dominant surface particulate size of 1–3 μm.

APPENDIX

The details of the optical modeling procedure are presented here as an appendix in order to justify the essential assumption that the diffuse reflectivity from ~1-3 μm laboratory samples represents the Martian soil.

For the determination of the complex indices of refraction, the total diffuse reflection and transmission measurements on limonite, montmorillonite, and basalt were made using a goniometric technique [41] at discrete wavelengths between 5865 and 2805 cm^{-1} using a circular variable filter of 2% resolution.

The results of the total diffuse transmission and reflection measurements on ~1 μm particle sizes of the samples are presented in Figs. A1 and A2, respectively, and the absorption portion of the optical complex index of refraction $n\kappa$ is presented in Fig. A3, calculated using the technique described by Egan et al. [8] and the Kubelka–Munk scattering theory. Both the limonite and the montmorillonite have a higher absorption between 3200 and 3600 cm^{-1} than elsewhere, but the relative change is about the same. The basalt has less of a change. The refractive portion of the complex index of refraction was determined by Brewster angle measurements from compressed powder samples of the limonite, basalt, and montmorillonite and is presented in Fig. A4. For $\nu = 3700\ cm^{-1}$, measurements were not made because of insufficient signal-to-noise ratio. The measurements were made at selected wavelengths greater than 3700 cm^{-1} using filters with a resolution of 40.

A comparison of the real index for our basalt (~1.6) with that of Pollack et al. [42] of about 1.5 indicates only a small difference, and the absorption components are ~0.01 and 0.004, respectively. The basalt sample of Pollack et al. [42] appears to be more glassy and less absorbing than the basalt sample described herein.

The determinations of the absorption coefficient of another sample of the same Amory, Mississippi, montmorillonite by Gillespie et al. [43] at wave-

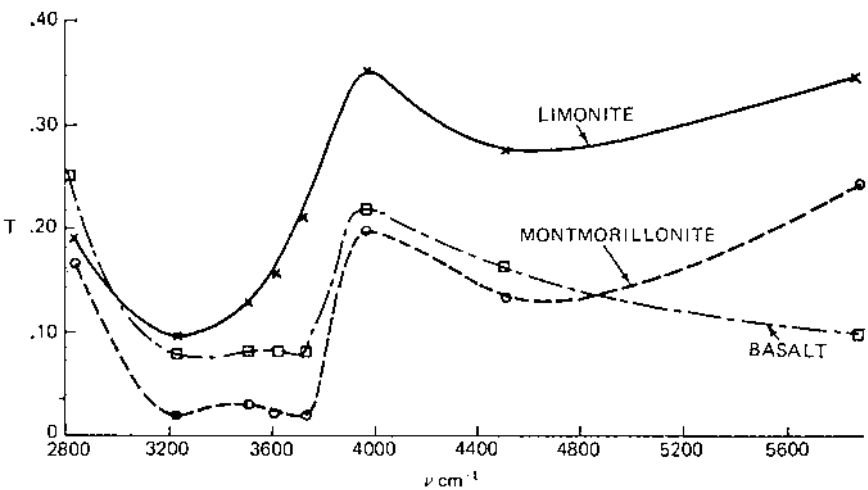

FIGURE A1 Total diffuse transmission of layered KBr pellets of limonite, montmorillonite, and basalt (equivalent thicknesses of 0.00029, 0.0024, and 0.0028 cm, respectively).

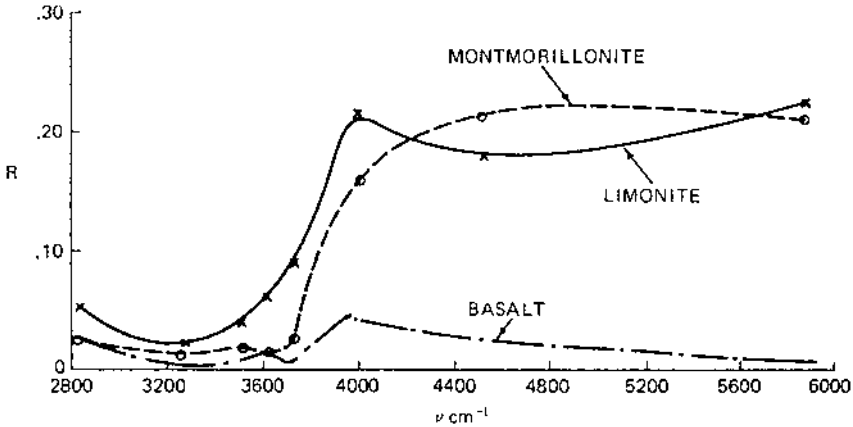

FIGURE A2 Total diffuse reflection of layered KBr pellets of limonite, montmorillonite, and basalt (equivalent thickness of 0.00029, 0.0024, and 0.0028 cm, respectively).

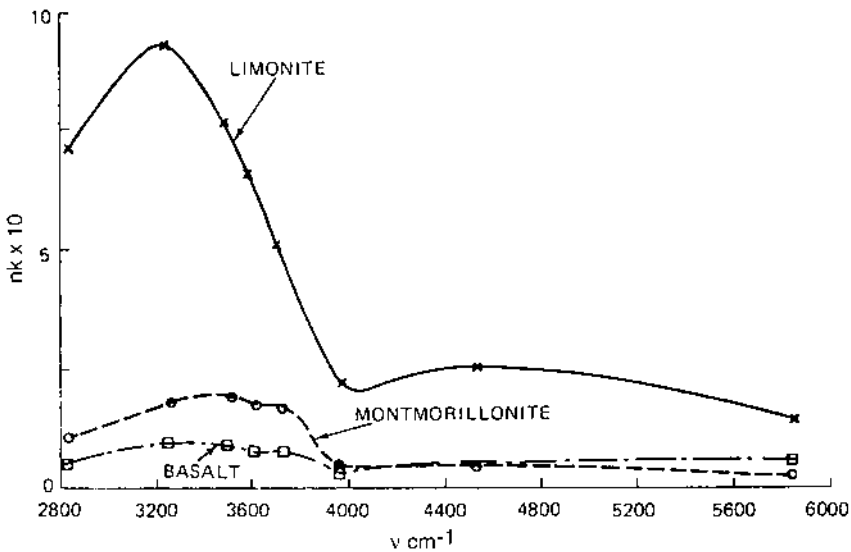

FIGURE A3 Absorption portion, n_K of optical complex index of refraction of limonite, montmorillonite, and basalt.

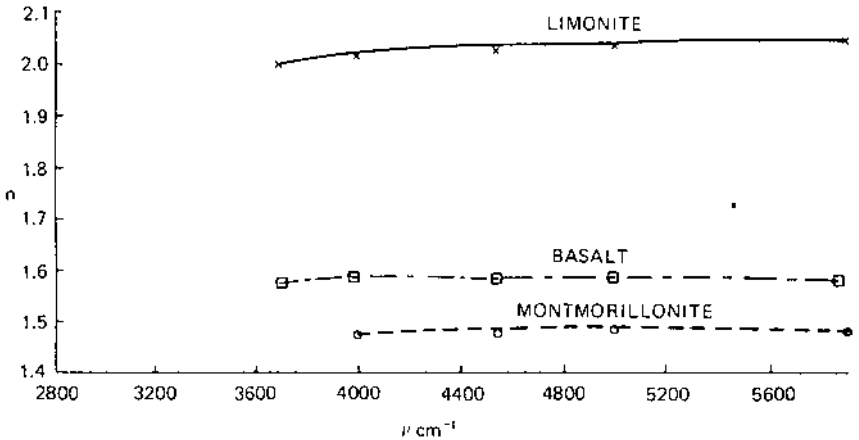

FIGURE A4 Refractive portion, *n*, of optical complex index of refraction of limonite, montmorillonite, and basalt.

lengths longer than 2 μm ($< 5000\ \text{cm}^{-1}$) are inaccurate because of poor signal-to-noise ratio in their measurements; however, they suggest a value at 2.5 μm wavelength that is at least an order of magnitude smaller than indicated by our more accurate layered pellet technique.

Having the optical complex indices of refraction of montmorillonite, limonite, and basalt (Figs. A3 and A4), we modeled the laboratory measurements (with the samples compressed into the surface layer of a KBr pellet). We also infer what the reflectance would be for a particulate surface composed of these three candidate materials by varying geometrical conditions such as particle size and asperity distribution and varying material-scattering properties. The geometrical optics theory developed by Egan and Hilgeman [26] takes into account the scattering by asperities and is applicable for particle radii $a \gtrsim \lambda$. For smaller particles, the Emslie and Aronson [44] fine particle theory can be used.

As a test of the surface model, laboratory pellet samples containing particles ≈ 1 μm in size were prepared as described in Egan et al. [8]. The results of modeling and measuring the reflectivity of these pellets are presented in Figs. A5, A6, and A7. The geometrical optics model produces only a fair match for the three candidate materials because it is at the lower limit of the size application; the parameters for the resulting "best match" curves are an effective particle diameter of 3 μm, extraordinarily high internal scattering for basalt and montmorillonite (internal scattering = 0.93 and 0.9, respectively, to lower the reflectance curves; see

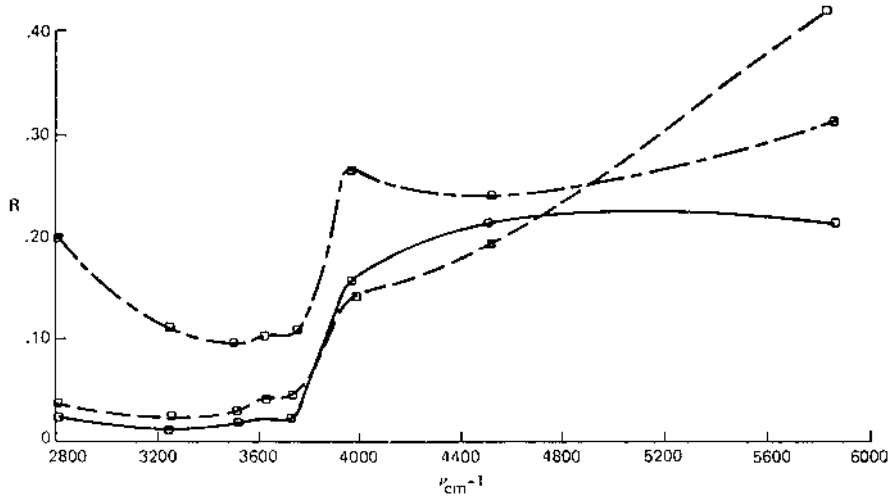

FIGURE A5 Comparison of reflectance of montmorillonite KBr layered pellet (solid curve) with that deduced from Egan and Hilgeman [26] (dash-dot curve) (particle diameter $d = 3$ μm; internal scattering SI = 0.9; total scattering NA = 0.1; absorption NE = $|n\kappa/\lambda|$) and from Emslie and Aronson [44] (dashed curve) ($V = 4 \times 10^{-12}$, $f = 0.3$, $N = 6 \times 10^{8}$).

discussion following), as well as very high scattering for all three samples. Because the sizes of the particles are in a transition region where they are comparable in size to the radiation wavelength, the Emslie and Aronson fine particle theory could also be applied. Here a good match occurred with 1 μm diameter particles, but the packing density had to be reduced considerably to bring the volume reflectance low enough to produce a good match. The match at 5865 cm^{-1} is not very good for the limonite, montmorillonite, or basalt.

It may be argued that these models do not replicate the exact pellet samples, but they are the best we have and serve as reasonable approximations. Note that, as might be expected, the fit of the fine particle theory is generally better at long wavelengths and that of the coarse particle theory, at shorter wavelengths (Figs. A5, A6, and A7). It may be that an appropriate bridging theory would improve the overall fit.

The effects of varying parameters of particle size, external scattering, and internal scattering are different. Generally as particles are made larger than λ, the reflectance of the surface decreases. As external scattering increases, the reflectance increases; as internal scattering increases, the reflectance decreases. The effect of varying total scattering is to displace the

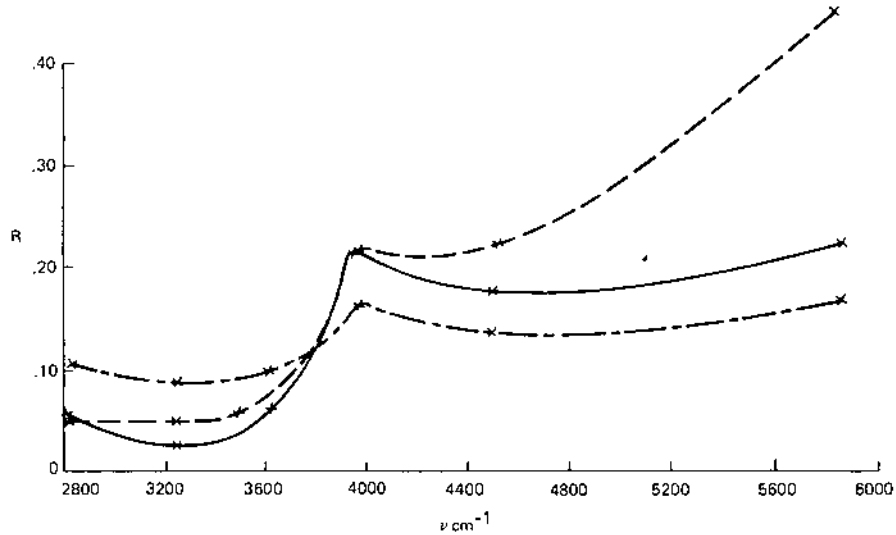

FIGURE A6 Comparison of reflectance of limonite KBr layered pellet (solid curve) with that deduced from Egan and Hilgeman [26] (dash-dot curve) (particle diameter $d = 3\ \mu$m; internal scattering SI = 0.6; total scattering NA = 1.0; absorption NE = $|n\kappa/\lambda|$) and from Emslie and Aronson [44] (dashed curve) ($V = 4 \times 10^{-12}$, $f = 0.3$, $N = 6 \times 10^{8}$).

baseline of the reflectance spectrum while preserving its shape. The effect of changing the particle surface reflectance is to change the shape of the spectrum.

When the particles are made smaller than λ, the reflectance of the surface increases, and the volume reflectance is proportional to the particles per unit volume.

The two scattering parameters for the geometrical optics model, SI [45] and NA [45], and the absorption parameter, NE [45], have a basis in the geometry of the scattering and absorption occurring in each particle. The total scattering of a single particle, NA, depends upon the external asperities and edges on the particles as well as internal grain boundaries; for very rough, inhomogeneous particles it may reach 1.0, and for smooth homogeneous particles, it can decrease below 0.01. The internal scattering SI, is that fraction of the total scattering (unity) that is internally scattered; generally it will be about 0.5 for rough surface particles, but for inhomogeneous particles it may reach 0.9. The absorption by asperities and edges, NE, is controlled by and proportional to the absorption coefficient for a given

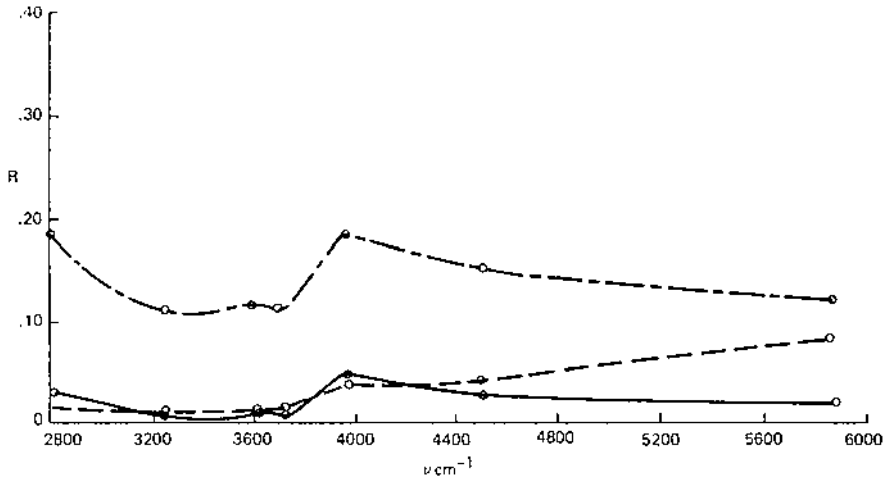

FIGURE A7 Comparison of reflectance of basalt KBr layered pellet (solid curve) with that deduced from Egan and Hilgeman [26] (dash dot curve) (particle diameter $d = 3$ μm; internal scattering SI = 0.93; total scattering NA = 1.0; absorption NE = $|n\kappa/\lambda|$) and from Emslie and Aronson [44] (dashed curve) ($V = 4 \times 10^{-12}$, $f = 0.3$, $N = 6 \times 10^7$).

material with a given particle geometry; it is set equal to $1/4\pi$ times the absorption coefficient in micrometers of the particles. Increasing the particles per unit volume for particles smaller than λ raises the reflectance at all wavelengths and flattens out the reflectance, producing an extremely poor match for all three samples. Decreasing the particle size for particles larger than the wavelength flattens out the curves and results in a poor match.

We adopt an albedo of about 0.4 at a wavelength of 4000 cm^{-1} [15] to match the estimated Russell–Bond albedos of the Martian disk, although Moroz [41] estimated the albedo to be closer to 0.2. We also require the albedo to be near zero at the CO_2 absorption band at 3567 cm^{-1}. To meet these dual requirements, modeling of the Martian surface reflection was attempted using the optical complex indices of refraction of montmorillonite, limonite, and basalt presented in Figs. A3 and A4. Particle diameters were tried ranging from 0.1 to 25 μm; internal scattering (SI) was varied from 0.50 to 0.95; the absorption, NE, was kept constant and equal to the absorption coefficient; and total scattering, NA, was varied from 0.01 to 1.0.

A single-size particle was used rather than a distribution because neither the theory developed by Egan and Hilgeman [26] nor that of Emslie and Aronson [44] treat a loosely compacted, multirefractive index, multisized

particulate medium. A single modal size must be used as representative of the distribution.

The closest model fit to the Martian soil was obtained with the three samples using the fine particle model of Emslie and Aronson [44] with a characteristic particle size of 3 μm. Because of the model limitations in their present state of development, the pellet reflections (Figs. A5, A6, and A7) were taken as being more realistic for calculating the Martian surface flux from incident solar radiation for comparison to Fig. 2. However, the models have proven useful in selecting particle sizes.

ACKNOWLEDGMENTS

We acknowledge the support of NASA for the observational portion of this program under Contract NAS-2-8664 and particularly thank N. Boggess, R. Cameron, and R. Mason, for their help in this program. We also thank J. Augustine for his efforts in the acquisition of laboratory data. We acknowledge the cooperation of the Viking program scientists in helpful discussions and in supplying us with preprint data: in particular, G. Soffen, B. Clark, R. Hargraves, H. Rose, and C. Spitzer. We also thank P. Forney for helpful discussions and the unpublished data on terrestrial analogs of Martian surface materials and C. Capen for Martian disk data during our observations. We thank H. Holt for his assistance in obtaining the Clay Spur, Wyoming montmorillonite sample.

REFERENCES

1. Clark, B.C. Private communication, 1976.
2. Moroz, V.I. The infrared spectrum of Mars (λ1.1–4.1μ). Astron. Zh. 1964, *41*, 350–361.
3. Goody, R.M. Atmospheric Radiation. Clarendon Press: Oxford, UK, 1964.
4. Loughnan, F.C. Chemical Weathering of the Silicate Minerals. American Elsevier: New York, 1969.
5. Sinton, W.M. On the composition of Martian surface materials. Icarus 1967, *6*, 222–228.
6. Clark, B.C.; Baird, A.K.; Rose, H.J. Jr.; Toulmin, P. III; Keil, K.; Castro, A.J.; Kelliher, W.C.; Rowe, C.D.; Evans, P.H. Inorganic analyses of Martian surface samples at the Viking landing sites. Science 1976, *194*, 1283–1288.
7. Baird, A.K.; Toulmin, P. III; Clark, B.C.; Rose, H.J. Jr.; Keil, K.; Christian, R.P.; Gooding, J.L. Mineralogic and petrologic implications of Viking geochemical results from Mars: interim report. Science 1976, *194*, 1288–1293.
8. Egan, W.G.; Hilgeman, T.; Pang, K. Ultraviolet complex refractive index of

Martian dust: laboratory measurements of terrestrial analogs. Icarus 1975, *25*, 344–355.
9. Biemann, K.; Oro, J.; Toulmin, P. III; Orgel, L.E.; Nier, A.O.; Anderson, D.M.; Simmonds, P.G.; Flory, D.; Diaz, A.V.; Rushneck, D.R.; Biller, J.A. Search for organic and volatile inorganic compounds in two surface samples from the Chryse Planitia region of Mars. Science 1976, *194*, 72–76.
10. Houck, J.R.; Pollack, J.R.; Sagan, C.; Schaack, D.; Decker, J.A. Jr. High altitude infrared spectroscopic evidence for bound water on Mars. Icarus 1973, *18*, 470–480.
11. Sagan, C.; Pollack, J.R. Anisotropic nonconservative scattering and the clouds of Venus. J. Geophys. Res. 1967, *72*, 469–477.
12. Shorthill, R.W.; Moore, H.L. II; Scott, R.F.; Hutton, R.E.; Liebes, S. Jr.; Spitzer, C.R. The "soil" of Mars (Viking I). Science 1976, *194*, 91–97.
13. Sagan, C.; Phaneuf, J.; Ihnat, M. Total reflection spectrophotometry and thermogravimetric analysis of simulated Martian surface materials. Icarus 1965, *4*, 43–61.
14. Pollack, J.B.; Sagan, C. An analysis of Martian photometry and polarimetry. Space Sci. Rev. 1969, *9*, 243–299.
15. Sagan, C.; Lederberg, J. The prospects for life on Mars: a pre-Viking assessment. Icarus 1976, *28*, 291–300.
16. Sinton, W.M. Spectroscopic evidence for vegetation on Mars. Astrophys. J. 1957, *126*, 231–239.
17. Rea, D.G.; O'Leary, B.T.; Sinton, W.M. Mars: the origin of the 3.58 and 3.69 micron minima in the infrared spectra. Science 1965, *147*, 1286–1288.
18. Danielson, R.E.; Gaustad, J.E.; Schwarzschild, M.; Weaver, H.F.; Woolf, N.J. Mars observations from Stratoscope, II. Astron J. 1964, *69*, 344–352.
19. Beer, R.; Norton, R.H.; Martonchik, J.V. Astronomical infrared spectroscopy with a Connes-type interferometer, II. Mars, 2500–3500 cm^{-1}. Icarus 1971, *15*, 1–10.
20. Strecker, D.W.; Erickson, E.F.; Witteborn, F.C.; Pollack, J.B.; Goorvitch, E. Medium resolution spectra of Venus, Mars, and Jupiter from 1.2 to 4.2 microns. Div. Plan. Sci., Am. Astron. Soc., 7th Ann. Mtg., Austin, TX, 1976.
21. Pimentel, G.C.; Forney, P.B.; Herr, K.C. Evidence about hydrate and solid water in the Martian surface from the 1969 Mariner Infrared Spectrometer. J. Geophys. Res. 1974, *79*, 1623–1634.
22. Herr, K.C.; Forney, P.B.; Pimentel, G.C. Mariner Mars 1969 Infrared Spectrometer. Appl. Opt. 1972, *11*, 493–501.
23. Forney, P.B. Private communication, 1976.
24. Kieffer, H. Spectral reflectance of CO_2–H_2O frosts. J. Geophys. Res. 1970, *75*, 501–509.
25. Egan, W.G.; Hilgeman, T. Optical properties of naturally occurring rhodochrosite between 0.33 μm and 2.5 μm. Appl. Opt. 1971, *10*, 2132–2136.
26. Egan, W.G.; Hilgeman, T. Spectral reflectance of particulate materials: a Monte Carlo model including asperity scattering. Appl. Opt. 1978, *17*, 245–252.
27. Forman, M.L.; Steel, W.H.; Vanasse, G.A. Correction of assymmetric inter-

ferograms obtained in Fourier spectroscopy. J. Opt. Soc. Am. 1966, *56*, 59–63.
28. Blackman, R.B.; Tukey, J.W. The Measurement of Power Spectra. Dover: New York, 1958.
29. Russell, R.W.; Soifer, B.T.; Forrest, W.J. Spectrophotometric observations of Mu Cephei and the Moon from 4 to 8 microns. Astrophys. J. 1975, *198*, L41–L43.
30. Nautical Almanac. U.S. Government Printing Office: Washington, DC, 1976.
31. Mitchell, R.I. New multicolor filter photometry of Mars. Commun. Lunar Planet. Lab. 1967, *6*, 289–294.
32. McClatchey, R.A.; Benedict, W.S.; Clough, S.A.; Burch, D.E.; Calfee, R.F.; Fox, K.; Rothman, L.S.; Garing, J.S. Air Force Cambridge Research Laboratory Atmospheric Absorption Line Parameters Compilation, AFCRL-TR-73-096, 1973. Available on magnetic tape from U.S. Department of Commerce, National Climatic Center, Federal Building, Asheville, NC 28801.
33. Gray-Young, L.D. Interpretation of high resolution spectra of Mars. II. Calculations of CO_2 abundance, rotational temperature, and surface pressure. J. Quant. Spectrosc. Radial. Transfer 1971, *11*, 1075–1086.
34. Aronson, J.R.; Strong, P.F. Optical constants of minerals and rocks. Appl. Opt. 1975, *14*, 2914–2920.
35. Huguenin, R.L. Mars: chemical weathering as a massive volatile sink. Icarus 1976, *28*, 203–212.
36. Capen, C.F. Private communication, 1976.
37. Toon, O.B.; Pollack, J.B.; Sagan, C. Physical properties of the particles composing the Martian dust storm of 1971–1972. Icarus 1977, *30*, 663–696.
38. Binder, A.B.; Cruikshank, D.P. The composition of the surface layer of Mars. Comm. Lunar Planet. Lab. 1966, *4*, 111–120.
39. Egan, W.G. Polarimetric and photometric simulation of the Martian surface. Icarus 1969, *10*, 223–227.
40. Huguenin, R.L. Mars spectra. Lunar Sci. 1977, *VIII*, 478–480.
41. Egan, W.G.; Hilgeman, T. Integrating spheres for measurements between 0.185 μm and 12 μm. Appl. Opt. 1975, *14*, 1137–1142.
42. Pollack, J.B.; Toon, O.B.; Khare, B.N. Optical properties of some terrestrial rocks and glasses. Icarus 1973, *19*, 372–389.
43. Gillespie, J.B.; Lindberg, J.D.; Smith, M.S. Visible and near-infrared absorption coefficients of montmorillonite and related clays. Am. Mineral. 1974, *59*, 1113–1116.
44. Emslie, A.G.; Aronson, J.R. Spectral reflectance and emittance of particulate materials. I. Theory. Appl. Opt. 1973, *12*, 2563–2572.
45. Deirmendjian, D.; Clasen, R.; Viezee, W. Mie scattering with Complex Index of Refraction. J. Opt. Soc. Am. 1961, *51*, 620–633.

15

The Interstellar Medium: Ultraviolet Complex Index of Refraction of Several Candidate Materials

I. INTRODUCTION

Interstellar extinction measurements were extended into the ultraviolet beyond 2200 Å by Stecher [1,2], Bless et al. [3], and Bless and Savage [4,5]. A conspicuous feature in many of the extinction curves occurs at about 2200 Å, apparently varying in shape. This same absorption feature occurs for stars in widely separated galactic regions and has been postulated to be caused by carbon, silica, iron, or combinations (see, e.g., Ref. 6) [29]. Also, interstellar silicate absorption has been observed near 10 μm in the infrared, and this has further emphasized the existence of silicates in the interstellar medium [7].

In order to examine the uniqueness of the present concept of the interstellar medium, a new group of minerals was chosen that (1) can be related to theories of the origin of the solar system and (2) have a reasonable possibility of existing in space, and we determined their fundamental optical properties in the ultraviolet as evidenced by the complex index of refraction. The optical complex index of refraction is a fundamental input parameter to Mie scattering (or any scattering theory for analyzing the interstellar medium). Another input parameter is the particle size distribution of the particulates (see, e.g., Ref. 8) [29].

Naturally occurring silicates have many scattering centers. The mixing of scattering with absorption has made previous measurements of these silicates unreliable. Accordingly, we developed and used a technique for

independent measurement of the refractive and absorptive components of the optical complex index of refraction that permits the removal of the effect of scattering with a modified Kubelka–Munk theory [9]; this technique is not subject to the inherently large errors in a Kramers–Kronig analysis (which does not include scattering). The technique is applicable to measurements from the ultraviolet to the infrared.

Candidate minerals were selected primarily from those highly probable in the solar system. A plagioclase feldspar—bytownite (Minnesota) with approximately 20% $NaAlSi_8O_8$ and about 80% $CaAl_2Si_2O_8$— and a clinopyroxene—augite (Canada) $(Ca,Na)(MgFe^{2+}Fe^{3+},Al)(Si,Al)_2O_6$—were

TABLE 1 Chemical Analyses of Samples

Mineral	Bruderheim[a] meteorite	Bytownite[b]	Augite[b]	Enstatite[b]	Diopside[b]	Troilite[b]	Pyrrhotite[b]
SiO_2	39.94	47.75	52.50	53.60	50.60	1.40	3.45
Al_2O_3	1.86	32.30	0.28	0.81	0.80	0.62	1.46
Fe_2O_3	—	0.06	2.64	3.88	3.74	—	—
FeO	12.94	0.28	4.20	9.76	2.56	—	—
MgO	24.95	0.43	14.28	30.50	16.13	2.07	0.36
CaO	1.74	15.69	25.00	0.44	24.95	0.25	3.76
Na_2O	1.01	2.54	0.36	0.05	0.32	0.02	0.03
K_2O	0.13	0.08	0.01	0.01	0.005	0.00	0.01
H_2O^+	0.10	0.54	0.24	0.16	0.22	—	—
H_2O^-	0.01					—	—
CO_2	—	0.15	0.10	0.18	0.08	—	1.65
TiO_2	0.12	0.03	0.01	0.01	0.13	0.00	0.00
P_2O_5	0.29	0.01	0.02	0.05	0.02	—	—
MnO	0.33	0.03	0.21	0.21	0.16	0.045	1.09
FeS	6.38	—	—	—	—	—	—
Fe	8.59	—	—	—	—	58.88	52.22
Ni	1.30	—	—	—	—	0.28	0.000
Co	0.05	—	—	—	—	—	—
Cr_2O_3	0.60		—	—	—	0.091	0.001
C	0.04	—	—	—	—	—	—
S	—	—	—	—	—	34.01	32.04
Cr	—	—	—	—	—	0.25	—
Cu	—	—	—	—	—	0.25	0.016
Pb	—	—	—	—	—	0.25	0.09
Zn	—	—	—	—	—	0.05	0.015
Total	100.38	99.89	99.85	99.66	99.71		

[a] Data from Ref. 16.
[b] Determined by K. Ramlal, Dept. of Earth Sciences, University of Manitoba.

selected; these minerals, both silicates, constitute on the average about 25% and 50%, respectively, of the lunar surface [10]. Also selected was the Bruderheim meteorite, enstatite (suggested initially by Huffman and Stapp [11]), diopside, troilite, and pyrrhotite. The Bruderheim meteorite is an olivine–hypersthene chondritic meteorite, which is the most common type found on the earth [12]. The enstatite (India), $(Mg,Fe)SiO_3$, was reported by Huffman and Stapp [11] to have a very strong absorption band at 2200 Å, and we obtained a sample from the same supplier. In addition, enstatite is predicted to condense out preferentially from certain primordial solar nebulae [13]. The diopside, $CaMg(Si_2O_6)$, is another pyroxene with high calcium [14], and the object was to determine the optical effect of the compositional variation. The troilite from Del Norte County, California (U.S. National Museum sample No. 94472), is stoichiometric hexagonal phase FeS, and a sample of the same material has been studied in the visual range as a means of optical structure–composition determinations [15]. Pyrrhotite, $Fe_{1-x}S$ (where $0 < x < 0.2$) is nonstoichiometric FeS; our sample was obtained from Zacatecas, Mexico, and was $Fe_{0.93}S$ as determined from X-ray powder diffractograms by R. B. Ferguson, Department of Earth Sciences, University of Manitoba. Also, he indicated that our sample was found to be ~30% hexagonal phase and ~70% monoclinic phase. Visual examination of the sample revealed some calcite ($CaCO_3$), which probably accounts for the Ca found by K. Ramlal in the chemical analysis (Table 1). Iron sulfides figure strongly in differentiating between models of the formation of the solar system [17].

The chemical analyses of the samples are listed in Table 1. These sample materials were selected for their significance in the understanding of the origins of our solar system. It is important to determine whether they also exist in the interstellar medium.

II. SAMPLES AND PROCEDURE

The absorption coefficient is obtained from our modified Kubelka–Munk scattering theory using the real index, the total diffuse transmission and reflection, and the effective thickness of the sample [9]. This procedure was followed for thin sections of augite, bytownite, enstatite, diopside, and the Bruderheim meteorite (see Table 2). For polycrystalline samples, such as our augite and bytownite, which have more than one index of refraction at each wavelength, the Brewster angle and diffuse reflection and transmission technique averages the indices.

The Bruderheim meteorite is very inhomogeneous; there are inclusions of iron nickel, olivine, hypersthene, pigeonitic pyroxene, plagioclase, kamacite, taenite, troilite, and chromite [16]. When a measurement of the real

Table 2 Diffuse Transmission and Reflection Samples

Sample	Thickness (cm)
Augite	0.010
Bytownite	0.0254
Bruderheim meteorite	
Thin section	0.010
KBr pellet configuration	0.0037
Diopside	0.0121
Enstatite	0.0635

index is made from the Brewster angle, it is a potpourri of the photometric and polarimetric effects of all the constituents. As a first-order approximation, the indices determined from an average section contain the effects of iron nickel and troilite inclusions (~20%). However, we were able to obtain a section for Brewster angle measurements that contained very little iron nickel and troilite (~1%); concurrently we pulverized a section of the meteorite and sieved the powder to eliminate most of the iron nickel (which did not pulverize). The powder was mixed with KBr to form a layer 0.018 cm thick on a 0.093 cm thick KBr substrate; the equivalent thickness of the meteorite layer was 0.0037 cm (Table 2). This procedure has been verified to be accurate with standard absorbing glasses and applies to nonhomogeneous rocks such as basalt [18].

However, for high-opacity semiconductors such as troilite and pyrrhotite, diffuse transmission measurements cannot be made because the absorption is too great relative to the smallest practical particle size. We therefore adopted an ellipsometric technique to determine the principal azimuth $\bar{\psi}$ at the pseudo-Brewster angle $\bar{\varphi}$ [19]; the real index n_r is then closely given by the relation

$$n_r = \frac{\sin\bar{\varphi}\,\tan\bar{\varphi}}{\sqrt{1+\tan^2\,2\bar{\psi}}}$$

and the absorption coefficient n, is given by

$$n_i = n_r \tan\,2\bar{\psi}$$

An older approach that relates the absorption coefficient to the ratio of the polarized components at the Brewster angle φ [20] cannot be used because of the surface scattering by the troilite and pyrrhotite.

The ellipsometer was a modification of the apparatus described by Egan et al. [9]. A Continental Optical Corporation quartz Babinet-Soleil compensator, mounted in a precision angle divider, was located just before the polarization analyzer on the sensor side. This permitted the principal azimuth to be located for radiation incident at the angle $\bar{\varphi}$ with the incident polarizer oriented at 45° to the vertical.

The optical complex indices of refraction may then be used in a Mie scattering program, for instance. The complex index of refraction is also applicable to other types of scattering programs such as cylinders [21]. We have used scalar parts I and II of an IBM 360 Mie scattering program developed by J. V. Dave [22]. Part I permits the computation of a Legendre series representing the scattering phase function of a spherical particle described by its size parameter $2\pi a/\lambda$ and refractive index (a is the radius of the sphere and λ the radiation wavelength). The values of the efficiency factors for absorption, Q_a, scattering, Q_g, and extinction, Q_e, are also obtained as program outputs. Computations may be made for size parameters up to about 160, but larger values may be used with some program modifications. Several hundred equally spaced, discrete-size parameters may be used, and the Legendre series may be stored for input to scalar part II; this program permits computation of the Legendre series representing the normalized scattering phase function of a unit volume (illuminated by an unpolarized, monochromatic, and unidirectional beam of radiation) containing a known size distribution of spherical particles of the same material. These coefficients may be obtained for three different size distribution functions: discontinuous power law, modified gamma, and log normal. We adapted these Dave–Mie scattering programs to a NOVA 800 minicomputer, producing a graphical plot of the scattering coefficients as a function of scattering angle.

III. RESULTS

The refractive portion n_r of the complex indices of refraction is plotted in Figs. 1a and 1b and listed in Table 3 for augite, bytownite, the Bruderheim meteorite (with and without iron nickel inclusions), troilite, pyrrhotite, diopside, and enstatite, all between 0.185 and 0.4 μm. The total diffuse transmissions and reflections on the thin sections are plotted in Figs. 2 and 3, and from these absorption coefficients n_r were calculated, plotted in Fig. 4, and listed in Table 3. The pyrrhotite and troilite absorption coefficients (Fig. 4b) were calculated from the ellipsometric measurements.

In detail, the silicates augite, bytownite, enstatite, and diopside have relatively little change in real index with wavelength between 0.185 and 0.4 μm (Figs. 1a and 1b); however, the Bruderheim meteorite samples revealed

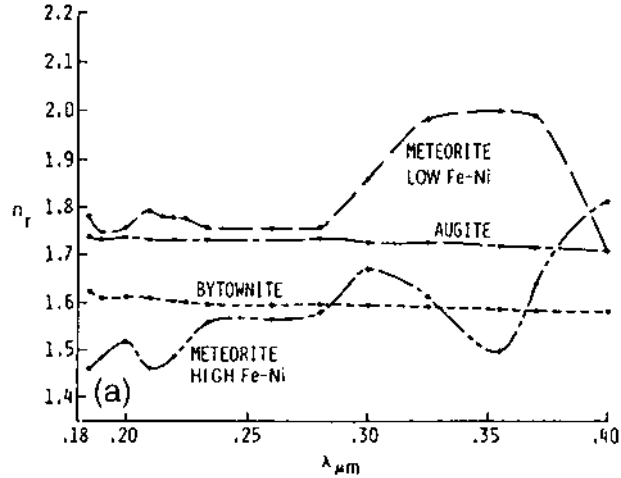

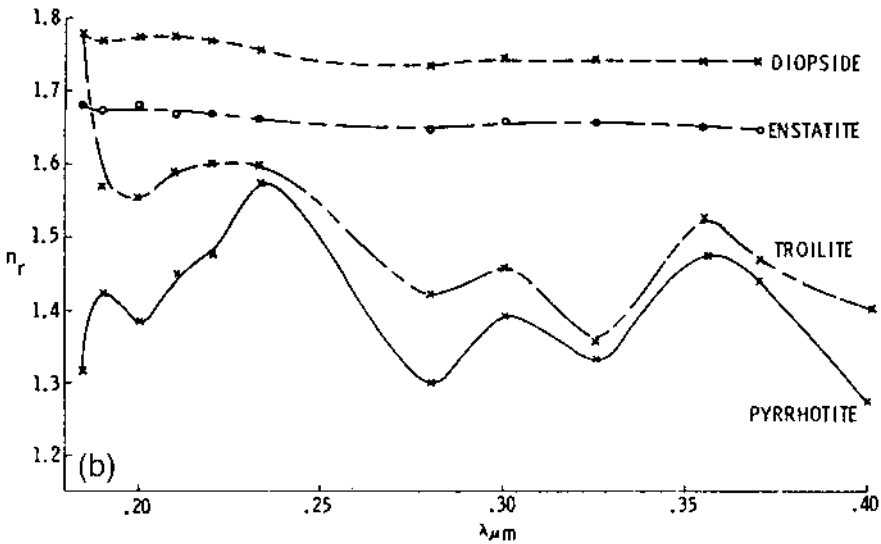

FIGURE 1 Refractive portion n_r of complex index of refraction between 0.185 and 0.4 μm. (a) Augite, bytownite, and Bruderheim meteorite with and without iron-nickel inclusions; (b) diopside, enstatite, troilite, and pyrrhotite.

TABLE 3 Ultraviolet Complex Indices of Refraction

	Bytownite		Augite		Thin section meteorite (high Fe-Ni)		Layered meteorite (low Fe-Ni)		Pyrrhotite		Troilite		Enstatite		Diopside	
λ (μm)	n_r	n_i	n_r	n_i	n_r	n_i	n_r	n_i	n_r	n_i	n_r	n_i	n_r	n_i	n_r	n_i
0.185	1.623	3.35×10^{-4}	1.741	10.05×10^{-4}	1.780	12.6×10^{-4}	1.459	17.3×10^{-4}	1.32	0.72	1.78	0.97	1.680	1.296×10^{-4}	1.783	6.4×10^{-4}
0.19	1.608	2.78×10^{-4}	1.732	9.17×10^{-4}	1.747	9.2×10^{-4}	1.485	16.1×10^{-4}	1.43	0.77	1.57	0.78	1.674	0.858×10^{-4}	1.767	5.0×10^{-4}
0.20	1.612	3.20×10^{-4}	1.739	9.93×10^{-4}	1.753	9.9×10^{-4}	1.519	15.4×10^{-4}	1.39	0.79	1.55	0.84	1.678	1.252×10^{-4}	1.775	6.6×10^{-4}
0.21	1.608	5.43×10^{-4}	1.733	12.98×10^{-4}	1.794	14.9×10^{-4}	1.458	17.5×10^{-4}	1.45	0.79	1.59	0.86	1.669	1.725×10^{-4}	1.775	7.6×10^{-4}
0.215	—	—	—	—	1.779	14.7×10^{-4}	1.460	—	—	—	—	—	—	1.593×10^{-4}	—	—
0.22	1.603	4.41×10^{-4}	1.731	13.28×10^{-4}	1.764	12.4×10^{-4}	1.487	17.9×10^{-4}	1.48	0.74	1.60	0.83	1.670	1.554×10^{-4}	1.767	7.1×10^{-4}
0.225	1.600	6.00×10^{-4}	—	—	–1.760	14.2×10^{-4}	1.500	—	—	—	—	—	—	1.988×10^{-4}	—	—
0.233	1.595	5.45×10^{-4}	1.728	13.15×10^{-4}	1.758	19.6×10^{-4}	1.559	20.6×10^{-4}	1.57	0.73	1.60	0.79	1.662	2.13×10^{-4}	1.757	8.7×10^{-4}
0.24	—	—	—	—	—	—	—	—	—	—	—	—	—	2.17×10^{-4}	—	—
0.26	1.596	2.35×10^{-4}	—	13.49×10^{-4}	1.756	13.5×10^{-4}	1.565	20.2×10^{-4}	—	—	—	—	—	2.82×10^{-4}	—	—
0.28	1.597	1.604×10^{-4}	1.729	14.81×10^{-4}	1.754	12.1×10^{-4}	1.579	22.1×10^{-4}	1.30	1.17	1.43	1.06	1.647	2.62×10^{-4}	1.732	8.6×10^{-4}
0.30	1.596	0.593×10^{-4}	1.728	14.09×10^{-4}	1.856	13.4×10^{-4}	1.673	23.7×10^{-4}	1.40	1.25	1.46	1.12	1.657	2.28×10^{-4}	1.746	8.2×10^{-4}
0.325	1.591	0.413×10^{-4}	1.731	11.77×10^{-4}	1.986	13.7×10^{-4}	1.633	20.6×10^{-4}	1.33	1.19	1.36	1.22	1.655	1.422×10^{-4}	1.740	7.0×10^{-4}
0.355	1.587	0.323×10^{-4}	1.720	9.31×10^{-4}	2.002	7.9×10^{-4}	1.495	15.7×10^{-4}	1.48	1.33	1.53	1.15	1.646	0.692×10^{-4}	1.743	5.6×10^{-4}
0.37	1.580	0.316×10^{-4}	1.712	8.64×10^{-4}	1.902	5.3×10^{-4}	1.642	17.1×10^{-4}	1.44	1.28	1.47	1.14	1.644	0.603×10^{-4}	1.739	5.2×10^{-4}
0.40	1.58	0.344×10^{-4}	1.708	8.67×10^{-4}	1.812	4.3×10^{-4}	1.701	18.4×10^{-4}	1.28	1.24	1.40	1.25	1.631	0.443×10^{-4}	1.722	5.2×10^{-4}

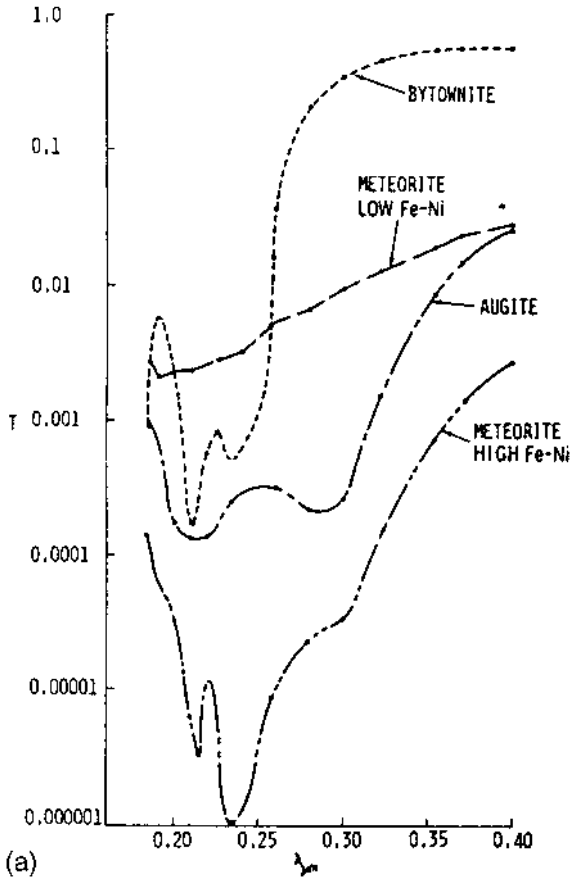

FIGURE 2 Total diffuse transmission of samples between 0.185 and 0.4 μm. (a) Augite, bytownite, and Bruderheim meteorite with and without iron-nickel inclusions; (b) diopside and enstatite.

significant variations, as did the pyrrhotite and troilite (Fig. 1b). There are distinct similarities between the pyrrhotite and troilite real indices except that the troilite had a significant but reproducible variation at 0.185 μm (Fig. 1b). The Bruderheim meteorite real-index variations are in part caused by the presence or absence of nickel-iron as well as other constituents.

However, the transmission curves for the thin sections are more significant because they would be expected to reveal an absorption feature in the vicinity of 0.22 μm that could be related to the corresponding interstellar absorption bump. It is seen that the bytownite and meteorite thin

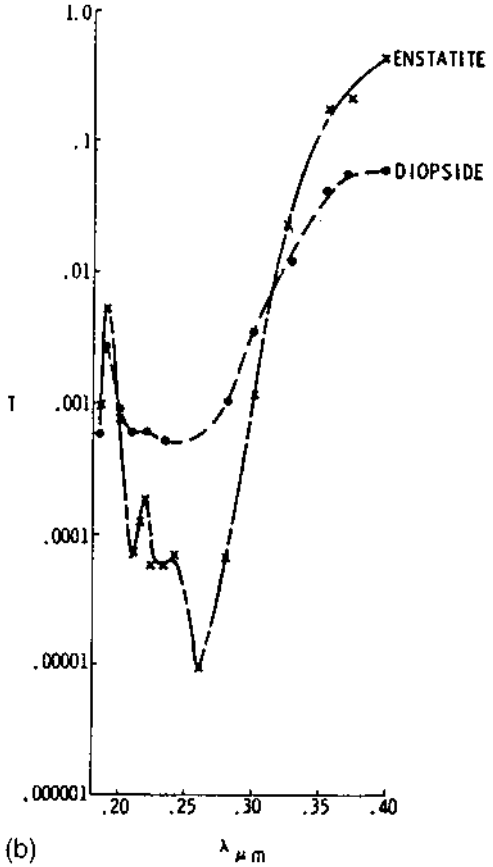

FIGURE 2 Continued.

sections (with high iron nickel) have absorption bands in the region of 0.22 μm (Fig. 2a); however, these transmission minima (absorption maxima) are double-peaked. The meteorite with low iron nickel has the minimum in the region of 0.22 μm broadened and smeared out by strong scattering; the scattering effects are subtracted out in the determination of the absorption coefficients later in this chapter. Even though augite has an absorption feature in the vicinity of 0.22 μm, there is a second absorption feature near 0.30 μm that eliminates it as a candidate for the interstellar medium (Fig. 2a).

One result is that the enstatite (Fig. 2b) has a complex transmission with intermediate peaks. The application of a Kramers–Kronig analysis to determine absorption for such a complex absorbing mineral would be question-

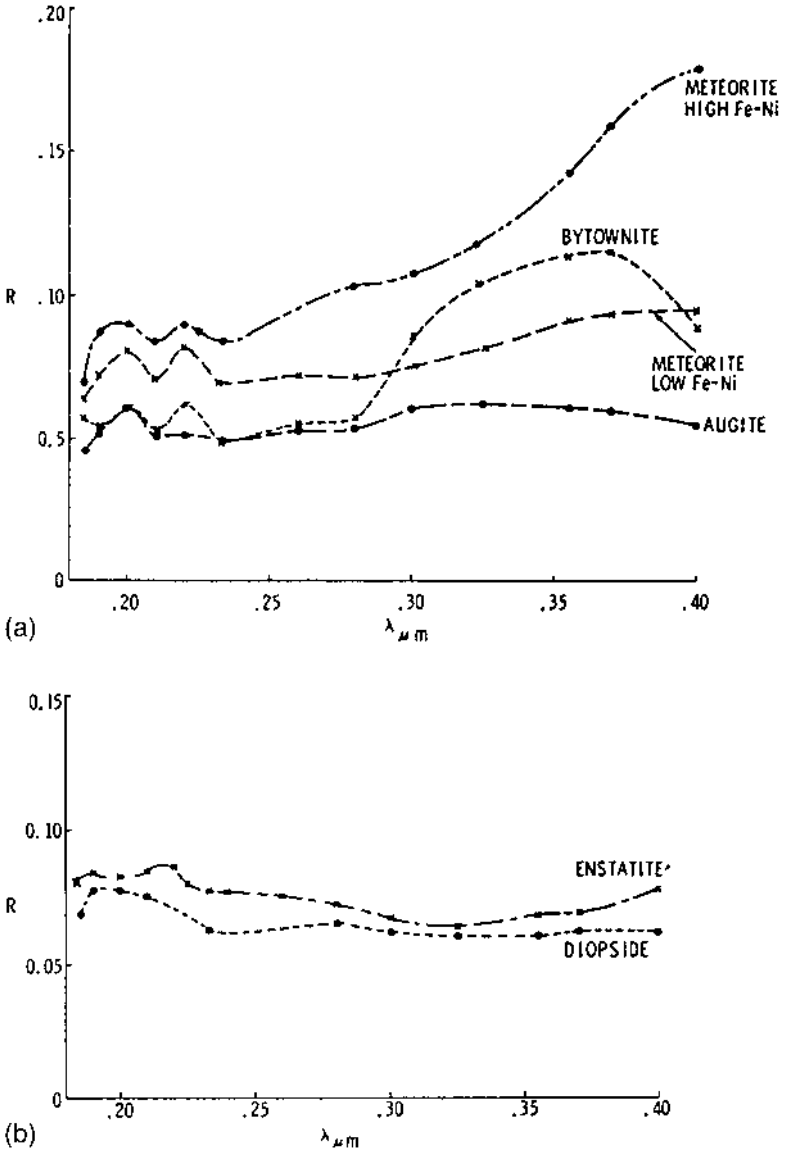

FIGURE 3 Total diffuse reflection of samples between 0.185 and 0.4 μm. (a) Augite, bytownite, and Bruderheim meteorite with and without iron-nickel inclusions; (b) diopside and enstatite.

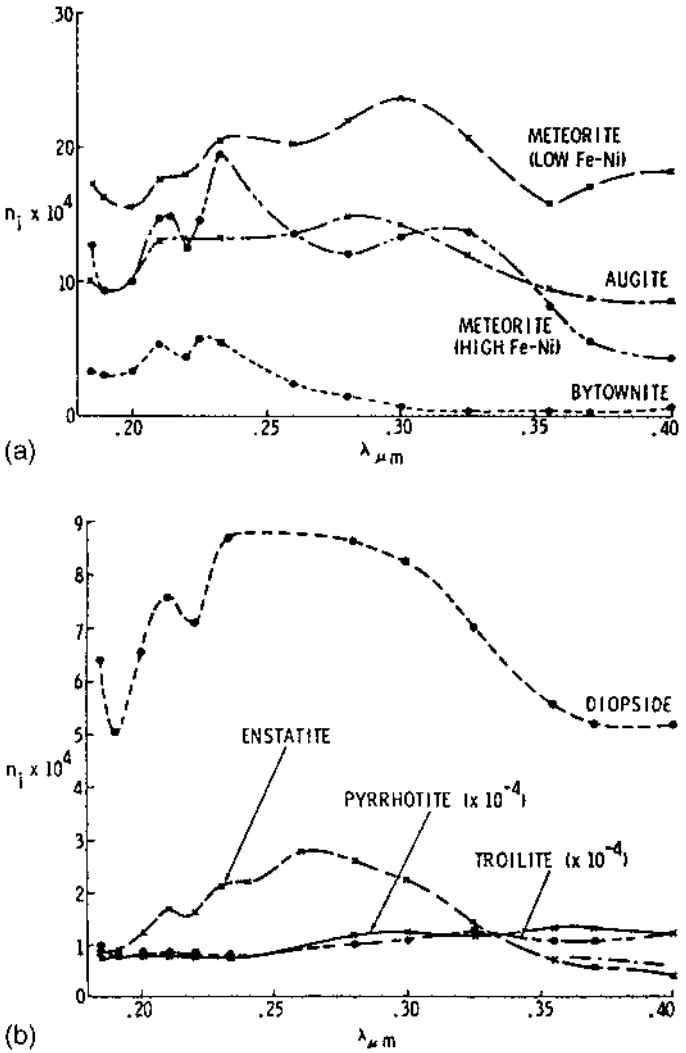

FIGURE 4 Absorption coefficient n_i of complex index of refraction between 0.185 and 0.4 μm. (a) Augite, bytownite, and Bruderheim meteorite with and without iron-nickel inclusions; (b) diopside, enstatite, troilite, and pyrrhotite.

able, even overlooking the fact that scattering is not included in a Kramers–Kronig analysis. There is an absorption in the region of 0.21 μm, and the ultimate location of the feature depends upon the separation of the scattering from the absorption, both of which cause the transmission results of Figs. 2a and 2b. The diopside (Fig. 2b) appears inappropriate as an interstellar medium candidate because of the much too broad absorption curve in the region of 0.22 μm.

The corresponding reflection measurements on these thin sections are shown in Figs. 3a and 3b. It should be pointed out that reflection measurements are relatively poor indicators of absorption bands, and only when there is a tremendous change in absorption will there be a relatively large change in reflection (consider, for instance, bytownite and high FeNi meteorite, Fig. 3a, and compare to corresponding transmission curves of Fig. 2a).

Using the data in Figs. 1–3 in our modified Kubelka–Munk scattering theory, we obtain the absorption coefficient n_i for the bytownite, augite, meteorite, enstatite, and diopside; these are plotted in Figs. 4a and 4b and listed in Table 3. The pyrrhotite and troilite absorption coefficients are plotted in Fig. 4b and also listed in Table 3. The probable error is ± 0.1 based on the accuracy of measurement of the principal azimuthal angle ψ.

By referring to the curves of Figs. 4a and 4b, we may infer which materials are appropriate for consideration as a possibility for the interstellar-medium. Bytownite and the Bruderheim meteorite with high iron nickel appear as possible candidates (save for the double peak in the 0.22 μm region); enstatite has a small absorption peak at 0.21 μm (as does diopside) and would bear consideration because the absorption coefficient decreases toward the visible.

Troilite and pyrrhotite are ruled out because they do not have absorption features in this wavelength region.

Using the Dave [22] scalar Mie scattering program and the optical complex indices of refraction in Table 3, we computed the normalized total extinction as a function of particle radius for bytownite, the Bruderheim meteorite with high iron nickel, and enstatite (shown in Figs. 5a, 5b, and 5c, respectively). The solid line shown in these figures delineates the extremes in ultraviolet interstellar extinction deduced from Bless and Savage [5].

It is seen that there is a significant structure near the 0.22 μm (0.455 μm^{-1}) peak when the particle radius becomes $\sim$0.001 μm. This structure is the result of the absorption variations near 0.22 μm for these materials. For larger particles ($\sim$0.1 μm radius), the Bruderheim meteorite is quite inappropriate (Fig. 5b), with the bytownite and enstatite still a possibility (Figs. 5a and 5c). Composite curves are not presented in order that trends in extinction may be readily seen as a function of particle radius. The bytownite would

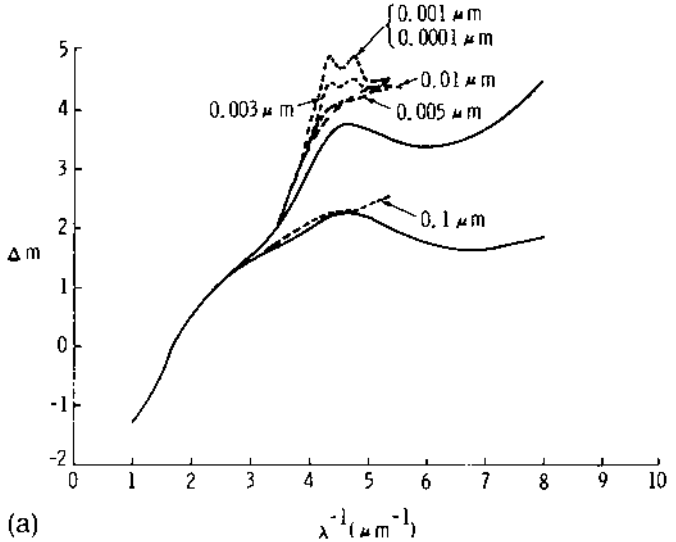

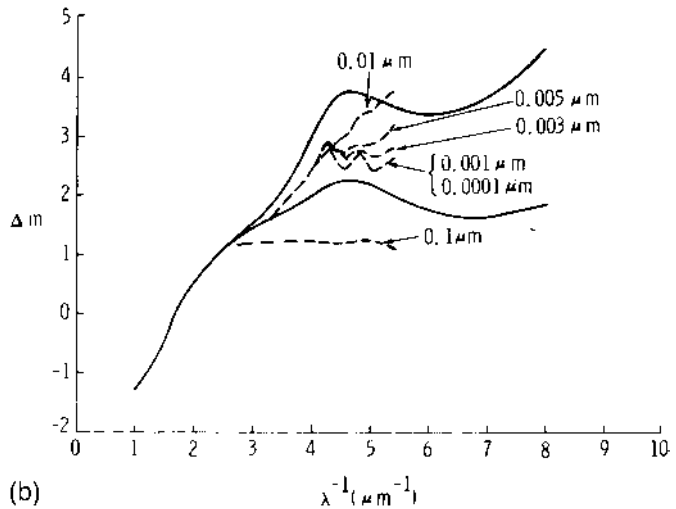

FIGURE 5 Differential absorption versus wavenumber for an interstellar medium consisting of various particle sizes. (a) Bytownite; (b) Bruderheim meteorite; (c) enstatite.

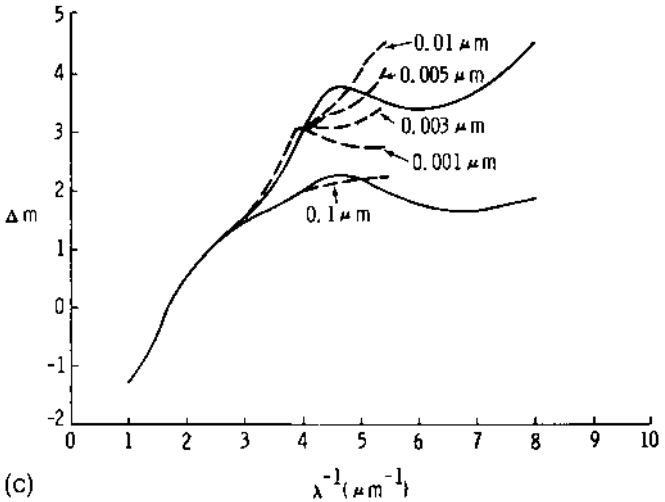

FIGURE 5 Continued.

appear to be a possibility for the interstellar medium only with a distribution of particle radii between 0.1 and 0.0001 μm. If a double peak were observed in the interstellar absorption feature at 0.22 μm, then smaller particles of bytownite or the meteorite would be more likely than the larger sizes. Enstatite appears to be ruled out because the strongest absorption feature is at about 0.26 μm (Fig. 5c and Table 3); this is in contrast to the measurements of Huffman and Stapp [11], which show an extraordinarily large absorption peak in the region of 0.22 μm; the difference appears to be the

TABLE 4 Albedo of Samples at 0.22 μm Wavelength

Sample	Particle radius	Albedo
Bytownite	0.001	0.009
	0.003	0.190
	0.005	0.520
Meteorite	0.001	0.005
	0.003	0.124
	0.005	0.400
Enstatite	0.001	0.031
	0.003	0.460
	0.005	0.800

result of the inability of Kramers–Kronig analyses to account for scattering and the complex nature of the enstatite absorption.

It is of interest to compare the albedo (ratio of scattering efficiency to extinction efficiency) of the candidate materials to that observed for the 0.22 μm interstellar absorption feature by Witt and Lillie [23]. This is presented in Table 4 for the bytownite, meteorite, and enstatite samples and is to be compared to the Witt and Lillie [23] observation of an albedo of $\leq$0.2. It is seen that the albedo of the candidate materials is critically dependent on particle size; a 0.003 μm particle radius for bytownite or the meteorite fulfills the observational requirement, but enstatite requires a smaller particle size.

IV. DISCUSSION

As a result of the measurements and calculations presented here, we have three alternatives as to the interpretation of the double peak that we infer at the 0.22 μm interstellar absorption maximum for the bytownite or Bruderheim meteorite type of material:

1. The double peak may not have been observed in UV extinction because the splitting is weak.
2. The materials we have measured are not valid as interstellar medium candidates because they have a double absorption peak near 0.22 μm.
3. The scattering phenomenon is more complicated than would be inferred from Mie scattering calculations.

We consider these three alternatives in order. The UV interstellar extinction observations of Bless and Savage [4,5] do not appear to reveal a double peak, at least to the clarity of the observations. Personal conversations with R. Bless (1975) and B. Savage (1975) confirmed their confidence in a single peak. Stecher's results [2] do not appear to suggest any structure (absorption maxima at $\sim$4.1 and $\sim$4.8 μm^{-1}) that could relate to the bytownite absorption peaks near these wavelengths (Fig. 5a). The original work of Bless and Savage [4] shows differences between the interstellar extinction curves, but later work by Savage [24] indicated that any fine structure would be less than 0.08 mag.

The second alternative, the appropriateness of the silicates that we observed, may be questioned. The silicates that we measured (augite, bytownite, enstatite, and Bruderheim meteorite material) do exist in the solar system and could be conjectured to exist in interstellar space. Cosmic abundances do not rule out these materials, and it is felt that they are reasonable candidates (see following).

The most attractive possibility appears to be the third alternative: that a distribution of nonspherical particles could shift the double peaks variously and thus smear the two peaks into one. Greenberg [25] show this wavelength shift for oblate and prolate spheroids. This would be in agreement with the current thinking that suggests the existence of particle sizes on the order of 0.005 μm [26]. The enstatite peak at $\sim$0.26 μm would require a large shift to bring it to the 0.22 μm location, and it is not clear that a simple change in particle shape could accomplish this.

Although a properly selected particle size distribution of graphite can be made to fit the absorption feature at 0.22 μm, it apparently will not absorb enough to fit the interstellar extinction at 0.1 μm (Hong, private communication, 1975). Irradiated quartz has been shown to give perhaps a better fit than we have presented [6].

Our suggestion that bytownite exists in the interstellar medium runs counter to the present astronomical thoughts on the interstellar medium. First, the bytownite has an extremely small absorption ($n_i \sim 10^{-3}$), and extremely small particle sizes are necessary for Mie scattering in order for the ratio of absorption to scattering to be large (i.e., 0.01–0.001 μm radius particles). Because of the small size of the particles, the quantity of material necessary to produce the observed interstellar extinction is less than for the conventionally accepted 0.1 μm particles. The justification for these statements is based on the assumption of particles small with respect to the wavelength. In this limit, absorption dominates scattering because the scattering efficiency Q_s is proportional to the fourth power of the size parameter x whereas the absorption efficiency Q_a varies linearly with x [21]. Because Q_a varies linearly with x, and the mass varies as the third power of x, the absorption efficiency per unit mass increases for small particle sizes. Also, with low absorption, the particle size dependence of the interstellar absorption is less critical, which is a simpler concept.

Another critical point is the fact that the cosmic abundances of Al, Ca, and Na (composing bytownite, for instance) are low compared to Mg, Fe, and Si (composing enstatite, for instance). Also, the deficiencies of these elements in the interstellar gas are large compared with cosmic abundances; C, Mg, Mn, and Fe are underabundant by a factor of slightly more than 10, and Ca, Al, and Ti are underabundant by a factor of 1000 or more [13]. The way out of this dilemma is postulated in the condensation of these elements in the dust, so that they do not appear in the gaseous form [13]. According to Purcell [27], a lower bound on the amount of material in the interstellar medium can be established (independent of the size and slightly dependent on the shape of the grains) on the order of 2.5×10^{-37} g/cm^3. The amount of material we require would be less than 10% of this amount.

Further, the existence of extremely small particles will not produce interstellar polarization at the same time as extinction; the extinction efficiency factors $Q_{\parallel}$ and $Q_{\perp}$ for infinite cylinders of refractive index $n_r = 1.66$ differ appreciably for size parameter $2\pi a/\lambda \sim 2.5$ [6]. We do not propose to exclude larger particle sizes from the interstellar medium but include them in a bimodal distribution such as suggested by Greenberg and Hong [26].

Yet another point to be considered is the effect of surface stresses and crystal structure on the absorption spectrum of small interstellar particles. Duley [28] shows that the dispersal of a solid material into particles with characteristic dimensions ranging from 100 to 1000 Å will generate new spectral features displaced $\sim 200\ \text{cm}^{-1}$ from those in the bulk. Thus this band shift would be expected to be small for the broad ultraviolet absorption bands in the vicinity of 2200 Å that we observed in bytownite, for instance.

We feel that there is still much room for further clarification in terms of interstellar medium models and further interstellar extinction observations. It should be borne in mind that the data we have presented cover a narrow wavelength range, and further elucidation in the visual and infrared is required for ultimate comparisons.

V. CONCLUSIONS

As a result of the UV determinations of the optical complex indices of refraction of candidate silicates, meteoritic and iron sulfide materials, it is possible that a suitable material for the interstellar medium is the plagioclase feldspar bytownite, comparison to interstellar extinction and albedo measurements. Bruderheim meteoritic material could be a possibility if a double peak existed in the interstellar extinction curve at 0.22 μm. Enstatite is ruled out as a possibility on the basis of the present measurements, because the absorption maximum is at the wrong wavelength (~ 0.26 μm). It further appears that bytownite might have a distribution of particles ranging from 0.1 to 0.001 μm in radius.

ACKNOWLEDGMENTS

The author wishes to thank J. Augustine for his conscientious optical measurements of the samples, J. S. White, Jr., Smithsonian Institution, for the sample of troilite, T. McGivney for his assistance in running the Mie scattering programs on the IBM 360 and 370 computers, and R. Reich and R. McGill for adapting the scattering programs to the NOVA 800 computer. I would also like to thank K. L. Day, Lunar and Planetary Laboratory,

University of Arizona, and J. M. Greenberg, SUNY at Albany, for comments on an initial version of this paper.

REFERENCES

1. Stecher, T.P. Astrophys. J. 1965, *142*, 1683.
2. Stecher, T.P. Astrophys. J. 1969, *157*, L125.
3. Bless, R.C.; Code, A.D.; Houk, T.E. Astrophys. J. 1968, *153*, 561.
4. Bless, R.C.; Savage, B.D. Ultraviolet Stellar Spectra and Ground-Based Observations; Houziaux, L., Butler, H.E., Eds.; Reidel: Dordrecht, 1970; 561.
5. Bless, R.C.; Savage, B.D. In The Scientific Results from the Orbiting Astronomical Observatory (OAO-2). Code, A.D., NASA SP-310.
6. Wickramasinghe, N.C.; Nandy, K. Rep. Prog. Phys. 1972, *35*, 157.
7. Knacke, R.F.; Gaustad, J.E.; Gillett, F.C.; Stein, W.A. Astrophys. J. 1969, *155*, L189.
8. Wickramasinghe, N.C. Interstellar Grains. The International Astrophysical Series; Chapman & Hall: London, 1964; Vol. 9, L189.
9. Egan, W.G.; Hilgeman, T.; Reichman, J. Appl. Opt. 1973, *12*, 1816.
10. Weill, D.F.; McCallum, I.S.; Bottinga, Y.; Drake, M.J.; McKay, G.A. Science 1970, *167*, 635.
11. Huffman, D.R.; Stapp, J.L. Nat. Phys. Sci. 1971, *229*, 46.
12. Mason, B. Meteorites; Wiley: New York, 1962.
13. Salpeter, E.E. Rev. Mod. Phys. 1974, *46*, 433.
14. Hurlbut, C.S. Dana's Manual of Mineralogy; Wiley: New York, 1966, 609.
15. Carpenter, R.H.; Balley, A.C. Am. Mineral. 1973, *58*, 440.
16. Baadsgaard, H.; Campbell, F.A.; Folinshee, R.E.; Cumming, G.L. J. Geophys. Res. 1961, *66*, 3574.
17. Lewis, J.L. Bull. Am. Astron. Soc. 1974, *6*/*3*(1), 337.
18. Egan, W.G.; Hilgeman, T.; Pang, K. Icarus 1975, *25*, 344.
19. Born, M.; Wolf, E. Principles of Optics; Macmillan: New York, 1959.
20. Egan, W.G.; Becker, J.F. Appl. Opt. 1969, *8*, 720.
21. Van de Hulst, H.C. Light Scattering by Small Particles; Wiley: New York, 1957.
22. Dave, J.V. Development of Programs for Computing Characteristics of Ultraviolet Radiation; NASA S80-RADTMO Goddard Space Flight Ctr.: Greenbelt, MD, 1972.
23. Witt, A.N.; Lillie, C.F. Astron. Astrophys. 1973, *25*, 397.
24. Savage, B.D. Astrophys. J. 1975.
25. Greenberg, J.M. J. Colloid Interface Sci. 1973, *39*, 513.
26. Greenberg, J.M.; Hong, S.S. Invited Paper at 8th Eslah Symp., 4–7 June 1974, Frascati, Italy.
27. Purcell, E.M. Astrophys. J. 1969, *158*, 433.
28. Duley, W.W. Bull. Am. Astron. Soc. 1974, *6*/*4* (1), 433.

16

Anomalous Refractive Index of Submicrometer-Sized Particulates

I. INTRODUCTION

Many attempts to model the optical properties of rough surfaces use radiative transfer theory in a phenomenological approach. Such a procedure does not concern itself with the causes of surface or body absorption and scattering and does not lead to an understanding of the optical interactions causing absorption and scattering.

A good physical model of a rough surface permits an understanding of the interaction with electromagnetic radiation and the specific modifications of a rough surface necessary to tailor bidirectional, specular, and diffuse reflectance as a function of incident radiation wavelength. One of the fundamental inputs to such a model is the optical refractive index of the surface material.

Without any a priori knowledge one would be tempted to use the bulk refractive index of the surface material. However, particles of small size comparable to the wavelength of the incident radiation ($\sim$1 μm in size) do not permit a macroscopic definition of refractive index (i.e., the ratio of the group velocity in the medium to that in free space). Perhaps the term effective refractive index would be more appropriate. The problem remains to determine the magnitude of the effective refractive index of submicrometer-sized particles and whether such index has any usefulness.

To address this problem, we have made refractive index measurements in the 0.400–1.105 μm wavelength region of compressed pellets of

submicrometer-sized particles of anatase, rutile, magnesium carbonate, barium sulfate, and sulfur. These materials are quite important as photometric standards and find wide use in integrating spheres. In the experimental investigation, < 1 μm sized powders of the aforementioned materials were compressed in a vacuum die with a hydraulic press. A 13 mm diameter sample, 7 mm thick, was formed with a die pressure of 3.3×10^7 dyn/mm^2. This produced a specular surface adequate for Brewster's angle reflection measurements. The refractive portion of the index of refraction of the powders was found by a Brewster's angle determination on these pellets at wavelengths between 0.400 and 1.105 μm [1].

The particle sizes range of the compressed samples was assessed using a scanning electron microscope. The anatase particles were approximately spherical, with sizes ranging from 0.1 to 0.2 μm. The rutile particles were more angular, with particles ranging from 0.1 to 0.3 μm, with a few as large as 0.5 μm. The magnesium carbonate was previously investigated [2] and found to consist of platelets 0.1 μm thick and ~ 1 μm along the edges. The barium sulfate particles were spheroidal, with the major axis ranging between 0.1 and 1.0 μm. The colloidal sulfur sample was found to have no discernible porosity on the compressed surface when examined with a scanning electron microscope.

The pore sizes of the anatase and rutile samples were roughly equal to the particle sizes. The magnesium carbonate had a range of pore sizes because of the platelet shape of the constituent particles. The barium sulfate pores varied because of the size range of the particles and were in the same range. The sulfur porosity was quite low, resulting in very small pores.

II. RESULTS

The results of the measurements are presented in the upper portion of Table 1; the comparison refractive index value (sodium D line determinations for the various crystal axes) together with the appropriate hardness values are also shown in Table 1. It is seen that the anatase, rutile, $MgCO_3$, and $BaSO_4$ powder samples all have indices of a refraction below the sodium D line bulk values at all wavelengths; the sulfur also follows this rule, except at a 0.400 μm wavelength. This is not surprising because sulfur is highly absorbing in the blue.

The reason for the lower values of the index of refraction for the powders appears to be related to the hardness. The hardness controls the degree to which the particles may be compressed to reconstitute the original bulk material. In essence, the reconstituted pellet samples have discontinuities between the particles that lower the effective index of refraction. This could result from air gaps between the particles or discontinuities in the micro-

TABLE 1 Index of Refraction of < 1 μm Powder Samples

Wavelength (μm)	Anatase	Rutile	$MgCO_3$	$BaSO_4$	Sulfur
0.400	1.470	1.749	1.467	1.479	2.067
0.500	1.489	1.670	1.473	1.454	1.912
0.600	1.543	1.630	1.470	1.441	1.884
0.633	1.577	1.628	1.470	1.441	1.875
0.700	1.623	1.628	1.468	1.419	1.860
0.800	1.654	1.632	1.470	1.415	1.843
1.0	1.684	1.663	1.469	1.420	1.847
1.105	1.706	1.682	1.461	1.419	1.848
Bulk values (Sodium D line, determinations for the various axes; λ = 0.5893 μm)					
	2.554	2.616	1.717	1.637	1.957
	2.493	2.903	1.515	1.638	
				1.649	
Mohs hardness					
	5.5–6	6–6.5	3.5–5	3–3.5	1.5–2.5
Volume fraction, X					
	0.42	0.57	0.50	0.52	0.91

structure. Essentially there is a spatial variation of the dielectric constant on a scale much smaller than the wavelength of the incident radiation.

A representation of the phenomenon appears to be contingent on determining the porosity of the samples (i.e., whether there are air gaps between the particles). Sample densities were determined from mass per unit volume (i.e., weighing each of the pellet samples and calculating the volume). The ratio of the sample density to the bulk density is the volume fraction. These determinations are presented in Table 1, where X is the volume fraction. For a standard comparison, a sample of Halon [a trade name of the Allied Chemical Corporation for a fine powder of polymerized tetrafluoroethylene (PTFE)] was compressed in the same die, and it achieved the bulk density within expected experimental variations of plastic samples. However, all other samples had significantly lower volume fractions, indicative of higher porosity.

A representation of this phenomenon might be achieved with the Maxwell-Garnett theory [3], which predicts changes in the complex dielectric constant of a mixture of spherical particles in an insulating matrix. This theory should also be applicable to the refractive portion of the optical complex index of refraction. The theory treats the two components in an asymmetrical manner. It assumes that the field acting on a grain resulting from all other grains is given by the local Lorentz field. The general expression involving the dielectric constant ε_S ($= n^2$) of the composite medium with

ellipsoidal grains with dielectric constant ε_A embedded in a matrix of dielectric constant ε_B is given by

$$\frac{\varepsilon_S - \varepsilon_B}{L\varepsilon_S + (1-L)\varepsilon_B} = X\frac{\varepsilon_A - \varepsilon_B}{L\varepsilon_A + (1-L)\varepsilon_B} \tag{1}$$

where L is the characteristic depolarization factor. The usual Maxwell-Garnett result is obtained for spherical grains ($L = 1/3$).

Table 2 (a) shows computations of the depolarization factor L based on the data in Table 1 (at 0.600 μm, as closest to 0.5893 μm). The depolarization factor for rutile is reasonable, but anatase and sulfur have low values and those for $MgCO_3$ and $BaSO_4$ are negative. Further, because of the asymmetrical nature of ε_A and ε_B, when they are interchanged the calculated value of L may be physically unrealizable (e.g., for $MgCO_3$, $L = -2.37$). Thus the Maxwell-Garnett theory fails to explain the experiment in all cases.

Going next to the effective medium theory [4], where the two components are treated equivalently, grains of dielectric constant ε_A and ε_B are embedded in a composite medium with effective dielectric constant ε_S. The effective medium is chosen so that the average field acting on any one grain from all other grains is zero. The effective medium dielectric constant ε_S is related by

$$X\frac{\varepsilon_A - \varepsilon_S}{\varepsilon_A + 2\varepsilon_S} + (1-X)\frac{\varepsilon_B - \varepsilon_S}{\varepsilon_B + 2\varepsilon_S} = 0 \tag{2}$$

Table 2 (b) shows a comparison of the first and second terms for the five compressed powder samples for $\lambda = 0.600$ μm. It can be seen that only the anatase and sulfur fulfill the requirements of the effective medium theory. Thus this theory is also inadequate to explain the data.

An empirical theory can be assumed for the dielectric constant ε_S, whereby when $X = 1$, $\varepsilon_S = \varepsilon_A$, and when $X = 0$, $\varepsilon_S = 1$. Thus,

$$\varepsilon_S = \varepsilon_A X + 1(1-X) \tag{3}$$

Table 2 (c) shows the results for a calculation of ε_S based on the data in Table 1 for $\lambda = 0.600$ μm. It is seen that the sulfur comes closest for the calculated ε_S, with rutile the poorest. It can be seen that this approach is generally quite inaccurate.

A variant in the empirical theory (but based on the index of refraction) suggested first by van de Hulst [5] is given by

$$n_S = n_A X + 1(1-X) \tag{4}$$

Table 3 (a) shows the results for n_S, again based on the data in Table 1 for $\lambda = 0.600$ μm. The results are good except for the rutile. Van de Hulst limits the application of the approximation [Eq. (4)] to the case where the

TABLE 2 Comparison of Dielectric Constant by Various Theories ($\lambda = 0.600\ \mu m$)

	Sample				
	Anatase	Rutile	$MgCO_3$	$BaSO_4$	Sulfur
ε_S (sample)	2.38	2.66	2.16	2.08	3.55
ε_A (published)	6.37	7.618	2.611	2.693	3.83
X (sample)	0.42	0.57	0.50	0.52	0.91
(a) Maxwell-Garnett theory					
Depolarization-factor L	+0.205	+0.446	−0.379	−0.228	+0.05
(b) Effective medium theory					
1st term	0.151	0.219	0.0325	0.0465	0.0234
2nd term	−0.139	−0.113	−0.109	−0.100	−0.0274
(c) Empirical theory for ε_S					
Calc. ε_S	3.26	4.77	1.81	1.88	3.58

complex refractive index is close to 1. It is thus expected that the rutile index would be poorly approximated.

As a last step, consider the expression given by Emslie and Aronson [6] for the Lorentz–Lorenz complex index of refraction $\bar{n}_{II}$:

$$\bar{n}_{II}^2 = 1 + \frac{2X\left\{\left[1 + 1/(n_A^2 - 1)\right]\ln(n_A)^2 - 1\right\}}{1 - X + \left[2X/(n_A^2 - 1)\right]\left\{\left[1 + 1/(n_A - 1)\right]\ln(n_A^2) - 1\right\}} \tag{5}$$

TABLE 3 Comparison of Index of Refraction by Various Theories ($\lambda = 0.600\ \mu m$)

	Sample				
	Anatase	Rutile	$MgCO_3$	$BaSO_4$	Sulfur
n_S (sample)	1.543	1.630	1.470	1.441	1.884
n_A (published)	2.524	2.760	1.616	1.641	1.957
X (sample)	0.42	0.57	0.50	0.52	0.91
(a) Empirical theory for n_S					
n_S	1.64	2.00	1.31	1.30	1.873
(b) Emslie–Aronson theory					
$\bar{n}_{II}$	1.453	1.817	1.295	1.311	1.849

This model assumes that a fine particle powder sample may be considered as an assembly of ellipsoids having the same volume as each of the irregularly shaped particles that have edges and asperities. Ellipsoids are mathematically tractable by the Lorentz–Lorenz technique, and by averaging over a range of ellipsoid shapes, dipole resonances, which produce high Fresnel reflectivities, are avoided. In analogy with the Lorentz–Lorenz method, each ellipsoid is enclosed in a coaxial ellipsoidal cavity having the same shape in the continuous medium with the average Lorentz–Lorenz index $\bar{n}_{ll}$.

Table 3 (b) (computed for $\lambda = 0.600$ μm) shows that the Emslie-Aronson theory produces fair agreement between the observed composite index n_S and calculated Lorentz–Lorenz value $\bar{n}_{ll}$. It might be thought that the absorption portion of the complex index of refraction could cause the remaining discrepancy, but the measured values are ~ 0.001 for all samples in the wavelength range presented.

Table 4 summarizes the results, giving the percent error in the dielectric constant at $\lambda = 0.600$ μm. The higher index materials (anatase and rutile) form one group, and the relatively lower index materials ($MgCO_3$ and $BaSO_4$) form another group. The sulfur because of its high volume fraction, has a very low error. It is seen that the Maxwell-Garnett theory gives the best average error (if the assumption of 1/3, true for spheres for the depolarization factor, is valid) and the Emslie–Aronson theory the next best, although the accuracy spread is not great. For the lower index materials the empirical relation for the dielectric constant yields the best result, but the spread of accuracy of the other theories is negligible. A sensitivity analysis of ε_S based on an assumed small inaccuracy in the mass fraction (X) determination resulted in a percentage increment in the dielectric constant of nearly the same amount (i.e., $+5\%$ increase in X produced a 3–5% increase in ε_S). Thus there is no inordinate variation in ε_S for a small inaccuracy in X.

TABLE 4 Comparison of Errors for ε_S with Various Theories ($\lambda = 0.600$ μm)

	High-index materials			Low-index materials			
Theory	Anatase	Rutile	Average	$MgCO_3$	$BaSO_4$	Average	Sulfur
Maxwell-Garnett ($L = 1/3$)	12.2	9.8	7.6	24.3	18.8	21.6	5.3
Effective medium	4.2	44.7	24.5	22.2	30.0	26.1	1.1
Empirical ε_S	40.0	77.4	58.7	16.2	9.6	12.9	0.8
Empirical n_S (van de Hulst)	13.0	50.4	31.7	20.4	18.8	19.6	1.1
Emslie–Aronson	11.3	24.1	17.7	22.2	17.3	19.8	3.9

In Table 4 it is seen that the Maxwell-Garnett and Emslie–Aronson theories yield nearly the same error for anatase, $MgCO_3$, $BaSO_4$, and sulfur; the Emslie–Aronson theory error is about 2.5 times as great as that of the Maxwell-Garnett theory for rutile. The reason for the close agreement in the majority of cases possibly lies in the similarity in their development, allowing for the assumption of a sphere depolarization factor of 1/3 in the Maxwell-Garnett theory. The generalization of the Maxwell-Garnett theory to ellipsoids, similar to the Emslie–Aronson approach, is described in a review paper by Granqvist and Hunderi [7].

III. CONCLUSION

The results presented here indicate that compressed pellets of submicrometer-sized particles have an effective refractive index lower than in the bulk caused by air spaces between the particles. The refractive indices were determined for a specific amount of compression. A lower compression would be expected to increase the porosity and lower the effective index more. This appears to be the first published experimental comparison of the Emslie–Aronson theoretical expression for the Lorentz–Lorenz index of refraction with other theories for the index of refraction in porous media.

In the analysis of the measurements given here, the tacit assumption is made that the indices of refraction for uniaxial and biaxial crystals (Table 1) may be averaged for comparison with the theoretical (ε_S), (Table 2) or the n_S (Table 3). This approach is reasonably valid in the spectral region between 0.400 and 1.105 μm, where no optical resonances are present. When optical resonances occur, the real portion of the index along one axis becomes less than unity, and one may not use an average of this index with that of another axis that could be greater than unity. Some form of weighted average would be necessary, and this would be a subsequent refinement on this work.

REFERENCES

1. Egan, W.G.; Hilgeman, T.W. Optical Properties of Inhomogeneous Material; Academic: New York, 1979.
2. Egan, W.G.; Hallock, H.B. Proc. IEEE 1969, *57*, 621.
3. Maxwell-Garnett, J.C. Phils. Trans. R on Soc. Lond., 1904; *203*, 385; 1906, *205*, 237.
4. Landauer, R. J. Appl. Phys. 1952, *23*, 779.
5. van de Hulst, H.C. Light Scattering by Small Particles; Wiley: New York, 1957.
6. Emslie, A.G.; Aronson, J.R. Appl. Opt. 1973, *12*, 2563.
7. Granqvist, C.G.; Hunderi, O. Phys. Rev. B 1977, *16*, 3513.

17

Ultraviolet Spectra of Organic Molecules and the Interstellar Medium

The polysaccharides cellulose and starch have been shown to give an excellent match to certain spectra of the interstellar medium [1]. The matching was based on comparisons of the laboratory spectra of polysaccharides in the 2–30 μm region with those of various astronomical objects, in particular dark clouds near the Trapezium [2,3]. Cellulose has broad absorption bands at 3, 10, and 20 μm devoid of the 10.3 μm high transmittance spike reported for crystalline silicates [4], the commonly accepted dominant interstellar material. It has been claimed that cellulose obviates the need for the presence of both H_2O ice and silicates in the interstellar medium [1]. Several organic molecules have already been found associated with dust grains in the interstellar medium. The dust grains offer protection from dissociation and could aid in the cellulose formation process [5]. The ultraviolet (UV) absorption in the interstellar medium can provide an additional identification technique for interstellar organic molecules, and this poses the question, What are the UV spectral characteristics of cellulose? We have tried to answer this question by measuring the UV spectrum of cellulose between 0.19 and 0.40 μm and comparing it to the observed UV spectrum of the interstellar medium [6]. The sample we chose was regenerated cellulose produced from wood pulp, known generally as cellophane.

I. RESULTS

The UV absorption spectrum for a 1 mil (0.025 μm) film was made on a Cary 14 spectrophotometer and is shown in Fig. 1. The transmission (expressed as optical density) is shown as a function of wavelength between 0.19 and 0.40 μm. A scale change takes place at the left of the figure, where the density range is then 1.0–2.0. It can be seen that the transmission is high from 0.40 μm to about 0.36 μm ($\sim$ 90%), dropping slowly to shorter wavelengths, with a sharp drop in transmission beginning at 0.23 μm and a transmission of 1% at 0.19 μm. There is no evidence of the extinction feature at 0.22 μm that is observed for the interstellar medium [6]. However, the opacity remains high toward shorter wavelengths, in agreement with interstellar medium observations [6].

In the infrared (IR) region, published spectra of cotton (cellulose) and other polysaccharides such as amylose, arabinogalactan, and mannan dispersed in KBr [7] are limited by having uncalibrated absorption coefficients. That is, scattering is not separated from absorption. This separation could be accomplished by use of additional measurements and a suitable theoretical approach [8]. However, using cellophane precludes the occurrence of significant scattering and eliminates this limitation. An IR spectrum of the same cellophane sample that was used for our UV measurements was taken on a Perkin-Elmer 457 spectrophotometer in the region between 2.5 and 40 μm (Fig. 2) and confirms it to be cellulose. The percent transmittance is shown as a function of wavelength (wavenumber). Interference fringes are evident at the shorter wavelengths, apparently the result of using different optical systems.

A calculation of the absorption coefficient at 3 and 10 μm may be made for the cellophane sample by scaling our observed absorption at 3.4 μm (Fig. 2) to those at 3 and 10 μm using previously published data on a lower

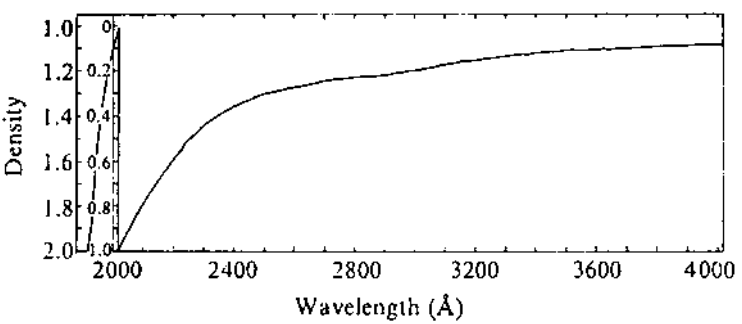

FIGURE 1 Ultraviolet transmission curve for 1 mil (0.025 mm) thickness of cellophane.

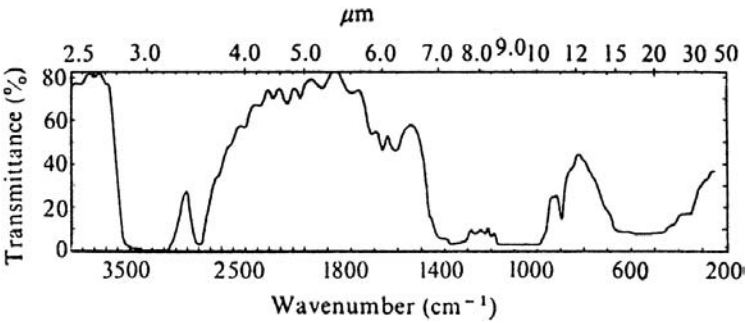

FIGURE 2 Infrared transmittance curve for 1 mil (0.025 mm) thickness of cellophane.

absorbing sample [7]. The results are that the absorption coefficient, α, is 870 cm^{-1} at both 3 and 10 μm.

Although the IR spectrum of cellulose is a good match to several observations of the interstellar medium [1] we feel that there are still arguments against it being a dominant constituent. First, absorption spectrum measurements of amorphous silicates [9] have shown a much better match to the 10 μm interstellar feature than previous measurements of crystalline silicates. The undesirable sharp transmission spike is not present for the amorphous form. There also remains the problem of explaining the extremely wide variation (0–∞) in the ratio of the strength of the 3–10 μm absorption bands observed in the interstellar medium [10]. Such a range of variation in band strength is difficult to account for by temperature and absorption variations and suggests at least a two-component medium. Further, late M-type stars constantly eject large quantities of silicates from their atmospheres [11]. These must then contribute to interstellar absorption unless some as yet unknown mechanism is capable of destroying silicates.

II. CONCLUSION

Finally, the UV measurements in Fig. 1 have shown that we need something other than cellulose in the interstellar medium to account for the 0.22 μm extinction feature. This absorption has previously been postulated as having been produced by three processes: by plasma oscillations in solids (graphite) [12], by solids having sharp UV absorption edges [silicates (Mg, Fe)SiO_3] [13], and by solids having UV absorption features in their bulk optical properties (irradiated quartz [14]; plagioclase feldspars [15].

We suggest another possibility for the 2200 Å feature. Consistent with the reported radiodetection of cyanooctatetene (C_3HN) in Holley's Cloud 2

[16] is the presence of a cyano or nitrile (C-N) group. Although this molecule has never been synthesized in the laboratory, it is known that similar bonded molecules have a UV absorption in the appropriate region. For instance, methacrylonitrile (C_3H_3N) has an absorption at 0.215 μm [17], near the 0.22 μm interstellar absorption. The nitrile group may thus be the cause of a UV absorption feature at the required wavelength. Another possibility is the carbonyl bond (C=O), which has an absorption near the required spectral region. For instance, formaldehyde, H_3CO, which has been confirmed as existing in the interstellar medium [18,19], has a strong absorption band at 1,850 Å. The actual location of the carbonyl absorption depends on the structure of the organic molecule with which it is associated. It has been noted that there is an underabundance of C, N, and O in the interstellar gas [20], and the presence of condensed organics may account for these missing elements.

We feel that although cellulose (or other organics) might exist in the interstellar medium, we are not yet prepared to reject the presence of H_2O ice and silicates.

REFERENCES

1. Hoyle, F.; Wickramasinghe, N.C. Nature 1977, 268, 610.
2. Forrest, W.J.; Soifer, B.T. Astrophys. J. 1976, 208, L129.
3. Forrest, W.J.; Houck, J.R.; Reed, R.A. Astrophys. J. 1976, 208, L133.
4. Day, K.L. Astrophys. J. 1975, 199, 660.
5. Goldanskii, V.I. Nature 1977, 268, 612.
6. Stecher, T.P. Astrophys. J. 1969, 157, L125.
7. Hoyle, F.; Olavesen, A.H.; Wickramasinghe, N.C. Nature 1978, 271, 229.
8. Egan, W.G.; Hilgeman, T. Icarus 1975, 25, 344.
9. Day, K.L. Astrophys. J. 1976, 210, 614.
10. Merril, K.M.; Russell, R.W.; Soifer, B.T. Astrophys. J. 1976, 207, 763.
11. Gehry, R.; Woolf, N. Astrophys. J. 1971, 165, 285.
12. Gilra, D.P. NASA 1972, SP-310, 295.
13. Huffman, D.R.; Stapp, J.L. Nature 1971, 229, 45.
14. Wickramasinghe, N.C. Nature 1971, 234, 7.
15. Egan, W.G.; Hilgeman, T. Astrophys. J. 1975, 80, 587.
16. Broten, N.W.; Avery, L.W.; MacLeod, J.M.; Oka, T.; Kroto, H.W. Presented at 151st Meeting Am. Astron. Soc., Austin, TX, 1978.
17. Dyer, J.R. Applications of Absorption Spectroscopy of Organic Compounds; Prentice-Hall: Englewood Cliffs, NJ, 1965.
18. Dickel, H.R.; Seacord, A.W. II; Gottesman, S.T. Astrophys. J. 1977, 218, 133.
19. Jaffe, H.H.; Orchin, M. Theory and Applications of Ultraviolet Spectroscopy; Wiley: New York, 1962.
20. Greenberg, J.M. Astrophys. J. 1974, 186, L81.

18

Complex Index of Refraction of Bulk Solid Carbon Dioxide

I. INTRODUCTION

This chapter presents the results of measurements of the complex index of refraction of commercially available solid carbon dioxide in the wavelength range 0.35–1.0 μm. Unlike the thin film techniques previously employed to determine the real portion of the index [1,2], the present method of measurement is relatively simple and obtains the real and imaginary portions. Our technique involves the determination of the Brewster angle on bulk solid CO_2; the absorption was determined from direct transmission measurements on thin sections of solid CO_2. A Perkin-Elmer 13U spectograph was modified to permit polarization measurements between angles of incidence of 23° and 90° over a 56.5 cm path length [3]. The ultraviolet (UV) and visible measurements were made with a Type 1P21 photomultiplier, and the infrared (IR) measurements were made with a Type 7102 photomultiplier. Narrowband interference filters were used in conjunction with the monochromator to eliminate errors caused by scattered light at wavelengths other than those under observation. Measurements were made at wavelengths of 0.35, 0.46, 0.56, 0.70, 0.97, and 1.0 μm.

The specimens were prepared from commercial Dry Ice manufactured at the Saltville, Virginia, plant of the Olin Mathieson Chemical Corp., New York. The Dry Ice was made with the addition of 50 ppm of water and 50 ppm of Kadol extra heavy white mineral oil (USP heavy); the mineral oil was manufactured by Sonneborn, division of Witco Chemical

Co., Inc., New York. These additives serve as a binder. Without them, the Dry Ice would crystallize and lose cohesion in a short time [4]. The optical absorption of water is known [5], and that of the mineral oil was measured and found to be negligibly small, between 0.35 and 1.0 μm. The index of refraction of the oil (pour point −25°C) is 1.4819 at a wavelength of 0.5893 μm [6]. It is assumed that the optical contribution of these impurities would be approximately proportional to their relative concentrations providing that they do not enter into the lattice structure of the CO_2 molecules. A check of the effect of the water absorption band at 0.97 μm on the transmission of the Dry Ice showed it to be below the resolution limit of our measurements.

II. PROCEDURE

Reflectance measurements were made with the Dry Ice sample immersed in a Pyrex cylinder that provided a thermally insulating atmosphere of CO_2. The Dry Ice specimen was polished by random rubbing contact with a smooth aluminum plate. If this procedure had not been followed, light scattering by the irregular surface of the solid Dry Ice would have made location of the Brewster angle difficult.

For light transmission measurements, an optically clear sample of Dry Ice was selected and polished to a thickness of about 1 cm. If optically clear Dry Ice had not been selected, the imaginary portion of the complex index could have been higher by a factor of 10 because of the greater amount of light scatter. The transmission was measured as a function of thickness as the Dry Ice was allowed to sublimate. The sample was polished prior to each measurement. If we assume that multiple internal reflections between the polished surfaces of the sample do not play an overwhelming role in the process, the slope of the loge transmission vs. thickness curve yields the absorption coefficient α, which is in turn related to the attenuation index κ by the expression

$$\kappa = \alpha\lambda_0/4\pi n \tag{1}$$

In the above relation λ_0 is the vacuum wavelength and n is the measured refractive index of the Dry Ice. The imaginary portion of the index of refraction, or absorption component, is then $n\kappa$.

To determine whether or not the presence of multiple reflections between the two polished surfaces of the sample would invalidate our use of Eq. (1), the transmission was measured for many thicknesses. The results for two separate wavelengths (0.46 and 1.0 μm) are presented in Fig. 1 and are representative of the results obtained at other wavelengths. Within experimental error, a straight line can be drawn through the points, indi-

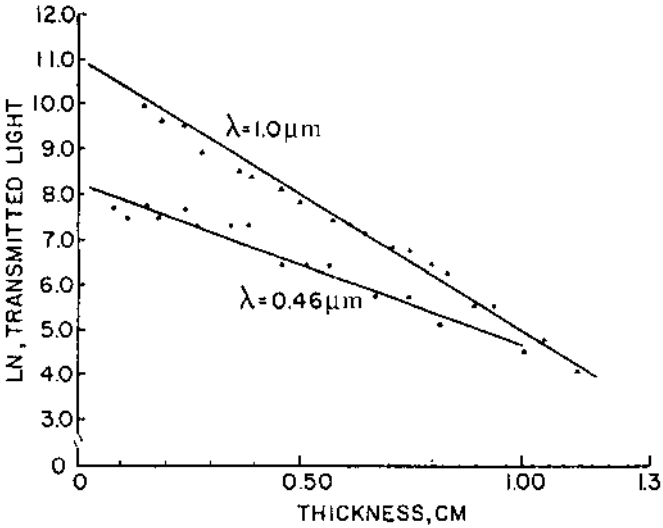

FIGURE 1 Transmission as a function of sample thickness and wavelength for bulk solid CO_2.

cating that multiple reflections do not appear to affect our assumption appreciably. If multiple reflections did in fact play an overwhelming role because of a low attenuation index, the natural log of transmission vs. thickness curve would not be a straight line but a bent curve because the transmission formula from which relation (1) is extracted, namely,

$$T = C \exp\left[-\frac{4\pi n\kappa}{\lambda_0} d\right] \tag{2}$$

is valid only for $[(4\pi n\kappa/\lambda_0)d] \gg 1$. From the results of Fig. 1 it appears that the Dry Ice does not take a high enough polish to produce any large number of specular multiple reflections, and an apparent attenuation index can be measured.

III. RESULTS AND DISCUSSION

The overall results of our experiments are presented in Fig. 2. The real portion of the complex index of refraction n was found to be 1.35 ± 0.05 between 0.35 and 1.0 μm. The attenuation index κ increases by a factor of 3.5 over the same wavelength interval. The values of the real portion of the index of refraction inferred from previous thin film measurements [1,2]

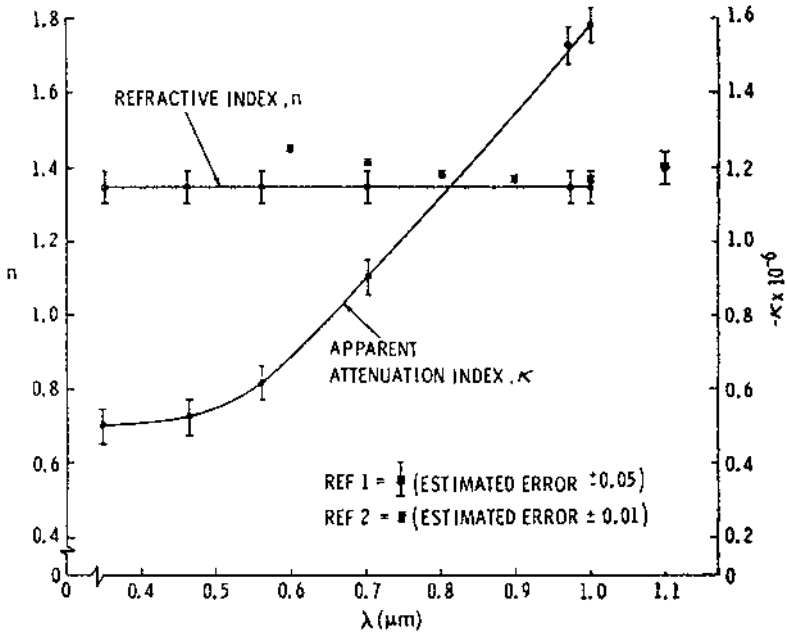

FIGURE 2 Variation of complex index for bulk solid CO_2 with wavelength.

are also plotted. The results obtained by both groups lie at or slightly above the extremes of our estimated experimental error. There appear to be two possible reasons for this. First, the measurements previously reported were made with the solid CO_2 at close to 77 K by virtue of condensation of CO_2 on a liquid nitrogen–cooled substrate. We could expect a higher index of refraction at 77 K than at our sublimation temperature of 195 K in accordance with the Lorenz–Lorentz equation because the density is greater. (The density of solid CO_2 decreases from 1.665 at 90 K to 1.565 at 193 K [7].) A second possibility is that surface or body scattering could slightly reduce the observed Brewster angle. If we assume that the scattering is a cosine function of the scattering angle (measured to the surface normal), the effect would be to bias the Brewster angle measurement toward a slightly smaller value. This could result in the observed slightly lower real portion of the index of refraction.

In addition, we observe an increased absorption toward the long-wavelength end of the spectral range investigated. This is contrary to the inferred absorption based on the increased index toward the shorter wavelengths observed by Tempelmeyer and Mills [2]. It would be inferred from

their data that an absorption band is approached at the shorter wavelengths, whereas our data indicate that the band occurs at the longer wavelengths. It is possible that surface or body scattering (included in the attenuation factor) may be greater in the infrared.

REFERENCES

1. Yamada, H.; Person, W.B. J. Chem. Phys. 1964, *41*, 2478.
2. Tempelmeyer, K.E.; Mills, D.W. J. Appl. Phys. 1968, *39*, 2968.
3. Egan, W.G.; Becker, J.F. J. Opt. Soc. Am. 1968, *58*, 1561; Grumman Research Department Memorandum RM-428J, 1968; Appl. Opt. 1969, *8*, 720.
4. McCauley, D.F. Olin Mathieson Chemical Corp. Private communication.
5. Irvine, W.M.; Pollack, J.B. Icarus 1968, *8*, 324.
6. Rhodes, R. Sonneborn Division, Witco Chemical Co., Inc. Private communication.
7. National Research Council. *International Critical Tables*; New York: McGraw-Hill, 1928; Vol. 3, 43 p.

19

Star Environments

This chapter describes spectral interferometric research from a Lear Jet airborne observatory to the search for water vapor in the stellar atmosphere. Specifically, late M-type stars (cool) were investigated; such stars as the Mira variables, which are given in starcharts by their right assention and declination.

I. INTRODUCTION

The Mira variables are the most common of all of the intrinsic variable stars in our galaxy. They are very red, bright giants with radii several hundred times the radius of the sun and effective temperatures in the range 2000–2500 K. The visible light variations are large and quite regular with periods of 100–700 days [1]. The Mira appear to be stars in the last stages of stellar evolution near the tip of the giant branch in the H–R diagram. Planetary nebulae may be products of evolution from the more massive ($\sim 2\ M_{\odot}$) Mira [2,3] that have ejected one or more shells of material.

The galactic kinematics show that the Mira of longer periods (greater than 350 days) have a more flattened distribution, coinciding with the galactic plane, than stars of shorter periods (less than 200 days) [4,5]. Wyatt and Cahn [6] state that the shorter period variables belong to an intermediate-age population between the younger, longer period variables concentrated near the plane of the galaxy and the oldest (nonvariable) stars in the galactic halo. A few Mira variables with periods of less than 200 days are found at the tip of the giant branches of metal-rich globular clusters 47 Tuc [7] and

NGC 6712 [8]. This is additional evidence that the shorter period Mira are members of an intermediate-age population not constrained to move in the galactic plane.

There is reason to believe that the Mira variables may be expelling copious quantities of material [9]. The estimate of the mass added to the interstellar medium calculated by Gehrz and Woolf, $2 \times 10^{-6} M_{\odot}/yr$, is even greater than that required by Deutsch [10] to reconcile theoretical stellar death rates with observed stellar number densities.

It is possible that condensation is taking place in the Mira, particularly in the circumstellar envelopes [11–13]. Observations in the microwave region show evidence for OH [14], H_2O [15], CO [16], SiO [17], and silicates [18], all in emissions. These constituents are also expected from the evidence for steam absorption in the stellar atmospheres [19,20] and predicted silicate condensation products [13].

At the temperatures of these long-period variables (2000–2500 K), the bulk of the radiation is emitted in the region 1–3 μm. The principal contributor to the atmospheric opacity in these oxygen-rich stars is H_2O, and the emergent flux is dominated by the absorption bands at 1.1, 1.4, 1.9, and 2.7 μm [21]. An analysis of the H_2O in Mira could provide the link between the photospheric H_2O absorption and the OH and H_2O circumstellar emission.

II. SEARCH FOR WATER VAPOR

The first detection of H_2O in Mira variables was by Kulper [19], who used a PbS spectrometer to observe the 1.1, 1.4, and 1.9 μm bands of Mira at 100 cm^{-1} resolution*. He noted that these bands were broader than the usual telluric bands due to the transitions from the excited upper states, which are populated at the stellar temperatures. Spinrad and Newburn [22] and Spinrad et al. [20] observed Mira, R Aq1, R Cas, and other variables in the 0.94 μm region on spectrographic plates and obtained H_2O abundances by observing a laboratory spectrum of hot steam and scaling from the H_2O observed in the earth's atmosphere. They were able to show H_2O abundance variations in Mira as it varied in phase. The H_2O bands at 1.4, 1.9, and 2.7 μm were observed in Mira and R Leo (resolution 150–300 cm^{-1}) from a balloon at 23 km altitude by Woolf et al. [23]. This was the first observation of stellar H_2O unobscured by telluric H_2O. Higher resolution (20 cm^{-1}) ground-based IR spectra of Mira and R Cas were obtained by McCammon et al. [24] using a

* To describe electromagnetic radiation, astronomers use cm^{-1} (wavenumber) and physicists use wavelength in μm, where $1/cm^{-1} = 1$ μm.

PbS spectrometer. Observations of R Cas and R Leo were conducted from the NASA/Kuiper Airborne Observatory (KAO) at 13 km altitude by Strecker et al. [25] using a variable filter spectrometer with 100 cm^{-1} resolution. At this low resolution, only color temperatures could be determined, not H_2O abundances.

The first measurement of H_2O in the infrared using a Fourier transform spectrometer (FTS) at 8 cm^{-1} were by Johnson et al. [26] and Johnson and Mendez [21]. They observed five Mira and corrected the spectra to an altitude of 13 km by observing the Moon both from the ground and from the NASA/Convair 990. Smith and Hilgeman [27] measured several Mira from the NASA/Lear Jet at 14 km using an FTS system operating at 10 cm^{-1}. Airborne spectra at 1.9 cm^{-1} were taken aboard the NASA/KAO by Hilgeman et al. [28].

These low resolution observations do not provide the resolution necessary to resolve the individual H_2O line profiles that are needed for accurate temperature and H_2O abundance determinations. Flaud et al. [29] observed R Cas at 0.12 cm^{-1} using an FTS and derived quantum numbers for many lines in the 4200–4500 cm^{-1} region and bands in the 5700–6400 cm^{-1} region. Additional high resolution spectra (0.15 cm^{-1}) of R Leo were obtained by Hinkle and Barnes [30]. Flaud et al. and Hinkle and Barnes used an isothermal "slab" atmospheric model to derive the H_2O abundances in R Cas and R Leo, respectively. The H_2O rate of formation and the line intensity have a strong temperature dependence; therefore the emergent flux is sensitive to the details of the structure of the atmosphere.

In the present study, ground-based spectra at 0.10 cm^{-1} resolution of R Aql and Mira and airborne spectra at 1.9 cm^{-1} of Mira and R Cas are used to analyze the hot H_2O in Mira. From the above discussion, the Mira periods may provide information about the general position of the Mira variables relative to the galactic plane as well as their age. Therefore these three stars were selected in the investigation of the atmospheric properties of Mira based on the range of their periods. The period of R Aql is 283 days, that of Mira is 332 days, and that of R Cas is 431 days.

The spectral region considered is 4400–4500 cm^{-1}, where H_2O lines are quite weak and are unsaturated in the star's atmosphere. The emergent flux is truly representative of the entire atmosphere, i.e., every layer contributes to the flux. Because this is also a transparent region in the earth's atmosphere [31], the H_2O lines can be observed unobscured by the telluric lines.

III. STELLAR MODELS

An attempt to unravel the complexities of the spectra of the cool Mira stars cannot proceed without realistic model atmospheres. Progress in constructing

these models has been slow due to the contribution of the several million molecular lines to the IR opacity. Review articles by Vardya [32], Carbon [33], and Merrill and Ridgway [34] summarize some of the problems involved.

All of the present cool models assume a static atmosphere in local thermodynamic equilibrium (LTE) with conservation of the energy flux. Only the models of Watanabe and Kodaira [35,36] relax the usual assumption of a plane-parallel atmosphere and treat the spherical case. The main difference between the models is in the treatment of the molecular opacity.

The first models with temperature values low enough to fall in the range of the Mira (Te $\leq$ 2500 K) were constructed by Auman [37]. The only molecular contribution to the opacity was H_2O, and the harmonic mean was used. Johnson [38] included the contributions of H_2O, CO, and CN as straight means averaged over intervals of 100 cm^{-1}. A more sophisticated approach was used by Johnson et al. [39], who included the effects of CN, CO, C_2, TiO, CH^+, NH, MgH, H_2O, and OH. The straight mean was used for H_2O, and all other molecules were treated by opacity sampling [40]. Tsuji [41] treats the opacity using the band model approximation where all the molecular lines are considered as equally spaced and equally intense. The spherical atmospheres of Watanabe and Kodaira [35,36] have H_2O calculated as a straight mean, TiO and OH by the band model approximation, and CO by the just-overlapping approximation.

The emergent flux for all of the above cool stellar models is at much too coarse a frequency grid to show the individual H_2O line profiles. This results, of course, from the opacity smoothing of the H_2O lines. The present approach is to compare the observational spectra on a line-by-line basis with synthetic models. The stellar temperature profile derived from the straight mean H_2O opacity is assumed to be valid, and the radiative transfer equation is solved using the individual H_2O line strengths to predict the high resolution emergent flux. This allows predictions of the stellar effective temperature and H_2O abundances that are closer to actual physical conditions than the isothermal "slab" approximation used in the past for modeling these types of stars. Radial velocities of the H_2O lines can also be measured and give information on the motion and position of the IR molecular region relative to the photosphere and circumstellar envelope.

IV. OBSERVATIONS

Model atmospheres are compared to actual Mira star spectra, and H_2O abundances are determined. Spectra were obtained from both ground-based and airborne spectrometer systems. A least squares fit is made between the observed and predicted spectra to derive the stellar H_2O content for each observation.

A. The Kuiper Airborne Observatory (KAO) Spectra

The research department of the Grumman Aerospace Corporation designed and constructed a Fourier transform spectrometer system to measure Mira star spectra from the 91 cm telescope aboard the NASA Kuiper Airborne Observatory (KAO) at altitudes up to 13.7 km. The KAO program was planned to observe H_2O in Mira stars in spectral regions obscured from ground-based observatories by telluric H_2O (1.9 and 2.7 μm bands) and CO_2 (2.7 μm band). It was found, however, that these regions are also opaque in the Mira star atmospheres, making abundance information almost impos-

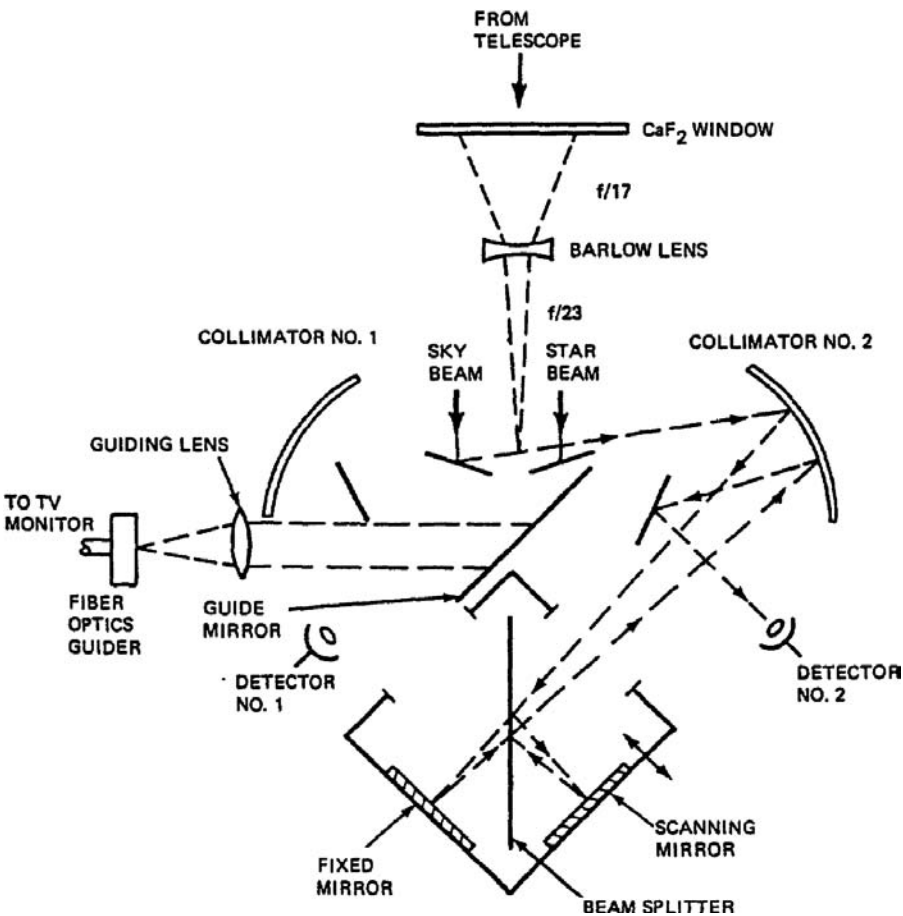

FIGURE 1 Schematic of optical path of Grumman interferometer system.

sible to obtain. Therefore, for this study the 4400–4500 cm^{-1} region containing only the weak H_2O bands were selected for closer examination, because this is a relatively transparent region in the Mira star atmospheres.

The Grumman spectrometer system operates in a dual-beam, dual-detector configuration to give automatic cancelation of the thermal emission due to sky, telescope, and spectrometer optics [27,28,42]. The configuration consists of a pressure bulkhead at the bent Cassegrain focus of the 91 cm telescope on which is mounted the acoustically isolated foreoptics–spectrometer–detector assembly. The telescope is open to the ambient atmospheric pressure (typically 150 mb at 13.7 km). A schematic diagram of the optical path of the Grumman system is shown in Fig. 1. [28,42] and in chapter 14. A CaF_2 window, transparent to infrared radiation, provides the pressure interface between the aircraft cabin and the telescope. A CaF_2 Barlow lens following the window transforms the f/17 telescope beam to f/23, which matches the spectrometer system. The f/23 beam is needed to achieve 1.9 cm^{-1} (apodized) spectral resolution [43]. If the beam acceptance solid angle is greater than f/23, the modulation of the interference fringes will be reduced for increasing displacement of the moving mirror in the spectrometer and the resulting resolution will be degraded from 1.9 cm^{-1}. This is the minimum resolution necessary for accurate H_2O abundance information. The beam splitter is CaF_2 with a silicon overcoating. The detectors are liquid nitrogen–cooled 0.5 mm lnSb cells with cold filters limiting the bandpass to 2800 $cm^{-1} < \nu < 6000\ cm^{-1}$. The observations used two 2.1 arc-min field-of-view apertures, one for star plus sky background and the

TABLE 1 H_2O Abundances in Mira Stars

Star	Phase	Abundance $\times 10^{21}$ mol/cm^2	T (K)	Reference
R Cas	0.48	7.4	1520	29
R Leo	0.00	6	1150	30
	0.14	3		
	0.20	2		
	0.49	25 + 38,−12		
	0.91	6 + 7,−2		
Mira	0.04	2 ± 1	1500	20
	0.67	11 ± 4		
	0.72	6 ± 2		
	0.78	12 ± 5		
	0.86	8 ± 3		
	0.87	7 ± 3		

other with only sky background. The optical centers of the two apertures are separated by 4.3 arc-min.

A HeNe laser of vacuum wavelength 0.6328 μm is sent through the spectrometer and is used to sample the interferogram signal from the star. Hundreds of scans are coherently added together to increase the signal-to-noise ratio (S/N), which is proportional to the square root of the observing time. The velocity of the spectrometers moving mirror is adjusted to give laser pulses every 1.0 ms. The unprocessed interferograms are stored on an analog tape recorder and at the same time digitized and sent to the computer aboard the KAO for processing. A Hamming function is used to apodize and interpolate the intermediate points in the spectra. The maximum path difference is chosen as $L = 0.487$ cm, giving an apodized resolution of 1.9 cm^{-1}.

The results of the observations are shown in Table 1.

REFERENCES

1. Kukarkin, B.V.; Kholopov, P.N.; Efremov, Yu.N.; Kukarkina, N.P.; Kurochkin, N.E.; Medvedeva, G.I.; Perova, N.B.; Federovich, V.P.; Frolov, M.S. General Cat. of Variable Stars. 3rd Ed. USSR Academy Science: Moscow, 1969.
2. Wood, P.R.; Cahn, J.H. Ap. J. 1977, 211, 499.
3. Cahn, J.H.; Wyatt, S.P. Ap. J. 1976, 210, 508.
4. Ikaunieks, J.J. Trans. Astrophys. Lab. Acad. Sci. Latvian SSR 1963, 11, 58.
5. Oswalds, V.; Risley, A.M. Publ. Leander McCormick Obs. 1961, 11, 147.
6. Wyatt, S.P.; Cahn, J.H. Preprint IAP 79-20 Dept. of Astronomy, Univ. of Illinois: Urbana, IL, 1970.
7. Arp, H.; Brueckel, F.; Lourens, J.v.B. Astrophys. J. 1963, 137, 228.
8. Sandage, A.; Smith, L.L. Ap. J. 1966, 144, 886.
9. Gehrz, R.D.; Woolf, N.J. Ap. J. 1971, 165, 285.
10. Deutsch, A.J. In: Mass Loss from Start, Hack, M., Ed.; Reidel: Urbana, IL, 1968; Vol. 1, 285.
11. Donn, B.; Wickramasinghe, N.C.; Hudson, J.P.; Stecker, T.P. Ap. J. 1968, 153, 451.
12. Wickramasinghe, N.C. Mon. Not. Roy. Astro. Soc. 1968, 140, 273.
13. Gilman, R.C. Ap. J. 1969, 155, L185.
14. Wilson, W.J.; Barrett, A.H.; Moran, J.M. Ap. J. 1970, 160, 545.
15. Schwartz, P.R.; Barrett, A.H. Ap. J. 1970, 159, L123.
16. Lo, K.Y.; Bechis, K.P. Ap. J. 1977, 218, L27.
17. Buhl, D.; Snyder, L.E.; Lovas, F.J.; Johnson, D.R. Ap. J. 1974, 192, L97.
18. Gillet, F.C.; Low, F.J.; Stein, W.A. Ap. J. 1968, 154, 677.
19. Kuiper, G.P. Commun. Lun. Planet. Lab (No. 23) 1963, 1, 179.
20. Spinrad, H.; Pyper, D.M.; Newburn, R.L.Jr.; Young, R.L. Ap. J. 1966, 143, 291.
21. Johnson, H.L.; Mendez, M.E. Astrophys. J. 1970, 75, 785.

22. Spinrad, H.; Newburn, R.L., Jr. Ap. J. 1965, 141, 965.
23. Woolf, N.J.; Schwarzschild, M.; Rose, W.K. Ap. J. 1964, 140, 833.
24. McCammon, D.; Munch, G.; Neugebauer, G. Ap. J. 1967, 147, 575.
25. Strecker, D.W.; Erickson, E.F.; Witteborn, F.C. Astrophys. J. 1978, 83, 26.
26. Johnson, H.L.; Coleman, I.; Mitchell, R.I.; Steinmetz, D.L. Commun. Lun. Planet. Lab. (No. 113) 1968, 7, 83.
27. Smith, L.L.; Hilgeman, T. Grumman Aero. Corp. Res. Dept. Memo. RM-684, 1979.
28. Hilgeman, T.; Smith, L.L.; Krassner, J. Grumman Aerospace Res. Dept. Rep. RE-608, 1980.
29. Flaud, J.M.; Camy-Peyret, C.; Maillard, J.P. Ann. Soc. Roy. Sci. Liege. Congress dAstrop. in press.
30. Hinkle, K.H.; Barnes, T.G. Ap. J. 1979, 227, 923.
31. McClatchey, R.A.; Benedict, W.S.; Clough, S.A.; Burch, D.E.; Calfee, R.F.; Fox, K.; Rothman, L.S.; Garing, J.S. AFCRL-TR-73-0096, 1973.
32. Vardya, M.S. Annu. Rev. Astron. Astrophys. 1970, 8, 87.
33. Carbon, D.F. Annu. Rev. Astron. Astrophys. 1979, 17, 477.
34. Merrill, K.M.; Ridgway, S.T. Annu. Rev. Astron. Astrophys. 1979, 17, 9.
35. Watanabe, T.; Kodira, K. Publ. Astron. Soc. Jpn. 1978, 30, 21.
36. Watanabe, T.; Kodira, K. Publ. Astron. Soc. Jpn. 1979, 31, 61.
37. Auman, J.R., Jr. Ap. J. 1969, 157, 799.
38. Johnson, H.R. NCAR Tech. Note, NCAR-TN/STR-95, 1974.
39. Johnson, H.R.; Bernat, A.P.; Krupp, B.M. Ap. J. Suppl. 1980, 236, 320.
40. Sneden, C.; Johnson, H.R.; Krupp, B.M. Ap. J. 1976, 204, 281.
41. Tsuji, T. Astron. Astrophys. 1978, 62, 29.
42. Hilgeman, E.; Smith. Comparison between Infrared Martian Disk spectra and optical properties of terrestrial analogs. Icarus 1978, 35, 209–226.
43. Vanasse, G.A.; Sakai, H. Fourier Spectroscopy in Progress in Optics; Wolf, E., Ed.; John Wiley and Sons, Inc.: New York, 1967; Vol. 6.

20

Optical Properties of Continental Haze and Cumulus and Orographic Clouds Based on Space Shuttle Polarimetric Observations

I. INTRODUCTION

Polarization has been used by astronomers and astrophysicists for more than 100 years for studies of stellar atmospheres, planetary surfaces, and the interstellar medium. However, its use with experimental data for analyzing the terrestrial atmosphere, clouds, and aerosols from space has eluded applications. Lyot [1] and Dollfus [2], in their seminal planetary research, used polarization to characterize planetary clouds and haze.

For many years, the high potential for polarimetry in atmospheric radiation and cloud studies has been recognized. There have been many demonstrations of this potential through qualitative studies [3–13]. To interpret space observations of polarization, one requires complex modeling techniques. This has been a major limitation to the quantitative application of polarimetric techniques for atmospheric and cloud remote sensing. For this reason any cloud and atmospheric measurement program using polarization must be based on a solid quantitative model and detailed polarimetric observations.

Because of the abstruse nature of the use of polarization in cloud studies, this approach is reviewed here. It is then applied to the analysis of Space Shuttle observations of orographic and marine stratocumulus clouds

as well as continental haze. These analyses lead to a definition of the relationship between the optical properties of haze and clouds and their microphysical properties. Essential parts of the approach are a sensitivity or error analysis study and a detailed discussion of data analysis methods to verify the feasibility of using polarization in terrestrial cloud and haze studies.

II. APPROACH

A first in the practical application of polarization was the characterization of the clouds of Venus. Hansen and Hovenir [14] were able to demonstrate the use of polarization to determine the effective radius a, variance b, and index of refraction of the Venus cloud droplets as a function of wavelength from the ultraviolet to the infrared. The effective radius is defined based on the scattering area of a particle, not simply the average radius. This is done because the scattering cross section, σ_{sca}, is the best single parameter describing scattered light. Similarly, b is defined based on the geometrical area of the particle. Hansen and Hovenir's technique used the measured Venus polarimetric phase function, shown for example in Fig. 1 for a wavelength of 0.55 μm. The phase angle is the angle between the solar radiation incident upon the clouds of Venus and the observational direction of earth-based telescopes. A full 180° phase-angle variation was obtainable because Venus is an inner planet (between the earth and the sun).

Figure 1 shows data points of Lyot [1] (○), Coffeen and Gehrels [15] (×), Dolfus and Coffeen [16] (+), and Veverka [17] (Δ). We see the critical dependence of the calculated polarimetric curve on the effective radius a at a wavelength of 0.55 μm, at an effective particle-size variance of 0.07, and at a real index of refraction of 1.44 (sulfuric acid). The best fit is obtained for an effective radius of 1.05 μm. Many calculations are necessary to zero in on the best model. The initial analyses of the clouds of Venus by Hansen and Hovenir were later confirmed and extended by Kawabata et al. [18].

It is essential to understand the philosophy of the technique of Hansen and Hovenir to apply the approach to terrestrial polarimetric modeling. For terrestrial clouds, we do not yet have a technique for obtaining the entire 180° phase function. For Space Shuttle imagery, we obtain only a 32° section of the phase function by virtue of the acceptance angle of the 100 mm lenses used to obtain the imagery. Thus we need to invoke the use of baseline data on clouds and fog to fill in the lack of phase-angle data.

A typical droplet-size distribution of a terrestrial fog is described in terms of submicrometer (unactivated nuclei) and supermicrometer (activated nuclei) droplets. Hindman and Bird [19] and others [20,21] have shown that both submicrometer and supermicrometer droplets occur concurrently in haze and cumulus clouds. Our assumed modeled distribution is thus de-

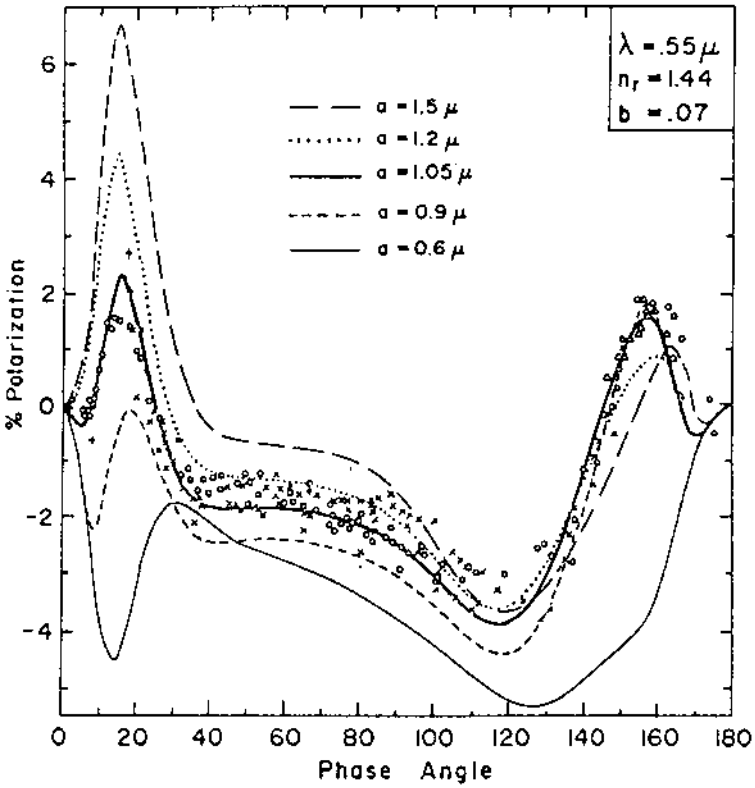

FIGURE 1 Observations and models of the percent polarization versus phase angle of sunlight reflected by the clouds of Venus in the visible wavelength region; the modeling is at a wavelength of 0.55 μm. The percent polarization sensitively defines the effective cloud particle radius *a*, variance *b*, and index of refraction n_r as a function of wavelength. The best fit to the observations (x, +, ○, Δ) are for an effective particle radius a = 1.05 μm. (From Ref. 14.)

scribed in terms of the Hansen–Hovenir [14,22] parameters to include both submicrometer and supermicrometer droplets, where

$$n(r) = \text{constant} \times [r^{(1-3b)/b} \exp(-r/ab)]$$

and

$$\text{constant} = N(ab)^{(2b-1)/b}/\Gamma[(1-2b)/b]$$

Here $a = 1.0$ μm and $b = 0.05$ μm, the size range extends from a radius of 0.0–3.0 μm, Γ is the gamma function, $n(r)\,dr$ is the number of particles per unit

volume, and N is the total number density of particles per unit volume. This size distribution is the Deirmendjian modified gamma function [23], which has been verified for measured size distributions of terrestrial water clouds [14,22].

As we show for clouds (Hawaii) and haze (New Madrid, MO), the percent polarization is significantly different for large droplets compared with small droplets and for pure water droplets compared with absorbing droplets. The value of the real refractive index also has an effect on the polarimetric curve. Generalizations as to the effect of parametric variations are difficult because of the detailed involvement of the parameters. Each application must be considered in detail, but the overall approach is identical with that used for the clouds of Venus.

III. EXPERIMENTAL PROGRAM

The data acquisition system uses two Hasselblad cameras, with a polarization analyzer on each camera and with the polarization filters oriented mutually perpendicular to each other [12]. The photographic imagery was taken through the overhead window of the Space Shuttle. For the Hawaii imagery, the orientation of the polarization analyzers was within $\pm 5^\circ$ of the principal plane (based on the maximum scene brightness seen in the camera viewfinder), and the analyzers themselves were perpendicular to better than 1° [12]. The three-color images were obtained in red, green, and blue with Ektachrome 5036 film (ASA 200). The spectral response is close to that shown in Figs. 8–10 of Ref. 3 for Ektachrome EH film (ASA 160). Subsequent digitization of the photographic imagery was accomplished at the National Aeronautics and Space Administration Video Digital Analysis Systems laboratory [12]. The digitization is necessary to allow application of a numerical algorithm for the analysis of the photographic images. Because the percent polarization is the ratio of the first two Stokes parameters [3], the spectral response of the film is canceled, provided the development process is carefully controlled. This is accomplished by quality control in the NASA (Houston, TX) photographic laboratory.

Color separation was achieved through the use of dichroic interference filters [12]. The red filter has 50% transmission at 585 nm, with 80% transmission at longer wavelengths and $\leq 1\%$ transmission at wavelengths of 380–550 nm. The green filter has 50% transmission at 505 and 575 nm, with $\leq 1\%$ transmission at 380–460 nm and 600–730 nm. Peak transmission at 540 nm is 70%. The blue filter has 50% transmission at 505 nm, 75% transmission at 390–480 nm, and $<1\%$ transmission at 540–750 nm. The resulting overall spectral function is the convolution of the film response and the color separation filters. Experimental limitations restricted the precise definition in this program.

Two areas were imaged in the current program: (1) the island of Hawaii and environs (photographs STS-51I-5/31-141 and STS-51I-50/50-46) and (2) the farmland area near New Madrid, Missouri (STS-28-85-033 and STS-28-86-033).

Figure 2 identifies the first area, Hawaiian orographic (mountain-produced) and marine stratocumulus clouds, and the volcanic ash calibration area. Figures 3–5 show the red, green, and blue equipolarimetric contour maps superimposed on Fig. 2. (The original publication [12] of the Hawaii image and contours required a 79% reduction of the contours to achieve perfect registration with the image.) The inclusion here of the Hawaii image and contours is necessary to correct the registration error in the previous paper [12].

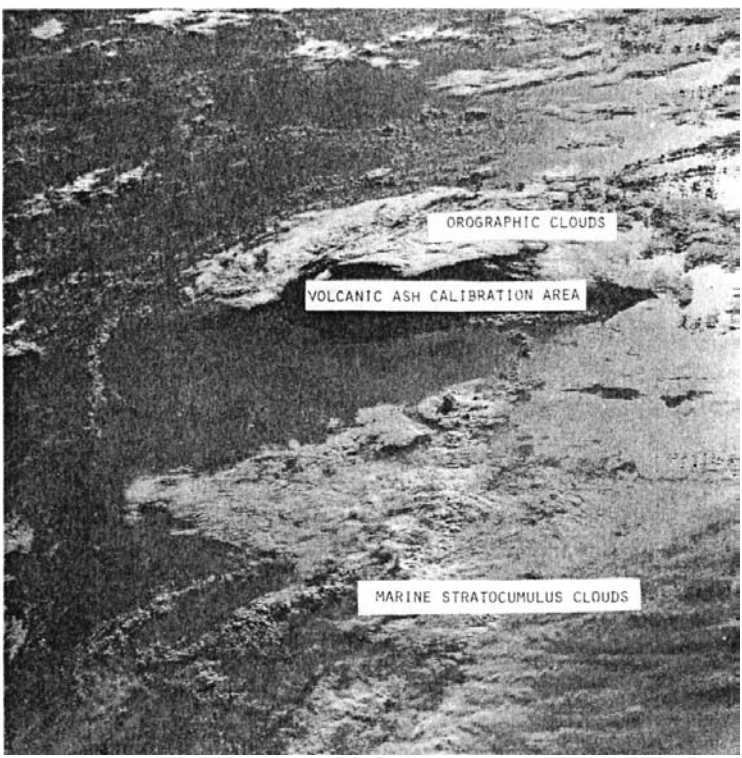

Figure 2 Island of Hawaii and environs observation area showing marine stratocumulus and orographic clouds. Also shown is the volcanic ash land mass used for calibration.

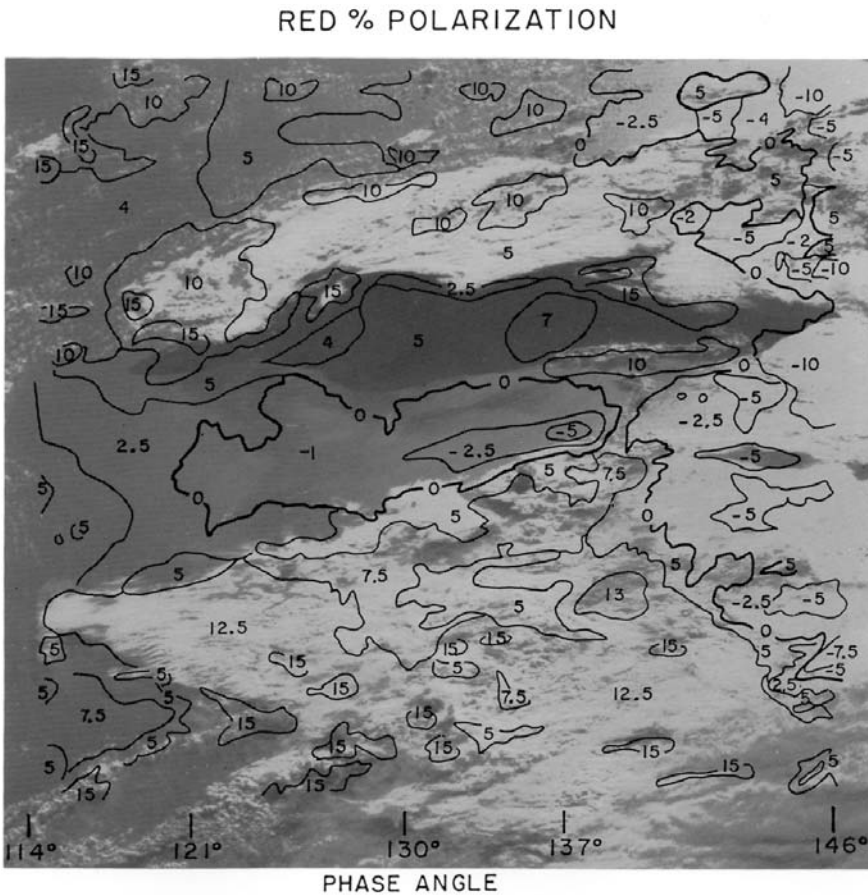

FIGURE 3 Equipolarimetric map of red spectral region overlaid on the imagery of Fig. 2.

The accuracy of the Hawaii polarimetric imagery is ±20% of each value of polarization computed. This was verified by the use of laboratory polarimetric and photometric measurements of Hawaiian volcanic ash in comparison with the Space Shuttle polarimetry observed over central Hawaii [12], taking into account the phase angle of the observations.

The other program studied was that of New Madrid, Missouri. The area is shown on the polarimetric 80 m resolution green band image in Fig. 6. The region is composed of many farms, which are identified by the characteristic polarimetric imagery corresponding to the crop type. The area is

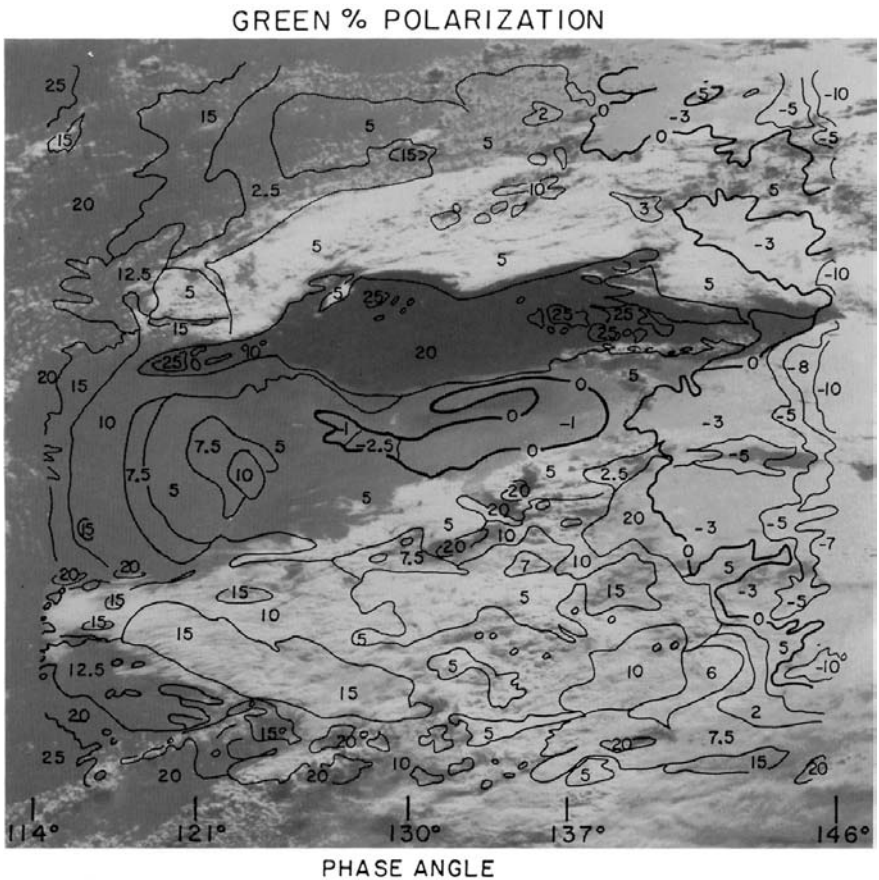

FIGURE 4 Equipolarimetric map of green spectral regions overlaid on the imagery of Fig. 2.

covered by a summer (August) haze; this can be seen from Figs. 7 and 8, which show the distribution of frequencies of percent polarization values and photometric levels in the digitized area. The surface polarizations may range from 0 to 100%, and the effect of the overlying atmosphere is to both polarize and depolarize the radiation emanating from the surface and to add polarization to the scattered incident solar radiation. The effect is to produce a shift (and compression) of the distribution of polarization in the red, green, and blue spectral regions, resulting in a shift of the distribution centroids from the continental haze. Thus in the blue spectral region, atmospheric scattering is greatest, photometric levels are highest, and apparent surface

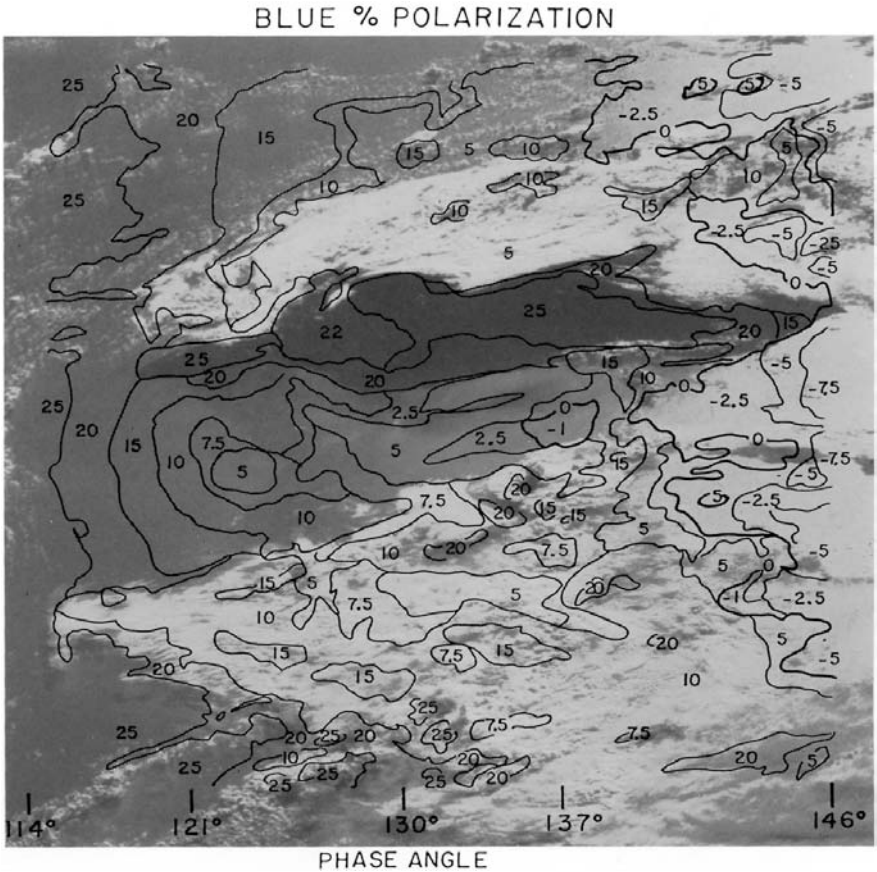

FIGURE 5 Equipolarimetric map of blue spectral region overlaid on the imagery of Fig. 2.

percent polarization is lowest (highest atmospheric depolarization); furthermore, in the red spectral region atmospheric scattering is lowest and the terrestrial surface percent polarization is more easily transmitted through the atmosphere (least atmospheric depolarization). The accuracy of the New Madrid polarimetric imagery is significantly better than that for Hawaii. The absolute accuracy is $\pm 1\%$ and the precision is $\pm 0.1\%$ as a result of improvements in data analysis techniques [24]. The use of in situ measurements on a sandbar (upper portion of Fig. 6) in the Mississippi River in comparison with Space Shuttle polarimetric and photometric observations allowed us to deduce atmospheric contributions; the red, green, and blue polarimetric

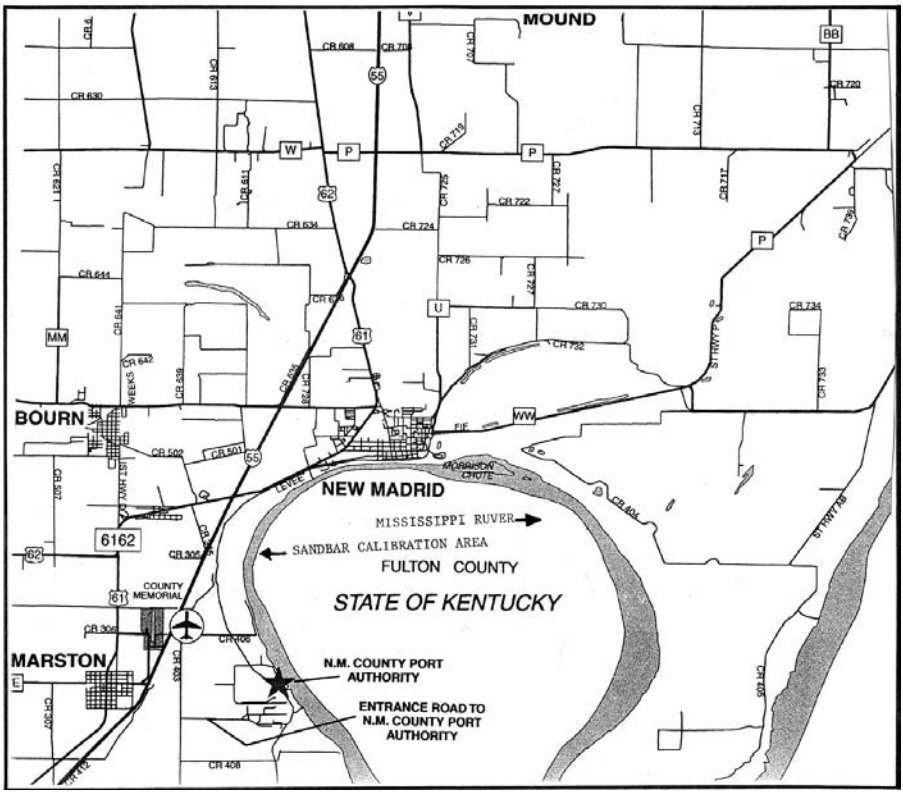

FIGURE 6 Green band 80 m resolution polarimetric image of New Madrid, Missouri, observation area. The Mississippi River sandbar calibration area is also shown.

contributions were 25.1%, 18.8%, and 9.3%, and the corresponding relative photometric contributions were 0.056, 0.166, and 0.271 [24].

The locations of the centroids of the polarimetric and photometric distributions should be related to the optical depths* of the atmosphere (the optical depth of the atmosphere would be expected to be inversely proportional to the percent polarization) [25].

* Optical depth, τ, is related to the transmission of the atmosphere, T, by the relation $T = \exp(-\tau)$.

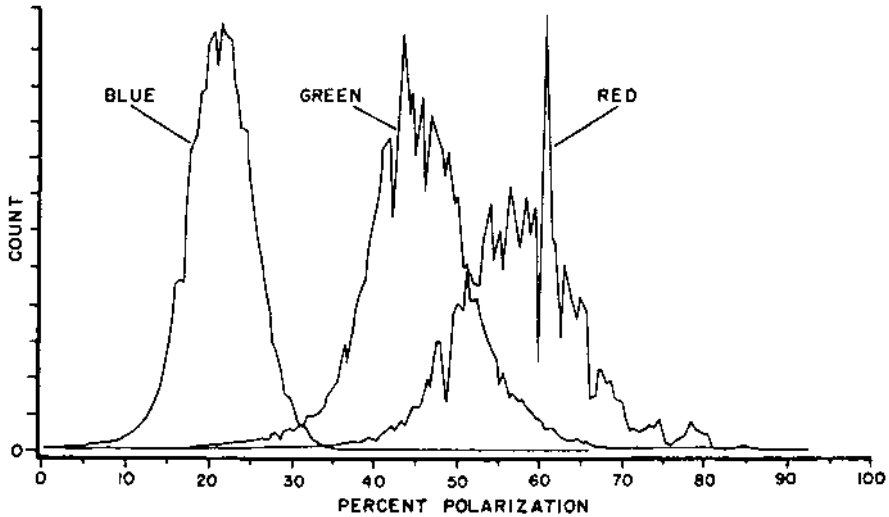

FIGURE 7 Plot of frequency distribution of percent polarization of New Madrid, Missouri, observation area. The effect of continental haze is to displace the distribution to lower polarization.

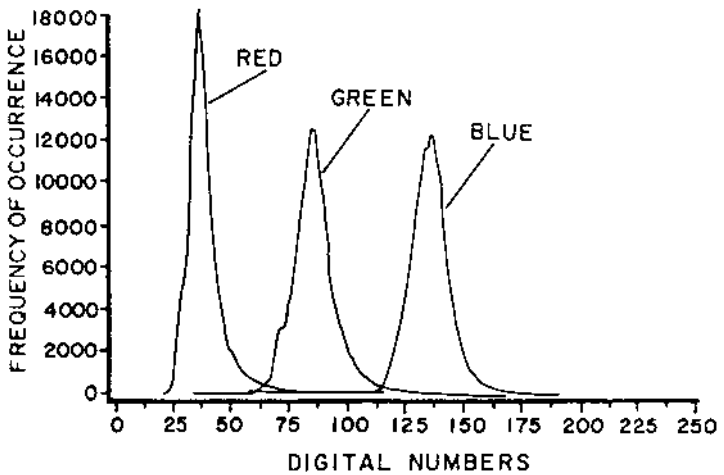

FIGURE 8 Plot of frequency distribution of photometric levels of New Madrid, Missouri, observation area. The effect of continental haze is to displace the distribution to higher brightness levels.

IV. CLOUD AND HAZE MODELS

The program used for the cloud and haze models was originally described by Hansen [22] and Hansen and Travis [26]. It was developed to describe the scattering and absorption of solar radiation by clouds. We adapted this program to analyze terrestrial clouds and haze with the help of Travis.

The program combines the parallel effects of Rayleigh scattering with the haze multiple scattering. Computations of the scattering and absorption by individual spherical droplets is accomplished using the Mie formulation, in which a particle size distribution is superimposed. The calculated scattering and absorption by the Mie particles (of complex index of refraction) is represented by the four Stokes parameters.

To account for multiple scattering, a doubling technique is used. The essence of the technique is such that if the reflection and transmission of each of two layers is known, the reflection and transmission of the combined layer are obtained by computing successive reflections back and forth between the two layers. If the two layers are chosen to be identical, the properties of a thick homogeneous layer can be constructed rapidly in a geometric (doubling) manner.

The model assumes no bottom layer (i.e., a completely absorbing surface). This assumption is valid for large optical depths of clouds ($\sim$10), however, for small optical depths (0 to $\sim$2), we require that the underlying surface have very low reflectance (of the order of a few percent). This assumption is not valid for the New Madrid imagery. For the New Madrid modeling, the optical depths are small, and the model can be used only to account for the atmospheric contributions to the photometry and polarization as previously determined [24].

The input angles of incidence and scattering were chosen to match the geometry of observation, allowing for the 32° acceptance angle of the Hasselblad cameras, and the azimuth angles were chosen accordingly. The output consisted of the parameters of percent polarization, the angle of the plane of polarization, and the four Stokes parameters of intensity, polarization difference, relative position of the plane of polarization, and circular polarization.

The Rayleigh scattering optical depth (τ) of the atmosphere is introduced with the air expression given by Hansen [22]:

$$\tau = 0.008569\lambda^{-4}(1 + 0.0113\lambda^{-2} + 0.00013\lambda^{-4}), \qquad \lambda \text{ in } \mu\text{m} \tag{1}$$

Comparisons of the present modeling results with the Monte Carlo calculations of Kattawar and Plass [6] for homogeneous cloud layers indicate agreement in polarization for their nimbostratus model in polarization for optical depths of 1 and 10. Dense clouds have optical depths of the order

of 10 [5]. The orographic clouds modeled here are shown by radiosonde observations to be physically 500 m thick above the Hilo, Hawaii, airport [12]. The relative cloud optical depth sensitivity for the Hansen [22] and Hansen–Travis [26] models agrees with that of Kattawar and Plass [6] for dense nimbostratus clouds.

V. CLOUD AND HAZE DATA ANALYSIS

A. Hawaii—Marine Stratocumulus and Orographic Clouds

The results of the Hawaii cloud modeling are shown in Figs. 9–11 with the modeled droplet size distribution described by Hindman and Bird [19] and others [20,21]. The refractive portion of the index of refraction is that for water at wavelengths of 0.435, 0.540, 0.600, and 1.00 μm. The range of phase angles is 117–153°.

Figure 9 is to be compared with Figs. 3, 4, and 5. As Figs. 3–5 show, the marinestratocumulus and orographic clouds have measured polarizations

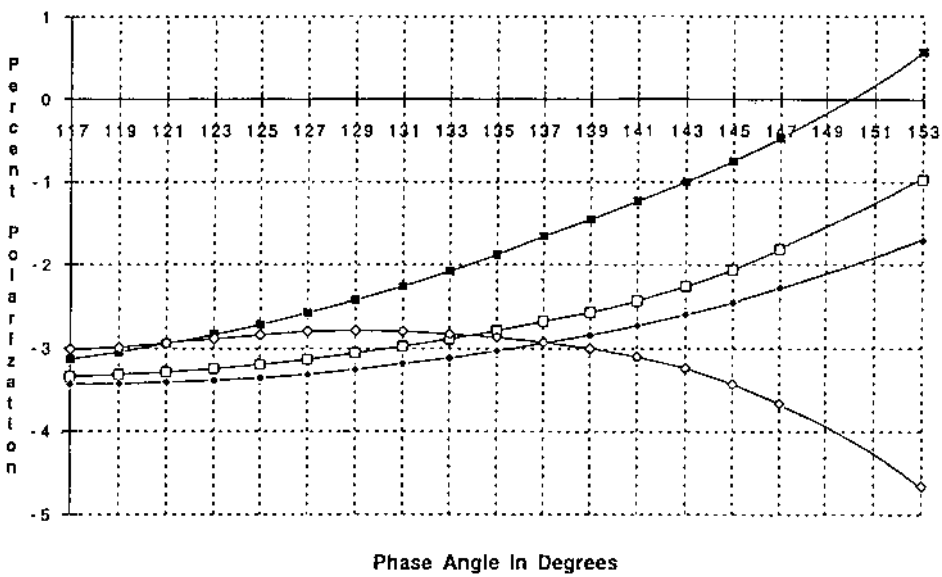

FIGURE 9 Hawaii cloud models of percent polarization versus phase angle for optical depth of 10 at four wavelengths: (■) 0.435 μm; (□) 0.540 μm; (♦) 0.600 μm; (◇) 1.00 μm. Models are for nonabsorbing marine stratocumulus and orographic clouds, which produce generally negative polarization.

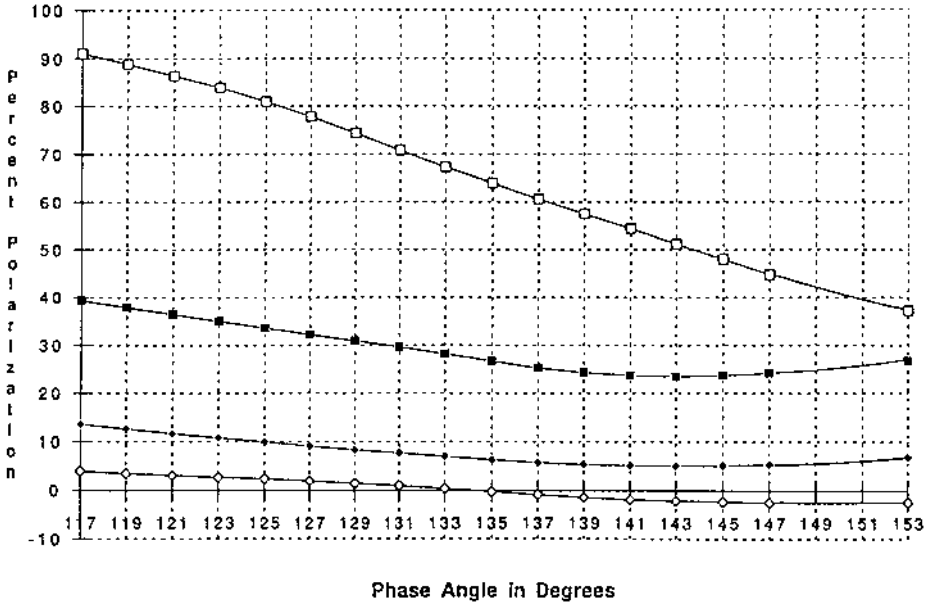

FIGURE 10 Hawaii cloud models of percent polarization versus phase angle for highly absorbing clouds (n_i = 0.1) at four wavelengths (optical depth = 10): (■) 0.435 μm; (□) 0.540 μm; (♦) 0.600 μm; (◇) 1.00 μm.

ranging from +15% to −10%. However, from Fig. 9 it can be seen that for the assumed particle size distribution at a wavelength of 0.600 μm, the polarization ranges from −3.4% to −1.7%. Therefore the measured −10% polarization at 146° and +15% polarization at 121° are unexplained by this assumed model.

If the particles were highly absorbing with the assumed particle size distribution, then the polarization would be +12% at 121° and +5% at 141° as shown in Fig. 10. This result also disagrees with measurements.

Because the experimental results do not agree with the model, in an effort to determine parametrically the specific dependence of the models on particle size, let us now consider separately the effect of small nonabsorbing particles (effective radius 0.1 μm) and large nonabsorbing particles (effective radius 50 μm) as shown in Fig. 11. In this figure the viewing angle is the abscissa instead of the phase angle. This presentation is appropriate because the phase angle depends on the viewing angle, and the phase angle has a smaller range for the extreme (±32°) camera rays. However, the model inputs are the (constant) solar incident angle and the (variable) viewing

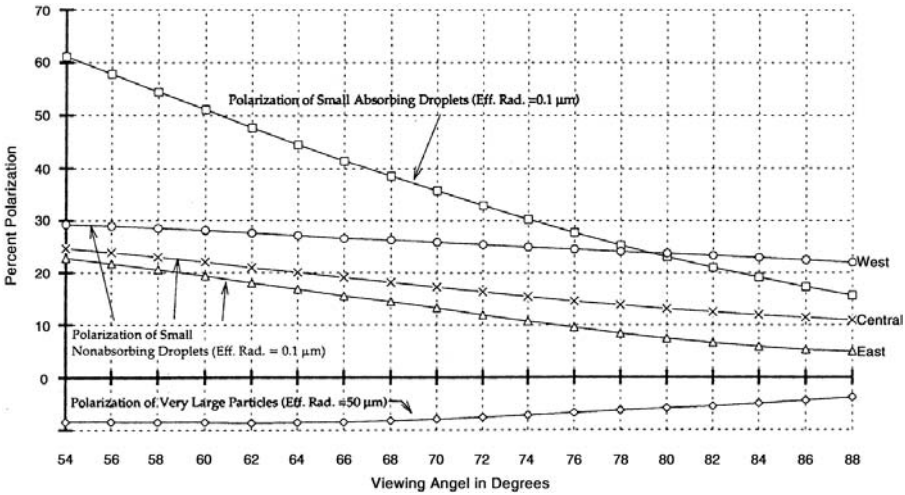

FIGURE 11 Parametric study of the modeled polarimetric properties at a wavelength of 0.600 μm of small (0.1 μm effective radius) and large (50 μm effective radius) droplets, showing the effect of absorption on 0.1 μm droplets. Also shown is the viewing angle effect proceeding from the western area (bottom) to the eastern area (top) of the Hawaii clouds.

angle, which then determine the phase angle. Thus the viewing angle (the angle between the normal and the terrestrial surface and the viewing direction) is the fundamental variable.

In Fig. 11, for the optical depth of 10, the largest droplets produce −9% polarization at a 54° viewing angle (117° phase angle) and −3% polarization at an 89° viewing angle (146° phase angle) at the 0.600 μm wavelength, whereas the small droplets (central area) produce a polarization range from +25% to +12% for the same range of viewing (phase) angles. Thus the results suggest that in the red band (Fig. 3), for the orographic clouds with polarizations ranging from −5% to +10%, the areas with +5% to +10% polarizations are predominantly composed of submicrometer water droplets, whereas the more westerly orographic clouds with −5% and −2% polarization are primarily composed of supermicrometer water droplets.

The marine stratocumulus clouds in the lower portion of the photograph have polarization of +5% to +15%; the positive polarization indicates predominantly submicrometer droplets, with the highest positive polarization indicating the dominance of the smallest submicrometer particles, which is in turn indicative of cloud formation with submicrometer

droplets being activated. If the particles were highly absorbing, the percent polarization would become much greater as shown in Fig. 11.

Submicrometer and supermicrometer droplets were inferred to exist in the Hawaii clouds from the modeling. The assumed droplet model underestimates the very small submicrometer particles compared with atmospheric measurements (Fig. 12), for example, but serves as a reasonable trial hypothesis. The figure is generally representative of clouds and haze but is not definitive for the Hawaii area. Because no atmospheric air truth was available, any droplet size distribution would be only an assumption. However, our model necessarily included both submicrometer and supermicrometer particles. A bimodal model would probably be more appropriate, again contingent on atmospheric ground truth at the time of the polarimetric observation.

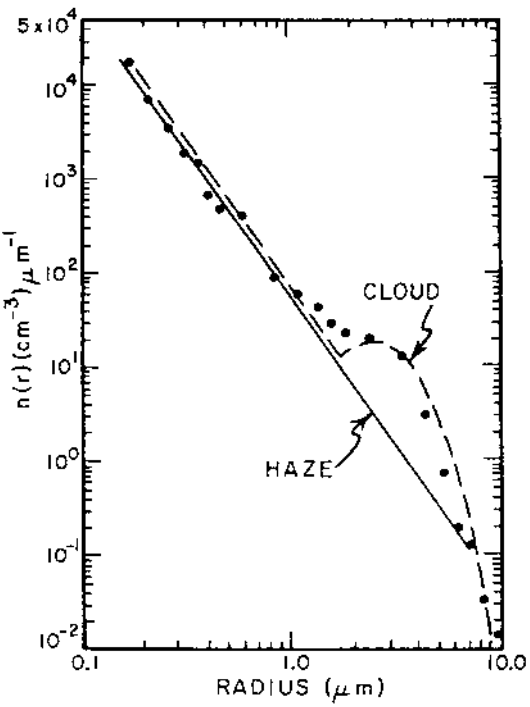

FIGURE 12 Representative cloud droplet size distribution measurement (dots) on 16 July 1976 at Trinidad, California. Submicrometer haze and supermicrometer cloud droplets are present. The actual particle size distribution during the polarization measurements was not available. (Adapted from Ref. 19.)

There is also an east–west asymmetry in Figs. 3–5; the upper portions of these figures are easterly (orographic clouds), and the bottom portions are westerly (marine stratocumulus clouds). The easterly percent polarizations are generally lower than the westerly percent polarizations; this is also shown by the modeling (Fig. 11). The highest positive polarizations occur at viewing angles near 54° (phase angles near 117°) as shown in Fig. 3.

If we refer to the green and blue percent polarizations in Figs. 4 and 5, there do not appear to be any significant differences between them and the red percent polarization in Fig. 3. Figure 9 indicates that the negative polarimetric characteristics are substantially similar at 0.435, 0.540, and 0.600 μm; at 1.0 μm (not observed experimentally) the polarization goes strongly negative at the larger phase angles. For strongly absorbing droplets the percent polarization becomes strongly positive (Fig. 10).

Calculations similar to those for Fig. 11 for cloud optical depths of 10 were made at wavelengths corresponding to the green and blue bands, with results similar to those shown at $\lambda = 0.600$ μm in Fig. 11. The three images are not precisely similar, and variations are probably caused by calibration effects.

B. New Madrid, Missouri, Haze

The farm area surrounding New Madrid, Missouri, shown in Fig. 6, produced the polarization and photometric distributions of Figs. 7 and 8. Through the use of the Mississippi River sandbar areas shown in Fig. 6, we are able to establish that the offsets of the polarimetric and photometric centroids in Figs. 7 and 8 are the result of both atmospheric scattering of haze droplets and the polarization and photometry of the terrestrial surface. The haze droplets were assumed to be composed of submicrometer and supermicrometer droplets as in the initial assumed droplet size. The centroid locations are listed in Table 1.

TABLE 1 Location of Centroids of Polarimetry and Photometry

Wavelength (μm)	Polarimetry (%)	Photometry (digital number)
0.600	57	35
0.540	45	88
0.435	21	151

Because of the model requirement that the underlying surface be nonreflecting, which is not valid for the New Madrid area, the Hansen–Travis model was used in a different manner. We required that the model supply the polarimetric atmospheric contributions in the red, green, and blue spectral regions of 25.1%, 18.8%, and 9.3% and the corresponding relative photometric contributions of 0.056, 0.166, and 0.271 [24]. These necessary contributions had been determined through the use of a sandbar calibration area in the Mississippi River.

Calculations were performed with the model for a range of optical depths in the red, green, and blue spectral regions. Typical results are shown in Figs. 13 and 14. By interpolating between the polarimetric curves (and photometric curves), the required atmospheric contributions yield the modeled total optical depths shown in Table 2. When the Rayleigh contribution is eliminated, the haze optical depths can be found (Table 2). The spectral variation is $\lambda^{-1.9}$, which is reasonable for continental atmospheric haze. Deirmendjian (Ref. 23, Fig. 29) also shows a wavelength variation of $\lambda^{-1.9}$ for his haze model, in agreement with the result of Table 1.

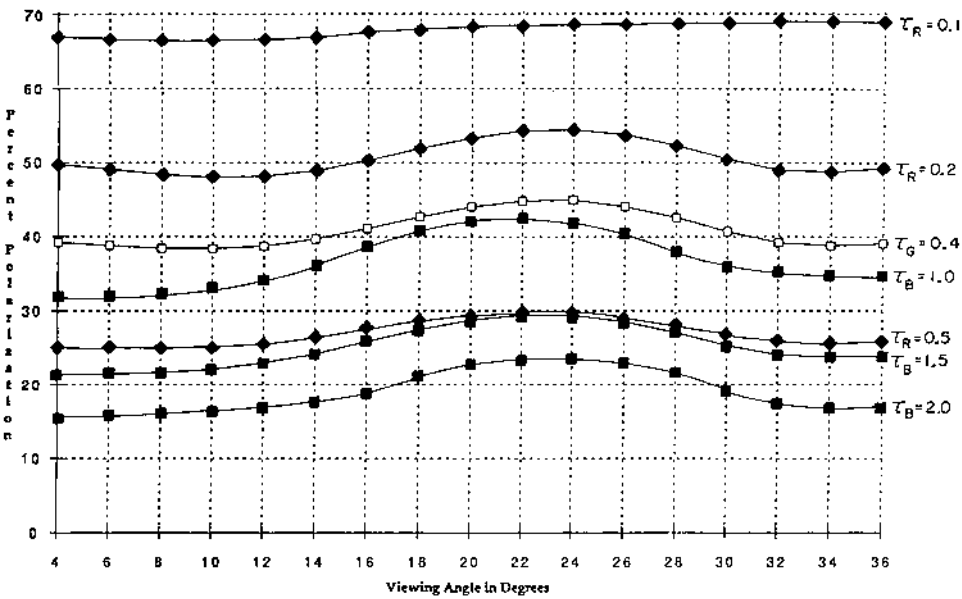

FIGURE 13 Plot of modeled percent polarization of atmosphere versus viewing angle for the New Madrid, Missouri, observation area at the three observational wavelengths: Red, λ = 0.600 μm; green, λ = 0.540 μm; blue, λ = 0.435 μm. τ, optical depth.

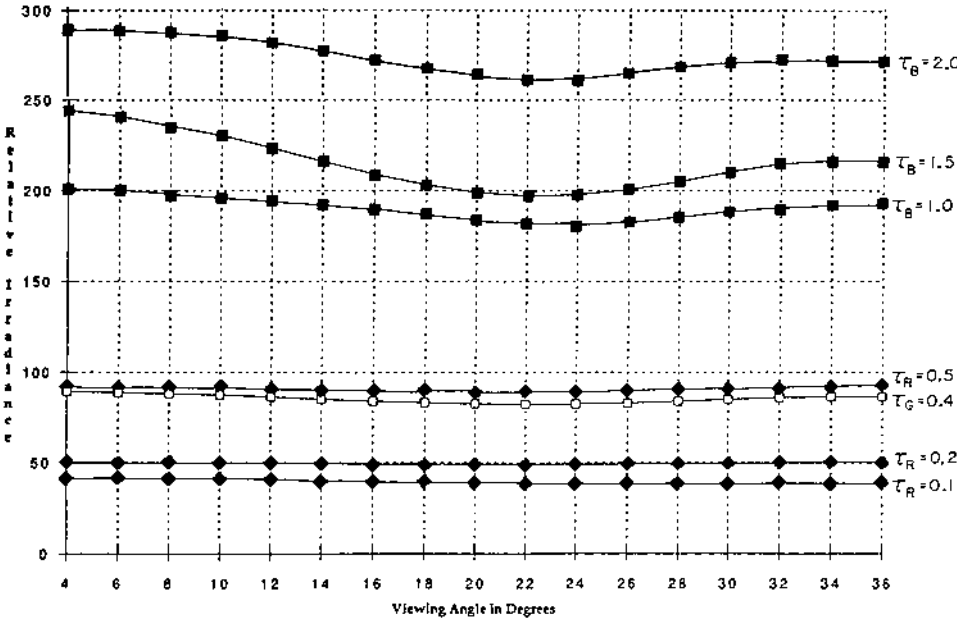

FIGURE 14 Plot of modeled relative irradiance of atmosphere versus viewing angle for the New Madrid, Missouri, observation area at the three observational wavelengths: Red, λ = 0.600 μm; green, λ = 0.540 μm; blue, λ = 0.435 μm. τ, optical depth.

It can be seen that the polarimetric sensitivity is greater than the photometric sensitivity, thus making polarimetry a superior discriminant.

The phase angle effect of percent polarization and photometry is not included in Figs. 7 and 8. The inclusion of the phase angle effect on polarimetry is very difficult because of the inhomogeneity of terrestrial farm areas, and the phase angle effect is generally different for each area. Furthermore,

TABLE 2 Modeled Optical Depths of New Madrid Area Haze

	Optical depth		
Wavelength (μm)	Total	Rayleigh	Haze
0.600	0.15	0.0682	0.08
0.540	0.20	0.105	0.10
0.435	0.40	0.254	0.15

the phase angle range in the Space Shuttle data is limited to 32° out of a range of 180° because of the limited acceptance angle of the camera lenses.

With the use of a polarimetric model, including the effect of the polarimetric and photometric phase functions of the underlying surface, it should be possible to deconvolve the phase function because each farm area could be characterized in terms of a specific phase function. This surface-modeling research is in progress [27].

VI. DISCUSSION

The feasibility of applying the Hansen–Travis radiative transfer program [25] to model Space Shuttle polarimetric observations has been examined for a wide range of droplet sizes. This model was used for the Hawaiin cloud models with optical depths of 10 as well as for New Madrid, Missouri, haze with calculated total optical depths in the range 0.08–0.15. We have no precise concurrent atmospheric air truth to justify the model for each application, although we have the Hilo radiosonde data [12]. It is important that observations of the cloud droplet size distributions be made during the polarimetric measurements. However, the polarimetric modeling confirms the hypothesis that cumulus clouds and haze are composed of both submicrometer and supermicrometer droplets. The limitation that the underlying surface must have zero reflectance restricts the application of a simple model except when suitable associated atmospheric photometric and polarimetric contributions are separately determinable (i.e., with the New Madrid data).

Because of the limited acceptace angle (32°) of the Hasselblad cameras, the entire polarimetric phase function (180°) is not obtained. The more angular phase function data that are available, the more accurate the polarimetric modeling will be. A scanning polarimeter would be the answer to obtaining more angular data. However, scanners introduce polarization unless a compensated two-mirror unit is used [28], as in the proposed Earth Observing Scanning Polarimeter [29]. Another cloud program could supply valuable cloud data if a polarization measurement program were included; this is not now done in the FIRE program.*

* FIRE (First International Satellite Cloud Climatology Program Regional Experiment), National Climate Program Office, Room 108, 11400 Rockville Pike, Rockville, MD 20952.The FIRE program is a multiagency effort conducted by NASA Langley Research Center, Hampton, VA 23655-5225. The program was originally a NASA program at Greenbelt, Maryland but is succeeded by programs designated with various acronyms such as CRYSTAL, FACE, SHEBA. A contact is professor David Randall, Colorado State University.

VII. CONCLUSIONS

We have shown that the use of percent polarization allows the characterization of marine stratocumulus clouds, orographic clouds, dense marine haze, and continental haze with respect to several properties.

The presence of submicrometer and supermicrometer droplets in cumulus clouds and haze has been inferred with polarimetry.

The particle size distribution within marine stratocumulus and orographic clouds is evident from polarimetry.

If clouds or haze contain highly absorbing particles such as aerosols, the result is high positive polarization in the visible spectral region for the geometry of the present Space Shuttle observations in the Hawaiian Island area.

An atmospheric optical depth as a function of wavelength can be deduced for continental haze with polarimetry from space. An accurate determination of the optical depths of the atmosphere is essential for climate modeling, aircraft visibility studies, and ground target identification.

It is necessary for simultaneous air truth measurements of clouds and haze to be available during polarimetric measurements to verify the deductions from polarimetry. The verified polarimetric measurements can then be used to determine properties of clouds and haze in the absence of air truth measurements.

High resolution is desirable for cloud observations, although haze is not as variable as cloud structure.

The inclusion of a suitable polarimetric surface model with the atmospheric radiative transfer model is necessary.

ACKNOWLEDGMENTS

We acknowledge the help and suggestions of L. Travis in the development of the present application of the modeling program. We thank R. Morales of the City University of New York (CUNY) Microcomputer Center for his help in producing the computer graphics and the CUNY computing staff for help in adapting programs to the CUNY system. We also thank the Kona Airport personnel and A. W. Hogan for meteorology discussions. We also thank the reviewers for their helpful comments and suggestions, especially H. Gordon.

This research was performed under National Aeronautics and Space Administration Contract NAS 9-17900, Lockheed Engineering and Sciences Company, Houston, Texas.

REFERENCES

1. Lyot, B. Research on the polarization of light from planets and some substances. Ann. Observatoire Paris Sect. Meudon. 8(1) (1929); Tech. Trans. TTF-187. NASA: Washington, DC, 1964.
2. Dollfus, A. Polarization de la lumiere renvoyee par les corps solides et les nuages naturels. Ann. Astrophys. 1956, 19, 83–113.
3. Egan, W.G. Photometry and Polarization in Remote Sensing; Elsevier: New York, 1985.
4. Deirmendijan, D. Scattering and polarization, properties of water clouds and hazes in the visible and infrared. Appl. Opt. 1964, 3, 187–196.
5. Coulson, K.L. Polarization and Intensity of Light in the Atmosphere; Deepak: Hampton, VA, 1988.
6. Kattawar, G.W.; Plass, G.N. Degree and direction of polarization of multiple scattered light. 1: Homogeneous cloud layers. Appl. Opt. 1972, 11, 2851–2865.
7. Kattawar, G.W.; Plass, G.N.; Catchings, F.E. Matrix operator theory of radiative transfer. 2: Scattering from maritime haze. Appl. Opt. 1973, 12, 1071–1084.
8. Kattawar, G.W.; Plass, G.N.; Guinn, J.A. Jr. Monte Carlo calculations of the polarization of radiation in the earth's atmosphere ocean system. J. Phys. Oceanogr. 1973, 3, 353–372.
9. Kattawar, G.W.; Plass, G.N. Asymptotic radiance and polarization in optically thick media: ocean and clouds. Appl. Opt. 1976, 15, 3166–3178.
10. Takashima, T.; Masuda, K. Degree of radiance and polarization of the upwelling radiation from an atmosphere–ocean system. Appl. Opt. 1985, 24, 2423–2429.
11. Dave, J.V. Intensity and polarization of the radiation emerging from a plane-parallel atmosphere containing monodispersed aerosols. Appl. Opt. 1970, 9, 2673–2684.
12. Egan, W.G.; Johnson, W.R.; Whitehead, V.S. Terrestrial polarization imagery obtained from the Space Shuttle: characterization and interpretation. Appl. Opt. 1991, 30, 435–442.
13. Coulson, K.L.; Whitehead, V.S.; Campbell, C. In Polarized Views of the Earth from Orbital Altitude. Blizzard, M.A., Ed. Ocean Optics VIII. Proc. Soc. Photo-Opt. Instrum. Eng. 1986, 637, 35–41.
14. Hansen, J.E.; Hoveni, J.W. Interpretation of the polarization of Venus. J. Atmos. Sci. 1974, 31, 1137–1160.
15. Coffeen, D.L.; Gehrels, T. Wavelength dependence of polarization. XV. Observations of Venus. Astron. J. 1969, 74, 433–445.
16. Dollfus, A.; Coffeen, D.L. Polarization of Venus. I. Disk observations. Astron. Astrophys. 1970, 8, 251–266.
17. Veverka, J. A polarimetric search for a Venus halo during the 1989 inferior conjunction. Icarus 1971, 14, 282–283.
18. Kawabata, K.; Coffeen, D.L.; Hansen, J.E.; Lane, W.A.; Sato, M.; Travis, L.D. Cloud and haze properties from Pioneer Venus polarimetry. J. Geophys. Res. 1980, 85, 8129–8140.

19. Hindman, E.E. II; Bird, R.E. Effects of haze droplets in fogs and clouds on the propagation of electromagnetic radiation. J. Rech. Atmos. 1980, 14, 385–389.
20. Squires, P. The microstructure and colloidal stability of warm clouds. Tellus X 1958, 256–261.
21. Cooper, W.A. In-situ observations of warm cloud microstructure. Preprints of Symposium on Role of Clouds in Atmospheric Chemistry and Global Climate Am. Meteorol. Soc.: Boston, MA, 1989; pp. 316–319.
22. Hansen, J.E. Multiple scattering of polarized light in planetary atmospheres. Part II. Sunlight reflected by terrestrial water clouds. J. Atmos. Sci. 1971, 28, 1400–1426.
23. Deirmendjian, D. Electromagnetic Scattering on Spherical Polydispersions; Elsevier: New York, 1969.
24. Egan, W.G.; Israel, S.; Johnson, W.R.; Whitehead, V.S. High-resolution space-shuttle polarimetry for farm crop classification. Appl. Opt. 1992, 31, 1542–1548.
25. Dave, J.V.; Furukawa, P.M. Intensity and polarization emerging from an optically thick atmosphere. J. Opt. Soc. Am. 1966, 56, 394–400.
26. Hansen, J.E.; Travis, L.D. Light scattering in planetary atmospheres. Space Sci. Rev. 1974, 16, 527–610.
27. Egan, W.G.; Maciulaitis, A. Modeling the Stokes parameters of surfaces. In Annual Meeting; OSA Tech. Vol. 15. Dig. Ser. Opt. Soc. Am.: Washington, DC, 1990; 260.
28. Egan, W.G. Proposed design of an imaging spectropolarimeter/photometer for remote sensing of earth resources. Opt. Eng. 1986, 25, 1155–1159.
29. Earth Observing System Reference Handbook; NASA Goddard Space Flight Center: Greenbelt, MD, 1990.

21

Volumetric Scattering and Absorption by Aerosols: Parametric Sensitivity in Mie Modeling and Comparisons to Observations

I. INTRODUCTION

Aerosols strongly affect visibility in the visible portion of the spectrum [1–3]. A wide range of values of the volume scattering and absorption coefficients has been reported [4]. The lack of agreement between observers can arise from accuracy limitations of the measurement instrumentation as well as variations in the aerosol sample and the sampling time and location. This serious problem was approached by the convening of the First International Workshop on Light Absorption by Aerosol Particles with the object of establishing instrumentation errors for various techniques. Various instruments were exposed to standardized aerosols, some typical of those in the atmosphere. These included ambient, Arizona road dust, ammonium sulfate [$(NH_4)_2SO_4$], carbon (soot), methylene blue (a dye), and mixtures of these. The result of this conference have been reported separately [5,6].

The purpose of this chapter is to use the experimental aerosol data of the workshop to predict aerosol instrumentation response and compare the predicted response with actual measurements. The measured aerosol size distribution and number density are used in Mie scattering calculation with measured optical complex indices of refraction to determine the volume scattering and absorption coefficients. In the course of these calculations the

size distribution and number density as well as the complex index of refraction are varied, and the sensitivity to these parameters is determined. Where disagreements exist between the calculated and measured volume scattering and absorption coefficients, a comparison and evaluation are made to assess whether the cause is a calculation inaccuracy or an instrumentation problem. Specific areas of improvement are suggested.

II. COMPUTATIONAL APPROACH

The Mie theory was developed to characterize the scattering and absorption by spherical particles with known optical complex index of refraction [7,8]. By imposing a size distribution and number density the volume absorption and scattering can be determined. A suitable program for calculating Mie scattering and absorption was developed by Dave [9]. The first portion of the program calculates the efficiency factors for scattering $Q_s(m,\chi)$ and absorption $Q_a(m,\chi)$ for particles with a specified index of refraction m over a designated size range χ. The size parameter χ equals $2\pi a/\lambda$, where a is the particle radius and λ is the radiation wavelength. The output is a tape that is used as input to the second portion of the program, which imposes a size distribution and number density to calculate the volume scattering and absorption coefficients. Three number density functions $n(r)$ are selectively available in the program; the quantity $n(r)$ represents the number of particles per cubic centimeter per unit radius (arbitrarily taken as 1 μm) interval at radius r.

The total number of particles per unit volume $N(r)$ in the radial range from $r_{\min}$ to $r_{\max}$ is given by

$$N(r) = \int_{r_{\min}}^{r_{\max}} n(r)\ dr$$

The volume scattering and absorption coefficients β_s and β_a are given by

$$\beta_s = \pi \int_{r_{\min}}^{r_{\max}} Qs(m,\chi) r^2 n(r)\ dr$$

$$\beta_a = \pi \int_{r_{\min}}^{r_{\max}} Qa(m,\chi) r^2 n(r)\ dr$$

The size distribution functions $n(r)$ given in order of increasing complexity by the Dave program are

1. Discontinuous power law [10]:

$$n(r) = C \qquad r_{\min} \le r \le r_m$$

$$n(r) = C(r_m/r)^{-(v+1)} \qquad r_m \le r \le r_{\max}$$

The quantity C represents the value of n(r) for the smallest particles (up to radius r_m), and v is the rate of decrease of n(r) with increasing radius.

2. Modified gamma function [11]:

$$n(r) = ar^{\alpha}\exp(-br^{\gamma}), \qquad r_{\min} \le r \le r_{\max}$$

The parameters α and γ are determined by matching the experimental curve. The quantity a is essentially given by the total number of particles per unit volume.

3. Lognormal function [12]:

$$n(r) = [\sigma r(2\pi)^{1/2}]^{-1}\exp\left[\frac{-(\ln r - \ln r_m)^2}{2\sigma^2}\right], \qquad r_{\min} \le r \le r_{\max}$$

For the lognormal distributions, values of $r_{\min}$ and $r_{\max}$ are computed from the following expressions:

$$r_{\min} = \exp(\ln r_m - 4\sigma), \qquad r_{\max} = \exp(\ln r_m + 4\sigma)$$

The first two functions are reasonably representative of the smoothly varying aerosol size distributions that are obtained by averaging over the histograms. The third function, lognormal, with $r_{\max}$ and $r_{\min}$ determined by the 4σ variances, is not easily specified in terms of histograms.

As inputs to the Dave program, appropriate complex indices of refraction are required as well as a size range of particles to be considered and the shape of the $n(r)$ number density function.

For the optical complex indices of refraction of soot, $(NH_4)_2SO_4$, methylene blue, and Arizona road dust, measured values of the refractive and absorptive portions were used [13]; the refractive portion was determined by a Brewster angle technique on compressed pellets [14], and the absorption portion from the application of a form of the Kubelka–Munk theory [14] on a thin layer of the sample on a KBr pellet. It is of interest to note that the determinations of the absorption portion for soot, $(NH_4)_2SO_4$, and methylene blue differ by less than one order of magnitude (generally determined by the application of some form of the Kubelka–Munk theory) as measured by the participants in the International Workshop on Light Absorption by Aerosol Particles [5]. Thus the values measured in Ref. 13 are taken to be reasonable. The number density $n(r)$ as a function of particle diameter was derived from histograms furnished to the aerosol conference participants [15].

The $n(r)$ curves were approximated by either the discontinuous power law or the modified gamma function. The observed particle diameters ranged from 0.006 to 9 μm; the analyses of this paper set $r_{\min} = 0.005$ μm ($d_{\min} = 0.01$ μm) and $r_{\max} = 4$ μm (dmax = 8 μm) close to the observed range.

The particle number density was experimentally determined by using three instruments [16]: (1) a Thermo Systems, Inc. Model 3030 electrical aerosol analyzer (EAA) for particles between 0.006 and 0.10 μm diameter: (2) a Particle Measuring Systems Model ASASP-X optical particle counter for particles between 0.1 and 0.5 μm diameter; and (3) a Royco Model 220 optical particle counter for particles between 0.5 and 9 μm diameter. Each counter was developed to be optimum within the size range used.

Soot appeared to present a problem with sizing by the EAA because the smallest carbon either did not charge or multiply charged, and it was not unusual to find a bin (representing a particle size) empty in the histogram. The ASASP-X was calibrated from a theoretical curve based on carbon particles and from one based on latex spheres provided by the manufacturer. The calibration may differ by as much as a factor of 2.5 [16]. The carbon particle and methylene blue data were reduced using the carbon calibration, and the ammonium sulfate, ambient, and road dust, by using the latex calibration. For mixtures of methylene blue and carbon with ammonium sulfate, the latex calibration was chosen for this study because of the lesser relative contribution of the absorbing part of the optical complex index of refraction of the additive. The overlap regions between the instruments were disregarded because a considerable discrepancy between the counts generally exists when the analyzers are used at the extremes of their ranges [17].

The particle number density was taken as the fundamental data item rather than the volume of the particles for three reasons: (1) The number density was directly measured, (2) the volume density is a derived quantity based on the assumption of a particular particle shape and density and thus is subject to error, and (3) the Mie scattering program requires particle number density as input.

The number density curves derived for the carbonaceous particles (soot), methylene blue, ammonium sulfate, ammonium sulfate plus soot, ammonium sulfate doped with 4.0% methylene blue, ambient, and Arizona road dust are presented in Figs. 1–7. The solid line histograms are the observed values, and the dashed lines are the curves that approximate the histograms with a modified gama function.

In attempting to match the number density distributions of Figs. 1–7 with an analytical function it was found that the discontinuous power law was a poor approximation for the shape of the histograms. Further, the calculated volume scattering and absorption coefficients were critically dependent on the breakpoint between the constant portion and the inverse radial dependence. However, the modified gamma function (which is also the Deirmendjian haze model [11]), which is also sensitive to the parameters discussed, does permit a better fit to the observed number densities; it was thus used for the

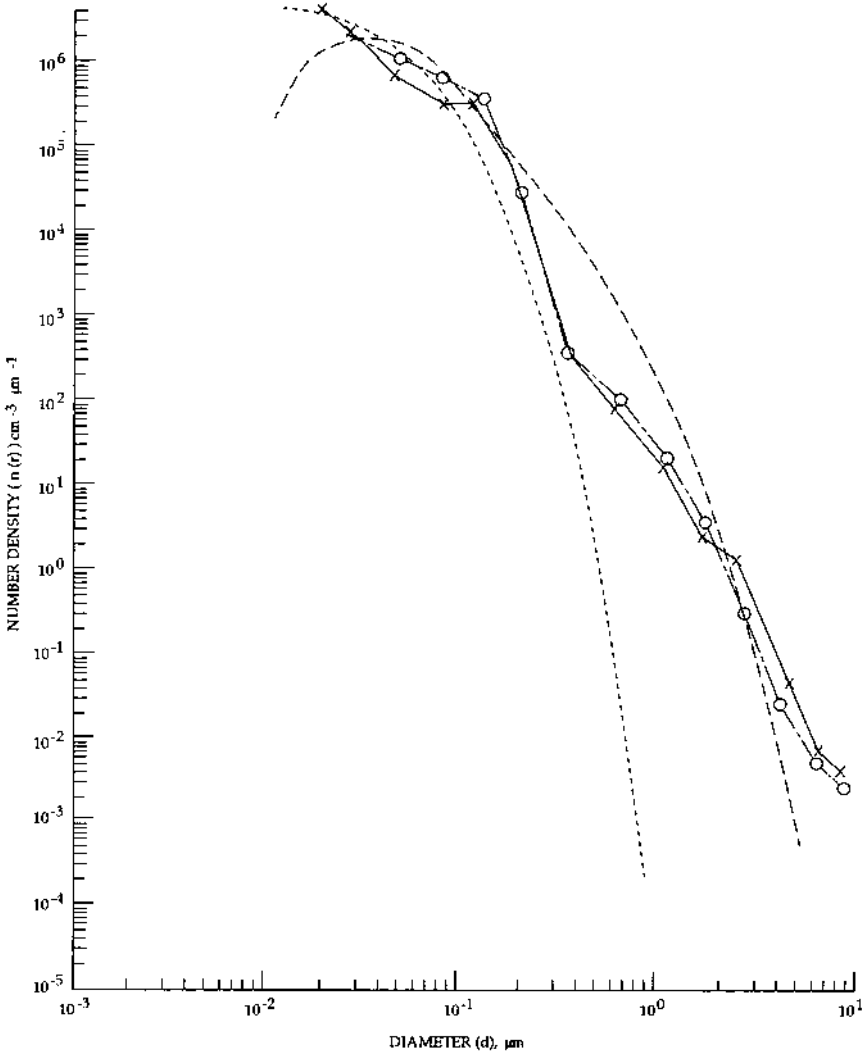

FIGURE 1 Sizes and concentrations of carbonaceous particles. (– – –) samples between 1500 h 38 s and 1505 h 18 s MDT on 1 Aug. 1980; (—) sampled between 1055 h 18 s and 1059 h 58 s on 4 Aug. 1980; (○) calculated with parameters listed in Table 1; (---) calculated for $\alpha = 2$, $\gamma = 1/2$, $b = 56.6$, and $a = 1.31 \times 10^{13}$.

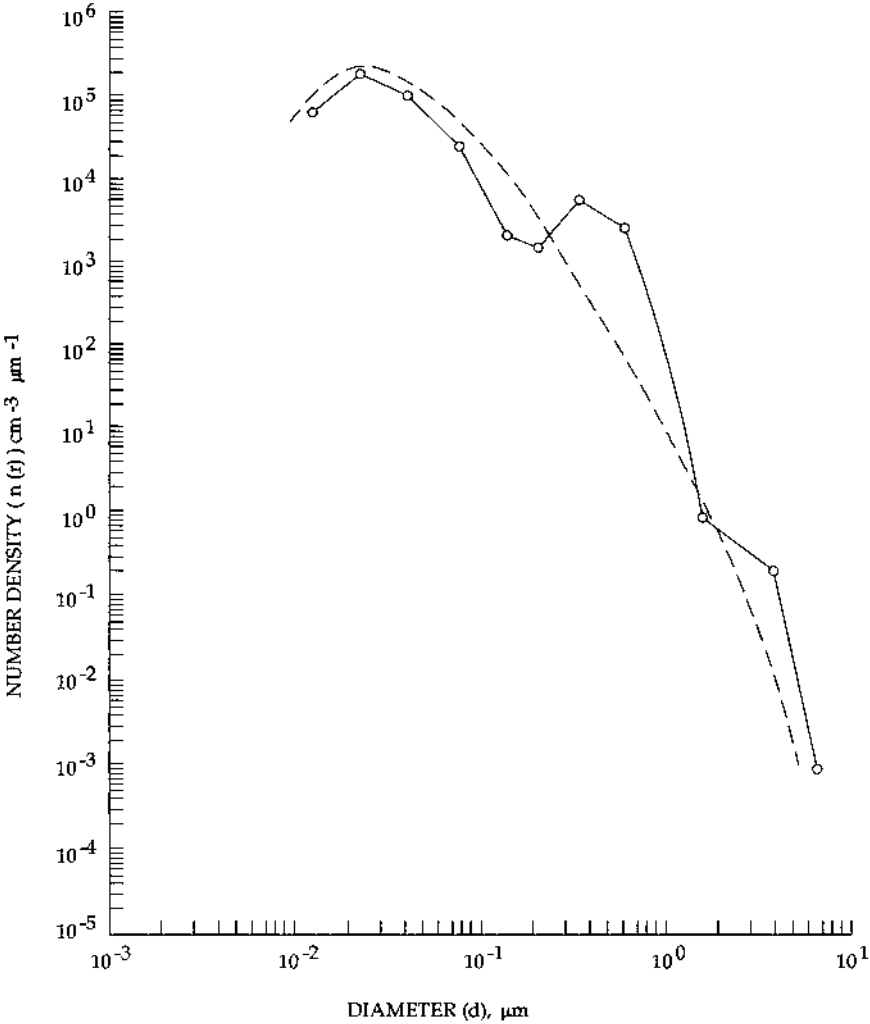

FIGURE 2 Sizes and concentrations of methylene blue particles. (—) Sampled between 1521 h 38 s and 1526 h 18 s MDT on 4 Aug. 1980; (- - -) calculated with parameters listed in Table 1.

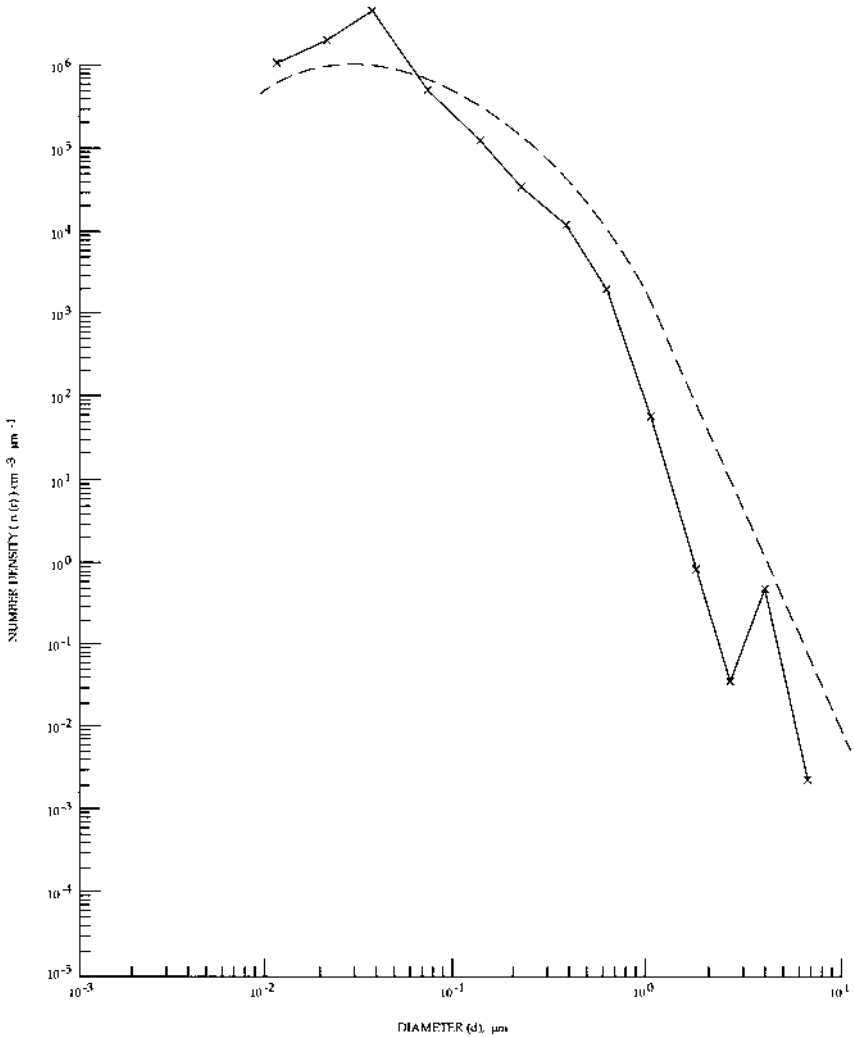

FIGURE 3 Sizes and concentrations of ammonium sulfate [$(NH_4)_2SO_4$] particles. (—) Sample between 1205 h 18 s and 1209 h 58s on 30 July 1980; (- - -) calculated with parameters listed in Table 1.

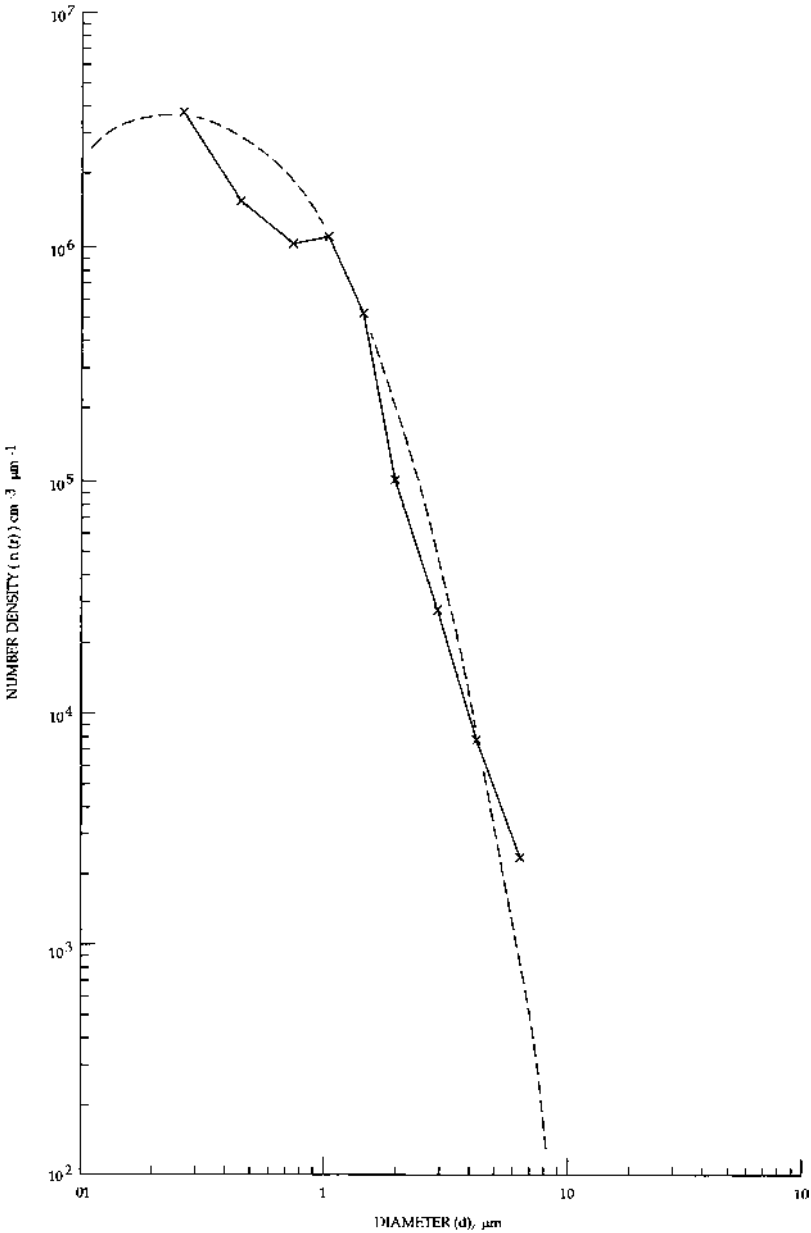

FIGURE 4 Sizes and concentrations of a 50:50 mixture of soot and $(NH_4)_2SO_4$ particles (—). Sampled between 1340 h 38 s and 1345 h 18 s on 4 Aug. 1980; (- - -) calculated with parameters listed in Table 1.

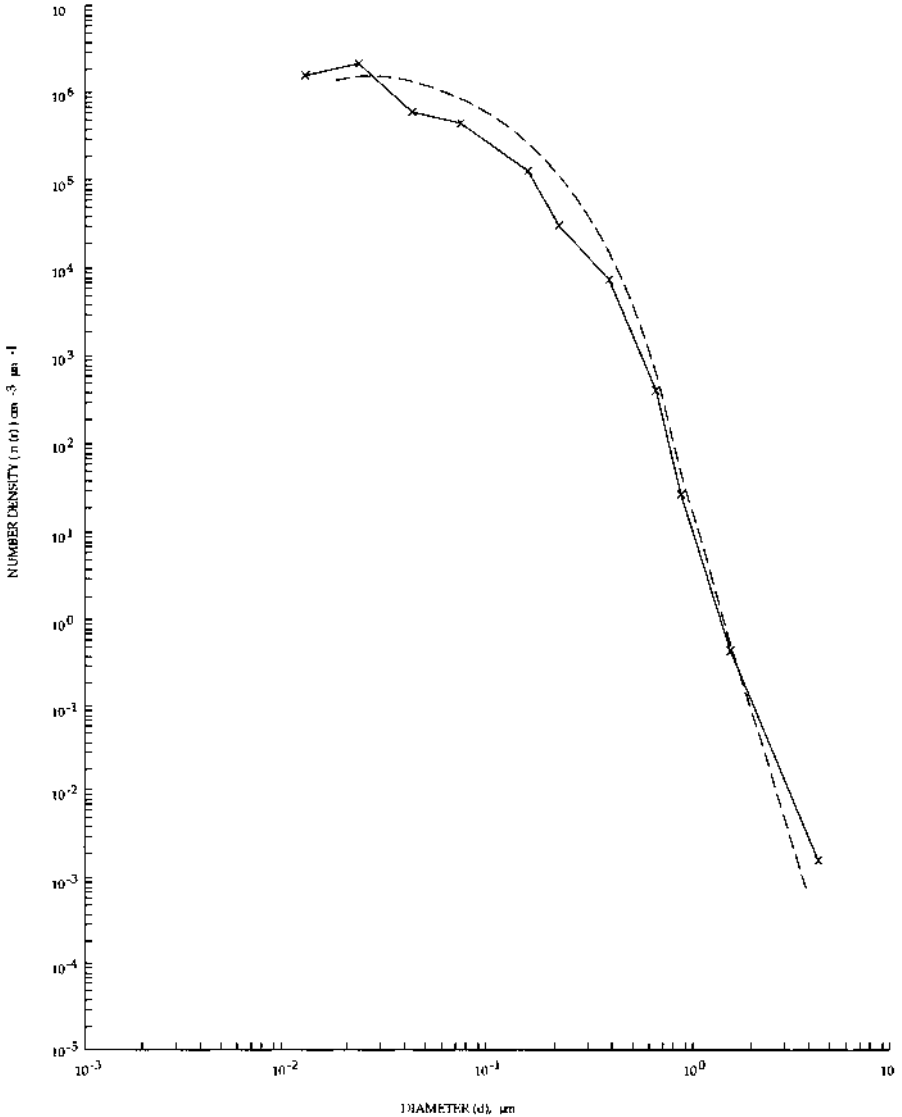

FIGURE 5 Sizes and concentrations of ammonium sulfate particles doped with 4.0% of methylene blue. (—) Sampled between 1715 h 18 s and 1719 h 58 s MDT on 30 July 1980; (- - -) calculated with parameters listed in Table 1.

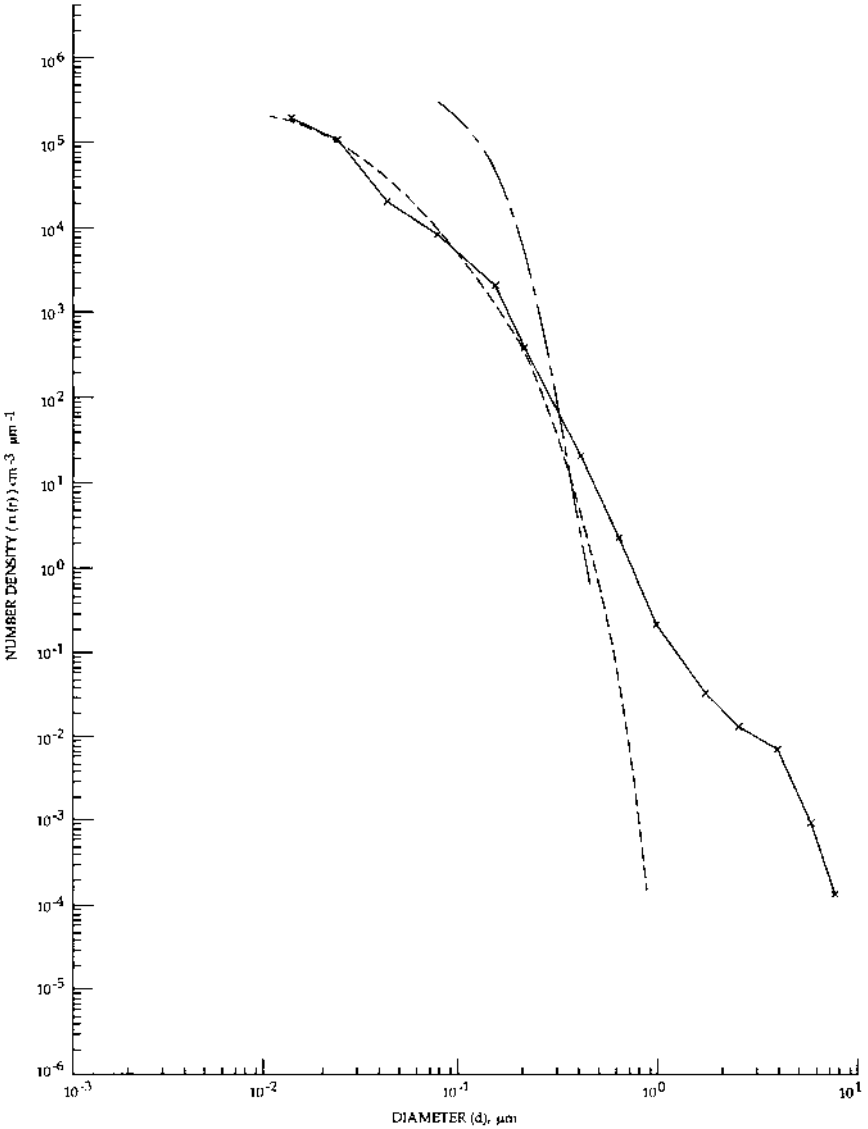

FIGURE 6 Sizes and concentrations of ambient particles. (—) Sampled between 1105 h 38 s and 1110 h 18 s MDT on 5 Aug. 1980; (- - -) mode A and (– – –) mode B, calculated with parameters listed in Table 1.

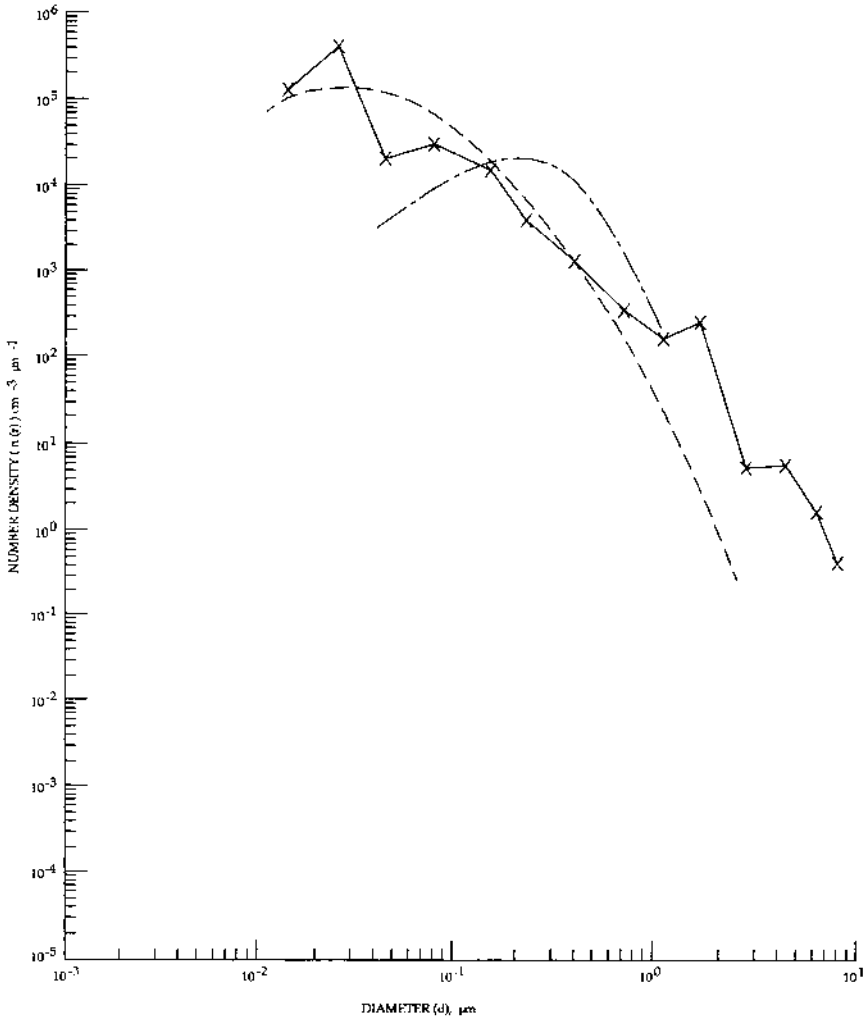

FIGURE 7 Sizes and concentrations of Arizona road dust particles. (—) Sampled between 1201 h 38 s and 1205 h 18 s MDT on 6 Aug. 1980; (- - -) mode A and (– - –) mode B, calculated with parameters listed in Table 1.

TABLE 1 Synopsis of Selected Calculations and Observations

1 Sample	2 Wavelength (μm)	3 $n + ik_0$[d]	4 β_s[a] Obs.	5 β_s Calc.
Soot	0.450	1.680 + *i*2.54E−2	2.55E−4	7.26E−4
8/4/80	0.550	1.660 + *i*3.55E−2	1.74E−4	6.31E−4
1000–1100	0.655	1.775 + *i*5.43E−2	1.29E−4	5.87E−4
	0.820	1.762 + *i*6.31E−2	8.07E−5	4.83E−4
Graphite powder	0.450	2.015 + *i*6.53E−3		8.87E−4
	0.550	2.040 + *i*7.41E−3		8.64E−4
	0.655	2.055 + *i*1.2E−2		8.06E−4
	0.820	2.060 + *i*1.48E−2		7.18E−4
Bulk graphite	0.450	1.69 + *i*6.57E−1		3.51E−4
	0.550	1.71 + *i*6.40E−1		3.29E−4
	0.655	1.775 + *i*5.08E−1		3.19E−4
	0.820	1.76 + *i*5.76E−1		2.73E−4
Methylene	0.450	0.987 + *i*2.03E−1	7.11E−4	4.28E−4
Blue (MB)	0.550	1.30 + *i*5.40E−1	4.09E−4	1.53E−3
8/4/80	0.655	1.57 + *i*1.70E−1	6.71E−4	2.00E−3
1500–1530	0.820	1.52 + *i*1.6E−2	1.63E−3	1.35E−3
$(NH_4)_2SO_4$	0.450	1.450 + *i*6.92E−6	8.84E−4	1.19E−5
7/30/80	0.550	1.448 + *i*7.94E−6	6.56E−4	6.07E−6
1130–1230	0.655	1.445 + *i*1.12E−5	5.39E−4	3.25E−6
	0.820	1.442 + *i*1.45E−5	3.44E−4	1.41E−6
$(NH_4)_2SO_4$ + soot	0.450	1.565 + *i*1.05E−1	1.83E−3	5.47E−4
8/4/80	0.550	1.580 + *i*1.17E−1	1.29E−3	3.84E−4
(50%/50%)	0.655	1.600 + *i*1.33E−1	1.03E−3	2.75E−4
1200–1330	0.820	1.602 + *i*1.53E−1	6.56E−4	1.59E−4
$(NH_4)_2SO_4$ + 4%	0.450	1.432 + *i*8.13E−3	5.91E−4	4.01E−4
MB	0.550	1.442 + *i*2.16E−2	4.18E−4	2.65E−4
7/30/80	0.655	1.450 + *i*6.81E−3	3.73E−4	1.95E−4
1700–1800	0.820	1.445 + *i*6.54E−4	2.27E−4	1.10E−4
Ambient air	0.450	1.339 + *i*1.80E−1	2.44E−5	4.06E−5
8/5/80	0.550	1.336 + *i*2.08E−1	1.70E−5	2.29E−5
1000–1200	0.655	1.333 + *i*2.29E−1	1.43E−5	1.34E−5
	0.820	1.332 + *i*2.74E−1	1.09E−5	6.69E−6
Arizona road dust	0.450	1.339 + *i*6.92E−3	2.80E−4	5.40E−4
(low conc)	0.550	1.336 + *i*7.94E−3	2.64E−4	4.00E−4
1130–1300	0.655	1.333 + *i*8.71E−3	2.80E−4	2.92E−4
	0.820	1.332 + *i*1.12E−2	2.49E−4	1.82E−4
Arizona road dust	0.450	1.339 + *i*1.38E−3		5.62E−4
(high conc)	0.550	1.336 + *i*1.10E−3		4.18E−4
	0.655	1.333 + *i*1.00E−3		3.04E−4
	0.820	1.332 + *i*1.10E−3		1.90E−4

[a] Bodhaine [18] (0.450, 0.550, 0.655, and 0.82 μm wavelengths).
[b] Heintzenberg [20] (0.550 μm wavelength).
[c] Rosen and Novakov [19] (0.6328 μm wavelength).
[d] Egan [13].
[e] Cowen [21] (0.56 μm wavelength).
[f] Deirmendjian [11].
[g] Rosen [27] (0.6328 μm wavelength).

6	7	8	9	10	11	12
		Modified gamma function parameters[f]				
β_s Obs.	β_a *Calc.*	α	γ	b	$r_c(\mu)$	a
1.76E−2–2.01E−2[e]	1.17E−4	1	0.5	17.9	0.0125	1.10E + 8
1.6E−3–2.0E−3[b]	1.26E−4					
1.1E−3–2.2E−3[c]	1.57E−4					
	1.40E−4					
	4.64E−5	1	0.5	17.9	0.0125	1.10E + 8
	4.39E−5					
	5.68E−5					
	5.36E−5					
	4.51E−4	1	0.5	17.9	0.0125	1.10E + 8
	4.52E−4					
	4.23E−4					
	4.10E−4					
1.38E−2–2.16E−2[e]	2.10E−3	2	1	35.8	0.0125	2.37E + 9
6.7E −4–2.1E−3[b]	3.83E−3					
1.7E −3–3.1E−3[c]	1.91E−3					
	1.73E−4					
5.5E −4–5.8E−4[c]	2.18E−9	1	0.5	16.3	0.015	4.93E + 8
3.4E −5–3.4E−4[b]	1.94E−9					
$<10^{-4}$[g]	2.22E−9					
	2.21E−9					
2.52E−2[e]	3.48E−4	2	0.5	35.8	0.0125	1.40E + 12
1.2E −3 to 7.1E−3[b]	3.03E−4					
4.4E −4 to 2.6E−3[c]	2.75E−4					
	2.35E−4					
2.69E−3[e]; 5.4E−4[c]	2.01E−5	2	0.5	32.6	0.015	3.38E + 11
1.0E−4[b]	4.76E−5					
	1.24E−5					
	8.76E−7					
	2.25E−4 (mode *A*)	2	0.5	56.6	0.005	4.37E + 12
	2.08E−4 (mode *B*)	2	1	100	0.02	9.24E + 10
8E−6[c]	1.90E−4					
	1.78E−4					
	2.49E−5 (mode *A*)	2	1	17.9	0.0125	5E + 8
	2.26E−5 (mode *B*)	2	1	20	0.100	1.18E + 7
<2E−5[g]	2.01E−5					
	1.96E−5					
	5.16E−6 (mode *A*)	2	0.5	17.9	0.0125	5E + 8
	3.25E−6 (mode *B*)	2	1	20	0.100	1.18E + 7
	2.39E−6					
	1.98E−6					

calculations. As previously indicated, the lognormal curve is not easily specified in terms of histograms and thus was not used.

The parameters for the dashed curves in Figs. 1–7 are listed in Table 1, columns 8–12. The calculated values for β_s and β_a from the Dave program are also listed in Table 1 for the associated optical complex indices of refraction and modified gamma function parameters. The best fit criteria are based on two requirements: (1) a good match of the theoretical curves (the modified gamma function) to the experimental histograms and (2) agreement of the calculated β_s (based on Mie theory) with the observed values of Bodhaine [18].

The wavelengths listed in Table 1 (0.450, 0.550, 0.655, and 0.820 μm) correspond to those of Bodhaine [18], who used the NOAA GMCC four-wavelength nephelometer on all samples to measure β_s. The measured β_a values were limited to 0.6328 μm [19], 0.550 μm [20], and 0.56 μm [21] and do not constitute a complete set for comparison with calculations. Three indices of refraction were used for the carbonaceous particle calculations (soot, graphite powder, and bulk graphite). The $(NH_4)_2SO_4$ + soot mixture calculation used a 50:50 combination of the indices of $(NH_4)_2SO_4$ and soot. The Arizona road dust was done with two absorption portions, one determined for a light concentration layer on a KBr pellet and another as a high concentration layer, the real index was assumed to be that measured for the Arizona road dust. It is to be noted that the real index of compressed particulate material is less than that of the bulk [22]. The ambient model and the Arizona road dust models required bimodal distributions; the ambient large particles were composed of agglomerates of 10 or more 0.4 μm estimated diameter particulates that peaked the $n(r)$ curve at 0.2 μm, and the largest Arizona road dust particulates had fines of 0.025 μm average diameter adhering to them.

III. COMPARISONS WITH OBSERVATIONS

A synopsis of selected calculations and observations is presented in Table 1. The observations of the volume scattering and absorption coefficients are listed, respectively, in columns 4 and 6 for comparisons with the calculations listed in columns 5 and 7. Agreement between the measured and calculated volume scattering coefficients β_s (compare columns 5 and 4) is good for soot, methylene blue, and ammonium sulfate doped with 4% methylene blue; ammonium sulfate + soot (50:50 mixture) is poorer but still within an order of magnitude. Ambient air and Arizona road dust are in close agreement with the calculated β_s bimodal distributions used. Ammonium sulfate has the poorest agreement, being approximately two orders of magnitude below that observed.

The figures (from which the calculations in Table 1 are derived) depict the effectiveness of the number density modeling and are discussed in sequence. In Fig. 1 the dashed curve (parameters in Table 1) is an average match to the two histograms obtained for carbonaceous particles. The quantity a in the modified gamma function is directly related to the maximum ordinate $n(r)$, and $r_c(\mu)$ is the mode radius (1.10E+8 and 0.0125 μm, respectively). The constants a, γ, and b determine the curve shape. Thus, if we increase b by a factor of 3.2 (dotted curve, Fig. 1) a five order of magnitude increase in a is required for $\gamma = 1/2$ and $\alpha = 2$, yielding the dotted curve. The values of β_s obtained from the dashed curve are within a factor of 6 of those observed (Table 1). It is to be noted that the particle sizes that contributes most strongly to the volume scattering function lie between 0.05 and 2 μm with the maximum sensitivity at $\sim$0.6 μm [23]. Hence the match of the theoretical curve to the experimental observations is most critical in this region.

Figure 2 shows the match between the theoretical curve (dotted) with the histogram obtained for methylene blue particles. Again, the overall agreement is good, both in Fig. 2 and within a factor of 4 between the calculated and observed values (Table 1). The peaking of the observed $n(r)$ at $\sim$4 μm diameter has a small effect relative to particles of $\sim$0.6 μm diameter.

Figure 3 for $(NH_4)_2SO_4$ reveals a match between the modified gamma function that sought to average the observations with emphasis around the peak. The observed values of β_s (Table 1) lie about two orders of magnitude above those calculated with the $n(r)$ curve in Fig. 3. The small $(NH_4)_2SO_4$ particles agglomerate extensively as shown by SEM photograph 29 [6,15] and it is probable that the particles counted in the larger size range (note the histogram peak at $\sim$4 μm diameter) produced an effect that would augment small-particle scattering and give the larger observed β_s.

Figures 4 and 5 present data on a 50:50 mixture of soot and $(NH_4)_2SO_4$ particles and $(NH_4)_2SO_4$ particles doped with methylene blue, respectively. Again there is good agreement between the theoretical curves and the histograms (particularly near the peak) as well as in the values of β_s (Table 1) to within a factor of 4.1 and 2.1 for the respective mixtures.

However, in Figs. 6 and 7 for ambient air and Arizona road dust, respectively, agreement of the calculated values with those observed could not be obtained with a single modified gamma function (mode A) that on the average matched the observed $n(r)$ histogram for the optically important sizes. A second mode (B) was required in addition to produce a good match to the observed β_s.

For ambient air the calculated values of β_s (Table 1) derived from the observed $n(r)$ (Fig. 6) (i.e., mode A) resulted in abnormally low values (about two orders of magnitude). However, the SEM photograph (No. 39) [5,15] of the particles revealed the larger particles detected by the counters to be

clusters of 10 or more particles of ~0.4 μm diameter. Thus mode *B* (Table 1) was added to mode *A* to include the estimated effect of these particles, simulating multiple scattering. With this modification, close agreement in magnitude of β_s was obtained (within a factor of 1.7) and the wavelength trend matched (decreased β_s with increased wavelength). However, the observed β_a is about two orders of magnitude below that calculated (Ref. 19, see footnote c, Table 1). It is possible that a variation in the concentration and size of the ambient aerosol (observed to change as a result of industrial activity and convection currents [23]) caused the difference.

Arizona road dust (a standard material available from General Motors Corp.) also posed a problem in that the calculated values of β_s were about four orders of magnitude below those observed using the measured $n(r)$ (see Fig. 7 and Table 1, mode *A*). However, an examination of the SEM photograph No. 31 [6,15] of the particle revealed fines adhering to the larger particles. These fines were estimated to be 0.2 μm in diameter, and a small contribution (mode *B*, Table 1) (see also Fig. 7) from them caused a considerable change in β_s; agreement within a factor of 1.9 was obtained with the observed value (Table 1). As mentioned previously Shaw [23] pointed out that particles of ~0.6 μm diameter have a great effect on β_s (real index of 1.5) at $\lambda = 0.5$ μm than at other sizes; the conclusion approximately holds for other indices near this one. Thus extreme sensitivity in β_s (and β_a) results when the $n(r)$ peak occurs near $r \sim 0.3$ μm. The use of the decreased value of the imaginary portion of the optical complex index of refraction (Arizona road dust, high concentration, Table 1) has only a slight effect on β_s (decrease) but causes an order of magnitude decrease in β_a. Also, incidentally, the calculated β_a is close to that observed by Rosen [27] (see footnote 9, Table 1).

In Table 1 there is a lack of detailed observations of the wavelength dependence of β_a, with measurements limited to $\lambda = 0.550$, 0.56, and 0.6328 μm. The agreement of the observed and calculated values of the volume absorption coefficient β_a (compare columns 6 and 7) are generally within an order of magnitude; $(NH_4)_2SO_4$ is a notable exception (about four orders of magnitude below observed) as well as ambient air (about two orders of magnitude above the one observation).

However, wavelength trends can be compared to volume scattering β_s where sufficient observations exist. There is a general trend for increased β_s as wavelength decreases, as modified by the contribution of the absorption portion of the optical complex index of refraction.

The results presented in Table 1 will now be discussed in detail. For soot the wavelength dependence of the observed β_s follows that calculated, but the calculated dependence is a stronger function of wavelength than that observed for soot. In contrast, the calculated trend is weaker for graphite powder and bulk graphite. The lack of precise agreement in the magnitude of

β_s is probably the result of an inaccurate representation of the counting statistics by the modified gamma distribution. The outcome of the β_s Mie scattering calculation has a stronger sensitivity to the real index variation (compare soot with graphite powder, Table 1) than to the imaginary portion (compare soot with bulk graphite, Table 1). The calculated value of β_a (column 7) is about one order of magnitude smaller than that measured by two observers [19,20] and two orders of magnitude below that measured by a third [21]. Graphite powder produces a lower β_a and bulk graphite a higher β_a, but both are lower than that observed. The lower calculated values are not too sensitive to the value of the imaginary portion of the index of refraction (compare soot with bulk graphite) and, because of the wide range of observed β_a, thus are inferred to be the result of measurement inaccuracy of β_a.

Methylene blue in comparison with graphite has a strong absorption band near $\lambda = 0.550$ μm, and the measured β_s is smaller than at the other three wavelengths; the calculated β_s is close to that at $\lambda = 0.655$ and 0.820 μm. The decrease in the calculated β_s at $\lambda = 0.450$ μm is attributed to an inaccuracy in the observed refractive portion of the index of refraction in the region of anomalous dispersion, putting it near unity with attendant low scattering. The values of β_s lie in good agreement with two observers [19,20] but below that of the third [21].

Ammonium sulfate presents a problem as evidenced by the calculated value of β_s being about two orders of magnitude below that measured. Although the calculated wavelength trend (decrease in scattering with increasing wavelength) matches that observed, the discrepancy in magnitude is attributed to increased scattering by the inhomogeneities of the agglomerated particulates (inferred from SEM photograph 29) [6,15]. The same calculated deficiency exists for β_a (about five orders of magnitude). It is inferred that the inhomogeneities in the agglomerated particulate provide multiple internal reflections (and scattering) and thus increase the effective path length in the particles with increased absorption.

The 50:50 mixture of $(NH_4)_2SO_4$ and soot (Table 1) has a calculated β_s of approximately one-third of that observed, with the wavelength trend matching (decreased β_s with increased wavelength). The overall index of refraction was approximated using a linear 50:50 combination of the $(NH_4)_2SO_4$ and soot real and imaginary indices of refraction. The calculated β_a is lower than that observed [(see footnotes b and c, Table 1), but close to that of Ref. 19 (see footnotes c, Table 1)].

The $(NH_4)_2SO_4$ with 4% methylene blue β_s values are in good agreement with those calculated, including the wavelength dependence. The better agreement of the mixture is probably caused by the dominant effect of the methylene blue absorption in reducing the effect of scattering by inhomogeneities in the $(NH_4)_2SO_4$. However, the calculated β_a values are one order of

magnitude below those of two observers [19,21] and two orders of magnitude below another [21]. The absorption (β_a) is particularly sensitive to the value of the imaginary component of the index of refraction. The use of a linear combination of indices of refraction of 4% methylene blue with 96% $(NH_4)_2SO_4$ is possibly not the best.

The ambient air and Arizona road dust required an augmented distribution to add more scattering to reproduce the observed values of β_s. The effect of particle shape on scattering and absorption has been investigated theoretically by a number of authors. Aronson and Emslie [24] note theoretically and experimentally the considerable effect that edges, asperities, and fines can have on the scattering and absorbing properties of particles. Thus it is not unreasonable to assume an additional particle number density function to characterize the effect of fines as well as particle edges and asperities. The trend of β_s with decreasing wavelength for ambient air is followed except at a 0.820 μm wavelength in the calculated results. The increase in β_s at this wavelength results from the measured change in the index of refraction. However, the Arizona road dust follows the expected trend for the calculated β_s.

IV. DISCUSSION

The use of Mie calculations based on first principles (i.e., Maxwell's equations, optical complex index of refraction, number density distribution of aerosols, and their sizes and shapes) to represent the physical situation of aerosol volume scattering β_s appears to be valid. The absorption data (β_a) are too inaccurate to permit a firm conclusion to be drawn. The magnitude of β_s and β_a are critically dependent on $n(r)$, particularly when there is a peak near $r \sim 0.3$ μm. The wavelength dependence of β_s (and β_a) depends on the real (and refractive) portions of the optical complex index of refraction less sensitively. Bodhaine indicated that the NOAA GMCC nephelometer measurements correlate very well with those observed over long path lengths [25] and thus are to be considered as a reliable indicator for β_s, and calculated agreement was strongly influenced by these observations in the modeling.

The volume absorption measurement β_a appears to be in some difficulty. Whereas there are differences between observers in the values of β_a on the same samples as well as in the statistics of $n(r)$, the β_a differences (approximately one order of magnitude for soot) correspond to those for the same observer for methylene blue. This indicates that the integrating plate method (IPM) that yielded a higher absorption for soot, methylene blue, and ammonium sulfate plus soot or 4% methylene blue may have a systematic error in these cases.

The soundness of the use of the particular indices of refraction [13] of Table 1 should be examined. Unfortunately, the real (refractive) portion

measurement of the aerosol standards has only one measurement counterpart, with a report of the real portion for methylene blue [26]. The real indices reported are higher then those in Table 1 at 0.450 μm (1.4 instead of 0.987) and 0.820 μm (2.1 instead of 1.52), and lower at 0.550 μm (1.2 instead of 1.30) and at 0.655 μm (1.3 instead of 1.57) [13,25]. Our measured region of anomalous dispersion was at 0.5 μm [13] instead of the 0.6 μm region shown by the dispersion analysis [26]. Although these disagreements are significant, we still favor the results in Table 1 because the real portion in Ref. 13 was determined using a dispersion analysis that has been shown to be invalid for scattering type materials [14], which include methylene blue. The justification of the use of the absorptive portion was covered in Section II.

The use of the histograms for $n(r)$, or the histograms for the number of particles within a size range, directly in the calculations for β_s and β_a is not generally valid. A given set of measurements of $n(r)$ is subject to statistical plus systematic errors. Because the physical processes involved in the formation of aerosols are described by differential equations producing smooth distributions, there is reason to believe that the actual size distribution should be smooth. The use of a smooth curve to represent the aerosol statistics thus appears to be the more accurate approach, provided a reasonable curve is chosen. The reasonableness of the histograms was checked by integrating the observed size distribution to determine the total mass that should be measured per cubic meter [16]; this was then compared with the ppm concentrations determined from a TSI Model 3200A particle mass monitor (PMM) and from nearly simultaneous filter collections [16]. In comparing the PMM and the integrated size distribution, although the ammonium sulfate measurements were within 25%, the methylene blue could be out by a factor of 6 (because of calibration problems [16]), Arizona road dust by a factor of 9 (it was inferred that most of the mass was in uncounted submicrometer particles [16]), and soot by a factor of 4 (because of instrument drift[16]). The mixture of soot and $(NH_4)_2SO_4$ was off by a factor of 2 (probably associated with the soot problem), but $(NH_4)_2SO_4$ and 4% methylene blue were within 1% (most of the mass was in the $(NH_4)_2SO_4$ [16]).

Unfortunately, the large errors in the PPM measurements make this comparison of limited use. It appears that in the overlapping regions of particle size analyses some statistical approach may be used to combine the observations to yield a better characterization of $n(r)$.

V. CONCLUSIONS

It is concluded that a Mie scattering calculation can be used with good accuracy to represent the volume scattering coefficients (β_s) of the standard aerosols that were generated at the First International Workshop on Light

Absorption by Aerosol Particles. The accuracy of the calculated magnitude of β_s and β_a depends strongly on the accuracy of the particle number density n(r) obtained from particle size analyzers. The best accuracies from the analyzer appear to be in the midregion of their specified range.

The calculated variation of β_s and β_a with radiation wavelength depends weakly on the variation of the refractive and absorptive portions respectively, of the optical complex index of refraction.

When particles are not spherical (and have fines adhering) or when they agglomerate, the net effect is to increase scattering (and absorption) by orders of magnitude ($\sim$1–4). Thus it is necessary to collect and characterize the particle shapes by scanning electron microscopy before attempting calculations.

Whereas the measurement of β_s appears to be consistent with calculations, the measurement of β_a appears to be in need of improvement because of lack of agreement between observers.

It was pointed out that the Brewster angle technique was a better technique for the determination of the refractive index than the dispersion approach, which gives significantly different results.

The absorption portion appears to be determined consistently by some form of the Kubelka–Munk theory on powder samples. The shape of the $n(r)$ curve, particularly for a particle radius of 0.3 μm, has an exceptionally great effect on the calculation of β_s and β_a. The calibration of particle size analyzers (i.e., with carbon or latex spheres) can vary with imaginary index of refraction of the sample.

REFERENCES

1. Egan, W.G. In Proceedings, Ninth International Symposium on Remote Sensing of the Environment; Environ. Res. Institute of Michigan: Ann Arbor, MI, 1974; 12, 1319–1343.
2. Egan, W.G.; Fischbein, W.L. In Proceedings, Tenth International Symposium on Remote Sensing of the Environment; Environ. Res. Inst. of Michigan: Ann Arbor, MI, 1975; 783–792.
3. Egan, W.G. In Proceedings, Fourteenth International Symposium on Remote Sensing of the Environment; Environ. Res. Inst. of Michigan: Ann Arbor, MI, 1980; 563–586.
4. Gerber, E. In Particulate Carbon: Atmospheric Life Cycle; Wolff, T., Klimish, R.L., Eds.; Plenum Press: New York, 1981; 145–158.
5. Gerber, H.E.; Hindman, E.E. Eng. Proc. Soc. Photo-Opt. Instrum. 1981, 277, 192.
6. Gerber, H.; Hindman, E., Eds. In Light Absorption by Aerosol Particles; Spectrum: Hampton, VA, 1981, 192.
7. Mie, G. Ann. Phys. 1908, 25, 377.

8. van de Hulst, H.C. In Light Scattering by Small Particles; Wiley: New York, 1957.
9. Dave, J.V. NASA Rep. No. S80-RADTMO. Goddard Space Flight Center: Greenbelt, MD, 1972.
10. Bullrich, K. Adv. Geophys. 1964, 10, 99.
11. Deirmendjian, D. In Electromagnetic Scattering on Spherical Polydispersions; American Elsevier: New York, 1969.
12. Aitchinson, J.; Brown, J.A.C. In The Lognormal Distribution; Cambridge Univ. Press: New York, 1957.
13. Egan, W.G. In Optical Properties of Standard Aerosols; Gerber, H., Hindman, E., Eds.; Light Absorption by Aerosol Particles Spectrum: Hampton, VA, 1981; 197–230.
14. Egan, W.G.; Hilgeman, T.W. In Optical Properties of Inhomogeneous Materials; Academic Press: New York, 1979.
15. Hindman, E. Workshop summary, histograms and SEM photographs of aerosol samples. Communication to attendees of First International Workshop on Aerosol Particles, 8 Aug. 1980.
16. Hindman, E.E.; Horn, R.D.; Finnegan, W.G. In Particle Generation Transport and Characterization at the First International Workshop on Light Absorption by Aerosol Particles; Gerber, H., Hindman, E., Eds.; Light Absorption by Aerosol Particles Spectrum: Hampton, VA, 1981; 71–122.
17. Hindman, E.E. Univ. Colorado. Fort Collins. Private communication, 1981.
18. Bodhaine, B.A. In The GMCC Four Wavelength Nephelometer; Gerber, H., Hindman, E., Eds.; Light Absorption by Aerosol Particles Spectrum: Hampton, VA, 1981; 149–160.
19. Rosen, H.; Novakov, T. In LBL Optical Attenuation Technique; Gerber, H., Hindman, E., Eds.; Light Absorption by Aerosol Particles Spectrum: Hampton, VA, 1981; 321–334.
20. Heintzenberg, J. In Workshop report; Gerber, H., Hindman, E., Eds.; Light Absorption by Aerosol Particles Spectrum: Hampton, VA, 1981; 267–274 and 379–386.
21. Cowen, S. In Light Absorption Measurements Using Integrating Plate Method; Gerber, H., Hindman, E., Eds.; Light Absorption by Aerosol Particles Spectrum: Hampton, VA, 1981; 189–196.
22. Egan, W.G; Hilgeman, T. Appl. Opt. 1980, 19, 3724.
23. Shaw, G.E. In Remote Sensing of Aerosol in the Free Atmosphere by Passive Optical Techniques; Gerber, H., Hindman, E., Eds.; Light Absorption by Aerosol Particles Spectrum: Hampton, VA, 1981; 335–356.
24. Aronson, J.R.; Emslie, A.G. Appl. Opt 1973, 12, 2573.
25. Bodhaine, B.A. NOAA/ARL. Private communication, 1981.
26. Volz, F.E. In Results on Aerosol Absorption; Gerber, H., Hindman, E., Eds.; Light Absorption by Aerosol Particles Spectrum: Hampton, VA, 1981; 357–372.
27. Rosen, H. Lawrence Berkeley Lab. Private communication, 1981.

22

Radiative Transfer Properties of the Sahara Region

I. INTRODUCTION

A report on the intercomparison of the results from 29 atmospheric model integrations generally concerned with numerical weather integration was presented by Gates [1]. The work was the result of the Atmospheric Model Intercomparison Project (AMIP) to simulate the climate of the 1979–1988 decade. One of the significant problems mentioned in the results is that of modeling the effect of aerosols [2,3]. An aerosol is defined as an airborne particle or collection of particles, although the word has been associated erroneosly with the propellent used in aerosol sprays. Clouds are not aerosols, but aerosols provide condensation nuclei upon which moisture condenses to form haze and clouds [4].

The continent of Africa contains two deserts: the Sahara, which is the largest in the world, and the Kalahari-Namib. It is reasonable to ask whether solar radiation reaching these desert areas will increase, decrease, or remain the same as a result of human activities that affect the quantity of mixed trace gases in the world's atmosphere (CO_2, N_2O, CH_4, CO, O_3, and H_2O vapor) in association with aerosols produced by Saharan dust storms. Remote sensing of the radiative transfer properties of the desert atmosphere is a function that is most effectively accomplished synopticaly with satellites. Radiative transfer, whether solar or terrestrial, is of particular importance to arid regions of the earth. It is important because it affects heat and water balance, which among other factors determine aridity and desertification.

At present more sophisticated techniques are being developed for the determination of the aridity indices: evapotranspiration and potential transpiration. This in turn requires detailed and accurate measurements of radiation transfer properties of the atmosphere to determine the radiation balance in the predictive modeling equations including trace components and aerosols.

There is conjecture as to whether the worldwide increased levels of atmospheric carbon dioxide and other trace gases are causing a general warming of the earth's climate because of a "greenhouse effect" [5]. Older observations show that they are in the southern hemisphere, where there has been a warming trend since 1945; but in the northern hemisphere there was a cooling trend, and in the equatorial region there was neither warming nor cooling [6]. In a later reference [7], the global mean annual mean surface air temperature in a 100-year run is compared with observational data to show the interannual variability of surface air temperature and longitudinal integrated upper air temperature based on 1951–1980 observations; additional observational data are presented on 1958–1985 radiosonde data [7a]. The surmise is that the "greenhouse" interrelationship is not as simple as originally supposed [8]. It has even been suggested that there is an inverse greenhouse effect caused by the concurrent presence of water vapor and carbon dioxide [9,10]. The inverse relationship between water vapor and carbon dioxide was confirmed by Egan and coworkers [11,12]. Further, Egan and Hogan [12] indicated that the variations in atmospheric carbon dioxide lag the water vapor changes hourly, daily, monthly, and annually. Further, methane, which is also on the increase worldwide, is thought to complicate matters [13] along with the effects of arctic haze. More recently, the warming trend has been shown to result from increases in the minimum temperatures rather than increases in the maximum temperature [14]. This results from increases in amounts of clouds and precipitation and decreasing sunshine.

To clarify the effect of desert dust aerosols, there have been a number of studies of the arid regions of the world. The hope was to understand the present radiative process and to predict future effects. One such study, the GARP Atlantic Tropical Experiment (GATE) occurred in 1971–1975 [15]. (The acronym GARP stands for Global Atmospheric Radiation Program.) An important aspect of the GATE was the determination of the radiative transfer properties of the Saharan dust during the storms.

Dust from Saharan storms may cover areas as large as 6×10^6 km^2, extending westward across the Atlantic Ocean to Florida and the Caribbean. The dust-covered area is frequently 0.1% of the globe, and immediate effects are seen on cloud formations, visibility, and radiative transfer [15].

In the GATE program, scientists from the Main Geophysical Observatory at Leningrad [15] and scientists of the Department of Atmospheric Science of Colorado State University [16] participated in a multidisciplinary

investigation involving detailed quantitative ship-, ground-, and aircraft-based observations of Saharan dust clouds. Satellite imagery was used only qualitatively to assess the origin and progress of the dust clouds; it was noted that the effects of the dust on the solar spectrum were very significant but the infrared effects were much less significant [16]. Basically there was a lack of data on the dust optical indices of refraction that would have permitted calculations to be made of the detailed wavelength-dependent absorption and scattering of the dust.

A more recent investigation of the radiative properties of Saharan desert aerosols was made using ground-based measurements [17]. The aerosol characteristics were consistent with the Shettle [18] desert models, but the properties were found to depend upon the background or dust storm conditions. An assumed refractive index of 1.55 - i0.005 was used with real and imaginary parts that were too large (see following).

Recently, the indices of refraction of six Saharan sand samples and that of Fe_2O_3, which imparts a brownish color to the sand, became available in the solar spectral region (0.185–1.1 μm). Also, chemical analyses of these sand samples are now available for comparison to the airborne samples collected during the GATE program [19]. The six Saharan samples include those from the Azelik flood plain, dune sands from Maradi, the Ténéré Desert, the Niger Valley, and Lake Chad.

In this chapter the visible and near-infrared indices of refraction of these Sahara sands and the particle size distribution and number density observed in the GATE program are used to calculate the scattering and absorption properties of the dust cloud with these new measured indices of refraction [19]; the two models that have not been used previously in this application are examined. A comparison of the calculated results to the observed solar spectral observations in the 0.4–0.9 μm wavelength region will be made with one model to verify the analytical approach. Then, using the long-wavelength infrared indices of refraction of these Sahara sands (spectral region 1.1–20 μm) in another model, the radiative transfer effects in the infrared region of the spectrum are approached theoretically.

The arid Sahara region exists because of the overlying prevailing wind flow patterns, the underlying terrain topography, and the atmospheric moisture transport. Superimposed upon these factors are the local atmospheric radiative transfer properties.

The Sahara desert is actually a region consisting of a number of smaller desert regions (geographically termed ergs), bounded on the north, east, west, and south by mountainous areas, and with a smaller central mountain range. These mountain regions strongly affect the atmospheric boundary layer circulation patterns as well as the rainfall resulting from upslope advection. There is an air mass flow from northeast to southwest

into the western Sahara "amphitheater" channeled by the Atlas Mountains of Morocco and Algeria on the north and the mountains of Sudan and Futa Jallon on the south. The underlying dune chains are the Erg Iguidy and Erg Chech. These ergs are hot and dry, and the rain is deposited on the north along the Mediterranean coast and in the south along the mountains.

In order for any change to occur in the radiative processes over desert areas of the western Sahara, where major dust storms are formed, there must first be a significant change in the wind circulation pattern and a concurrent change in moisture transport. The local radiative transfer properties of the atmosphere, as affected by the underlying terrain, influence the buildup of dust storms.

The earth's global circulation pattern is basically that of a heat engine fed by solar radiation, with maximum input in equatorial regions and cold sinks at the poles. The solar radiative input to the earth is affected by stratospheric optical-chemical reactions and by the tropospheric chemistry. During atmospheric circulation processes, which occur almost continously, aerodynamic forces operate to augment frequently, as well as perpetuate, certain atmospheric circulation properties. In any analysis of a particular region, the scope should be kept very broad in order to consider as completely as possible the interactions of all radiative transfer contributions. The database available for this report is essentially information about the troposphere above the western Sahara, although the radiative transfer models implicitly have the effects of the stratosphere.

II. DATABASE

There are four sources of the data used in the analyses presented here. The major source is the Kondratiev et al. [15] report on the aerosol in the GATE area. A second source is the Minnis and Cox report [16], and the third is a book [19] listing the chemical composition and complex indices of refraction of six Saharan sands that may become airborne as dust aerosols. The fourth source is the ERBE Experiment Team's [20] report on the Earth Radiation Budget Experiment.

The data of Kondratiev et al. [15] consist of atmospheric soundings, dust aerosol number density, size distribution and chemical analysis, solar radiation attenuation, upwelling and downwelling fluxes (longwave and shortwave), flux divergence, and albedo. Many of these observations were from aircraft. Satellite observations from ATS-1, ATS-6, SMS-1, NOAA-2, and NOAA-3 and ship observations gave dust cloud estimates.

The Minnis and Cox [16] data consist of aircraft measurements from four broadband Eppley hemispheric radiometers, both downlooking and uplooking, two in the 0.285–2.8 μm band and two in the 4–50 μm band.

Associated parameters are listed, such as temperature, dew point, static pressure, time, logbook estimates of dust cloud cover, and various aircraft heading and location data.

The listing of the chemical composition of six Saharan aerosols (Ref. 19, p. 399) and the complex indices of refraction in the wavelength range 0.185–1.105 μm (Ref. 19, pp. 457–462) furnish data that allow previously unavailable quantitative input into the radiative transfer models of the Saharan dust storms. The indices of refraction have been deduced using a radiative transfer theory that permits the elimination of the scattering that occurs in the potassium bromide pellets that contain the Saharan aerosol dusts [21]. The transmission technique used by Volz [22,23a,b] with potassium bromide pellets unfortunately results in an absorption portion at least one magnitude greater than those measured by [19] on the Saharan aerosols; the real portions measured are also less, as deduced from a Brewster angle measurement, than assumed by Tanré et al, [17].

The ERBE Experiment Team data [20] include emitted infrared radiation, albedo, and estimated scene types on 15 November 1984 as well as measurements of the solar constant.

III. MODELING

There are basically two spectral regions for modeling: (1) the ultraviolet, visible, and near-infrared solar spectral region, where emission effects can be neglected, and (2) the longer wavelength region (greater than 3 μm wavelength), where atmospheric emission effects are significant. The reason for this distinction arises from the architecture of the models. Radiative transfer models are considerably more complicated when the emission as well as absorption and scattering of atmospheric aerosols and molecules must be inserted into the model. Essentially, at the shorter wavelengths, incident solar energy is converted into heat, to be reradiated at longer wavelengths. This heat is radiated from atmospheric aerosols and molecules at temperatures corresponding to their particular altitudes as well as from the earth's surface at a temperature of ~300 K. The peak emission wavelength at a temperature of 300 K is at 10 μm, with the emission trailing off to negligible at wavelengths of 3 and 80 μm. Thus emission models are required at wavelengths longer than 3 μm, which also must include absorption and scattering by aerosols and molecules.

In this chapter, two models are used. The shorter wavelength model is the Dave vector radiative transfer model, and the longer wavelength model is the LOWTRAN 5 program. A detailed description of the Dave program is available [19]. Inputs are the complex indices of refraction of the atmospheric Saharan dust aerosols, their size distribution and number

density, the atmospheric pressure–height distribution (tropical for this report), ozone variation with altitude, optical reflectance of the underlying terrestrial surface, and the sun zenith angle. The effects of particle shape are included in the specification of the particle size distribution by using the technique described by Egan [24]. When particles are of irregular shapes or when they agglomerate, the effect is to produce increased scattering, the amount depending upon the size and number of asperities or constituents in the agglomerates [24]. These effects are taken into account by choosing the particle size and number density distribution. Outputs are optical depth as a function of wavelength and upward and downward radiances as a function of zenith angle and azimuth of the viewing direction. The Dave program is run for one wavelength at a time; wavelengths chosen in the present modeling program are 0.36, 0.400, 0.500, and 1.0 μm to cover the ultraviolet through the visible to the near-infrared. The Dave radiative transfer program is essentially that developed by Hansen and Travis [25] to analyze light scattering in planetary atmospheres. The technique involves the use of Mie single scattering of a distribution of particle sizes, then multiple scattering. The multiple scattering is described using a doubling (or adding) method to obtain the intensity, linear polarization (its degree and direction), and circular polarization. The accuracy depends upon the incident and scattering directions and is limited only by the number of Fourier terms in an expansion of azimuth-dependent functions. The program has been used to define the optical complex index of refraction of the clouds of Venus [26] as well as the particle radius in the clouds to three figure accuracy.

The LOWTRAN 5 program [27] is a computer code that characterizes atmospheric transmittance and thermal radiation emitted by the atmosphere and earth at wavelengths from 350 to 40,000 cm^{-1} (0.25–28.6 μm) at a spectral resolution of 20 cm^{-1}.* The LOWTRAN 6 code that supercedes LOWTRAN 5 includes solar and lunar scattering, spherical refractive geometry subroutines, the same water vapor continuum model, modified aerosol, cirrus cloud, and rain models. The LOWTRAN 7 code [28] has been criticized in the water vapor modeling aspect, in that there are inconsistencies with optical and microwave measurements that are yet to be resolved [29,30]. There have been ongoing discussions about the accuracy of the H_2O absorption bands, particularly the contributions of the H_2O vapor continuum. For our purposes, the simpler LOWTRAN 5 model is used as a first cut at the long-wavelength infrared modeling. Comparisons of the LOWTRAN 5 with measurements is given in Appendix F of Kneizys et al,

* To describe electromagnetic radiation, astronomers use cm^{-1} (wavenumber) and physicists use wavelength in μm, where $1/cm^{-1} = 1$ μm.

[27] for some important water vapor 6.3 μm and carbon dioxide 4.3 and 15 μm bands. It is seen that the LOWTRAN calculations agree closely with measured spectral transmittance. Sea level transmittance and atmospheric radiance measured from the Nimbus 4 satellite also closely agree.

A. Dave Vector Model

The complex indices of refraction for inputs to the Dave program were selected from the optical constants available for five sand samples [19]; two were chosen for the calculations. Aeolian dust is derived from the surface soil particles from wind erosion. The airborne particles are thus derived from the surface material and have the same indices of refraction [31]. They were Sahara sand 1 from the Azelik flood plain and Sahara sand 5, which was dune sand from the Niger Valley close to Niamey. These sand samples were those closest to the region of the western Sahara where the major dust storms develop. They also represent a range of the real portion of the index of refraction of $\sim$1.5 for Sahara sand 1 and $\sim$1.3 for Sahara sand 5. The imaginary portions are similar to those of the other sand samples except for Sahara sand 4 from the Lake Chad area. Five wavelengths were used in the calculations, and these and the complex indices for the two Sahara sands are shown in Table 1.

The variation of the number density of the sand aerosols $n(r)$ is taken as r^{-3} based on the data of Kondratyev et al. (Fig. 10 of Ref. 15). The observed spectrum of particle size shows a slower decrease in number density than the usual r^{-4}. The vertical profile of aerosol concentration in Fig. 1 was adapted from Fig. 14 of Kondratyev et al, [15]. The aerosol layer boundaries are indicated, and the concentrations as observed and the one used here are shown.

TABLE 1 Complex Indices of Refraction for the Sahara Sands

Sahara sand sample	Wavelength (μm)	n_r	n_i
1	0.33	1.487	0.228E−2
5	0.33	1.258	0.106E−2
1	0.400	1.494	0.177E−2
5	0.400	1.267	0.656E−3
1	0.500	1.484	0.156E−2
5	0.500	1.269	0.378E−3
1	1.0	1.448	0.682E−3
5	1.0	1.231	0.210E−3

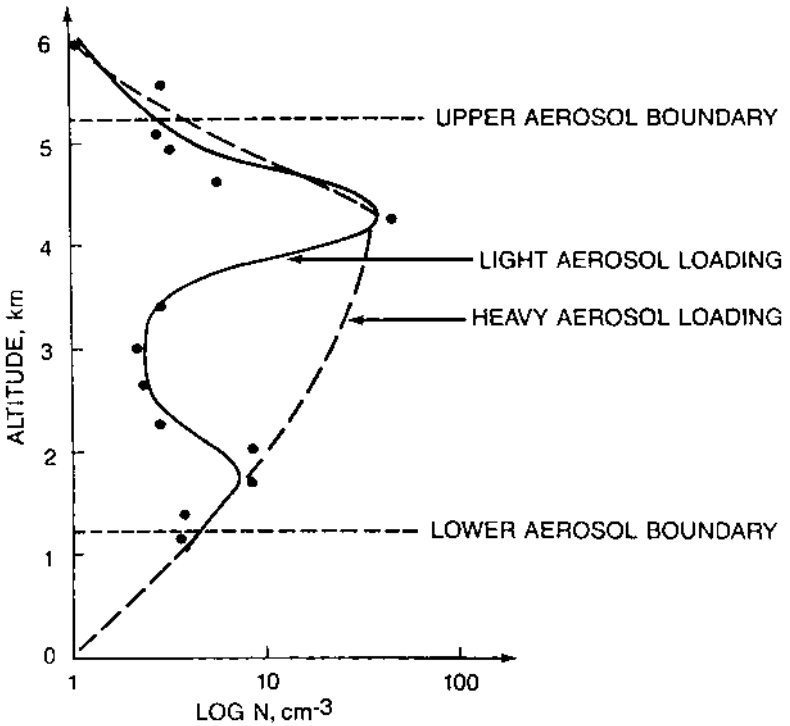

FIGURE 1 Vertical profiles of measured aerosol concentration [log (N, cm^{-3})]. (——) Aerosol concentration (light loading); (– –) heavy loading aerosol concentration; (- - -) aerosol layer boundaries. (Adapted from Ref. 15.)

The observed aerosol concentration (light loading) is a minimum within the cloud, where the mass concentration was observed to be a maximum; it was also noted that the larger particles were conglomerates of smaller particles. For the present modeling, two distributions were used. The dashed curve was taken to be an approximate representation of the actual (unconglomerated) particle number density (heavy loading). The particle size range was taken to lie between radii of 0.400 and 18.00 μm. Particle radius does agree with Gillette [31] for particles at 1 m above ground. The dry parent soil particles are much larger, but those that have been transmitted great distances are much smaller [31]. The rural aerosol model with 5 km surface visibility is justified for the infrared computations, because that visibility is sometimes observed in dust. The vertical profile of the rural model boundary layer condition approximates that given in Fig. 1. The DAVE program computes the fluxes.

The pressure–height atmospheric distribution was taken as the AFGL "tropical," as was the ozone vertical distribution [32]. The ozone band absorption is included parametrically in the model as a function of wavelength. The sun zenith angle was taken as 0°. A sun zenith angle of 0° was taken as an approximation for noon sun at a latitude of 20°N during the period of measurement in July 1974 [33]. The data used for comparison were not specifically segmented to time of day (sun elevation) or latitude.

Two diffuse surface reflectivities were used: 0.0 and 0.5. The 0.5 value was taken to represent the average visual reflectivity of the Sahara sands, taking into account the bidirectional reflectance function (Ref. 19, p. 134), and the 0.0 reflectivity was used to determine the effects of atmospheric transmission alone on the incident radiation over a low albedo surface such as the ocean.

By-products of the modeling are the plane and circular polarization produced by atmospheric scattering.

B. LOWTRAN 5 Model

The LOWTRAN model [27] includes the band-averaged effects of CO_2, N_2O, CH_4, CO, N_2, O_2, HNO_3, and H_2O vapor. The H_2O vapor continuum has been included empirically based on limited experimental measurements. For the present long-wavelength modeling, the 5 km visibility rural extinction model was used as representative of the heavy dust conditions when the meteorological visibility dropped to 8.7–12 km [15]. The visibility model does not represent surface visibility, but that extending to the top of a well-mixed boundary layer. The rural aerosols are assumed to be composed of 70% water-soluble substance and 30% dustlike aerosols [34]. The water-soluble and dustlike aerosols have refractive indices between $\sim$1.2 and 1.4 in the 1–5 μm region and absorptions of $\sim 10^{-3}$. Volz [22] indicates that dustlike aerosols are comparable to Sahara dust. A tropical model is applicable because the model surface temperature of 300 K is close to that observed in the Sahara and is comparable to other available models. The dustlike aerosols have very high absorption in the 9–14 μm region, as do the Saharan aerosols. A tropical model atmosphere was used, with a background stratospheric aerosol profile and extinction. A 20 cm^{-1} resolution was used in the model, and the wavelength range was 12,500.0-500.0 cm^{-1} (0.8–20.0 μm). Vertical paths were used in the model looking both downward and upward. Vertical paths were assumed as an approximation to take into account the varying geometry of sensor acceptance and solar incidence angles. The ground emissivity was assumed to be unity because of the high absorption of the Sahara sands in the 8–14 μm spectral region (corresponding to the wavelengths of maximum thermal emission range of the terrestrial surface).

IV. RESULTS

The results of the modeling are presented in two parts:

1. The Dave vector program radiance values for wavelengths of 0.33, 0.400, 0.500, and 1.0 μm, with comparisons to the observations of Kondratyev et al. [15] and those of Minnis and Cox [16]
2. The LOWTRAN 5 radiance calculations in the spectral range 12,500 to 500 cm^{-1}, and comparisons to the long-wavelength results in the two aforementioned reports

To check the effect of increasing the mixed gas level from that in the LOWTRAN 5 model (330 ppm) to a level 330 ppm greater, the mixed gas ratio was increased by that amount. The mixed gases include CO_2, N_2O, CH_4, CO, N_2, and O_2. Although the increase will also have the effect of increasing N_2 and O_2 molecular scattering, the effect is small in the longer wavelength infrared. The inclusion of all of these gases will be a more stringent test of a possible "greenhouse effect" than the use of CO_2 and CH_4 alone. The tropical profiles are selected for H_2O vapor and O_3.

A. Dave Vector Program Results

The results of the Dave vector program modeling are presented in Tables 2–4 and in Figs. 2–5. Essentially, the information presented indicates the effect of aerosols on the atmospheric transport of radiation in the wavelength range from the ultraviolet through the near-infrared.

In detail, Table 2 lists the total aerosol and Rayleigh optical depths for the AFGL tropical atmosphere model with the two aerosol loadings shown in Fig. 1. The two sets of values for the complex indices of refraction

TABLE 2 Total Aerosol and Rayleigh Optical Depths

	Dave program			Kondratyev				
		Dusty desert		Kara Kum Desert		Atlantic Ocean		
λ (μm)	Sahara sand aerosol	Light	Heavy	9/19 Clear	9/10 Dusty	7/20 Clear	6/24 Dusty	Rayleigh
0.33	1	0.211	0.599	0.184	0.345	0.198	0.421	0.5634
	5	0.222	0.630					
0.400	1	0.217	0.615					0.3825
	5	0.234	0.664					
0.500	1	0.227	0.643					0.1508
	5	0.241	0.684					
1.0	1	0.439	0.903	0.078	0.254	0.097	0.322	0.00724
	5	0.393	0.809					

TABLE 3 Percent Plane Polarization Effects of Sahara Dust as Seen from 44.7 km Altitude[a]

		Percent polarization for aerosol (type 1) loading as shown		
λ (μm)	Surface albedo	None	Light	Heavy
0.33	0.0	8.87	8.57	7.95
	0.5	2.75	3.02	3.13
0.400	0.0	8.85	8.26	7.28
	0.5	1.91	2.14	2.30
0.500	0.0	8.26	7.51	5.85
	0.5	0.70	0.97	1.13
1.0	0.0	7.66	6.28	4.06
	0.5	0.03	0.59	0.71

No circular or elliptical polarization greater than 0.004%.
[a] Solar zenith angle = 0°; sensor zenith angle = 30°.

used in the model are those listed in Table 1. In Table 2, a comparison of the Sahara sand aerosol optical depths is made to the Kondratyev et al. [15] results over the Kara Kum Desert and over the Atlantic Ocean; results at only two wavelengths (0.33 and 1.0 μm) are given in their report.

It is seen from Table 2 that the difference between optical depths using Sahara sand 1 or 5 aerosol is at most ~10% for the light and heavy dust loadings. Because the difference is small, Sahara sand aerosol 1 with the

TABLE 4 Photometry Effects of Sahara Dust as Seen from 44.7 km Altitude[a]

		Atmospheric radiance relative to clear atmosphere, (type 1) loading as shown		
λ (μm)	Surface albedo	None	Light	Heavy
0.33	0.0	0.1585	0.1911	0.2483
	0.5	0.5060	0.5471	0.6615
0.400	0.0	0.1086	0.1291	0.1551
	0.5	0.4993	0.4880	0.4743
0.500	0.0	0.04216	0.06430	0.09246
	0.5	0.4969	0.4781	0.4503
1.0	0.0	0.001868	0.04955	0.08955
	0.5	0.4997	0.4668	0.4444

[a] Solar zenith angle = 0°; sensor zenith angle = 30°.

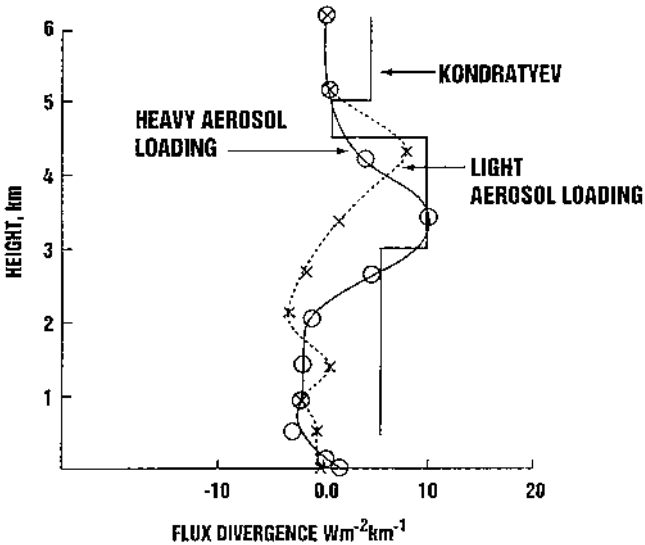

FIGURE 2 Short-wavelength solar flux divergence versus altitude for light and heavy aerosol loadings and a 0.5 ground albedo. A comparison is also shown to calculations of Kondratyev et al. [15].

somewhat larger refractive and absorption indices was used for subsequent analyses. Also, it is seen that the Dave optical depths are higher than the Kondratyev et al. [15] results, particularly at 1.0 μm wavelength. It is possible that the Sivkov technique used to determine optical depths may be inapplicable for the cases considered. Sivkov [35] uses the expression τ_λ^* equal to the aerosol optical thickness and the index of power to which the wavelength is raised in the Angstrom formula $\tau_\lambda^* = \beta\lambda^{-n}$ to characterize the degree of aerosol attenuation selectivity. Aerosol optical thickness at $\lambda = 1$ μm corresponds to the Angstrom index of atmospheric turbidity β. It also appears that the "clear" atmosphere measured by the Kondratyev group contained a significant amount of aerosols. The large aerosol optical depth at 1.0 μm wavelength in the Dave model may be the result of a resonance that is stronger for Sahara sand 1 aerosol than for sand 5 aerosol because of its higher real index of refraction [36]. It also appears that it may result from iron oxide contaminants in sample 1 (see Sec. V).

The optical properties of spheres do not have a one-to-one correspondence with irregular particles. The phase functions may be brought into agreement in a number of ways. One way is to modify the semiempirical theory of Pollack and Cuzzi [37] or use Mie particles with a fictitious

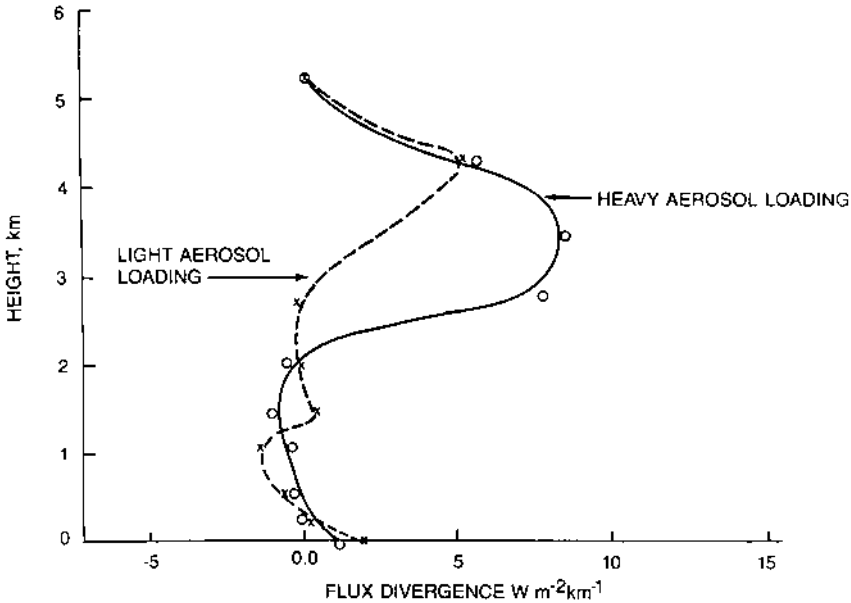

FIGURE 3 Short-wavelength solar flux divergence versus altitude for light and heavy aerosol loadings and a 0.0 ground albedo.

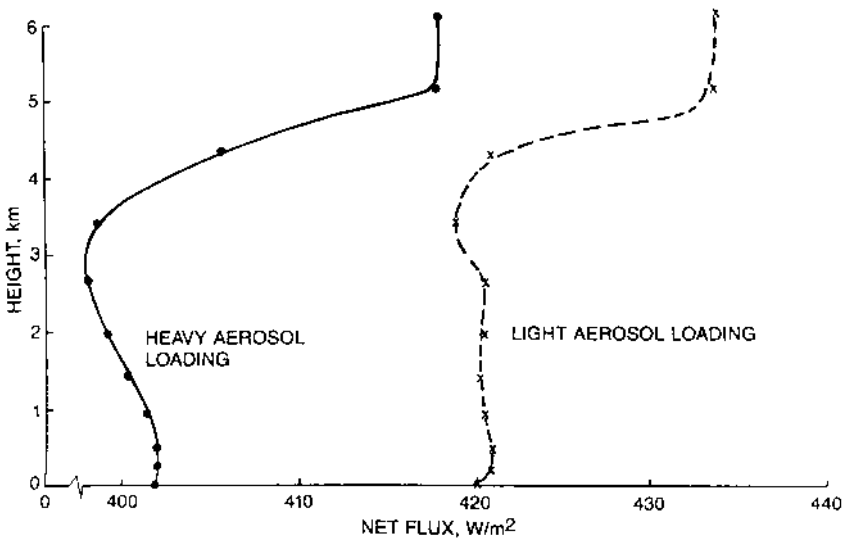

FIGURE 4 Net short-wavelength solar downward flux versus altitude for light and heavy aerosol loadings and a 0.5 ground albedo for 0.33–1.0 μm wavelength.

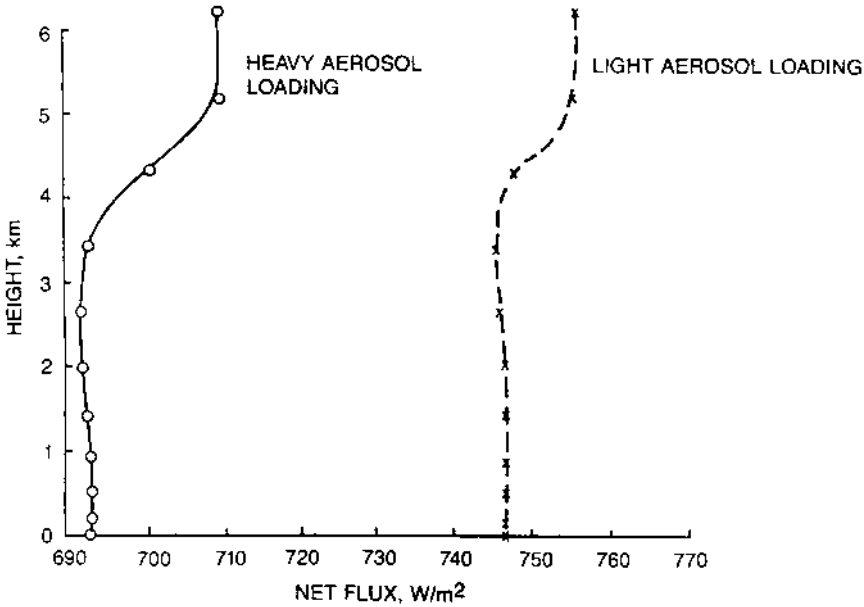

FIGURE 5 Net short-wavelength solar downward flux versus altitude for light and heavy aerosol loadings and a 0.0 ground albedo for 0.33–1.0 μm wavelength.

absorption [38]. Another technique used by Egan [24] is to modify the number and size distribution of the aerosol particles; the latter technique is used here.

The polarimetric and photometric properties of Sahara dust as seen from space (44.7 km altitude) are shown in Tables 3 and 4. These properties are affected strongly by the surface albedo; because of this, two typical values of diffuse surface albedo were used: 0.5 for a terrestrial sand surface and 0.0 for an ocean surface.

The percent polarization (Table 3) is seen to vary inversely with radiation wavelength for both aerosol loadings, as would be expected from the wavelength dependence of scattering. For a 0.0 albedo surface, the polarization varies inversely with aerosol loading, whereas for a 0.5 albedo underlying surface, the polarization varies directly with aerosol loading. The reason for the inverse variation with aerosol loading for the lower albedo surface is that the corresponding lower surface albedo permits the depolarizing effect of aerosol multiple scattering to dominate and thus reduce the observed polarization. For the higher surface albedo, the forward-scattering, highly polarized component of aerosol scattering arising from the surface-scattered radiation will dominate, resulting in the higher polarization shown.

A comparison of the 0.0 ground albedo (simulating sea areas) with the Space Shuttle polarimetric observations of oceanographic areas reveals a strong wavelength dependence of polarization of 20%, 10%, 5% for blue, green, and red spectral regions, respectively [4]. The Space Shuttle observations were for a phase angle of 121°, whereas the DAVE model phase angle is 30° (the phase angle is the angle between the solar incident and sensor viewing directions). Egan [39] found that the percent polarization of sea areas varies directly with the phase angle and that at smaller phase angles the polarization is less.

The photometry (Table 4), as seen from space, shows less well defined photometric trends. For the 0.0 albedo surface, the radiance varies directly with aerosol loading and inversely with wavelength. For the 0.5 albedo surface, the variation with aerosol loading is opposite at wavelengths of 0.400, 0.500, and 1.0 μm, and there is a general inverse radiance trend with wavelength (exception at 1.0 μm, no aerosols). Also for 0.33 μm, surface albedo = 0.5, there is a strong radiance increase from light to heavy loading, whereas for the next wavelength there are decreases. This is explained by the backscatter of radiation that enters into the calculation; the effect of surface backscattering to the atmosphere is weakest at 0.33 μm and strongest at longer wavelengths for the 0.5 surface albedo.

The photometric and polarization effects have been presented to establish the relationship between photometry and polarization for the test cases shown.

To determine the energy distribution of the incident radiation, we employ two approaches. One is the determination of total radiation flux divergence, and the other is the calculation of the net flux downward. The flux divergence is the radiant energy variation with altitude (i.e., the radiant energy absorbed by various levels of the atmosphere). The net flux downward is another way of representing the net decrease of radiant energy as it progresses downward through the atmosphere. These data are presented in Figs. 2–5 and represent the energy available to heat the aerosol-laden atmosphere and the underlying terrestrial surface.

Two cases are considered: (1) an underlying surface with an albedo of 0.5 (Figs. 2 and 4) and (2) an underlying surface of 0.0 albedo (Figs. 3 and 5). A comparison to the data of Kondratyev et al. [15] is shown in Fig. 2. In Fig. 2, the flux divergence is plotted versus altitude from the surface to a height of 6.17 km; it is seen that the heavy aerosol loading has a greater flux divergence than the light aerosol loading. The net solar flux (Fig. 4) accessible for atmospheric aerosol heating to the 6 km level is 14 W/m^2 for the light aerosol loading and 19 W/m^2 for the heavy aerosol loading, as may be seen from Table 5. The effect of both aerosol loading is to reduce the radiative flux reaching the ground, although radiative transfer to the

TABLE 5 LOWTRAN 5 Long-Wavelength Results[a]

H1 (km)	*H2* (km)	Θ (deg)	Mode	Mixed gas ratio	Integrated path flux (W/m^2)	Transmission (avg)
100	0	180	1,0,2	1.0	440.55	0.5636
100	0	180	1,0,2	1.3	436.90	0.5621
100	0	180	1,2,2	1.0	431.29	0.3797
100	0	180	1,2,2	1.3	427.72	0.3784
0	100	0	1,0,2	1.0	488.44	0.5636
0	100	0	1,0,2	1.3	488.98	0.5621
0	100	0	1,2,2	1.0	487.53	0.3797
0	100	0	1,2,2	1.3	489.01	0.3784
1	0	180	1,0,2	1.0	677.64	0.6340
1	0	180	1,0,2	1.3	677.64	0.6327
1	0	180	1,2,2	1.0	664.64	0.4893
1	0	180	1,2,2	1.3	664.70	0.4881

[a] *H1* is position of observer.

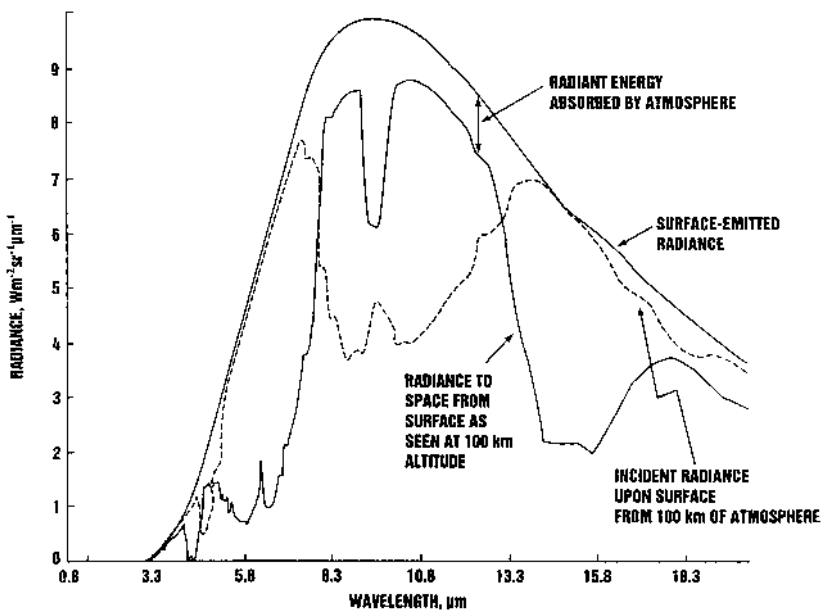

FIGURE 6 Long-wavelength radiances as a function of wavelength for heavy aerosol–laden atmosphere for 300 K surface temperature.

aerosol increases. For the condition of 0.5 ground albedo, no aerosols, and only Rayleigh atmospheric scattering, the net flux reaching the ground would be 460 W/m^2. The calculated peak flux divergence is similar to that of Kondratyev et al. [15]. The small difference is probably caused by the aerosol model not being in exact agreement with the aerosol observations.

For the 0.0 albedo case, the flux divergence (Fig. 3) follows trends similar to those of the 0.5 albedo but with higher peak flux divergence because of the lack of surface-reflected radiation. As a result, there is a greater net flux decrease (Fig. 5) for both the heavy and light aerosol loadings to

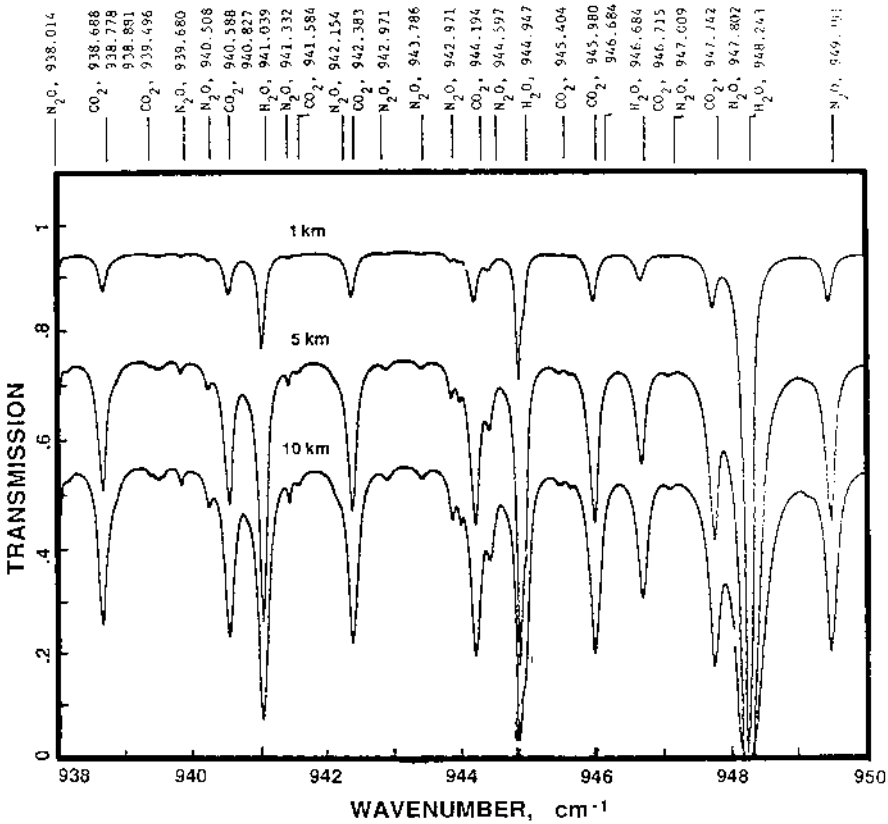

FIGURE 7 Typical boundary layer transmission of the earth's atmosphere between wavelengths of 10.661 and 10.526 μm (938–950 cm^{-1} wavenumbers) using rural aerosols and H_2O continuum of LOWTRAN 5 in a line-by-line model. The H_2O continuum is the main cause of the displacement of the maximum transmission below 1.0.

the surface and at the surface. The net flux reaching a 0.0 albedo ground surface with the absence of aerosols and only Rayleigh scattering would be 793 W/m^2.

B. LOWTRAN 5 Program Results

The LOWTRAN 5 program results are presented in both graphical (Figs. 6 and 7) and tabular (Tables 5 and 6) forms. In Table 5 is shown the effect of increasing the mixed gas concentrations by 1.3. Figure 6 shows the blackbody radiance ($W\ m^{-2}\ sr^{-1}\ \mu m^{-1}$) from the terrestrial desert surface and also that at an altitude of 100 km after passing through the earth's heavy aerosol-laden atmosphere. It is seen that the absorption is far from uniform, being essentially the result of the absorption of water vapor, carbon dioxide, and methane. The radiation incident upon the terrestrial surface from 100 km altitude through the atmosphere is also shown. The 30% increase in mixed gases has a barely perceptible effect on these curves, basically because the mixed gas absorption is swamped by the H_2O continuum, as shown, for instance, in Fig. 7. This agrees in principle with the statement in Houghton et al. [2] that the "greenhouse effect" is dominated by water vapor. The greatest changes occur where the atmospheric transmission is very low, as shown in Fig. 8. The radiance effects are best seen by reference to Table 5, the results of which are summarized in Table 6, and by reference to Fig. 9, which shows the effect on surface radiation as a function of precipitable water vapor.

TABLE 6 Incremental Long-Wavelength Path Radiance Changes for LOWTRAN 5 from 1.3 Change in Mixed Gases and Aerosols

Configuration	Flux change (W/m^2)	Mixed gases	Aerosols
Radiant flux to space	+ 9.26	1.0	Clear minus dusty
at 100 km	+ 9.18	1.3	Clear minus dusty
Incident ground radiant	+ 0.91	1.0	Clear minus dusty
flux at 0 km	− 0.03	1.3	Clear minus dusty
Radiant flux from ground	+13.0	1.0	Clear minus dusty
to 1 km	+12.94	1.3	Clear minus dusty
Radiant flux absorbed	−47.89	1.0	Clear
by atmosphere	−52.08	1.3	Clear
	−50.63	1.0	Dusty
	−61.29	1.3	Dusty
Net radiant flux absorbed	+ 4.19	1.3 minus 1.0	Clear
by atmosphere	+10.66	1.3 minus 1.0	Dusty

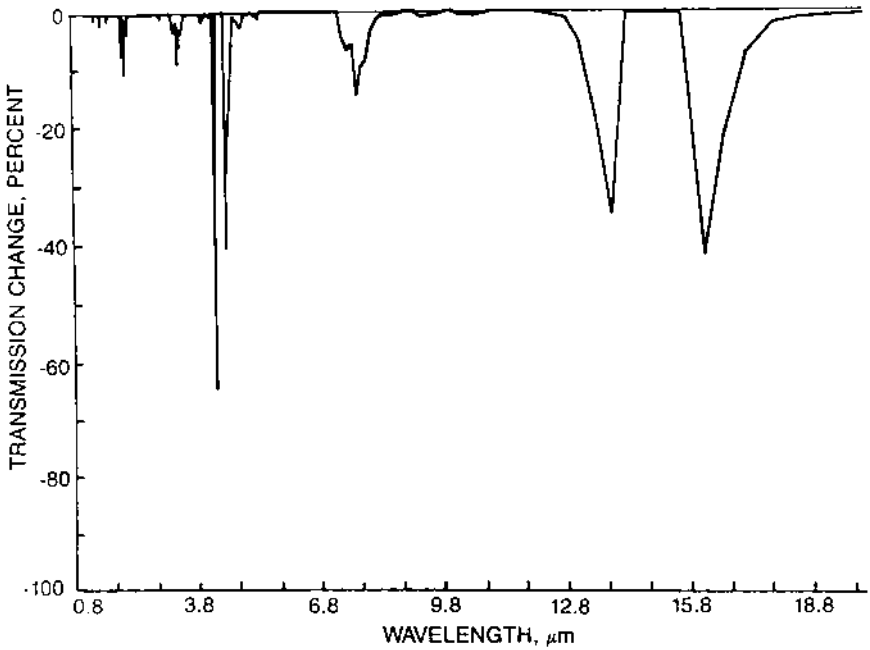

FIGURE 8 Percent decrease in clear atmospheric transmission from an increase of 30% in CO_2, N_2O, CH_4, CO, N_2, and O_2 with H_2O continuum and HNO_3 held constant. The large percent decreases occur in very low transmission spectral regions and thus have negligible effect on overall atmospheric transmission.

The LOWTRAN 5 results in Table 5 represent the radiances (W/m^2) seen with the observer at height *H1*, looking toward height *H2*. The 1, 0, 2 mode designates the tropical model atmosphere, no aerosol attenuation in the calculation, and a vertical path between two altitudes. The 1, 2, 2 modifies the model to include an aerosol extinction that yields a 5 km meteorological range. The program is executed in both radiance and transmittance modes.

It is seen, by referring to Table 5, that the upward atmospheric transmission is slightly reduced in instances where the mixed gas ratio is increased by 30%. In Table 6, it is seen that the flux to space is decreased by the presence of aerosols (first two lines of the table) but the increase in mixed gases reduces the flux change. The radiative flux incident upon the ground is increased by 0.91 W/m^2 by aerosols but increases slightly for an increase in mixed gases (next two lines of the table). The flux from the ground (0 km) upward remains relatively constant (fifth and sixth lines). In the remain-

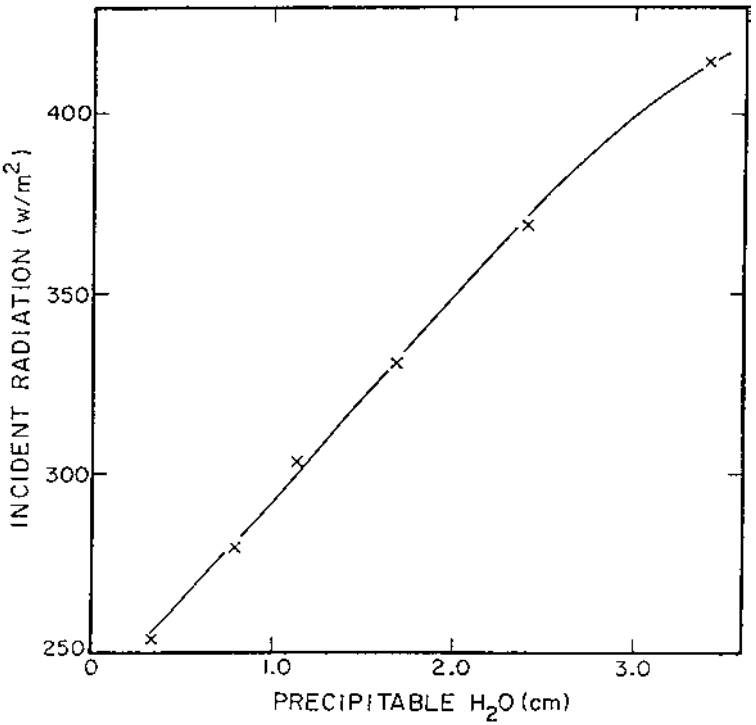

FIGURE 9 LOWTRAN 5 atmosphere infrared modeled effect of precipitable water on radiant flux incident on earth's surface (ϵ=1).

der of the table it is seen that an increase in aerosols or in mixed gases increases the flux absorbed by the atmosphere to augment the short-wavelength radiation absorbed.

V. DISCUSSION

The results just presented represent a new application of two radiative transfer programs (the Dave vector model and LOWTRAN 5) to the problems of radiative transfer and remote sensing over the Sahara Desert and the impact of an increase in mixed gases in the presence of water vapor, nitric acid, and ozone. The Dave program indicated an aerosol heating flux of 14 or 19 W/m^2 for light and heavy aerosol loading, respectively. The net flux striking the terrestrial surface (downward minus upward) was seen to be significantly dependent upon ground albedo as noted by Coakley and

Cess [40] as well as on the associated atmospheric aerosol loading. It is also to be noted that a change in the actual aerosol constants in the Dave program, corresponding to two different Saharan sands, produced a 10% change in optical depths of the atmosphere.

The use of the visible and near-infrared complex indices of refraction of Sahara sand 1 in the Dave program instead of Sahara sand 5 is justified to serve as a first look at the effect of varying the complex index of refraction alone in radiative transfer calculations. An interesting comparison of Table 2 with data of Tanré et al. [17] shows that the optical depth at 1.0 μm is about twice that at the shorter wavelengths. The reason is that Sahara sands 1 and 5 have a significant Fe and Fe_2O_3 content [19], which produces a brownish coating on the sand similar to "desert varnish" [41,42]. A better selection for the 1.0 μm calculations would have been Sahara sand 3 from Erg du Ténéré, which is almost due east of M'bour, the site of the Tanré et al. [17] ground station. Sahara sand 3 had low FeO and Fe_2O_3 [19] and hence weak absorption at 1.0 μm; this would produce dominant scattering at 1.0 μm to decrease the aerosol optical depth (Table 2) and reduce the polarization (Table 3). Thus, polarization can delineate absorptive aerosols, here evident in the characterization of iron oxide in aerosols. As the theory and experimental observations become more refined, so will the modeling. In the infrared region, the emissivity of the terrestrial surface was assumed to be unity, a reasonable approximation for silicate sand, which has a high absorption in the 10 μm spectral region.

The Dave model generally confirms the observations of Kondratyev et al. [15] for heavy aerosol loading and Sahara sand 5. Compared to the NCAR model global average results [40], the solar radiative flux absorbed at the surface is reduced by $\sim$11.5 W/m^2 for low latitude land surfaces in the NCAR model compared to the present determination of 14–19 W/m^2. The NCAR Community Climate Model [40] model of Shettle and Fenn [34] is for downward solar radiation in a clear sky. A comparison of the results shown in Table 4 with the ERBE Experiment Team [20] imagery with reflected sunlight albedo of $\sim$10% over sea areas and $\sim$50% over the western Sahara shows fairly close agreement for a clear sky. Thus the present modeling appears reasonable and also yields wavelength-dependent photometry and polarization of the aerosol cloud as remotely sensed from space [43].

The LOWTRAN 5 model output is particularly interesting because it shows the wavelength-dependent fluxes to space and to the terrestrial surface including effects of the mixed gases and H_2O vapor. The tropical AFGL model that was used for the calculations is a good approximation to the actual Sahara Desert conditions. For more precise work, the measured atmospheric properties of temperature, pressure, O_3, and H_2O vapor could

be used as the input. The H_2O vapor in the LOWTRAN 5 vertical path to space is 3.35 g/cm^2, and that of the concurrent H_2O continuum is 0.0689 g/cm^2. For actual soundings at Dakar, Senegal, under dusty conditions, the path to space contained 3.01 g/cm^2, and under clear conditions, 5.12 g/cm^2 (from Fig. 2 of Ref. 16). Thus, the LOWTRAN 5 model is realistic in terms of the H_2O vapor modeling. It should be mentioned that LOWTRAN 5 may be modified to permit the transmission functions of each absorber in the mixed gases to be calculated separately and also to extend the calculations to other absorbers [44].

The experimental finding that in the infrared spectral region, changes in the effective emissivities of the atmosphere in the presence of dust are ambiguous but rarely exceed the uncertainties of observations is confirmed by the LOWTRAN 5 modeling. Tables 5 and 6 show that the presence of aerosols can decrease the incident radiance on the ground by 0.91 W/m^2, and with a 30% increase in the mixed gases can effect a small increase of 0.03 W/m^2. The long-wavelength infrared indices of refraction of the Sahara sands were determined in the 2–10 μm region using an interferometer-spectrometer and the Kubelka–Munk radiative transfer theory to eliminate scattering from absorption [45]. The results confirm the use of the LOWTRAN 5 values as a close approximation. The average transmission of the atmosphere decreased by 0.0015 for a clear atmosphere with a 30% increase in the mixed gases and by 0.0013 with a mixed gas increase in the presence of aerosols. If one considers only the band between 7.5 and 13.9 μm, these figures are 0.0032 and 0.0029, respectively. The incident flux to the ground is changed by less than 1 W/m^2 by a 30% increase in mixed gases in the presence of aerosols.

In one instance, the ERBE Experiment Team [20] found that the infrared upward flux from clear Saharan regions at night was about 260 W/m^2 in cloud-free areas, whereas the daytime upward flux computed from LOWTRAN 5 was 441 W/m^2 (Tables 5). The difference is attributed to the fact that the daytime desert sand temperature was assumed to be 300 K, whereas at night the temperature would be significantly lower, reducing the spectral emmissivity by a factor of ~2 [46].

Also, it appears that polarization can be a valuable adjunct to photometry in the remote sensing of Saharan dust aerosol. The use of polarization requires the development of a new class of sensors that would permit spectral imaging polarimetry as well as photometry [21].

VI. CONCLUSIONS

From the analyses presented, it is concluded that a 30% increase in mixed atmospheric gases (CO_2, N_2O, CH_4, CO, N_2, O_2) (in the presence of the

LOWTRAN 5 fixed H_2O vapor, nitric acid, and O_3) causes infrared transmission changes of 0.0015 and 0.0013 for clear and aerosol-laden atmospheres, respectively. These changes are quite small. Radiant flux changes with aerosol loading serve to augment those already existing for the incident solar radiation. It appears that the mixed gas absorption bands are swamped by the H_2O absorption bands, and even though there are significant changes in the mixed gas transmission, they are evident only where the atmosphere is weakly transmitting.

The effect of aerosol loading decreases the long-wavelength ground flux by 0.91 W/m^2, and with a 30% concurrent increase in mixed gases (CO_2, N_2O, CH_4, CO, N_2, O_2) the flux is increased by 0.03 W/m^2. The infrared fluxes are computed by LOWTRAN 5 by integrating over the long-wavelength interval and the total downward flux by assuming approximately uniform radiance and multiplying by 2π steradians.

The incident solar radiation absorbed by the aerosol layer under the observed conditions lies between 14 and 19 W/m^2.

The original data of Hansen et al. [6] appear to be borne out in the low latitude region of the western Sahara basin.

Hence one would conclude that for the near future there will be negligible change in radiative transfer processes for the western Sahara as a result of a 30% increase in mixed gases for the aerosol conditions of this report.

REFERENCES

1. Gates, W.L. AMIP: the Atmospheric Model Intercomparison Project. Bull. Am. Meteorol. Soc. 1992, 73, 1962–1970.
2. Houghton, J.T., Jenkins, G.J., Ephraums, J.J., Eds. Climate Change. The IPCC (Intergovenmental Panel on Climate Change) Scientific Assessment; Cambridge Univ. Press: New York, 1990; 1962–1970.
3. Houghton, J.T., Callander, B.A., Varney, S.K., Eds. Climate Change 1992. Supplementary Report to the IPCC Scientific Assessment; Cambridge Univ. Press: New York, 1992; 1962–1970.
4. Egan, W.G.; Israel, S.; Sidran, M.; Hindman, E.E.; Johnson, W.R.; Whitehead, V.S. Optical properties of continental haze and cumulus and orographic clouds based on Space Shuttle polarimetric observations. Appl. Opt. 1993, 32, 6841–6852.
5. National Academy of Sciences. Changing Climate: Report of the Carbon Dioxide Assessment Committee Natl. Acad. Press: Washington, DC, 1983.
6. Hansen, J.; Johnson, D.; Lacis, A.; Lebedeff, S.; Lee, P.; Rind, D.; Russell, G. Climate impact of increasing atmospheric carbon dioxide. Science 1981, 213, 957–966.
7. Hansen, J.; Fung, I.; Lacis, A.; Rind, D.; Lebedeff, S.; Ruedy, R.; Russell, G.

Global climate changes as forecast by Goddard Institute for Space Studies three-dimensional model. J. Geophys. Res. 1988, 93, 9341–9364.
7a. Egan, W.G.; Huth, P.C.; Mihocko, G.A.; Hogan, A.W. Relation of mean air temperatures to other climate indicators. EOS Trans. Am. Geophys. Union 1993, 73, 68.
8. Idso, S.B. Carbon dioxide and global temperature: what the data show. J. Environ. Quality 1983, 12, 159–163.
9. Idso, S.B. The climatological significance of doubling of earth's atmospheric carbon dioxide concentration. Science 1980, 207, 1462–1463.
10. Idso, S.B. Reply to A.J. Crane's "Comments on Recent Doubts About the CO_2 Greenhouse Effect." J. Appl. Meteorol. 1982, 21, 748.
11. Egan, W.G.; Hogan, A.W.; Zhu, H. Physical variation of water vapor, and the relation with carbon dioxide. Geophys. Res. Lett. 1991, 18, 2245–2248.
12. Egan, W.G.; Hogan, A.W. Analysis of atmospheric carbon dioxide–water vapor inverse relationships at Mauna Loa. Trans. Am. Geophys. Union 1994, 75, 89.
13. Cess, R.D.; Hameed, S.; Hogan, J.S. Response of the Global Climate to Changes in Atmospheric Chemical Composition Due to Fossil Fuel Burning. A.S.M.E. Paper n 80-WA/HT-3, Nov. 16–21, 1980, Meeting.
14. Plantico, M.S.; Karl, T.R.; Kukla, G.; Gavin, J. Is recent climate change across the United States related to rising levels of anthropogenic greenhouse gases? J. Geophys. Res. 1990, 95, 16,617–16,637.
15. Kondratyev, K.Ya; Barteneva, O.D.; Chajsursky, L.I.; Chernenko, A.P.; Grishechkin, V.S.; Ivlev, L.S.; Ivanov, V.A.; Korzov, V.I.; Lipatov, V.B.; Prokofyev, M.A.; Tolkatchev, V.K.; Vasiliev, O.B.; Zhvalev, V.F. Aerosol in the GATE Area and Its Radiative Properties. NOAA Rep. No. NOAA-77020207. NTIS Rep. No. PB 265264. 1976.
16. Minnis, P.; Cox, S.K. Magnitude of the radiative effects of the Sahara dust layer. Thesis. NTIS Rep. No. PB286835, Colorado State University, 1978.
17. Tanré, D.; Devaux, C.; Herman, M.; Santer, R. Radiative properties of desert aerosols by optical ground-based measurements at solar wavelengths. J. Geophys. Res. 1988, 93, 14,223–14,231.
18. Shettle, E.P. Optical and radiative properties of a desert aerosol model. In Proceedings of a Symposium on Radiation in the Atmosphere; Fiocco, G., Ed. Deepak: Hampton, VA, 1984; 74–77.
19. Egan, W.G. Photometry and Polarization in Remote Sensing; Elsevier: New York, 1985.
20. ERBE Experiment Team First data from the Earth Radiation Budget Experiment (ERBE). Bull. Am. Meterol. Soc. 1986, 67, 818–824.
21. Egan, W.G. Proposed design of an imaging spectropolarimeter/photometer for remote sensing of earth resources. Opt. Eng. 1986, 25, 1155–1159.
22. Volz, F.E. Infrared optical constants of ammonium sulfate, Sahara dust, volcanic pumice, and fly ash. Appl. Opt. 1973, 12, 564–568.
23a. Volz, F.E. Infrared Refractive Index of Atmospheric Substances. Appl. Opt. 1972, 11, 755–759.

23b. Volz, F.E. Infrared Absorption by Atmospheric Aerosol Substances. J. Geophys. Res. 1972, 77, 1017–1031.
24. Egan, W.G. Volumetric scattering and absorption by aerosols: parametric sensitivity in Mie modeling and comparisons to observations. Appl. Opt. 1982, 21, 1445–1453.
25. Hansen, J.E.; Travis, L.D. Light scattering in planetary atmospheres. Space Sci. Rev. 1974, 16, 527–610.
26. Hansen, J.E.; Hovenir, J.W. Interpretation of the polarization of Venus. J. Atmos. Sci. 1974, 31, 1137–1160.
27. Kneizys, F.X.; Shette, E.P.; Gallery, W.O.; Chetwynd, J.H., Jr.; Abreu, L.W.; Selby, J.E.A.; Fenn, R.W.; McClatchey, R.A. Atmospheric Transmittance/Radiance: Computer Code LOWTRAN 5. Air Force Geophys. Lab. Rep. AFGL-TR-80-0067. NTIS Rep. No. ADA088215. Bedford, MA, 1980.
28. Kneizys, F.X.; Shettle, E.P.; Abreu, L.W.; Chetwynd, J.H., Jr.; Anderson, G.P. Users Guide to LOWTRAN 7: Interim Scientific Report. Air Force Geophys. Lab. Rep. TR-88-0177. NTIS Rep. ADA-206773. Bedford, MA, 1988.
29. Peter, R.; Schmidt, B. Comparison of columnar water vapor determined from microwave emission and solar transmission measurements. Presented at CoMEAS '93 Conference, Mar. 22–25, 1993, Albuquerque, NM.
30. Schmidt, B.; Peter, R.; Matzler, C. Intercomparisons of columnar water vapor retrievals obtained with a sun photometer and microwave radiometer. Progr. Electromagn. Res. Symp. Proc. Jet Propulsion Laboratory, Calif. Inst. Technol. Pasadena, CA, July 12–16, 1993, p. 67.
31. Gillette, D.A. In Production of dust that may be carried great distances. T.L. Pewe., Ed. Desert Dust: Origin Characteristics, and Effect on Mars. Spec. Paper 186.Geol. Soc. Am.: Boulder, CO, 1981.
32. McClatchey, R.A.; Fenn, R.W.; Selby, J.E.A.; Volz, F.E.; Garing, J.S. Optical Properties of the Atmosphere. 3rd Ed. Air Force Cambridge Res. Lab. Environ. Res. Paper No. 411, Rep. AFCRL-72-0497. NTIS Rep. No. AD-753075. Bedford, MA, 1972.
33. Smith, J.T., Jr., Ed. Manual of Color Aerial Photography. Amer. Soc. Photogrammetry: Falls Church, VA, 1968; 70.
34. Shettle, E.P.; Fenn, R.W. Models of the Aerosols of the Lower Atmosphere and the Effects of Humidity Variations on Their Optical Properties. Air Force Geophys. Lab. Rep. AFGL-TR-79-0214, 17 Sept., 1979, Bedford, MA.
35. Sivkov, S.J. Calculation Techniques for Solar Radiation Characteristics. Gidrometeoizdat (Agricultural Meteorology) 1968, 1, 247.
36. Van de Hulst, H.C. Light Scattering by Small Particles; Wiley: New York, 1957.
37. Pollack, J.B.; Cuzzi, J.N. Scattering by non-spherical particles of size comparable to a wavelength: a new semi-empirical theory and its application to tropospheric aerosols. J. Atmos. Sci. 1980, 37, 868–881.
38. Nakajima, T.; Tanaka, M.; Yamano, M.; Shiobara, M.; Arao, K.; Nakanishi, Y. J. Metrol. Soc. Jpn. 1989, 67, 279–291.

39. Egan, W.G. Aircraft polarimetric and photometric observations. Proc. 5th Symp. Remote Sensing, Univ. Michigan 1968, 169–189.
40. Coakley, J.A.; Cess, R.D. Response of the NCAR Community Climate Model to radiative forcing by the naturally occurring tropospheric aerosol. J. Atmos. Sci. 1985, 42, 1677–1692.
41. Binder, A.B.; Cruikshank, D.P. Lithological and mineralogical investigation of the surface of Mars. Icarus 1966, 5, 521–525.
42. Binder, A.B.; Cruikshank, D.P. The composition of the surface layer of Mars. Commun. Lunar Planet. Lab. 1966, 4, 111–120.
43. Kneizys, F.X.; Shettle, E.P.; Gallery, W.O.; Chetwynd, J.H., Jr.; Abreu, L.W.; Selby, J.E.A.; Fenn, R.W.; Clough, S.A. Atmospheric Transmittance/ Radiance: Computer Code LOWTRAN 6. Air Force Geophys. Lab. Rep. AFGL-TR-83-0187. NTIS Rep. No. ADA137786. Bedford, MA, 1983.
44. Pierluissi, J.H.; Tomiyama, K.; Gomez, R.B. Analysis of the LOWTRAN transmission functions. Appl. Opt. 1979, 18, 1607–1612.
45. Egan, W.G.; Hilgeman, T. Optical Properties of Inhomogeneous Materials; Academic Press: New York, 1979.
46. Wolfe, W.L., Ed. Handbook of Military Infrared Technology. Res. Dept. of the Navy, Office of Naval: Washington DC, 1965:1607–1612

23

Meteorological Analysis of Chemical Exchange Events in the Arctic Basin

I. INTRODUCTION

The atmospheric transport of industrial pollutants and other mid-latitude substances to the Arctic closely parallels the transport of continental materials to the oceans. In 1978, the National Academy of Sciences sponsored a workshop, which produced a report, "Tropospheric Transport of Pollutants and Other Substances to the Ocean." This chapter reviews the progress that has been made since that report was issued, with respect to regional and local processes influencing atmospheric transport and exchange of particulate substances to selected places at the arctic surface. More general surveys of larger scale transport to the Arctic are collected in special volumes edited by Schnell [1] and Rahn [2]. In addition, we present results of an analysis of the diurnal variation of CO_2, temperature, and dew point temperature for the summer of 1986 at Barrow, Alaska.

Meteorological analysis and climatic averages show that tropospheric air flowing from lower latitudes continuously passes aloft over the polar regions. Balloon soundings of particle concentration [3] show a continuum in the stratosphere, where aerosols of tropical volcanic origin overspread the poles. There is an almost continuous reservoir of air of recent mid-latitude exposure above the Arctic. To understand the ecological influences associated with a contaminant, it is necessary to define local exchange and precipitation processes that can bring it into contact with the surface at a selected point.

Relatively long-term measurements of the fallout of radionuclides injected by mid-latitude (30–60° N) nuclear tests were analyzed using the model of Lal and Rama [4]. The data show that about 5% of the material was transported into the Arctic (60–90° N). These nuclides are attached to particulate material, supporting a hypothesis that an average of 5% of particulates reaching the mid-latitude troposphere can be exchanged into the Arctic. Aerosol measurements made in a more idealized setting in the Antarctic show that the remains of cyclonic systems, called "salt storms" by Shaw [5] and Parungo et al. [6], cause manifold increases in aerosol concentration at the surface. An analysis by Hogan and Gow [7] indicates that most of the precipitation of water and sodium substances to the polar plateau may occur in just a few days. Here we examine three meteorological events that resulted in exchange among atmospheric layers or increased surface concentrations of aerosol substance, as a review of some processes that may result in particle precipitation to specific places on the arctic surface. The frequency and seasonality of these processes may exert a major influence on the effects caused by allocthonic contaminants.

II. A REVIEW OF SIGNIFICANT ARCTIC EXCHANGE EVENTS

Figure 1 shows a typical arctic boundary layer and lower tropospheric temperature structure. Tropospheric air from lower latitudes flows poleward above an inversion that inhibits exchange of air and particulate matter with the boundary layer when the surface is dominated by snow, ice, or frozen soil. The troposphere cools radiatively, and this cooling causes subsidence with concurrent adiabatic heating in the lower layers. Heat is being removed from the atmosphere radiatively, and this is not an isentropic process. Snow- and ice-covered surfaces provide accelerated radiative cooling, and the minimum lower atmospheric temperature occurs near the surface, originating the near-surface inversion layer. The reduction in temperature results in an increase in the relative humidity of air within the inversion layer, and limited exchange of air across the inversion associated with wind differences often produces ice-saturated air near the inversion. There is a limited and sporadic exchange of water and particulate substance in the vicinity of the inversion, as evidenced by the frequent, but intermittent, precipitation of small ice crystals in this layer.

Summer in the continental Arctic is characterized by ice-free lakes and tundra vegetation. Inversions may form over vegetated or dry soil surfaces during midnight sun hours, but midday solar radiation may heat the surface enough to cause a lapse in the lower layer, as shown at the right in Fig. 1. This induced instability may allow free exchange with the lower troposphere for

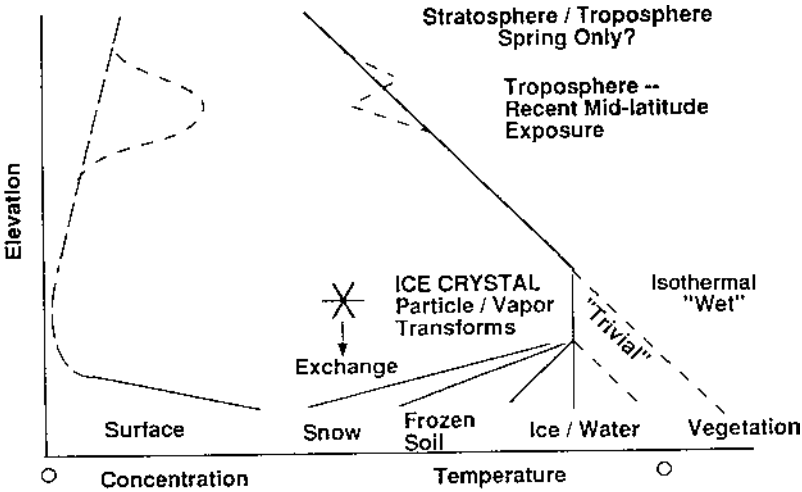

FIGURE 1 An idealized diagram showing typical temperature and particle concentrations with respect to height above the arctic surface. The maximum aerosol concentration is often adjacent to the surface [8,9]. Defined layers of midlatitude material aloft, as shown by the dashed layer coincident with a temperature discontinuity [10,11], are also sometimes found.

several hours each summer day in continental areas and can be described and analyzed using established methods. The following sections describe the examination of local aerosol exchange to the boundary layer coincident with apparently persistent inversions.

A. Transport and Exchange of Particulate Material Accompanying Warm Advection

Robinson [12] and Shaw [5] showed quite convincingly that enhanced aerosol concentration accompanies heat advected to the surface of the Antarctic Plateau. This heat and moisture characterize maritime polar air in the remnants of cyclonic systems [13] that occasionally invade the continent. Leaitsch et al. [14] and Hogan et al. [8] examined a similar warming event near Igloolik, Northwest Territories, Canada, and gave chronologies of several aerosol components, as shown in Fig. 2. Surface aerosol concentration was near the threshold of instrumental detection before 20 February, although photochemical production of small particles was observed during the brief daily periods of sunlight. A cyclonic system intruded from the Atlantic sector in February, warming the layers just above the surface and producing light

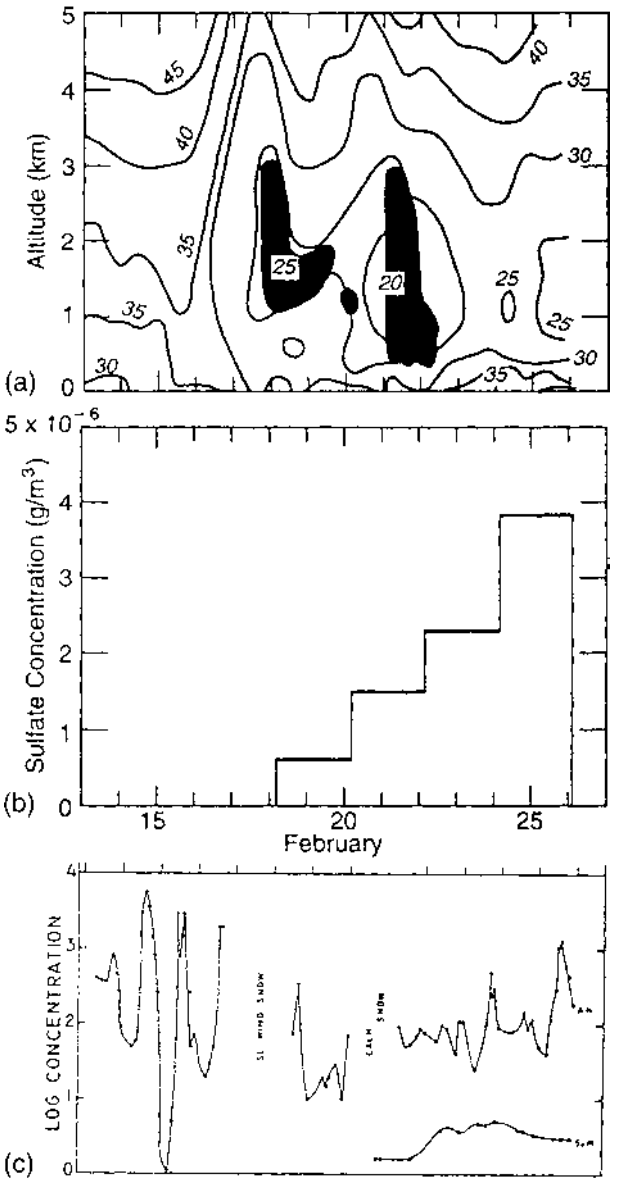

FIGURE 2 (a) A cross-sectional analysis of temperature structure above the Hall Beach sounding, coordinated in time with (b) aerosol sulfate and (c) surface aerosol observations at Igloolik, NWT. The inset bar graph displays the increase in sulfate aerosol, measured by Atmospheric Environmental Service of Canada [14], following, but not coincident with, warm moist advection. All temperatures are negative.

snow. A second intrusion of warm air followed, as shown in the cross section in Fig. 2, but little surface warming occurred and the characteristic inversion persisted.

The total aerosol concentration increased slightly in conjunction with this warm advection. The total aerosol mass and the sulfate component of aerosol, measured by Atmospheric Environmental Service of Canada (AES)

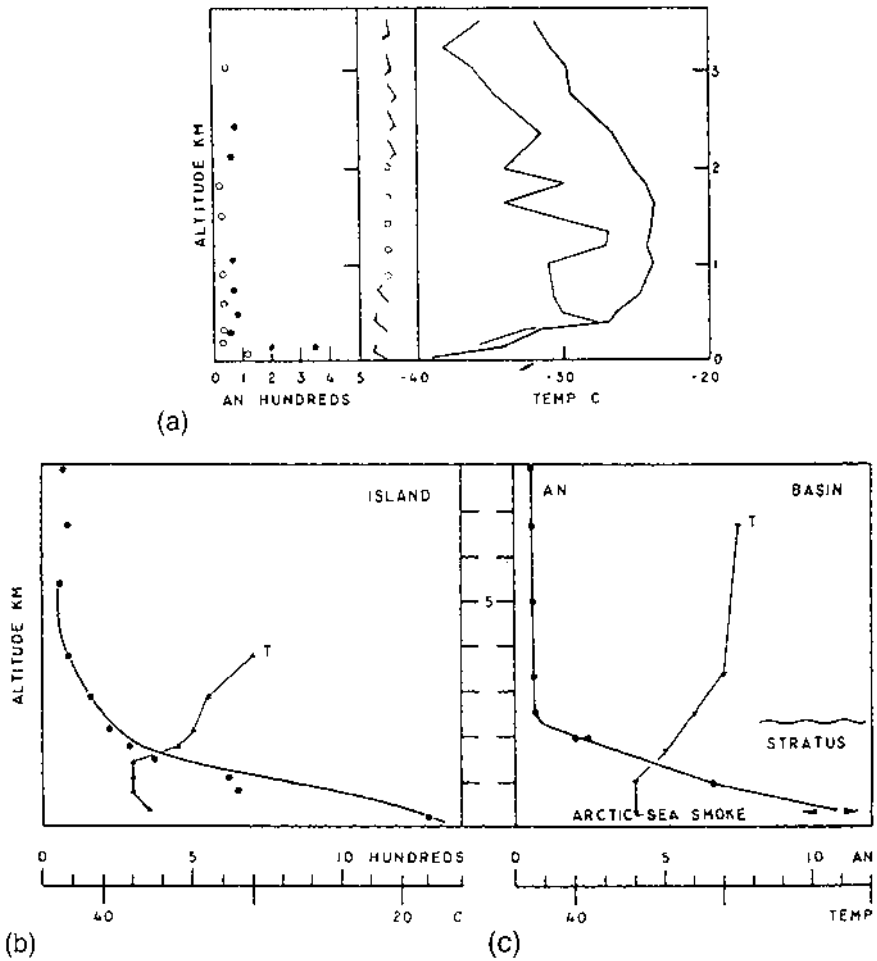

FIGURE 3 Vertical profiles of (a) atmospheric wind, (b) temperature, and (c) aerosol in Foxe Basin, on 26 February 1982. A maximum in aerosol concentration was observed adjacent to the surface over both land and open water, although aerosol concentration was near the limit of detection 500 m aloft.

at a contamination-free site, in the surface layer did not respond immediately to the advection event. The concentration continually increased through 26 February, however, when vertical profiles of aerosol concentrations were obtained. The vertical profiles of aerosol concentration are shown in coordination with temperature and wind structure in Fig. 3. The concentration of particles is greatest near the surface over both land and steaming open water, whereas concentrations approach the threshold of detection a few hundred meters above. This poses a significant question in interpreting transport and exchange mechanisms in the Arctic. The increase in aerosol concentration measured at the surface between 20 and 26 February may have been associated with mid-latitude air advected to the region and exchanged through the inversion by wind shear and ice crystal mechanisms, as shown in Fig. 4. The increase may have been associated with dispersion of marine aerosol from the numerous leads and areas of open water in the Arctic archipelago. The source cannot be uniquely identified from the data set.

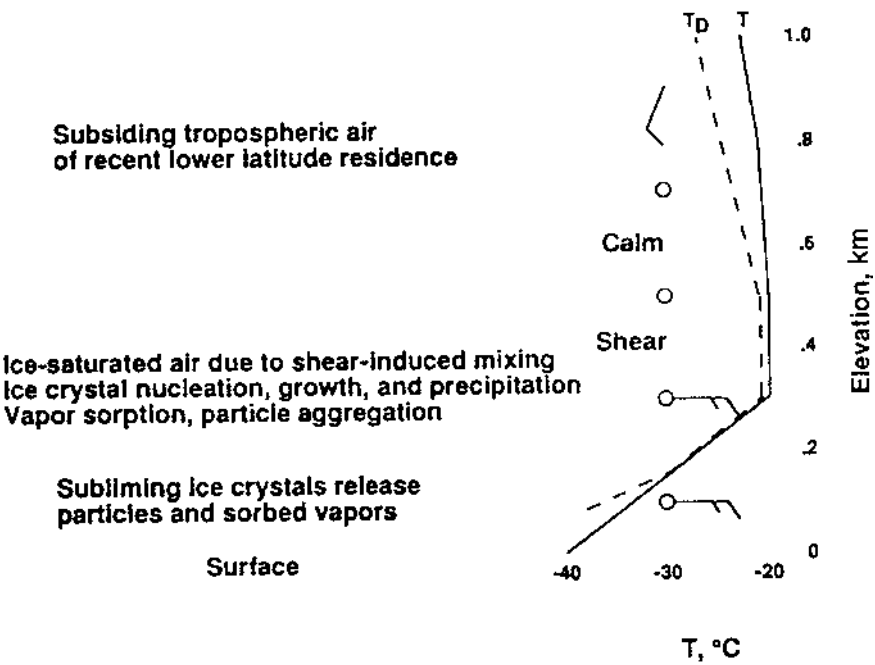

FIGURE 4 A diagramatic representation of near-surface exchange and precipitation processes that may occur over the Arctic in winter.

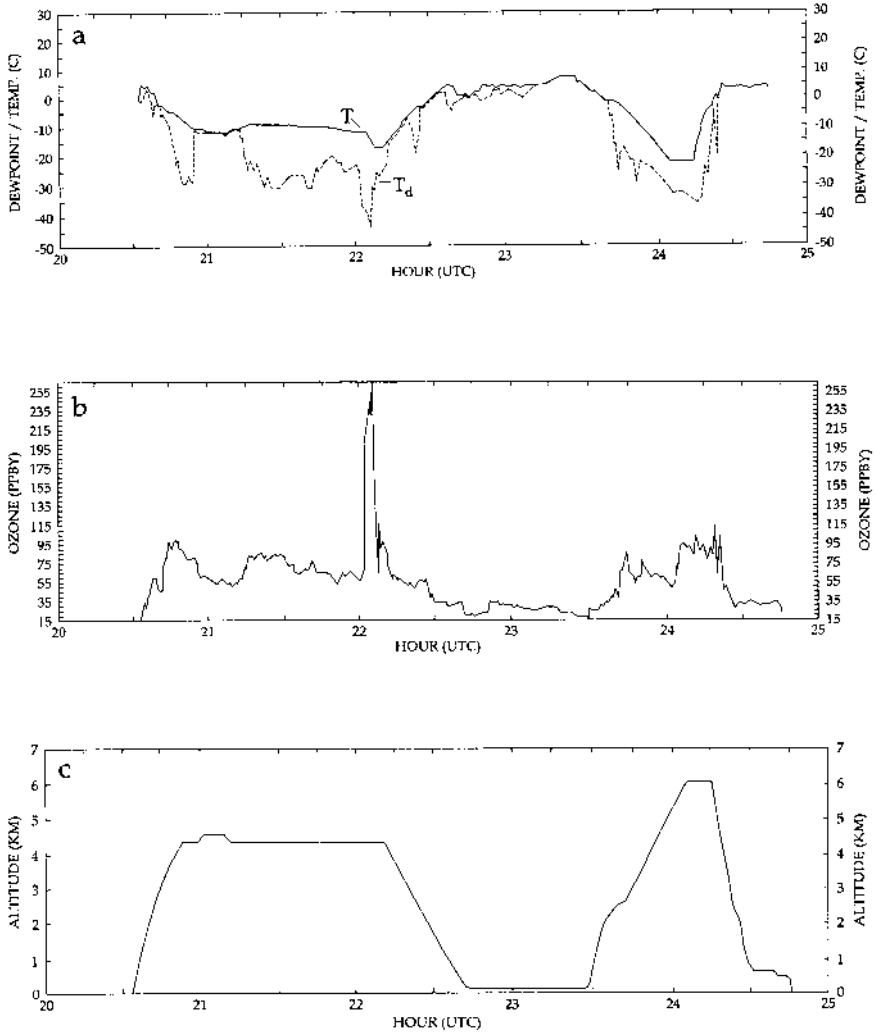

FIGURE 5 Aircraft measurements of (a) temperature T and dew point T_d, (b) ozone, and (c) aircraft flight altitude from Mission 8 (NASA ABLE-3A).

B. Vigorous Atmospheric Exchange in the Arctic Summer

Deep mixing was observed in the Arctic by Shapiro et al. [15] and reported from measurements made during the 1988 NASA ABLE-3A (Arctic Boundary Layer Expedition). The experimental results of ABLE-3A are discussed in J. Geophys. Res., Vol. 97, No. D15.

Aircraft measurements made during ABLE-3A show a layer of dry ozone-enriched air (>200 ppbv) encountered over Barrow at approximately 4 km above sea level on 15 July (Fig. 5). A time series cross section analysis for Barrow shown in Fig. 6 indicates that subsidence occurred following

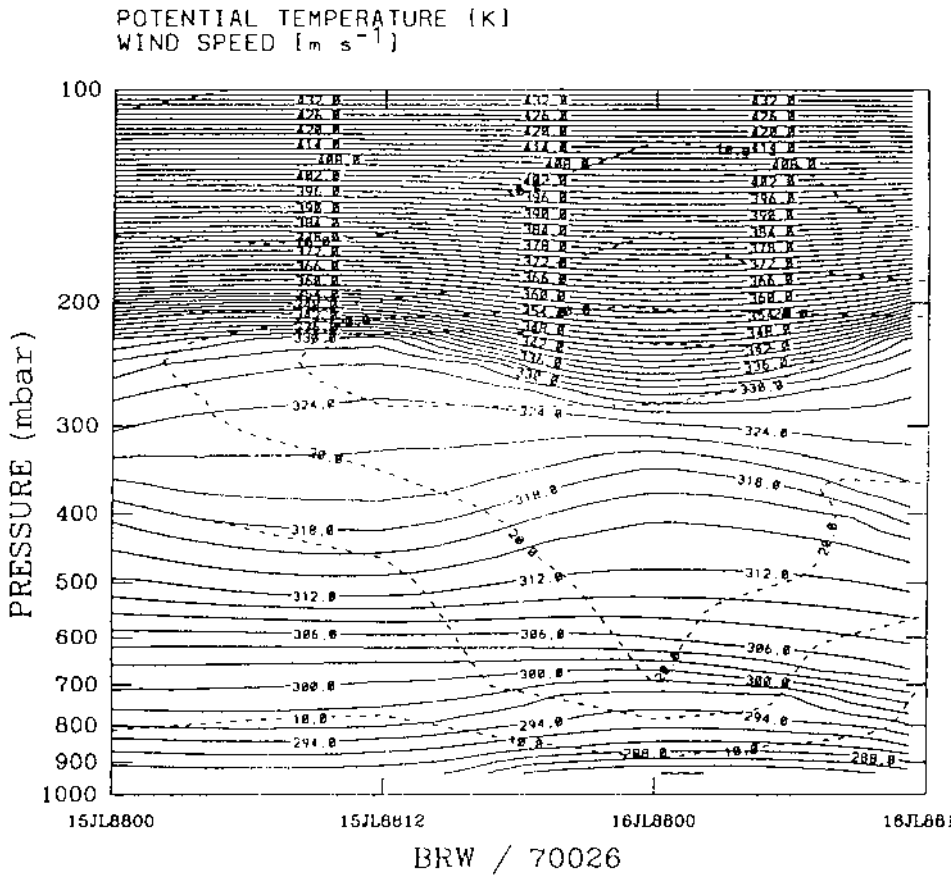

FIGURE 6 Time series cross-sectional analysis for Point Barrow. Note passage of weak trough at 1200 UT on 15 July 1988.

the passage of a weak trough at 1200 UT (Universal Time) on 15 July 1988. Although not shown, upper air meteorological charts verified a trough of low pressure over Barrow at 1200 UT at 500 mbar, with a strong short wave moving on a west-to-east track. Moderate downward motions were found behind the trough with decreasing potential vorticity advection. The high concentration of ozone found over Barrow apparently was transported from

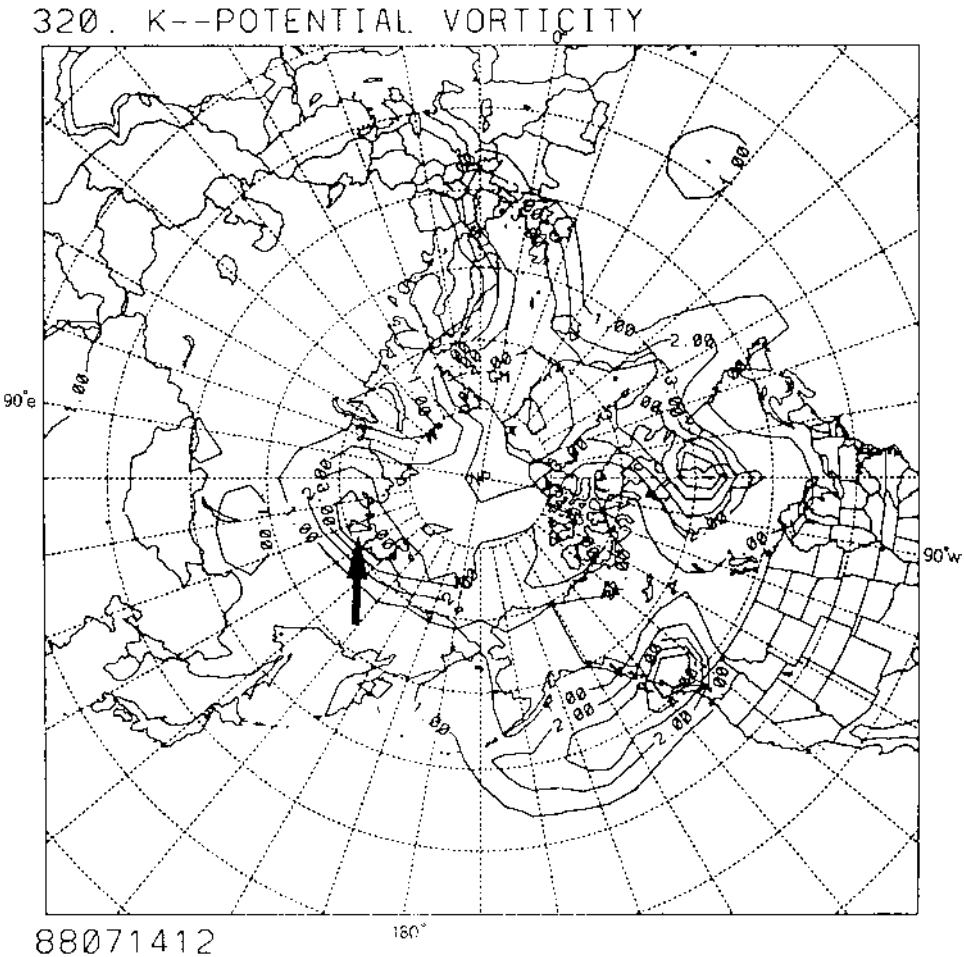

FIGURE 7 Ertel's potential vorticity (PV) chart for 1200 UT on 14 July 1988. Units are in (10^{-5} K m^2 kg^{-1} s^{-1}). Note PV maximum centered near 70° N, 120° E (denoted by arrow).

a region of high potential vorticity centered near 70° N, 130° E at 1200 UT on 14 July 1988. This region of maximum vorticity is shown in Fig. 7 along the 320 K isentropic surface for 1200 UT on 14 July 1988.

Back-trajectory analysis [16] along the 320 K isentrope (Fig. 8) indicates that ozone-enriched air arriving over Barrow on 15 July could have originated from this high potential vorticity (PV) region. Further time series cross-sectional analysis showed a tropopause fold [17] occurring at 1200 UT on 14

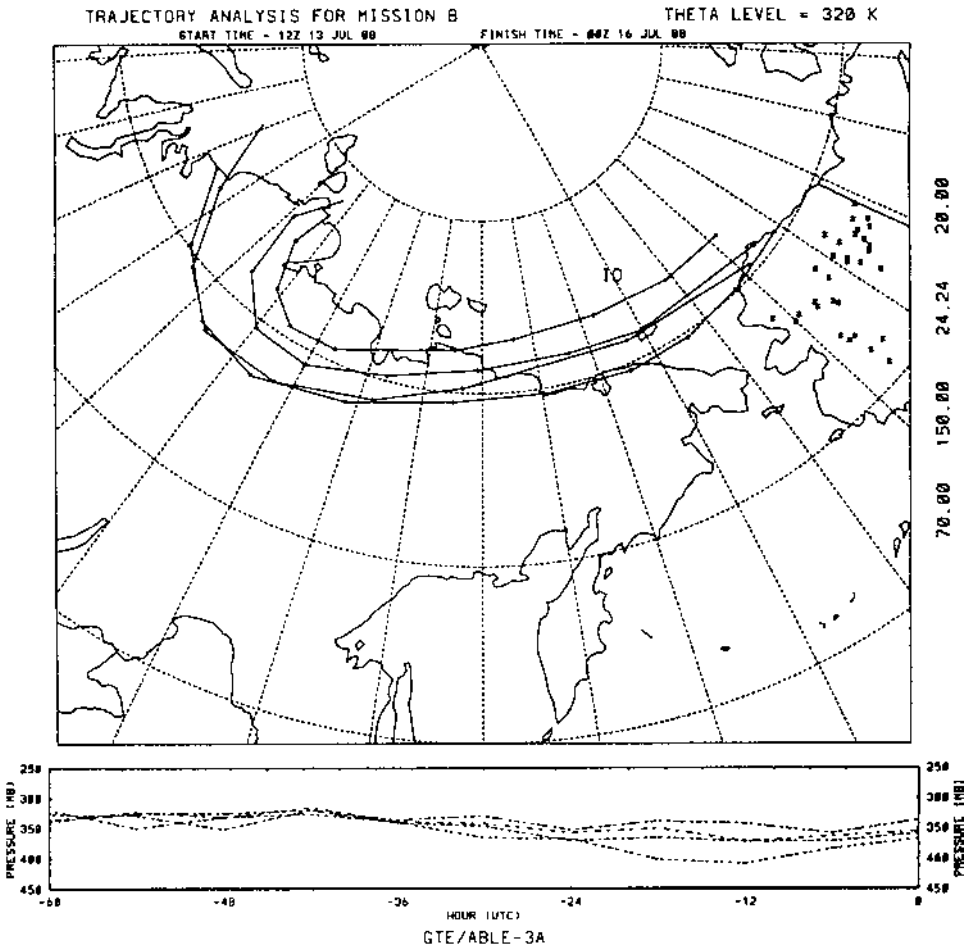

FIGURE 8 Back-trajectory computed for 320 K isentropic surface using Haagensen and Shapiro [16] trajectory model. Barrow was used as the starting point, and the trajectory was computed 2.5 days backward in time.

July 1988 near 68° N, 112° E (Fig. 9). Ozone-enriched air was apparently advected along the 310 K isentropic surface from the 380 mbar to the 550 mbar level (Fig. 8, lower part).

This deep mixing of stratospheric air was accompanied by concurrent changes in the total column of ozone. An enhanced area of total ozone for the same region is supported by the TOMS (Total Ozone Mapping Spectrometer) data [18]. Interestingly, as the wave tracked eastward from the region of high

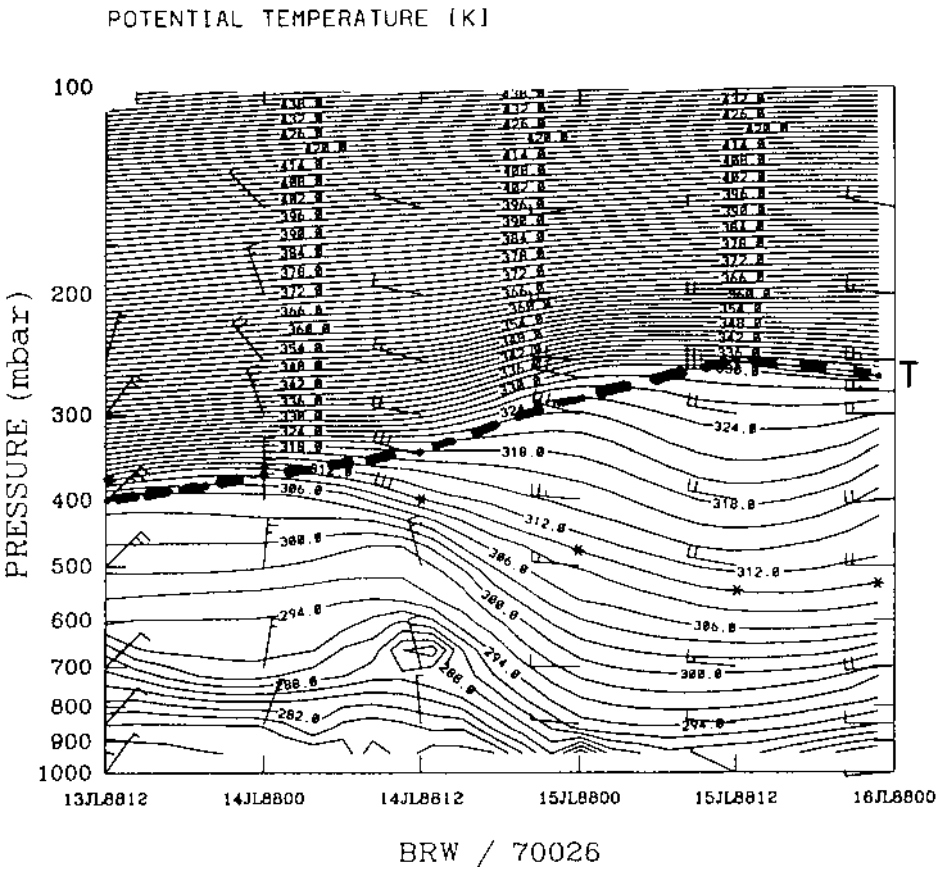

FIGURE 9 Partial time series cross-sectional analysis illustrating tropopause fold occurring at 1200 UT on 14 July 1988. The 310 K isentropic surface is given by asterisks (*). Barrow was used as the starting point. NMC gridded data and global rawinsonde data were used to generate this cross section. The tropopause, T, is indicated by the dashed line.

PV, concurrent changes in the total ozone column could be observed in the TOMS data. Preliminary interpretation of TOMS satellite data shows a change of approximately 40 Dobson units (DU) with the progression of this particular wave. Further studies are needed to determine how well tropospheric–stratospheric exchange in the Arctic can be correlated with changes in the total column of ozone.

C. Summer Particle Exchange in the Arctic Basin

The Barrow NOAA/CMDL (formerly GMCC) observatory site was carefully selected for examining the properties of northern hemisphere air that had experienced precipitation mechanisms in the Arctic Basin. The prevailing surface wind at Barrow is from the east-northeast (the seaward direction), but tropospheric winds a few hundred meters aloft are generally from the southerly sector. The surface wind is generally stronger than the wind at 1 km above the surface at Barrow, similar to the profile observed at Igloolik.

Hogan et al. [8] proposed that any component of diurnal variation of aerosol concentration attributable to contributions from plant terpenes might be observable at Barrow, where maritime arctic air passes over tundra vegetation. A series of experiments were conducted in August, using very sensitive aerosol measurement and sizing devices, over the tundra from the shore to the NOAA/CMDL station (Fig. 10). Major tundra fires occurred coincidentally during the experiment period, causing a heavy smoke layer to flow over Barrow and into the Arctic Basin in the lower troposphere. This smoke-filled layer is shown in a photograph provided by Dr C. Racine. The base of this smoke layer above Barrow was about 500 m above the surface, according to pilot reports.

A composite of figures from Hogan et al. [8] is given in Fig. 10, showing a chronology of aerosol and meteorological events surrounding the period of tundra fires. Boundary layer transport and flow are consistently from the Arctic Sea near Barrow. Flow from the interior of Alaska occurs above the surface during the summer, and this flow transports the smoke northward above Barrow. The size distribution of surface aerosol during the smoke passage is shown, in comparison with those of other Barrow surface aerosols, in Fig. 11. The contribution of the smoke to the surface aerosol is quite obvious when the size distributions are compared. The method of smoke exchange into the surface layer is not obvious, as few data are available over the arctic ice where mixing occurs.

The smoke transport occurred on the days surrounding 30 July, during the period of continuous but varying daylight at Barrow, and there is an obvious diurnal cycle in summer. Figure 12 shows the mean daily variation of temperature, dew point temperature, and carbon dioxide observed during

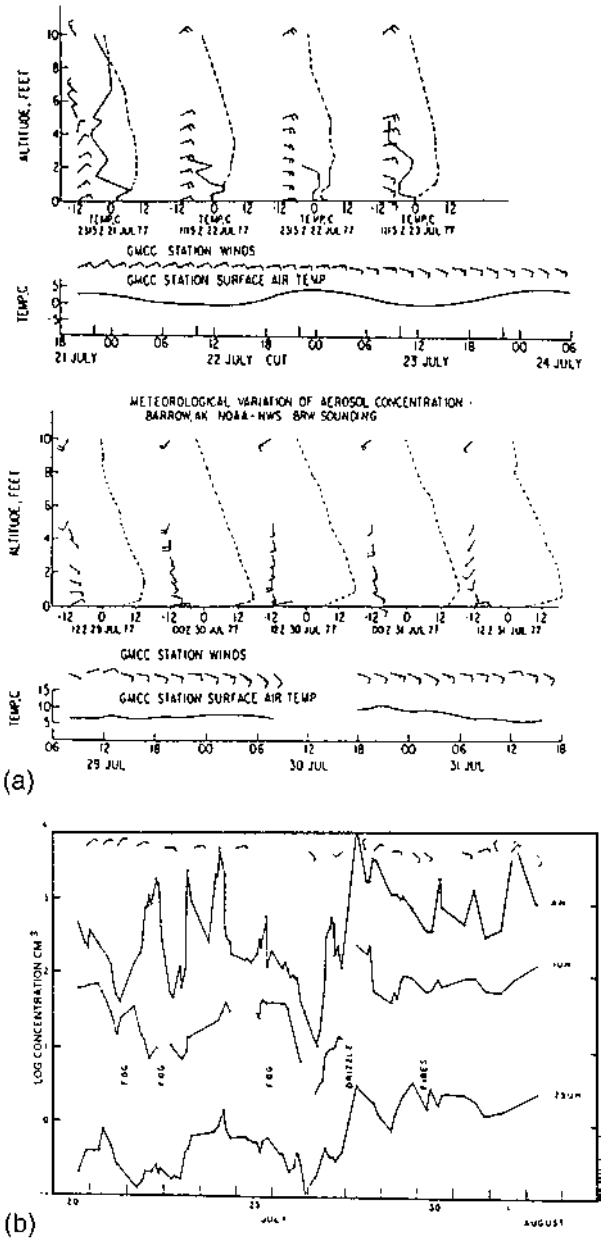

FIGURE 10 Chronologies of (a) atmospheric temperature structure and winds coordinated with (b) surface observations at Barrow coincident with passage of a tundra fire smoke layer on 30 July 1977. The lower panel provides a chronology of surface aerosol observations surrounding this period [8].

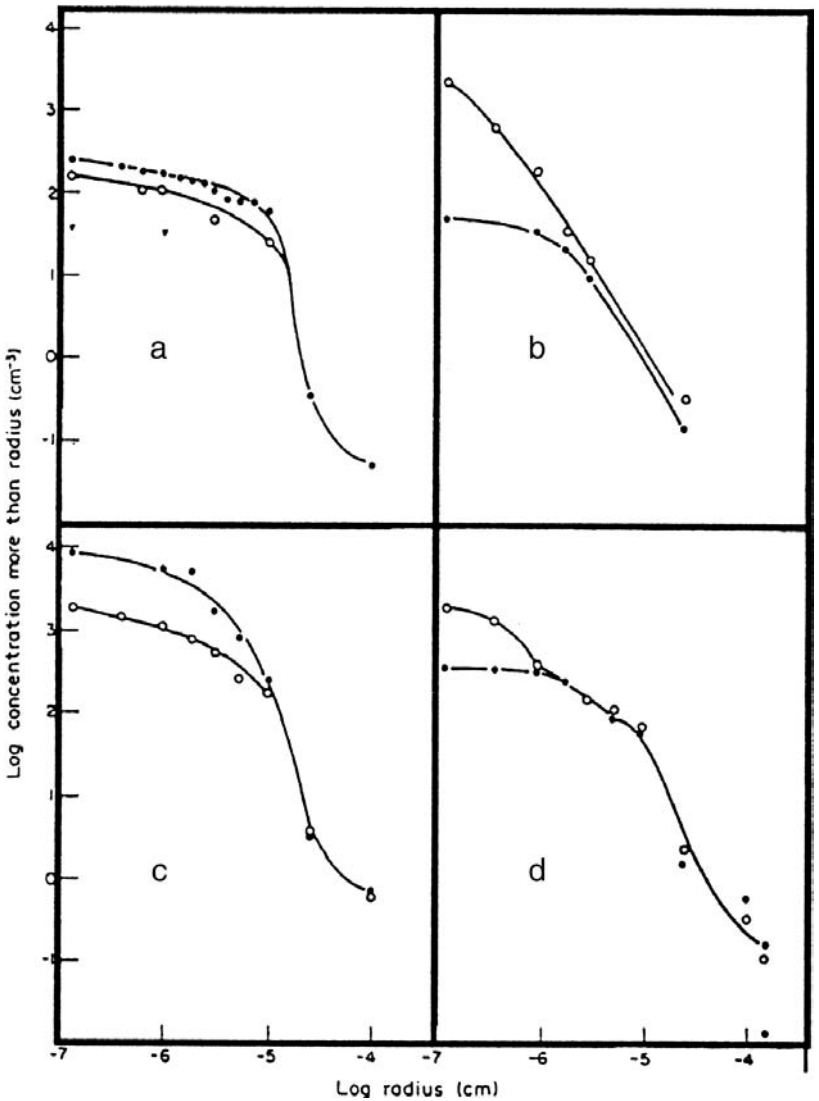

FIGURE 11 Examples of aerosol size distribution observed at Barrow GMCC Observatory. The curves in (a) refer to foggy conditions; (b) clearing conditions following fog; (c) air from settlement; and (d) tundra fire smoke. The difference among the size distributions observed when fire smoke was passing overhead (d) and more typical Arctic Basin aerosol borne on the same wind (b) is quite obvious. Open circles refer to near local noon observations, and the solid circles refer to early morning observations.

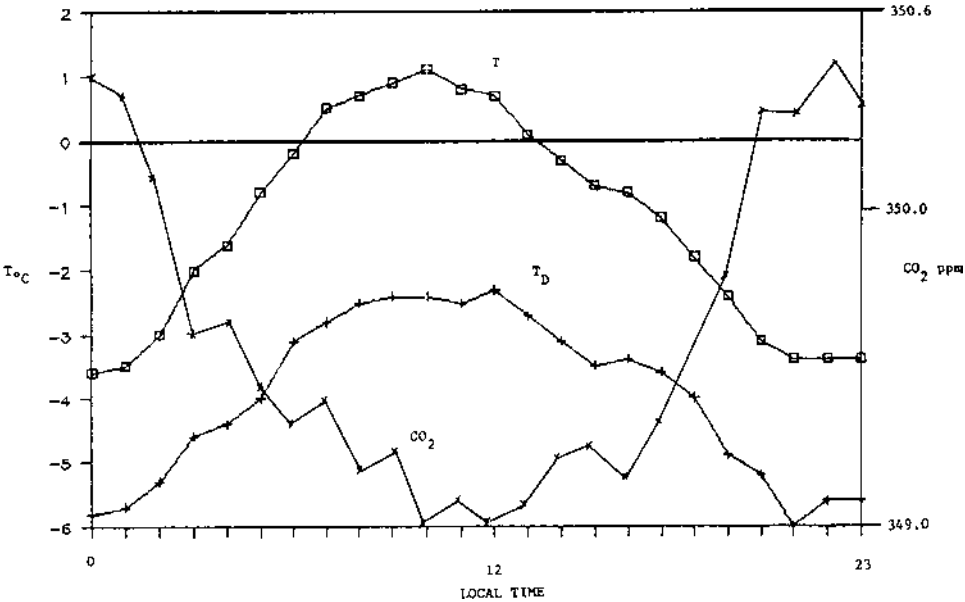

FIGURE 12 The mean hourly temperature, dew point temperature, and CO_2 concentration observed at Barrow during continuous daylight between 7 May and 3 August 1985. Calculated from archived data provided by NOAA/CMDL.

continuous daylight at Barrow between 7 May and 3 August 1985, calculated from archived data supplied by NOAA/CMDL. Surface air at Barrow has a trajectory over the ice of the Arctic Ocean, presenting a mean summer temperature that is below freezing. There is sufficient solar heating of the surface, along the short path separating the ice edge and the observing station, to increase the mean temperature to greater than freezing around midday. Note that the dew point temperature, like CO_2, has an apparent diurnal variation. The dew point temperature reflects the mixing ratio of water vapor in air, a conservative property that usually has no diurnal variation except for a possible source or sink. Likewise, the CO_2 should not change.

To explain the dew point temperature variation, the possibility of diurnal heating of the surface may be sufficient to induce exchange of the lower tropospheric air to the surface, to balance the warmed air that has entered the troposphere. This exchange would also result in diluting smoke from this layer into the surface layer. It is not possible to determine if this exchange occurred near or over the station or at some other place along the trajectory, from where it was advected to the station.

The CO_2 summer diurnal variation and inverse relation to H_2O vapor is more difficult to explain. There is no diurnal winter variation at Barrow. Initially, a major question is the source of the CO_2 and associated inverse H_2O vapor variation and why there is a diurnal variation. It can be surmised that there is some sort of CO_2 exchange mechanism rather than photosynthesis on the tundra or in the ocean. It is also possible that the air seen at Barrow has left the land and, with a curvilinear trajectory, returned to Barrow in the clean air sector. Anomalous air temperatures with respect to wind direction may accompany frontal passage. It was not possible to determine whether the air had come from the Arctic Basin or had recently left the land, although apparently arriving from the Arctic Basin.

All meteorological analyses show that air flows into the Arctic Basin. Because CO_2 and H_2O vapor have been shown in laboratory experiments to be linked [19–21] one could infer that the curvilinear motion of the upper air over the ice-free ocean would permit CO_2 to exchange to the air [22], concurrently with evaporative water vapor with a latent heat exchange to cool the air. This would not occur in winter over sea ice, as verified by winter meteorological observations.

A meteorological low frontal passage is a short-term event that would not be expected to affect the overall average curvilinear flow pattern from meteorological highs. The reason for the separation of the curvilinear flow from the surface is the strong surface inversion that blocks the advection to the surface. High barometric pressure causes the easterly flow out of the Arctic Basin, with the return flow following advection over the warm ice-free open sea areas, where the temperature inversion is weakened.

The observed diurnal variation must be related to the diurnal movement of the sun, even though total sun exists throughout the entire day during the summer. Local noon at Barrow occurs concurrently with the carbon dioxide minimum and the temperature and humidity maxima. The minimum could be attributed to increased photosynthesis during midday, which would deplete the CO_2 as previously indicated. The solar incident angle is less at noon than at other times of the day, producing a greater solar incident flux on the surface of the Arctic Basin and increasing the average hourly temperature.

III. DISCUSSION

The nature of global circulation is such that the Arctic receives a nearly continuous flow of tropospheric air from lower latitudes. This air generally experiences cloud-forming and precipitation processes at the polar front, and long-term studies of radionuclides indicate about 5% of midlatitude contaminants are exchanged into the Arctic, as a mean value. These exchanges are probably brief, because the particulate content of arctic surface air is often

indistinguishable from that of filtered air, even when extremely sensitive aerosol detectors [8] are used. The three cases described in this chapter reflect this episodic nature.

There are rarely enough meteorological data to uniquely analyze these episodes. The diversity of snow, ice, water, and vegetation on the arctic surface provides local sources of heat and particulates that invalidate the simple heat–particle transport model successfully used in the Antarctic. Local heat inputs may enhance local surface–troposphere exchange, but simultaneously complicate interpretation by adding local contamination. There is a major need for development of very sensitive sampling methods that can resolve changes in contamination concentrations on time scales comparable to those of meteorological events. Even these sampling methods cannot uniquely differentiate local from distant contamination, and an easily measured tracer is needed to provide uniqueness.

Spring and summer are frequently the dominant periods of exchange to the surface for several substances of midlatitude origin. Vigorous exchange of both stratospheric and lower tropospheric components to the near-surface layers can occur concurrently with the discontinuities in the tropopause about the jetstream or polar front [17], even at arctic latitudes, as shown by Shapiro et al. [15] and Raatz et al. [23]. Diurnal heating can produce clear air exchange over the continental Arctic in summer, even at the latitude of Barrow.

The inherent stability of air over snow-covered ground and the minimal solar heating of the arctic surface effectively decouple the arctic surface from the troposphere flowing above. The exchange mechanism that we have cited is infrequent and of a scale smaller than ordinary synoptic analyses. We can only describe exchange events that have occurred in proximity to the observing station.

IV. CONCLUSION

We can only imprecisely define the times and places of exchange of tropospheric contaminants to the arctic surface, even if the sampling site is adjacent to a meteorological station, as at Igloolik and Barrow. Only the general area of deep exchange can be defined by a combination of satellite sounders and cross-sectional analysis.

Meteorological analysis indicates that air of recent midlatitude history is almost continuously in the arctic troposphere, but the greatest particulate concentrations are frequently found below this layer adjacent to the surface. The maximum aerosol concentration at the surface has been observed to lag, by days, the arrival of warm air advected a few hundred meters above. The arctic exchange model described in Fig. 4 may provide a mechanism to account for these seeming inconsistencies, but a thorough examination of arctic

surface sources is necessary to eliminate the possibility of local contamination causing this layer.

A review of the CMDL Barrow data, along with data from recent arctic air chemistry experiments, might provide a reliable tracer of midlatitude contamination in arctic surface air. Identification of such a tracer would greatly enhance the analysis of frequency and seasonality of precipitation of midlatitude contaminants on the arctic surface. The inverse relationship of CO_2 to H_2O vapor, which appears to occur worldwide, also provides an analytical tool for interpreting arctic circulation patterns. The CO_2 concentrations are conserved across sharp temperature gradients, where H_2O vapor concentrations may not be. Hence CO_2 becomes a valuable chemical tracer.

REFERENCES

1. Schnell, R.C. Arctic haze and the Arctic Gas and Aerosol Sampling Program (AGASP). Geophys. Res. Lett. 1984, 11, 361–364.
2. Rahn, K.A. Progress in arctic air chemistry 1980–84. Atmos. Environ. 1985, 19, 1987–2208.
3. Hofmann, D. Balloon borne measurements of middle atmospheric aerosols and trace gasses in Antarctica. Rev. Geophys. 1988, 26, 113–130.
4. Lal, D.; Rama. Characteristics of global tropospheric mixing based on manmade ^{14}C, ^{3}H, and ^{90}Sr. J. Geophys. Res. 1966, 71, 2865–2874.
5. Shaw, G.E. Antarctic aerosols: a review. Rev. Geophys. 1988, 21, 89–112.
6. Parungo, F.; Bodhaine, B.; Bortniak, J. Seasonal variation in antarctic aerosol. J. Aerosol Sci. 1979, 12, 491–504.
7. Hogan, A.W.; Gow, A.J. Particle transport to the snow at the South Pole: the beginning of a tropospheric history. Tellus 1993, 45B, 188–207.
8. Hogan, A.W.; Barnard, S.C.; Kebschull, K.; Townsend, R.; Samson, J.A. Aerosol variation in the western hemisphere Arctic. J. Aerosol Sci 1984, 15, 13–33.
9. Wendling, P.; Wendling, R.; Ringer, W.; Covert, D.S.; Heindzenberg, J.; Moerl, P. Calculated radiative effects of arctic haze during a pollution episode in spring 1983 based on ground based and airborne measurements. Atmos. Environ. 1985, 19, 2181–2193.
10. Flyger, H.; Hansen, K.; Megaw, W.J.; Cox, L.C. The background level of the summer tropospheric aerosol over Greenland and the North Atlantic Ocean. J Appl. Meteorol. 1973, 12, 161–174.
11. Flyger, H.; Heidam, N.Z.; Hansen, K.; Megaw, W.J.; Walther, E.G.; Hogan, A.W. The background level of the summer tropospheric aerosol, sulphur dioxide and ozone over Greenland and the North Atlantic Ocean. J Aerosol Sci. 1976, 7, 107–140.
12. Robinson, E. Polar meteorology and climatology 1979–1982. Rev. Geophys. Space Phys. 1983, 21, 1048–1064.
13. Murphey, B.B.; Hogan, A.W. Meteorological transport of continental soot to Antarctica. Geophys. Res. Lett. 1991, 19(1), 33–36.

14. Leaitsch, R.; Melnichuk, S.; Hogan, A.W. Some physical and chemical properties of the arctic winter aerosol in northeastern Canada. J. Appl. Meteorol. 1983, 23, 916.
15. Shapiro, M.A.; Schnell, R.D.; Parungo, F.P.; Oltmans, S.E.; Bodhaine, B.A. El Chichon volcanic debris in the arctic troposphere fold. Geophys. Res. Lett. 1984, 11, 421–424.
16. Haagensen, P.L.; Shapiro M.A. Isentropic Trajectories for Derivation of Objectively Analyzed Meteorological Parameters. Tech. Note NCAR/TN-149. Boulder, CO: National Center for Atmospheric Research, 1979.
17. Danielsen, E.F. Stratospheric–tropospheric exchange based on radioactivity, ozone, and potential vorticity. J. Atmos. Sci. 1968, 25, 502–518.
18. Guimaraes, P., McPeters, R., Eds. TOMS Gridded Ozone Data, 1978–1988. Published in CD-ROM by NASA, Upper Atmosphere Research Program, Greenbelt, MD, 1990.
19. Ohtaki, E. Application of an infrared carbon dioxide and humidity instrument to studies of turbulent transport. Bound. Layer Meteorol. 1984, 29, 85–107.
20. Zhu, H.; Egan, W.G.; Hogan, A.W. Cold precipitation of CO_2 and water vapor in a model marine system (Abstr.). Trans. Am. Geophys. Union. 1990, 71, 471.
21. Egan, W.G.; Hogan, A.W.; Zhu, H. Physical variation of water vapor and the relation with carbon dioxide. Geophys. Res. Lett. 1991, 18, 2245–2248.
22. Etcheto, J.; Boutin, J.; Merlivat, L. Seasonal variation of the CO_2 exchange coefficient over the global ocean using satellite wind speed measurements. Tellus 43B, 247–255.
23. Raatz, W.E.; Schnell, R.C.; Bodhaine, B.A.; Oltmans, S.J.; Gammon, R.H. Air mass characteristics in the vicinity of Barrow, Alaska, 9–19 March 1983. Atmos. Environ. 1985, 19, 2127–2134.

24

Optical Enhancement of Aircraft Detection Using Polarization

I. INTRODUCTION

Various techniques have been used to obtain multispectral imagery of ground and aircraft targets: visual, infrared, and radar [1–12]. The technique of polarization has long been used effectively in radar, where the coherence length (monochromaticity) of the radar waves is great.

In optics, the passive use of optical wavelengths, passively admits the use of sensor polarization. Polarization should be considered as high spectral and spatial resolution photometry, because the measurements are made relative to a plane from the target defined by the incident and scattered radiation directions (this plane is the plane of vision or the principal plane) [2].

A set of four measurements are made, with the sensor oriented to detect radiation (1) parallel to the principal plane, (2) perpendicular to the principal plane, (3) at 45° to the principal plane, and (4) at 135° to the plane. These measurements describe the Stokes parameters, the first being the total radiation intensity, the second being the polarization difference between the perpendicular and parallel components, and the third being derived from the 45° and 135° measurements, to define measurements at some angle to the principal plane. The fourth Stokes parameter characterizes the circular polarization.

The Stokes parameters are obtained with a Kodak CIR (color infrared) camera [13–20].

II. MEASUREMENTS

The sensor configuration of the Kodak color infrared camera DCS460 is shown in Fig. 1a. The focal plane array uses a silicon CCD element, which for the DCS460 has dimensions of 2048 × 3072 pixels approximately 1 mil (20 μm) in size. There are four elements per pixel—two sensitized for green, one for red, and one for blue; this is called a Bayer pattern (Fig. 1b).

In order to sense the short-wavelength infrared, blocking filters are used (Fig. 1c). All sensors are sensitive to the short-wavelength infrared as well as the designated color. The 700–800 μm filter allows the green, red, and infrared to pass. The 500–800 μm filter keeps the short-wavelength blue from reaching the blue-sensitive element. Thus the green, red, and "blue" elements sense the infrared as well as their indicated color. Thus the "blue" element detects the short-wavelength infrared alone. A Kodak algorithm based on nearest neighbor and next nearest neighbor perform color interpolation to produce three-color coaligned full image polarization from the initial color images.

III. IMAGERY

The visual appearance of a camouflaged C-130 aircraft is shown in Fig. 2, and the percent polarization is shown in Fig. 3, where greater brightness represents increased percent polarization. The percent polarizations of different areas of the same camouflaged C-130 aircraft are shown in Fig. 4.

In Fig. 4, the percent polarizations are annotated in green, and near infrared sequentially at each symbol. The sky designations 1,2,3, and 4 are arbitrarily located, whereas the tail (T1,T2); side fuselage 2 and 3; upper fuselage sideview 1,2, and 3; propeller; and underwing 1 are areas selected to quantify the percent polarization of the camouflaged aircraft.

Some areas (T1,T2) are shadowed with a typical polar diagram shown in Fig. 5 for T2. The percent polarization is positive and 1 relatively high (about 24%), as compare to the clear sky of −5% in the green and −1 in the near-infrared yields high polarization contrast. The photometric contrast is of the order of 2 or 3, but since the sky has a strong polarization (negative sign), there is no positive polarization in the sky regions in the principal plane. Thus, in the computer rendition, the negative polarizations become zero positive polarization and infinite contrast. Sky 2 has some positive polarization in the near-infrared, probably as a result of haze from a scattered cloud.

In Fig. 5 the green and near-infrared polarization measurements are plotted as a polar diagram, showing a limited specular reflection at a viewing angle of about 45°. The green has a higher reflectance. Superimposed on the polar diagram is the near-infrared percent polarization, which reaches a peak of 28%, although at 0° it is about 16%. A curve is shown of the diffuse

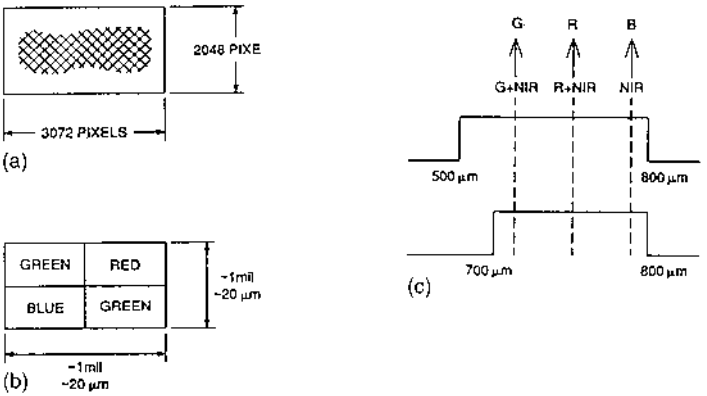

Figure 1 (a) Configuration of focal plane array of Kodak DCS460 CIR camera. (b) Bayer focal plane sensor array. (c) Blocking filter arrangement.

Figure 2 Visual photograph of camouflaged C–130 aircraft.

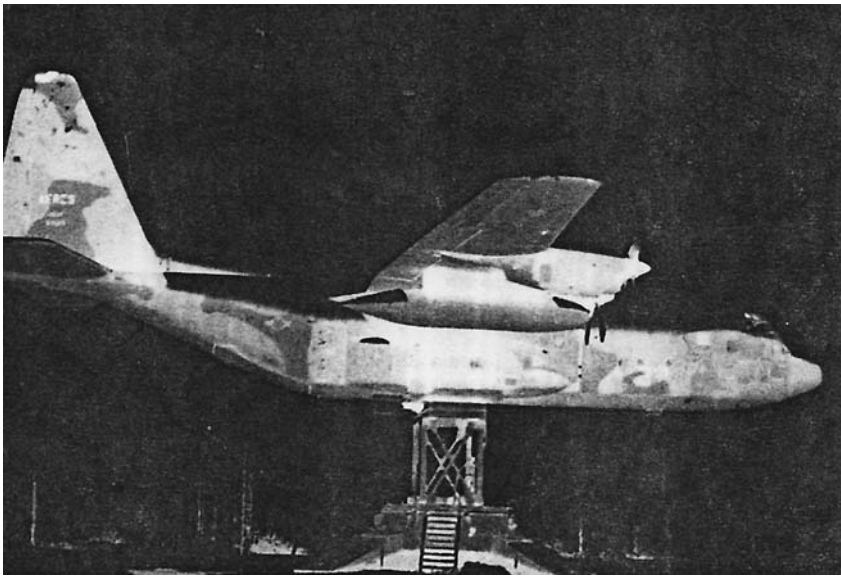

Figure 3 Multispectral photograph of C–130 aircraft.

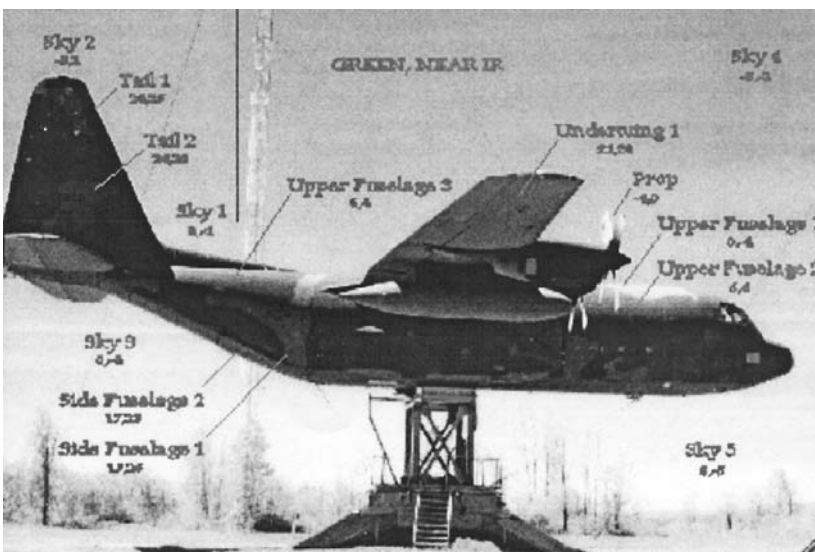

Figure 4 Photo of camouflaged aircraft of Figs. 1–3 with percent polarization annotated.

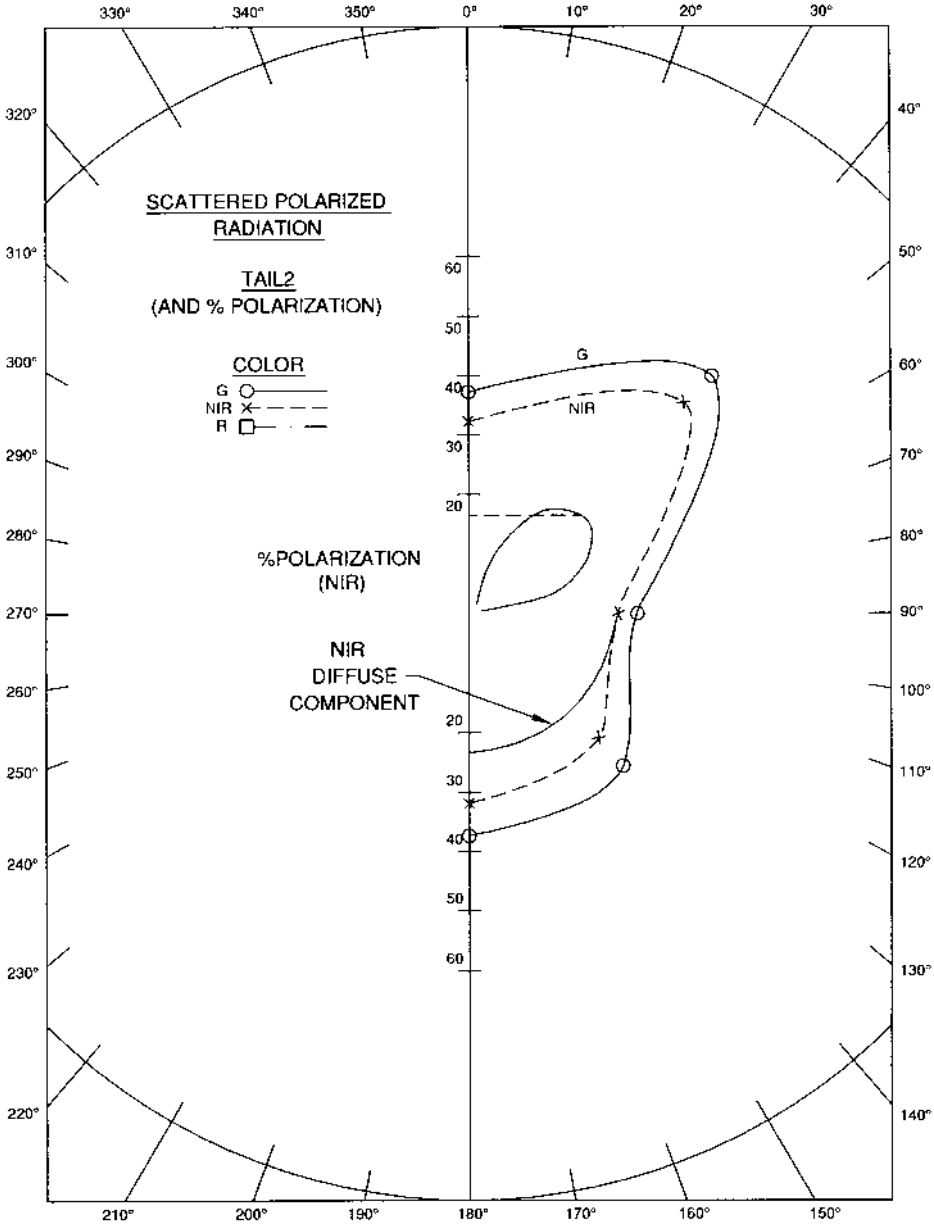

Figure 5 Polarization of tail 2.

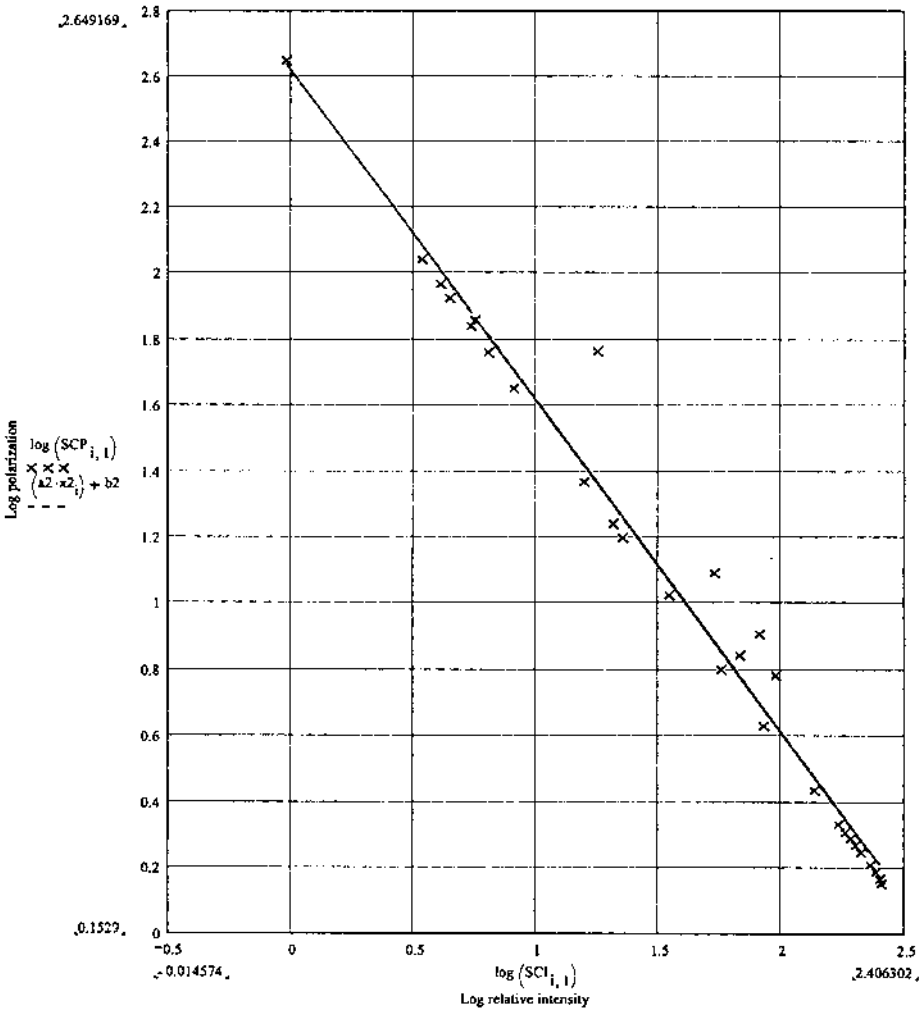

Figure 6 Plot of the logarithm of the digital scene radiance vs. the logarithm of the polarization for the scenes, containing sunlit artificial targets of different albedo, vegetation and camouflage nets and targets in different degrees of shadow.

background contribution of the surface reflectance in the near-infrared (Fig. 6 and 7).

Figures 8–12 depict, on polar plots, the relative polarization measured at 0°, 45°, 90°, and 135° polarimetric analyzer positions. The measurements were made of various areas of a C-130 aircraft, as annotated in Fig. 4. The sky polarizations are characterized in Figs. 13 and 14.

In Figs. 8 and 9, percent polarizations of two locations on the upper fuselage are represented, and Figs. 10 and 11 characterize the side fuselage. Specularity is apparent in the positive polarizations in the green and near-infrared for upper fuselage sideview 2 and 3. However, upper fuselage 1 apparently reflects (scatters) sky radiation, and the apparent percent polarization is less.

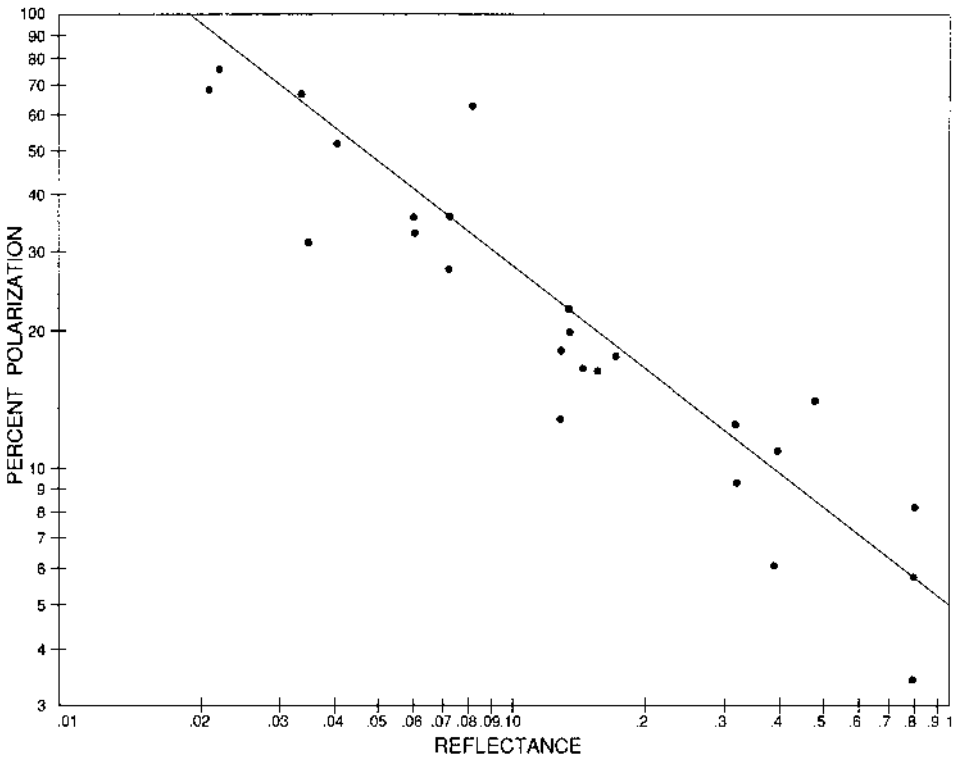

Figure 7 Curve of the diffuse background contribution of the surface reflectance in the near-infrared.

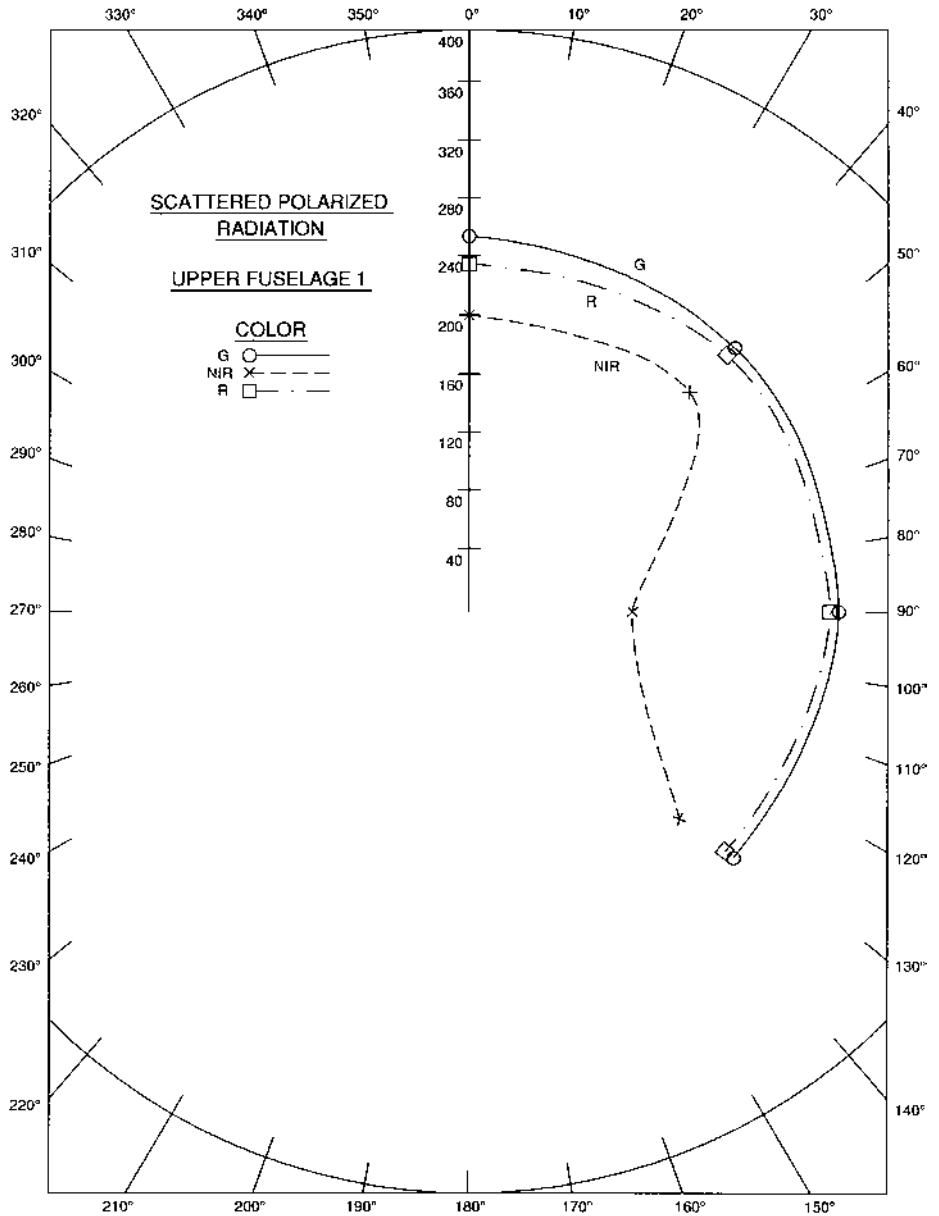

Figure 8 Polarization of upper fuselage 1.

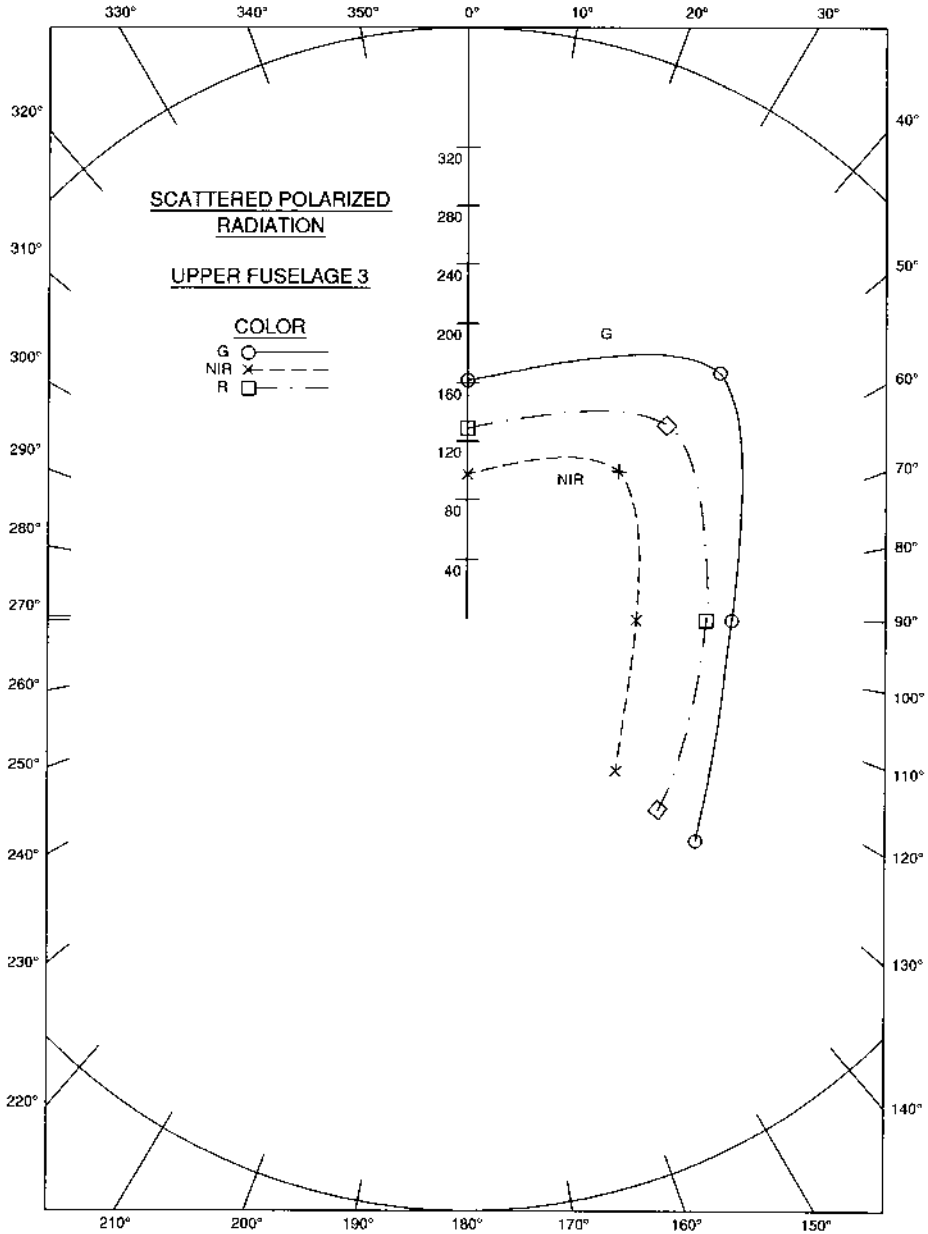

Figure 9 Polarization of upper fuselage 3.

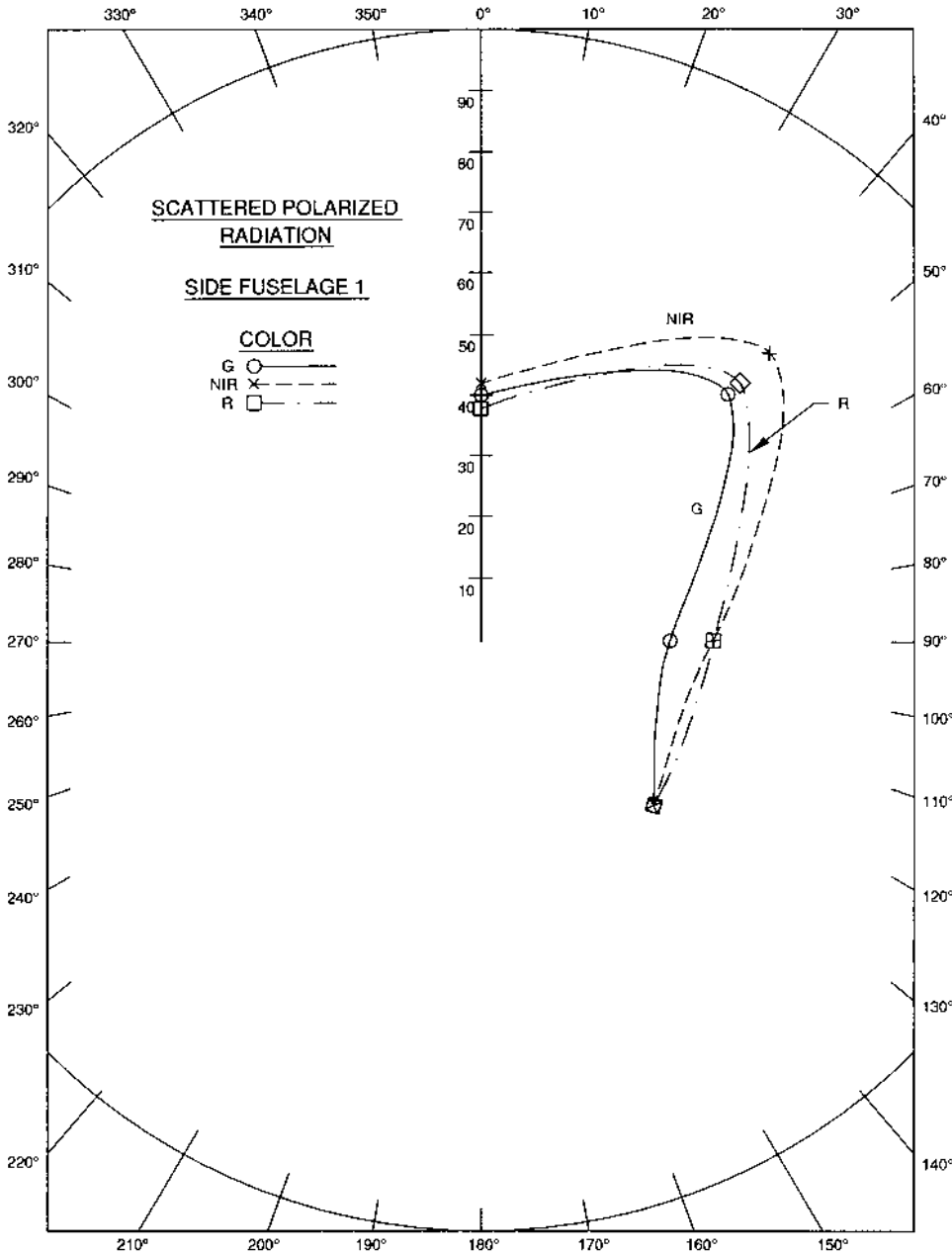

Figure 10 Polarization of side fuselage 1.

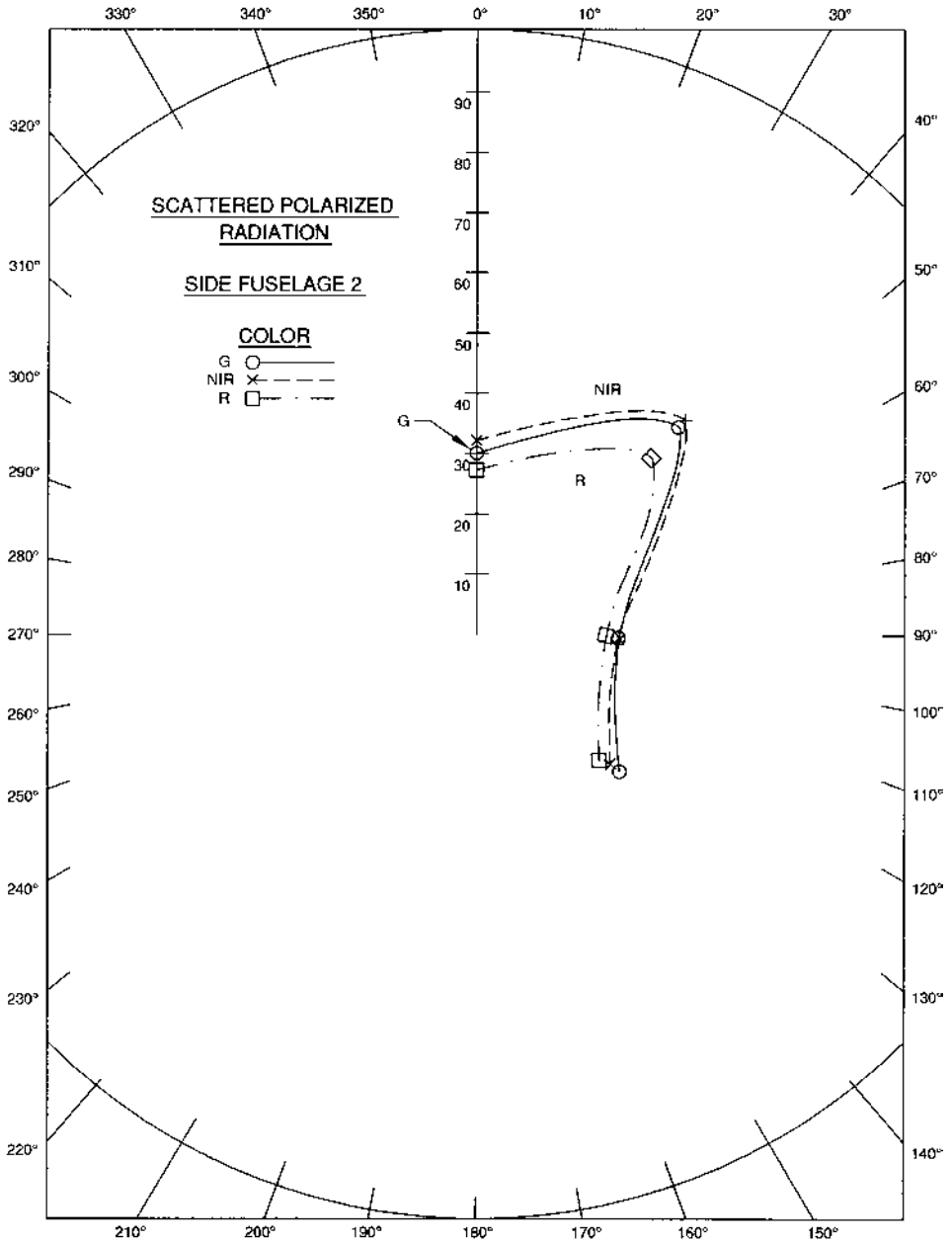

Figure 11 Polarization of side fuselage 2.

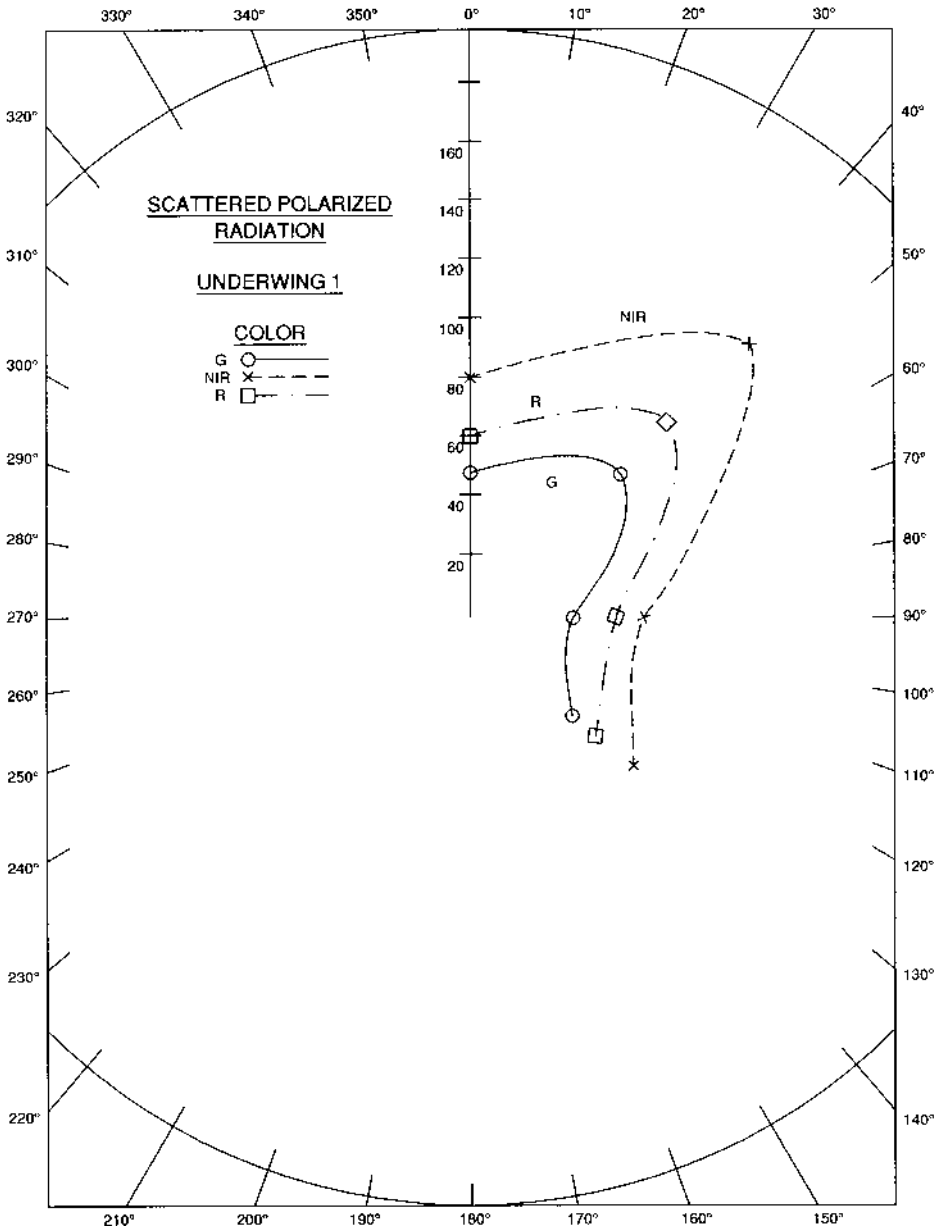

Figure 12 Polarization of underwing 1.

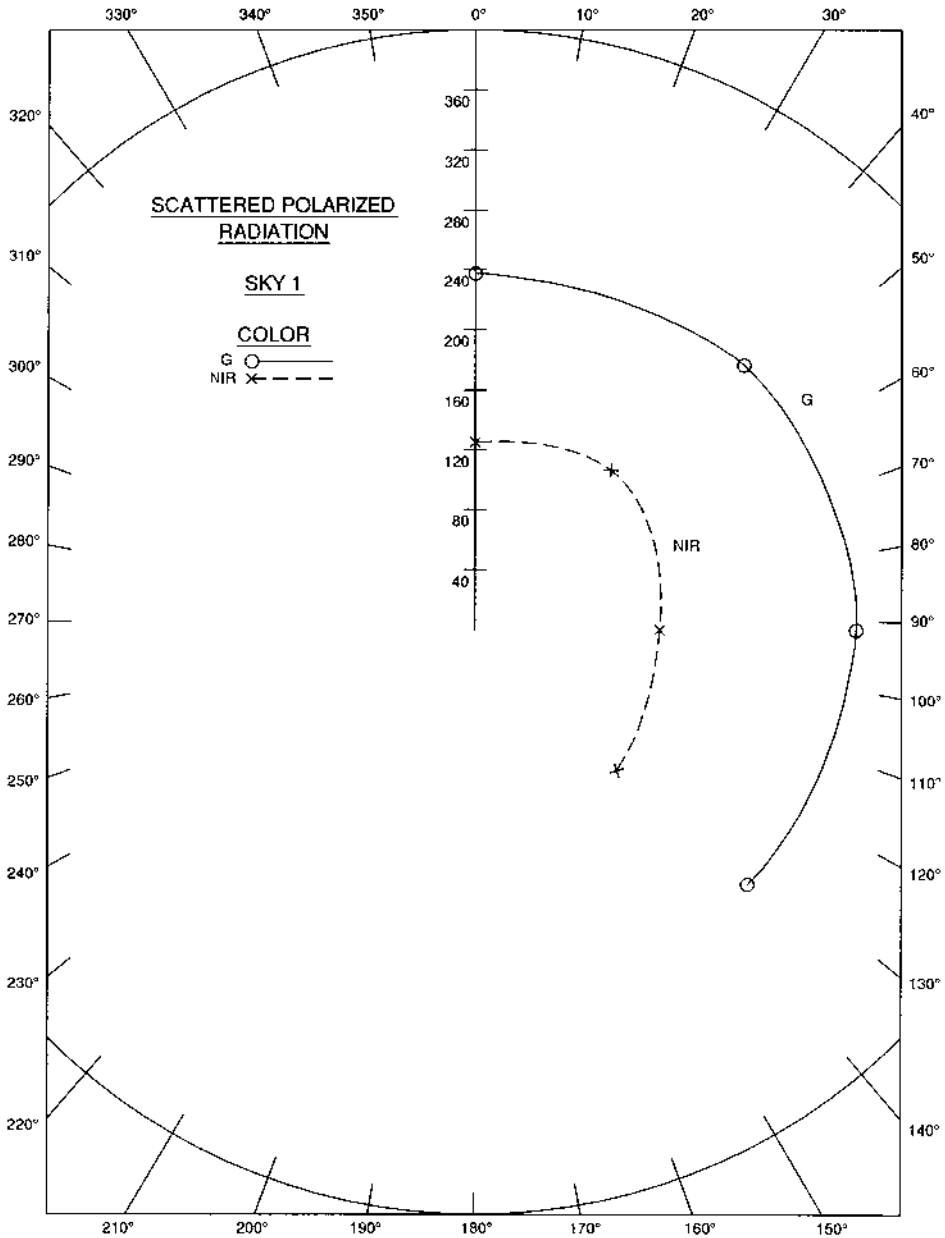

Figure 13 Polarization of sky 1.

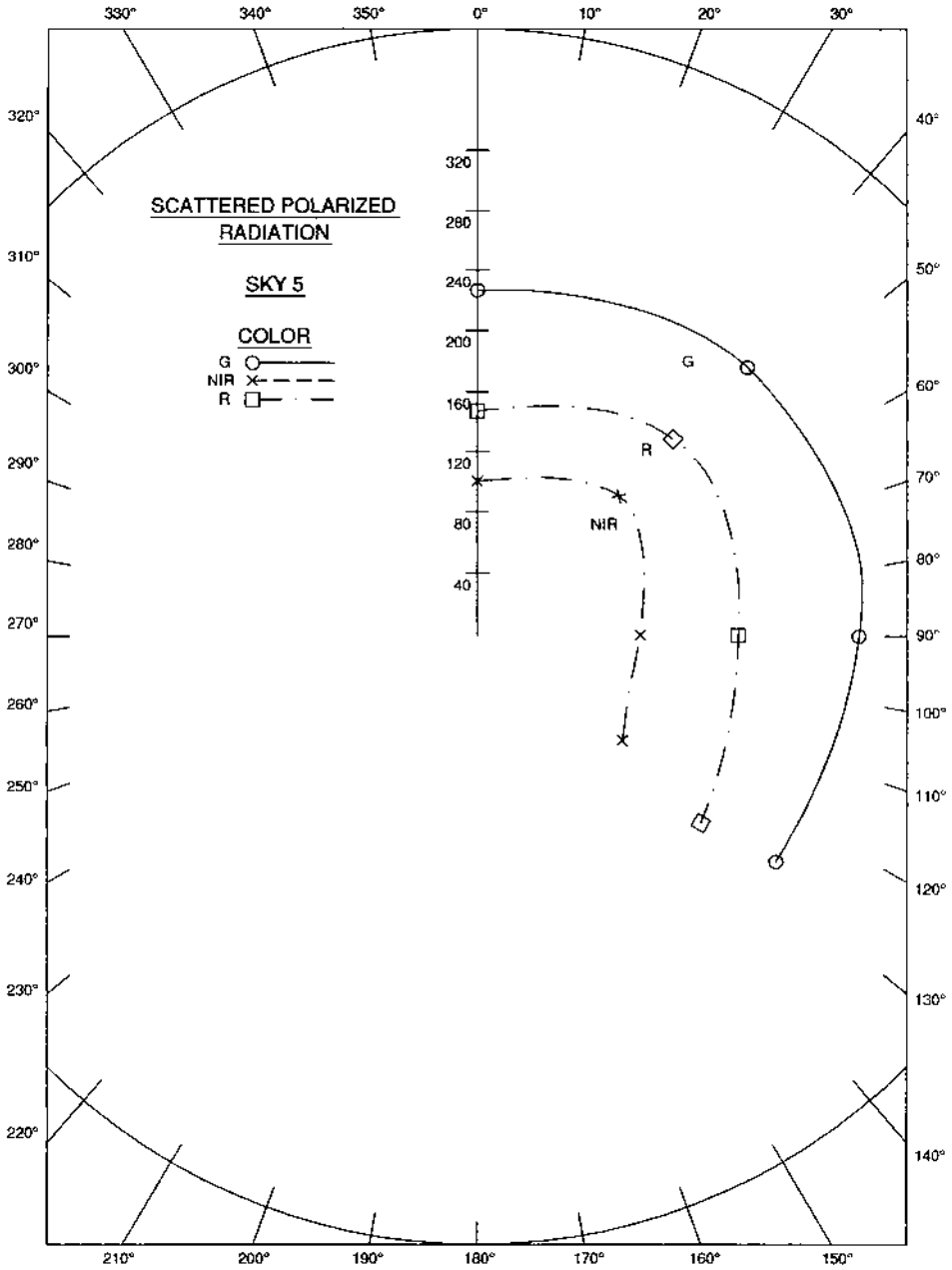

Figure 14 Polarization of sky 5.

Upper fuselage 3 has a distance scattering peak at 45° in the green, red, and near-infrared. However, upper fuselage 1 shows peaking only in the near-infrared, possibly the result of scattering of sky radiation.

Figures 10 and 11 characterize the percent polarization of two sections of the side fuselage. They both show a quasi-specular peak at 45° as a result of the sun reflection; the solar elevation angle is 65°. In comparison with Figs. 8 and 9, where green has the highest polarization, here in the shadowed areas infrared has the highest polarization. The relative polarized brightness is less than in Figs. 8 and 9 by about a factor of 3–4, as a result of the shadowing.

Figure 12 serves to represent the percent polarization of the shadowed underwing area. Even though it is shadowed (with low scattered polarization intensity, compared with Figs. 8 and 9) there is a quasi-specular peak at 45°.

Figures 13 and 14 are representative of sky percent polarization, Fig. 13 being the clear sky near the fuselage and Fig. 14 in the boundary atmospheric haze layer. Both curves are fairly symmetrical in the polar pattern, with green being strongest above the infrared polarized components. The green would be expected to be stronger than the red or infrared because of stronger (though weak) Rayleigh scattering.

IV. DISCUSSION

Contrast of a target against the background is an important factor leading to identification. Contrast is highly dependent on the background against which the target is seen. In some instances photometry may be superior to polarization. In any case, the contrast is generally wavelength-dependent. A subsidiary identification is based on the geometrical shape of the target.

Shadowing is a particular photometric property of surfaces and objects that can lead to their identification. The texture of a surface affects the shadowing and thus the photometric scattering function. In polarization, microshadowing by particles on a surface, or surface roughness, leads to asymmetrical scattering and ultimately the characterization (signature) of a surface. In any case, the appropriate recognition technique depends upon the particular target and its background.

V. CONCLUSIONS

It has been shown that a C–130 camouflaged aircraft has enhanced polarimetric contrast in multispectral imagery of green, red, and the near-infrared against a sky background. Identification is facilitated by the use of Stokes parameters.

Imagery discussed here was collected using a Kodak color infrared (CIR) camera with a focal plane array. The polarimetric resolution is of the

order of 1%, allowing the discrimination of various aircraft areas from a maximum of about 24%.

Because the sky may be negatively polarized under certain conditions, the computer representation for the negative is designated zero, leading to infinite contrast. This, of course, depends upon viewing conditions and on how close to zero the measured zero is.

REFERENCES

1. Baum, B.R.; Tullock, A.P.; Bailey, L.G. A survey of epicuticular waxes among some species of Triticum. 1. Ultrastructure of glumes and some leaves as observed with the scanning electron microscope. Can. J. Bot. 1980, 58, 2467–2480.
2. Egan, W.G. Photometry and Polarization in Remote Sensing. Elsevier: New York, 1985.
3. Vanderbilt, V.C.; Grant, L.; Daughtry, C.S.T. Polarization of light scattered by vegetation. Proceedings of IEEE 1985, Vol. 73, 1012–1024.
4. Vanderbilt, V.C.; Grant, L.; Biehl, L.L.; Robinson, B.F. Specular, diffuse and polarized light scattered by two wheat canopies. Applied Opt. 1985, 24, 2408–2418.
5. Vanderbilt, V.C.; Grant, L. Polarization photometer to measure bidirectional reflectance factor. Opt. Engng. 1986, 25, 566–571.
6. Grant, L. Diffuse and specular properties of leaf reflectance. Remote Sens. Environ. 1987, 22, 309–322.
7. Wickland, D.E. Future directions for remote sensing in terrestrial ecological research. In: Theory and Applications of Optical Remote Sensing; Asrar, G.; Ed. Wiley Interscience: New York, 1989; 691–724.
8. Kharuk, V.I.; Yegorov, V.V. Polarimetric indication of plant stress. Remote Sens. Environ. 1990, 33, 35–40.
9. Philpot, W.; Duggin, M.J.; Raba, R.; Fu-an, Tsai. Analysis of reflectance and fluorescence spectra for atypical features: fluorescence in the yellow-green. Jol of Plant Pathology 1996, Vol. 148, 567–573.
10. Duggin, M.J.; Kinn, G.J.; Bohling, E. Vegetative target enhancement in natural scenes using multiband polarization methods. Proc. SPIE Conference on Polarization: Measurement, Analysis and Remote Sensing, July 30-August 1; San Diego: California, 1997; pp. 288–295.
11. Duggin, M.J.; Kinn, G.J.; Schrader, M. Enhancement of vegetation mapping using Stokes parameter images. Proc. SPIE Conference on Polarization: Measurement, Analysis and Remote Sensing, July 30-August 1; San Diego: California, 1997; pp. 307–313.
12. Riddell, J.; Kelch, D.J.; Sin; Sira, D.; Hill, R.K.; Stoner, W.; Dionne, C.; Nguyen, S.T. Spectral polarization characteristics of soils and landmines. Int. Symp. On Spectral Sensing Research, 1999.

13. Title, A.M. Improvement in birefringent filters 4: the alternate partial polarization filter. Appl. Optics 1976, 15(11), 2871–2879.
14. Walraven, R. Polarization imagery. Optical Engng. 1981, Vol. 20, 15–18.
15. Parulski, K. A. Color Filters and Processing Alternatives for One-Chip Cameras. IEEE Trans. Electron Devices, ED-32, 1985; 1381–1389.
16. Brainard, K.H. Bayesian Method for Reconstructing Color Images from Trichromatic Samples. Proceedings, IS&T's 47th Annual Conference/ICPS, 1994; 375–380.
17. North, J.A. PhD Thesis, State University of New York at Syracuse, 1995.
18. North, J.A.; Duggin, M.J. Stokes vector imaging of the polarized skydome. Applied Optics 1997, Vol. 36, 723–770.
19. Duggin, M.J.; Egan, W.G.; Gregory, J. Measurements of polarization of targets of differing albedo and shadow depth. SPIE 1999, Vol. 3699, 27–37.
20. Duggin, M.J. Imaging polarimetry in scene element discrimination. SPIE 1999, Vol. 3754, 108–117.

25

Detection of Vehicles and Personnel Using Polarization

I. INTRODUCTION

The visual detection of vehicles and personnel depends upon a number of factors: reflected/emitted color (photometry), contrast (spectral resolution), shapes, and motion. Optical polarization has not been used although radar, its relative, has been readily accepted and applied. There are clear analogs between radar optics and light optics. Radar is used in four polarized modes to observe vertical (V), horizontal (H), and cross-polarized (HV, VH) reflectance. In addition, because of the high spectral coherence length of radar signals (monochromaticity), radio interferometry can be used as in astronomy. Like that of the angular resolution of radar is governed by the size of the antenna aperture, but the bigger the antenna the weaker the signal that can be observed.

At present the monochromaticity of laser radiation is not good enough to permit polarized interferometry of targets. This chapter discusses the reflectance of selected targets and backgrounds. The targets are military vehicles and a soldier's uniform; the backgrounds are various types of deciduous and evergreen foliage and desert areas of the Sahara and the Sinai.

The Sahara is very important in ocean visibility studies because Saharan dust storms propagate aerosols westward over the Atlantic Ocean. During photometric and polarimetric measurements in a study in St. Thomas, U.S. Virgin Islands, surface visibility had dropped to less than 3 miles as a result of a Saharan dust storm [1].

II. CONTRAST, POLARIZATION, AND PHOTOMETRY

Military camouflaged vehicles and aircraft have fairly diffuse (nonspecular) coatings that generally have a uniform reflectance as a function of viewing angle and wavelength. However, in polarization, there are distinct differences (Fig. 1) particularly as a function of scattering angle (also termed phase angle, from astronomical notation) [2]. There is a small wavelength dependence for the military vehicle (truck). There is an inverse relationship between the surface reflectance and percent polarization of the military vehicle.

Wavelength (μm)	Reflectance	% Polarization at 90 μm
0.359	0.039	68
0.500	0.079	62
1.0	0.070	53

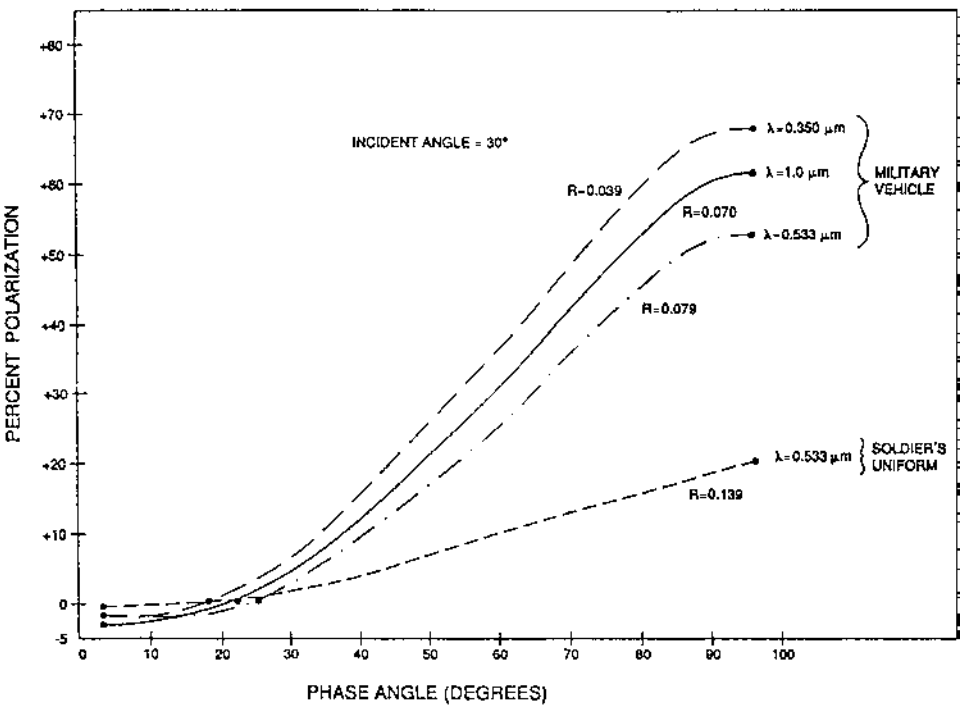

FIGURE 1 Percent polarization versus scattering angle (phase angle).

The variation in percent polarization with phase angle (scattering angle) is quite typical, ranging from −3% through an inversion angle of about 20° to a maximum polarization at about 90°. Percent polarization is a dimensionless quantity defined as

$$\% \text{ Polarization} = \frac{I_{\perp} - I_{\parallel}}{I_{\perp} + I_{\parallel}} \times 100$$

Percent polarization is independent of the absolute polarized reflectance and allows easy comparisons of optical properties.

The soldier's clothing is a neutral gray, with a lower reflectance than the vehicle, yet with significant polarization.

Table 1 lists the photometric and polarimetric properties of various targets and sand backgrounds. The origins of the Sahara and Sinai sands are shown in Table 2. It can be seen that the desert sands are relatively bright

TABLE 1 Comparison of Polarimetric and Photometric Characteristics of Various Targets

Target	Polarization[a]	Reflectance[a]
Soldier's uniform	20	14
Military vehicle	52	7
Peach leaves	2.5	41
Oak leaves	17	43
Red pine needles	8	42
Dry soil	5.5	35
Sand (beach)	10	70
Rhododendron leaves	22	100
Maple leaves	10	40
Sahara sand		
1	22	17
2a	4	61
2b	6.5	56
3	5.5	53
4	8	44
5	8	43
Sinai sand		
	5.5	50
1	27	14
2	9	35
3	7	41
4	35	11

[a] Percentage at 96° scattering angle, wavelength 1.0 μm.

TABLE 2 Locations of Sahara and Sinai Desert Sand Samples

Sahara sand samples
1. Azelik flood plain
2. a. Maradi: surface dune sample
   b. Maradi: 30 cm below the dune surface
3. Amakon: dune sand from Tenere Desert, east of Aïr
4. N'g'uigmi (diatomite from Lake Chad area)
5. Dune sand from Niger Valley close to Niamez

Sinai Desert sand samples
1. Calcareous serozems, 4 km east of Beit-Shean near Kibbutz Ma'oz Haim
2. Loessial serozems, near Tel-Malkhata, 23 km east of Beer-Sheva
3. Sand dunes located near Yamit on northern coast of Sinai Peninsula
4. Terra rossas, brown rendzinas and pale rendzinas, and Sinai sand from 10 km south of Elat, Sinai Peninsula

Source: Ref. 2.

(except Sahara sand 1 and Sinai sand 4) and have low polarization. Thus the military vehicle, with 52% polarization, is readily identified in the desert by using polarization; however, it is relatively dark (7% reflectance) and generally has a significant contrast photometrically. Which technique is most effective depends upon the background, which is not always the same; in some cases photometry is better and simpler than polarization. The evergreen rhododendron is an exception because its leaves are shiny and give a high polarized reflectance. The soldier's uniform has a significant contrast both photometrically and polarimetrically.

Sahara sand 1 (from the Azlik flood plain) is darker, presumably due to organic matter. Sinai sand 4 is darker because of the brown rendzinas and pale rendzinas material, with resulting high polarization. Otherwise, the sands have a high percentage of silicon dioxide, with relatively low absorption and with real index. Thus they strongly scatter light, which renders them bright.

III. DISCUSSION AND CONCLUSIONS

Depending upon the region, because recognition depends upon contrast, a chameleon approach has been proposed to camouflage targets. There is no general surface or coating that will not be detectable to either photometry or polarization or a combination of the two.

High resolution (photometric or polarimetric) requires large optics that are difficult to fly in aircraft but are suitable for satellites, either stationary or in near-earth orbit.

Selection of optical wavelength bands or the use of hyperspectral imagery is one possible approach, especially where distinct absorption bands occur. Such bands occur for chlorophyll in the near-infrared or for water vapor at 0.96 μm.

REFERENCES

1. Egan, W.G. Boundaries of ERTS and aircraft data within which useful water quality information can be obtained. Environ. Lett. 1974, *6*, 95–101.
2. Egan, W.G. Photometry and Polarization in Remote Sensing. New York: Elsevier, 1985.

26

Optical Remote Sensing of the Sea: A Caribbean Example

I. INTRODUCTION

This chapter reviews the optical remote sensing of sea properties: chlorophyll content, turbidity, land/water boundaries, bathymetric seafloor biota, and oil slicks. The need for absolute calibrated measurements of these properties is emphasized, whereby the bulk absorption and scattering properties of the sea may be deduced despite the disturbing effects of the sea surface wave structure and the absorption and scattering properties of the atmosphere. Two atmospheric models are discussed (LOWSUN and the Dave radiative transfer model) to permit correction for atmospheric effects. The Cox and Munk representation of sea surface wave slope probability is also considered for optical modeling of reflection from the sea surface.

Finally, an example of detailed ground calibration with sea surface and atmospheric modeling is presented. The region considered is in St. Thomas, U.S. Virgin Islands, where a region of the harbor was studied in detail optically and biologically, with multispectral imagery obtained from both an aircraft and LANDSAT I.

The "bottom line" is the quantitative relation of the imagery to the biological and chemical processes occurring in the sea. These processes affect seawater optical absorption and scatter caused by particulate and chemical loading of the sea.

The visible and near-infrared remotely sensed signals from the sea are influenced by three significant factors (Fig. 1): (1) the bulk absorption and

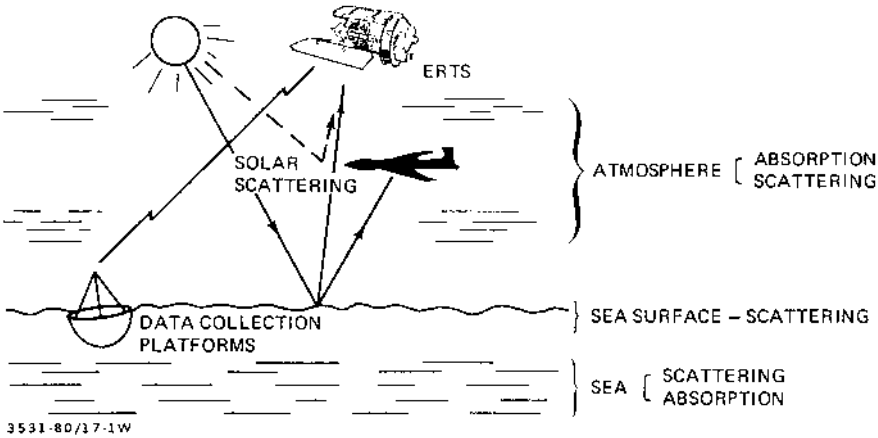

FIGURE 1 Optical remote sensing applications ($0.4 < \lambda < 1.1$ μm).

scattering properties of the sea, (2) the wave structure and reflecting characteristics of the sea surface, and (3) the absorption and scattering properties of the atmosphere. All three factors are functions of wavelength and the fundamental optical properties of the absorbers and scatterers. Various optical models can be used to correct for the effects of the latter two factors and thus obtain the bulk optical scattering and absorption properties of the sea itself. The reason we want the bulk optical properties of the sea is that these relate to the biological and chemical processes in it.

In this chapter we consider applications to determinations of chlorophyll, turbidity, water quality, depth, seafloor biota, oil slicks, land/water boundaries, and the effects of wave action, atmospheric scattering, and absorption on remotely sensed signals (Fig. 1).

When we speak of the sea with respect to remote sensing, we define it in this overview to include open water areas of reasonable extent, i.e., oceans, bays, lakes, deltas, and estuaries. Further, we consider work in the optical region of the spectrum, that is, at wavelengths of 0.400–1.0 μm. The analyses considered are limited to this spectral region and what can be deduced with optical (visible, near-IR) remote sensing.

The approach used for the Caribbean example in this review is "fundamentalist," that is, relating specific fundamental ground truth biology and chemistry to the optical properties of scattering and absorption in the sea and ultimately to the remotely sensed radiance. The intervening effects of atmospheric scattering and absorption are taken into account with verified models

of varying complexity from LOWTRAN 4 to an elaborate multilayer radiative transfer model. The sea surface roughness is treated with a variation of the Cox and Munk [1] representation of particular wave facet slopes.

The LOWSUN model adapted from LOWTRAN 4 is a precursor of the subsequent LOWTRAN/MODTRAN codes and does not include multiple scattering. Multiple scattering is sometimes important, particularly in the blue spectral regions with hazy or dusty atmospheres. However, the detailed satellite data that were taken are of interest because of the extensive calibration program. The analyses do not include the effects of polarization, which are covered in Chapter 31 describing the polarization modifications of MODTRAN 5. Multiple scattering is included in MODTRAN 5.

Underlying the entire review is an unrelenting emphasis on quantitative calibration. This must not be taken to impure the quality of much good remote sensing work that has been accomplished to date, but training areas are not as conveniently available in sea areas as on land to make comparisons. The use of training areas is not possible in the sea for several reasons. Local wind conditions, which may vary near land areas, affect the sea surface roughness, which in turn changes the photometric properties as a function of time. Further, large areas with similar solar incident radiation angles, with controlled and defined turbidity and chlorophyll, carotenoid, or effluent waste contents do not generally occur.

Also, to enable intercomparisons between observational data, a careful calibration and control program must be maintained despite the difficulty. For instance, the quantitative contribution of varying atmospheric absorption and scattering must be deduced for each remote sensing observation, this is particularly true for the higher resolution photometry of LANDSAT D. The LANDSAT D (now LANDSAT IV) Thematic Mapper (TM) has 256 photometric quantization levels compared with 64 for the MSS on LANDSATs I, II, and III. Also, the instantaneous field of view (IFOV) of the TM is 30 m compared with 79 m for the Multispectral Scanner (MSS) on LANDSATs I, II, and III (82 m on LANDSAT IV).

II. CHLOROPHYLL SENSING

Tassen et al. [2] emphasized through a model that in the remote sensing of water bodies the upwelling radiance is typically low and only a minor part contains information about the water and substances in it. They also recognized the large contributing factor of atmospheric scattering and sun and sky glitter (which they call atmospheric effects). Their analysis adopts a phenomenological approach based on reflectance ratios taken as the ratio of the upwelling radiance just below the water surface to the downwelling radiance

just above the surface. These reflectance ratios are measured at wavelengths of 0.431, 0.667, and 0.548 μm, the first two being at maximum and the last at minimum chlorophyll absorption. As a result of their analyses, a chlorophyll retrieval expression was evaluated that showed no detailed conclusion except that there is a strong dependence of wind speed over the sea and visibility on the sediment content of the water.

Hovis and Clark [3] showed that chlorophyll *a* and phaeopigments dominate absorption in the blue and also demonstrated good agreement with an algorithm between in situ measurements with upwelled radiance. However, the blue optical spectral region is where atmospheric scattering effects are strongest and mask the remotely sensed radiance measurements. Further, Hovis and Clark took note of the importance of data processing to remove the effects of atmospheric path radiance and ocean surface reflectance.

The remote detection of chlorophyll by fluorescence is still being used by at least four groups (cited in Ref. 4); two of these groups are looking at oil spill detection by fluorescence. Typically, laboratory measurements of chlorophyll *a* are based on ultraviolet excitation with broadband ultraviolet (centered at 0.400 μm) and sensing in the red at a wavelength of 0.685 μm (see, e.g., Ref. 5). The technique has also been adapted to in situ marine environment measurements in the Gulf Stream [5,6] and in estuarine waters [7,8].

Remote sensing of chlorophyll fluorescence requires an ultraviolet source and spacecraft- or aircraft-borne sensors. It is very difficult to sense the density and diversity of phytoplankton (chlorophyll-bearing organisms) from space because atmospheric effects on the signal are of the same order as diversity effects. Placement of an active fluorometer on a low-flying helicopter or aircraft appears feasible [4,9]. There is a problem with strong scattering in the atmosphere of the ultraviolet excitation radiation, which reduces the excitation energy reaching the sea surface. Also required is a separate determination of the attenuation coefficients of radiation in the sea at the excitation and fluorescence wavelengths. These may vary if the water is turbid as in estuarine environments.

III. TURBIDITY SENSING

Turbidity sensing in the sea is on a firmer footing than chlorophyll sensing because its broadband scattering characteristics match the broadband spectral sensing characteristics of aircraft and spacecraft optical sensors. One study of water quality in Lake Powell, Utah [10], concluded that at a wavelength of 0.58 μm the reflected radiance (measured by an aircraft at 600 m altitude) was directly correlated to the suspended sediment concentration. Even though this study made use of a 500-channel spectroradiometer

in the wavelength region 0.4–1.1 μm, the broadband nature of the particulate scattering is demonstrated, with peak reflected radiance occurring at 0.58 μm (probably from calcium carbonate) and a shoulder at 0.64 μm (probably from siliceous particulate matter or sediment such as clay). Although Merry does not provide a quantitative relationship between turbidity and radiance, an allusion is made to this possibility. The low altitude surveys were conducted on clear, low wind days, resulting in negligible atmospheric correction; however, atmospheric scattering could still be appreciable toward the shorter wavelength end of the spectrum.

Another marine pollution study of interest was one of Tokyo Bay in 1972–1976 [11]. Industrial and municipal wastes flow from four rivers into the bay along with fresh water. The reference for the data reduction was "clear open sea water" similar to the idea of Scherz and Van Domelen [12] of using "clear lake" as a photometric reference. Saitoh et al. [11] assumed that the total radiance on a flat surface and the atmospheric transmittance did not change over the frame; it should be pointed out that, judging from personal observations, in the environs of Tokyo, where Tokyo Harbor is located, there is hardly an area where the air transmittance is constant. Saitoh et al. [11] deduced five classes of water reflectance representative of different suspended materials without relating to the optical scattering and absorption in the five classes of water as a function of wavelength. The interdisciplinary nature of the study is commendable, though, with excellent data handling to show contrasts.

Proceeding to a study of water of the San Francisco Bay delta from a U-2 aircraft using an Ocean Color Scanner [13], a region with high turbidity, high chlorophyll content, and high suspended solids was found that was termed "a region of high biological activity," though no calibration is presented. Khorram [13] makes use of correlation coefficients to show significance but does not attempt any absolute photometric calibration. Also, the surprising comment is made in the paper that the regions of high biological activity were not locatable with aerial photography of the "highest quality." This conflicts with Egan's observations [14,15] of representative areas of high biological activity in St. Thomas harbor, where an area of high chlorophyll content, high turbidity, and high suspended solids could easily be discerned from both ERTS-1 bulk MSS data and from I^2S 4 camera precision-calibrated and processed imagery. However, there could be differences in the scattering and absorption properties of the contaminants of the San Francisco Bay delta water or in the solar incident radiation that rendered the particulates invisible.

Similar "quick look" contrasts are shown with processed images that show the effect of land use on estuarine water quality [16] in Apalachicola

Bay, Florida, for instance. The criticism of lack of calibration was aptly put in a talk by Dr. R. Dewling of the Environmental Protection Agency in Edison, New Jersey, to the effect that "uncalibrated black boxes cannot be used to enforce any environmental standards laws," 1980. Moreover, observers cannot intercompare data from uncalibrated quick look imagery.

IV. LAND/WATER BOUNDARIES

Satellite optical sensor photometric data of the sea have application to cartography. Although this may not appear to be within the realm of remote sensing of the open sea, it is relevant to remote sensing of bay and lake areas. The relevance exists because highly accurate location of ground truth points on satellite photometric data are necessary to achieve correct correlations. The same requirements required for aircraft scanner imagery and can be supplied by GPS (ground positioning satellite), but photographic imagery may also require cartographic correction.

Two techniques have been used to produce high geometric accuracy: resampled computer tapes and photomap bases. One uses the navigational satellite surveyer method, and the other uses the map-matching method [17]. The MSS Channel 5 (0.6–0.7 μm) was used for the analyses.

The navigational satellite surveyor method required high contrast pixels representative of readily identified field elements and ground control points that could be accurately located with a navigational satellite to ± 30 (with averaging to ± 5 m). Systematic geometric corrections are made for earth rotation, mirror scan velocity variations, satellite altitude variations, and oversampling along the scan line direction. The average absolute error for this technique was 49.9 m. This method is applicable to regions where accurate maps are not available. Where accurate maps are available, no field work is required, and once the pixel column and row numbers (from the image) and the longitude and latitude (from the map) of each corner of a frame are known, a map tape and photomap base can be produced. The average absolute error for this technique is 68.3 m. For the LANDSAT-D Thematic Mapper with an IFOV of 30 m, the absolute average error would be expected to be between 20 and 30 m.

Although MSS Band 5 (0.6–0.7 μm wavelength) was used for the cartographic mapping described above, there is a preference for MSS bands 6 and 7 (0.7–0.8 and 0.8–1.1 μm, respectively) because the land/water boundaries can be more clearly seen.

Cartographic applications do not require the accurate photometric calibrations that are necessary for remote determination of water quality and chlorophyll.

V. BATHYMETRY

Where the sea is adequately transparent, the reflectivity of the benthic environment is known. Algorithms were developed to use MSS bands 4 and 5 (0.5–0.6 μm and 0.6–0.7 μm, respectively) to discern depths in the Bahama test range [18]. A 30% bottom reflectance was assumed, and attenuation coefficients of $k = 0.00975\ \text{cm}^{-1}$ (MSS4) and $k = 0.00325\ \text{cm}^{-1}$ (MSS5). Maximum detectable depth was 40 m, with the best accuracy being 2½% when the key variables of water attenuation and bottom reflectivity are known. Much concern is shown for detector radiometric calibration, but sea surface wave conditions and atmospheric scattering and absorption are not considered. However, an algorithm developed for a specific sea area bathymetric application that works from a non-fixed (i.e., "floating") reference is hardly applicable elsewhere except by coincidence. It is pointed out that with LANDSAT operating in the high gain mode over the sea (3× higher gain) improved depth-sensing accuracy is possible.

The bathymetric techniques described are useful for reef location, but a further application deals with the effects of tidal fluctuation on the spectral characteristics of submerged reef areas [14]. Biña and Ombac [19] show concern about atmospheric corrections; in the absence of atmospheric data, the brightness of radiation scattered in the atmosphere to the satellite would be the same as that over a zero brightness area (taken as over deep clear water), and the maximum brightness of 100% ground reflectance plus atmosphere to the satellite taken over the white coralline sand of the Apo Reef. Neither atmospheric absorption nor sea surface corrections are considered.

Another version of depth measurement is given by Chong et al. [20], who lump the atmospheric radiance and sea surface scatter into a term for the radiance observed over deep sea. The sea depth is deduced from the decrease in radiance observed as the depth of the sea increases for a given bottom reflectance.

VI. OIL SLICKS

Many techniques have been proposed for the remote sensing of oil slicks. We consider only the UV, visible, and IR spectral regions here. There must be sufficient photometric contrast between the oil and the seawater background to enable positive identification. The nature of the oil and sky lighting sensor viewing conditions critically affect the recognition, particularly because the oil generally forms a monomolecular layer on the surface of the sea. From an overhead viewing station oils generally appear to be yellow, brown, or

brownish black because of their strong UV absorption characteristics, which extend into the visible spectrum. All crude and semirefined oils fluoresce when excited by UV light as a result of the polyaromatic and heterocyclic compounds in the oil.

The real portion of the refractive index of oils is generally higher than that of seawater in the visible and near-IR portion of the spectrum, and consequently oil reflectivity is somewhat higher. However, the smoothing effect of oils on the sea surface appears to make the most promising approach to oil slick detection, the use of the sun glitter pattern of polarimetry [21]. The glitter pattern is quite different with an oil film, with greater reflectivity of the sea surface, and at most angles in the glitter pattern the polarization of the reflected light is higher.

VII. BULK SCATTERING AND ABSORPTION IN THE SEA AND RELATION TO ECOLOGY

The optical properties of seawater are affected by the chemical and biological processes occurring within it. Extinction of radiation may be used to represent the effect on radiative transfer in the water. Extinction is the sum of scattering and absorption effects, and in turbid water the scattering and absorption can be both molecular and particulate. Particulate scattering can result from hydrosols or the particles themselves. Thus a more detailed analysis would determine scattering and absorption in seawater, the appropriate sum of which would give the conventional extinction parameters used in correlation to biological and chemical parameters.

Going further, scattering and absorption depend upon the scattering angle (the angle between the incident radiation and the scattered radiation), the size and shape of the scattering and absorbing particles, and their complex index of refraction. Most of these characteristics are unknown or poorly known at present for the hydrosols and particulates present in seawater. Thus, as a first obvious step, separate determinations of the absorption and scattering coefficients as a function of wavelength allow us to proceed one step beyond the present concept of extinction as the basic correlation parameter in seawater.

As a result of progress in radiative transfer models, it is possible to construct a two-flux model that permits the separation of scattering from absorption in seawater from three simple in situ spectrophotometric measurements. Essentially, the reflectance of a diffusely reflecting white panel is measured just above and $\sim$30 cm and $\sim$150 cm below the surface of the sea. A submarine viewing tube is used for the underwater photometric measurements, which are made using daylight as the radiation source. The photometer is mounted at the top of the viewing tube; the unit can be used

with interchangeable narrowband interference filters to select the appropriate wavelength of interest. The three measurements permit reflectance values R_1 and R_2 to be calculated from the ratios of the 30 cm and 150 cm depth measurement, respectively, to the surface measurement at a specific wavelength. The set of equations representing these conditions has been solved in terms of a nomogram that permits both the scattering and absorption coefficients to be obtained [22]. Then, separately, if the equivalent thickness of the dominant biological or chemical substance is known, the absorption portion of the optical complex index of refraction may be calculated [23]. The refractive portion of the optical complex index of refraction is about 1.28 at 0.500 μm for chlorophyll-bearing materials. The optical complex indices of refraction of sediments such as clays have been published for wavelengths between 0.185 and 2.7 μm [23]. Phase functions may be computed assuming Mie scattering and taking the relative refractive portion of the complex index of refraction as the difference between that of the particulates and that of seawater.

An application of this optical approach is presented in Section XI for a Virgin Islands test site.

Thus when the scattering and absorption coefficients of seawater have been obtained, their relation to the ecology may be determined. Chlorophyll has maximum absorption at wavelengths of 0.431 and 0.667 μm; thus the absorption coefficient would be greatest at these wavelengths if chlorophyll were present. Its determination requires narrowband filter measurements (at these wavelengths) of the reflected and scattered radiation to deduce the presence of chlorophyll. If the photometric accuracy of a broadband sensing system (i.e., MSS4: 0.6–0.7 μm) is high enough, then the effect of the narrow chlorophyll absorption band within the larger (0.6–0.7 μm) absorption band can be sensed. With absolute calibration, absolute chlorophyll levels can be specified, not just those relative to "clear" water.

Particulates in the sea (as well as molecules of water) exhibit Rayleigh scattering increasing to the inverse fourth power of wavelength. This is essentially why pure water is blue. Larger particulates generally scatter at some weaker inverse power of wavelength. Silicate particles have weak absorption, but clays containing iron minerals would be expected to absorb more strongly toward the blue. Turbidity is a complex parameter, but it is closely related to scattering. It is measured by relating to standards in a Hatch Model 2100A Turbidometer, for example.

Turbidity in the sea is readily sensed remotely because of the radiative scattering associated with the brightening effect in the water. Benthic diversity has been found to be inversely correlated with turbidity in a Virgin Island study [24]. Thus it is suggested that benthic diversity is indicative of long-term water quality conditions. Water chemistry parameters were found to be dy-

namic, and instantaneous measurements are thus inferred to be stochastic and unrepresentative of parametric conditions.

As indicated in Fig. 1, much of the ground truthing can be accomplished through the use of data collection platforms. For instance, the transmission properties of water (from which the absorption and scattering of water are determined) as well as those of chlorophyll can be measured in situ by fluorescence.

VIII. ATMOSPHERIC EFFECTS

Atmospheric effects have not been given the consideration they deserve in remote sensing of the sea. Empirical corrections have been used (see Refs. 15, 19, and 20, for instance). However, with the need for absolute calibration to enable data between different observers to be compared and quantitative specifications for water properties to be made, absolute and exact corrections for atmospheric effects are necessary. Further, with the higher photometric resolution on the Thematic Mapper of LANDSAT IV (256 quantization levels compared to 64 on the MSS on LANDSATs I, II, and III), almost an order-of-magnitude improvement is necessary in the photometric data reduction to make use of the full capabilities of the newer instrumentation.

To correct for atmospheric effects, a measurement of the pertinent optical atmospheric properties is necessary together with the application of an appropriate optical model. The optical properties are the aerosol sizes, vertical distribution, complex index of refraction, and vertical molecular profile of the atmosphere. These properties could be inferred using satellite measurements of the brightness of ground targets and atmospheric radiance (both as a function of wavelength) together with simultaneous ground truth radiance measurements at the targets (buoys on the sea may be used). Interpretation of these measurements would require a model in order to obtain explicit optical properties because all of the optical properties of the atmosphere tie into each measurement. The disentangling of the optical properties is quite formidable (see, e.g., Ref. 25). For the present, the AFGL standard atmospheres and aerosol parameters [26] are most conveniently used in standard atmospheric models.

Two validated, accurate atmospheric correction programs are discussed here. The first is the atmospheric transmittance/radiance computer code LOWTRAN 4 [27]; the second is the multilayer Dave radiative transfer code [28]. These are not the only atmospheric correction codes, but they are both accessible to the public and can be run on generally available computers. Following this, some experimental techniques for atmospheric corrections are discussed.

The LOWTRAN program can be run on a personal computer. The Dave program requires a computer with a large memory capacity plus a conversion of the original Fortran program to a CD or Zip disk with at least 1 MB of data storage. The program is available from the NASA Center for Aerospace Information, Report No. 75N10746 in hard copy or microfiche. Although the program was developed 30 years ago, the modeling is still valid and useful for detailed polarization analyses.

LOWTRAN 4 is a computer code that predicts the atmospheric transmittance and radiation emitted by the atmosphere and earth in the wavelength region between 0.25 and 28.5 μm. The spectral resolution is 20 cm^{-1}, which is 0.000125 μm at 0.25 μm and 1.62 μm at 28.5 μm. The model takes into account all the absorption effects of water vapor, uniformly mixed gases, ozone, nitrogen, continuum, water vapor continuum at 10 μm, molecular scattering, aerosol extinction, UV ozone, and nitric acid. Six standard geographical and seasonal atmospheric models and four standard aerosol models are included with provision for substitution of nonstandard or experimental values. Two modes of operation are possible, to compute atmospheric transmittance alone or to compute both radiance and atmospheric transmittance for any given path geometry. The card deck is available from the National Climatic Center, Federal Building, Ashville, NC 28801. The program has evolved into the MODTRAN Program.

In the original LOWTRAN 4 program, emission from aerosols and molecules was included in the line of sight. However, aerosol and molecular scattering were considered only as scattering out of the line of sight, not into it.

Contributions to atmospheric emission from radiation scattered one or more times was neglected. A modification of LOWTRAN 4 to include solar scattering into the line of sight (but not multiple scattering), called LOWSUN, was presented by Smith et al. [29]. Scattered first-order solar radiation becomes an important source of background radiation at wavelengths greater than 5 μm.

The digitized absorption coefficients in LOWTRAN 4 are those for moderate atmospheric paths and generally tend to underestimate transmittance for very long paths and overestimate transmittance for very short paths.

The Dave radiative transfer program [28] is intended for research investigations where a plane parallel nonhomogeneous atmosphere may be assumed. A variety of aerosol particle size distributions may be employed as well as number density in a vertical atmospheric profile over a Lambert ground of specified reflectivity. Rayleigh scattering of molecules and aerosols is included as well as absorption by ozone and aerosols. The program may be expanded into a line-by-line model of molecular absorbers such as carbon

dioxide and water [30]. The program is not an efficient one for production runs with a specific atmospheric model, because four separate subprograms must be executed before the radiances are obtained at various levels in the atmosphere. However, a detailed description of the Fortran program and a tape are available from NASA.

Part I of the scalar Dave radiative transfer program computes the coefficients of the Legendre series representing the scattering phase function of a spherical particle from its size and complex index of refraction. The output, consisting of these coefficients for hundreds of discrete but equally spaced values of the size parameters, is stored on magnetic tape for input to Part II. An option exists in Part I to print the values of the Legendre coefficients and values of the intensity of the scattered radiation for each size parameter at scattering angle increments of 1° from 0° to 180°.

Part II computes the coefficients of a Legendre series that characterize the normalized scattering phase function of a unit volume that is illuminated by monochromatic, unpolarized, and unidirectional radiation. The volume contains one of three specified size distributions of spherical particles (i.e., discontinuous power law, modified gamma, or log-normal). The output is in punch card form for input to Part III.

Part III computes the Fourier coefficients of a series representing a normalized scattering phase function of a unit volume for the zenith angles β ($=\cos^{-1}\mu$) and β' ($=\cos^{-1}\mu'$) of the directions of the incident and scattered radiation. The argument of the Fourier series is the difference between the azimuth angles ($\varphi' - \varphi$) of the meridian phase containing these two directions. The Fourier coefficients are computed as $\theta = 0°$ (2°) 180° and $\theta' = 0°$ (2°) 180°.* The output of this program is stored on magnetic tape for input into Part IV (or part V) of the DAVE program.

Part IV computes the scattered intensity emerging at selected levels of a plane-parallel, nonhomogeneous atmosphere that contains an arbitrary vertical distribution of aerosol number density and/or ozone. The atmosphere is bounded at the lower end by a Lambert ground of specified reflectivity. The basic radiative transfer equation is separated into a series of mutually independent integrodifferential equations representing the *n*th Fourier component of the scattered intensity. The argument of the Fourier series is the azimuth angle difference ($\varphi' - \varphi$). These integrodifferential equations are then individually solved by dividing the atmosphere into a finite number of layers (160, 80, 40, 32, 20, or 16) and using the Gauss–Seidel iterative procedure. As mentioned previously, atomic absorption in LOWTRAN/MODTRAN

* 0° (2°) 180° signifies 0° to 180° in 2° increments.

nodes lines may be incorporated into the ozone absorption portion of the program. This was accomplished, for instance, by using a separate layered atmosphere molecular absorption program and dovetailing it into the Dave [28] program [30].

It should be mentioned in passing that Plass and Kattawar [31,32] used the Monte Carlo method to solve the atmosphere–ocean radiative transfer problem. The technique was extended in the atmosphere–ocean system to calculate flux and radiance [33–35], and the complete Stokes vector was calculated by Kattawar et al. The Dave [36], radiative transfer program also has a vector form that permits calculation of the polarimetric scattering and absorption properties of the atmosphere similar to the scalar model.

Experimentally, satellite optical data can be corrected for variable target irradiance, atmospheric attenuation, and atmospheric backscatter. One technique employed a radiant power measuring instrument (RPMI) to determine target irradiance, atmospheric transmittance for one air mass, and sky radiance seen by the space sensor [37]. The global irradiance H (i.e., sun plus sky over the hemisphere) is easily measured for each spectral band of the sensor. However, the beam transmittance for one air mass would have to be inferred with a single-point measurement technique, with resulting limited accuracy. The sky radiance could be measured directly from a satellite but also could be inferred from ground-based measurements of backscatter if satellite observations were unavailable. A measurement is made on the ground of radiation scattered at an angle corresponding to that scattered to the spacecraft, and a correction is made for the difference in air masses between the direction of observation and direction of the spacecraft. This technique can be used only when the solar zenith angle is greater than 45°. Modeling is otherwise necessary to extrapolate from available measurement angles to the desired angle.

A variant on this technique was used by Egan [6] to correct LANDSAT I imagery for water quality in the Virgin Islands. The radiances from standard test panels (resulting from the sun and sky illumination) were measured at ground level in the MSS sensor bands 4 and 5. A comparison of the observed ground measurement with the simultaneous satellite sensor observation of a large photometric target (a beach area) revealed that a correction was necessary for atmospheric scattering and absorption. The multiplicative correction for scattering and subtractive absorption was inferred for ERTS-1 bands 4 and 5 (0.5–0.6 and 0.6–0.7 μm, respectively) from tables of astrophysical quantities [38]. This correction produced reasonable results but hardly the ultimate in precision.

Another experimental approach was described by Griggs [39], who used the results of Plass and Kattawar [31,40] that showed that outgoing radiance

varies with aerosol content and that when the underlying surface albedo is low it is a very sensitive function. The ocean or sea fulfills this requirement. Further calculations by Plass and Kattawar [34] and by Ludwig et al. [41] indicated that the upward radiance depended strongly on the total number of aerosols but not on the vertical distributions. Thus upward radiance measurements can be directly related to the total vertical aerosol content and thus the mass loading, using a relationship given by Griggs [39].

IX. EFFECT OF WAVES AND SUN GLINT

Very seldom is the sea surface smooth. If it were, the major upwelling radiation would be that from sky scattering and sea-reflected radiation as well as scatter from suspended particulates and molecules of water and ocean salts. The 0.5° wide image of the sun would be seen only at the specular reflection angle. However, as the wind ruffles the ocean surface, wave facets appear, Fresnel's reflection laws apply for each facet, and the sun glitter pattern broadens. The broadening of the glitter pattern and the sky reflection are governed by a probability distribution of the wave facet slopes. The wave slope distribution was first determined (photographically) by Cox and Munk [42], who give an analytical expression for the normalized slope probability. The expression is not symmetrical up- and downwind but is symmetrical cross-wind. An example of the probability distribution is shown in Fig. 2 for wind speeds of 2.62 m/s [5 knots (kn)] and 4.19 m/s (8 kn). (These particular wind speeds were chosen because they have subsequent application to the Caribbean example discussed in Section XI).

The x and y slope probabilities shown in Fig. 2 are normalized to the rms cross-wind and upwind slopes, and the $+y$ direction is the wind direction [42,43]. We see in Fig. 2 that the probabilities for y slopes are not symmetrical up- and downwind for either 2.62 or 4.19 m/s and that the probability for downwind slopes is greater. It is seen that the high cross-wind (x) slopes are less probable than the same y cross-wind slopes for a given wind speed. Note that the 2.62 m/s y slopes overlap the 4.19 m/s cross-wind slopes. Note also that there is a finite (though small) probability for even the highest slopes.

The use of the probability expression for sun glint depends upon the elevation angle of the sun. The normalized probability of those facets that are oriented to produce a specular reflection multiplied by the solar radiance (with a Fresnel reflection from each facet so oriented) will yield the solar radiance scattered by the wind-ruffled sea. Thus there is always a finite amount of sun glitter produced by the reflection of solar radiation from the sea, and the glitter will generally require consideration in photometric corrections of satellite imagery of the sea at high solar elevation angles (small

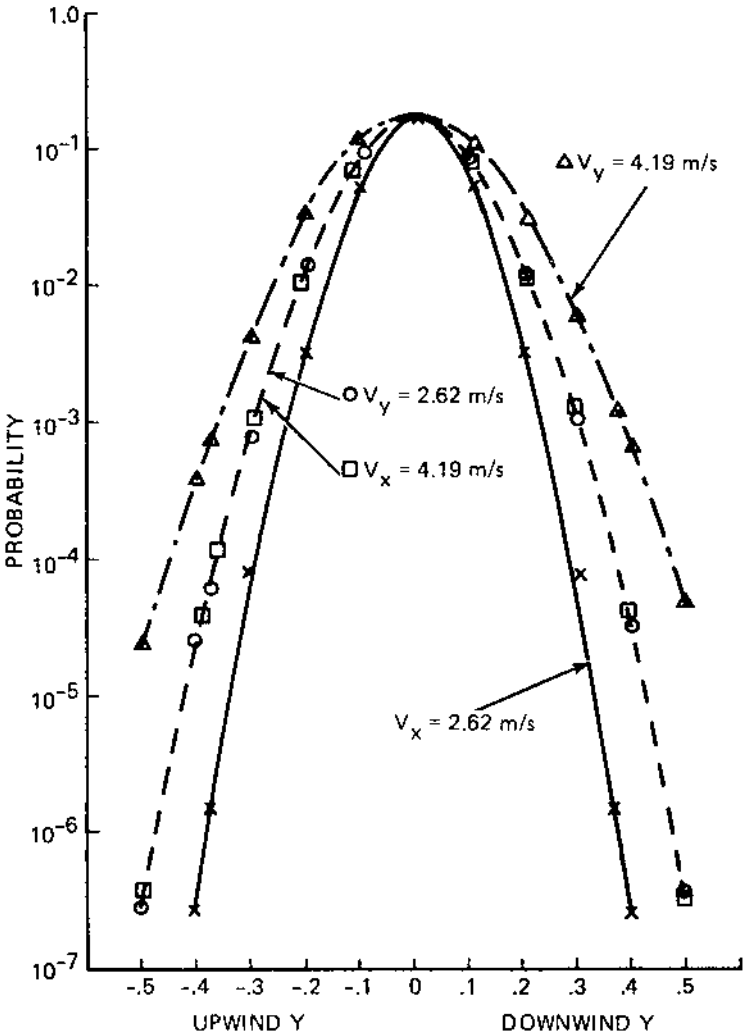

FIGURE 2 Normalized probability distribution for sea wave slopes.

zenith angles). This correction for sun glint at long wavelengths is described by Egan et al. [44].

The specular reflection of the sky from the wave facets may appear simple at first look. However, near industrialized coastal areas, a heavy, low altitude aerosol layer may occur that causes the sky brightness to vary from horizon to zenith; this variation must be taken into account for photometric corrections based on sky brightness.

There are a number of papers by the Texas A &M University group that consider the radiance distribution over a wind-ruffled sea [21,45–47]. They consider the atmosphere–ocean system as a unit in their analyses using the Monte Carlo method to solve the radiative transfer problem [45,46]. In the most recent paper, the complete azimuthally asymmetrical form of the wave slope distribution is applied to deduce the effect of wind direction and magnitude on the sun glitter pattern as well as the polarization of the reflected radiation. One paper deals with the glitter pattern alone, showing isophotes of time-averaged intensities for the glitter pattern on a wind-ruffled sea; the curvature of the earth is taken into account, and the percent polarization is computed [47]. It also mentions that quantitative data for comparison were lacking, although qualitative comparisons to photographs appear good [47]. These analyses do not take into account varying properties of the sea resulting from augmented scattering and absorption from pollutants, or the possibility of absorption by aerosols (the spherical aerosols were assumed to have a real index of refraction of 1.55 [45]).

X. SEAFLOOR BIOTA DISTRIBUTION

The quantitative determination of seafloor biota such as turtle grass or shoal grass based on sea bottom reflectance when the water depth is less than 1 or 2 optical attenuation lengths has been possible (in St. Andrew Bay, Florida) [48]. The effects are caused by water depth and low bottom reflectance (due to seafloor biota). The two effects are separated by using an algorithm that combines information from two satellite sensor bands. The Turner [49] method for atmospheric radiative transfer used Lyzenga et al. [48] is a two-stream iterative model especially designed for hazy atmospheres [50]. An approximate form is used for the scattering phase function, and although the model has an appreciable error with high reflectivity surfaces, it provides quite accurate results at small optical depths for upward diffuse, downward diffuse, and total downward radiances. The elevation angle effects of source and observer are not included, and more detailed modeling would be beneficial.

It should be pointed out that the conventional maximum likelihood classification technique (training area approach) does not map bottom features accurately under a variable depth of water [48].

XI. A CARIBBEAN EXAMPLE—STUDY AREA AND APPROACH

As an illustration of current techniques (applicable to all multispectral scanners), data obtained from NASA Experiment No. 589 [24] will be reanalyzed using computer modeling techniques developed subsequent to the original observations. The original experiment was conducted in the St. Thomas harbor at Charlotte Amalie in the U.S. Virgin Islands. The scope of NASA Experiment No. 589 included optical, biological, and chemical ground truthing of the harbor water, I^2S (International Imaging Systems) four-band aerial photography, and interpretation of LANDSAT I Multispectral Scanner bands 4 (0.5–0.6 μm) and 5 (0.6–0.7 μm). A very accurate and comprehensive sea area optical calibration and control program was developed for the LANDSAT and aircraft imagery obtained at that time. The database is representative of the best that can be obtained.

The optical survey area is shown in Fig. 3, with a biological and optical transect superimposed; there are seven optical stations (Nos. 1–7) and 20 biological stations (Nos. 101–120). The area was interesting because a number of sources were present to degrade the seawater quality and hence affect the ecology of the area, namely, 3×10^6 gal/day of raw sewage, 150,000 gal/day of waste effluent from a blackstrap molasses plant, discharge from a desalinization/power plant of coolant water [21,000 gallons per minute (gpm) at 38°C and 2000 gpm of brine at 70 ppt], and a solid waste ocean dump. It should be noted that in the interceding time, a sewage treatment plant was added, and the ecology is recovering.

ERTS-1 (LANDSAT I) MSS data were acquired on October 17, 1972, scene #1086-14162 at 10:16 a.m. local time. The acquisition of the optical in situ data was tighly scheduled to match the time of satellite passage as closely as possible. The biological and chemical harbor water data acquisition program extended over three satellite passes from October 10 to November 22. Aircraft imagery of the harbor used the I^2S four-band camera (blue, 0.410–0.470 μm; green, 0.475–0.580 μm; red, 0.590–0.690 μm; near-infrared, 0.740–0.900 μm). The optical calibration measurement consisted of (1) in situ measurements of harbor water at the seven optical stations along the harbor transect (shown in Fig. 3) and (2) spectral reflectance measurements of color test panels and the coral beach sand at Brewer's Bay Beach for use as a calibration standard for ERTS-1 and aircraft data.

The original optical analysis of the in situ harbor water data (Table I of Ref. 6) presented extinction coefficients at wavelengths of 0.433, 0.533, and 0.633 μm; the theoretical basis did not exist for separating out the scattering and absorption portions of the extinction. However, concurrent reflectance measurements of a diffuse white panel did exist to which the reflectance

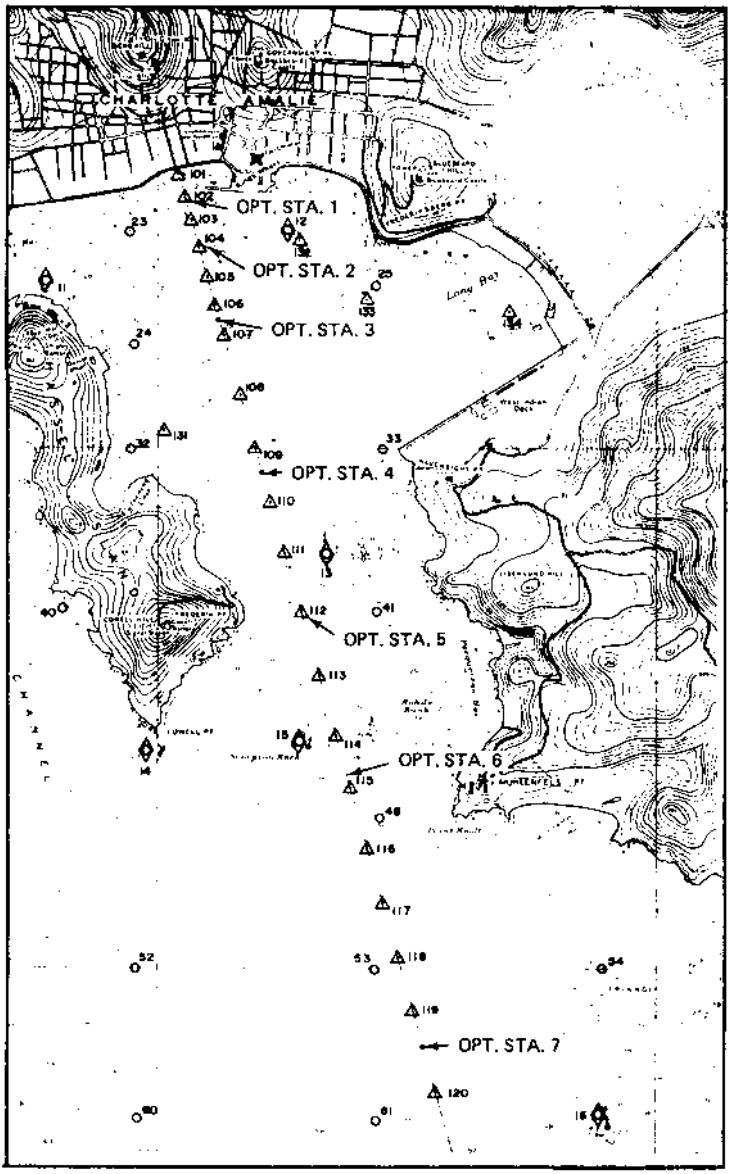

FIGURE 3 Optical study area in the St. Thomas harbor. The optical stations lie along the biological transect between stations 102 and 120.

measurements at two water depths could be related. (See Sec. VII). Thus, the reanalysis of the data now yields the bulk absorption and scattering coefficients of the harbor water (for the seven optical transect stations) and is presented in Fig. 4. It is seen that the absorption, k, is strongest near the shore, where the sewage effluent concentration is greatest. (See Fig. 5, which correlates turbidity, chlorophyll, and carotenoids.) Toward the open sea, the absorption approaches that for pure seawater. The scattering, s, is greatest where the turbidity is highest, except for the blue band, where the scattering increases toward the open sea. This phenomenon is verified by the blue-band aircraft photography (Table XI of Ref. 5).

The first thing to do with this in situ optical absorption and scattering data is to relate them to the biological and chemical data and then, using appropriate atmospheric corrections, relate them to the aircraft and satellite

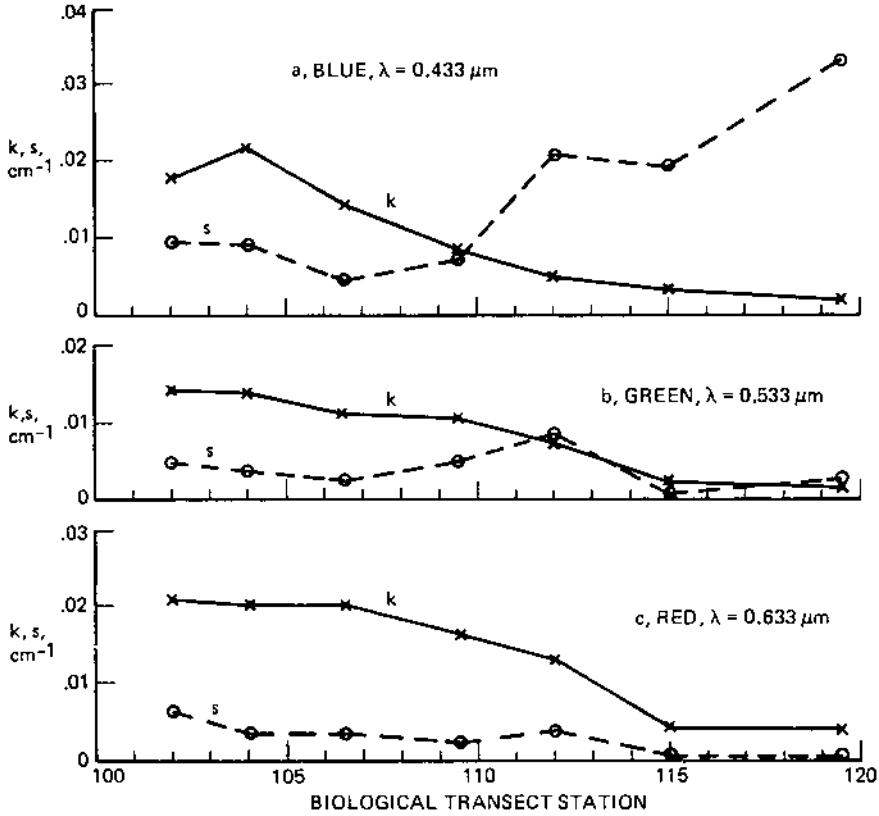

FIGURE 4 Scattering and absorption properties of seawater along optical transect in St. Thomas harbor on Oct. 17, 1972.

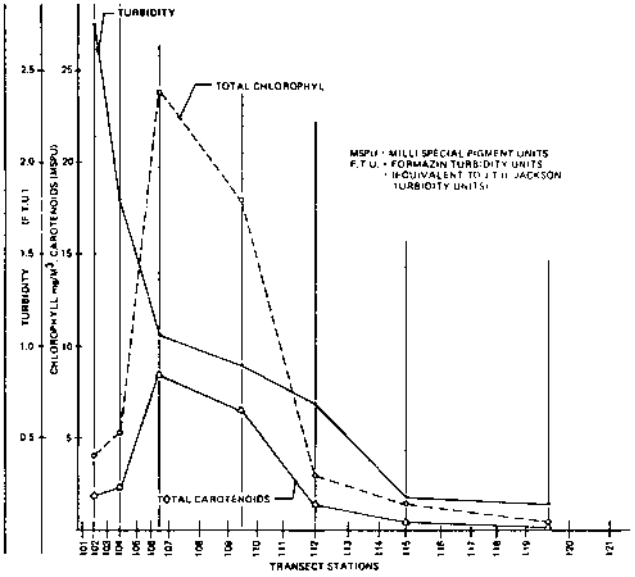

FIGURE 5 Graphical correlation of turbidity, chlorophyll, and carotenoids along the harbor transect.

data. Figure 6 shows a synopsis of some of the relationships that are evident. For instance, in situ scattering of particulates in seawater is proportional to the turbidity, because the particulates have very little absorption. The determinations of scattering could be made at any wavelength, but the scattering would be greatest at the shortest wavelength. However, the shorter wavelengths are least easily sensed from aircraft and satellite sensors because of the masking effects of molecular and aerosol scattering, which increase with decreasing wavelengths.

Absorption at $\lambda = 0.433$ μm is proportional to chlorophyll concentration, which generally increases the reflectance of seawater because of the combination of scattering and absorption from the chlorophyll-containing phytoplankton in the seawater. The same hypothesis would be expected to apply to "red tides." Similarly, plankton diversity as well as fecal coliform content would be indicated by increased scattering in seawater caused by seawater turbidity. Other variables (such as dissolved nitrates and phosphates, plankton diversity, fecal coliform bacteria, and particulate humic acids) have been found to be functionally related to the observed scattering and absorption [24].

The effect of scattering and absorption on the sea reflectivity can be calculated by radiative transport theory for seawater [22]. Going a step

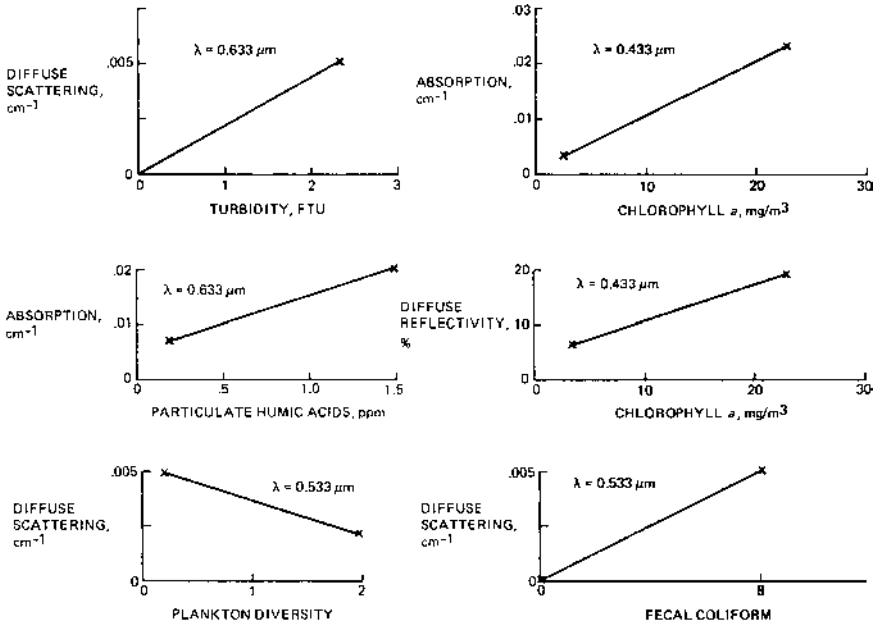

FIGURE 6 Seawater properties amenable to optical remote sensing (St. Thomas harbor test site).

further, the radiative transfer scattering and absorption in seawater is a function of the complex index of refraction of the scatterers and absorbers as well as their size and shape (see, e.g., Ref. 23). Typically, coral has a refractive index of ~ 1.5, making the index relative to seawater ~ 0.2. Using Mie scattering for nonabsorptive particles, the scattering can be calculated and the coral sand particle density in seawater inferred for a certain particle size distribution. A similar calculation may be made for chlorophyll, where the absorptive portion of the complex index will have the dominant effect.

Going now to the ERTS-1 remotely sensed data, it was found that computer-compatible tapes (CCTs) were the most accurate MSS output that were available. The ERTS-1 photographic imagery was found unsuitable for quantitative data reduction by microdensitometry for various reasons. There were horizontal striations in the band 5 imagery because of nonuniform channel gains and displacements of some lines. There are also photographic nonlinearities that must be corrected in data reduction.

Basically, the ERTS-1 bulk CCT printout was aligned to match the shoreline Coast and Geodetic Survey Chart No. 993 of St. Thomas Harbor (Fig. 7). This located the pixels within one element so that those representing the harbor transect (shown superimposed) could be determined. An addi-

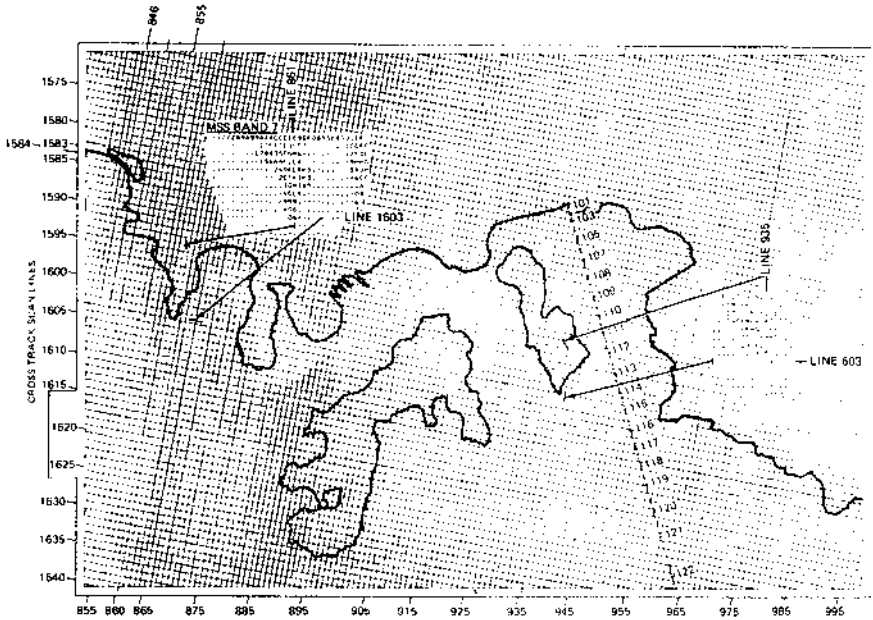

FIGURE 7 ERTS-1 MSS bulk CCT computer printout grid of scene 1086–14162. Scaled to match Chart #933, St. Thomas, USVI.

tional cluster smoothing was employed whereby each pixel on the transect was averaged with the four surrounding it to reduce noise. During the pixel data analysis, it was found that a perspective harbor map could be produced using computer graphics techniques (Fig. 8) [24]. Also, water depths could be mapped (to depths as great as 18 m) to reveal coral reefs (Fig. 9); the dotted line outlines the reef, and the solid line outlines the land.

The effect of sun glint on the ERTS imagery was below 0.005 mW cm^{-2} sr^{-1} for 50° surface winds of 2.62 m/s that existed during the overpass (refer to Fig. 2). Later in the day the winds picked up to 4.19 m/s (also indicated on Fig. 2) from 90°. The effect on the ERTS-1 imagery was negligible in this case also.

The effect of atmospheric absorption is shown in Table 1. A tropical model was used for the LOWSUN and Dave models. The complex index of refraction for the Dave model (real = 1.53; imaginary = 0.0065 at 0.45 μm and 0.007 at 0.55 and 0.65 μm) was obtained from an AFGL listing [26]. The aerosol size distribution was conventional with particle radii ranging from 0.02 to 10.0 μm, constant number density between 0.02 and 0.1 μm, and an r^{-3} number density falloff above 0.1 μm radius. The vertical number distribution

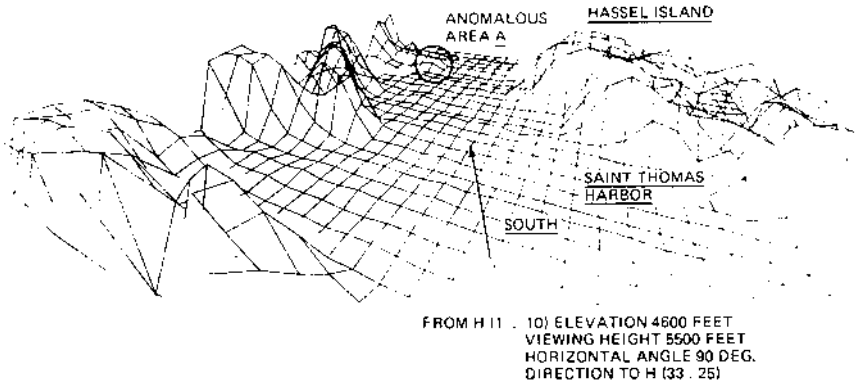

FIGURE 8 ERTS MSS CCT data (viewing angle north to south). (From Ref. 24.)

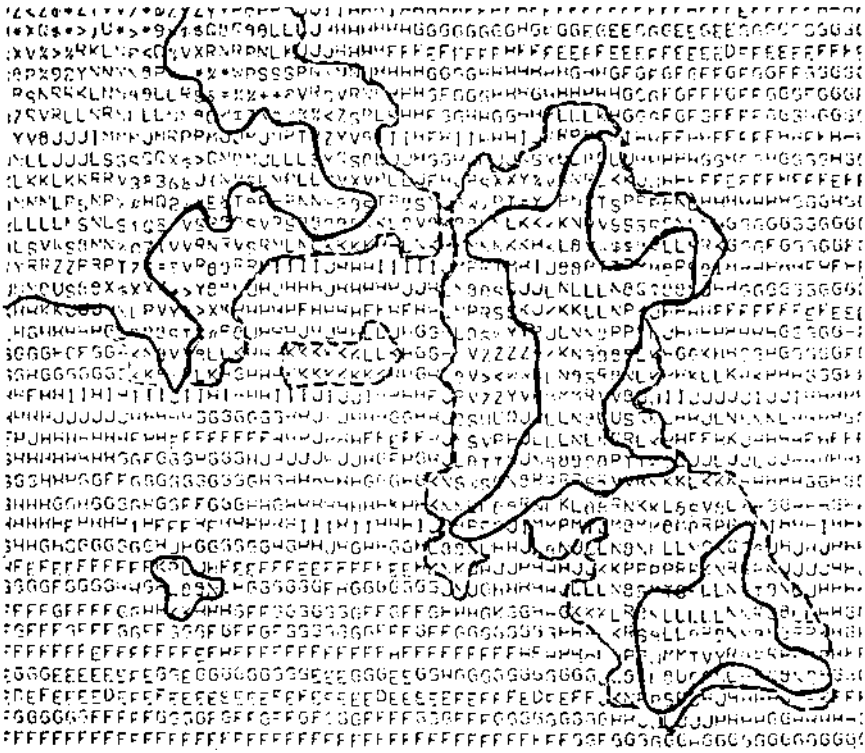

FIGURE 9 Bulk MSS band 4 data land water boundary derived from band 7. Contour lines separate MSS values $\leq J$ from values $\geq K$. (From Ref. 24)

TABLE 1 Comparison of Atmospheric Corrections to Satellite Data

LANDSAT MSS band	Clear atmospheric attenuation (%)			Atmospheric scattered radiance (mW cm^{-2} sr^{-1})		
	Egan[a]	LOWSUN	Dave[b]	Egan[a]	LOWSUN	Dave[b]
4 (0.5–0.6 μm)	17	22	35	0.13	0.17	0.04
5 (0.6–0.7 μm)	10	15	29	0.04	0.09	0.03

[a] Ref. 15.
[b] Ref. 28.

was taken from Braslau and Dave [51], and a Junge layer is included at ~20 km altitude.

In Table 1, the comparison of the atmospheric corrections to the satellite MSS band 4 and 5 data show that the original [15] approximate corrections are near the LOWSUN results (solar scattering included), but the Dave program shows about twice the LOWSUN attenuation and considerably lower scattering than LOWSUN. The differences are the result of the different models, with the LOWSUN and Dave models being the best ones; and even these may differ by a factor of nearly 2 in the absorption and greater in the scattering.

The differences between the LOWSUN and Dave results are even greater at a very low altitude of 0.668 km (see Table 2) and less at a somewhat

TABLE 2 Comparison of Atmospheric Corrections at 0.668 km Altitude

	Clear atmospheric attenuation (%)		Atmospheric scattered radiance (mW cm^{-2} sr^{-1})	
	LOWSUN	Dave	LOWSUN	Dave
LANDSAT MSS band 4 (0.5–0.6 μm)	3	14	0	0.008
LANDSAT MSS band 5 (0.6–0.7 μm)	2	13	0	0.007
I^2S blue (0.410–0.470 μm)	5	16	0	0.01
I^2S green (0.475–0.580 μm)	3	14	0	0.008
I^2S red (0.590–0.690 μm)	3	13	0	0.007

TABLE 3 Comparison of Atmospheric Corrections at 1.892 km Altitude

	Clear atmospheric attenuation (%)		Atmospheric scattered radiance (mW cm^{-2} sr^{-1})	
	LOWSUN	Dave	LOWSUN	Dave
LANDSAT MSS band 4 (0.5–0.6 μm)	8	22	0	0.008
LANDSAT MSS band 5 (0.6–0.7 μm)	6	21	0	0.013
I^2S blue (0.410–0.470 μm)	11	26	0	0.024
I^2S green (0.475–0.580 μm)	9	22	0	0.019
I^2S red (0.590–0.690 μm)	6	21	0	0.013

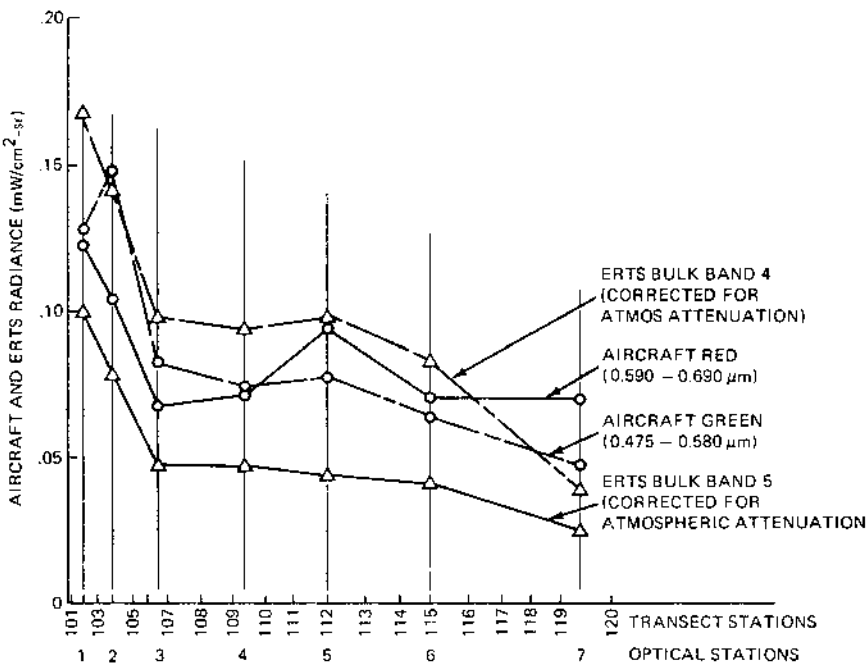

FIGURE 10 Comparison of ERTS-1 bands 4 and 5 and aircraft green and red harbor transect optical data.

higher altitude of 1.892 km (see Table 3). The LOWSUN program tends to overestimate the transmittance for short paths (see Sec. VIII), and this could explain the discrepancy.

As a result of applying the Dave atmospheric correction (Tables 1 and 2) to the original ERTS-1 bands 4 and 5 and the aircraft I^2S photographic data, we obtain Fig. 10. The match of the ERTS-1 band 5 to the aircraft green is improved, the band 5 curve being moved upward by a factor of about 2.6. Band 4 was moved upward by a factor of about 1.1, the match being quite good.

XII. SUMMARY AND OUTLOOK

From the concepts presented in this chapter, it is quite evident that a quantum step forward is necessary in atmospheric and sea surface wave corrections for remote sensing. The computer codes are available for these corrections using sea surface and atmospheric models that already exist. The atmospheric models are required to produce angular radiance computations when, for instance, source and sensor are not one above the other. The accuracy of existing detailed atmospheric models depends upon knowledge of the properties of aerosols, that is, the variations in complex index of refraction, effect of nonsphericity, and effects of turbulence in the atmosphere.

Polarization is just emerging as an additional tool in optical remote sensing, but polarization is nothing more than precise photometry. It is currently possible to account for the polarimetric-photometric effects of the atmosphere in terms of Stokes parameters as well as the polarimetric properties of sea wave reflection. It is possible that one of the new directions of remote sensing will be polarization.

REFERENCES

1. Cox, C.; Munk, W. Some problems in optical oceanography. Marine Res. 1955, 14, 63–78.
2. Tassen, S.; Sturm, B.; Diana, E. A sensitivity analysis for the retrieval of chlorophyll contents in the sea from remotely sensed radiance. Proc. 13th Int. Symp. Remote Sensing Environ. ERIM, Ann Arbor: MI, 1979; 713–727.
3. Hovis, W.A.; Clark, D.K. Remote sensing of chlorophyll and derived pigments. Proc. 13th Int. Symp. Remote Sensing Environ. ERIM, Ann Arbor: MI, 1979; 711.
4. Jarrett, O., Jr.; Brown, C.A., Jr.; Campbell, J.W.; Houghton, W.M.; Poole, L.R. Measurement of chlorophyll a fluorescence with an airborne fluorosensor. Proc. 13th Int. Symp. Remote Sensing Environ. ERIM, Ann Arbor: MI, 1979; 703–710.

5. Egan, W.G. Manned submersible optical remote sensing within the Gulf Stream. Proc. 6th Int. Symp. Environ. Willow Run Laboratories, Inc. Univ. Michigan, Ann Arbor: MI, 1969; 721–735.
6. Egan, W.G. Measurement of the fluorescence of Gulf Steam water with submerged in-situ sensors. Marine Technol. Soc. J. 1974, 10, 40–47.
7. Egan, W.G.; Cassin, J.M.; Hair, M.E. Interdisciplinary monitoring of the New York Bight. Environ. Lett. 1972, 2, 205–215.
8. Egan, W.G.; Cassin, J.M. Correlation of in-situ fluorescence and bio-luminescence with biota in the New York Bight. Biol. Bull. 1973, 144(2), 262–275.
9. Farmer, F.H.; Brown, C.A., Jr.; Jarrett, O., Jr.; Campbell, J.W.; Staton, W.L. Remote sensing of phytoplankton density and diversity in Narragansett Bay using an airborne fluoresensor. Proc. 13th Int. Symp. Remote Sensing Environ. ERIM, Ann Arbor: MI, 1979; 1793–1805.
10. Merry, C.J. The correlation and quantification of airbrone spectroradiometer data to turbidity measurements at Lake Powell, Utah. Proc. 13th Int. Symp. Remote Sensing Environ. ERIM, Ann Arbor: MI, 1979; 1309–1316.
11. Saitoh, S.; Iisaka, J.; Asaoka, O. Marine pollution analysis in Tokyo Bay by Landsat 1 and 2. Proc. 13th Int. Symp. Remote Sensing Environ. ERIM, Ann Arbor: MI, 1979; 1657–1679.
12. Scherz, J.P.; Van Domelen, J.F. Water quality indicators obtainable from aircraft and LANDSAT images and their use in classifying lakes. Proc. 10th Int. Symp. Remote Sensing Environ. ERIM, Ann Arbor: MI, 1974; 447–460.
13. Khorram, S. Remote sensing of water quality in the San Francisco Bay Delta. Proc. 13th Int. Symp. Remote Sensing Environ. ERIM, Ann Arbor: MI, 1979; 1591–1601.
14. Egan, W.G. Water quality determination in the Virgin Islands from ERTS-A data. Proc. 8th Int. Symp. Remote Sensing Environ. ERIM, Ann Arbor: MI, 1972; 685–708.
15. Egan, W.G. Boundaries of ERTS and aircraft data within which useful water quality information can be obtained. Proc. 9th Int. Symp. Remote Sensing Environ. ERIM, Ann Arbor: MI, 1974; 1319–1343.
16. Hill, J.M.; Stout, K. Impacts of land use on estuarine water quality. Proc. 13th Int. Symp. Remote Sensing Environ. ERIM, Ann Arbor: MI, 1979; 385–395.
17. Vincent, R.K.; Harrow, R.A.; Vincent, D.K. Cartography with combined LANDSAT and navigational satellite data. Proc. 13th Int. Symp. Remote Sensing Environ. ERIM, Ann Arbor: MI, 1974; 983–992.
18. Polcyn, F.C.; Lyzenga, D.R. Landsat bathymetric mapping by a multitemporal processing. Proc. 13th Int. Symp. Remote Sensing Environ. ERIM, Ann Arbor: MI, 1979; 1269–1276.
19. Biña, R.T.; Ombac, E.R. Effects of tidal fluctuations on the spectral patterns of Landsat coral reef imageries. Proc. 13th Int. Symp. on Remote Sensing Environ. ERIM, Ann Arbor: MI, 1979; 1293–1308.
20. Chong, Y.J.; Liang, T.Y.; Yeo, A.C.; Vong, V.K. Remote sensing of the sea around Singapore. Proc. 13th Int. Symp. Remote Sensing Environ. ERIM, Ann Arbor: MI, 1979; 1807–1814.

21. Guinn, J.A., Jr.; Plass, G.N.; Kattawar, G.W. Sunlight glitter on a wind-ruffled sea: further studies. Appl. Opt 1979, 18(6), 842–849.
22. Egan, W.G.; Hilgeman, T. *In situ* separation of scattering and absorption in fluids. Appl. Opt 1980, 17(22), 7324–7327.
23. Egan, W.G.; Hilgeman, T. Optical Properties of Inhomogeneous Materials. Academic Press: New York, 1979.
24. Coulbourn, W.C.; Egan, W.G.; Olsen, D.A.; Heaslip, G.B. NASA-ERTS-1 Experiment 589, Determine Boundaries of ERTS and Aircraft Data Within Which Useful Water Quality Information Can Be Obtained. Final Contract Report. Goddard Space Flight Center: Greenbelt, MD, 1973.
25. Abreu, V.J.; Hays, P.B. Influence of atmospheric absorption on satellite auroral observations. Appl. Opt 1979, 18, 3324–3327.
26. McClatchey, R.A.; Selby, J.E.A. Atmospheric Attenuation of Laser Radiation from 0.76 to 31.25 μm. Report No. AFCRL-TR-74-0003, Environmental Research Paper No. 460. AFCRL: Bedford, MA, 1974.
27. Selby, J.E.A.; Kneizys, F.X.; Chetwynd, J.H., Jr.; McClatchey, R.A. Atmospheric Transmittance/Radiance: Computer Code LOWTRAN 4, Report AFGL-TR-78-0053, Environmental Research Papers, No. 626, Air Force Geophysics Laboratory, Hanscom AFB, Massachusetts, 01731.
28. Dave, J.V. Development of Program for Computing Characteristics of Ultraviolet Radiation. NASA Rep. No. S80-RADTMO. Goddard Space Flight Center: Greenbelt, MD, 1972.
29. Smith, L.L.; Krassner, J.; Egan, W.G.; Hilgeman, T.; Selby, J.E.A. A recommended modification of LOWTRAN4 to include first order solar scattering. Paper 195–25, Soc. Photogr. Instrum. Eng.; 1979.
30. Egan, W.G.; Fischbein, W.L.; Smith, L.L.; Hilgeman, T. High resolution Martian atmosphere modeling. Icarus 1980, 41, 166–174.
31. Plass, G.N.; Kattawar, G.W. Monte Carlo calculations of light scattering from clouds. Appl. Opt 1968, 7, 415–419.
32. Plass, G.N.; Kattawar, G.W. Radiance and polarization of the earth's atmosphere with haze and clouds. J. Atmos. Sci 1971, 28, 1187–1198.
33. Plass, G.N.; Kattawar, G.W. Radiative transfer in an atmosphere–ocean system. Appl. Opt 1969, 8, 455–466.
34. Plass, G.N.; Kattawar, G.W. Monte Carlo calculations of radiative transfer in the earth's atmosphere ocean system. Pt. 1. Flux in the atmosphere and ocean. J. Phys. Oceanogr 1972, 2, 139–145.
35. Kattawar, G.W.; Plass, G.N. Monte Carlo calculations of radiative transfer in the earth's atmosphere ocean system. Pt. 2, Radiance in the atmosphere and ocean. J. Phys. Oceanogr 1972, 2, 146–156.
36. Kattawar, G.W.; Plass, G.N.; Guinn, J.R. Jr. Monte Carlo calculations of the polarization in the earth's atmosphere–ocean system. J. Phys. Oceanogr 1973, 3, 353–372.
37. Rogers, R.H.; Peacock, K. A technique for correcting ERTS data for solar and atmospheric effects. Paper I–3, Proc. of 3rd ERTS Symp., 10–14 Dec. Washington, DC: NASA Goddard Space Flight Center, 1973.

38. Allen, C.W. Astrophysical Quantities. London: Athlone Press, 1963.
39. Griggs, M. Determination of the aerosol content in the atmosphere from ERTS-1 data. Proc. 9th Int. Symp. Remote Sensing Environ. ERIM, Ann Arbor: MI, 1974; 471–481.
40. Plass, C.N.; Kattawar, G.W. Polarization of the radiation reflected and transmitted by the earth's atmosphere. Appl. Opt 1970, 9, 1122–1130.
41. Ludwig, C.B.; Griggs, M.; Malkmus W.; Bartle, E.R. Monitoring Air Pollution by Satellites. NASA CR-2324.
42. Cox, C.; Munk, W. Measurement of the roughness of the sea surface from photographs of the sun's glitter. J. Opt. Soc. Am 1954, 44(11), 838–850.
43. Cox, C.; Munk, W. Slopes of the sea surface deduced from photographs of sun glitter. Bull. Scripps Inst. Oceanogr 1956, 6(9), 401–486.
44. Egan, W.G.; Hilgeman, T.; Krassner, J. Thermal infrared polarization produced by roughness variations in the sea surface. Proc. 13th Int. Symp. Remote Sensing Environ. ERIM, Ann Arbor: MI, 1979; 1633–1641.
45. Plass, G.N.; Kattawar, G.W.; Guinn, J.A. Jr. Radiative transfer in the earth's atmosphere and ocean: influence of ocean waves. Appl. Opt 1975, 14(8), 1924–1936.
46. Plass, G.N.; Kattawar, G.W.; Guinn, J.A. Jr. Radiance distributions over a ruffled sea: contributions from glitter, sky, and ocean. Appl. Opt 1976, 15(12), 3161–3165.
47. Plass, G.N.; Kattawar, G.W.; Guinn, J.S. Jr. Isophotes of sunlight glitter on a wind-ruffled sea. Appl. Opt 1977, 16(3), 643–653.
48. Lyzenga, D.R.; Scuchman, R.A.; Arnone, R.A. Evaluation of an algorithm for mapping bottom features under a variable depth of water. Proc. 13th Int. Symp. Remote Sensing Environ. Ann Arbor, MI: ERIM, 1979; 1767–1780.
49. Turner, R.E. Radiative transfer on real atmospheres. ERIM Rep. No. 190100-24-T.
50. LaRoccca A.J.; Turner, R.E. Atmospheric Transmittance and Radiance: Methods of Calculation. ERIM Rep. No. 107600-10-T, 1975, pp. 74–75.
51. Braslau, N.; Dave, J.V. Effects of aerosols on the transfer of solar energy through realistic model atmospheres. J. Appl. Meterol 1973, 12(4), 601–615.

27

Physical Variation of Water Vapor and the Relation with Carbon Dioxide

I. INTRODUCTION

The seasonal, geographic, and secular variation of carbon dioxide vapor concentration in the mixing layer has been measured with unprecedented precision since 1957 [1–4]. Pales and Keeling [5], Komhyr et al. [1], and Gammon et al. [6] describe the annual and seasonal variation of carbon dioxide at fixed stations, which was simulated by Heimann and Keeling [7]. Tans et al. [8] reviewed atmospheric and marine carbon dioxide concentrations relative to the carbon budget of the earth and proposed that a major net carbon dioxide sink must be present in the extratropical Northern Hemisphere to account for the latitudinal variation observed. Hogan et al. [9] applied the data from some of these same carbon dioxide concentration archives to analysis of the seasonal change of antarctic aerosol concentrations. They found a relationship among the annual range of water vapor and carbon dioxide concentrations at several stations where these data sets coexisted, which were uniquely small at the South Pole. We offer some additional analysis of the concentration of water vapor in air with respect to the carbon dioxide concentration as a contribution to understanding the atmospheric chemical budget.

Points indicating the annual range of the partial pressure of water vapor as a function of latitude, taken from meteorological stations collocated with or near CO_2 reporting stations, are overlain on the presentation of seasonal amplitude of carbon dioxide concentration given by Gammon et al.

[6] in Fig. 1. The annual range of water vapor pressure at several of these stations was obtained by comparing the 99th percentile of minimum dry bulb temperature with the 99th percentile of maximum wet bulb temperature given in the Engineering Weather Data [10]. The water vapor data presented by Hogan et al. [9] for the Barrow, Mauna Loa, and Samoa GMCC stations is from cooled mirror records of Herbert, tabulated in GMCC annual reports; the data for Palmer, Antarctica, is from the nearby station at Alt. Brown, and those for the South Pole are from mixing ratio measurements, using a phosphorus pentoxide conductivity cell, of Hogan et al. [11].

The water vapor data presented in Fig. 1 are derived from longer records and are somewhat greater at Barrow and Cold Bay, Alaska, than orig-

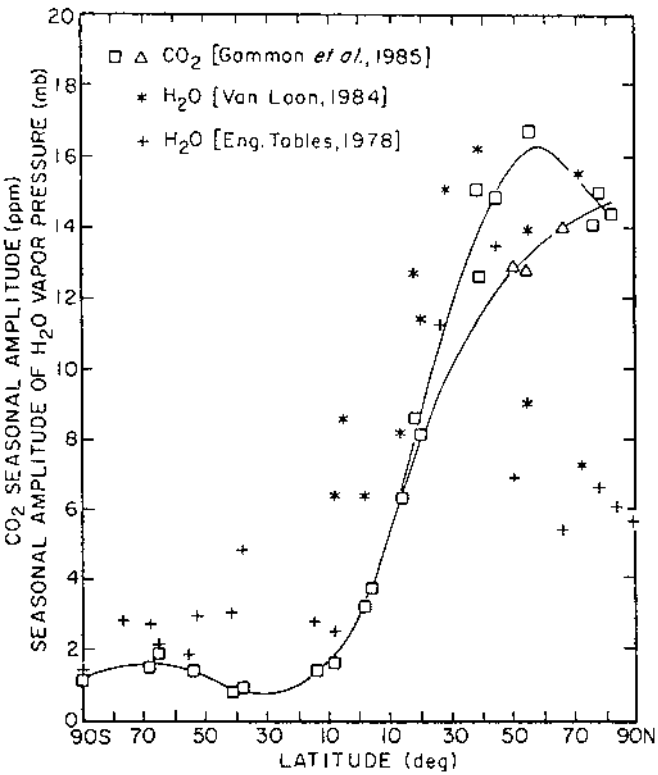

FIGURE 1 Comparison of the annual amplitudes of the variation of the partial pressures of CO_2 and water vapor with latitude. The amplitude of CO_2 has been extracted from Gammon et al. [6]. The water vapor data were extracted from NOAA sources, Engineering Weather Data [10], and Van Loon [13].

inally repored. The uniformity of the polar maritime (mP) air mass source regions surrounding Antarctica and the uniformity of the antarctic ice as a sink for heat and water substances combine to produce the uniquely small variation given at the southermost latitude. Coastal antarctic stations receive mP air from offshore, and this same air, in the form of antarctic maritime (mA) air from inshore directions, which increases the seasonal amplitude in water vapor pressure relative to the interior of Antarctica. Samoa has a very small variation in water vapor compared to the mean vapor pressure measured there. It has been demonstrated [12–14] that three air masses with distinguishably different source regions influence Samoa but that these air masses are similar in physical and chemical properties. The island stations north of Samoa have considerably greater seasonal variation in water vapor concentration. This is a consequence of monsoonal flows (Seychelles), the greater seasonal difference in air masses that occurs over the oceans of the northern hemisphere, and the greater latitudinal range of the polar front in the northern hemisphere. The Alaskan and Canadian coastal stations reflect the variation in water vapor in air masses from very different source regions. These source regions have very great seasonal variation as well. The Arctic stations do not reflect the strong meridional flow of midlatitude air aloft, which occurs during summer, due to the persistence of ice cover in the Arctic basin. These stations have seasonal variation in water vapor approximating that of the drifting ice stations in the basin [15].

Figure 1 has been scaled in such a manner that the maximum amplitude of water vapor variation approximates the maximum amplitude of carbon dioxide variation given by Gammon et al. [6]. The range of vapor pressures shown have also been compared with similar figures given in Komhyr et al. [1–3] and Tans et al. [8], which provide similar latitudinal trends using slightly different families of stations. The amplitude of annual variation of water vapor pressure with respect to latitude resembles the amplitude of carbon dioxide concentration in Fig. 1. The presentations of Van Loon [13] of seasonal mean marine water vapor pressure in several sections show Atlantic–Pacific consistency in the southern hemisphere but inconsistency among the Atlantic, eastern Pacific, and western hemisphere Pacific poleward of 45 N latitude, which is similar to the modeled and observed carbon dioxide trend presented by Gammon et al. [6]. These presentations of annual variation of concentration with respect to latitude mimic the variation in the length of the continental arc with respect to latitude on the earth's surface. The greatest interstation variation in annual range of concentrations coincides with the latitude band of greatest seasonal and zonal variation in air mass characteristics.

The seasonal variations of water and carbon dioxide vapor pressures measured at a station in the maximum variation zone (Cold Bay, Alaska) and

a station of comparable southern latitude (Palmer Station, Antarctica) are shown in Fig. 2. Although the two stations are surrounded on the poleward side by extremely different terrain, both have similar locations relative to the polar fronts and persistent low pressure centers in winter. These two stations have seasonal amplitudes in carbon dioxide concentration approaching the maximum (Cold Bay) and minimum (Palmer) observed by Komhyr et al. [1–3]. The axes in Fig. 2 have been adjusted so that the seasonal variations of CO_2 at the two stations have equal graphical amplitudes. The data are extracted from Komhyr's fitting of twice monthly observations, and the time locations of peaks and inflections are limited to this resolution [1–3]. The seasonal variations of carbon dioxide and water vapor are nearly opposite in phase,

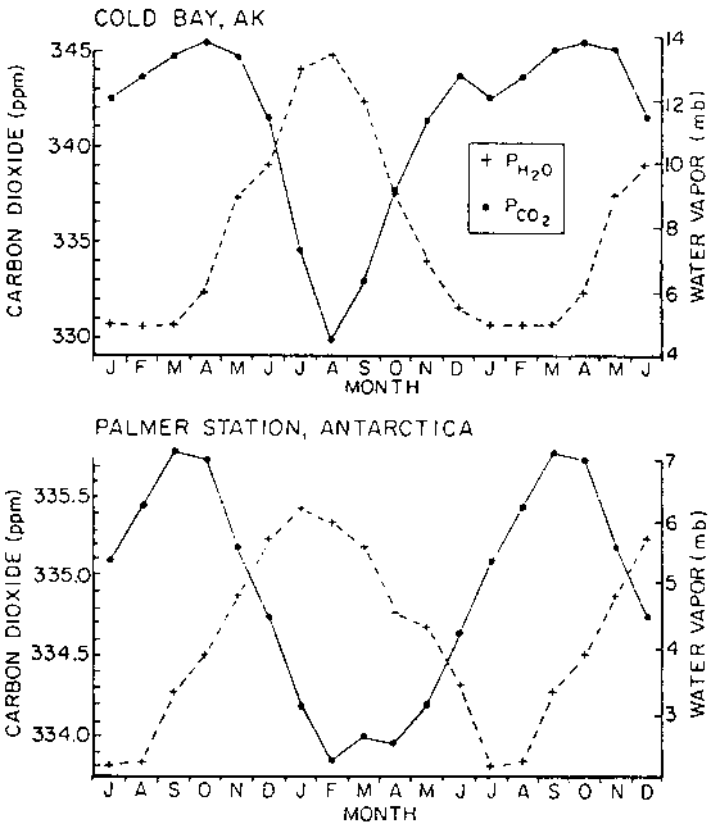

FIGURE 2 Mean monthly variation of CO_2 concentration from Gammon et al. [6] and Komhyr et al. [2], and mean monthly H_2O vapor concentration at Cold Bay and Palmer Station. The plotted lines are to aid visualization.

but the relative seasonal variations of these geographically dissimilar stations are quite similar. It should be noted that the meteorological seasons of high southern latitudes are delayed relative to those of high northern latitudes due to the persistence of a circumpolar vortex for more than 30 days following the equinox. Similar phase relations but of different amplitudes are found when the seasonal variations of these parameters are compared for the South Pole, Barrow, and Samoa.

Further comparison of the seasonal variations of CO_2 and H_2O concentrations is given in Fig. 3 for the same stations as Fig. 2. The monthly mean concentration of CO_2 is plotted against that month's mean water vapor concentration. The annual progression of the relationship is noted by designating the calendar months by 1,2,3, ... on the plot and connecting the points sequentially. It is seen that the slopes of the increasing segments (i.e., 4–7 on Palmer and 8–12 on Cold Bay) are similar.

It is inviting to speculate from Fig. 3 that changes in botanical growth or exchange mechanisms may occur concurrently with the inflections in the CO_2 vs. H_2O diagram. Objective analysis cannot be accomplished because the secular increase in CO_2 concentration has been appropriated through the year, perhaps enhancing or diminishing the actual rate of change at some times within the year. The dates of onset of meteorological spring and autumn and the relative mix of ice and water surface over the high latitude seas display extreme year-to-year variability. A general trend is evident from consideration of Figs. 1, 2, and 3; there is a widespread opposite phase relation of water vapor and carbon dioxide that is reflected in the data from all reporting stations.

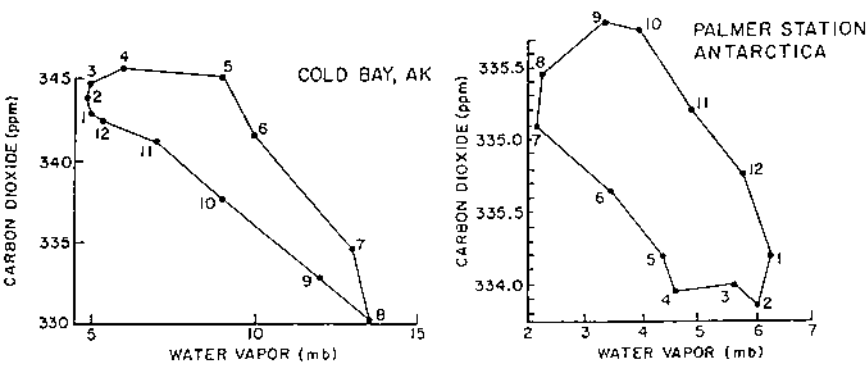

FIGURE 3 Comparison of monthly mean values of CO_2 and H_2O vapor concentrations at the same stations as Figure 2.

The variations in CO_2 and H_2O shown in the figures reflect the variation in air masses at the several observing stations. The station locations and sampling protocol used to produce the CO_2 database were carefully established to provide consistent samples of the representative air of the stations' latitudes, without local contamination. Usually this requires the station to be located on an upwind shore where climatically the wind is confined to a "clean air sector" on a majority of days during every season. The air masses representative of the region are mixed and exchanged in the clean air sector, and the integrated result is sampled at the observing station. The similarity of seasonal water vapor and carbon dioxide amplitude tends to verify that the sampled air is indeed the well-mixed representative.

Understanding the world CO_2 budget requires resolution of changes in CO_2 concentration on the order of fractional parts per million with respect to dry air at several distant observation stations. There is no doubt that the standards, calibration, and measurement procedures in use have evolved to yield the most precise geophysical measurements of our era. Is it possible that the nature of the physics of water and carbon dioxide in the atmosphere puts some fraction of each in solution or association that makes that fraction unmeasurable?

Cragin et al. [16] showed that glacial melt water approaching the purity of reference distilled water retains carbon dioxide unless it is carefully degassed. Antarctic ice, even though stored for several years, requires outgassing of CO_2 prior to analysis. Experiments with simulated precipitation while preparing a continuous flow precipitation sampler [17] showed that it was possible to greatly supersaturate water with CO_2 and that this supersaturation would persist for many days at 20°C ambient temperature. Many temporary surface sinks of carbon dioxide accompany every exposed water surface. There also appear to be temporary sinks in the association of carbon dioxide and water vapor in air that may place some carbon dioxide in an unmeasurable form.

This is evident when we compare the water vapor diffusion coefficient (cm^2/s) in air (0.220) and in CO_2 (0.1387); the diffusion coefficient of water vapor is less in a CO_2 atmosphere than in air [18]. Application of Graham's law indicates that the apparent mean mass of a water molecule increases by a factor of 1.2 through association with the surrounding carbon dioxide molecules, to provide the change in diffusion coefficient observed. Many CO_2:H_2O clathrates exist [19,20]. Experiments with pulsed molecular beam Fourier transform microwave spectrometry [21], molecular beam electron resonance spectroscopy [22], and chemical/acoustic observations show that CO_2:H_2O dimers exists. Thermodynamic considerations indicate that the relative occurrences of these dimers and other possible trimers of carbon dioxide are small. This "small" amount of hidden CO_2, on the order of a

fraction of a part per million, may also be important in the analysis of the global budget.

A laboratory experiment was conducted to investigate water vapor–carbon dioxide interaction on the laboratory scale [23]. A tank of synthetic air orginally containing 800 ppm of carbon dioxide with water vapor corresponding to a dew point of less than −69°C [24] was connected through a flow divider and cold trap to an infrared Fourier transform spectrometer [25]. This permits the flow to be alternately routed through a cold trap without other change. Zero air from another cylinder was also connected to the flow divider, through a precision wet test meter that provided saturated air at a chosen flow rate. Mixing equal amounts from the two supplies produces air of 400 ppm CO_2 and 10°C dew point that is not greatly dissimilar from surface air.

The apparent concentration of CO_2 was measured at 2357 cm^{-1} and water vapor at 3738 cm^{-1}, using 10 and 114 cm path length gas cells. Several mixtures were passed through the cold trap, at −77°C, and the dried gas mixture was measured with the spectrometer. The relative response of sensed CO_2 partial pressure to inlet water vapor pressure is given in Fig. 4, which shows that the collection of carbon dioxide by the cold trap increased as water vapor concentration increased in the inlet stream. The measurement is highly

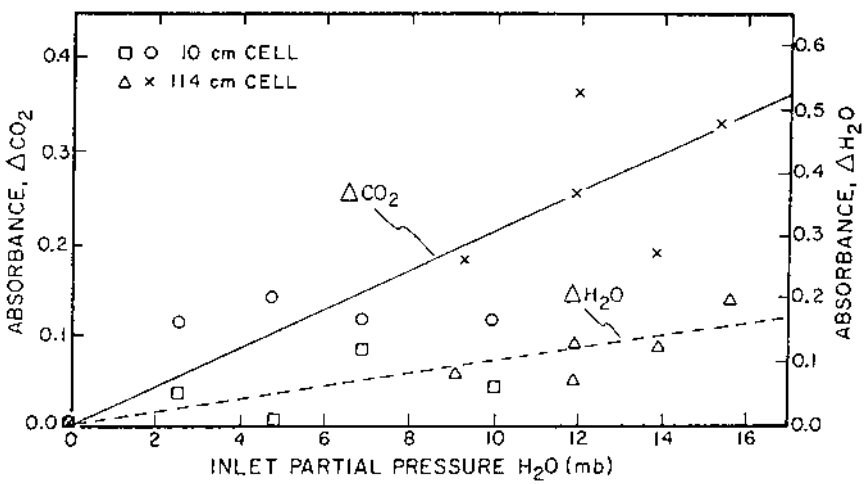

FIGURE 4 Removal of CO_2 and H_2O vapor as a function of inlet partial pressure of H_2O vapor by a −77°C cold trap as measured by a BOMEM interferometer-spectrometer. Solid line is plot of CO_2 absorbances for the 10 cm cell (○) and 114-cm cell (×). Dashed line is plot of H_2O absorbance for 10 cm cell (□) and 114 cm cell (Δ).

accurate, but the precision is limited due to the 4 cm^{-1} resolution of the spectrometer used in the experiment. The data support a hypothesis that CO_2 may be temporarily stored in unmeasurable form through cocondensation or coprecipitation in liquid or solid water [26] or dissolution into water vapor.

The surface concentration of water vapor varies by more than a factor of 200 over the earth. Even a small interaction of carbon dioxide and water vapor may induce some of the variation shown in Figs. 1–3.

II. DISCUSSION AND CONCLUSION

We interpret the similarity in latitudinal dependence of the annual range of variation in water vapor and carbon dioxide concentrations as indicative of the response to the summation of several common physical processes. The similarity of the seasonal variation of carbon dioxide compared to the seasonal variation of water vapor at two geographically divergent but meteorologically similar stations again indicates response of the CO_2 concentration to physical stimulae. Our previous work demonstrated that Antarctic aerosol concentrations vary meteorologically; Robinson et al. [27], Cronn et al. [28], and Cronn and Schilling [29] found meteorological variation in the concentration of halocarbon vapors; there may be similar variation in carbon dioxide concentration [30].

This presents nearly unbounded questions. Can it be that the major sources of carbon dioxide lie on land and the major source of water vapor is the sea, producing latitudinal and seasonal variations of the concentrations of these substances that are merely summations of out-of-phase components? Or are temporary sinks storing carbon dioxide in water and producing local and air mass scale variations in carbon dioxide as the water varies in both concentration and phase?

It would appear that experiments including precise water vapor measurements on relatively small time and space scales are necessary to support the current global scale experiments addressing the secular variation in carbon dioxide concentration and the atmospheric carbon budget. A laboratory experiment is certainly in order to examine the vapor-phase interaction and coprecipitation of carbon dioxide and water. There is also a need for field experiments over the sourceless ice sheets to examine the meso- and microscale variability of carbon dioxide within air masses due solely to meteorological processes.

REFERENCES

1. Komhyr, W.D.; Harris, T.B. Measurements of atmospheric CO_2 at the U.S. GMCC baseline stations. Special Environmental Report No. 10, WMO - No. 460, 9–19, 1976.

2. Komhyr, W.D.; Gammon, R.H.; Harris, T.B.; Waterman, L.S.; Conway, T.J.; Taylor, W.R.; Thoning, K.W. Global atmospheric CO_2 distribution and variations from 1968–1982 NOAA/GMCC CO_2 flask sample data. J. Geophys. Res. 1985, 90, 5567–5596.
3. Komhyr, W.D.; Harris, T.B.; Waterman, L.S.; Chin, J.F.S.; Thoning, K.W. Atmospheric carbon dioxide at Mauna Loa Observatory. 1. NOAA Global Monitoring for Climatic Change measurements with a nondispersive infrared analyzer 1974–1975. J. Geophys. Res. 1989, 94, 8533–8547.
4. Keeling, C.D.; Whorf, T.P.; Wang, C.S.; Bellamy, R.D. The concentration of atmospheric carbon dioxide at ocean weather station P from 1969 to 1981. J. Geophys. Res. (D) 1985, 90 (D6), 10,511–528.
5. Pales, C.J.; Keeling, C.D. The concentration of atmospheric carbon dioxide in Hawaii. J. Geophys. Res. 1965, 70, 6053–6076.
6. Gammon, R.H.; Sundquist, E.T.; Fraser, P.J. Atmospheric Carbon Dioxide and the Global Carbon Cycle, DOE/ER - 0239, 1985.
7. Heimann, S.M.; Keeling, C.D. Meridional eddy diffusion model of atmospheric transport of CO_2.1. Seasonal carbon cycle over the tropical Pacific Ocean. J. Geophys. Res. A 1986, 91 (D7), 7765–7781.
8. Tans, P.P.; Fung, I.Y.; Takahashi, T. Observational constraints on the global atmospheric CO_2 budget. Science 1990, 247, 1431–1438.
9. Hogan, A.W.; Egan, W.G.; Samson, J.A.; Barnard, S.C.; Riley, D.C.; Murphy, B. Seasonal variation of some components of Antarctic troposheric air. Geophys. Res. Lett. 1990, 17, 2365–2368.
10. Engineering Weather Data, AFM 88-29. TM 5785 NAVFAC P-89. Depts. of Air Force, Army, and Navy, 1 July 1978.
11. Hogan, A.W.; Barnard, S.C.; Samson, J.A.; Winters, W. The transport of heat, water vapor and particulate material to the South Polar Plateau. J. Geophys. Res. 1982, 87, 4287–4292.
12. Bortniak, J.C. The wind climatology of American Samoa. NOAA Tech. Memo. ERL ARL - 98, 1981.
13. Van Loon, H., Ed. World survey of climatology. Climate of the Oceans 1984, 15, 716.
14. Halter, B.C.; Harris, J.M.; Conway, T.J. Component signals in the record of atmospheric concentration in American Samoa. J. Geophys. Res. 1988, 93, 15914–15918.
15. Vowinckel, E.; Orvig, S. The climate of the north polar basin. In World Survey of Climatology, Vol. 14, Climate of the Polar Regions; Orvig, S., Ed.; Elsevier: New York, 1970; 129–252.
16. Cragin, J.H.; Geovinetto, M.B.; Gow, A.J. Baseline acidity of precipitation at the South Pole during the last 2 millennia. Geophys. Res. Lett. 1987, 14, 789–792.
17. Hogan, A.W. Some characteristics of chemical precipitation. Tellus 1983, 35B, 121–130.
18. Washburn, E.W. International Critical Tables of Numerical Data Physics, Chemstry and Technology. McGraw-Hill, for Natl. Res. Council; New York, 1928.
19. Miller, S.L. Clathrate hydrates of air in Antarctic ice. Science 1969, 165, 489–490.
20. Davidson, D.W.; Garg, S.K.; Gough, S.R.; Handa, Y.P.; Ratcliff, C.I.; Tse, J.S.;

Repmeester, J.A. Some structural and thermodynamic studies of clathrate hydrates. J. Inclusion Phenom. 1984, 2, 231–238.
21. Peterson, K.I.; Klemperer, W. Structure and internal rotation of H_2O–CO_2, HDO–CO_2 and D_2O–CO_2 van de Waals complexes. J. Chem. Phys. 1984, 80 (60), 2439–2445.
22. Peterson, K.I.; Suenram, R.D.; Lovas, F.J. The structure of the CO_2-CO_2-H_2O van der Waals complex determined by microwave spectroscopy. J. Chem. Phys. 1989, 90 (11), 5964–5970.
23. Zhu, H.; Egan, W.G.; Hogan, A.W. Cold recipitation of CO_2 and water vapor in a model marine system [Abstr.]. Trans. AGU 1990, 71, 471.
24. Linde Specialty Gases. Catalog L3500 F, 1985.
25. Bomem/Hartmann and Brown AG, DA3 Manual, March 1985.
26. Coyne, P.J.; Kelley, J.J. Variations in carbon dioxide across an Antarctic snowpack during spring. J. Geophys. Res. 1974, 79, 799–802.
27. Robinson, E.; Rasmussen, R.A.; Krasnec, J.; Pierotti, D.; Jakubovic, M. Halocarbon measurements in Alaskan troposphere and lower stratosphere. Atmos. Environ. 1977, 11, 215–223.
28. Cronn, D.R.; Barnesberger, W.L.; Menzia, F.A.; Waylett, S.F.; Ferrara, T.W.; Howard, H.M.; Robinson, E. Atmospheric trace gas trends at Palmer Station, Antarctica 1982–1983. Geophys. Res. Lett. 1986, 13, 1272–1275.
29. Cronn, D.R.; Schilling, K. Atmospheric trace gas studies in Antarctica. Rev. Geophys. 1988, 26, 497–518.
30. Schwerdtfeger, W. The climate of the Antarctic. In World Survey of Climatology, 14, Climate of the Polar Regions; Orvig, S., Ed.; Elsevier: New York, 1970; 253–355.

28

Oil Spill Analysis

I. INTRODUCTION

Low resolution visual polarimetric photographic imagery of the Galveston Bay oil spill from a tanker accident on July 28, 1990, was obtained and analyzed. The low resolution imagery (30–100 m) was obtained concurrently with high resolution imagery (1 m) and is representative of what would be seen by a polarimetric satellite. Orthogonal red-green-blue (RGB) polarimetric images obtained with color photography were digitized by Kodalux onto a CD ROM. These polarimetric images were then used to calculate the percent polarization. The positive and negative percent polarized radiation scattered by each of the sea surface waves is seen individually in high resolution imagery. (Percent polarization is defined as positive when the dominant radiation is perpendicular to the plane of incidence and negative when it is parallel.) The analysis of low resolution polarimetry is approached in a different manner than that of high resolution; in high resolution polarimetry, individual waves are imaged, and the positively polarized sky and scattered solar radiation is seen as well as the negatively polarized internally scattered radiation from the back surfaces of the waves. In low resolution imagery, all of the polarized radiation is averaged, and this would be seen by one of the proposed satellite polarimeters. By using the statistically averaged percent polarization in density slices, the areal extent of the oil coating is readily characterized, and the relationship between the oil thickness and the percent polarization is readily determined. Percent polarization has the advantage over photometry and image enhancement in that absolute calibration is retained by virtue of the

fact that percent polarization is the ratio of reflected to scattered radiative components and variations in the incident illumination cancel out. Absolute calibration is essential for any quantitative evaluation of oil spill effects just as it is necessary for any legal or enforcement action as well as the evaluation of ecological effects.

II. IMAGERY

The location of the oil spill in Galveston Bay is show on the chart in Fig. 1; it was in Redfish Bay adjacent to the Houston Ship Channel. The barge was pulled off to the side after the oil spill. A few days after the spill, the oil dispersed as shown in Fig. 2.

Figure 3 is a low-resolution photographic image corresponding to Fig. 2 but taken in polarized scattered radiation from the sea. The dispersal of the oil in the harbor is clearly visible as the brighter areas.

Figure 4 shows a high resolution polarimetric image of the spill; the waves on the surface of the sea can be seen. In this figure the heavier oil areas appear the darkest, indicating the highest polarization.

Figure 5 is a very high resolution polarimetric image of a section of the oil spill with the heavy oil appearing darker (higher polarization) and the hydrosols lighter (lower polarization). The circled areas were chosen arbitrarily with the percent polarization and standard deviations shown.

Figure 6 shows aerial photographs of the spill area. Polarization images of the oil spill are shown in blue (0.433 μm), green (0.533 μm), and red (0.633 μm) spectral regions. The green spectral band (Fig. 6b) most clearly defines the oil spill. Note that the highest polarization in these images appears white, opposite to Fig. 5 images, where it is darker.

Figure 7 shows in detail the calculated percent polarizations. The hydrosol areas tend to have lower polarization.

Figure 8 is a representation of the polarization of the solar (and cloud) radiation scattered by the sea. Haze in the atmosphere is seen as an artifact producing a polarization contrary to the polarization of the sea for the particular solar incident geometry. The deconvolution of the sea surface polarization requires an appropriate model and appropriate input parameters for the aerosol haze.

The oil film on the surface of the sea is characterized in Fig. 9. The oil is less dense than the water and hence floats; the oil film can produce an interference effect with light (because of its thickness), and this produces a rainbow effect. The thinner oil films produce a lower polarization as shown in Fig. 10.

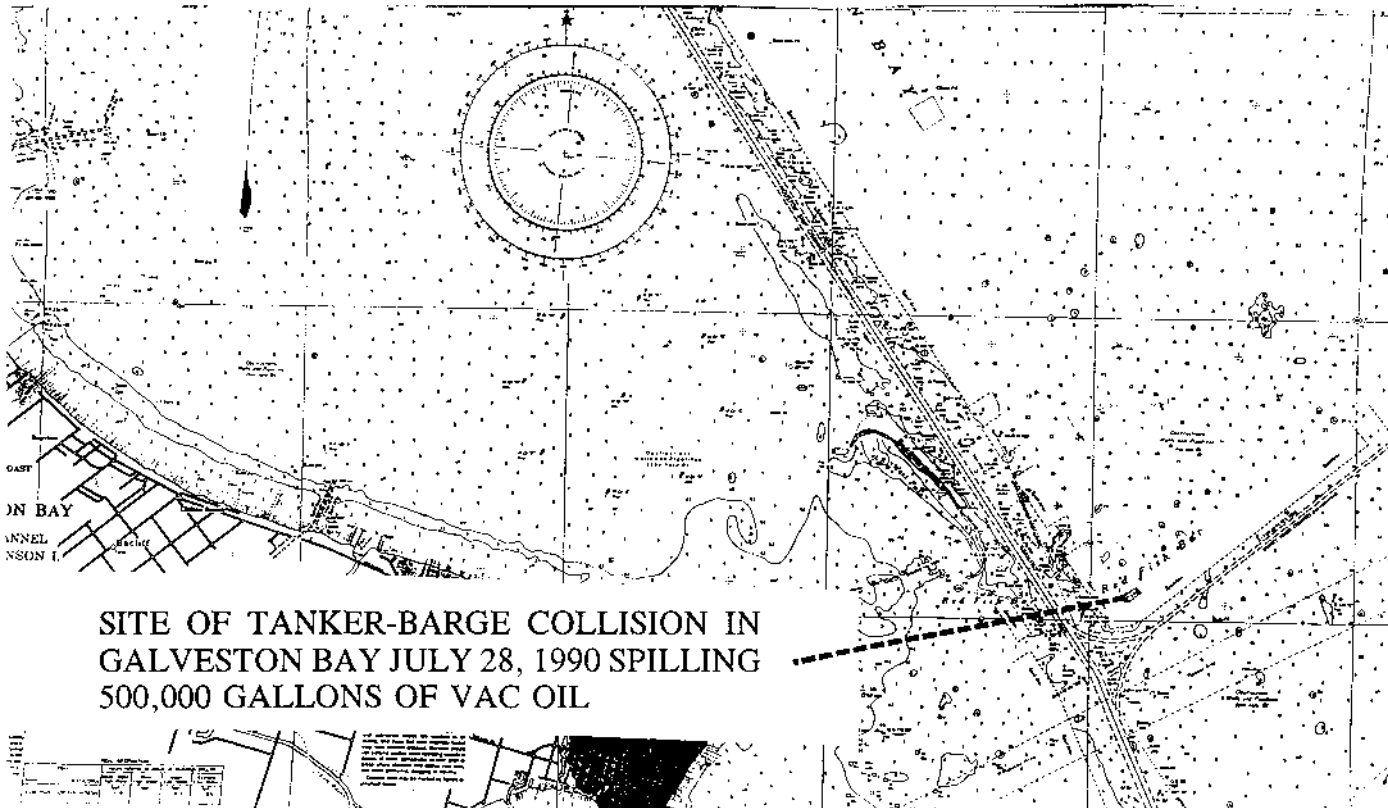

FIGURE 1 The site of the tanker–barge collision on July 18, 1990, which caused a spill of 500,000 gallons of VAC oil, an intermediate refinery product that was to be further cracked to produce gasoline and other hydrocarbon by-products. The collision occurred in the Houston Ship Channel.

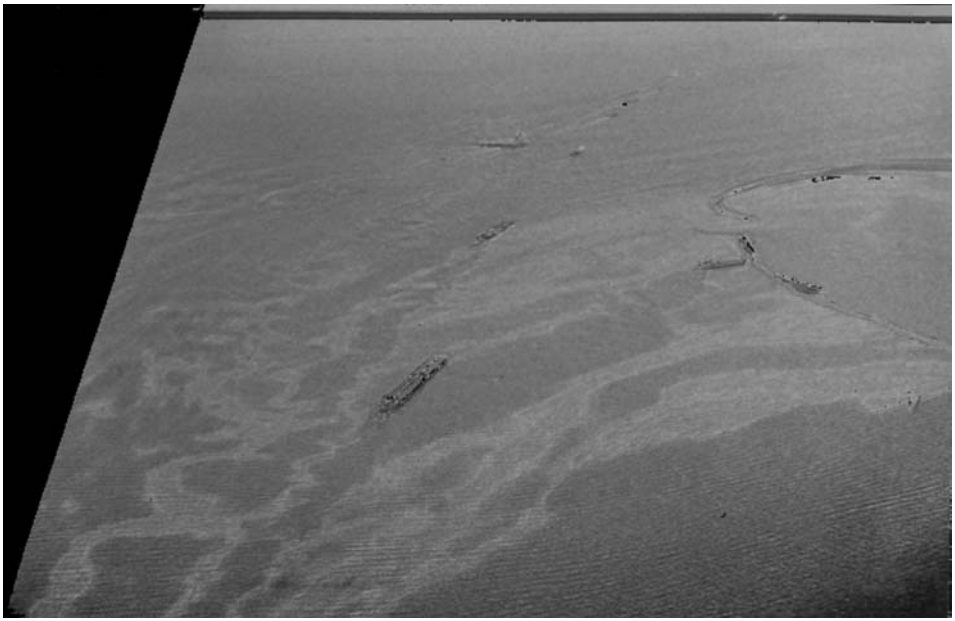

FIGURE 2 A low resolution black-and-white polarimetric image of the oil spill area with the barge located in the lower central portion of the image. The streaming high polarization of the oil distribution is plainly seen in the polarimetric (wideband) image as bright high polarization.

III. CONCLUSION

In analyses of visual photographic polarimetric mapping of the Galveston Bay oil spill from the tanker accident on July 28, 1990, statistical fluctuations in the percent polarization values of adjacent pixels made the demarcation between surface oil films of differing thicknesses uncertain. The statistical fluctuations were caused by the superimposing of the orthogonal red-green-blue (RGB) polarimetric images obtained by color photography, which were digitized by Kodalux onto a CD ROM. To obviate this problem, an averaging process was required to reduce the effects. By using the statistically averaged percent polarization in density slices, the areal extent of the oil coating is readily characterized, and the relationship between the oil thickness and the percent polarization readily determined. Oil film thicknesses from micrometers to millimeters can be delineated. The best spatial resolution possible with this technique is of the order of 1 m. Both negative and positive percent

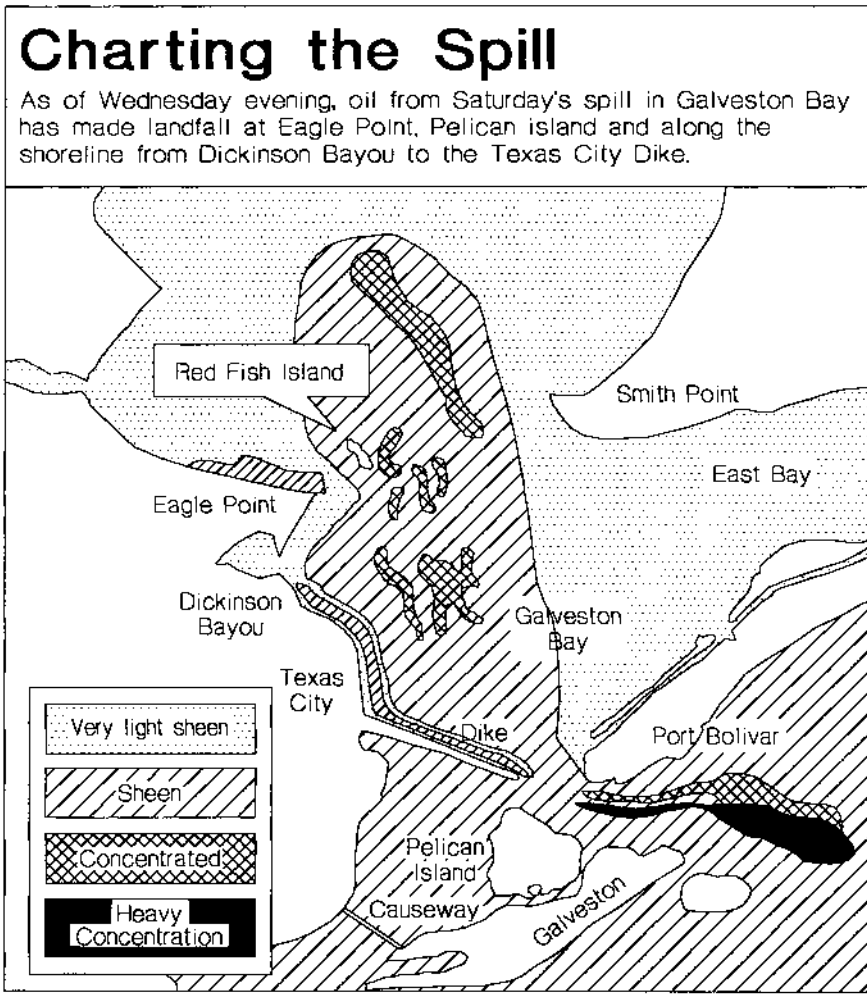

FIGURE 3 The Houston *Daily News* charted the spill in a general way but not in the detail shown in Fig. 2.

polarizations occur, indicating that not only surface scattering but also internal scattering occurs at the sea surface.

Percent polarization has the advantage over photometry and image enhancement in that absolute calibration is retained by virtue of the fact that percent polarization is the ratio of the parallel to the perpendicular reflected/scattered radiative components, and thus any variations in the incident illu-

FIGURE 4 High-resolution polarimetry image of the oil spill. The wave structure of the sea surface can be plainly seen as well as the distribution of the oil spill. The heavy oil areas appear darker here indicating the highest polarization.

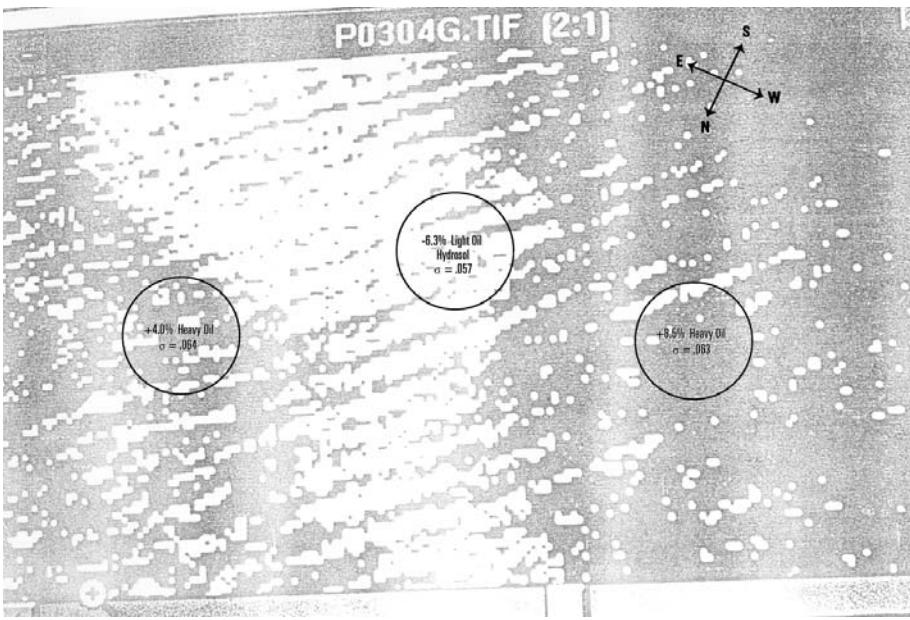

FIGURE 5 A very high resolution polarimetric image of the oil spill areas, with the heavy oil spills, appearing darkened, indicating highest polarization.

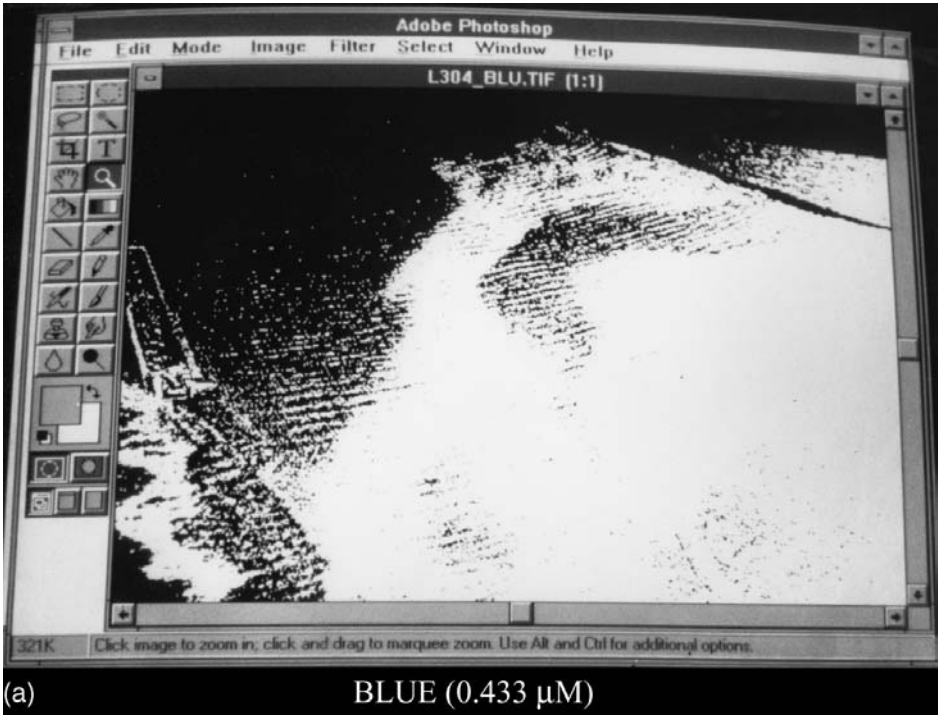

FIGURE 6 (a) Blue (0.433 μm), (b) green (0.533 μm), and (c) red (0.633 μm) optical wavelength measurements of imagery. Note that in this image the highest polarization is shown in white, opposite to the previous image in which dark areas indicated high polarization. The strongest polarization is in the blue spectral region, and the lowest in the red. This is related to the oil thickness, the lighter oil having a lower percent polarization.

mination affects both the parallel and perpendicular components and is canceled out in the ratio. The retention of absolute calibration is essential for the quantitative evaluation of oil spill effects that is necessary for any legal or enforcement action as well as for the evaluation of ecological effects.

Simple uncalibrated optical polarimetry of the reflected and scattered radiative components parallel to the plane of vision is useful in delineating oil or other surface or subsurface contaminants. This does not require computational procedures and can be used in real time with simple optical sensors.

Illustrated results of the analyses were presented with applications to in situ observations as well as to aircraft and satellite imagery.

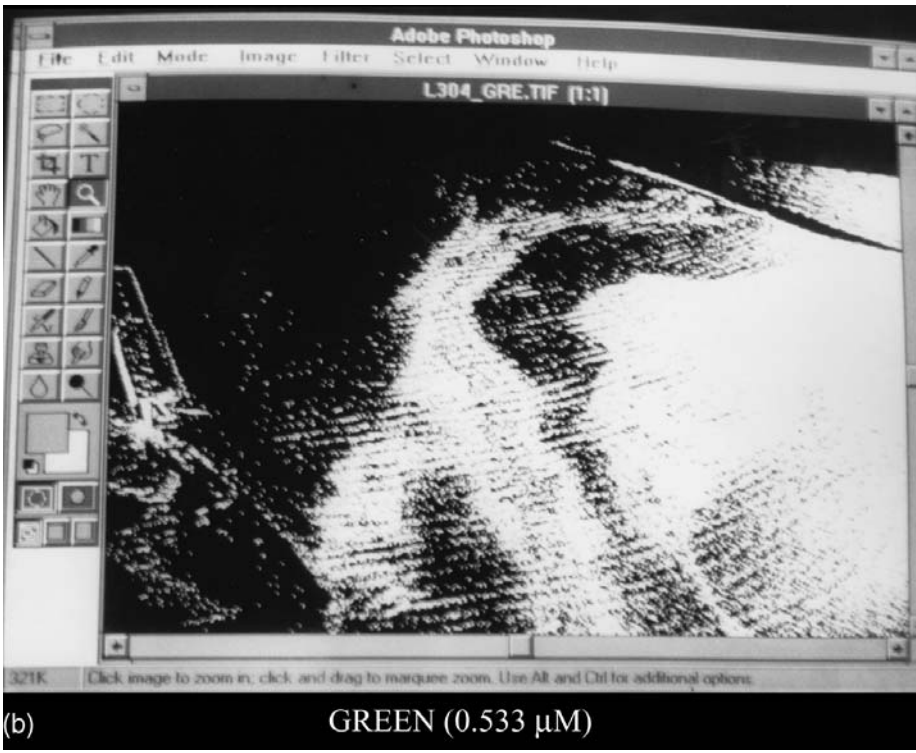

FIGURE 6 Continued.

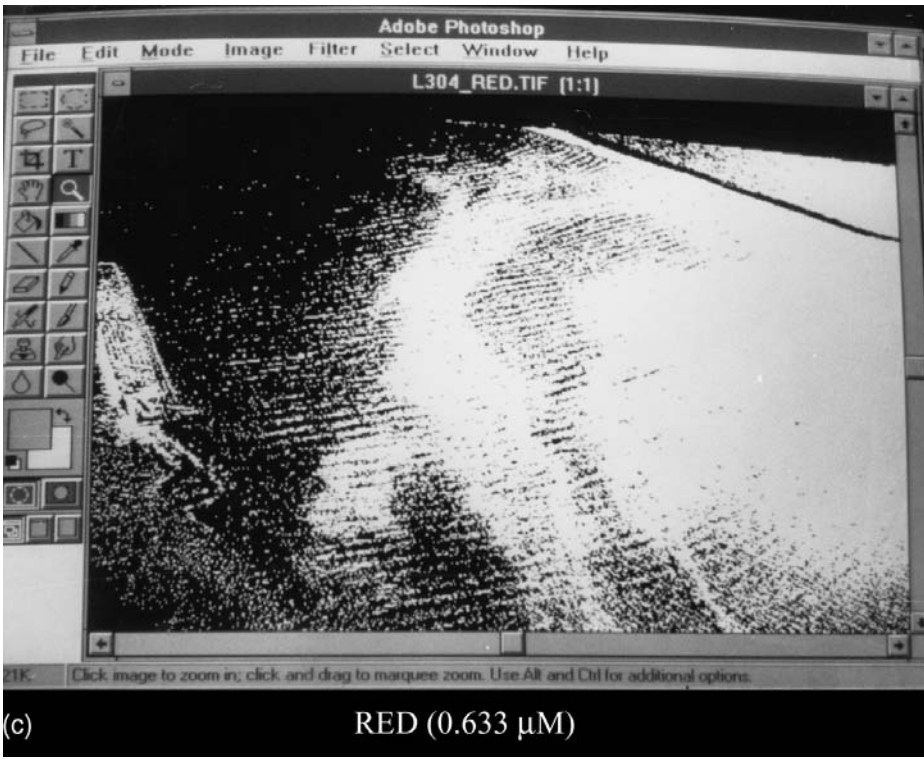

FIGURE 6 Continued.

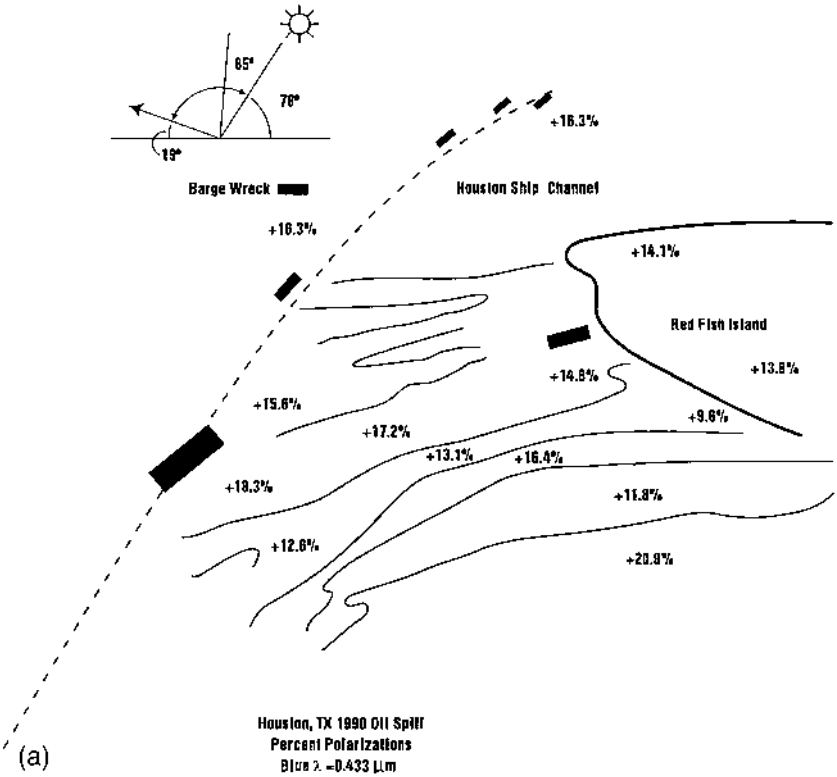

FIGURE 7 (a)–(c) Numerical values of the percent polarization illustrated in corresponding parts of Fig. 6. It is seen that the blue (0.433 μm) percent polarizations are higher in the heavy oil areas where the hydrosols are mixed in. The solar/viewing geometry is indicated on the figure at the time of observation. The barge location is shown as a rectangular block.

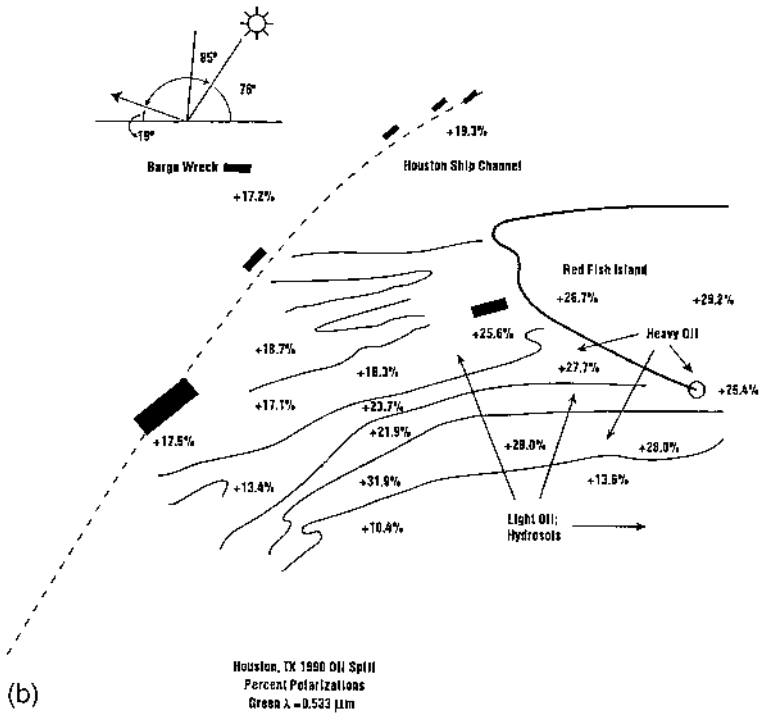

FIGURE 7 Continued.

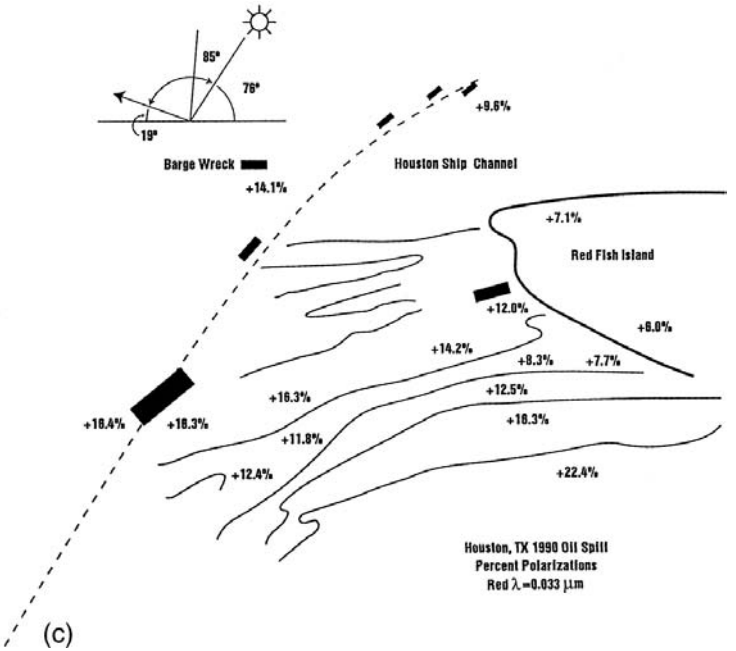

FIGURE 7 Continued.

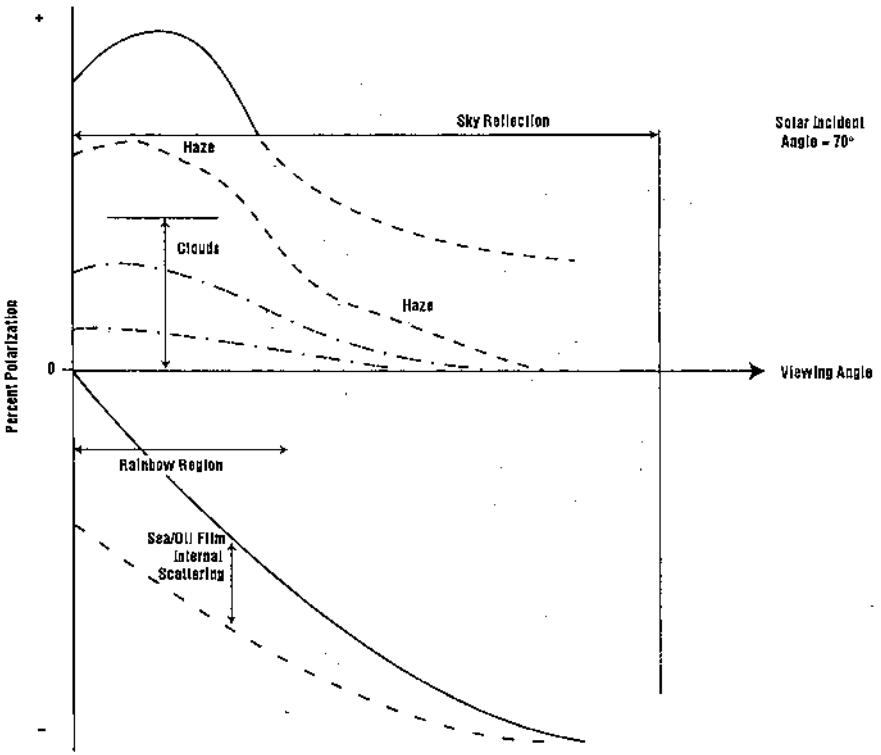

FIGURE 8 The polarization of solar radiation scattered from the sea. There is radiation scattered from sky reflections, clouds, and haze as well as in internal scattering.

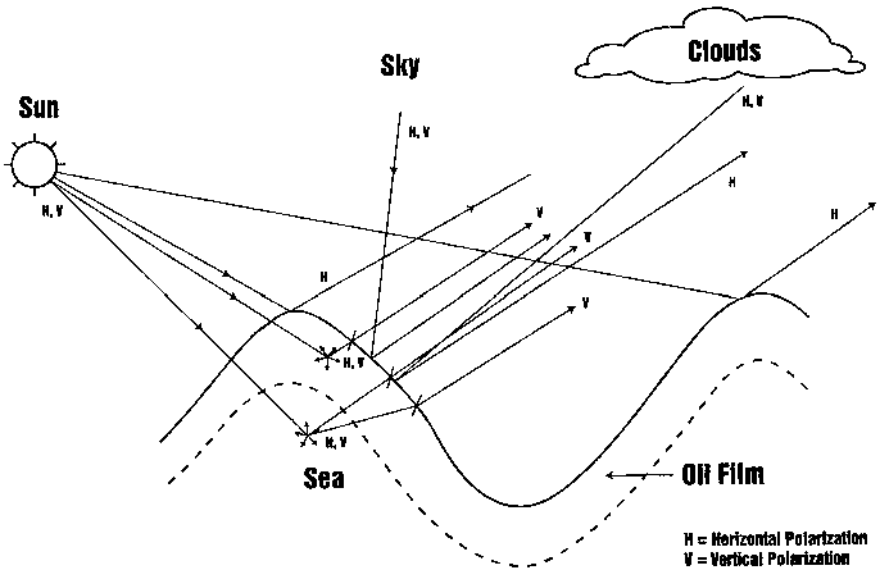

FIGURE 9 The effect of surface waves on the surface-scattered and internally scattered radiation. For thicker oil film, there is more absorption by the surface coating and high polarization (Figure 7), where a higher polarization is observed in the green from the green hydrosols than from the red or blue. Figure 7 is a black and white rendition of polarization, where white is higher polarization and black is lower. The explanation is that the hydrosols are of lower absorption than the oils and therefore absorb less radiation and produce higher polarization.

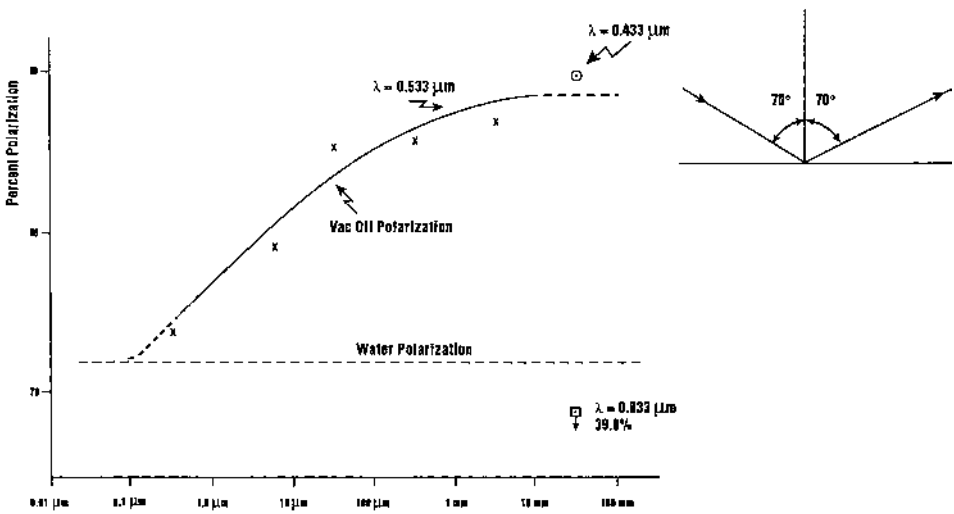

FIGURE 10 The increase in percent polarization as the oil film thickness increases is shown for the green (0.533 μm) incident radiation.

29

Infrared Optical Constants of Sahara Sand, Volcanic Ash, and Water-Soluble Aerosols

I. INTRODUCTION

The Volz technique for determining the absorption indices of atmospheric aerosols was adapted and improved for use in the LOWTRAN and MODTRAN models. The modified technique uses the Kubelka–Munk scattering theory to separate scattering from absorption in measurements with potassium bromide pellets containing the aerosols, resulting in absorption indices that are significantly lower in the window regions than those previously used in models. Calibrations were achieved using lasers and a sulfur-coated integrating sphere. Also, finite wavelength effects cause a relocation of the observed absorption bands.

An essential component in the LOWTRAN and MODTRAN infrared atmospheric models is the optical properties of aerosols. The original determinations of the infrared optical constants of Sahara sand, volcanic ash, and water-soluble aerosols were from compressed samples and powders of the samples in potassium bromide pellets [1]. In potassium bromide pellets, there is significant scattering among the particles, which causes an apparent increase in the absorption. This can result in a measured absorption that is one to two orders of magnitude greater than the true absorption.

In this chapter we trace the development of various techniques for separating scattering from absorption in potassium bromide pellets, leading to accurate values of the infrared absorption index of some representative

TABLE 1 Scattering Models That Include Absorption

1. Two-flux model [Kubelka–Munk (K-M) Theory]
2. Two-flux model with surface scattering (M-K-M)
3. Six-flux model
4. Modified dispersion model
5. Mie scattering
6. Radiative transfer
7. Multiple scattering model
   - Doubling
   - Successive orders of scattering
   - Invariant embedding
   - The Monte Carlo method

Source: Ref. 2.

aerosols. There are at present seven scattering models that include absorption (Table 1). We consider the simplest, the two-flux model [Kubelka–Munk (K-M) theory], which requires the least computing time, with atmospheric constituents shown in Table 2.

The two variables of scattering and absorption in potassium bromide pellets require two measurements to separate them uniquely. The theoretical models generally require the measurement of total diffuse transmission and absorption by the pellet sample. This is best accomplished by using an integrating sphere, although point-by-point equivalent measurements can be made. Visible range integrating spheres with a magnesium oxide coating are readily available for use in the wavelength range of 0.185–2.8 μm. One such is the Gier–Dunkle system. We have used this system to determine the total diffuse transmission and reflection of various mineral and aerosol samples at wavelengths of 0.185–2.8 μm. However, the question arises as to the accuracy of the technique in determining the absorption indices of the (scattering) powders contained in the potassium bromide pellets.

To check the validity of the measurements, a standard Corning CS1-64 colored glass with known visible to near-infrared absorption indices as a function of wavelength was used for calibration. The diffuse transmission and

TABLE 2 Atmospheric Constituents Used in the Modeling

pH[a]	NO_2[a]	NO_3[a]	Cl^-[a]	SO_4[a]	Na[a]	TOC[a]	TIC[a]	CO_2[a]	Pollen	CO_3[a]	Cu[a]	Zn[a]
4.8	0.32	<0.05	1.2	5.0	0.11	2	<1	<4	Yes	2.0	54	61

[a] Parts per million (ppm).

reflection of powdered and sintered samples were measured; pellets were made containing uniformly distributed glass powders and others with the glass powder forming a layer on the surface of the pellet [2]. Scattering analyses were made using the Kubelka–Munk theory and the modified Kubelka–Munk (M-K-M) theory; the most accurate results were obtained using the layered samples and the M-K-M model. Typical results for a Sahara sand are shown in Fig. 1 (top) for the absorption portion of the absorption index of refraction; shown in Fig. 1 (bottom) is the refractive portion in the wavelength region 0.185–1.105 μm. The refractive portion was determined using a Brewster angle measurement as described in Ref. 2.

However, for infrared measurements, an integrating sphere system was required that would operate in the 0.8–20 μm spectral region. Gold-coated integrating spheres have been used for total transmission and reflection measurements on samples, and a check of the validity of gold as a diffuse coating for an integrating sphere was in order. Whether the gold was shiny,

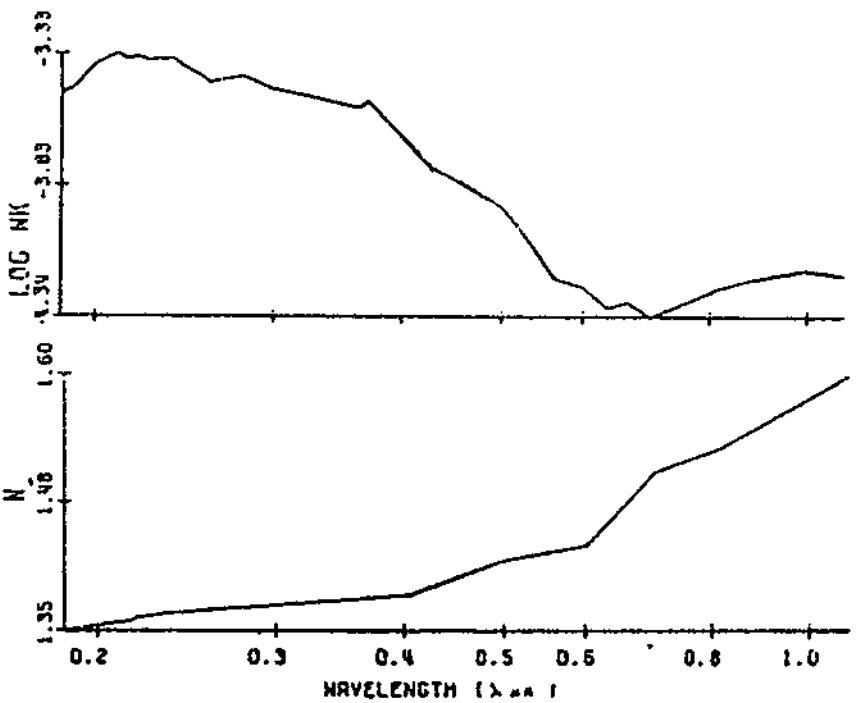

FIGURE 1 Sahara sand No. 3: Amokon dune sand from Tenere Desert East from Aïr.

dull, sintered, or sand-blasted, point-by-point measurements of the gold surfaces showed that they were not diffuse and had a low hemispherical reflectance. In the literature, papers appeared describing flowers of sulfur as a diffuse standard [3,4]. This appeared to be a good coating for the 0.8–20 μm spectral region. The question then arose as to how to obtain an integrating sphere with detectors in the long-wavelength infrared region.

An integrating sphere system was constructed that could be checked for accuracy in the UV-visible-near-IR spectral region and then adapted to the longer wavelength infrared by constructing a duplicate system with a sulfur coating. Many integrating sphere systems are described in the literature, and the main point in the design is that the first scattering from the sample should not be seen by the detector in reflection, nor the direct incident beam in transmission. Thus, an integrating sphere system was constructed as shown in Fig. 2 [2], which allowed the use of photomultipliers in the UV-Vis-NIR regions, and, for the duplicate system, indium antimonide in the near-infrared, and arsenic-doped silicon in the far-infrared. Because the latter detectors have to be cryogenically cooled, the reduction in sensitivity produced by the external location had to be tolerated. A detector immersed in the sphere would have been better.

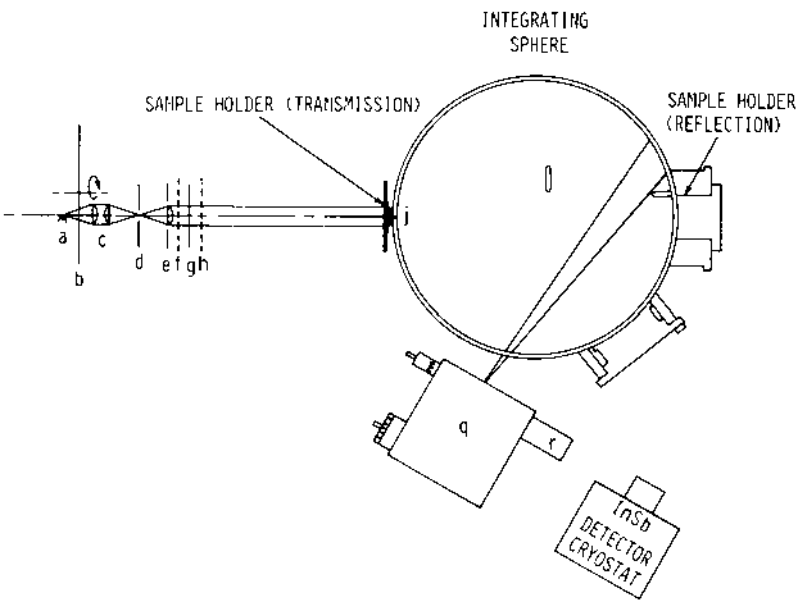

FIGURE 2 Layout of optical system for integrating sphere. (From Ref. 2.)

Another problem arose: Source strengths proved to be inadequate for reasonable measuring times. To obviate this problem, lasers were used: a HeNe laser for 1.159 and 3.159 μm and a carbon dioxide laser for 9.2 and 10.6 μm. The accuracy of the UV-Vis-NIR system (with a barium sulfate coating) was compared to the Gier-Dunkle System and found to yield closely comparable results, thus validating the extension to the sulfur-coated integrating sphere. We further compared samples at 1.139 μm in both the barium sulfate and sulfur-coated integrating sphere systems using the HeNe laser, with results in close agreement. Then we used the diffuse transmission and reflection measurements to calibrate measurements of transmission and reflection from a Perkin-Elmer Model 283B infrared recording spectrophotometer in the 2.5–50 μm spectral region (similar to the Volz technique [1]). Data were analyzed

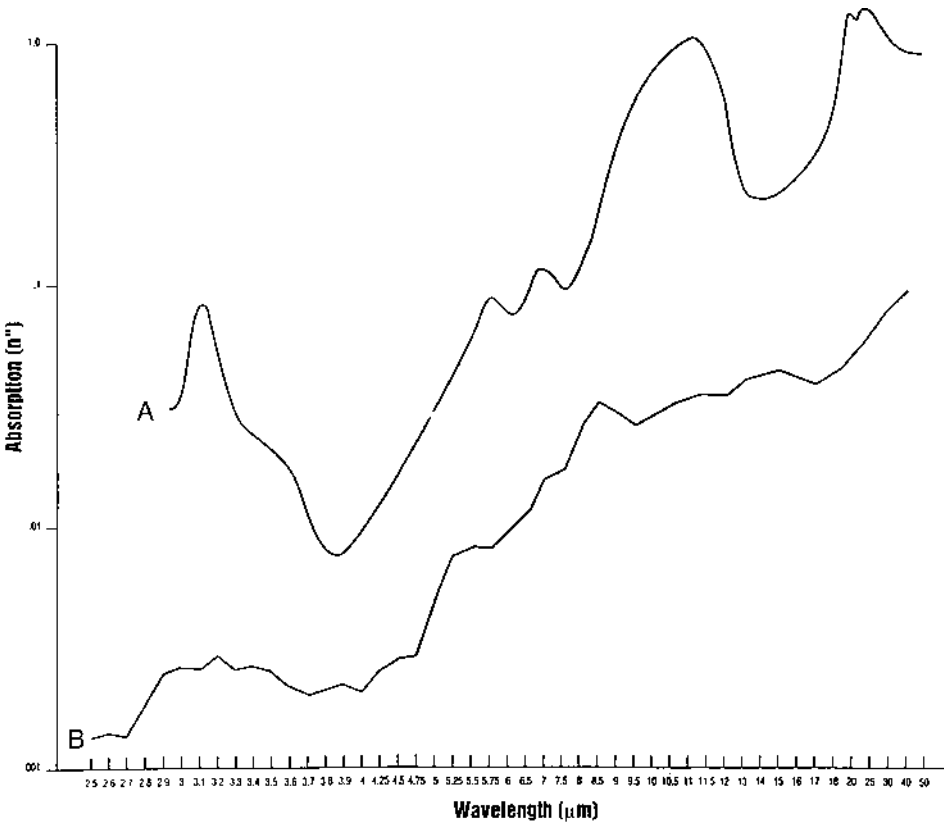

FIGURE 3 Absorption versus wavelength for Sahara dust. Curve A from Ref. 1, curve B from Ref. 5.

TABLE 3 Complex Indices of Refraction of Sahara Sands and Mount Saint Helens Volcanic Ash

Sample	Sahara samples	Mount Saint Helens
SiO_2	54.75	63.40
Al_2O_3	15.84	16.92
Fe_2O_3	6.74	2.46
FeO	0.25	2.72
MgO	2.83	2.14
CaO	2.08	5.07
Na_2O	0.96	4.65
K_2O	2.51	1.43
H_2O^+	6.03	
H_2O	5.45	
CO_2	1.38	
TiO_2	0.95	0.68
P_2O_5	0.17	
MnO	0.112	
S		0.397
F		0.0389
Total:	100.05	99.91

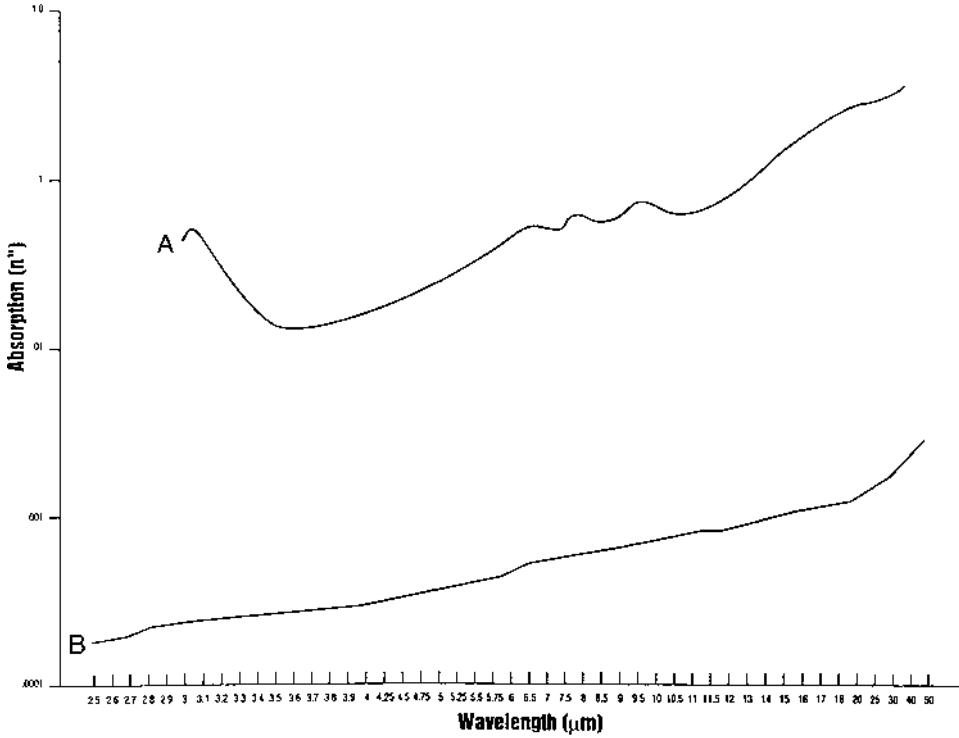

FIGURE 4 Absorption versus wavelength for water-soluble aerosols. Curve A from Volz [1]; curve B (Kubelka–Munk) from Ref 5.

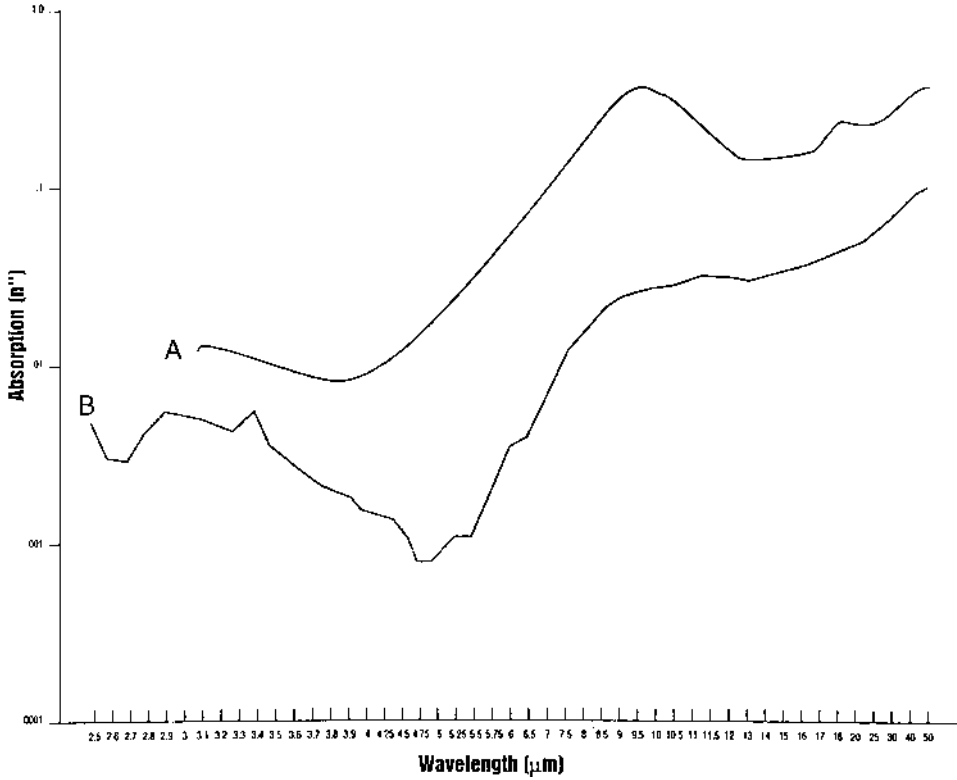

FIGURE 5 Absorption versus wavelength for volcanic dust. Curve A from Volz [1]; curve B (Kubelka–Munk) from Ref 5.

using the K-M theory, and the results for a Sahara sand are shown in Fig. 3 (Table 3) in comparison with the results of Volz [1].

It is seen that the separation of the scattering component produces an absorptive portion of the index of refraction that is one to two orders of magnitude less on the Sahara sand sample than that of Volz [1]. The results are similar for water-soluble aerosols and volcanic soil (Figs. 4 and 5) (see also Table 3). The spectral resolution is limited by the long time constant used in the spectrophotometer for reasonable scan times. It appears that scattering

FIGURE 6 (a) Complex indices of Refraction of Sahara sand, volcanic ash, and aerosols [5]. (b) Refractive portion of refractive indices for samples Sahara dust, volcanic dust, [5] and water-soluble aerosols. (From Ref. 1.)

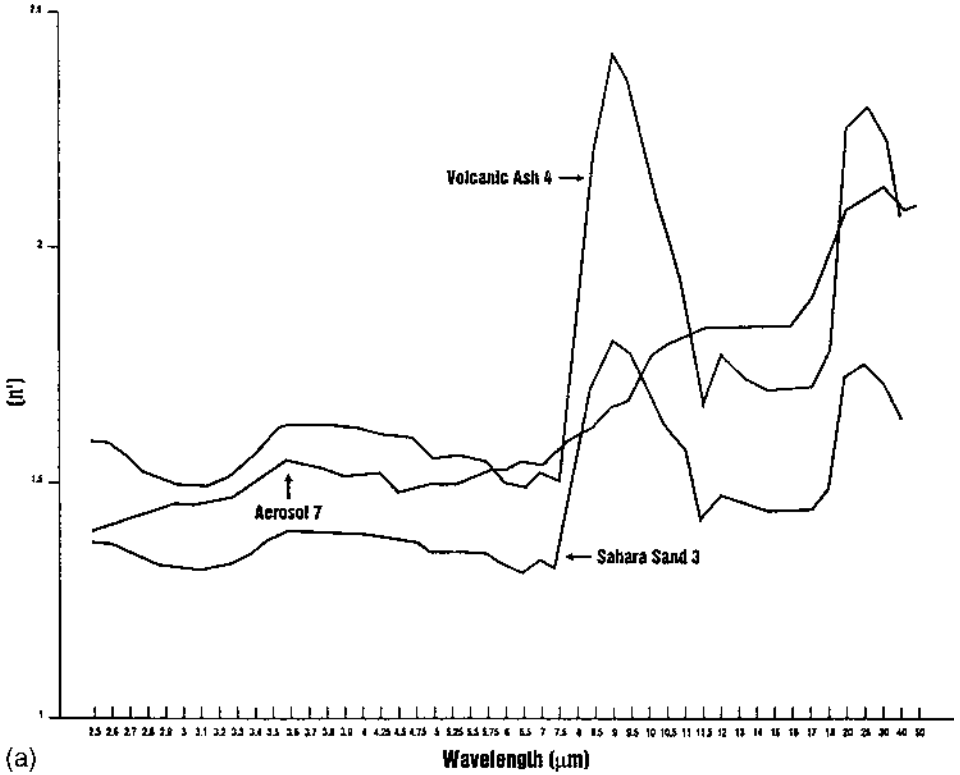

(a)

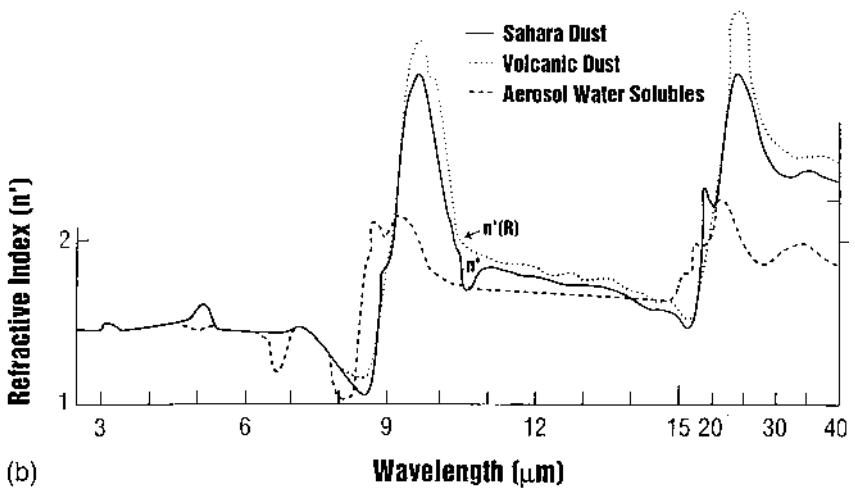

(b)

has not been completely eliminated, and further analyses would be desirable using the M-K-M scattering theory.

There are also differences between the Volz measurements of the refractive indices of the samples as evidenced by Figs. 6a and 6b. These differences could possibly be caused by sample differences, finite-wavelength effects, or differences in measurement techniques. However, the silicate bands are evident in the volcanic ash and Sahara sand samples.

REFERENCES

1. Volz, F.E. Infrared optical constants of ammonium sulfate, Sahara dust, volcanic pumice, and flyash. Appl. Opt. 1973, 12, 564–568.
2. Egan, W.G.; Hilgeman, T.W. Optical properties of inhomogeneous materials; Academic Press: New York, 1979.
3. Agnew, J.T.; McQuistan, R.B. Experiments concerning infrared diffuse reflectance standards in the range 0.8–20.0 microns. J. Opt. Soc. Am. 1953, 43, 999–1007.
4. Kronstein, M.; Kraushaar, R.J.; Deacle, R.E. Sulfur as a standard of reflectance in the infrared. J. Opt. Soc. Am. 1963, 53, 458–465.
5. Egan, W.G.; Joseph, J., Jr. Infrared optical constants of sahara sand, volcanic ash, and water soluble aerosols. 18th Annual Review of the Conference on Atmospheric Transmission, Bedford, MA, 1995, pp. 202–203.

30

Optical Properties of Standard Aerosols

I. INTRODUCTION

The earth's atmosphere is known to contain numerous micrometer-sized aerosol particles that are composed of silicate dust, ammonium sulfate [$(NH_4)_2SO_4$], amorphous carbon, sodium chloride, water, and solutions of nitric, sulfuric, and hydrochloric acids. In order to characterize the optical behavior of these particles so that their effect on atmospheric optical transmission, scattering, and absorption may be determined, their fundamental optical properties (i.e., the complex index of refraction) must be determined.

Many techniques have been described in the literature for the determination of the complex index of refraction [1]. The refractive (real) and absorptive (imaginary) portions are usually measured separately as a function of wavelength. The refractive portion of a bulk or compressed powder sample of an inhomogeneous material can be determined from the Brewster angle, and the absorption portion from the application of the basic or modified Kubelka–Munk theories [1]. The Kubelka–Munk approach requires that a finely dispersed powder of the material under investigation be embedded in a potassium bromide (KBr) pellet.

The majority of the absorption measurement techniques determine the absorption portion alone, but the Kramers–Kronig technique produces both the refractive portion and the absorption portion. However, this technique is not valid when scattering is present as in the ultraviolet, visible, and near-infrared portions of the spectrum [1]. It is desirable and necessary to compare the results of the determinations of the complex index of refraction by various techniques in order to assess their validity.

II. EXPERIMENTAL APPROACH

Aerosol samples were collected during the period 4 August to 7 August 1980 from the high-density pipeline source furnished by the Cloud Simulation and Aerosol Laboratory of the Department of Atmospheric Science, Colorado State University, Fort Collins, Colorado. The collections were made using Millipore Type PVC5 filters supported by AP10 MF support pads in the 37 mm, three-section, in-line monitor. A Millipore vacuum pressure pump was used at 10 L/min flow during the collection runs. The samples acquired and the collection durations are listed in Table 1. The samples furnished were soot (amorphous carbon), $(NH_4)_2SO_4$, methylene blue, Arizona dust, ambient air, and mixtures of soot and $(NH_4)_2SO_4$. The Millipore filters were weighed before and after the collections to determine the quantity of aerosol collected during each run; the filters were reinserted into the filter housing for storage after the final weighing, along with a small amount of silica gel desiccant. The desiccant was separated from the sample by a partition made from the blue filter pad spacers, and the holder openings were sealed with plastic plugs; in this way the samples could be carried back to the Grumman Optics Laboratory for sample preparation for total diffuse reflectance and transmission measurements with a $BaSO_4$-coated integrating sphere [1]. Also, samples of

TABLE 1 List of Sample Collections Made from the High-Concentration Line Located in the Downstairs Laboratory (Except as Noted) Using Vacuum Pump and Millipore PVC5 Filters on Pad in Holders

Date	Aerosol material	Time on	Time off	Sample holder No.
8/4/80	Propane soot	1030	1045	3
8/4/80	Propane soot	1045	1125	2
8/4/80	Propane soot + $(NH_4)_2SO_4$	1152	1212	4
8/4/80	Propane soot + $(NH_4)_2SO_4$	1212	1400	5
8/4/80	Methylene blue	1500	1545	6
8/4/80	Methylene blue	1525	1527	7
8/5-6/80	Ambient air	1035	0830	8
8/6/80	Arizona road dust	1040	1300	1
8/6/80	Propane soot + $(NH_4)_2SO_4$	1445	1700	9
8/7/80	Propane soot	1000	1040	10
8/7/80	Propane soot + $(NH_4)_2SO_4$	1045	1340	11
8/7/80	Humidified soot + $(NH_4)_2SO_4$ (upstairs)	1420	1550	12
8/8/80	$(NH_4)_2SO_4$	1130	1200	13
8/8/80	$(NH_4)_2SO_4$	1200	1535	14

bulk $(NH_4)_2SO_4$, methylene blue, and Arizona dust (which were used to generate the aerosols) were brought back for determinations of the refractive portion of the index of refraction using the Brewster angle technique on compressed pellets of these materials. Soot was obtained (in the form of lampblack from Fischer (stock No. C-198). The soot was amorphous, as verified by an X-ray diffraction measurement. However, the soot particles were coated with a layer of sulfur; the sulfur presumably condensed on the particles during the burning of high sulfur oil under the conditions of oxygen-deficient combustion necessary to produce the soot. The soot was also used in a Brewster angle determination of the refractive portion of the index of refraction. As a point of comparison, spectroscopically pure graphite ("graphite 1") was also investigated using ellipsometry to determine the refractive and absorptive portions; also, a powder of the graphite was prepared in a KBr pellet to determine the absorptive portion using the Kubelka–Munk theory for comparison.

The sample collection filters were removed from their holder upon arrival at the Grumman Optics Laboratory, and the material collected on the filter surface was mixed with a small measured quantity of KBr and dispersed using an agate mortar and pestle. This sample was then inserted into a Barnes 13 mm KBr die, and another thicker layer of KBr powder was placed above it. Compression of the composite at a pressure of 3.3×10^7 dyn/mm^2 resulted in a thin layer of powder sample in the KBr pellet. It was found that the $(NH_4)_2SO_4$ aerosol samples could not be prepared because the sample embedded itself into the filter because the filter pore sizes were too large. Future collections of $(NH_4)_2SO_4$ aerosol would require the use of glass fiber collection filters such as Millipore Type AP40.

Optical measurements of total diffuse transmission and reflection were made using a modified Perkin-Elmer Model 13U spectrograph with a $BaSO_4$-coated integrating sphere. Initial measurements (reported here) were made at selected wavelengths between 0.185 and 1.105 μm. From the measurements, the Kubelka–Munk (K-M) or modified Kubelka–Munk (MKM) theories were used to calculate the absorption coefficient of the samples independent of the scattering [1]. For the application of the MKM theory, the real portion of the refractive index of the sample is necessary. This index was determined from Brewster angle measurements on compressed pellets composed completely of powders of $(NH_4)_2SO_4$, methylene blue, lampblack, and Arizona dust; a sample block of spectroscopically pure graphite was also used for measurements of the real index. For the highly opaque samples (lampblack, graphite, and methylene blue), ellipsometric measurements were made to determine the absorption portion of the index of refraction.

Calculations of the absorption portion of the complex index of refraction were made on an IBM 370/168 computer, and the refractive portions of

the index were made using a least squares curve fit program on an HP-9810-A computer plotter. Comparisons of the present set of measurements to previously published data on $(NH_4)_2SO_4$, graphite, and atmospheric aerosols are made.

III. RESULTS AND DISCUSSION

The results of the measurements of total diffuse reflectance and transmission (between wavelengths of 0.185 and 1.105 μm) on the samples, as well as the calculated imaginary index (n_2), are presented in Figs. 1–11 and Tables 2–12; also included is the Brewster angle determination of the refractive portion of the index (n_1). For the high-opacity samples (graphite 1, methylene blue, and lampblack), the results of the ellipsometric measurements are presented separately in Figs. 12–14 and Tables 13–15. A similar set of results of measurements on pure $(NH_4)_2SO_4$ in a KBr pellet is shown in Fig. 15 and Table 16. In the figures, the logarithm (base 10) of the total diffuse transmission (T), the total diffuse reflection (R), and the refractive and absorption portions of the refractive index (n_1 and n_2, respectively) are plotted as a function of the wavelength in micrometers. The effective thickness specified is the equivalent thickness of a layer of the aerosol material that is suspended in the KBr pellet. The tables give numerical values (estimated error $< \pm 10\%$) for the data presented in the figures. It is to be noted that in the notation of Egan and Hilgeman [1] $n = n_1$ and $K_0 = n_2$.

The optical properties n_1 and n_2 are the significant results, whereas the diffuse transmission and reflection are presented mainly as a point of information. In the event that better theories for obtaining the optical complex index of refraction become available, they may be applied to these raw data.

A comparison of the optical properties n_1 and n_2 of Arizona dust aerosol (Fig. 1 and Table 2) with samples prepared from the bulk sample (Figs. 2 and 3; Tables 3 and 4) indicate that the aerosol sample has about one order of magnitude higher absorption than the bulk samples. The aerosol sample would generally consist of smaller particles with a lower real refractive index, which is inferred to be the result of quantum size effects (QSE) (see, for instance, Egan and Hilgeman [2]). This lower effective index would increase scatter in the KBr matrix and increase absorption as concentration is lowered, as was found.

Propane soot (Figs. 4 and 5; Tables 5 and 6) shows general agreement in magnitude of n_2 between the two samples, with the lower concentration sample (Fig. 4) showing a slightly higher absorption. However, both absorptions are lower than that for bulk soot (Fig. 14 and Table 15), which is also attributed to QSE and possibly to the effect of the sulfur contaminant.

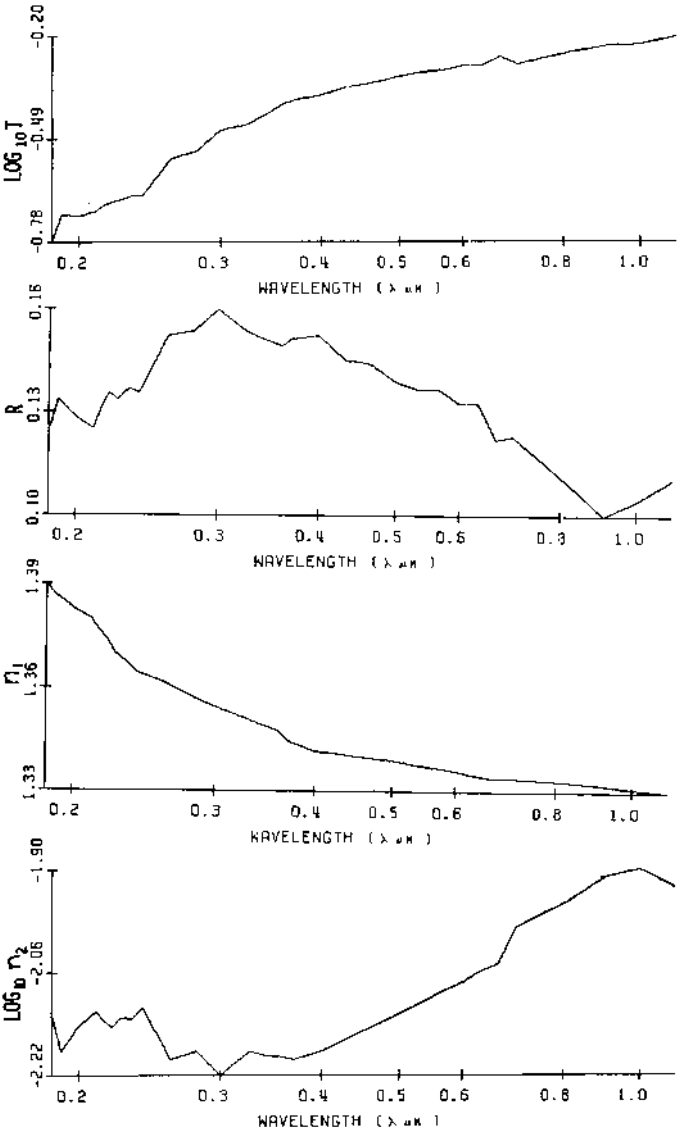

FIGURE 1 Arizona dust, CSU aerosol sample No. 1, compressed KBr pellet (effective thickness 0.000149 cm); n_1 from Brewster angle measurement.

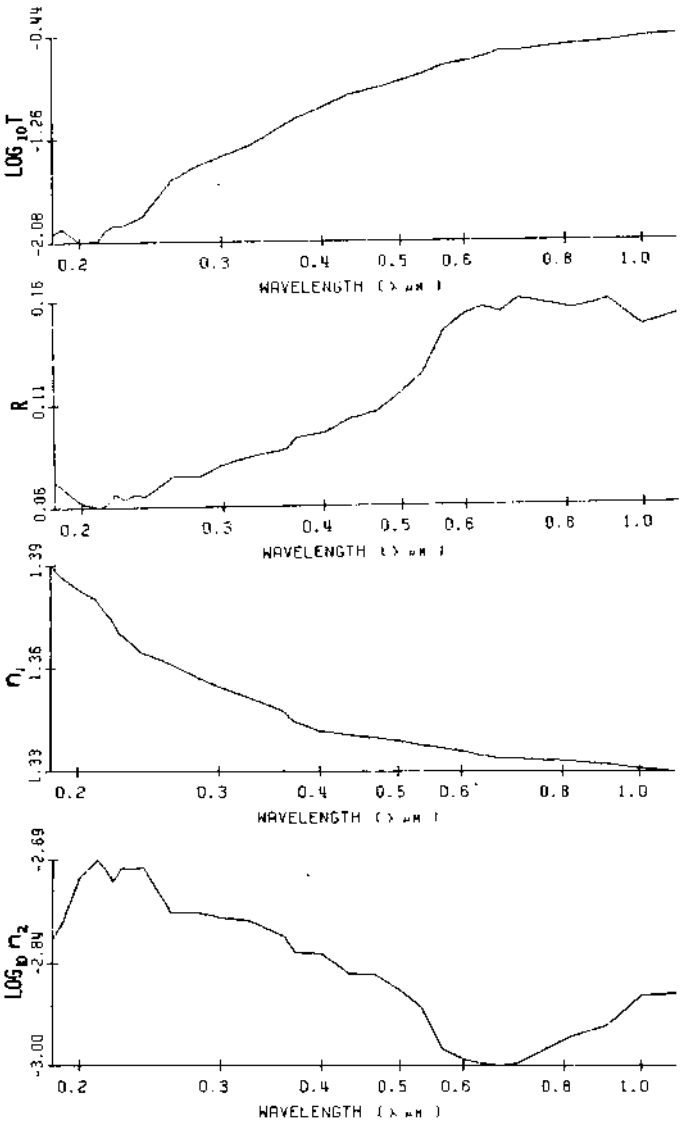

FIGURE 2 Arizona dust, prepared from raw dust, CSU sample No. 1A, compressed KBr pellet (effective thickness 0.00263 cm); n_1 from Brewster angle measurement.

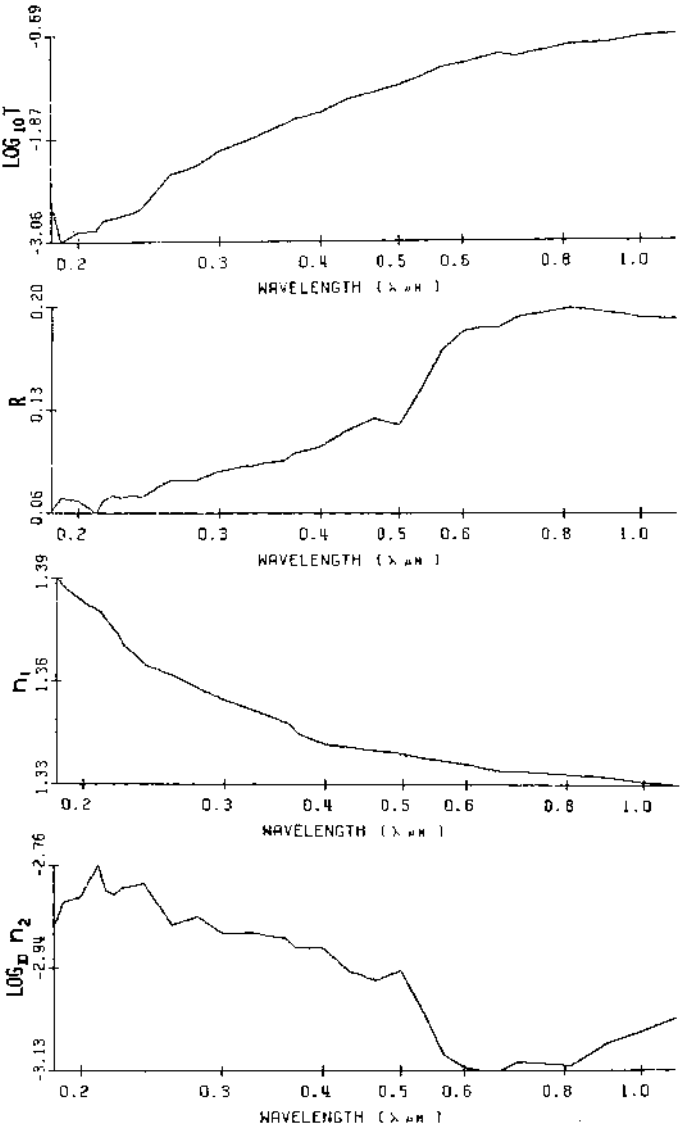

FIGURE 3 Arizona dust, prepared from raw dust, CSU sample No. 1B, compressed KBr pellet (effective thickness 0.00448 cm); n_1 from Brewster angle measurement.

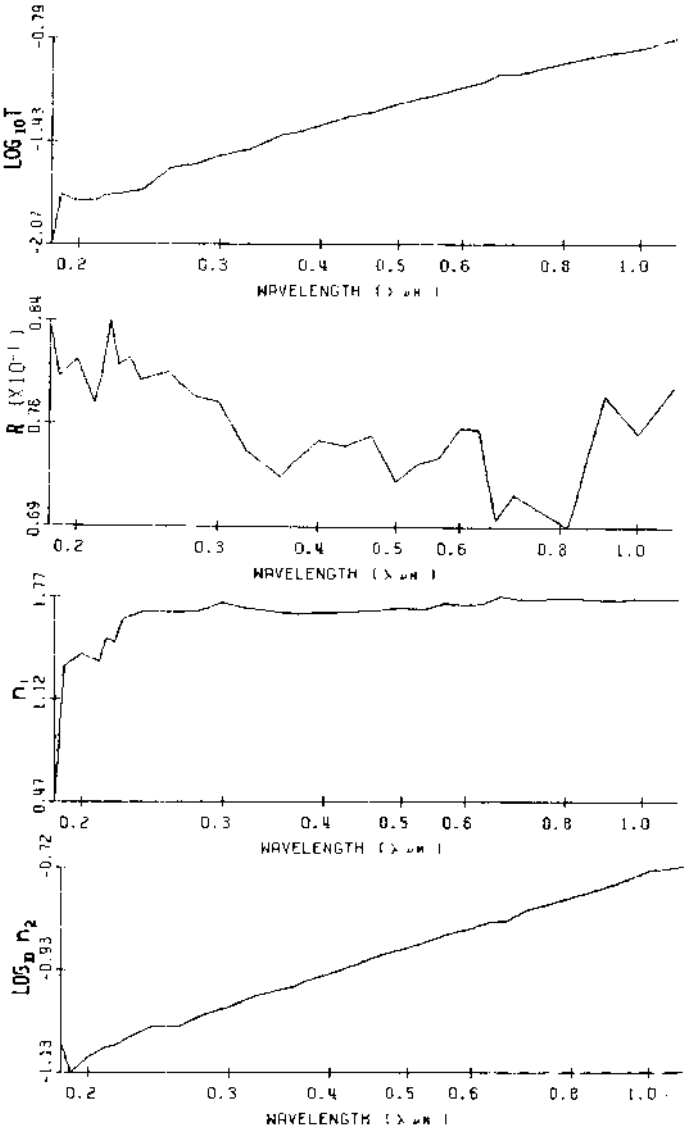

FIGURE 4 Propane soot, CSU aerosol sample No. 2, compressed KBr pellet (effective thickness 0.0000831 cm); n_1 from Fig. 14.

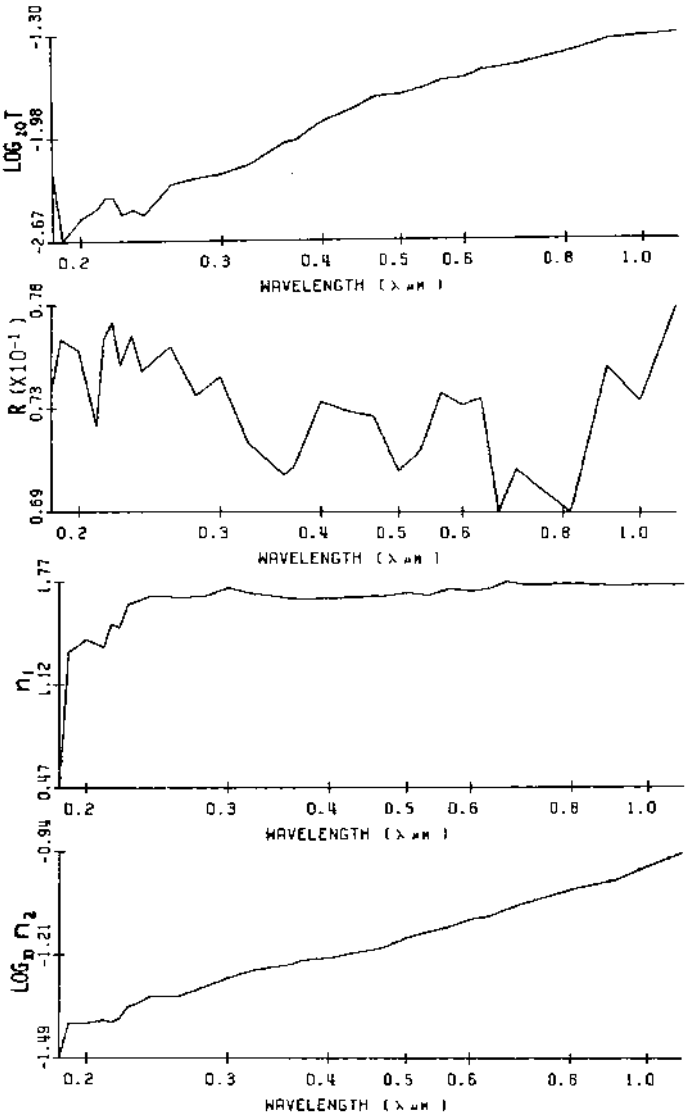

FIGURE 5 Propane soot, CSU aerosol sample No. 2A, prepared from CSU sample No. 2, compressed KBr pellet (effective thickness 0.000229 cm); n_1 from Fig. 12.

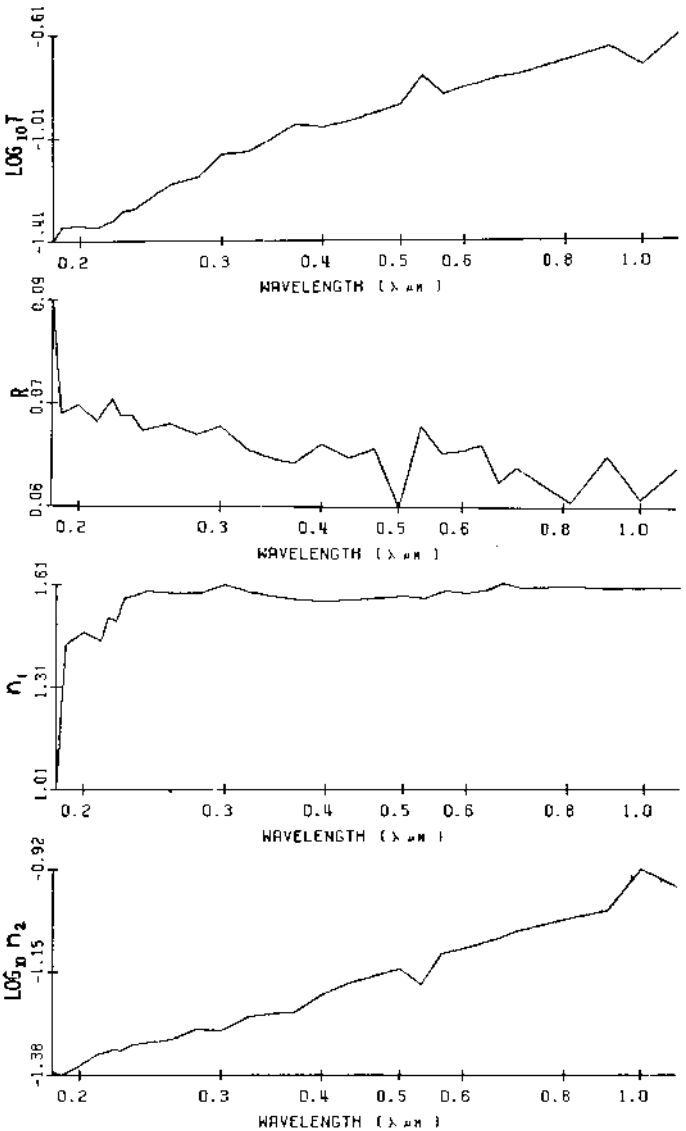

FIGURE 6 Propane soot + $(NH_4)_2SO_4$, CSU aerosol sample No. 5, compressed KBr pellet (effective thickness 0.000112 cm); n_1 is average from Figs. 12 and 15.

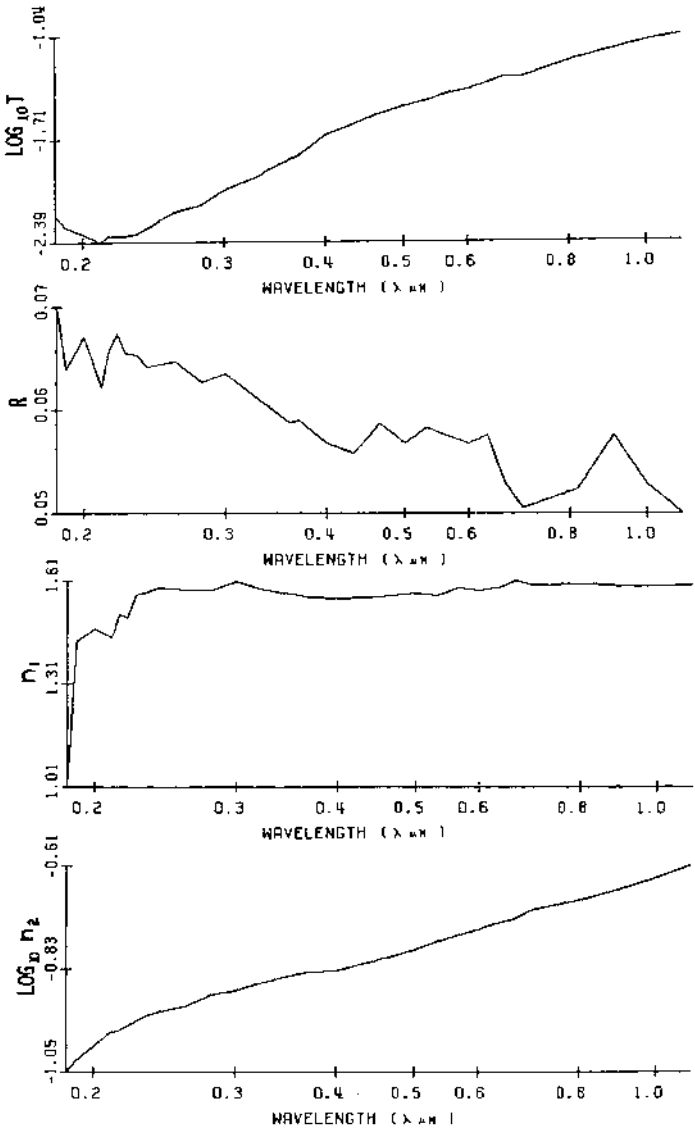

FIGURE 7 Propane soot + $(NH_4)_2SO_4$, CSU aerosol sample No. 5A, prepared from CSU sample No. 5, compressed KBr pellet (effective thickness 0.0000850 cm); n_1 is average from Figs. 12 and 15.

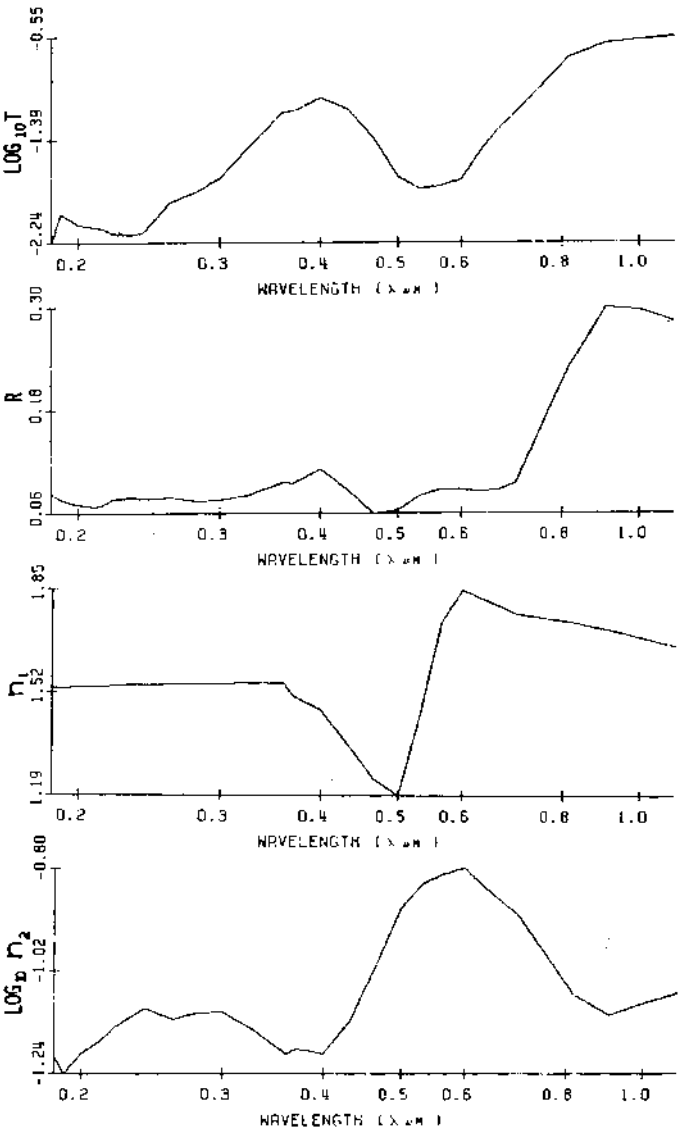

FIGURE 8 Methylene blue, CSU aerosol sample No. 6, compressed KBr pellet (effective thickness 0.00012 cm); n_1 from Fig. 13.

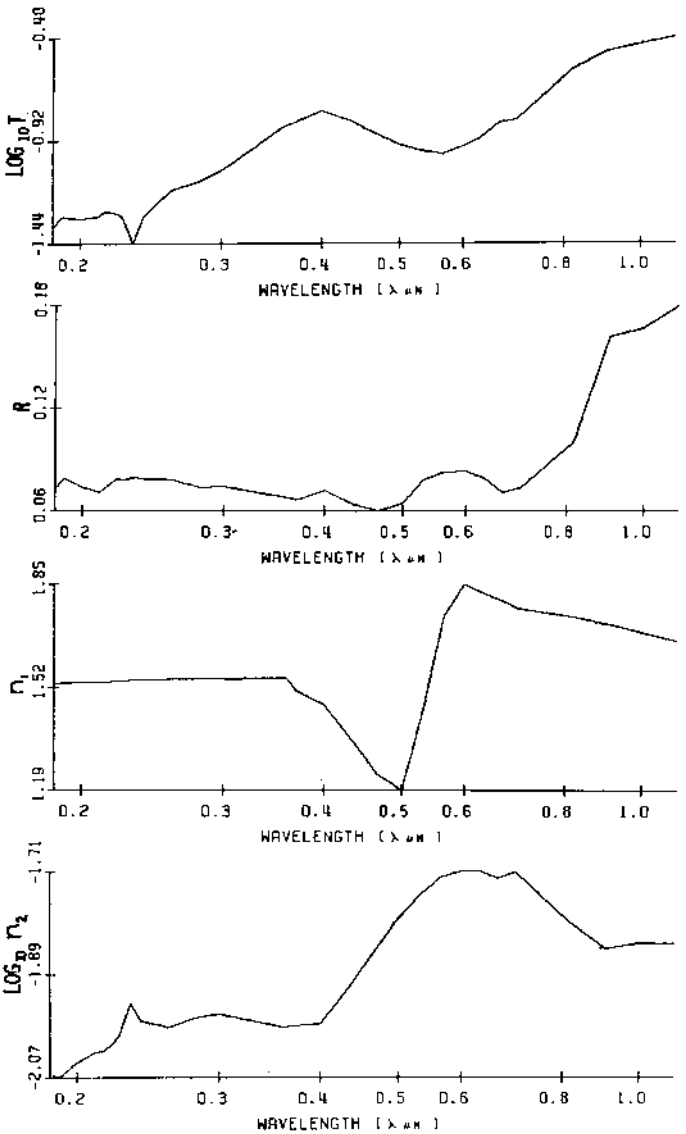

FIGURE 9 Methylene blue, prepared from bulk methylene blue, CSU sample No. 6A, compressed KBr pellet (effective thickness 0.000536 cm); n_1 from Fig. 13.

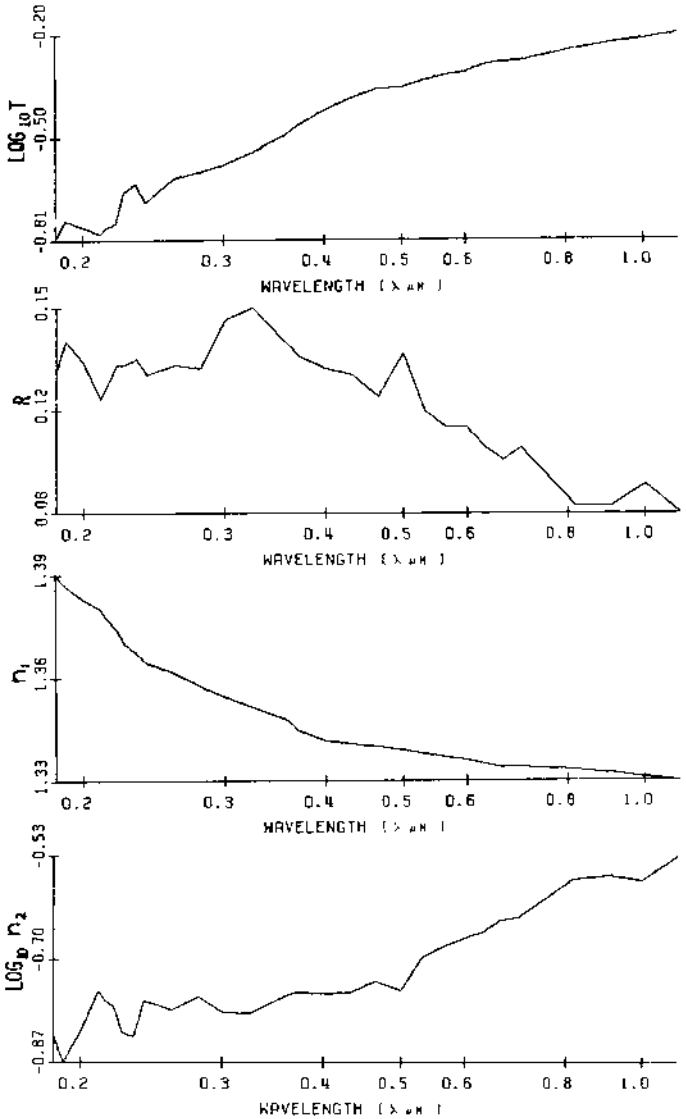

FIGURE 10 Ambient air, Fort Collins, Colorado, CSU aerosol sample No. 8, compressed KBr pellet (effective thickness 0.00000737 cm); n_1 from Table 2.

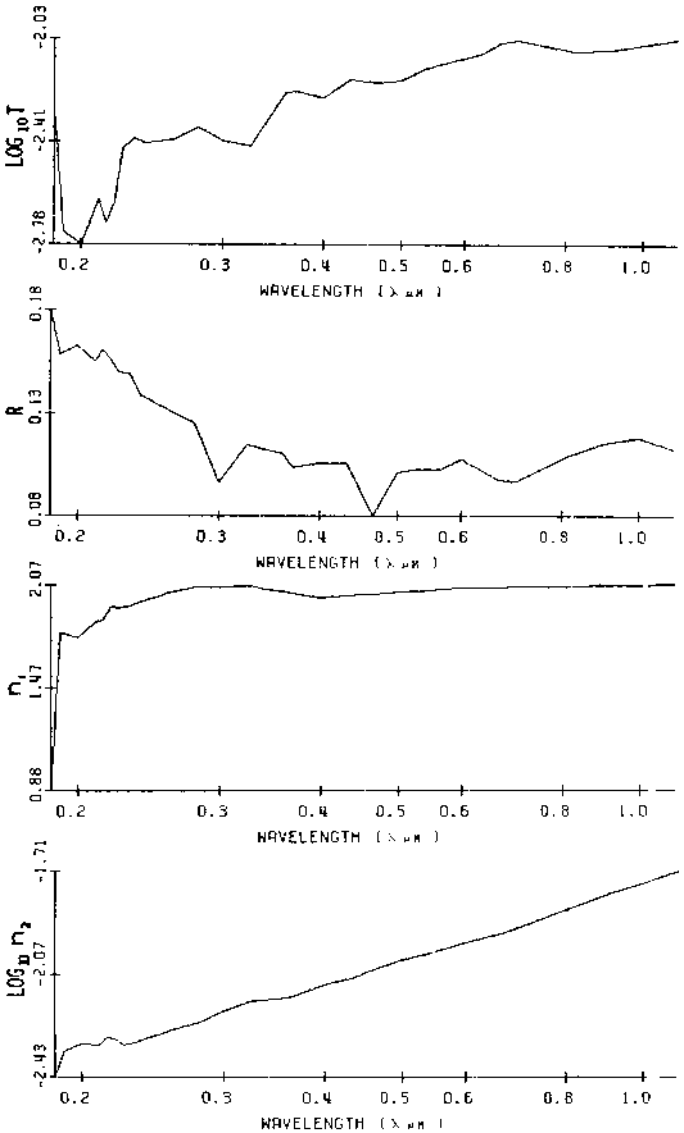

FIGURE 11 Spectroscopically pure graphite, CSU sample "graphite," compressed KBr pellet (effective thickness 0.00208 cm).

TABLE 2 Arizona Dust (Fig. 1)

$\lambda(\mu m)$	Log T	R	Log n_2	n_1
0.185	−0.783	0.125	−0.213 × 10	1.390
0.190	−0.706	0.134	−0.219 × 10	1.387
0.200	−0.710	0.129	−0.215 × 10	1.383
0.210	−0.695	0.126	−0.212 × 10	1.380
0.215	−0.678	0.131	−0.214 × 10	1.377
0.220	−0.668	0.136	−0.215 × 10	1.374
0.225	−0.664	0.134	−0.213 × 10	1.370
0.233	−0.650	0.137	−0.213 × 10	1.367
0.240	−0.652	0.136	−0.212 × 10	1.364
0.260	−0.545	0.152	−0.220 × 10	1.361
0.280	−0.523	0.153	−0.219 × 10	1.357
0.300	−0.463	0.159	−0.222 × 10	1.354
0.325	−0.446	0.153	−0.219 × 10	1.351
0.360	−0.387	0.149	−0.220 × 10	1.347
0.370	−0.378	0.151	−0.220 × 10	1.344
0.400	−0.364	0.152	−0.219 × 10	1.341
0.433	−0.338	0.145	−0.217 × 10	1.340
0.466	−0.327	0.144	−0.215 × 10	1.339
0.500	−0.310	0.139	−0.213 × 10	1.338
0.533	−0.298	0.137	−0.211 × 10	1.337
0.566	−0.293	0.137	−0.209 × 10	1.336
0.600	−0.280	0.133	−0.208 × 10	1.335
0.633	−0.277	0.133	−0.206 × 10	1.334
0.666	−0.255	0.123	−0.206 × 10	1.333
0.700	−0.276	0.124	−0.199 × 10	1.333
0.817	−0.241	0.111	−0.195 × 10	1.332
0.907	−0.223	0.102	−0.191 × 10	1.331
1.000	−0.215	0.106	−0.190 × 10	1.330
1.105	−0.196	0.112	−0.193 × 10	1.329

TABLE 3 Arizona Dust (Fig. 2)

λ(μm)	Log T	R	Log n_2	n_1
0.185	−0.201 × 10	0.073	−0.281 × 10	1.390
0.190	−0.198 × 10	0.069	−0.278 × 10	1.387
0.200	−0.208 × 10	0.062	−0.271 × 10	1.383
0.210	−0.207 × 10	0.060	−0.269 × 10	1.380
0.215	−0.200 × 10	0.062	−0.270 × 10	1.377
0.220	−0.195 × 10	0.067	−0.272 × 10	1.374
0.225	−0.195 × 10	0.064	−0.270 × 10	1.370
0.233	−0.192 × 10	0.066	−0.270 × 10	1.367
0.240	−0.187 × 10	0.066	−0.270 × 10	1.364
0.260	−0.159 × 10	0.075	−0.277 × 10	1.361
0.280	−0.147 × 10	0.075	−0.277 × 10	1.357
0.300	−0.140 × 10	0.080	−0.277 × 10	1.354
0.325	−0.132 × 10	0.084	−0.278 × 10	1.351
0.360	−0.115 × 10	0.087	−0.280 × 10	1.347
0.370	−0.110 × 10	0.092	−0.283 × 10	1.344
0.400	−0.102 × 10	0.094	−0.283 × 10	1.341
0.433	−0.917	0.101	−0.286 × 10	1.340
0.466	−0.866	0.104	−0.286 × 10	1.339
0.500	−0.807	0.113	−0.289 × 10	1.338
0.533	−0.752	0.122	−0.291 × 10	1.337
0.566	−0.684	0.141	−0.298 × 10	1.336
0.600	−0.650	0.149	−0.299 × 10	1.335
0.633	−0.618	0.152	−0.300 × 10	1.334
0.666	−0.573	0.150	−0.300 × 10	1.333
0.700	−0.569	0.156	−0.300 × 10	1.333
0.817	−0.520	0.151	−0.296 × 10	1.332
0.907	−0.499	0.155	−0.294 × 10	1.331
1.000	−0.469	0.143	−0.289 × 10	1.330
1.105	−0.440	0.148	−0.289 × 10	1.329

TABLE 4 Arizona Dust (Fig. 3)

$\lambda(\mu m)$	Log T	R	Log n_2	n_1
0.185	-0.262×10	0.061	-0.287×10	1.390
0.190	-0.306×10	0.069	-0.283×10	1.387
0.200	-0.294×10	0.068	-0.282×10	1.383
0.210	-0.293×10	0.059	-0.276×10	1.380
0.215	-0.280×10	0.067	-0.281×10	1.377
0.220	-0.279×10	0.071	-0.282×10	1.374
0.225	-0.277×10	0.070	-0.280×10	1.370
0.233	-0.273×10	0.071	-0.280×10	1.367
0.240	-0.267×10	0.070	-0.280×10	1.364
0.260	-0.229×10	0.081	-0.287×10	1.361
0.280	-0.219×10	0.081	-0.285×10	1.357
0.300	-0.201×10	0.087	-0.288×10	1.354
0.325	-0.190×10	0.091	-0.288×10	1.351
0.360	-0.172×10	0.095	-0.289×10	1.347
0.370	-0.166×10	0.099	-0.291×10	1.344
0.400	-0.158×10	0.104	-0.291×10	1.341
0.433	-0.143×10	0.115	-0.295×10	1.340
0.466	-0.135×10	0.123	-0.297×10	1.339
0.500	-0.127×10	0.119	-0.295×10	1.338
0.533	-0.117×10	0.143	-0.302×10	1.337
0.566	-0.107×10	0.169	-0.310×10	1.336
0.600	-0.102×10	0.182	-0.312×10	1.335
0.633	-0.967	0.185	-0.313×10	1.334
0.666	-0.914	0.185	-0.313×10	1.333
0.700	-0.936	0.192	-0.311×10	1.333
0.817	-0.810	0.198	-0.312×10	1.332
0.907	-0.783	0.195	-0.308×10	1.331
1.000	-0.728	0.192	-0.306×10	1.330
1.105	-0.690	0.191	-0.303×10	1.329

TABLE 5 Propane Soot (Fig. 4)

$\lambda(\mu m)$	Log T	R	Log n_2	n_1
0.185	-0.207×10	0.083	-0.108×10	0.472
0.190	-0.176×10	0.080	-0.113×10	1.331
0.200	-0.180×10	0.081	-0.110×10	1.409
0.210	-0.179×10	0.078	-0.108×10	1.367
0.215	-0.176×10	0.080	-0.108×10	1.508
0.220	-0.175×10	0.084	-0.107×10	1.491
0.225	-0.175×10	0.081	-0.106×10	1.633
0.233	-0.174×10	0.081	-0.105×10	1.659
0.240	-0.173×10	0.079	-0.104×10	1.684
0.260	-0.159×10	0.080	-0.104×10	1.678
0.280	-0.157×10	0.078	-0.102×10	1.684
0.300	-0.152×10	0.078	-0.100×10	1.737
0.325	-0.148×10	0.074	-0.976	1.697
0.360	-0.139×10	0.072	-0.959	1.674
0.370	-0.137×10	0.073	-0.951	1.665
0.400	-0.133×10	0.075	-0.933	1.668
0.433	-0.128×10	0.075	-0.915	1.675
0.466	-0.124×10	0.075	-0.894	1.687
0.500	-0.119×10	0.072	-0.882	1.701
0.533	-0.116×10	0.073	-0.866	1.689
0.566	-0.113×10	0.074	-0.851	1.731
0.600	-0.109×10	0.076	-0.843	1.716
0.633	-0.106×10	0.076	-0.829	1.729
0.666	-0.102×10	0.069	-0.827	1.775
0.700	-0.102×10	0.071	-0.805	1.753
0.817	-0.932	0.069	-0.776	1.762
0.907	-0.886	0.078	-0.753	1.750
1.000	-0.857	0.076	-0.725	1.753
1.105	-0.790	0.079	-0.717	1.757

TABLE 6 Propane Soot (Fig. 5)

$\lambda(\mu m)$	Log T	R	Log n_2	n_1
0.185	-0.221×10	0.074	-0.149×10	0.472
0.190	-0.267×10	0.076	-0.139×10	1.331
0.200	-0.252×10	0.076	-0.139×10	1.409
0.210	-0.245×10	0.072	-0.139×10	1.367
0.215	-0.238×10	0.076	-0.139×10	1.508
0.220	-0.238×10	0.077	-0.138×10	1.491
0.225	-0.249×10	0.075	-0.135×10	1.633
0.233	-0.246×10	0.076	-0.134×10	1.659
0.240	-0.249×10	0.075	-0.132×10	1.684
0.260	-0.229×10	0.076	-0.132×10	1.678
0.280	-0.225×10	0.074	-0.130×10	1.684
0.300	-0.222×10	0.075	-0.127×10	1.737
0.325	-0.216×10	0.072	-0.125×10	1.697
0.360	-0.201×10	0.070	-0.124×10	1.674
0.370	-0.201×10	0.071	-0.123×10	1.665
0.400	-0.188×10	0.073	-0.122×10	1.668
0.433	-0.180×10	0.073	-0.120×10	1.675
0.466	-0.172×10	0.073	-0.119×10	1.687
0.500	-0.170×10	0.070	-0.117×10	1.701
0.533	-0.166×10	0.071	-0.115×10	1.689
0.566	-0.161×10	0.074	-0.114×10	1.731
0.600	-0.159×10	0.073	-0.112×10	1.716
0.633	-0.154×10	0.074	-0.111×10	1.729
0.666	-0.153×10	0.069	-0.109×10	1.775
0.700	-0.150×10	0.071	-0.108×10	1.753
0.817	-0.142×10	0.069	-0.103×10	1.762
0.907	-0.134×10	0.075	-0.101×10	1.750
1.000	-0.132×10	0.073	-0.977	1.753
1.105	-0.130×10	0.078	-0.941	1.757

TABLE 7 Propane Soot + $(NH_4)_2SO_4$ (Fig. 6)

$\lambda(\mu m)$	Log T	R	Log n_2	n_1
0.185	-0.141×10	0.093	-0.137×10	1.005
0.190	-0.135×10	0.072	-0.138×10	1.432
0.200	-0.135×10	0.074	-0.136×10	1.468
0.210	-0.136×10	0.071	-0.133×10	1.444
0.215	-0.134×10	0.073	-0.133×10	1.511
0.220	-0.133×10	0.075	-0.132×10	1.500
0.225	-0.129×10	0.072	-0.132×10	1.568
0.233	-0.129×10	0.072	-0.131×10	1.578
0.240	-0.126×10	0.070	-0.131×10	1.588
0.260	-0.119×10	0.071	-0.130×10	1.582
0.280	-0.116×10	0.069	-0.128×10	1.582
0.300	-0.107×10	0.070	-0.128×10	1.606
0.325	-0.106×10	0.066	-0.125×10	1.583
0.360	−0.979	0.064	-0.124×10	1.569
0.370	−0.955	0.064	-0.124×10	1.561
0.400	−0.967	0.067	-0.120×10	1.560
0.433	−0.943	0.065	-0.118×10	1.563
0.466	−0.910	0.066	-0.116×10	1.568
0.500	−0.879	0.056	-0.114×10	1.575
0.533	−0.764	0.071	-0.118×10	1.569
0.566	−0.839	0.066	-0.111×10	1.590
0.600	−0.812	0.066	-0.110×10	1.582
0.633	−0.790	0.067	-0.109×10	1.588
0.666	−0.770	0.060	-0.108×10	1.610
0.700	−0.762	0.063	-0.106×10	1.599
0.817	−0.699	0.056	-0.103×10	1.602
0.907	−0.654	0.065	-0.101×10	1.596
1.000	−0.728	0.057	−0.925	1.596
1.105	−0.606	0.063	−0.962	1.598

TABLE 8 Propane Soot + $(NH_4)_2SO_4$ (Fig. 7)

λ(μm)	Log T	R	Log n_2	n_1
0.185	−0.222 × 10	0.072	−0.105 × 10	1.005
0.190	−0.229 × 10	0.065	−0.103 × 10	1.432
0.200	−0.234 × 10	0.069	−0.997	1.468
0.210	−0.239 × 10	0.063	−0.967	1.444
0.215	−0.235 × 10	0.067	−0.964	1.511
0.220	−0.235 × 10	0.069	−0.954	1.500
0.225	−0.235 × 10	0.067	−0.945	1.568
0.233	−0.233 × 10	0.067	−0.931	1.578
0.240	−0.230 × 10	0.066	−0.925	1.588
0.260	−0.220 × 10	0.066	−0.910	1.582
0.280	−0.215 × 10	0.064	−0.886	1.582
0.300	−0.205 × 10	0.065	−0.878	1.606
0.325	−0.197 × 10	0.063	−0.859	1.583
0.360	−0.185 × 10	0.060	−0.842	1.569
0.370	−0.183 × 10	0.060	−0.837	1.561
0.400	−0.170 × 10	0.057	−0.835	1.560
0.433	−0.163 × 10	0.056	−0.818	1.563
0.466	−0.156 × 10	0.060	−0.805	1.568
0.500	−0.151 × 10	0.057	−0.790	1.575
0.533	−0.147 × 10	0.059	−0.771	1.569
0.566	−0.143 × 10	0.058	−0.760	1.590
0.600	−0.139 × 10	0.057	−0.744	1.582
0.633	−0.136 × 10	0.058	−0.732	1.588
0.666	−0.132 × 10	0.053	−0.723	1.610
0.700	−0.131 × 10	0.051	−0.703	1.599
0.817	−0.120 × 10	0.052	−0.677	1.602
0.907	−0.113 × 10	0.058	−0.656	1.596
1.000	−0.108 × 10	0.053	−0.632	1.596
1.105	−0.104 × 10	0.050	−0.606	1.598

TABLE 9 Methylene Blue (Fig. 8)

λ(μm)	Log T	R	Log n_2	n_1
0.185	−0.224 × 10	0.080	−0.120 × 10	1.535
0.190	−0.200 × 10	0.072	−0.124 × 10	1.536
0.200	−0.209 × 10	0.067	−0.119 × 10	1.537
0.210	−0.211 × 10	0.064	−0.117 × 10	1.539
0.215	−0.213 × 10	0.067	−0.116 × 10	1.540
0.220	−0.216 × 10	0.073	−0.114 × 10	1.541
0.225	−0.217 × 10	0.074	−0.113 × 10	1.543
0.233	−0.217 × 10	0.075	−0.111 × 10	1.544
0.240	−0.216 × 10	0.074	−0.110 × 10	1.545
0.260	−0.191 × 10	0.076	−0.112 × 10	1.547
0.280	−0.182 × 10	0.072	−0.111 × 10	1.548
0.300	−0.171 × 10	0.072	−0.111 × 10	1.549
0.325	−0.146 × 10	0.078	−0.114 × 10	1.551
0.360	−0.117 × 10	0.094	−0.119 × 10	1.552
0.370	−0.116 × 10	0.092	−0.119 × 10	1.510
0.400	−0.105 × 10	0.110	−0.120 × 10	1.467
0.433	−0.114 × 10	0.085	−0.113 × 10	1.356
0.466	−0.138 × 10	0.057	−0.101 × 10	1.243
0.500	−0.170 × 10	0.061	−0.887	1.190
0.533	−0.180 × 10	0.077	−0.835	1.451
0.566	−0.177 × 10	0.085	−0.815	1.750
0.600	−0.172 × 10	0.085	−0.802	1.854
0.633	−0.150 × 10	0.082	−0.840	1.829
0.666	−0.132 × 10	0.084	−0.873	1.803
0.700	−0.117 × 10	0.092	−0.903	1.778
0.817	−0.712	0.232	−0.107 × 10	1.752
0.907	−0.602	0.302	−0.111 × 10	1.727
1.000	−0.577	0.300	−0.109 × 10	1.701
1.105	−0.548	0.286	−0.107 × 10	1.676

TABLE 10 Methylene Blue (Fig. 9)

$\lambda(\mu m)$	Log T	R	Log n_2	n_1
0.185	-0.135×10	0.070	-0.207×10	1.535
0.190	-0.130×10	0.076	-0.207×10	1.536
0.200	-0.131×10	0.070	-0.205×10	1.537
0.210	-0.130×10	0.068	-0.203×10	1.539
0.215	-0.128×10	0.071	-0.203×10	1.540
0.220	-0.128×10	0.075	-0.202×10	1.541
0.225	-0.130×10	0.075	-0.200×10	1.543
0.233	-0.144×10	0.076	-0.194×10	1.544
0.240	-0.130×10	0.075	-0.197×10	1.545
0.260	-0.116×10	0.075	-0.199×10	1.547
0.280	-0.112×10	0.071	-0.197×10	1.548
0.300	-0.107×10	0.071	-0.196×10	1.549
0.325	−0.983	0.0672	-0.197×10	1.551
0.360	−0.845	0.065	-0.198×10	1.552
0.370	−0.824	0.064	-0.198×10	1.510
0.400	−0.770	0.069	-0.198×10	1.467
0.433	−0.815	0.061	-0.192×10	1.356
0.466	−0.879	0.057	-0.185×10	1.243
0.500	−0.939	0.061	-0.180×10	1.190
0.533	−0.971	0.075	-0.175×10	1.451
0.566	−0.983	0.079	-0.172×10	1.750
0.600	−0.951	0.080	-0.171×10	1.854
0.633	−0.900	0.076	-0.171×10	1.829
0.666	−0.830	0.068	-0.172×10	1.803
0.700	−0.812	0.070	-0.171×10	1.778
0.817	−0.572	0.097	-0.180×10	1.752
0.907	−0.471	0.158	-0.185×10	1.727
1.000	−0.438	0.163	-0.184×10	1.701
1.105	−0.400	0.176	-0.184×10	1.676

TABLE 11 Ambient Air, Fort Collins, Colorado (Fig. 10)

$\lambda(\mu m)$	Log T	R	Log n_2	n_1
0.185	−0.807	0.131	−0.829	1.390
0.190	−0.750	0.141	−0.875	1.387
0.200	−0.767	0.134	−0.822	1.383
0.210	−0.788	0.122	−0.755	1.380
0.215	−0.767	0.127	−0.770	1.377
0.220	−0.759	0.133	−0.780	1.374
0.225	−0.664	0.133	−0.825	1.370
0.233	−0.638	0.135	−0.831	1.367
0.240	−0.693	0.130	−0.769	1.364
0.260	−0.623	0.133	−0.786	1.361
0.280	−0.604	0.132	−0.763	1.357
0.300	−0.585	0.148	−0.789	1.354
0.325	−0.548	0.152	−0.791	1.351
0.360	−0.491	0.140	−0.760	1.347
0.370	−0.469	0.136	−0.757	1.344
0.400	−0.421	0.132	−0.757	1.341
0.433	−0.386	0.130	−0.756	1.340
0.466	−0.359	0.123	−0.737	1.339
0.500	−0.354	0.137	−0.753	1.338
0.533	−0.334	0.118	−0.695	1.337
0.566	−0.318	0.113	−0.677	1.336
0.600	−0.310	0.113	−0.664	1.335
0.633	−0.288	0.106	−0.652	1.334
0.666	−0.279	0.102	−0.632	1.333
0.700	−0.276	0.106	−0.629	1.333
0.817	−0.241	0.087	−0.563	1.332
0.907	−0.223	0.087	−0.557	1.331
1.000	−0.211	0.094	−0.564	1.330
1.105	−0.196	0.085	−0.525	1.329

TABLE 12 Spectroscopically Pure Graphite (Fig. 11)

λ(μm)	Log T	R	Log n_2	n_1
0.185	−0.229 × 10	0.181	−0.243 × 10	0.879
0.190	−0.274 × 10	0.159	−0.234 × 10	1.797
0.200	−0.278 × 10	0.163	−0.231 × 10	1.767
0.210	−0.262 × 10	0.155	−0.232 × 10	1.856
0.215	−0.270 × 10	0.161	−0.229 × 10	1.867
0.220	−0.263 × 10	0.156	−0.230 × 10	1.947
0.225	−0.243 × 10	0.150	−0.232 × 10	1.939
0.233	−0.240 × 10	0.149	−0.231 × 10	1.951
0.240	−0.241 × 10	0.138	−0.229 × 10	1.975
0.260	−0.240 × 10	0.131	−0.226 × 10	2.031
0.280	−0.236 × 10	0.124	−0.224 × 10	2.059
0.300	−0.240 × 10	0.094	−0.220 × 10	2.062
0.325	−0.242 × 10	0.113	−0.216 × 10	2.065
0.360	−0.223 × 10	0.109	−0.215 × 10	2.035
0.370	−0.222 × 10	0.102	−0.214 × 10	2.026
0.400	−0.225 × 10	0.104	−0.210 × 10	2.000
0.433	−0.218 × 10	0.104	−0.208 × 10	2.010
0.466	−0.219 × 10	0.077	−0.205 × 10	2.020
0.500	−0.218 × 10	0.099	−0.202 × 10	2.030
0.533	−0.214 × 10	0.101	−0.200 × 10	2.038
0.566	−0.212 × 10	0.101	−0.198 × 10	2.045
0.600	−0.210 × 10	0.106	−0.196 × 10	2.053
0.633	−0.208 × 10	0.101	−0.194 × 10	2.054
0.666	−0.204 × 10	0.096	−0.192 × 10	2.055
0.700	−0.203 × 10	0.095	−0.190 × 10	2.057
0.817	−0.207 × 10	0.108	−0.183 × 10	2.060
0.907	−0.207 × 10	0.114	−0.178 × 10	2.064
1.000	−0.205 × 10	0.117	−0.174 × 10	2.067
1.105	−0.203 × 10	0.111	−0.171 × 10	2.071

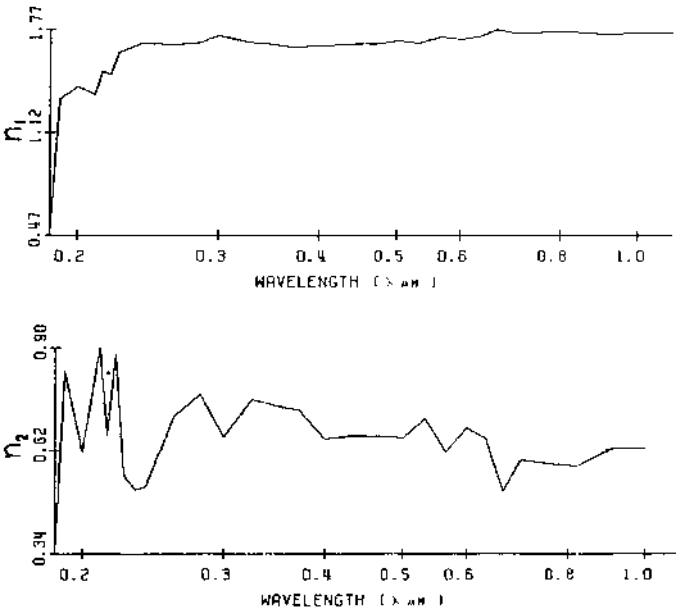

FIGURE 12 Spectroscopically pure graphite, bulk sample, CSU sample "graphite I."

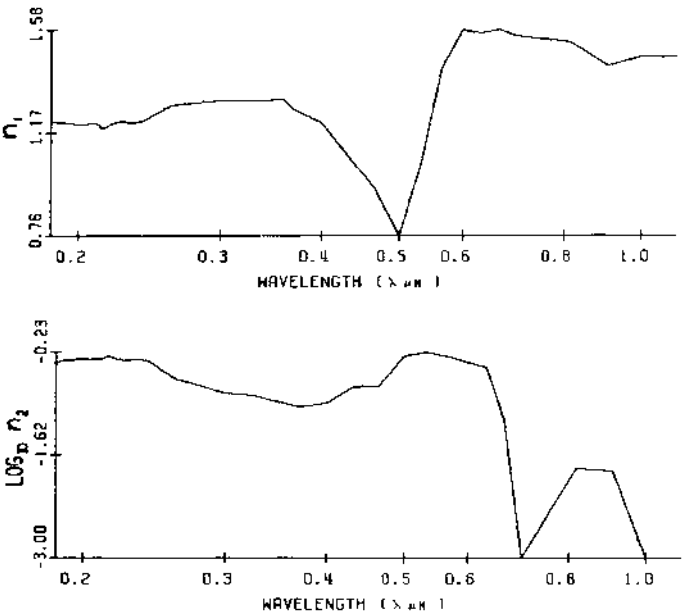

FIGURE 13 Bulk methylene blue.

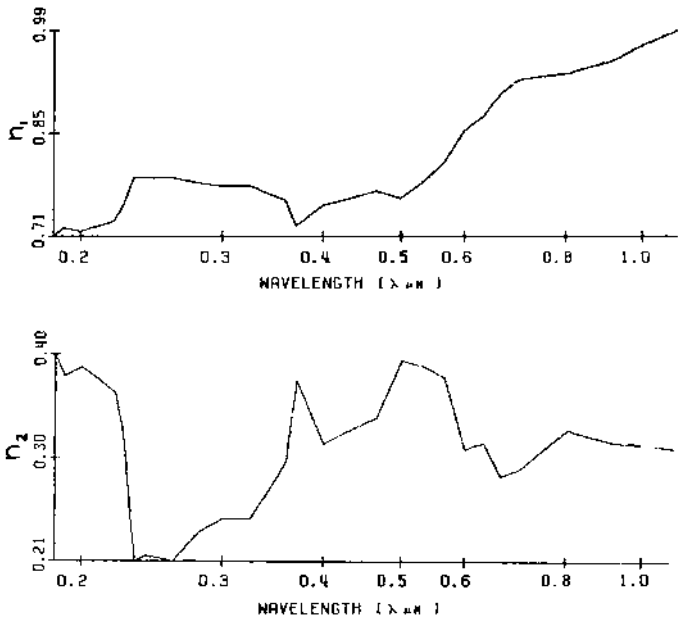

FIGURE 14 Bulk lampblack.

The mixture of propane soot and $(NH_4)_2SO_4$ (Figs. 6 and 7; Tables 7 and 8) reveals an absorption n_2 dominated by soot, the higher absorber, as expected, with the lower concentration sample showing a slightly higher absorption.

Methylene blue (Figs. 8 and 9; Tables 9 and 10) shows an anomalous refractive effect on n_1 in the blue, with a slight corresponding increase in n_2. The sample prepared from the bulk (Fig. 9) shows an order-of-magnitude larger value for n_2 than the finer aerosol sample (Fig. 8). The bulk sample analyzed with the ellipsometric technique (Fig. 13; Table 14) has a much higher absorption; this too is inferred to be the result of QSE.

The ambient aerosol collected over a 22 h period had the optical absorption properties shown in Fig. 10 and Table 11. The absorption is comparable to that of a "dirty" silicate.

A comparison of absorption n_2 for particulate grahite (Fig. 11, Table 12) with absorption for the same material in bulk form (Fig. 12, Table 13) shows a two-orders-of-magnitude decrease in the absorption portion, which is also presumed to be caused by QSE. The characteristics of the bulk graphite are different from those of amorphous carbon (Fig. 14, Table 15), which has a

TABLE 13 Spectroscopically Pure Graphite (Fig. 12)

$\lambda(\mu m)$	n_1	n_2
0.185	0.472	0.338
0.190	0.133 × 10	0.834
0.200	0.141 × 10	0.616
0.210	0.137 × 10	0.897
0.215	0.151 × 10	0.659
0.220	0.149 × 10	0.881
0.225	0.163 × 10	0.550
0.233	0.166 × 10	0.511
0.240	0.168 × 10	0.519
0.260	0.168 × 10	0.711
0.280	0.168 × 10	0.771
0.300	0.174 × 10	0.653
0.325	0.170 × 10	0.758
0.360	0.167 × 10	0.731
0.370	0.166 × 10	0.728
0.400	0.167 × 10	0.649
0.433	0.168 × 10	0.658
0.466	0.169 × 10	0.656
0.500	0.170 × 10	0.652
0.533	0.169 × 10	0.703
0.566	0.173 × 10	0.616
0.600	0.172 × 10	0.680
0.633	0.173 × 10	0.650
0.666	0.177 × 10	0.608
0.700	0.175 × 10	0.591
0.817	0.176 × 10	0.576
0.907	0.175 × 10	0.623
1.000	0.175 × 10	0.624
1.105	0.176 × 10	0.626

TABLE 14 Bulk Methylene Blue (Fig. 13)

$\lambda(\mu m)$	n_1	n_2
0.185	0.121×10	0.431
0.190	0.120×10	0.453
0.200	0.120×10	0.474
0.210	0.120×10	0.468
0.215	0.118×10	0.517
0.220	0.120×10	0.473
0.225	0.121×10	0.459
0.233	0.121×10	0.467
0.240	0.121×10	0.456
0.260	0.127×10	0.254
0.280	0.128×10	0.205
0.300	0.129×10	0.163
0.325	0.130×10	0.154
0.360	0.130×10	0.116
0.370	0.126×10	0.108
0.400	0.121×10	0.118
0.433	0.107×10	0.201
0.466	0.946	0.204
0.500	0.756	0.512
0.533	0.105×10	0.586
0.566	0.143×10	0.522
0.600	0.158×10	0.426
0.633	0.156×10	0.364
0.666	0.158×10	0.716×10^{-1}
0.700	0.155×10	0.100×10^{-2}
0.817	0.152×10	0.160×10^{-1}
0.907	0.143×10	0.150×10^{-1}
1.000	0.147×10	0.100×10^{-2}
1.105	0.147×10	0.100×10^{-2}

TABLE 15 Bulk Lampblack (Fig. 14)

$\lambda(\mu m)$	n_1	n_2
0.185	0.711	0.404
0.190	0.723	0.383
0.200	0.718	0.392
0.210	0.725	0.379
0.215	0.728	0.373
0.220	0.732	0.367
0.225	0.750	0.328
0.233	0.792	0.206
0.240	0.791	0.211
0.260	0.792	0.206
0.280	0.784	0.234
0.300	0.780	0.247
0.325	0.780	0.247
0.360	0.761	0.301
0.370	0.725	0.379
0.400	0.753	0.319
0.433	0.763	0.333
0.466	0.773	0.344
0.500	0.763	0.399
0.533	0.786	0.394
0.566	0.812	0.383
0.600	0.857	0.314
0.633	0.876	0.320
0.666	0.907	0.288
0.700	0.926	0.294
0.817	0.935	0.333
0.907	0.952	0.321
1.000	0.974	0.319
1.105	0.994	0.315

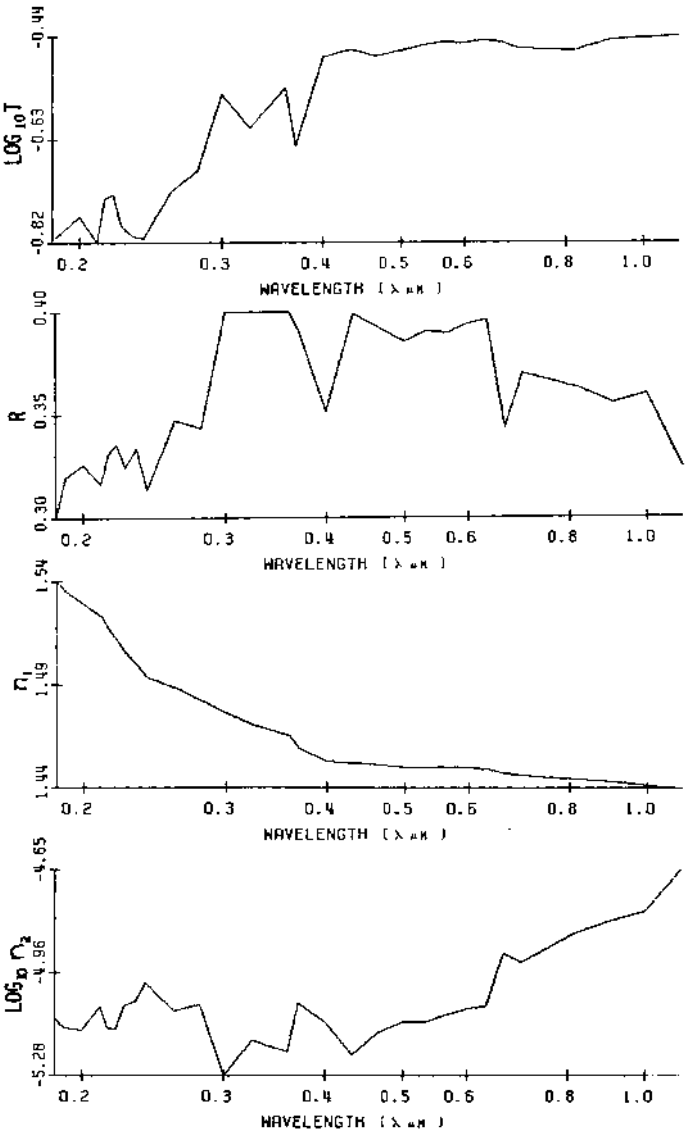

FIGURE 15 Pure $(NH_4)_2SO_4$, compressed pellet (effective thickness 0.0475 cm).

TABLE 16 Pure $(NH_4)_2SO_4$ (Fig. 15)

λ(μm)	Log T	R	Log n_2	n_1
0.185	−0.818	0.302	−0.510 × 10	1.537
0.190	−0.804	0.321	−0.513 × 10	1.532
0.200	−0.775	0.327	−0.514 × 10	1.526
0.210	−0.824	0.318	−0.507 × 10	1.520
0.215	−0.740	0.332	−0.513 × 10	1.514
0.220	−0.733	0.337	−0.513 × 10	1.509
0.225	−0.793	0.326	−0.506 × 10	1.503
0.233	−0.812	0.335	−0.505 × 10	1.497
0.240	−0.815	0.315	−0.499 × 10	1.491
0.260	−0.726	0.348	−0.508 × 10	1.486
0.280	−0.688	0.344	−0.506 × 10	1.480
0.300	−0.544	0.399	−0.528 × 10	1.474
0.325	−0.609	0.399	−0.517 × 10	1.468
0.360	−0.532	0.399	−0.520 × 10	1.463
0.370	−0.644	0.390	−0.506 × 10	1.457
0.400	−0.474	0.352	−0.511 × 10	1.451
0.433	−0.460	0.398	−0.521 × 10	1.450
0.466	−0.472	0.391	−0.514 × 10	1.449
0.500	−0.462	0.385	−0.511 × 10	1.448
0.533	−0.452	0.390	−0.511 × 10	1.448
0.566	−0.447	0.389	−0.509 × 10	1.448
0.600	−0.450	0.393	−0.507 × 10	1.448
0.633	−0.444	0.395	−0.506 × 10	1.447
0.666	−0.447	0.344	−0.490 × 10	1.445
0.700	−0.458	0.370	−0.493 × 10	1.444
0.817	−0.462	0.363	−0.484 × 10	1.442
0.907	−0.444	0.356	−0.480 × 10	1.441
1.000	−0.439	0.360	−0.478 × 10	1.439
1.105	−0.435	0.326	−0.465 × 10	1.438

lower real index (the result of QSE and the sulfur coating) and an absorption decrease in the 0.26 μm region in the ultraviolet (UV). Bulk graphite has an absorption increase toward the UV (Fig. 12, Table 13) as corroborated by Wickramasinghe [3].

Also presented are the properties n_1 and n_2 for $(NH_4)_2SO_4$ (Fig. 15, Table 16), assuming the bulk sample to be representative of the aerosol and neglecting QSE. A comparison with the results of Toon et al. [4] shows the same value for the refractive portion in the range considered, but the comparison shows quite a bit less variation in the absorption portion. There is a slight decrease in n_2 with wavelength, whereas the observations of Toon et al. [4] indicate a decrease of nearly three orders of magnitude, which is suggestive of an error due to failure to eliminate the effect of scattering in the observed thin crystals.

REFERENCES

1. Egan, W.G.; Hilgeman, T.W. Optical Properties of Inhomogeneous Materials; Academic Press: New York, 1979.
2. Egan, W.G.; Hilgeman, T. Anomalous refractive index of submicron-sized particles. Appl. Opt. 1980, 19 (22), 3724–3727.
3. Wickramasinghe, N.C. Intersteller Grains; Chapman and Hall: London, 1967.
4. Toon, O.B.; Pollack, J.B.; Khare, B.N. Optical constants of several atmospheric aerosol species: ammonium sulfate, aluminum oxide, and sodium chloride. J. Geophys. Res. 1976, 81 (33), 5733–5748.

31

Polarization Modeling Using MODTRAN 3.7

I. INTRODUCTION

Remote sensing of oceans of the world has become an important environmental considerations because the colors of the ocean and estuaries are key indicators of pollution as well as of biological phenomena. The atmosphere above the ocean contains dust and aerosols [1] that produce a significant bias in the observations. Industrial smokes and exhaust particles are of particular importance as well as dusts from the deserts of the world. Of prime importance is the dust from the Sahara and Gobi deserts, which can lower visibility to a few kilometers over distances of hundreds of kilometers from the sources by affecting photometry (brightness).

Polarization observations can be used to deconvolve the optical effects of aerosols. The behavior of Sahara dust is opposite that of nonabsorbing aerosols such as marine or clean continental aerosols or the desert aerosol, in terms of behavior of the epsilon (optical complex index of refraction) function with wavelength [2].

In this chapter observations of the Sahara dust aerosol by Kondratyev et al. [1] are analyzed in terms of two photometric/polarimetric models using optical measurements of the complex index of refraction of two selected Sahara dusts (out of five measured). Albedo effects on the atmosphere and the effects on polarization are examined with the models. A sensitivity analysis is made to resolve the effects of changing particle size and number density of the aerosol as well as changes in the optical complex index of refraction.

Although the analysis is based on Sahara sand, the results may not be strictly applicable to the Gobi or Kalahari deserts. Also, as will be seen, there is great variability in the sands of the Sahara, and results would be expected to vary depending upon the geology. However, the optical principles are general and still apply.

II. ATMOSPHERIC MODELS

As mentioned in the Introduction, two optical models are considered. These are

1. The Dave vector code for three-dimensional polarization modeling
2. The LOWTRAN 3.7 code modified for polarization

The Dave code is very detailed, with a Fourier series expansion of the Stokes vector followed by a Legendre expansion of the scattering functions. A variety of atmospheric models (size and number distributions of particulates as well as the complex index of refraction) can be used. The output is a true three-dimensional characterization of the polarization and photometry of the atmosphere [3–6].

The MODTRAN 3.7 polarization version [4] is an adaptation of the one-dimensional MODTRAN photometric codes (height) but was expanded to three dimensions geometrically, with photometry and polarization. Size and number distributions of the aerosol are included as well as the optical complex index of refraction.

III. INPUT DATA

The input data for the models consist mainly of two parts: (1) the characterization of the aerosol (size, number density) and (2) optical complex index of refraction. A height number density distribution (measured) is shown in Fig. 1 [1] with an associated heavy aerosol loading as a function of altitude as well. There is no distinction to characterize the agglomeration of small particles that is known to occur. Also, the dispersion of points in the plot indicates that there is also variability in the number density. In addition, the size distribution was indicated to be the inverse of the radius to the third power.

The optical complex indices of refraction of the sand types are listed for wavelengths from the ultraviolet to the near-infrared [2,3]:

1. Azelik Flood Plain
2. Dune sand from Niger Valley near Niamez

There is a large variability in both the real and imaginary indices of refraction.

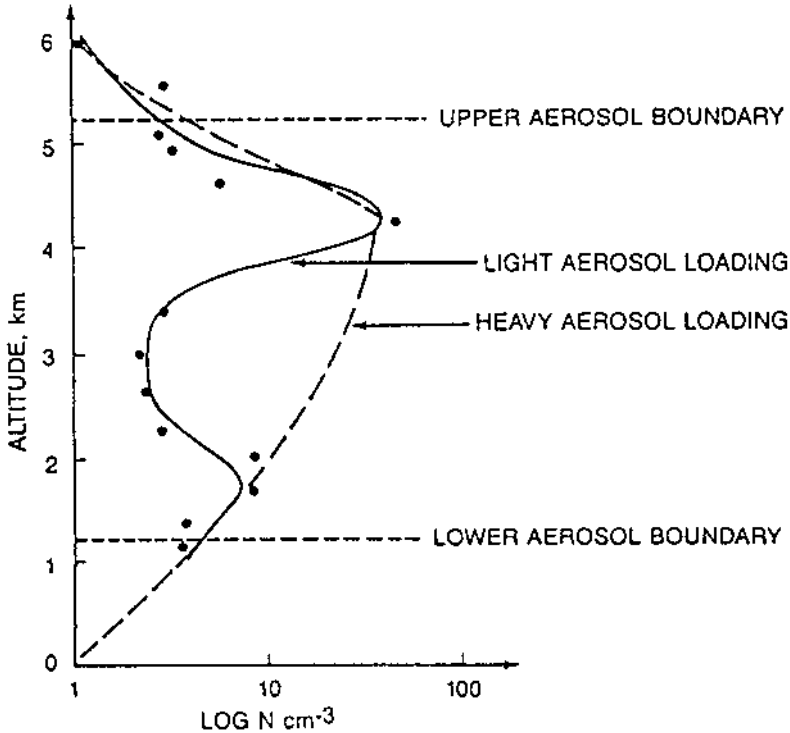

FIGURE 1 Vertical profiles of aerosol concentration measured (log $N\ \mathrm{cm}^{-3}$): (—) aerosol concentration (light loading); (– –) heavy loading aerosol concentration; (- - -) aerosol layer boundaries.

Figure 2 indicates the indices of refraction used in the MODTRAN 3.7 code [2].

Figure 3 shows the effect of particle size on the normalized extinction coefficient, a significant effect. This is also evident in Table 1, which lists the effect of particle size distribution on the extinction coefficient, single-scattering albedo, the asymmetry factor, and modal distribution. Mode 1 is a single size, and mode 3 is a log normal distribution from micrometer to submicrometer size. It is seen that for the larger particulates the wavelength variation reverses from that of the smaller, the smaller following a Rayleigh distribution.

Figure 4 indicates that the aerosol epsilon (complex index of refraction) is significantly affected by the aerosol type (maritime, urban, or continental). Note that these curves are only averages and are subject to much variation (Table 2).

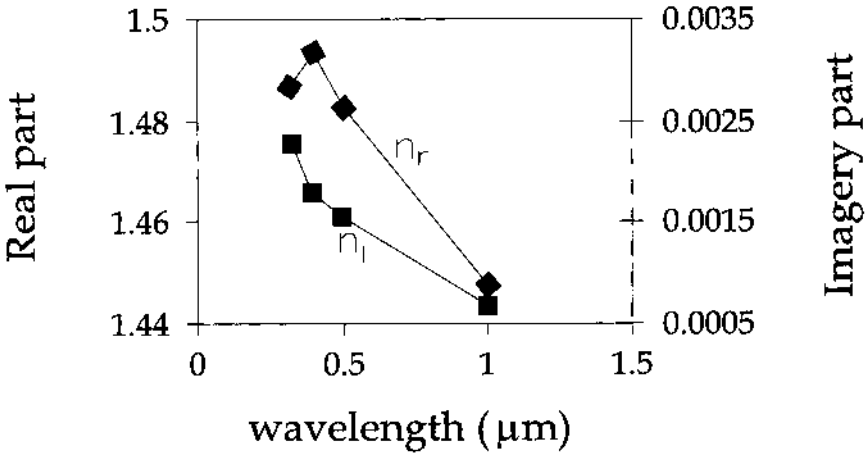

FIGURE 2 Refractive index of desert aerosol.

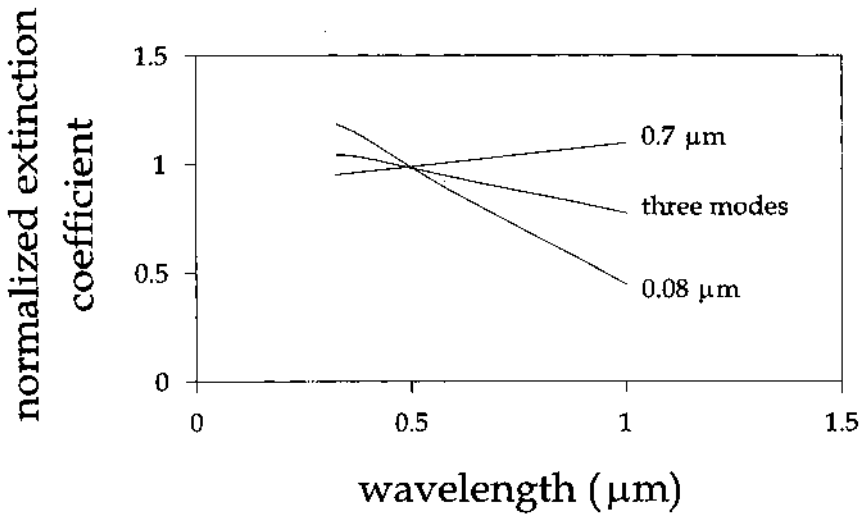

FIGURE 3 Effect of particle size on the normalized extinction coefficient.

TABLE 1 Optical Properties of Atmosphere with Desert Aerosol Loading at Wavelengths of 0.330–1.000 μm

Particle size and wavelength	Extinction coefficient	w_0	g	Mode
0.08 μm				
0.330	0.1408E−03	0.9786E+00	0.7036E+00	1
0.400	0.1331E−03	0.9853E+00	0.6959E+00	1
0.500	0.1169E−03	0.9886E+00	0.6965E+00	1
1.000	0.5121E−04	0.9953E+00	0.6672E+00	1
0.2 μm				
0.330	0.8539E−03	0.9503E+00	0.7200E+00	1
0.400	0.8797E−03	0.9671E+00	0.7058E+00	1
0.500	0.9057E−03	0.9767E+00	0.7057E+00	1
1.000	0.7909E−03	0.9943E+00	0.7229E+00	1
0.3 μm				
0.330	0.1794E−02	0.9280E+00	0.7461E+00	1
0.400	0.1844E−02	0.9516E+00	0.7254E+00	1
0.500	0.1924E−02	0.9653E+00	0.7160E+00	1
1.000	0.2007E−02	0.9923E+00	0.7261E+00	1
0.4 μm				
0.330	0.3067E−02	0.9085E+00	0.7696E+00	1
0.400	0.3133E−02	0.9374E+00	0.7466E+00	1
0.500	0.3251E−02	0.9543E+00	0.7318E+00	1
1.000	0.3597E−02	0.9899E+00	0.7265E+00	1
0.7 μm				
0.330	0.8914E−02	0.8606E+00	0.8141E+00	1
0.400	0.9022E−02	0.9011E+00	0.7914E+00	1
0.500	0.9223E−02	0.9258E+00	0.7744E+00	1
1.000	0.1019E−01	0.9819E+00	0.7383E+00	1
Three modes				
0.330	0.6848E−03	0.8958E+00	0.7826E+00	3
0.400	0.6861E−03	0.9267E+00	0.7662E+00	3
0.500	0.6855E−03	0.9440E+00	0.7542E+00	3
1.000	0.6902E−03	0.9854E+00	0.7246E+00	3

Source: Ref. 2.
w_0 = single scattering albedo
g = assymetry factor

IV. RESULTS

The results of the modeling and comparisons to the measurements of Kondratyev et al. [1] are presented in Tables 3 –7 and Figs. 4–6.

Table 3 lists the results of the application of the Dave polarized radiative transfer program for wavelengths of 0.330, 0.400, 0.500, and 1.0 μm for aerosols 1 and 5 for both light and heavy aerosol loading. Also listed are the Kondratyev photometric optical depth observations for two examples of clear and dusty atmosphere. As a comparison, Rayleigh scattering optical depths are indicated. It is seen that there are large discrepancies in the optical depths in both clear and dusty aerosol conditions (Table 4).

However, the MODTRAN 3.7 polarization results show precise agreement in optical depths. Table 5 lists the predicted polarizations, which have not been verified. Table 6 presents a more detailed listing of the optical properties of the desert atmosphere with heavy aerosol loading. Also shown are the results for four wavelengths of the optical depths of the single scattering albedo (w), the asymmetry factor (g), and the percent polarization for aerosol mode 3 (the log normal distribution).

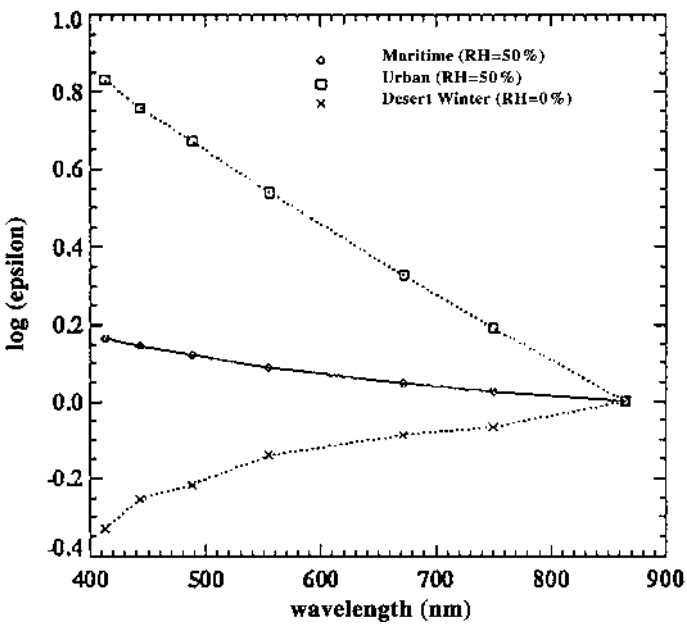

FIGURE 4 Epsilon values for maritime, clean continental, and desert aerosols.

TABLE 2 Complex Indices of Refraction for the Sahara Sands

Sahara sand sample	Wavelength (μm)	n_r	n_i
1	0.33	1.487	0.228E−2
5	0.33	1.258	0.106E−2
1	0.400	1.494	0.177E−2
5	0.400	1.267	0.656E−3
1	0.500	1.484	0.156E−2
5	0.500	1.269	0.378E−3
1	1.0	1.448	0.682E−3
5	1.0	1.231	0.210E−3

Source: Ref. 2.

In Table 7 are presented the results of both the Dave model and the original Liu MODTRAN polarimetric model. A blue/red optical depth ratio is presented to show that the dust aerosol produces a reddening of the sea surface.

In Fig. 5a, it is shown that the degree of polarization increases with increases in viewing angle, and in Fig. 5b that it decreases with optical depth increase.

A polar plot of degree of polarization at 0.550 μm, optical depth 0.4, and incident solar angle of 41° is shown in Fig. 6, where the dotted lines des-

TABLE 3 Total Aerosol and Rayleigh Optical Depths

	Dave program [3]			Kondratyev [1]				
				Kara Kum Desert		Atlantic Ocean		
Wavelength (μm)	Sahara sand aerosol	Dusty desert Light	Dusty desert Heavy	9/19 Clear	9/10 Dusty	7/20 Clear	6/24 Dusty	Rayleigh
0.33	1	0.211	0.599	0.184	0.345	0.198	0.421	0.5634
	5	0.222	0.630					
0.400	1	0.217	0.615					0.3825
	5	0.234	0.664					
0.500	1	0.227	0.643					0.1508
	5	0.241	0.684					
1.0	1	0.439	0.903	0.078	0.254	0.097	0.322	0.00724
	5	0.393	0.809					

Source: Refs. 1 and 3.

TABLE 4 Optical Thickness for the Heavy- and Light-Loaded Desert Aerosol over the Atlantic

Wavelength (μm)	Heavy-loaded desert aerosol		Light-loaded desert aerosol	
	Calc.	Meas.	Calc.	Meas.
0.33	0.345	0.345	0.184	0.184
0.40	0.339		0.176	
0.50	0.325		0.158	
1.00	0.253	0.254	0.077	0.078

Source: Ref. 1.

ignate viewing angles and the solid lines are the computed degree of polarization intersecting the dotted lines at different azimuths. The calculations are in general agreement with polarization observations made with a helicopter-mounted polarimeter off Andros Island in the Bahamas.

V. DISCUSSION

The results presented indicate that desert aerosols cause the sea to appear reddened by the Sahara sands. However, the optical properties of the sea are highly variable, depending upon time, location, and biological activity. As an example, in Fig. 7 is shown an optical transect in St. Thomas Harbor in the U.S. Virgin Islands, with measurements presented in Figs. 8 and 9. The variation of chlorophyll and turbidity is shown in Fig. 9 and detailed optical absorption and scattering are shown in Fig. 8. At the time of observation, raw sewage was being discharged into the harbor. This has since changed because of the construction of sewage treatment plants. It is to be noted that there is no specific value of absorption or scattering coefficient associated with the observation; every case must be characterized individually.

TABLE 5 Polarization for the Heavy- and Light-Loaded Desert Aerosol

Wavelength (μm)	Heavy-loaded	Light-loaded
0.33	6.90	8.24
0.40	6.48	7.12
0.50	6.44	7.42
1.00	3.43	5.06

Source: Ref. 5.

TABLE 6 Optical Properties of Atmosphere with Heavy Desert Aerosol Loading

Wavelength (μm)	Opt. depth	w	g	Mode	Polarization
0.33	0.345	0.843	0.778	3	7.34%
0.40	0.339	0.874	0.770	3	7.25%
0.50	0.325	0.894	0.771	3	7.4%
1.0	0.253	0.958	0.771	3	4.39%

Source: Ref. 4.

VI. CONCLUSION

It has been shown that MODTRAN 3.7, adapted to include polarization, can be used to characterize the atmospheric effects of an apparent reddening caused by Sahara dust aerosols. The effect is a decrease in percent polarization of about 1% between light and heavy aerosol loading. The degree of polarization increases with viewing angle but decreases with optical depth.

Polarimeters have a resolution of 0.1% and thus are capable of measuring ocean color.

TABLE 7 Percent Polarization Comparison of MODTRAN 3.7 with Dave Vector Model for Desert Aerosols

Wavelength (μm)	Normal	Light	Optical depth	Heavy	Optical depth
Dave model[a] [5]					
0.33	8.87%	8.57%	0.211	7.95%	0.599
0.400	8.85%	8.26%	0.217	7.28%	0.615
0.500	8.26%	7.51%	0.227	5.85%	0.643
1.0	7.66%	6.28%	0.439	4.06%	0.903
AFGL desert model [4]					
0.33		11.8%	0.22	10.9%	0.63
0.400		10.6%	0.22	9.8%	0.63
0.500		8.8%	0.22	6.5%	0.63
0.550				7.33%	0.4
0.8		6.99%	0.22	4.8%	0.63
BLUE/RED Dave	1.16%	1.36%		1.97%	
AFGL		1.69%		2.27%	

Solar zenith angle =0°; viewing angle =30°; surface albedo =0 (ocean); and altitude =44.7 km.
[a] Aerosol Type 1 Sahara loading (Kondratyev).

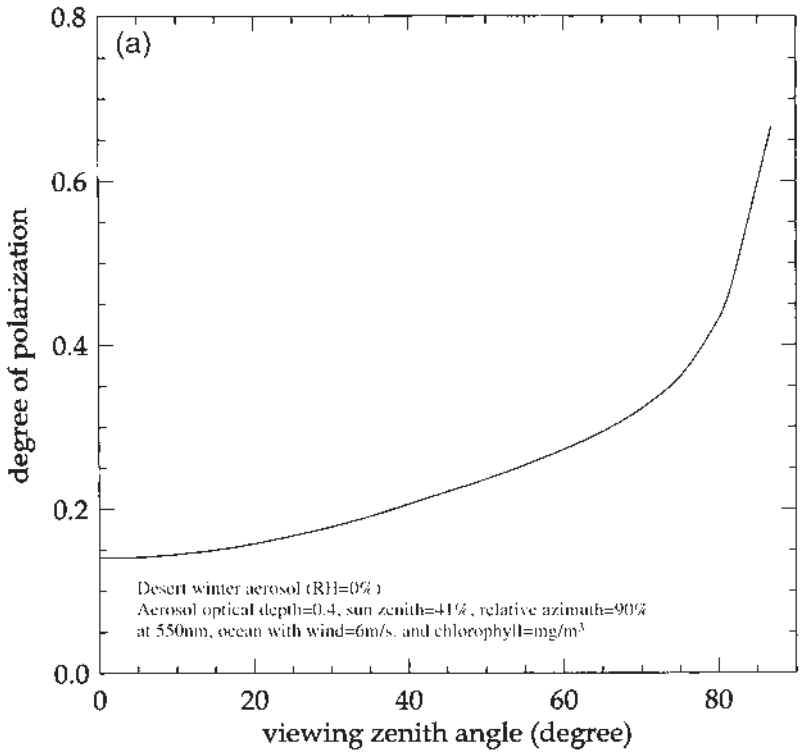

FIGURE 5 (a) Variation of the degree of polarization to the viewing zenith angle. (b) Variation of the degree of polarization to the desert aerosol optical depth.

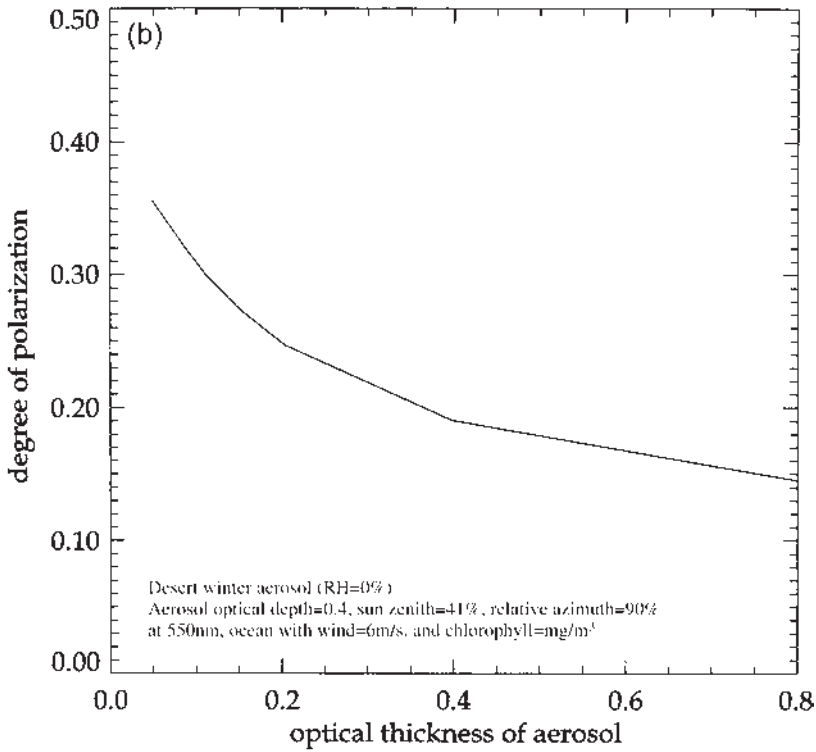

FIGURE 5 Continued.

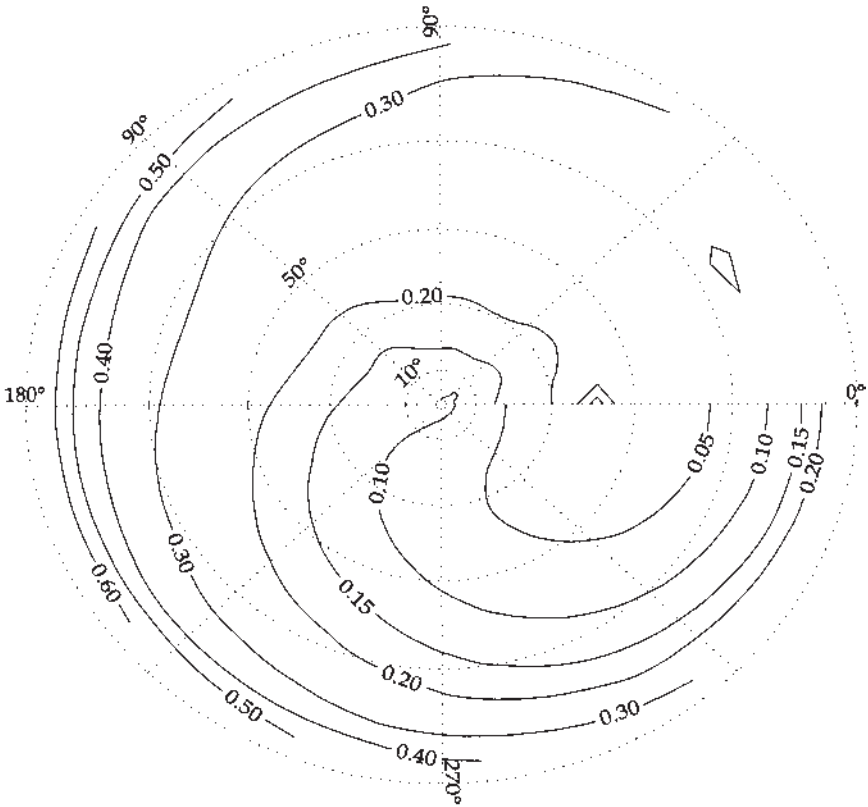

FIGURE 6 Sun zenith angle of 41 degree. Degree of polarization for λ = 550 nm, opt = 0.4, and $\theta_{sun} = 41^{\circ}$.

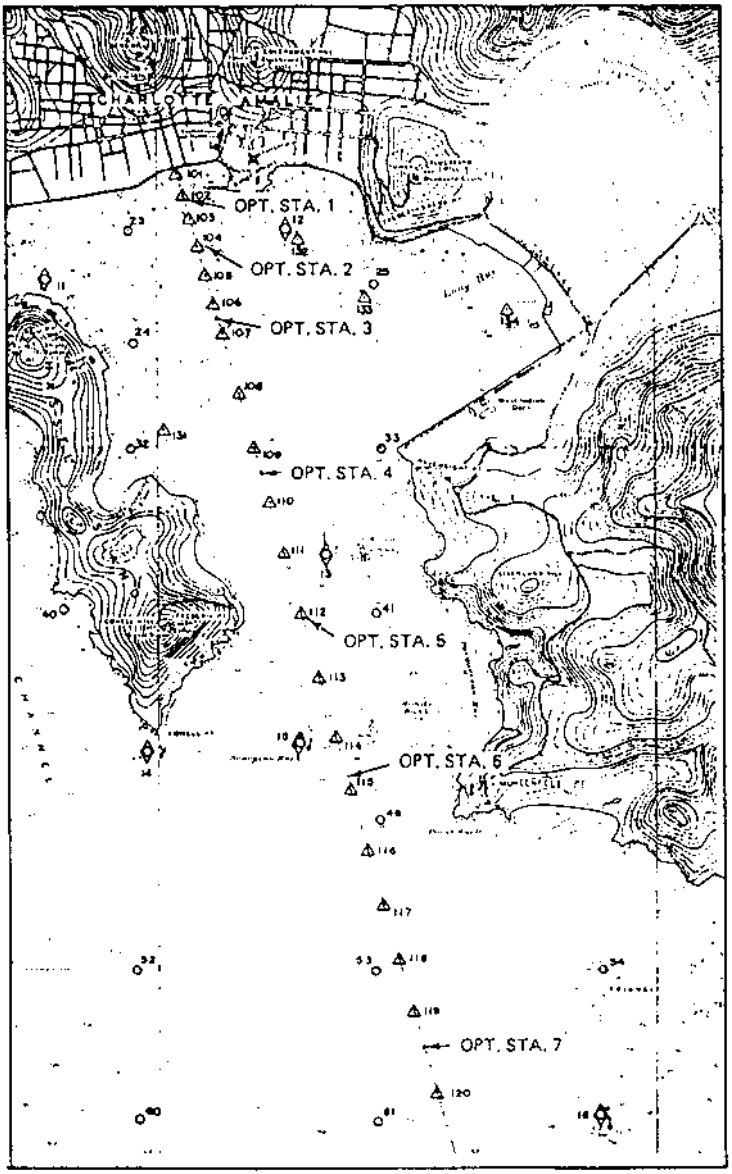

FIGURE 7 Optical study area in the St. Thomas Harbor. The optical stations lie along the biological transect between stations 102 and 120.

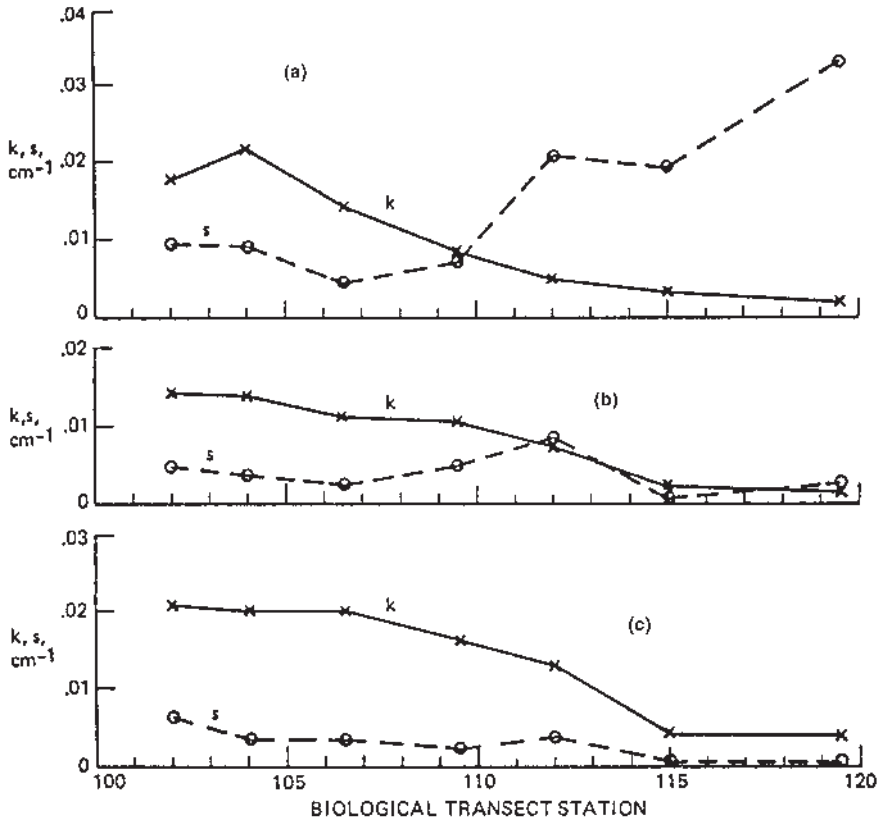

FIGURE 8 Scattering and absorption properties of seawater along optical transect in St. Thomas Harbor on October 17, 1972. (a) Blue, $\lambda = 0.433\ \mu m$; (b) green, $\lambda = 0.533\ \mu m$; (c) red, $\lambda = 0.633\ \mu m$.

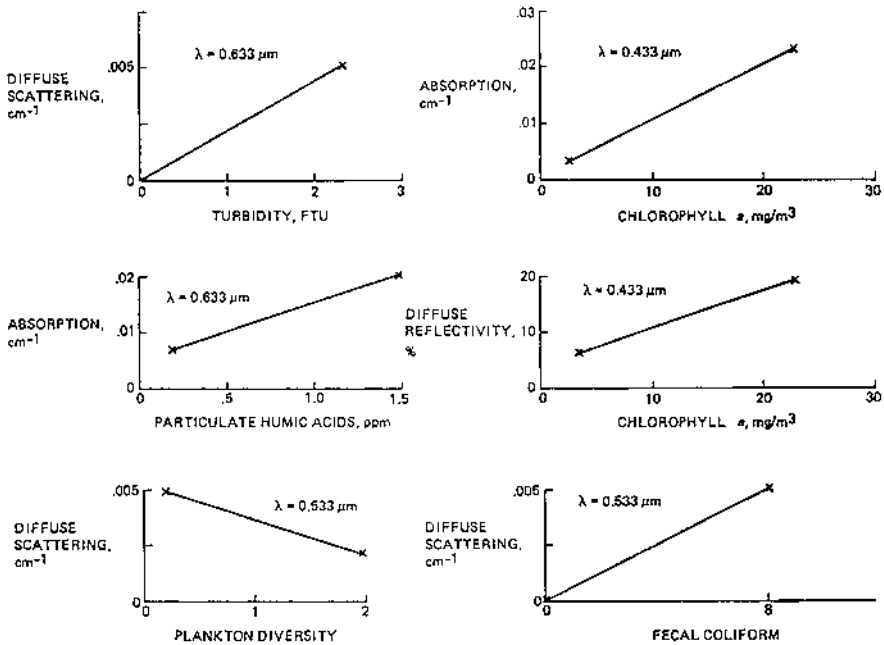

FIGURE 9 Seawater properties amenable to optical remote sensing (St. Thomas Harbor test site).

REFERENCES

1. Kondratyev, K.Ya.; Barteneva, O.D.; Chajsursky, L.I.; Chernenko, A.P.; Grishechkin, V.S.; Ivlev, L.S.; Ivanov, V.A.; Korzov, V.I.; Lipatov, V.B.; Prokofyev, M.A.; Tolkatchev, V.K.; Vasiliev, O.B.; Zhvalev, V.F. Aerosols in the GATE Area and Its Radiative Properties. NOAA Rep. No. NOAA-77020207, NTIS Rep. No. PB 265264, 1976.
2. Egan, W.G. *Photometry and Polarization in Remote Sensing*; Elsevier: New York, 1985.
3. Egan W.G.; Hilgeman, T. *Optical Properties of Inhomogeneous Materials*; Academic Press: New York, 1979.
4. Egan, W.G.; Liu, Q. Polarized MODTRAN 3.7 applied to analyze desert aerosol radiative transfer. Presented at 23rd Annual Review Conference on Atmospheric Transmission Models, Radiation Laboratory, Hanscom AFB, MA, June 2000.
5. Egan, W.G. Radiative transfer properties of the Sahara region. Remote Sensing of Environ. 1994, *50*, 182–193.
6. Egan, W.G.; Selby, J.E.A. Extension of LOWTRAN/MODTRAN codes to polarization. Presented at 22nd Annual Review Conference on Atmospheric Transmission Models, Base Theater, Hanscom AFB, MA, 7–10 June 1999.